MARTIN MARIETTA ENERGY SYSTEMS LIBRARIES

3 4456 0376526 3

ORNL/TM-12363

ornl

OAK RIDGE NATIONAL LABORATORY

MARTIN MARIETTA

Ceramic Technology Project Semiannual Progress Report for April 1992 Through September 1992

Prepared for
U.S. Department of Energy
Assistant Secretary for
Energy Efficiency and Renewable Energy
Office of Transportation Technologies
Materials Development Program

CERAMIC TECHNOLOGY PROJECT

CERAMIC TECHNOLOGY PROJECT • DOE/ORNL •

OAK RIDGE NATIONAL LABORATORY
CENTRAL RESEARCH LIBRARY
CIRCULATION SECTION
4500N ROOM 175
LIBRARY LOAN COPY
DO NOT TRANSFER TO ANOTHER PERSON
If you wish someone else to see this report, send in name with report and the library will arrange a loan.

MANAGED BY
MARTIN MARIETTA ENERGY SYSTEMS, INC.
FOR THE UNITED STATES
DEPARTMENT OF ENERGY

This report has been reproduced directly from the best available copy.

Available to DOE and DOE contractors from the Office of Scientific and Technical Information, P.O. Box 62, Oak Ridge, TN 37831; prices available from (615) 576-8401, FTS 626-8401.

Available to the public from the National Technical Information Service, U.S. Department of Commerce, 5285 Port Royal Rd., Springfield, VA 22161.

This report was prepared as an account of work sponsored by an agency of the United States Government. Neither the United States Government nor any agency thereof, nor any of their employees, makes any warranty, express or implied, or assumes any legal liability or responsibility for the accuracy, completeness, or usefulness of any information, apparatus, product, or process disclosed, or represents that its use would not infringe privately owned rights. Reference herein to any specific commercial product, process, or service by trade name, trademark, manufacturer, or otherwise, does not necessarily constitute or imply its endorsement, recommendation, or favoring by the United States Government or any agency thereof. The views and opinions of authors expressed herein do not necessarily state or reflect those of the United States Government or any agency thereof.

ORNL/TM-12363

332
96

Metals and Ceramics Division

CERAMIC TECHNOLOGY PROJECT SEMIANNUAL PROGRESS REPORT FOR APRIL 1992 THROUGH SEPTEMBER 1992

D. R. Johnson
Project Manager

Date Published: July 1993

NOTICE: This document contains information of a preliminary nature. It is subject to revision or correction and therefore does not represent a final report.

Prepared for
U.S. Department of Energy
Assistant Secretary for Energy Efficiency and Renewable Energy
Office of Transportation Technologies
Materials Development Program
EE 51 01 00 0

Prepared by the
OAK RIDGE NATIONAL LABORATORY
Oak Ridge, Tennessee 37831-6285
managed by
MARTIN MARIETTA ENERGY SYSTEMS, INC.
for the
U.S. DEPARTMENT OF ENERGY
under Contract DE-AC05-84OR21400

MARTIN MARIETTA ENERGY SYSTEMS LIBRARIES

3 4456 0376526 3

REPORTS PREVIOUSLY ISSUED

ORNL/TM-9325	Period March 1983-September 1983
ORNL/TM-9466	Period October 1983-March 1984
ORNL/TM-9497	Period April 1984-September 1984
ORNL/TM-9673	Period October 1984-March 1985
ORNL/TM-9947	Period April 1985-September 1985
ORNL/TM-10079	Period October 1985-March 1986
ORNL/TM-10308	Period April 1986-September 1986
ORNL/TM-10469	Period October 1986-March 1987
ORNL/TM-10705	Period April 1987-September 1987
ORNL/TM-10838	Period October 1987-March 1988
ORNL/TM-11116	Period April 1988-September 1988
ORNL/TM-11239	Period October 1988-March 1989
ORNL/TM-11489	Period April 1989-September 1989
ORNL/TM-11586	Period October 1989-March 1990
ORNL/TM-11719	Period April 1990-September 1990
ORNL/TM-11859	Period October 1990-March 1991
ORNL/TM-11984	Period April 1991-September 1991
ORNL/TM-12133	Period October 1991-March 1992

Research sponsored by the U.S. Department of Energy, Assistant Secretary for Energy Efficiency and Renewable Energy, Office of Transportation Technologies, as part of the Ceramic Technology Project of the Materials Development Program, under contract DE-AC05-84OR21400 with Martin Marietta Energy Systems, Inc.

CONTENTS

SUMMARY 1

0.0 PROJECT MANAGEMENT AND COORDINATION 3

1.0 MATERIALS AND PROCESSING 5

INTRODUCTION 5

1.1 MONOLITHICS 7

1.1.1 Silicon Carbide 7

High Temperature Hexoloy SX Silicon Carbide (Carborundum) 7

1.1.2 Silicon Nitride 16

Characterization of Attrition Milled Silicon Nitride Powder (NIST) 16

Microwave Sintering of Silicon Nitride (ORNL) . . . 21

Cost Effective Sintering of Silicon Nitride Ceramics (SIU-C) 35

1.1.4 Processing of Monolithics 43

Improved Processing (Norton) 43

Improved Processing (ORNL) 56

Rheology and Particle Packing of Chem- and Phys-Adsorbed, Alkylated Silicon Nitride Powders (University of California) 64

1.2 CERAMIC COMPOSITES 87

1.2.2 Silicon Nitride Matrix 87

Characterization of Grain Boundary Phases in Silicon Nitride Ceramics (University of Michigan) 87

Optimization of Mechanical Properties of Silicon Nitride Ceramics (University of Michigan) 92

In-Situ Reinforced Silicon Nitride (GCCD) 93

1.2.3 Oxide Matrix 98

Dispersion-Toughened Ceramic Composite (ORNL) . . . 98

1.2.4 Silicate Matrix 115

Low Expansion Ceramics for Diesel Engine Applications (VPI) 115

1.3 THERMAL AND WEAR COATINGS 137

Fabrication and Testing of Corrosion-Resistant Coatings (ORNL) 137

Development of Adherent Coatings to Reduce Contact Stress Damage of Ceramics (Boston University) . . . 138

Wear-Resistant Coatings (Caterpillar) 149

Thick Thermal Barrier Coating (TTBC) Systems for Low Heat Rejection Diesel Engines (Caterpillar) 154

1.4 JOINING 168

1.4.1 Ceramic-Metal Joints 168

Joining of Ceramics for Heat Engine Applications (ORNL) 168

1.4.2 Ceramic-Ceramic Joints 172

Analytical and Experimental Evaluation of Joining Silicon Carbide to Silicon Carbide and Silicon Nitride to Silicon Nitride for Advanced Heat Engine Applications Phase II (Norton) 172

2.0 MATERIALS DESIGN METHODOLOGY 193

INTRODUCTION 193

2.2 CONTACT INTERFACES 195

2.2.1 Static Interfaces 195

Elastic Properties and Adherence of Thin Films and Coatings (University of Tennessee) 195

2.2.2 Dynamic Interfaces 197

Development of Standard Test Methods for Evaluating the Wear Performance of Ceramics (ORNL) 197

2.3 NEW CONCEPTS 200

Advanced Statistical Concepts of Fracture in Brittle Materials (GE) 200

3.0 DATA BASE AND LIFE PREDICTION 203

INTRODUCTION 203

3.1 STRUCTURAL QUALIFICATION 205

Microstructural Analysis of Structural Ceramics (NIST) 205

Mechanical Properties and Microstructural Characterization of Si_3N_4 Ceramics (ORNL) 211

Project Data Base (ORNL) 218

3.2 TIME-DEPENDENT BEHAVIOR 223

Fracture Behavior of Toughened Ceramics (ORNL) . . 223

Cyclic Fatigue of Toughened Ceramics (ORNL) 229

Rotor Data Base Generation (ORNL) 242

Toughened Ceramics Life Prediction (NASA Lewis Research Center) 254

Life Prediction Methodology (Allison) 269

Life Prediction Methodology (GAPD) 279

3.3 ENVIRONMENTAL EFFECTS 305

Environmental Effects in Toughened Ceramics (University of Dayton) 305

3.4 FRACTURE MECHANICS 332

Testing and Evaluation of Advanced Ceramics at High Temperature in Uniaxial Tension (North Carolina A&T State University) 332

Standard Tensile Test Development (NIST) 340

Development of a Fracture Toughness Microprobe (Rice) 353

3.5 NONDESTRUCTIVE EVALUATION DEVELOPMENT 356

Nondestructive Characterization (ORNL) 356

NDE Standards for Advanced Ceramics (ORNL) 370

X-ray Computed Tomographic Imaging (ANL) 371

Nuclear Magnetic Resonance Imaging (ANL) 379

4.0 TECHNOLOGY TRANSFER 385

4.1 TECHNOLOGY TRANSFER 385

4.1.1 Technology Transfer 385

Technology Transfer (ORNL) 385

IEA Annex II Management (ORNL) 387

Characterization of Ceramic Powders (NIST) 390

Ceramic Mechanical Property Test Method Development (NIST) 394

CERAMIC TECHNOLOGY PROJECT SEMIANNUAL PROGRESS REPORT FOR APRIL 1992 THROUGH SEPTEMBER 1992

SUMMARY

The Ceramic Technology Project was originally developed by the Department of Energy's Office of Transportation Systems (OTS) in Conservation and Renewable Energy. This project, part of the OTS's Materials Development Program, was developed to meet the ceramic technology requirements of the OTS's automotive technology programs.

Significant accomplishments in fabricating ceramic components for the Department of Energy (DOE), National Aeronautics and Space Administration (NASA), and Department of Defense (DoD) advanced heat engine programs have provided evidence that the operation of ceramic parts in high-temperature engine environments is feasible. However, these programs have also demonstrated that additional research is needed in materials and processing development, design methodology, and data base and life prediction before industry will have a sufficient technology base from which to produce reliable cost-effective ceramic engine components commercially.

An assessment of needs was completed, and a five-year project plan was developed with extensive input from private industry. In July 1990 the original plan was updated through the estimated completion of development in 1993. The objective of the project is to develop the industrial technology base required for reliable ceramics for application in advanced automotive heat engines. The project approach includes determining the mechanisms controlling reliability, improving processes for fabricating existing ceramics, developing new materials with increased reliability, and testing these materials in simulated engine environments to confirm reliability. Although this is a generic materials project, the focus is on the structural ceramics for advanced gas turbine and diesel engines, ceramic bearings and attachments, and ceramic coatings for thermal barrier and wear applications in these engines. This advanced materials technology is being developed in parallel and close coordination with the ongoing DOE and industry proof-of-concept engine development programs. To facilitate the rapid transfer of this technology to U.S. industry, the major portion of the work is being done in the ceramic industry, with technological support from government laboratories, other industrial laboratories, and universities.

This project is managed by ORNL for the Office of Transportation Technologies, Office of Transportation Materials, and is closely coordinated with complementary ceramics tasks funded by other DOE offices, NASA, DoD, and industry. A joint DOE and NASA technical plan has been established, with DOE focus on automotive applications and NASA focus on aerospace applications. A common work breakdown structure (WBS) was developed to facilitate coordination. The work described in this report is organized according to the following WBS project elements:

0.0 Project Management and Coordination

1.0 Materials and Processing

- 1.1 Monolithics
- 1.2 Ceramic Composites
- 1.3 Thermal and Wear Coatings
- 1.4 Joining

2.0 Materials Design Methodology

- 2.2 Contact Interfaces
- 2.3 New Concepts

3.0 Data Base and Life Prediction

- 3.1 Structural Qualification
- 3.2 Time-Dependent Behavior
- 3.3 Environmental Effects
- 3.4 Fracture Mechanics
- 3.5 Nondestructive Evaluation Development

4.0 Technology Transfer

- 4.1 Technology Transfer

This report includes contributions from all currently active project participants. The contributions are arranged according to the work breakdown structure outline.

0.0 PROJECT MANAGEMENT AND COORDINATION

D. R. Johnson
Oak Ridge National Laboratory

Objective/scope

This task includes the technical management of the project in accordance with the project plans and management plan approved by the Department of Energy (DOE) Oak Ridge Operations Office, and the Office of Transportation Technologies. This task includes preparation of annual field work proposals, initiation and management of subcontracts and interagency agreements, and management of ORNL technical tasks. Monthly management reports and bimonthly reports are provided to DOE; highlights and semiannual technical reports are provided to DOE and program participants. In addition, the program is coordinated with interfacing programs sponsored by other DOE offices and federal agencies, including the National Aeronautics and Space Administration (NASA) and the Department of Defense (DoD). This coordination is accomplished by participation in DOE and NASA joint management meetings, annual interagency heat engine ceramics coordination meetings, DOE contractor coordination meetings, and DOE Energy Materials Coordinating Committee (EMaCC) meetings, as well as special coordination meetings.

1.0 MATERIALS AND PROCESSING

INTRODUCTION

This portion of the project is identified as project element 1.0 within the work breakdown structure (WBS). It contains four subelements: (1) Monolithics, (2) Ceramic Composites, (3) Thermal and Wear Coatings, and (4) Joining. Ceramic research conducted within the Monolithics subelement currently includes work activities on low cost Si_3N_4 powder, green state ceramic fabrication, characterization, and densification, and on structural, mechanical, and physical properties of these ceramics. Research conducted within the Ceramic Composites subelement currently includes silicon carbide, silicon nitride, and oxide-based composites. Research conducted in the Thermal and Wear Coatings subelement is currently limited to oxide-base coatings and involves coating synthesis, characterization, and determination of the mechanical and physical properties of the coatings. Research conducted in the Joining subelement currently includes studies of processes to produce strong, stable joints between zirconia ceramics and iron-base alloys. As part of an expanded effort to reduce the cost of ceramic components, a new initiative in cost effective machining has been started.

A major objective of the research in the Materials and Processing project element is to systematically advance the understanding of the relationships between ceramic raw materials such as powders and reactant gases, the processing variables involved in producing the ceramic materials, and the resultant microstructures and physical and mechanical properties of the ceramic materials. Success in meeting this objective will provide U.S. companies with new or improved ways for producing economical, highly reliable ceramic components for advanced heat engines.

1.1 MONOLITHICS

1.1.1 Silicon Carbide

High Temperature Hexoloy SX Silicon Carbide

S. K. Lau and G. V. Srinivasan

- **Introduction:**

Hexoloy SX has been demonstrated to possess higher toughness and strength than Hexoloy SA®*.[1] Its toughness is about 50% to 100% higher than that of SA and its typical room temperature MOR value ranges between 620-915 MPa (90-133 ksi). Moreover, these are only preliminary data, it is believed that the mechanical properties can be further improved via proper optimization of composition, powder selection and processing conditions.

- **Scope and Objective:**

The approach taken for this work is to first establish a complete mechanical property database and conduct detailed microstructural characterization on the first generation SX material currently available. After that, the emphasis will then be focused on the selection of a best SiC powder source and the optimization of processing conditions for this first generation material via a systematic designed experimental method. In parallel, a Carborundum in-house sponsored program with the objective of identifying a second generation additive composition with improved high temperature properties will also be conducted. Once this second generation composition is identified, the information will be fed into the current program. Then further experiments will be conducted to optimize the properties of this second generation SX material. Finally, the complete property database will then be established for the second generation composition.

The three major objectives for the current program are as follows: (1) to establish property database and conduct detailed characterization for the current best SX material, (2) to improve the processing conditions of that material via a designed experimental method, and (3) to develop a second generation SX material with improved properties.

- **Task 1 Objective:** Complete Characterization of Generation I SX-SiC Material.

Completed, details reported in last semi-annual report.

- **Task 2 Objective:** SiC Powder Selection.

Completed, details reported in last semi-annual report.

- **Task 5 Objective:** Development of an Improved Dispersion Process.

Completed, details reported in last semi-annual report.

- **Task 3 Objective:** Property Optimization for Generation I SX-SiC

The objective of Task 3 was to optimize Hexoloy SX-G1 properties through a designed experiment approach by varying the three most influential processing parameters, namely, the sintering temperature, the post-treatment temperature and the post-treatment pressure. The upper and lower limits for each of these factors are listed below:

---

* Hexoloy SA, registered trade mark of Carborundum Company

Sinter Temperature:	ST_1 and ST_2
Post-Treat Temperature:	PT_1 and PT_2
Post-Treat Pressure:	P_1 and P_2

A main factor plus interaction model was used to design this series of experiments. The upper and lower limits of these three factors form a design experiment cube. Totally, there were 10 sets of experimental conditions, with 8 at the corners of the cube and 2 experiments at the center of the cube (Fig. 1).

The responses used to monitor these experiments included room temperature MOR and toughness, MOR and toughness at 1232°C, and dynamic fatigue at 1232°C.

To prepare the test samples, the powder processing technique first chosen was turbomilling because this process had demonstrated the potential of achieving very high mechanical properties as reported in Task 5. However, processing reproducibility remained a major issue. The most difficult part of this process was to overcome the chipping of the grinding media which resulted in significantly lower density and strength. Alternate approaches to overcome the chipping problem were evaluated, including the use of sintered SX media and milling with no or lower amounts of grinding media. However, these initial attempts were unsuccessful. It was determined that more effort was required to overcome this problem. Carborundum, therefore, recommended the use of the traditional milling process used in Task 1 to complete the remaining Task 3 work while an internal Carborundum program was carried out to define acceptable turbomilling conditions.

With the concurrence of the ORNL technical monitor. A new SX-G1 mix was then prepared. All the 10 experiments were successfully conducted. The final densities obtained were between 97.7% to 100.0% T.D. with 6 out of 10 conditions showing densities over 99.3% T.D.

The appropriate mechanical testing and microstructural characterization were then conducted according to the contract specifications.

The responses as a function of densification conditions are shown in Table 1. The densification conditions are normalized, i.e., -1 for the lower limit and +1 for the upper limit of the conditions. There is no significant change in K_{1c} for various densification conditions, while a significant change in RT MOR is evident as a function of densification conditions.

A maximum average MOR at room temperature of 140 ksi was obtained for the processing conditions of lower sintering temperature, higher post-treatment temperature and pressure. This strength is 24% higher than that of the previous Task data (113 ksi). It was observed that the higher MOR at RT also resulted in a higher MOR at 1232°C. Furthermore, no slow crack growth was evident from dynamic fatigue studies at 1232°C for any of the densification conditions.

Fractographic observation confirmed that the strength limiting defects are still the silicon rich "pools". These pools are actually clusters of phases resulting from reactions of yttrium aluminates with SiC as suggested in Task 1. It appears that the severity of the reaction is lower at lower sintering temperatures and higher post-treatment pressures.

To better analyze the experimental data, contour plots were also generated. From these figures (figures 2 to 7), it can be concluded that lower sintering temperature is preferred for achieving maximum final density and strength. Higher post-treatment temperature and pressure also yield higher strength. More importantly, the analysis from the designed experiment also reveal that the optimum post-treatment conditions are in fact falling outside of the experimental cube implying that the mechanical properties can still be further improved.

Deliverables of 20 MOR bars were then fabricated using the best densification conditions from the design experiments. However, this first batch of bars yielded a lower than expected MOR (108 ksi vs. 140 ksi). This may indicate the current process is very susceptable to minor variations in processing conditions. A new batch of plates were sintered and post-treated. Satisfactory densities were obtained. The plates have been sent out for machining into MOR bars.

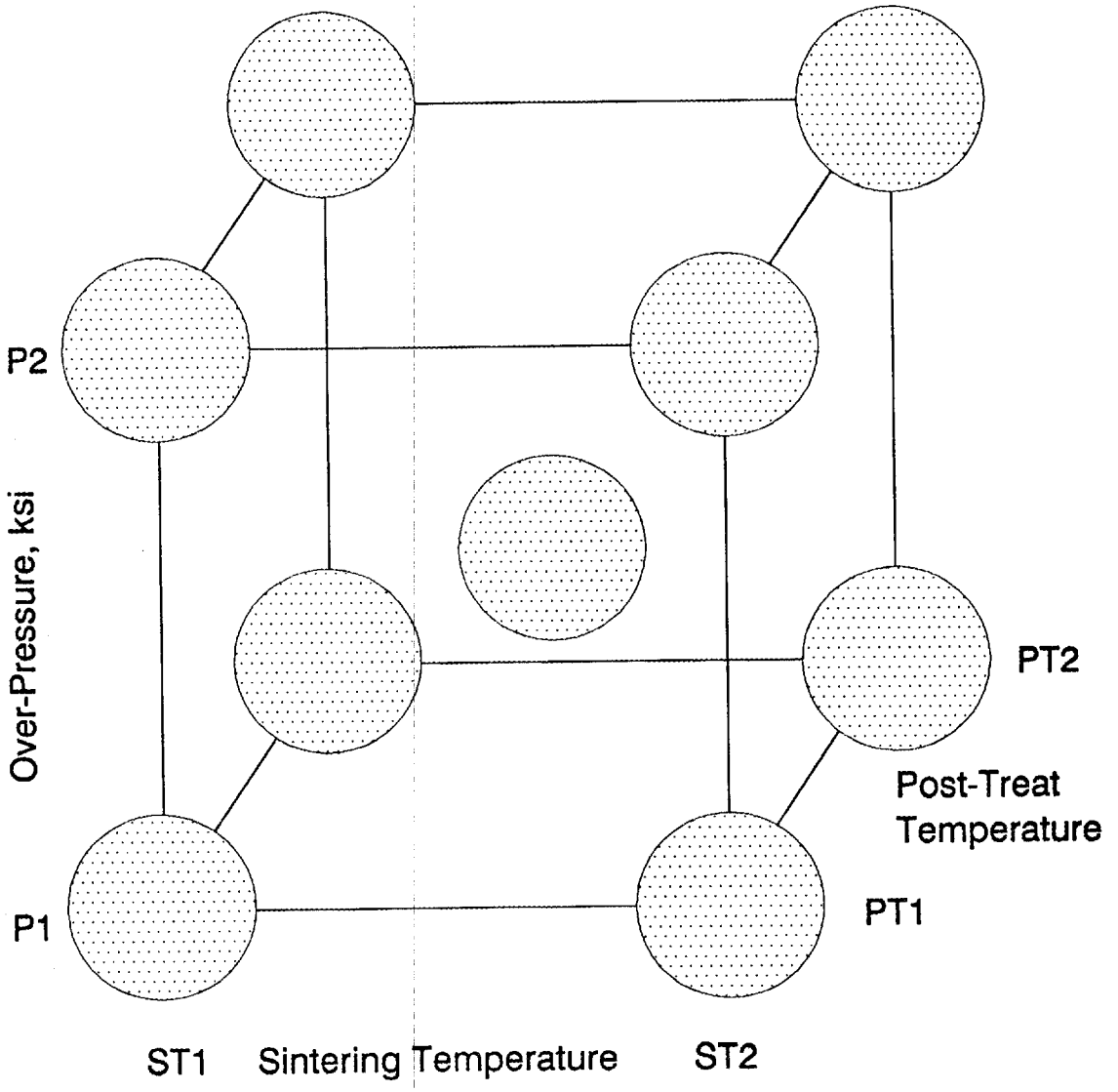

Figure 1. Experimental Design Matrix

Table 1
Task 3 - Experimental Conditions and Mechanical Property Results

				MOR, ksi		Chevron Notch Toughness MPa $m^{\frac{1}{2}}$	
Sin. Temp.	PT. Temp.	PT. Pressure	PT. Density %	RT	1232°C	RT	SCG* Parameter N
0	0	0	99.9	128	76	4.9	No SCG
+1	-1	+1	97.7	84	60	5.2	No SCG
-1	+1	-1	99.5	103	66	5.4	No SCG
+1	+1	+1	100.0	124	60	4.9	No SCG
-1	+1	+1	99.9	140	76	4.7	No SCG
0	0	0	99.9	115	72	4.9	No SCG
-1	-1	+1	99.3	105	62	4.4	No SCG
+1	-1	-1	98.0	79	54	4.6	No SCG
-1	-1	-1	97.7	80	57	4.3	No SCG
+1	+1	-1	98.2	84	58	5.5	No SCG

*Slow Crack Growth. No SCG means N is approaching infinity.

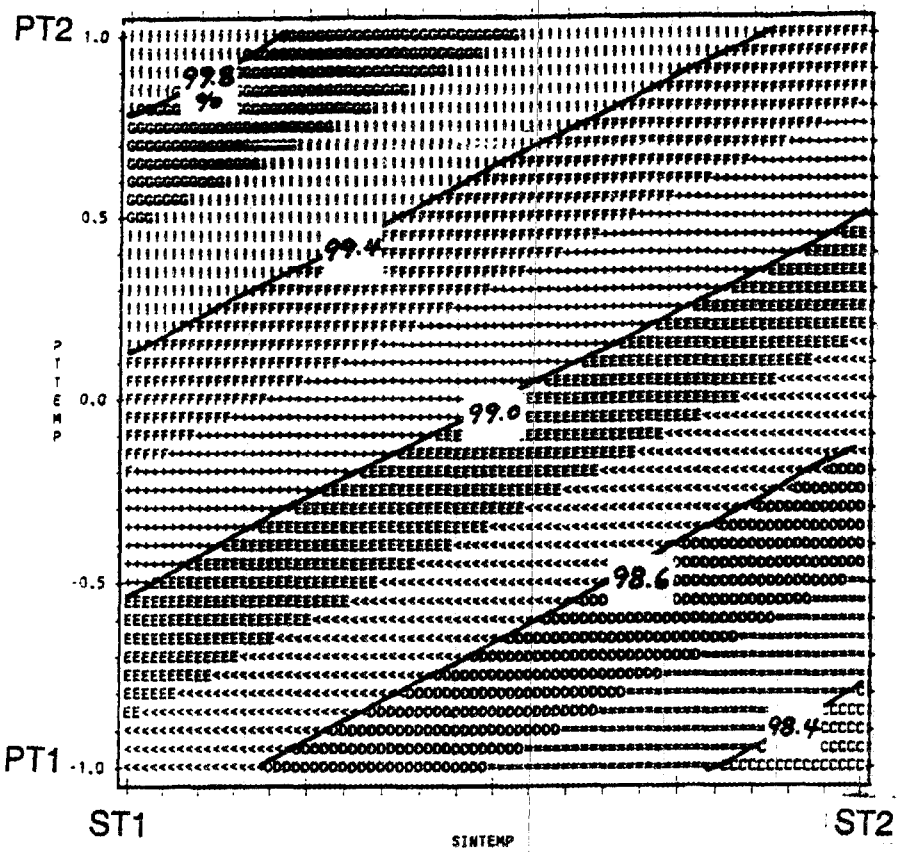

Figure 2
Final Density
vs. Sinter
Temperature and
Post-Treat
Temperature

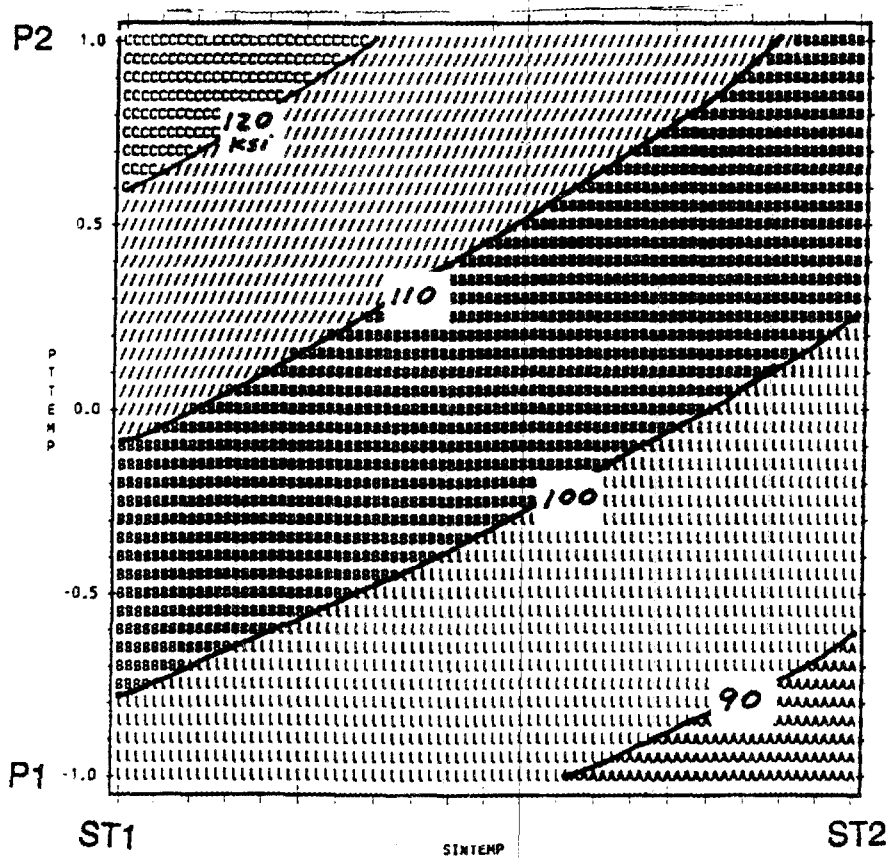

Figure 3
R.T. Strength
vs. Sinter
Temperature and
Post-Treat
Temperature

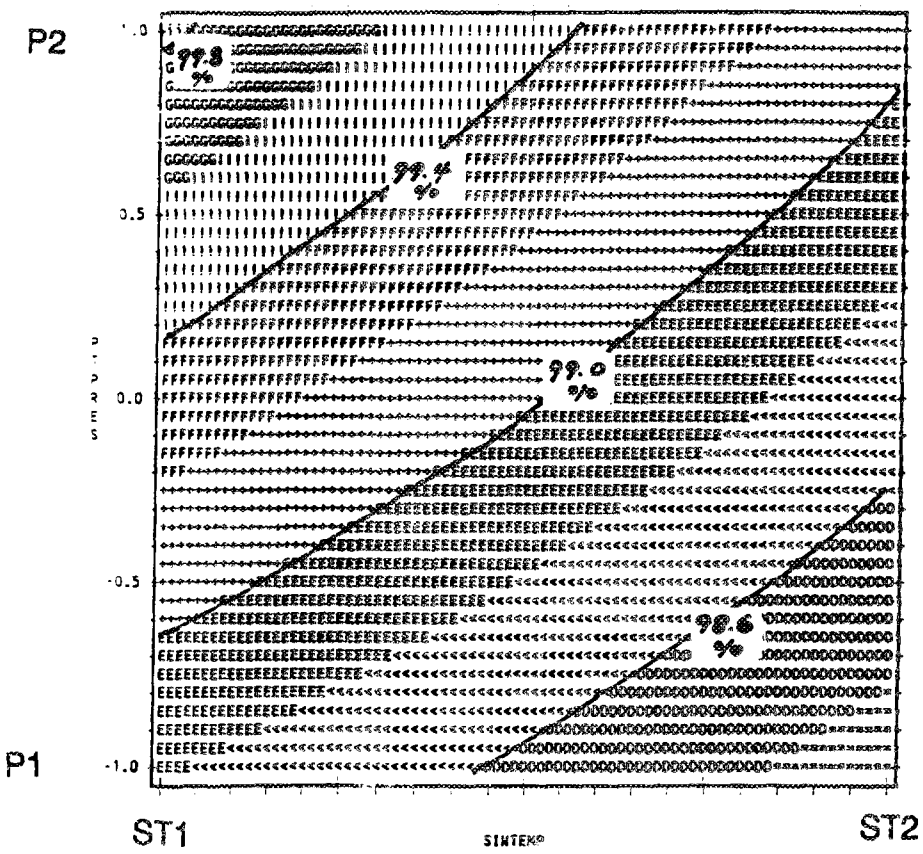

Figure 4
Final Density
vs. Sinter
Temperature and
Post-Treat
Pressure

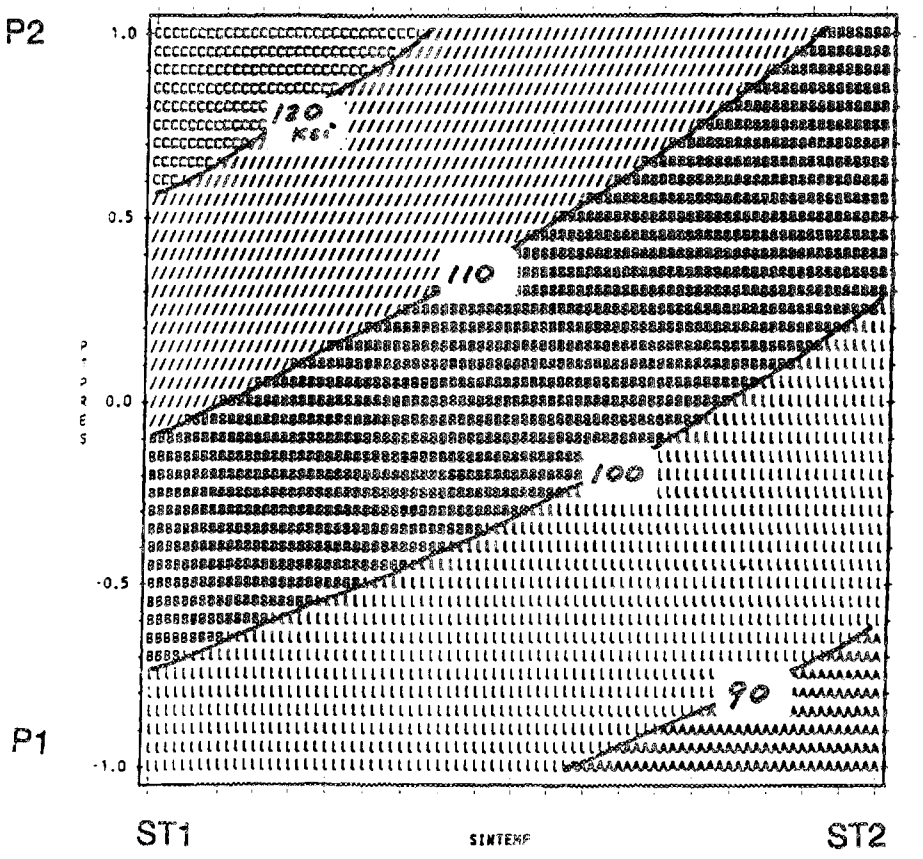

Figure 5
R.T. Strength
vs. Sinter
Temperature and
Post-Treat
Pressure

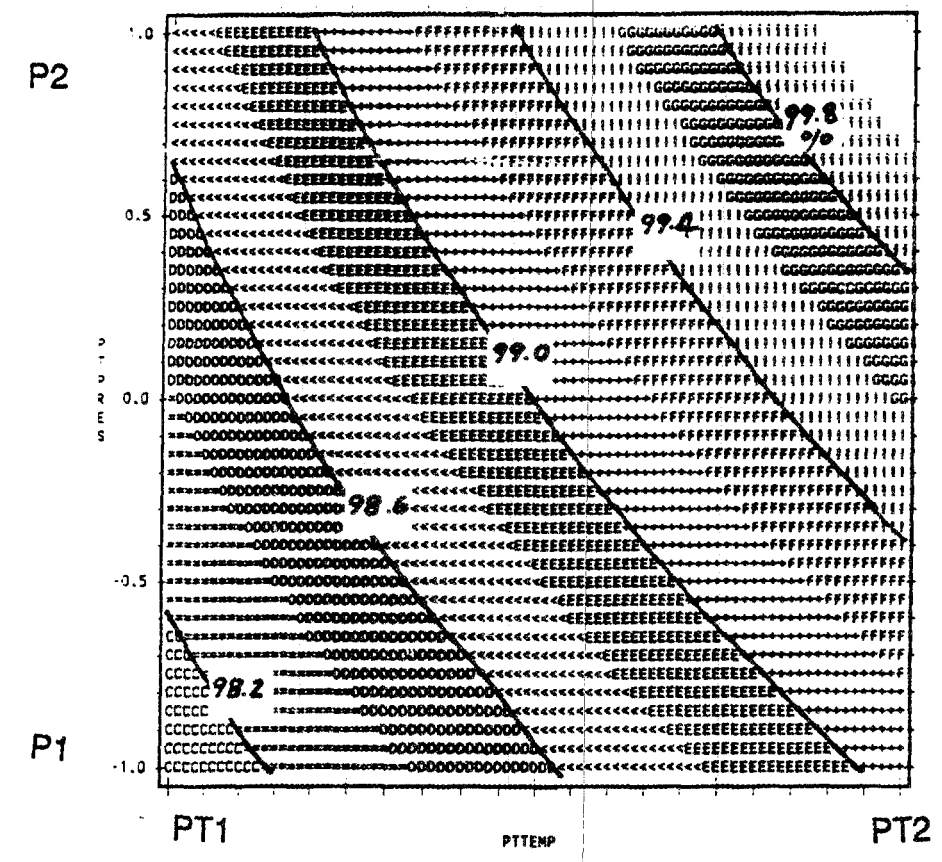

Figure 6
Final Density
vs. Post-Treat
Pressure and
Post-Treat
Temperature

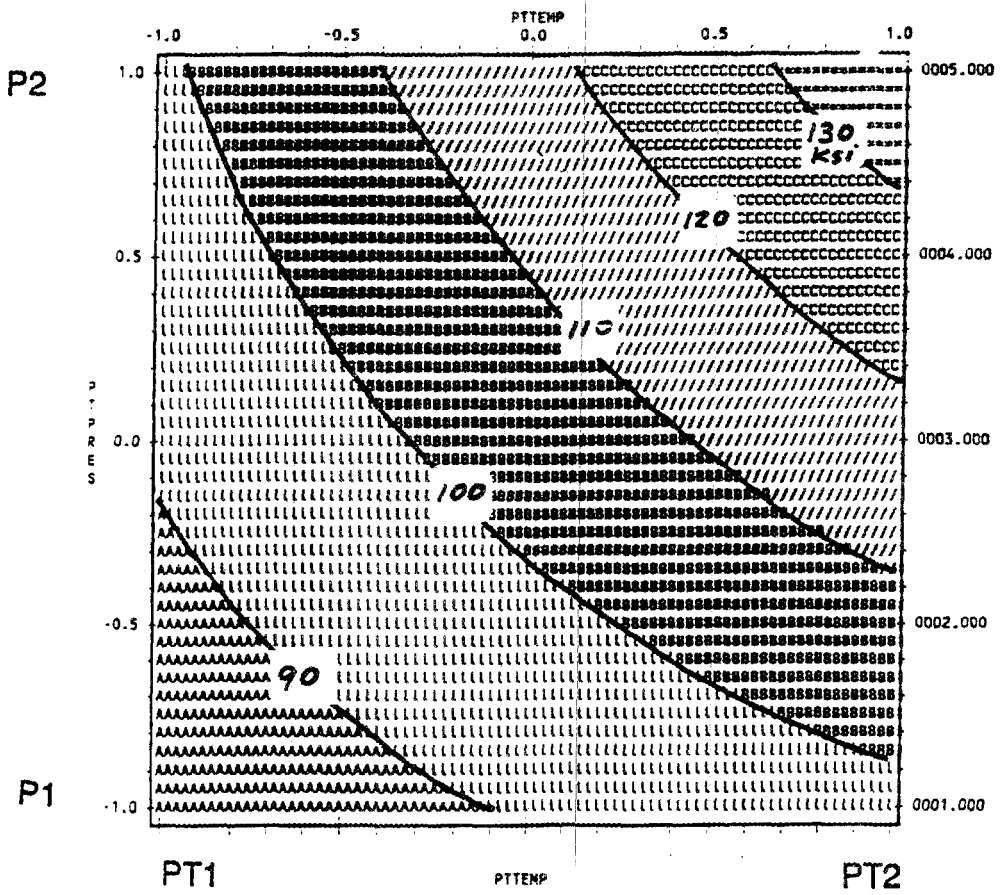

Figure 7
R.T. Strength
vs. Post-Treat
Pressure and
Post-Treat
Temperature

- **Task 4 Objective:** Continue Optimization of SX-G1

Prior to the start of Task 4, under a Carborundum in-house sponsored program, efforts to develop a second generation SX composition (SX-G2) as well as improve the processing conditions of turbomilling were conducted. Results obtained revealed that although there were several compositions identified to possess wider processing windows, the SX-G1 composition developed previously after several years of intensive work still remains the best one as far as RT and high temperature MORs are concerned. On the other hand, these internal efforts have also successfully identified approaches to improve the reproducibility of the turbomilling process which in turn can be expected to further enhance the mechanical properties.

Based on these considerations, Carborundum believed that it was not warranted at this point to conduct the full mechanical property characterization on SX-G2 as outlined in the original program plan. Instead, the technical approach proposed for Task 4 is to conduct a second series of design experiments to further improve the SX-G1 composition using the results described above and those reported under Task 3. The proposed experimental conditions are:

Powder Processing Techniques:	Improved Turbomilling Process
Sinter Temperature:	ST_3 to ST_4
Post-Treat Temperature:	PT_3 to PT_4
Post-Treat Pressure:	P_3 to P_4

The upper and lower limits for each of the furnacing parameters are selected based on the findings described earlier as well as previous Carborundum in-house research data. For example, although it has been found that lower sintering temperatures and higher post-treatment temperatures are preferred, Carborundum in-house data has shown that below T_3, SX-G1 cannot be sintered to the minimum density required to achieve >99% post-treatment density. This defines the lower temperature limit. While on the other hand, at above T_4, excessive silicon pool formation will occur, which defines the upper temperature limit. Regarding the post-treatment pressure, preliminary in-house data revealed that at or above P_4, the mechanical properties obtained are rather poor. Similar observations on Si_3N_4 furnacing indicated that too high a gas pressure could have the effect of "pumping" gaseous species into the material microstructure and retarding the sintering cycle. The upper limit for the post-treatment pressure has, therefore, been set at P_4.

It is estimated that a total of 11 experiments are needed to complete the experimental matrix. After the evaluation of the resulting mechanical data, including MOR at room temperature and 1232°C, toughness at room temperature and 1232°C, and dynamic fatigue at 1232°C, the optimum furnacing conditions will be selected. Two sets of samples will then be fabricated using these conditions. The first set of samples will be characterized for tensile strength and MOR at room temperature, 1000, 1232 and 1371°C. The slow crack growth and creep behavior of the optimized G1 material is not expected to be different from the earlier G1 material tested for Task 1. Hence experiments involving slow crack growth and creep need not be conducted again. The second set of samples will be delivered to ORNL for other detailed evaluation and characterization.

Upon the approval from ORNL for this revision to Task 4, powder processing work for Task 4 was then initiated.

After an initial series of experiments to define the optimum turbomilling processing conditions, turbomilling was carried out in several batches at Southern Illinois University to yield 40 pounds of premix. These powder batches were then further processed at Carborundum. The particle size analysis and BET surface area measurements are consistent from batch to batch. The surface area increased from about 15 sq. m/gm. to about 22 sq. m/gm after this improved milling process. The powder was then spray dried. Green plates have been pressed and baked out. The sintering and post-sintering experiments under the new design conditions are in progress.

Plan - complete the design experiments, conduct limited mechanical property evaluation to identify the optimum processing conditions. Prepare samples for full property characterization.

- **Communications/Visits/Travel:**

None.

- **Problems Encountered:**

Sensitivity to processing variables has resulted in a lower than expected strength in the test bars for the deliverables under Task 3. It is hoped that an enhanced turbomilling procedure combined with the further optimized process conditions from Task 4 will reduce this variability.

- **Publications:**

None.

1.1.2 Silicon Nitride

Characterization of Attrition Milled Silicon Nitride Powder

S. G. Malghan and D. B. Minor
(National Institute of Standards and Technology)

Objective/Scope

Currently, the starting materials in the manufacture of silicon nitride ceramic components are fine powders. These fine sized powders tend to form agglomerates due to the van der Waals attractive forces. For improved reliability in the manufacture of ceramic components, the agglomerates in the powders should be eliminated since they form defects. In addition, the powders should have an appropriate range of size distribution and specific surface area for achieving a near-theoretical density of the ceramic after densification. These factors necessitate the use of powder milling as one of the major powder processing unit operations. Therefore, milling of powders is an integral unit operation in the manufacture of silicon nitride components for advanced energy applications. The production and use of these powders require the use of efficient milling techniques and understanding of characteristics of the milled powders in a given environment. High energy attrition milling appears to offer significant advantages over conventional tumbling and vibratory mills.

The major objectives of this project are: 1. establish repeatability of particle size distribution and other relevant characteristics of slurries milled in a high energy agitation mill (HEAM); 2. determine processing and densification characteristics of powders milled in HEAM; and 3. compare properties of powder, and resulting ceramic obtained by milling in the HEAM vs. vibratory ball mill in a collaborative project with Norton Company.

Technical Progress

Measurement Errors: Experiments to evaluate repeatability of milled powder properties and comparison with vibratory milling have been initiated. These repeatability experiments have been planned in consultation with a statistician. One of the goals of this study is to estimate various errors in the characterization of milled powders. For example, in the determination of particle size distribution, errors due to measurement and sampling have to be included in the overall statement of repeatability. We investigated the measurement error in considerable detail, in the analysis of milled powders. It turned out to be a non-trivial issue since equipment limitations and aging of powder in aqueous environment were major problems. Procedure for the determination of measurement error consisted of retaining and reusing the same dispersion over and over. This is not too difficult in the use of Horiba LA-900 particle size analyzer. However, loss of a small fraction of the particles cannot be ruled out. We have minimized this error by development a of careful sample collection procedure.

Additionally, reagglomeration of particles in dilute suspension is a critical issue. Since the procedure calls for reusing the same sample over a period of one week by different operators, no changes to the sample are to be made. We found that dispersion in the original sample could not be held stable after the first day. As a result, we were unable to evaluate measurement error by this procedure. Subsequently, we have explored the possibility of obtaining a compound effect which includes errors due to measurement and sample. In this method, one sample of dispersion from a 1.0 g of powder in 20 ml water was prepared and subsequent subsamples were obtained from it. These data show that a relative standard deviation for d_{50} is at 3%, if we eliminate aging during week-end.

Repeatability Experiments: In the meantime, we initiated milling tests to define repeatability. The first experiment was completed and essential data were obtained. It appears that only 60 minutes of milling is sufficient to increase the specific surface area from 6 to 9 m^2/g. This milling test showed that the mixture of SNE-10, 5 and 3 had a very low viscosity at 50% V loading, which indicates that the packing density of the particles is better than that of the SNE-5 and 3 mixture. The particle size distribution and specific surface area during milling exhibited a linear relationship with milling time. The milled slurry was cast into 3 in. x 3 in. blocks of approximately 3/8 in. thick. Initially, we experienced considerable difficulties in obtaining a crack-free green body. Discussions with Dr. Vimal Pujari, Norton Company, revealed that the gypsum blocks had to be wetted prior to pouring the slurry for casting. Pretreatment of the gypsum block by wetting for 5 to 10 min. appears to be sufficient to prevent fast drying at the initial period. The tests conducted in this exercise indicate that dry gypsum blocks tend to remove water from the slurry at a fast rate which appears to induce drying cracks due to inhomogeneous draining of water.

Milled powders containing 4% Y_2O_3 in dry form have been analyzed for particle size distribution and specific surface area, and slurries have been analyzed for pH, conductivity, electrokinetic sonic amplitude (ESA), and isoelectric pH. These data have been collected at 0, 20, 32, 50 and 80 min. milling time so that milling kinetics can be evaluated. The milling kinetics data show that most of the size reduction has taken place in the first 20 minutes, indicating that deagglomeration is the primary mechanism in the initial stages. Since deagglomeration is accompanied by a significant increase in specific surface area, it indicates that the agglomerates containing smaller particles in the as-received powder have undergone deagglomeration. Mechanistically, the largest agglomerates are the first to undergo nearly-complete deagglomeration, followed by the next size smaller particles. Strength of bond between the primary particles in these powders appears to be strong since application of ultrasonics at 30 watts from 3 min. was not sufficient to fracture these agglomerates. As a result of such mechanism which is typical for this powder, we are able to arrive at 8-9 m^2/g specific surface area within 60 minutes.

A comparison of particle size distribution from all five tests indicates expansion of the repeatability band with the increase of particle size. In otherwords, at d_{10} the data are more reproducible than at d_{50}, where the subscripts of d stand for percent weight of particles finer than the stated size in micrometers. In addition, at shorter milling times, reproducibility is better than at longer milling times. The data are being analyzed using statistical methods to observe trends. There are no obvious reason to explain the range of variability. The slurry data also show some degree of variability in repeatability. The initial pH_{iep} at 6.4 ± 0.3 of slurry containing silicon nitride powder, water, 1000 ppm polymethacrylate surfactant and 4% yttria remains almost at the same level even after milling for 80 min., while the specific surface area changed from 5.8 ± 0.3 m^2/g to 11.2 ± 1.0 m^2/g.

A batch of milled slurry from the latest test has been sent to Dr. V. K. Pujari, Norton-St. Gobain, for slip casting followed by densification. The green body showed a higher density than that of slurry produced in a vibratory mill. Additional milling tests will be conducted based on the results of this evaluation.

Analysis of Slurry Preparation: The slurry preparation step, involving mixing of water, dispersant, followed by a slow addition of silicon nitride powder, was studied in detail using electroacoustic, pH and conductivity measurements. The slurry preparation procedure involves the use of a high speed mixer and orderly addition of ammonium hydroxide (to pH = 9.5 ± 0.2), and polymethacrylate dispersant. The silicon nitride powder addition to this solution is carried out over a period of 30-40 minutes while the mixer is operated at a high speed to keep the slurry in suspension. Once approximately 30% v/v slurry is prepared, the slurry is passed through the mill for size reduction. In the first 10 min. of milling, the entire powder is added to reach a slurry density of 50% v/v. The powder addition is carried out by adding slowly, but steadily at the same rate throughout the 10 min. The slurry is milled for an additional 11 min. to a total 21 min. when the Y_2O_3 powder is added within a 2 min. interval. The milling is continued up to a total of 80 min. Samples are taken at 0, 20, 32, 50 and 80 min. during milling, and set of analyzed for physical and surface chemical properties. Table 1 shows a typical data of pH, electrokinetic sonic amplitude (ESA), conductivity and pH_{iep}. These data show an excellent agreement at 80 min., while the agreement of these data is not as good as one proceeds from 80 min. to 0 min. milling. Therefore, as milling proceeds for a longer period, the slurry components have a longer time to become homogeneous. The variation in these parameters in the initial stages of milling is primarily due to the lack of homogeneity, different levels of deagglomeration, and different concentration of powder as a function of milling time in the slurry. It is logical to assume that the sooner we achieve overall homogeneity during the milling period, higher the likelihood of getting repeatable slurry parameters. In the remaining tests, we plan to further tighten the procedure to achieve a higher level of repeatability.

Milling of Experimental Powder: At the request of Dr. V. K. Pujari, Norton-St. Gobain Company, we examined the feasibility of milling -100 mesh silicon nitride powder produced by their proprietary process. Using the procedure described above, a 2 kg sample of the powder was milled in an aqueous environment, and the resulting samples were analyzed by the measurement of a slurry properties. This experiment on milling of slurry containing 50% v/v powder demonstrate the feasibility of milling a coarse size powder. In the milling of Ube powders, most of the size reduction is primarily due to deagglomeration of strongly held particles. As a result, power consumption in the mill is very small. However, the new powder studied contains large particles and agglomerates exhibiting trimodal size distribution. In addition, the agglomerates appear to be much stronger. Therefore, the power consumption in the mill was on the order of 20 amps, which is two times the power drawn during milling of Ube powders. The initial trimodal particle size distribution changed to bimodal and finally to monomodal within 30 minutes.

Table 1. Comparison of pH, Conductivity, ESA and pH_{iep} of the Milled Samples

	Test No.	Sample Time (min.)	0	20	32	50	80
I. pH	41		8.2	9.4	9.6	9.5	9.7
	42		8.5	8.3	8.4	8.8	8.6
	43		8.0	7.9	8.2	8.4	8.5
	44		7.4	8.9	8.9	8.6	8.5
II. ESA	41		-0.34	-0.60	-0.44	-0.53	-0.52
	42		-0.45	-0.47	-0.49	-0.47	-0.51
	43		-0.37	-0.50	-0.47	-0.50	-0.49
	44		-0.49	-0.51	-0.52	-0.50	-0.49
III. Conductivity	41		22	54	53	71	83
	42		22	59	64	73	85
	43		22	43	46	52	68
	44		42	42	46	49	60

IV. pH_{iep}	41	6.7	6.7	7.1	7.1	6.9
	42	6.7	5.8	6.4	6.6	6.4
	43	6.2	5.3	6.0	6.1	6.4
	44	5.1*	6.4	6.2	6.0	6.3

* Ultrasonicated before pH_{iep} measurement

Status of Milestones

On target.

Communications/Visits

Dr. V. Pujari, St. Gobain-Norton Company visited NIST in September to carry out milling test.

Publications

None

Microwave Sintering of Silicon Nitride

T. N. Tiegs, J. O. Kiggans, P. A. Menchhofer, and K. L. Ploetz
(Oak Ridge National Laboratory)

Objective/scope

The objective of this research element is to identify those aspects of microwave processing of silicon nitride that might (1) accelerate densification, (2) permit sintering to high density with much lower levels of sintering aids, (3) lower the sintering temperature, or (4) produce unique microstructures. The investigation of microstructure development is being done on dense silicon nitride materials annealed in the microwave furnace. The sintering of silicon nitride involves two approaches. The first approach comprises heating of silicon nitride and sialon powder compositions in the 2.45- or 28-GHz units. The second approach deals with using reaction-bonded silicon nitride as the starting material and is done entirely in the 2.45-GHz microwave furnace.

Technical highlights

Sintered Reaction-Bonded Silicon Nitride (SRBSN) - In continuing work on SRBSN materials, several specimens were fabricated, nitrided, and sintered in the 2.45-GHz microwave furnace. The compositions for these samples are shown in Table 1. Summaries of the results on nitridation and sintering are shown in Tables 2 and 3, respectively. The conventional processing is done in two separate steps for nitridation and sintering, whereas the microwave processing is done in one continuous operation. The samples that achieved high densities, >95 % T. D., were machined into mechanical property test specimens. A summary of the strengths determined to date is given in Table 4.

Previously, it has been shown that the mechanical properties of the MWSRBSN are not equal to ceramics made from the higher-cost powders, but are appropriate for a number of applications at lower temperatures and stress levels.[1] At ambient temperature, typical strength, toughness (K_{Ic}), and hardness values of the current materials are 480 MPa, 4.8 MPa$\sqrt{m}$, and 14 GPa, respectively. It would be desirable to improve both the strength and toughness of the materials. Consequently, additional samples were fabricated using different processing procedures and materials to improve these properties. For example, isopropyl alcohol (IPA) has been substituted for the water in the milling step. This reduces the oxygen pickup and improves nitridation of the silicon at lower temperatures, thereby increasing the a-Si_3N_4 content of the compacts prior to high-temperature sintering.[2] This should result in more elongated grain growth and an increased fracture toughness. Use of IPA will also reduce agglomeration of the silicon and decrease the aging time that was problematic in the previous samples. The newer samples are also nitrided with approximately 5 vol % He in the N_2-H_2 atmosphere to further increase the a-Si_3N_4 content in the compacts.[2] Additional compositions are being fabricated to investigate the effects these will have on densification behavior and properties. Nominal compositions will include Si_3N_4-9% Y_2O_3-3% Al_2O_3 and Si_3N_4-5% Y_2O_3- 2% MgO-3% Al_2O_3.

Table 1. Compositions of sintered reaction-bonded silicon nitride materials.

Sample	Silicon purity (wt %)	Mean particle size (μm)	Additive content[a] (wt %)	a-Si_3N_4 content (wt %)	Material cost - ($/lb) as-fabricated[b]	Material cost - ($/lb) as-sintered[c]
TM-138	< 0.5[1]	3.4	11.5.% R. E.[3]	5[4]	4.06	2.90
TM-139	< 0.05[2]	4.2	11.5 % La_2O_3[6]	5[5]	7.29	5.17

[a]All compositions contain the same molar content of sintering additives.
[b]Material cost based on purchase price in 10-kg lots. Cost will decease at larger quantities.
[c]Assumes a yield of 58% from nitridation of silicon.
[1]Elkem Metals Co., Buffalo, N.Y.; grade metallurgical Si.
[2]Elkem Metals Co., Buffalo, N.Y.; grade Si-HQ.
[3]Molycorp, White Plains, N.Y.; grade 5210, rare-earth mixture (<1% CeO_2).
[4]Starck, Berlin, Germany; grade S1 Si_3N_4.
[5]Starck, Berlin, Germany; grade LC-10N Si_3N_4.
[6]Molycorp, White Plains, N.Y.; grade 5205, >99.9% La_2O_3.

Table 2. Summary of results on nitridation of reaction-bonded silicon nitride compositions. Samples were heated to 1480°C in a 24-h period. Atmosphere was nitrogen-4% hydrogen.

Sample	Heating type	Silicon weight gain (%)	Fraction silicon reacted (%)
TM-138I, TM-138J	Conventional	52.8	81
TM-139J, TM-139K	Conventional	48.1	74
TM-139N, TM-139O	Microwave	55.9	86

Table 3. Summary of densification results on sintered reaction-bonded silicon nitride compacts during microwave and conventional heating.

Sample	Heating type	Sintering conditions (°C/h)	Density (g/cm3, % T. D.)
TM-138I	Conventional	1800/4	3.06, 91.3
TM-138E, TM-138F	Microwave	1800/4	3.18, 94.8
TM-139J	Conventional	1800/4	3.20, 95.4
TM-139G, TM-139H	Microwave	1800/1	2.92, 86.5
TM-139L, TM-139M	Microwave	1800/2	3.23, 96.4

Table 4. Summary of flexural strength of SRBSN samples.

Sample No.	Densification technique	Flexural strength (MPa)	
		25°C	1000°C
TM-138E	Microwave	466 ± 34	338 ± 52
TM-138F	Microwave	422 ± 34	325 ± 9
TM-139J	Conventional	415 ± 54	269 ± 31

Cooperative Research and Development Agreements (CRADAs) - Three CRADAs have been started in the area of microwave processing of silicon nitride. The first CRADA is with Garrett Ceramic Components (GCC)/Allied-Signal and involves annealing of specimens of silicon nitride with high additive contents (>5%). Compositions include AS-44, GN-10, and AS-700. A second CRADA with Norton also involves annealing of silicon nitride in the microwave but with additive contents less than 5%. Most of the work was involved with NT-154 with a range of a-phase contents. Norton was also involved in the third CRADA where reaction-bonded silicon nitride was fabricated in the microwave. The results were directly compared to materials fabricated by conventional heating.

Specimens of AS-44 silicon nitride from GCC/Allied-Signal have been annealed. Conditions used were 1600 to 1800°C for times of 2 to 10 h. The samples were machined into test specimens and tested for mechanical properties. Results of the fast fracture strength and fracture toughness are shown in Table 5. As shown, the stress-rupture behavior at elevated temperatures was significantly improved over the baseline material. Samples of GN-10 silicon nitride have been fabricated and microwave annealed. Samples are currently being machined into test bars.

Table 5. Summary of results on microwave annealing of GS-44 silicon nitride.

Properties	Baseline	Microwave exposure Conditions		
		1600°C/10 h	1700°C/10 h	1800°C/2 h
Flexural Strength (MPa)				
25°C	961 ± 10	931 ± 5	910 ± 3	931 ± 3
900°C	697 ± 7	690 ± 11	710 ± 5	634 ± 9
1100°C	434 ± 3	448 ± 7	386 ± 5	413 ± 5
Fracture Toughness (MPa√m)	8.04 ± 0.16	8.05 ± 0.14	8.09 ± 0.14	7.79 ± 0.51
Stress-Rupture				
900°C-413 MPa	0.0 h	>24 h	4.21 h	0.01 h
900°C-379 MPa	0.3 h	>24 h	>24 h	0.07 h

Samples of Norton NT-154 with high a-phase contents have been annealed. The results are reported in a following section. A second set of samples was microwave annealed and is currently being machined into test specimens. Additional samples of Norton NT-154 with high a-phase contents have been annealed, machined into test specimens, and tested under dynamic fatigue conditions identical to previous samples. The results are shown in Table 6. Another set of samples is currently ready to be microwave annealed.

Samples of Norton reaction-bonded silicon nitride have been fabricated and microwave reaction-bonded and sintered. The results are summarized in a following section.

References

1. T. N. Tiegs, J. O. Kiggans, and K. L. Ploetz "Cost-Effective Sintered Reaction-Bonded Silicon Nitride for Structural Ceramics," to be published in *Ceram. Eng. Sci. Proc.*, American Ceramic Society.

2. R. G. Stephen and F. L. Riley, "The Influence of Pre-Oxidation on the Processing of Silicon Powder," pp. 307-14 in *4th International Symposium on Ceramic Material Components for Engines*, ed. R. Carlsson, T. Johansson, and L. Kahlman, Elsevier Applied Science, New York, 1992.

3. B. Q. Lei, D. Ashkin, T. Johansson, and T. Lindbäck, "Optimization of the Silicon Nitridation Process," pp. 633-40 in *4th International Symposium on Ceramic Material Components for Engines*, ed. R. Carlsson, T. Johansson, and L. Kahlman, Elsevier Applied Science, New York, 1992.

Status of milestones

All milestones on schedule

Table 6. Summary of dynamic fatigue results at 1370°C on microwave-annealed NT-154.

Sample	Dynamic fatigue exponent, N	α-Si_3N_4 content (%)
MW8	12.7	16
MW9	17.3	4
MW10	22.0	23

Communications/visits/travel

Travel by T. N. Tiegs to Washington, D.C., on April 9, 1992, to attend the CTAHE Bi-monthly Project Meeting. A presentation was made entitled, "Cost-Effective Sintered Reaction Bonded Silicon Nitride for Structural Ceramics."

Travel by T. N. Tiegs from April 12-16, 1992, to Minneapolis, Minnesota, to attend the American Ceramic Society Annual Meeting and present a paper entitled, "Cost-Effective Sintered Reaction Bonded Silicon Nitride for Structural Ceramics."

Travel by J. O. Kiggans from April 27-30, 1992, to San Francisco, California, to attend the Materials Research Society Fall Meeting and present a paper entitled, "Characterization of Sintered Reaction-Bonded Silicon Nitride by Microwave Processing."

Travel by T. N. Tiegs from August 11-24, 1992 to Melbourne, Australia, to attend the Austceram'92 Meeting and present a paper entitled, "Sintered Reaction Bonded Silicon Nitride for Structural Ceramics."

Travel by J. O. Kiggans from September 21-22, 1992, to West Lafayette, Indiana, to present a seminar to the Purdue University Graduate Seminar entitled, "Microwave Processing of Ceramics."

Problems encountered

None

Publications

J. O. Kiggans and T. N. Tiegs, "Characterization of Sintered Reaction-Bonded Silicon Nitride by Microwave Processing" to be published in *Proceedings of the Materials Research Society Fall Meeting*, San Francisco, California, April 27-30, 1992.

T. N. Tiegs and J. O. Kiggans, "Cost-Effective Sintered Reaction-Bonded Silicon Nitride for Structural Ceramics" to be published in *Ceram. Eng. and Sci. Proc.*, American Ceramic Society.

Development of Microwave Processing of Silicon Nitride Components for Advanced Heat Engine Applications Reaction Bonded and Sintered Reaction Bonded Silicon Nitride - C. A. Willkens (Saint-Gobain/Norton Industrial Ceramics Corporation)

CRADA No. ORNL 90-0036

Objective/Scope

Microwave processing offers potential advantages, such as decreased nitriding and sintering times, nitriding of larger cross-sections and unique microstructures, as compared to traditional sintering techniques. This CRADA project will apply Microwave processing technology developed at ORNL to unfired reaction bonded silicon nitride (RBSN) and sintered reaction bonded silicon nitride (SRBSN) materials processed at NRDC. Powder compacts produced at NRDC will be brought to ORNL for microwave nitriding and sintering studies. The properties of microwave nitrided and/or sintered silicon nitride will be directly compared against same lot materials traditionally "fired" at NRDC.

Technical Progress

RBSN

Presintered silicon powder tiles were microwave nitrided at ORNL using the 6 kW, 2.5 GHz furnace. Three types of silicon, having different particle size distributions, purity and green density were evaluated. A narrow particle size distribution, having a green density of ~1.45 g/cc was nitrided using a temperature cycle having a number of different ramp rates, but no intermediate soaks except for a final 1hr soak at 1440°C. Four 2 x 4 x 0.2 inch tiles were nitrided in a cycle. Figure 1 shows the microwave power output during the cycle. The decrease at ~1200°C was due to the controller compensating the output due to detection of the reaction exotherm. Sample temperature is monitored at the tile surface with a thermocouple during the cycle. One of the four samples had a small region of silicon meltout of the bottom. Otherwise, the samples looked very uniform after nitriding. A broader, coarser particle size distribution, having a green density of 1.53 g/cc, was microwave nitrided in a separate cycle. The power output is shown in Figure 2. This run was smoother than the previous run with only a single decrease in power to maintain ramp rate. A very smooth ramp rate was maintained throughout the cycle, even at low temperatures. Again, the samples looked very uniform after nitridation. Table 1 compares results of the microwave nitrided tiles with the results from same lot tiles nitrided by conventional furnacing at NRDC. The weight gains are very similar. Samples were machined into bend bars at NRDC and sent to ORNL for mechanical property evaluation. Microstructural characterization of the baseline, RBSN - Narrow, showed a slightly higher free silicon level for the microwave nitrided (0.4%) as compared to the traditionally nitrided (0.2%) The alpha content was similar at 81% for microwave and 83% for traditionally nitrided. The room temperature bend strengths (MIL-STD-1942A, Sample Size B) were similar, a limited

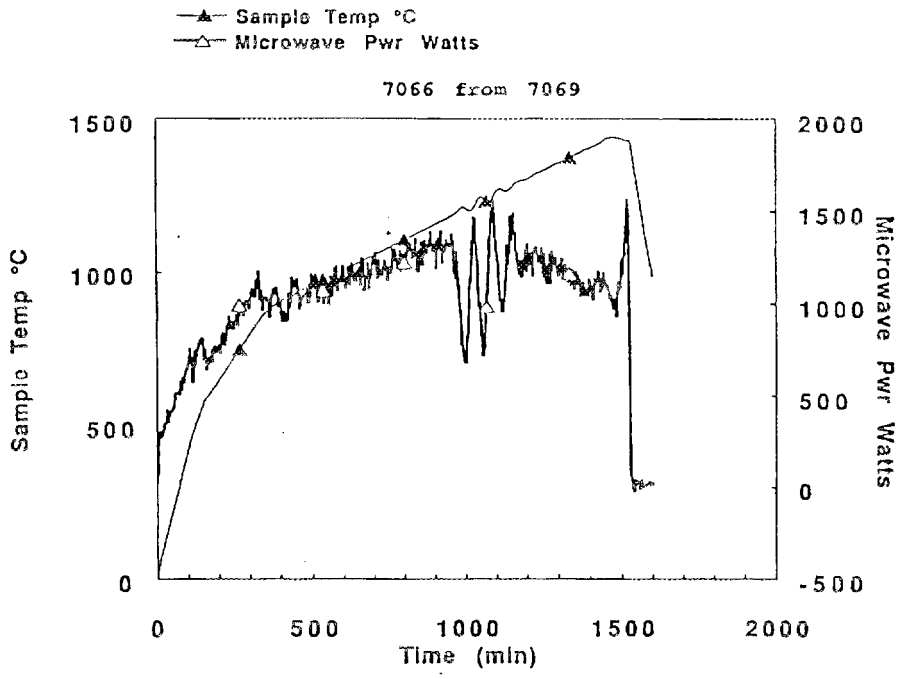

Figure 1: Microwave Nitriding of Presintered Silicon Tiles - Narrow Particle Size Distribution

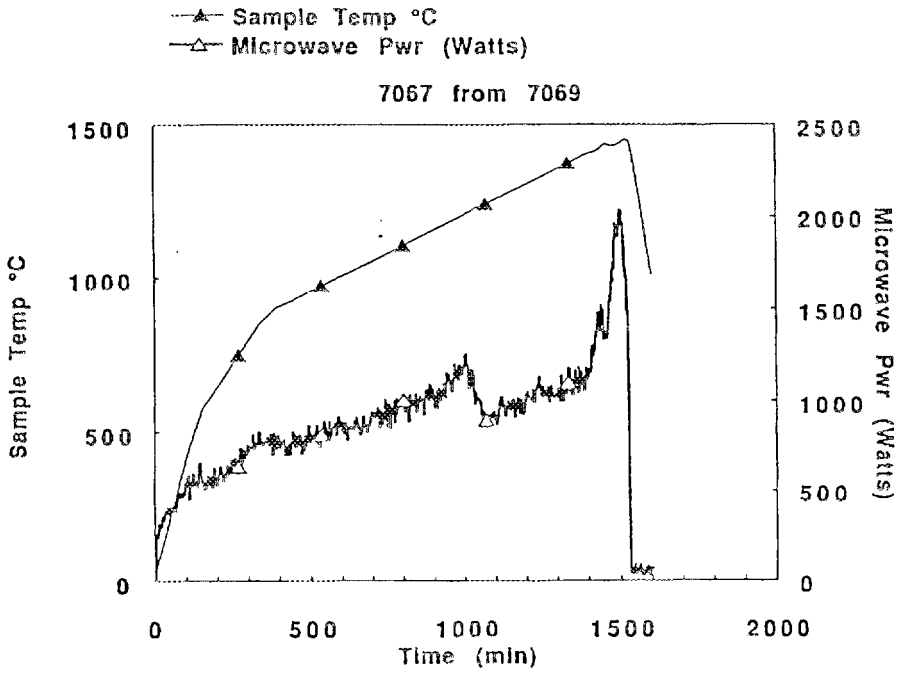

Figure 2: Microwave Nitriding of Presintered Silicon Tiles - Broad, Coarse Particle Size Distribution

number of bars (3) of each have been tested. Testing was on machined surfaces. A higher purity silicon was used for sample 6120. The iron level of this silicon was 200 ppm as compared to ~2000 ppm for the above samples. The weight gains were similar (Table 1), and both showed a slight amount of meltout.

Table 1 - Current RBSN Results

Sample	Nitride Technique	(%) Weight Gain	(%) Alpha	(%) Silicon	(MPa) RT Strength
RBSN - Narrow	conventional	62.9	83	0.2	194 ± 4
RBSN - Narrow	microwave	63.1	81	0.4	234 ± 26
RBSN - Broad	conventional	60.0			
RBSN - Broad	microwave	61.5			
RBSN - Pure	conventional	62.7			
RBSN - Pure	microwave	61.3			

SRBSN:

SRBSN precursor tiles that were conventionally nitrided at NRDC were microwave sintered at ORNL in the 6 kW, 2.5 GHz microwave furnace. One of the compositions was also nitrided and sintered in a single microwave cycle. Two compositions were evaluated, SRBSN-A (lower eutectic) and SRBSN-B (higher eutectic). Both are experimental compositions from NRDC, not commercial products. Two tiles, 3 x 3 x 0.300 inch, of a given composition were sintered in each microwave cycle. Sample 6120/7044, composition B, was nitrided conventionally using two different final soak temperatures, 1370°C (Sample 6120/7044) and 1440°C (Sample 6120/6220). The 1370°C soak temperature resulted in ~5% residual silicon. Table 2 shows the current results from the SRBSN study. Tiles of Composition B, that had no free silicon and also a lower alpha silicon nitride content after conventional nitriding (6120/6220), did not heat by microwave at low temperature (<500°C). Both microwave and conventionally sintered tiles of 7078/7084 showed residual silicon and microporosity. Failure origins were large grains of silicon, up to 60 μM, that appeared to have coalesced during sintering. Tiles of 7078, Composition A, were also supplied for nitriding and sintering in a single microwave cycle. The density of this sample was slightly lower than the combination of conventional nitriding and microwave sintering. Figure 3 shows the microwave power output during the sintering cycle for 6120/7044. The decrease in power at ~1490°C is thought to be due to formation of the intergranular liquid phase resulting in dielectric relaxation. Figure 4 shows the output for 7078/7084. The rise in power starting at ~1100°C is due to the increase in temperature ramp rate called for by the controller. The decrease at ~1250°C is believed due to either nitridation of any residual free silicon or the formation of the intergranular liquid phase resulting in dielectric relaxation. Figure 5 shows the output for 7078/8055 where nitridation and sintering were done in a single microwave cycle. Future work will focus on these single-cycle materials using composition A.

Table 2 - Current SRBSN Results

Sample	Composition	Sinter Technique	(g/cc) Density	(MPa) RT Strength
6120/7044	B	conventional	3.18	496
6120/7044	B	microwave	3.25	460
6120/6220	B	conventional	3.19	448
6120/6220	B	microwave	poor heating	
7078/7084	A	conventional	3.30	448 ± 34
7078/7084	A	microwave	3.32	413 ± 62
7078/8055	A	microwave nitride + sinter	3.25	248

Samples were machined into bend bars at NRDC and sent to ORNL for mechanical property evaluation. Composition 7078/7084 showed full conversion to beta silicon nitride for both microwave and traditional sintering methods. Polished sections showed the amount of residual porosity and free silicon was significant, resulting in the relatively low strength and fracture toughness. Both were nitrided traditionally using a low final soak temperature. The same composition (7078/8055) was both microwave nitrided and sintered in a single cycle. There was also a significant amount of residual silicon and porosity. The amount of porosity is related to the amount of residual silicon and increases going from the outside to the inside of the compact. A portion of the porosity may in fact be silicon pullouts. The relatively low eutectic temperature of this composition is likely causing for partial sintering to occur prior to full nitridation. Composition 6120/7044 microwave had a density of 3.26 g/cc and showed only minor porosity (~1-2 micron diameter). Preparation of additional samples of Composition 7078 was hindered due to a hydration problem with one of the sintering additives. This resulted in cracking of the tiles prior to the presinter step. Additional samples are being prepared using Composition 6120 variations, which will be both microwave nitrided and sintered in the same cycle.

Status of Milestones

On schedule.

Publications

None

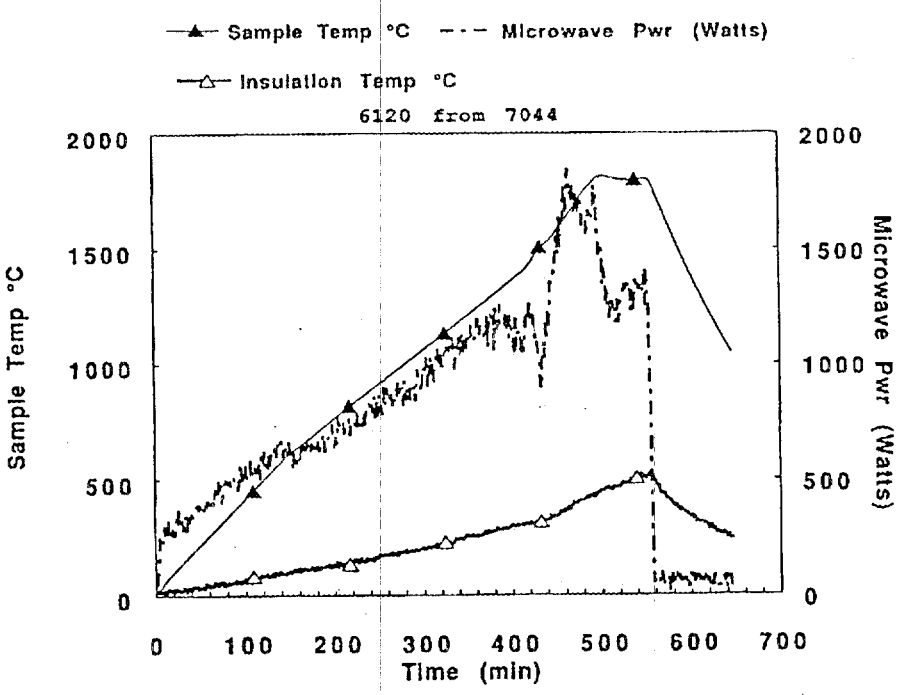

Figure 3: Microwave Sintering Power Output of SRBSN Sample 6120/7044

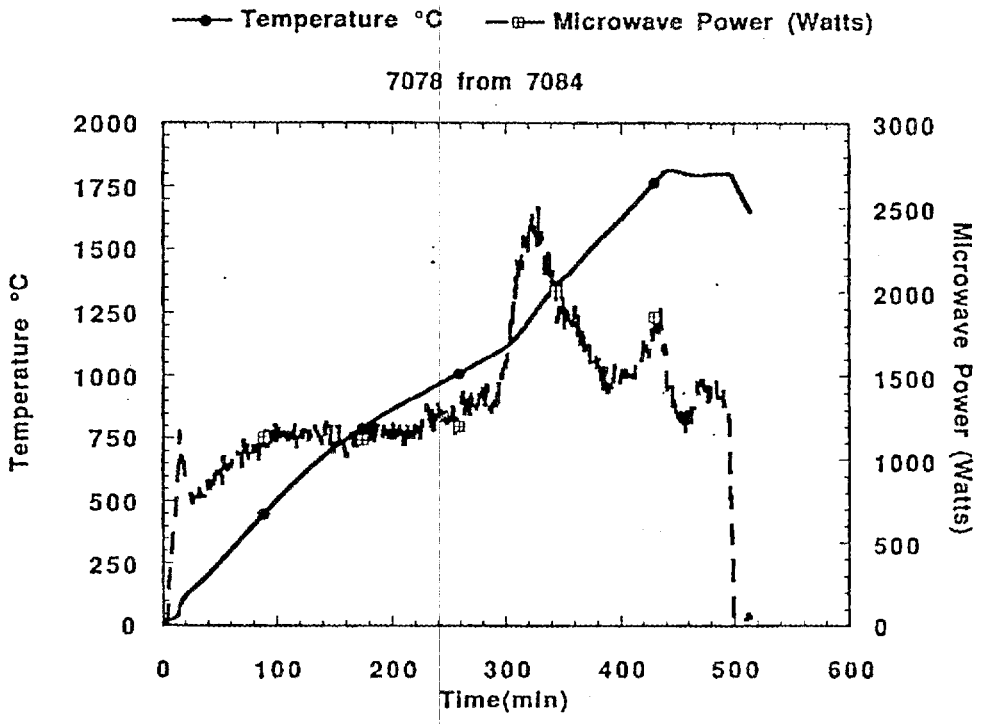

Figure 4: Microwave Sintering Output of Pre-Nitrided SRBSN Sample 7078/7084

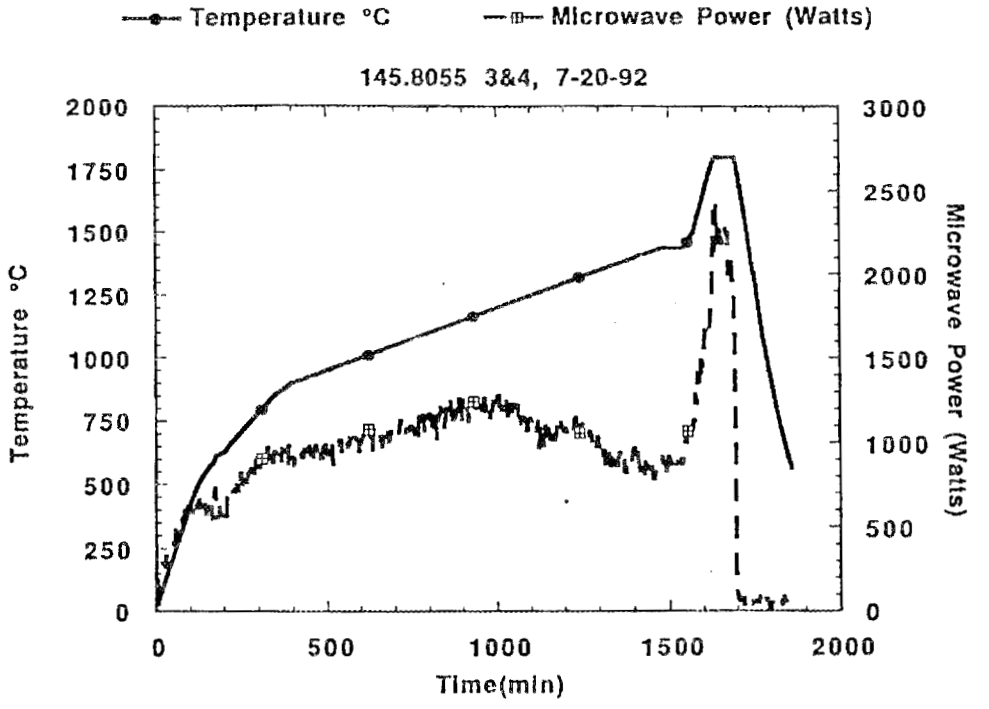

Figure 5: Microwave Combined Cycle Nitriding and Sintering of Pre-sintered Silicon Sample 7078/8055

MICROWAVE ANNEALING

R.L.Yeckley(SGNIC), T.N.Tiegs, J.O.Kiggans, K.L.Ploetz(ORNL)

CRADA No. ORNL 90 - 0037

Objective/Scope

The purpose of the annealing trials is to improve the fracture toughness and creep resistance of HIP silicon nitride with 4% yttria by promoting growth of elongated grains.

Technical Progress

Earlier microwave experiments at ORNL found that sintered silicon nitrides with retained alpha silicon nitride would complete transformation during annealing. In addition to the transformation, significant grain growth occurred with some toughness improvement. In these same trials, HIP silicon nitrides with 100 % β silicon nitride did not show any grain size changes. Microwave annealing improve the high temperature deformation resistance of both materials. Therefore, the first series of microwave annealing trials investigated the changes occurring to HIP silicon nitride with untransformed alpha silicon nitride. The alpha content before annealing was 24%. Below a certain annealing temperature no transformation was observed as seen in table 1.

Mechanical Properties - Mechanical testing was done with a 3 mm by 4 mm flexure bar on a 4-point quarter point fixture with an outer span of 40 mm. Toughness was determined by the indentation fracture procedure. The indent load was 10 kilograms. All the annealed fracture toughness values are lower than the silicon nitride after HIPing. The grain boundary crystallization accounts for part of the toughness decreases. Yttrium disilicate was not detected in the as HIP material. Yttriia disilicate was present after all annealing trials. The toughness of MW2, 3, 4, and 7 is typical of as HIP silicon nitride with yttria disilicate. The lowest toughness were found in annealing trials during which further α to β transformation occurred. The greater toughness decrease is expected to be due to a number of factors such as: anneal temperature, time at temperature, extent of crystallization.

Table 1. Microwave Anneal Property Summary.

	Fracture Toughness		1370 Strength		Phase Analysis	
ID	MPa m1/2	st dev	Avg	st dev	%alpha	$Y_2Si_2O_7$
MW1	4.84	0.018	79	4.6	0.3	alpha
MW2	5.45	0.05	101.05	12.5	25.4	gamma
MW3	5.37	0.1	94.7	4.6	21	alpha
MW4	5.39	0.19	76.2	5.1	7	alpha
MW5	5.18	0.13	80.1	3.5	0	alpha
MW6	4.02	0.7	72.9	6.5	0	gamma
MW7	5.5	0.14	94.1	7.5	21	gamma
HIP	5.69	0.09			24	n.d.

The higher 1370° C fast fracture strengths and improved resistance to slow crack growth are obtained from the lower temperatures within the microwave anneal matrix. In general, crystallization of the intergranular phase and associated changes to the microstructure are expected to be the primary factors improving the high temperature behavior. The stressing rate exponents determined from flexure tests at 1370 are in Table 2. Testing was done with a 3 mm by 4 mm flexure bar on a 4-point quarter point fixture with an outer span of 40 mm. The stress exponent for standard NT154 is 16.7. Only the microwave anneal MW2 showed a significant improvement in the stress exponent. The MW2 fracture surfaces at the low stressing rates of .001 MPa/s did not exhibit any apparent slow crack growth. Typically, slow crack growth is observed at stressing rates of 0.1 MPa/s. MW2 will be duplicated and further analysis is planned to verify this experimental point.

Table 2. Slow crack growth exponent at 1370 C.

ID	1370 Dynamic Fatigue N
MW1	16.6
MW2	65.7
MW3	18.3
MW4	22.6
MW5	13.3
MW6	13.9
MW7	16.9

The improved dynamic fatigue behavior of MW2 occurred even though this material still had 25% α Si_3N_4 and a finer grain size than NT154. A two step microwave anneal trial has been completed. The first step at high temperature completes the α to β transformation. The second step at the same conditions as MW2 will crystallize the grain boundary phase. The dynamic fatigue behavior of this material will be compared to MW2.

Annealing Trials - Improved slow crack growth at 1370 C was measured for one of the microwave annealing trials completed. No evidence of increased silicon nitride aspect ratio was observed for any of the annealing conditions. A final set of annealing trails are planned. These last annealing trials will focus around the apparent optimum condition for slow crack growth determined in previous experiments.

Cost Effective Sintering of Silicon Nitride Ceramics (SIU-C)

D. E. Wittmer (Associate Professor, Southern Illinois University at Carbondale, Carbondale, IL 62901

Objective/Scope

The purpose of this work is to investigate the potential of cost effective sintering of Si_3N_4 through the development of continuous sintering techniques and the use of lower cost Si_3N_4 powders and sintering aids.

Technical Highlights

The project research goals for Phase I are divided into 4 major tasks:

Task 1. Conduct economic comparisons of continuous sintering with batch sintering.

Task 2. Assess the effects of heating rate on densification, microstructure and properties.

Task 3. Determine feasibility of using lower cost Si_3N_4 powders.

Task 4. Determine feasibility of using alternate materials and furnace design to improve load and throughput.

Task 5. Final Report.

Task 1. Conduct economic comparisons of continuous sintering with batch sintering.

This task was essentially completed during this reporting period. Further work was conducted on comparative analyses of the costs involved with continuous sintering and batch sintering. Different furnace sizes and constructions were considered which would allow for the sintering of a large number of parts roughly the size of a small roller cam follower. Additional refinements of the economic model were made which allowed for variations in furnace volume and throughput for both the belt and batch furnaces. Also the cost of the Si_3N_4 powder and processing cost of the part were considered. Some specific results for different furnace configurations for sintering a 5 gram Si_3N_4 part are given in Table I. Assumptions were made of the same process hours per week and that the scale-up of the batch furnace would reduce the

yield. A $200/kg processed powder cost was used in determining the actual part cost, this number could be reduced with the use of lower cost Si_3N_4 powder and sintering aids and automated shape fabrication. The yield was used in determining the total Si_3N_4 consumption and is reflected in the overall cost per part (including powder processing). This model does not allow for unexpected furnace down-time, annual maintenance, or overheads.

Table I. Sample of Sintering Cost Comparisons for Belt and Batch Furnaces

Property	Belt Furnace			Batch Furnace		
	6W-36L Tungsten	6W-36L Double Pass	12W-72L Graphite	6X6X15 Tungsten	12X12X12 Graphite	24X18X36 Graphite
Process Hrs Per Week	168	168	168	168	168	168
Parts Per Year (million)	4.44	8.88	17.75	0.8	2.25	12.9
Yield %	98	98	98	90	70	70
$/Part Sintering	0.05	0.03	0.02	0.92	0.18	0.08
$/KG Sintering	9.399	6.81	4.51	187.76	36.63	16.17
$/Part Including Powder	1.07	1.05	1.02	2.03	1.61	1.51

Task 2. Assess the effects of heating rate on densification, microstructure and properties.

As reported previously, several batches of Si_3N_4 containing sintering aids were processed to uniform green density by processing methods developed as part of subcontract 19X-SA796C, WBS Element 1.1.1.6 Improved Processing of Ceramics Composites (SIU-C). The processing

employs turbomilling[1] for homogenization of the Si_3N_4 powders and sintering aids, followed by pressure casting, drying, and isopressing. The Si_3N_4 compositions and formulations prepared included:

- A4Y13--4 wt.% Al_2O_3 (Ceralox), 13 wt.% Y_2O_3 (Starck) and 83 wt.% Si_3N_4 (2 batches using Starck LC-10 and Ube E-10)

- A4Y13--4 wt.% Al_2O_3 (Ceralox), 13 wt.% Y_2O_3 (Starck) and 83 wt.% Si_3N_4 (Ube E-10) containing 5 wt. % β-Si_3N_4 seed.

- A4Y6--4 wt.% Al_2O_3 (Ceralox), 6 wt.% Y_2O_3 (Starck) and 90 wt.% Si_3N_4 (3 batches using Starck LC-10, Starck LC-12SX and Ube E-10)

- A4L6--4 wt.% Al_2O_3 (Ceralox), 6 wt.% La_2O_3 (Molycorp) and 90 wt.% Si_3N_4 (3 batches using Starck LC-10, Starck LC-12SX and Ube E-10)

- A2Y8--2 wt.% Al_2O_3 (Ceralox), 8 wt.% Y_2O_3 (Starck) and 90 wt.% Si_3N_4 (2 batches using Starck LC-10 and Ube E-10)

- A6L8--2 wt.% Al_2O_3 (Ceralox), 8 wt.% La_2O_3 (Molycorp) and 90 wt.% Si_3N_4 (2 batches using Starck LC-10, Starck and Ube E-10)

- A4Y6L7-4 wt.% Al_2O_3 (Ceralox), 6 wt.% Y_2O_3 (Starck) 7 wt.% La_2O_3 (Molycorp) and 83 wt.% Si_3N_4 (Ube E-10)

Several of these Si_3N_4 formulations (in the form of disks approximately 7.5 cm in diameter by 1.5 cm thick) were sintered in the Centorr Furnaces 6-BF belt furnace in flowing N_2 at 1625, 1675, 1725, 1750, 1775, 1800, 1825 and 1850°C for 30 to 90 min,. with poor to excellent density results. Compositions sintered at 1800°C and above were severely decomposed and reacted with the Mo boat material. This was anticipated due to the lack of N_2 over-pressure to retard the Si_3N_4 decomposition. At lower temperatures most of the compositions sintered with very good to excellent results. In order to eliminated cracking due to thermal shock, it was necessary to run the belt furnace with the first hot-zone off for compositions with lower sintering aid additions.

---

[1] The turbomill is a high shear mixing/grinding apparatus originally developed by the Bureau of Mines and is presently being manufactured by Noble Technologies Group, RR 1, Box 120B Ridgewood Drive, Gilmanton, NH 03237 (603) 267-6344

Some disks were selected from the initial sintering runs which produced relatively high sintered densities. Some of these disks were machined into standard test bars, while for others the faces were machined to determine the extent of surface reactions. Table II shows the results from density

Table II. Density and Flexural Strength Results for Some Selected Sintering Trials

Sample ID	Composition	Sintering Conditions	Density (%TD)	Flexural Strength (MPa)
9-1	A2Y8-E10	Belt Furnace 1625/90 min. 1st Zone Off	3.07 (94%)	880
20-5	A4Y6L7-E10	N_2 Overpressure 1750/240 min.	3.30 (99.1%)	972
20-9	A4Y6L7-E10	Belt Furnace 1625/90 min. 1st Zone Off	3.28 (99.4%)	974
23-6	A4Y13-E10 5% β-Seed	Belt Furnace 1625/90 min. 1st Zone Off	3.32 (99.5%)	929
24-10	A4Y13-E10	Belt Furnace 1625/90 min. 1st Zone Off	3.32 (99.5%)	918
23-1	A4Y13-E10 5% β-Seed	Belt Furnace 1725/90 min.	3.32 (99.5%)	915
24-2	A4Y13-E10	Belt Furnace 1725/90 min.	3.32 (99.5)	1084

measurements and flexural testing for some of the selected disks. As seen in this table, A4Y13, A4Y13 with 5% β-Si_3N_4 seed, and A4Y6L7 were sintered to near full density with excellent flexural strengths. Also, A2Y8-E10 (Ube E-10 Si_3N_4) gave excellent flexural strength for only 94% dense material. Microstructural examination is currently underway on all compositions; however it is expected that, in order achieve such strength in low density material, the porosity is very fine and well dispersed (as has been observed in other continuously sintered Si_3N_4).

Following the initial sintering trials, additional sintering trials are were made to observe the sintering rate dependence on temperature for the lower liquid phase additions. Specifically the A2Y8, A2L8, A4Y6,and A4L6 compositions, using both Starck and Ube Si_3N_4 powders, were sintered in the Centorr 6-BF belt furnace in the temperature range of 1675 to 1750°C for 30 to 90 min. Typical data for the best sintering runs are given in Table III.

Table III. Best to Date Sintered Densities of Si_3N_4 Compositions Sintered in the Belt Furnace

Composition	Firing Temp °C	Firing Time min	Bulk Density g/cc	% Theor. Density
A4Y6-LC10	1700	60	3.116	95.6
A4Y6-LC12	1725	90	3.212	98.5
A4Y6-E10	1700-1750	60-90	3.25	99.5
A2Y8-LC10	1750	90	2.916	89.5
A2Y8-E10	1750	90	3.265	100
A4L6-LC10	1675	60	3.046	93.4
A4L6-LC12	1700	60	3.141	96.4
A4L6-E10	1750	90	3.230	99.1
A2L8-LC10	1750	90	3.030	92.9
A2L8-E10	1725-1750	90	3.231	99.1
A4Y13-ASN34	1675-1725	30-90	3.33	100

The disks represented in Table III are presently being machined into standard test bars for flexural strength and fracture toughness measurements.

As seen in Table III, ASN-34 Si_3N_4 from Performance Ceramic Co. (92% α-Si_3N_4, with a surface area of 9.5 m^2/g and an O_2 content of 1.8 %) in the A4Y13 formulation was sintered to 100% of theoretical density in the belt furnace at 1675-1700°C for 30 to 90 min.

Also as part of this task, several samples of Norton Co. NT-451, provided by Norton/TRW, Salem, NH, were successfully sintered to greater than the target density in separate belt furnace runs. The effect of continuous sintering on the microstructure and properties was examined by Norton/TRW and found to be comparable to their best batch sintered material.

Due to the success of continuously sintering Si_3N_4 a modification of the present contract has been granted to continue this task as a milestone for another year. The concentration will be to generate more data by sintering a large volume of Si_3N_4 for a specific formulation.

Task 3. Determine feasibility of using lower cost Si_3N_4 powders.

This task was initiated through the use of 3 commercially available Si_3N_4 powders as part of Task 2. These 3 Si_3N_4 powders have a range of purity and cost, with the LC-10 being the lower cost and purity and Ube E-10 being the higher in cost and purity. Formulations prepared from both LC-10 and E-10 were sintered to high densities in the belt furnace, however those prepared from the E-10 Si_3N_4 had somewhat higher densities for the same sintering conditions. Several Si_3N_4 powders and a small amount of spherical Si_3N_4 milling media have been received from Performance Ceramics, Peninsula, OH for testing. ASN-34, containing 92% α-Si_3N_4 with a surface area of 9.5 m^2/g and an O_2 content of 1.8 %, was processed by the standard turbomilling and pressure casting methods in the A4Y13 formulation. The Si_3N_4 milling media on loan from Performance Ceramics was used during turbomilling. For a 2 h milling cycle there was no measurable wear on the media. As reported in the previous task, disks prepared from the A4Y13-ASN34 mix were sintered in the belt furnace to complete density for a wide range of temperatures and times.

Additional formulations containing low cost Si_3N_4 powders from Performance Ceramics Co. and low cost Lanthana concentrate from Molycorp were prepared in a A2Y4La_c4 formulation. The slurries tended to gel at fairly low solids content and produced very low as-cast green densities. The sintered density of these disks was on the order of 75 to 80% of theoretical at 1700°C.

As part of the contract extension, this task will also be continued.

Task 4. Determine feasibility of using alternate materials and furnace design to improve loading and throughput.

This task was completed during this reporting period. Initially the use of alternate construction materials and design of the belt were investigated to improve the loading and part throughput. The impact of improving the loading and throughput on the per part cost were incorporated as part of the input in the economic modelling in Task 1. A change in the belt design was tested which allowed for at least double the load capacity of the previous design. In addition, alternate setter and crucible materials were investigated as a means of improving heating uniformity and reducing the reactions between the Si_3N_4 parts and the setter. These modifications were tested successfully in Task 2.

Also, the construction materials for the furnace elements and belt are a major issue in determining both the load capacity and operating costs for a continuous sintering furnace. Several options have been considered which need to be addressed by further research.

Contract Modification

Due to the demonstrated potential of continuous sintering for compositions with reduced sintering aids, additional funding was requested for the following tasks: 1) refine economic model and design for a chosen furnace, 2) continue the evaluation of sintering parameters on properties of selected Si_3N_4 composition, 3) continue evaluation of low cost Si_3N_4 powders.

Given the success of this additional research, it is anticipated that Phase II would involve the design, construction and testing of a pilot scale belt furnace with improved load bearing capacity for specific heat engine component, 3) sintering of parts provided by industrial partner(s) and 4) continued evaluation of sintering parameters on properties of selected Si_3N_4 composition, and Phase III would involve conducting pilot scale production of heat engine components, and the assessment of properties, production yields and manufacturing costs related to continuous sintering of actual heat engine component(s).

Status of Milestones

1.	Conduct economic comparisons of continuous sintering with batch sintering.	Completed
2.	Assess the effects of heating rate on densification, microstructure and properties.	On Schedule
3.	Determine feasibility of using lower cost Si_3N_4 powders.	On Schedule
4.	Determine feasibility of using alternate materials and furnace design to improve load and throughput.	Completed
5.	Final Report	On Schedule

Publications

None

Presentations

None

1.1.4 Processing of Monolithics

Improved Processing

V. K. Pujari, D. M. Tracey, M. R. Foley, A. K. Garg, N.I. Paille,
P. J. Pelletier, L.C. Sales, C. A. Willkens, R. L. Yeckley (Norton Company)

OBJECTIVE/SCOPE

The goals of the program are to develop and demonstrate significant improvements in processing methods, process controls, and nondestructive evaluation (NDE) which can be commercially implemented to produce high-reliability silicon nitride components for advanced heat engine applications at temperatures to 1370°C. Achievement of these goals shall be sought by:

- The use of silicon nitride - 4% yttria composition which is consolidated by glass encapsulated HIP'ing.
- The generation of baseline data from an initial process route involving injection molding.
- Fabrication of tensile test bars by colloidal techniques - injection molding and colloidal consolidation.
- Identification of (critical) flaw populations through NDE and fractographic analysis.
- Correlation of measured tensile strength with flaw populations and process parameters.
- Minimization of these flaws through innovative improvements in process methods and controls.

The quantitative program goals are: 1) mean RT tensile strength of 900 MPa and Weibull modulus of 20, 2) mean 1370°C fast fracture tensile strength of 500 MPa, and 3) mean 1230°C tensile stress rupture life of 100 hours at 350 MPa.

TECHNICAL PROGRESS

Process optimization efforts were completed during the reporting period according to the Stage II experimental plan which involved processing 16 iterations of buttonhead tensile bars. The iterations served as factorial designed experiments based on control variables established in Stage I of the Program. The outcome of successive iterations relative to targeted mechanical properties was used to establish the optimum control variable combinations/levels for the Stage III final process demonstration scheduled between 6/1/92 and 11/30/92.

Stage II Process Optimization

In Stage II colloidal consolidation processing methodology was optimized using a series of process iterations each starting with Si_3N_4 - 4% Y_2O_3 mill batches capable of yielding approximately 75 buttonhead tensile rods. These in turn were used for the determination of the tensile strength distribution representative of the iteration. Each iteration served as an experiment in a test matrix which was designed using the critical process parameters identified in Stage I of the program. Extensive NDE

and fractography data were generated to establish the nature of failure precursors for guidance on the process improvements necessary for strength and reliability enhancement in subsequent iterations.

From the strength and fractography data generated during the latter part of Stage II, HIP parameters, post-machining treatment and machining related flaws were found to be significant. Therefore, controlled experiments were designed to reevaluate the HIP and post-machining treatments and to optimize the machining process to a level sufficient for the current study, as described below:

i) Evaluation of HIP and Post-Machining Treatments

Specimens from Iteration AC were tested to confirm the optimized HIP cycle and post-machining heat treatment. Fast fracture tensile strength data for 36 room temperature and 8 high temperature (1370°C) tests are summarized in Tables 1 and 2. Specimens were processed with either the standard or optimized HIP cycle and either with no post-machining heat treatment or with a modification of the previously optimized treatment.

The room temperature data clearly show that the optimized HIP cycle produces higher strength specimens (830 vs. 702 MPa) than the standard cycle. The modified heat treatment degrades strength (630 vs. 702 MPa, 678 vs. 830 MPa), contrary to the strength enhancement found with the optimized heat treatment. The data also suggests a high temperature strength degradation (348 vs. 379 MPa) attributable to the modified heat treatment. These results validate the optimized HIP cycle and post-machining heat treatment as SOP (Standard Operating Procedure) for Stage III process demonstration.

Table 1: Room Temperature Tensile Strength -Iteration AC

HIP	Heat Treatment	Average Strength (MPa)	Standard Deviation (MPa)	Number Specimens
Std	None	702	95	17
Std	Mod	630	24	4
Opt	None	830	98	10
Opt	Mod	678	101	5

Table 2: 1370°C Tensile Strength - Iteration AC

HIP	Heat Treatment	Average Strength (MPa)	Standard Deviation (MPa)	Number Specimens
Std	None	368	54	2
Std	Mod	372	44	2
Opt	None	379	99	2
Opt	Mod	348	10	2

ii) Machining Process Optimization

Four distinct machining procedures were evaluated for their influence on tensile strength. Specimens from Iteration AA (mill Batch CO29) were used in the study. Consistent with the focus on machining damage effects, the specimens were not given heat treatments for the purpose of this study. A total of 72 specimens from 3 HIP runs were machined and tested in the study.

Customary practice expresses surface finish specification in terms of the average roughness R_a. Early Stage II work resulted in a reduction of the R_a spec from 16 μin (0.4 μm) to 10 μin at the buttonhead radius and to 8 μin along the gage length. The current study maintained these R_a specs but varied the rough grinding procedure. The four procedures considered differed according to intermediate grinding steps, diamond wheel type and depths of cut. On the basis of the grinding parameters employed, the machining procedures would be ranked according to operational precision from #1 to #4, with #4 being the most precise procedure.

In spite of the major differences in operational precision, the resultant tensile strength data showed no statistically significant dependence on procedure, Figure 1, even though R_y (maximum peak to valley) Talysurf surface finish values were significantly higher for procedures #1 and #2 when compared to procedures #3 and #4.

The mean strengths found in this study are consistent with the 900 MPa room temperature target, given the absence of strength enhancing heat treatment. Therefore the primary consideration in choosing a machining procedure for Stage III was attaining a minimum variability of strength and high Weibull modulus. Table 3 lists the mean and standard deviation found for each procedure. Since procedure #1 had the smallest standard deviation, it was chosen as SOP for Stage III demonstration.

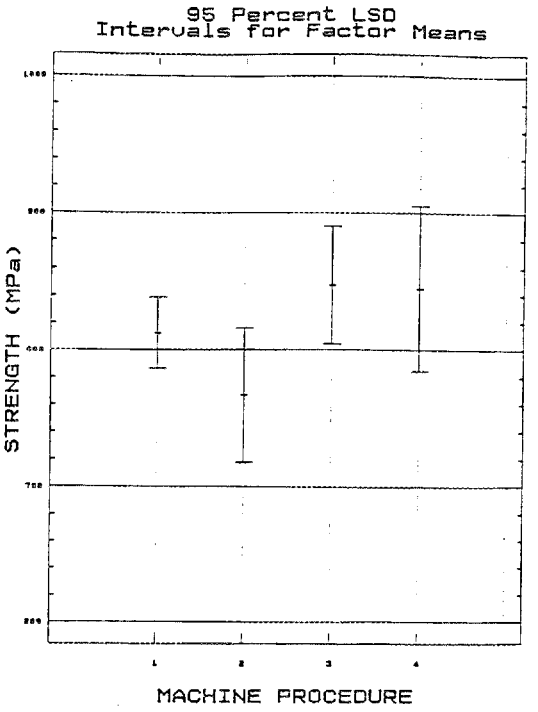

Figure 1

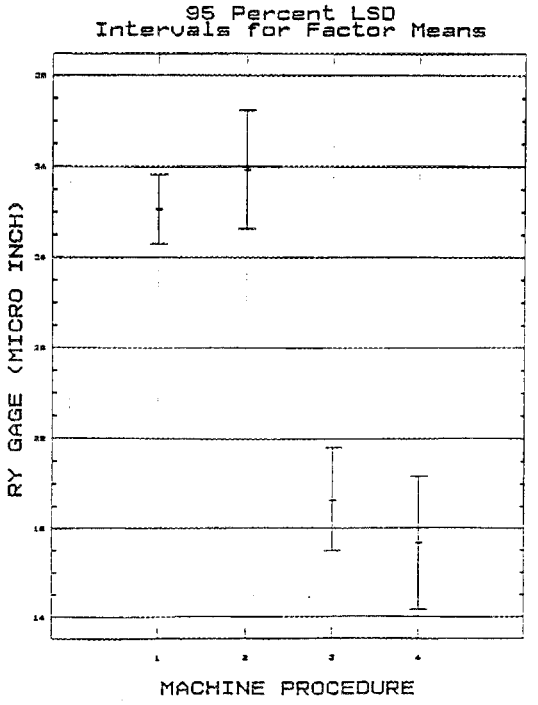

Figure 2

Table 3: Machining Procedure Strength Data

Procedure	Mean	Standard Deviation	Count
1	812.5	18.4	31
2	767.0	34.7	10
3	847.3	30.2	14
4	845.0	42.5	9

iii) Fabrication of MLP (Machined from Large Piece) Specimens

Fabricability of the 50 mm diameter MLP specimen using the colloidal consolidation technique was demonstrated during the reporting period. These specimens were also fully densified using the HIP process. To examine the uniformity through the cross-section, MOR bars (3 x 4 x 50 mm) were machined from various sections of the specimen for room temperature and 1370°C fast fracture flexure strength and fracture toughness (4-point indentation strength) measurements.

The fast fracture flexure strength data are presented in a Weibull plot in Figure 3. Room temperature tests were performed on a group of specimens which were oxidized and on a group given no heat treatment. Similar to previous experience in testing NSF tensile bars, the oxidation treatment was found to enhance the characteristic strength, but diminish the Weibull modulus: (1018 MPa, 12) vs. (873 MPa, 24). Excellent 1370°C strength was measured (660 MPa, 46) especially in view of the fact that these specimens were not given a post-HIP crystallization heat treatment. Seven fracture toughness tests were performed and these provided an average toughness of 6.8 $\pm$ 0.36 MPa$\sqrt{m}$.

Stage III Demonstration Set Fabrication and Testing

Large scale production of NCX-5102 net shape formed buttonhead tensile bars using SOP established in Stage II commenced during the reporting period for demonstration of the optimized aqueous processing methodology. This demonstration will conclude by November 30, 1992. A minimum of 300 room temperature fast fracture tests will be conducted to establish the strength distribution associated with the optimized methodology. A minimum of 25 specimens will be tested to establish elevated temperature fast fracture strengh (1370°C) and stress rupture (1230°C) properties.

In this section, current issues and data related to the demonstration effort are discussed. All required tensile bars have been processed through the steps of milling, casting and HIP densification and are being machined and tensile tested as per schedule. Details of Stage III processing activities are summarized below:

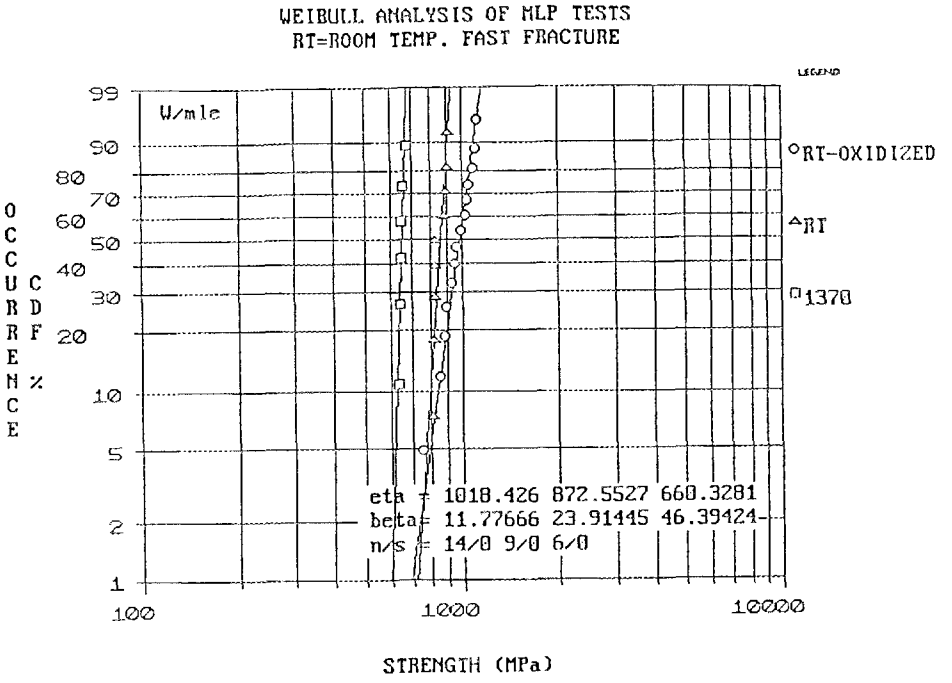

Figure 3

i) Powder Milling

Six 30 kg batches (CO34 - CO40) were prepared using the closed loop aqueous milling procedure. Using established SPC, the required physical and chemical properties of the powder suspensions have been assured. Amongst various characterization techniques, the casting rate of the suspension is measured to establish its suitability for cast density uniformity. An upper control limit (UCL) has been established for the slope of the thickness squared vs time curve in casting trials using puck shaped samples. As discussed below and indicated in Figure 4, batches CO34 - CO36 were found unsuitable for casting.

In the early stages of the Stage III activities, a new lot of powder (Lot E) was found to be significantly different than previous lots (Lots A,B,C,D). Lot E powder showed a measurably higher isoelectric point (IEP) thus affecting dispersion and casting rate. Lot E powder after milling showed decreased casting performance in regard to cast density. Only part of this decrease was attributable to a narrower particle size distribution, primarily due to a finer E03. Samples of milled powder, with yttria, prepared using Lot D and Lot E silicon nitride were sent to Dr. Subhas Malghan at NIST for measurement of the isoelectric point using the Matec ESA 8000. The Lot E powders gave a higher isoelectric point than the Lot D powder. Samples of only the starting silicon nitride powder were then measured at Matec in Hopkinton, MA on the Matec ESA 8000. The raw E03 and E10 powder also showed a trend of decreased IEP for Lot D as compared to Lot E. Using our PenKem System 7000 Acoustophoretic Titrator (PenKem, Bedford Hills, NY), these relative

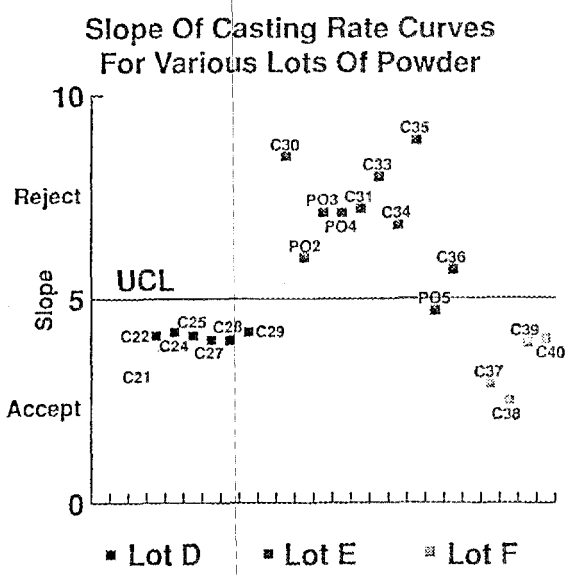

Figure 4

differences were confirmed. Various conditioning treatments were evaluated for adjusting the surface chemistry of the powder, and shown to be successful by the PenKem 7000. FTIR analysis using a Nicolet 510P, diffuse reflectance, confirmed the effectiveness of the conditioning treatments on controlling the surface groups. These treatments were then introduced for preparing small batches, and were shown to be effective in drastically improving the casting behavior as compared to the untreated Lot E Ube silicon nitride powder. Large batches (CO34 and CO35) were then prepared using one of these treatments. Only partial improvement in casting behavior was obtained, and this correlated well with the isoelectric point. Apparently this particular conditioning treatment did not scale-up well. Adjustments to the milling process (CO36) resulted in additional improvements (decreased isoelectric point) but did not meet prior casting results with Lot D. Pre-shipment samples of Lot F powders were received and measured by Sedigraph and PenKem 7000. These Ube lots were shown to have preferred particle size distribution and isoelectric point as compared to Lot E. Iteration batches CO37 through CO40 were processed with the new Lot F silicon nitride powder. The casting results were the best to date, even compared to Lot D. The final size distribution and isoelectric point correlated nicely with the improved casting performance. As a consequence of this experience, specification for isoelectric point has been added for qualification of incoming powder and milled slurry.

ii) Casting

The milled aqueous suspensions mentioned above were processed through closed loop, computer controlled casting equipment. A programmed pressure profile was designed and applied automatically to assure reproducibility of casting. From each milled batch approximately 120 NSF bars were cast. Cast weight and green density were monitored as SPC parameters.

iii) Densification

The cast bars are densified using a glass encapsulated HIP process optimized during Stage II of this processing program. The HIP process was optimized to achieve fracture toughness in the 6.2 - 6.5 MPa√m range and greater than 90% yield.

A lower control limit of 99.5% theoretical density (3.23 g/cc) has been set for the HIP operation. Density values for over 400 acceptable Stage III tensile rods are plotted in Figure 5.

iv) Mechanical Testing

The inspection and testing of Stage III net shape formed buttonhead tensile bars are being carried out following the procedure outlined in the flow diagram of Figure 6. Briefly this involves measurements for dimensional tolerances and surface finish, NDE for volume and surface flaws, loading to fast fracture at a 60 MPa/sec rate using Instron buttonhead supergrips, optical and SEM fractography and finally, analysis of the strength, NDE and fractography data.

To date, 409 tensile rods have been qualified through the HIP operation for machining. Approximately 40 rods per week are being machined until the end of October. As of September 30, a total of 101 room temperature tensile tests had been completed. Of these, 89 were successful gage section fractures. The remaining rods fractured either in the transitron region (5), shanks (5) or buttonheads (2). Elevated temperature testing, (fast fracture and stress rupture) is scheduled for October and November. SEM fractography of the 89 gage failures has been completed. Preliminary analysis of the strength, NDE and fractography data is being pursued.

v. Non Destructive Evaluation

a. Microfocus X-ray

Radiography is being employed at various points of the process for detection of contaminants in the raw material and slip and for detection of defects in the green and final machined specimens. During the reporting period, this in-process inspection technique was instrumental in detecting an air leak in the casting system. A sudden rise in radiographic void indications led to the discovery of a leak which was causing air entrapment voids in the cast specimens.

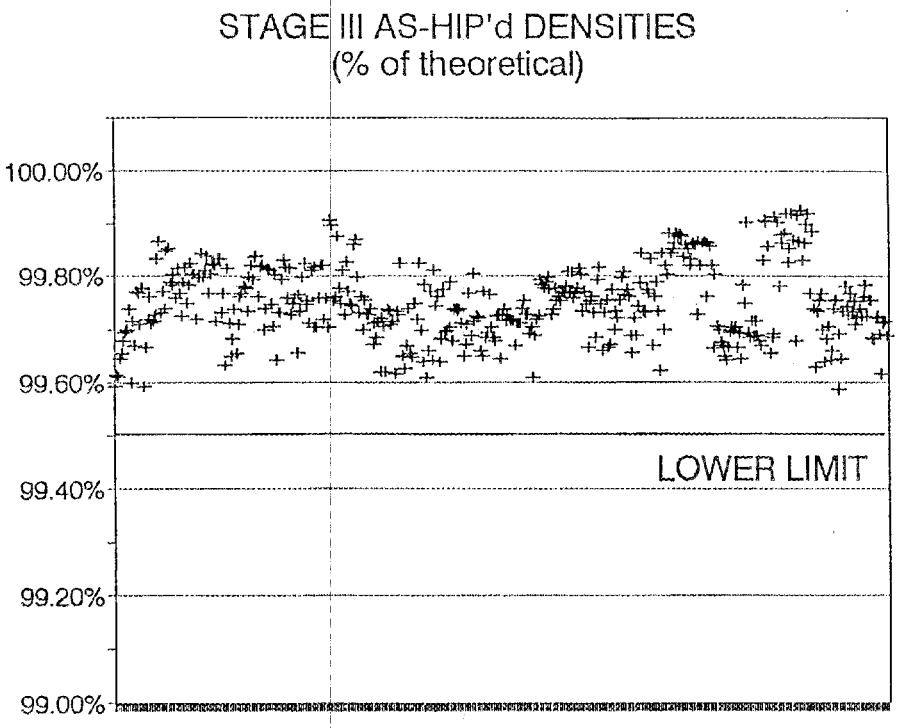

Figure 5

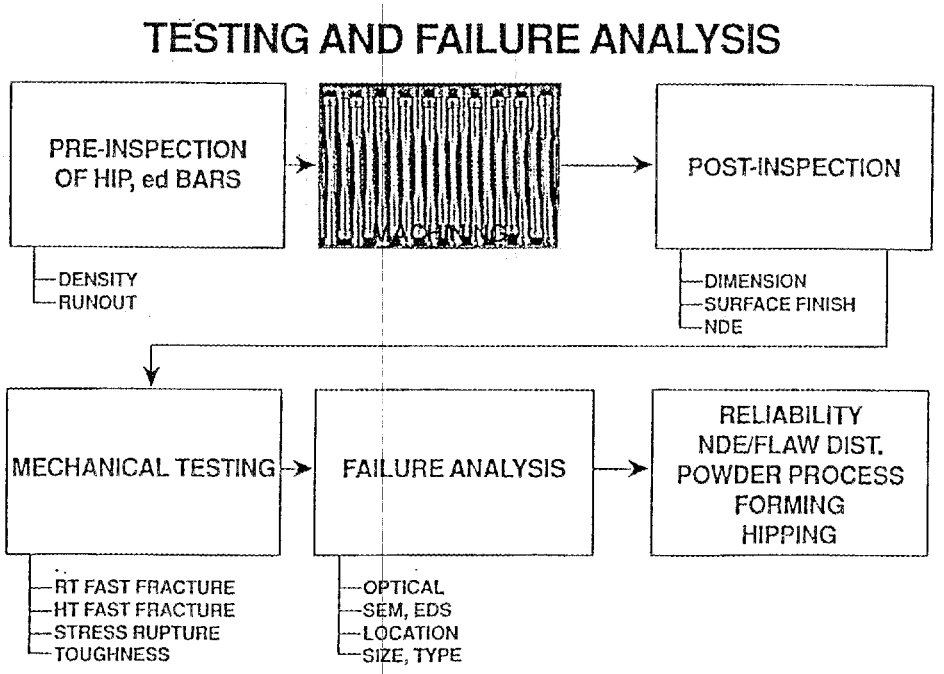

Figure 6

Corrective actions were completed after only a minor interruption in the casting process.

MFX was also used to evaluate the effect of chemical treatment of the plaster of Paris molds on the low density region that develops at the filtration surface. The study was pursued as part of the Lot E powder evaluation discussed above. Radiographs of tensile rod cross sections clearly established that the treatment substantially reduces the depth of penetration of this low density zone (from 1.2 to 0.3 mm).

The machined and ready to test tensile bars have also been examined for volume flaws by MFX. Of the 148 bars examined so far, six were found to contain high density inclusions suspected to be introduced from the mold material.

b. Ultrasonics

A set of 13 machined NSF bars from Iteration AE were examined for volume flaws (using 100 MHZ toric transducer) and surface/sub-surface machining flaws (using focused 100 MHZ spherical transducer in surface wave mode).

The specific toric transducer used in this study scanned an annuler region between 1.5 and 2.5 mm below the surface. No detectable flaws were found in the gage section of the bars. Two other toric transducers are required to scan the remaining volume of the gage section. So far several unsuccessful attempts have been made to fabricate these two transducers. The fragile nature of PVDF transducer material resulted in premature cracking during stretching and casting operations of the PVDF films.

Surface and sub-surface machining flaws were examined using the surface wave imaging procedure described in the February-March 1992 bi-monthly report. Machining scratches and surface pits above the 40 μm detection limit were clearly observed in the C-scans of some of the bars. C-scans of two separate specimens are shown in Figure 7. The vertical direction in those C-scans represents the "unwrapped" cylindrical surface of the bars. This evaluation procedure will be utilized on a select basis for Stage III NSF bar QA.

c. NMR Spectroscopy

NMR has been utilized by Dr. R. Botto at Argonne National Laboratory to obtain fundamental suspension characterization data to compliment standard measurements such as pH, viscosity, IEP, zeta potential and casting rate. During this period, tests were conducted to establish adsorption isotherms of 40% Si_3N_4 stock slurries prepared with two different surfactants, S-1 and S-2.

A standard NMR method for monitoring adsorption of surfactant on the surface of the ceramic powder was developed previously. This method involves standardization of integrated signal intensity from methyl protons in a

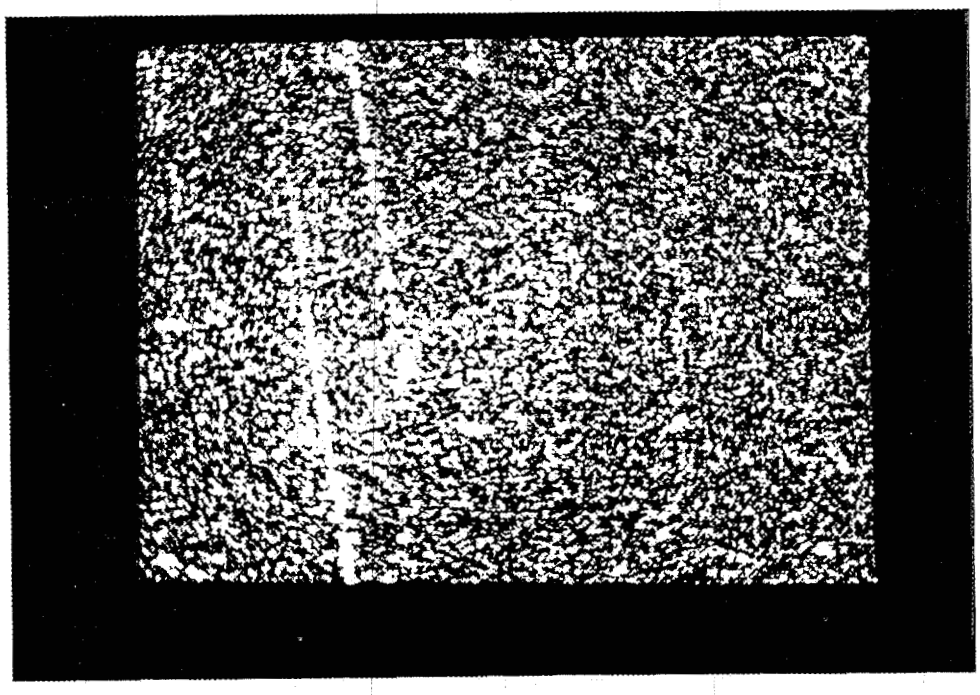

a) Specimen with machining scratch and surface pits

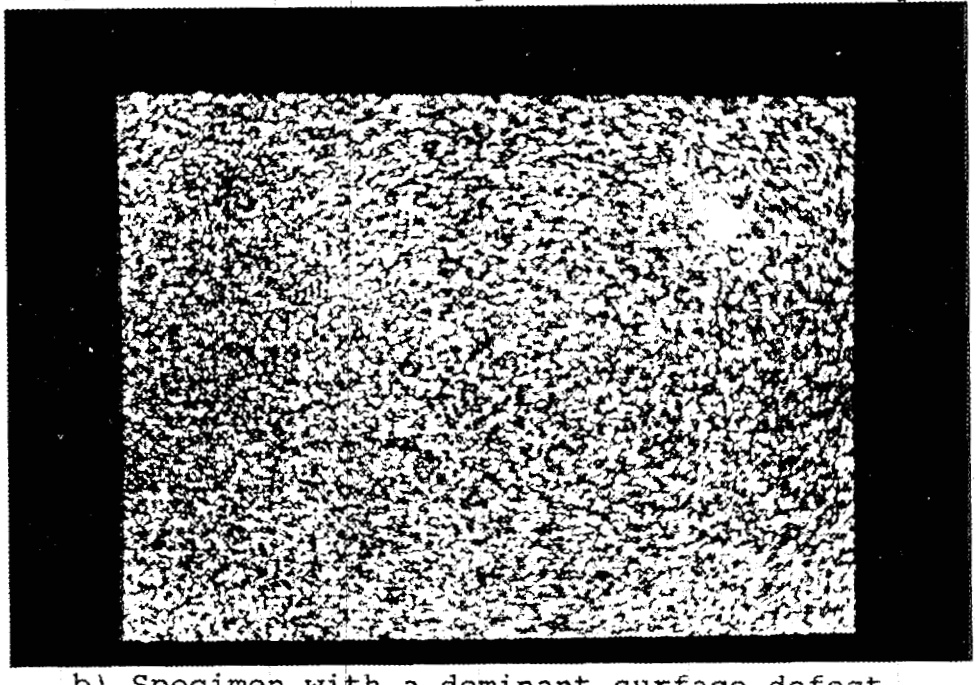

b) Specimen with a dominant surface defect

Figure 7: UT C-scans of "unwrapped" gage surfaces

standard solution of the surfactant against the signal from an analytically prepared aqueous NMR reference standard. The NMR reference chosen was 3-(trimethylsilyl) propionic -2,2,3-d_4 acid, sodium salt (TSP).

Subsequently, this method was found to be suitable for monitoring the adsorption of the surfactant S-2. The ^1H NMR of surfactant S-2 exhibits an intense, well resolved ^1H NMR signal necessary for quantitation in D_2O solution. However the ^1H NMR spectrum of S-1 in D_2O lacked such an intense characteristic NMR signal. The overlapping ^1H frequencies reduce the resolution and signal intensity in the NMR spectrum of surfactant S-1 severely, this rendering ^1H NMR spectroscopy unsuitable for monitoring the adsorption of the type S1 surfactant.

The adsorption of surfactant S-2 in a D_2O slurry of Si_3N_4 (containing 37.5 wt% solids) was measured as a function of time at two initial concentrations. Within experimental error, no adsorption of surfactant S-2 was observed over a period of eight days at either the 1 wt% or 0.1 wt% initial level. At this point the experiment was terminated.

The water ^1H NMR relaxation times T_1 and T_2 were previously observed to change as the Si_3N_4 slurry aged. Clearly, liquid-solid interfacial changes must be occurring as a function of time. The initial surfactant concentrations in this preliminary study were substantially higher than those typically used in investigations of this type. Perhaps adsorption equilibrium was reached quickly and/or the initial surfactant concentrations used were too high to observe changes in signal intensity with adsorption of the surfactant. Therefore, the experiment will be repeated using initial S-2 levels in the range of 0.01 wt% to 0.001 wt%. When a suitable initial concentration level has been determined, the adsorption of surfactant S-2 will be monitored as a function of time, and the adsorption isotherm of surfactant S-2 in a 40% Si_3N_4 slurry will be determined.

Status of Milestones

All milestones are on schedule. Key milestone #114108 - "Complete Factorial Design Experiments for Process Optimization" completed on schedule April 30, 1992.

Publications

1. "NMRS Characterization of Ceramic Slurry for Pressure Casting", A.K. Garg, V.K. Pujari, D. French and R. Botto was presented at the ACS Annual Meeting in Minneapolis, MN, April 15, 1992 by A.K. Garg.

2. "Green Microstructure Control in the Colloidal Consolidation of Silicon Nitride", was presented by V.K. Pujari at the 23rd Annual Meeting of the Fine Particle Society/Symposium on Ceramics, Las

Vegas, Nevada, July 16, 1992.

3. "An Investigation of Residual Stresses in Machined Silicon Nitride", D.J. Snoha and M.R. Foley, Army Materials Technology Laboratory TR 92-46, July 1992.

4. "Processing Methodology for the Production of Reliable High Strength Silicon Nitride" by V.K. Pujari et.al. was submitted August 25, 1992 for Preprints of Automotive Technology Development CCM, November 2-5, 1992.

5. "In-Process Inspection and Control for High Reliability Si_3N_4" was presented by D.M. Tracey at the DoE/ORNL Advanced Ceramic Manufacturing Workshop, Washington, D.C., September 22, 1992.

6. "High Strength Silicon Nitride Production Through Advanced Processing", by D.M. Tracey, V.K. Pujari, M.R. Foley, L.C. Sales and P.J. Pelletier has been accepted for presentation at the MRS fall meeting, Boston, MA, Nov. 30 - Dec. 4, 1992.

7. "Microstructural Development of HIP'ed Si_3N_4 With 4% Y_2O_3" by R.L. Yeckley and M.J. Mangaudis has been scheduled as a poster paper at the MRS fall meeting, Boston, MA, Nov. 30 - Dec. 4, 1992.

8. "Process Control Methods in the Consolidation of Highly Concentrated Suspensions", V.K. Pujari, L.C. Sales, and N.I. Paille has been scheduled as a poster paper at the MRS fall meeting, Boston, MA, Nov. 30 - Dec. 4, 1992.

Improved Processing

S. D. Nunn, O. O. Omatete, C. A. Walls, N. Bell, and K. L. Ploetz
(Oak Ridge National Laboratory)

Objective/scope

To determine and develop the reliability of selected advanced ceramic processing methods. This program is to be conducted on a scale that will permit the potential for manufacturing use of candidate processes to be evaluated. The emphasis is on silicon nitride. Issues of practicality; safety, hygiene, and environmental issues; and in-process testing methods are to be addressed in addition to technical feasibility. The methodology includes selection of candidate processes and evaluation of their range of applicability to various kinds of commercially available ceramic powders.

Technical highlights

1. Silicon Nitride Gelcasting

Several silicon nitride compositions were prepared using two of the new gelcasting systems that are being evaluated as lower-toxicity replacements for acrylamide. The two systems are: methacrylamide monomer (MAM) with polyethylene glycol dimethacrylate (PEG1000DMA) crosslinking agent and MAM with methylene bisacrylamide (MBAM) crosslinker. The compositions that were prepared are shown in Table 1. All of the compositions contained UBE Si_3N_4, either grade E-10 (0.2 μm average particle size) or a blend of grades E-03 (1.0 μm), ESP(0.7 μm), and E-10. In addition, oxides were added as sintering aids.

The compositions prepared in the MAM/PEG system contained silicon nitride powder plus 6 wt % yttria and 4 wt % alumina as sintering aids. It was found that a slip containing 45 vol % ceramic was too viscous to allow adequate deairing when UBE E-10 silicon nitride was used (batch 1). In general, it is more difficult to disperse fine powders such as the E-10 silicon nitride, which results in a high viscosity slip. Batch 2, having the same composition but prepared using a blend of UBE silicon nitride grades E-10 (10 wt %), ESP (30 wt %), and E-03 (60 wt %), had a low viscosity and was easily deaired and cast. No air bubbles were observed in the cast parts after they were removed from the molds. Samples cast from this batch had a green density of 1.7 g/cm^3 (53% theoretical) after drying. The samples were fired at 1750°C for 4 h under 1 atm of nitrogen, and the sintered density was 96% of the theoretical density.

Several silicon nitride batches were gelcast using the MAM/MBAM system. These compositions are also shown in Table 1. The batches contained 45 vol % ceramic and were prepared with various sintering aids and either UBE E-10 silicon nitride or a blend of UBE silicon nitride grades E-10, ESP, and E-03. The batches were mixed using a turbo mill to produce low-viscosity slurries which were cast and gelled.

Samples prepared with UBE E-10 containing 8.5 wt % La_2O_3 and 2.0 wt % Al_2O_3 (batches 3 and 4) were fired at 1750°C for 4 h and at 1800°C for 5 h. The density

Table 1. Gelcast silicon nitride batch compositions

Batch number	Gelcast system	Si_3N_4 grade*	Weight %				
			Si_3N_4	Y_2O_3	La_2O_3	Al_2O_3	SiO_2
1	MAM/PEG	E-10	90.00	6.0		4.0	
2	MAM/PEG	E-03	54.00	6.0		4.0	
		ESP	27.00				
		E-10	9.00				
3	MAM/MBAM	E-10	89.50		8.5	2.0	
4	MAM/MBAM	E-10	89.50		8.5	2.0	
5	MAM/MBAM	E-03	53.70		8.5	2.0	
		ESP	26.85				
		E-10	8.95				
6	MAM/MBAM	E-10	91.80		7.4		0.8
7	MAM/MBAM	E-10	91.80		7.4		0.8
8	MAM/MBAM	E-10	91.80		7.4		0.8
9	MAM/MBAM	E-10	92.00	6.0		2.0	

*UBE Industries, Grades E-10, ESP, and E-03.

of the samples from the 1750°C firing was 97%, while those fired at 1800°C had a density of 98%, as summarized in Table 2. Gas-pressure sintering (GPS) of this composition did not significantly increase the density.

Fired ceramics from batch 4 were machined into modulus of rupture (MOR) bars and tested in 4-point bending for flexural strength. The samples fired at 1750°C had a strength of 580 ± 129 MPa; those fired at 1800°C had a strength of 574 ± 120 MPa. While these strengths are respectable for sintered silicon nitride, the standard deviations are quite high. Examination of the fracture surfaces revealed that the low-strength samples failed at internal pores, which appeared to have been formed by trapped air bubbles. These pores were much finer than those that have been observed in the past but were still serious, strength-limiting defects.

A similar composition (batch 5) prepared using a blend of UBE grades, as in batch 2, sintered to only 91% density when fired conventionally and 94% when gas-pressure sintered. While the blend resulted in a very fluid and easily cast slip, the large fraction of relatively coarse silicon nitride particles appears to strongly inhibit densification.

Table 2. Gelcast silicon nitride property measurements

Batch number	Firing method*	Temp. (°C)	Time (h)	Pressure (psi)	Density (g/cc)	Density (%)	Strength (MPa)	Toughness (MPa√m)
2	Conv.	1750	4	15	3.12	96.0		
3	Conv.	1750	4	15	3.25	96.9		
3	Conv.	1800	5	15	3.28	98.0		
3	GPS	1850	2	100				
		1900	1	300	3.29	98.3		
4	Conv.	1750	4	15	3.25	96.9	580 ± 129	
4	Conv.	1800	5	15	3.28	97.9	574 ± 120	
5	Conv.	1750	4	15	3.06	91.3		
5	Conv.	1800	5	15	2.80	83.7		
5	GPS	1850	2	100				
		1900	1	300	3.16	94.4		
6	Conv.	1800	5	15	2.83	86.0		
6	GPS	1850	2	100				
		1900	1	300	3.28	99.6		
7	Conv.	1800	5	15	2.48	75.4		
7	GPS	1850	2	100				
		1900	1	300	3.26	99.0	339 ± 51	3.85 ± 0.19
8	GPS	1850	2	100				
		1900	1	300	3.22	97.7		
9	GPS	1850	2	100				
		1900	1	300	3.23	99.2	673 ± 76	7.05 ± 0.06

*Samples were fired conventionally (1 atm N_2) or by a two-step gas-pressure sintering method.

MAM/MBAM compositions containing La_2O_3 and SiO_2 as sintering aids (batches 6, 7, and 8) were difficult to sinter conventionally but achieved very high densities (98 to 100%) by GPS. However, the mechanical properties (measured on gas-pressure sintered batch 7) were poor. As shown in Table 2, the fracture strength was only 340 MPa. The fracture toughness, measured by the controlled surface flaw method, was about 3.9 MPa√m. These samples are being examined for microstructural features, which may explain the cause of the low strength and toughness.

Batch 9, which used the MAM/MBAM gelcasting chemistry and contained yttria and alumina sintering aids, reached high density by GPS and had very good mechanical properties. The density was greater than 99%, the average fracture strength was 674 MPa, and the fracture toughness was about 7.0 MPa√m. These samples are also being examined to characterize the microstructure and to determine the fracture origins.

Evaluation of these new gelcasting systems and modifications to improve the gelcasting process will continue.

2. Sintered Reaction Bonded Silicon Nitride (SRBSN) Gelcasting

The gelcasting of Si for forming SRBSN parts is being evaluated in the MAM/MBAM gelcasting systems. The initial attempts at preparing gelcast batches have been unsuccessful due to the reactivity of Si metal in the aqueous slurry. Pretreatment of the Si powder by aging in water at room and at elevated temperatures, oxidizing in air at 800°C, and partially nitriding the powder at 1200°C are methods that have been tried to passivate the powder surface and reduce reactivity. Thus far, these efforts have been unsuccessful.

In addition, batches have been prepared using isopropyl alcohol or a mixture of alcohol and water to reduce gas evolution at the Si surface. While this method helped during the milling process, gas formation was observed when the catalyst and the accelerator were added to the batch prior to casting. Further efforts will be required to determine the best possible processing conditions for preparing gelcast silicon.

3. Alumina Gelcasting

An alumina batch was prepared and gelcast using the MAM/MBAM system. The alumina powder used was Reynolds RCHP DBM with 0.05 wt % MgO, which is a sinterable grade of alumina having an average particle size of less than 0.5 μm. The solids loading in the gelcast slurry was 60 vol %. The mixture had a low viscosity and was easily cast and deaired. The resulting tiles were sintered at 1500°C for 4 h and reached a density of 3.95 g/cm^3 (99.3%). MOR bars were cut from the samples for flexure strength testing. The bend strength was 527 $\pm$ 160 MPa. This compares very favorably with typical values of 300 to 450 MPa for dense, high-purity alumina. The standard deviation was quite high, and examination of the fracture surfaces revealed that the low-strength samples failed at regions of inhomogeneity, which may have resulted from poor mixing or nonuniform gelation. No evidence was observed of pores resulting from trapped air bubbles in the gelled material.

4. Alternate Gelcasting Systems - Gel Characterization

Several alternative low-toxicity gelcasting systems are being evaluated to replace the neurotoxic acrylamide system. Two, in particular, the MAM-PEG and the MAM-MBAM systems, have shown excellent promise as replacements for the acrylamide system. However, during the initial investigation of the gelation process, there is a need to characterize the gel in order to determine the physical properties that may define acceptable gels. In the past, this has been done qualitatively by visual observation and by pushing a glass rod into the gel. To obtain quantitative physical characterization of the gels, it is necessary to measure some rheological properties of the gels.

Samples of the three gels: acrylamide, MAM-PEG, and MAM-MBAM, labeled A, B, and C, respectively, were sent to the laboratories of three rheometer vendors for characterization. All three laboratories ran oscillatory experiments in both frequency sweep and amplitude (strain) sweep modes. The following parameters were

measured: G', the storage or elastic modulus; G'', the loss or viscous modulus; η^*, the complex viscosity; and *tan* δ, the damping or loss ratio (G''/G'). These measurements yield quantitative data for characterizing the gels. Two of the laboratories also carried out creep and relaxation tests on the gels.

The data showed that the gels were viscoelastic, with the elastic component being larger than the viscous component for all three gels as shown in Table 3, an abbreviated summary of some of the test results. (The values for a given gel vary somewhat from one lab to another due to variations in test conditions and the dependence of the properties on both the amplitude and the frequency of the applied strain.) The viscous component for gel C, the MAM-MBAM system, was much larger than for the other two gels as shown in Table 3 and clearly illustrated by the data plot from Lab 2, which is shown in Fig. 1.

Table 3. Characteristic properties of the gels at 5 Hz

Laboratory	Gel A	Gel B	Gel C
		G'	
		Storage or Elastic Modulus, kPa	
1	32.0	25.0	35.0
2	23.0	20.0	18.0
3	22.0	17.0	19.0
		G''	
		Loss or Viscous Modulus, kPa	
1	4.20	3.80	16.00
2	0.55	0.51	5.30
3	2.10	2.10	6.00
		tan δ (G''/G')	
		Loss or Damping Ratio	
1	0.131	0.152	0.457
2	0.024	0.025	0.279
3	0.095	0.123	0.316

Figure 2 (also from Lab 2) compares G', the elastic moduli for the three gels, at varying frequencies. The elastic moduli for gels A and B show negligible variation over the frequency range, while that of gel C shows a wide variation. This implies that gels A and B are well crosslinked compared to gel C, which has a much lower level of crosslinking. This result agrees well with the qualitative observations and with the level of crosslinking monomers actually incorporated into the original

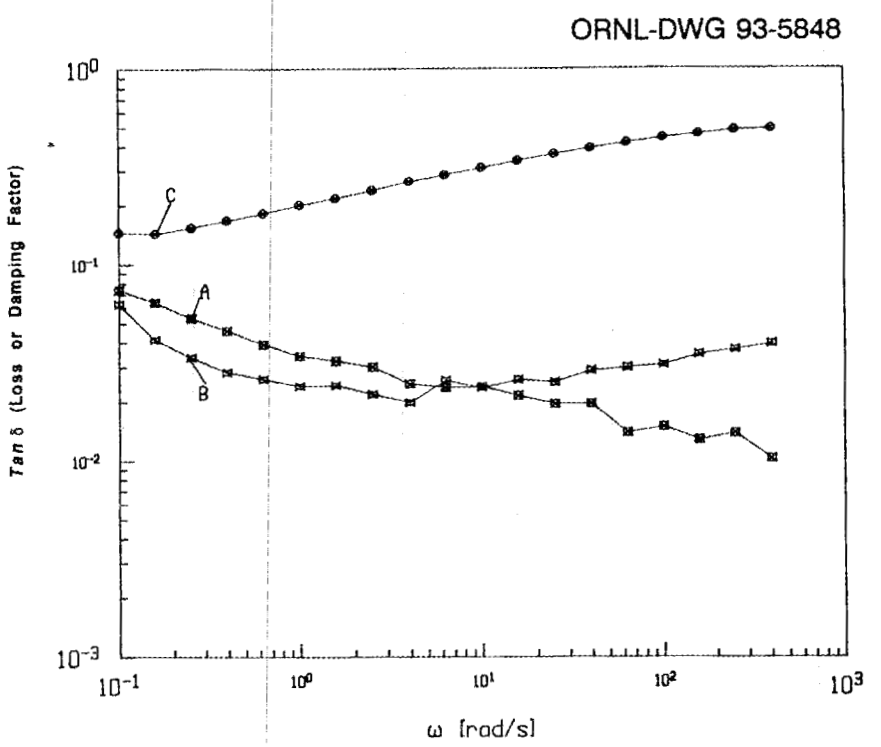

Fig. 1. Comparison of *tan* δ in frequency sweeps.

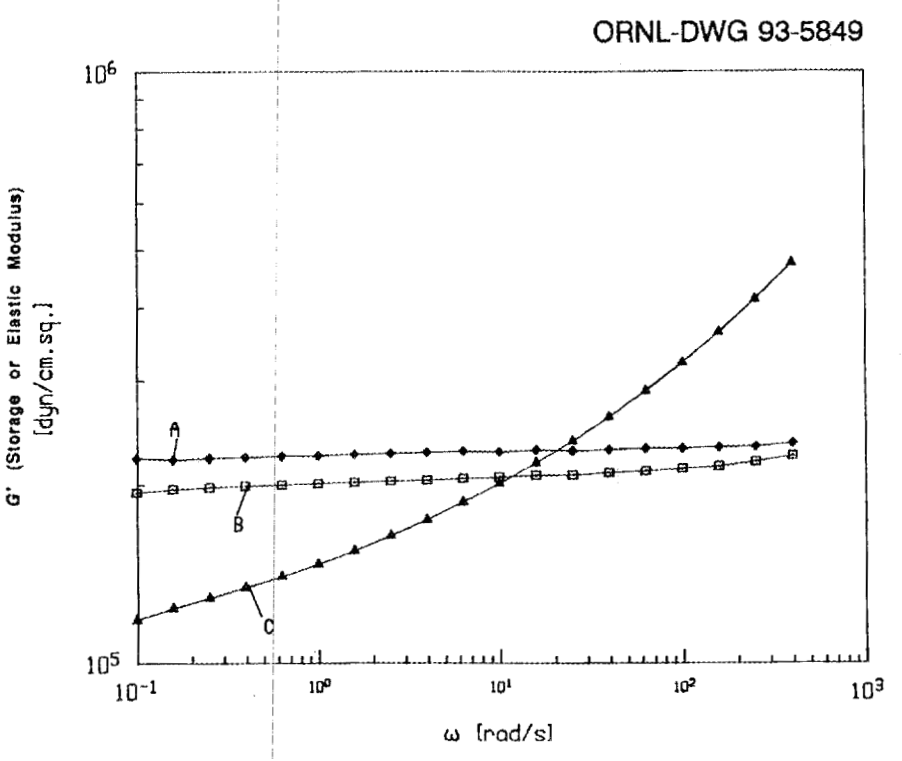

Fig. 2. Comparison of *G'* in frequency sweeps at room temperature.

monomer solutions. The test results indicate that an appropriate rheometer may be used to characterize the gels, thus enabling the quantitative selection of gels for alternative low-toxicity systems.

5. Garrett Cooperative Research and Development Agreement (CRADA)

As a follow-on to the previous Collaborative Research Agreement (CRA) between ORNL and Garrett Ceramic Components (GCC), work on the gelcasting of silicon nitride components will continue under an extension of the CRA. Research under the previous agreement demonstrated the feasibility of using gelcasting to produce complex-shaped components (automotive turbocharger rotors) using GCC's GN-10 Si_3N_4 composition. Mechanical property testing showed that gelcast Si_3N_4 could be produced that had mechanical properties comparable to GCC's slipcast Si_3N_4. Under the new agreement, ORNL will incorporate one of the new gelcasting chemical systems that has improved environmental, safety, and health ratings. (Previous work was done in the acrylamide system. The acrylamide monomer has a high toxicity rating.) Work will focus on achieving low-viscosity slips containing high-volume fractions of Si_3N_4 powder and on complete removal of the organic materials during binder burnout. Garrett will fire gelcast samples using glass-encapsulation hot isostatic pressing and measure the mechanical properties.

Binder burnout - One of the new gelcasting systems being evaluated is the MAM and the crosslinking agent polyethylene glycol dimethacrylate (PEG DMA). A sample of the dried MAM/PEG gel was examined using thermogravimetric analysis to determine the temperatures when decomposition occurs. As shown by the plot in Fig. 3, the weight loss curve exhibits sharp inflections (rapid changes in the rate of weight loss) at about 170 and 355°C. These temperatures will be used to help establish an efficient binder burnout schedule for removing the polymers from parts cast using this gel system.

Status of milestones

On schedule

Publications and presentations

O. O. Omatete, "Rheology of Zirconia-Alumina Gelcasting Slurries," presented at the 1992 Spring Meeting of the Materials Research Society, San Francisco, California, April 27 - May 1, 1992.

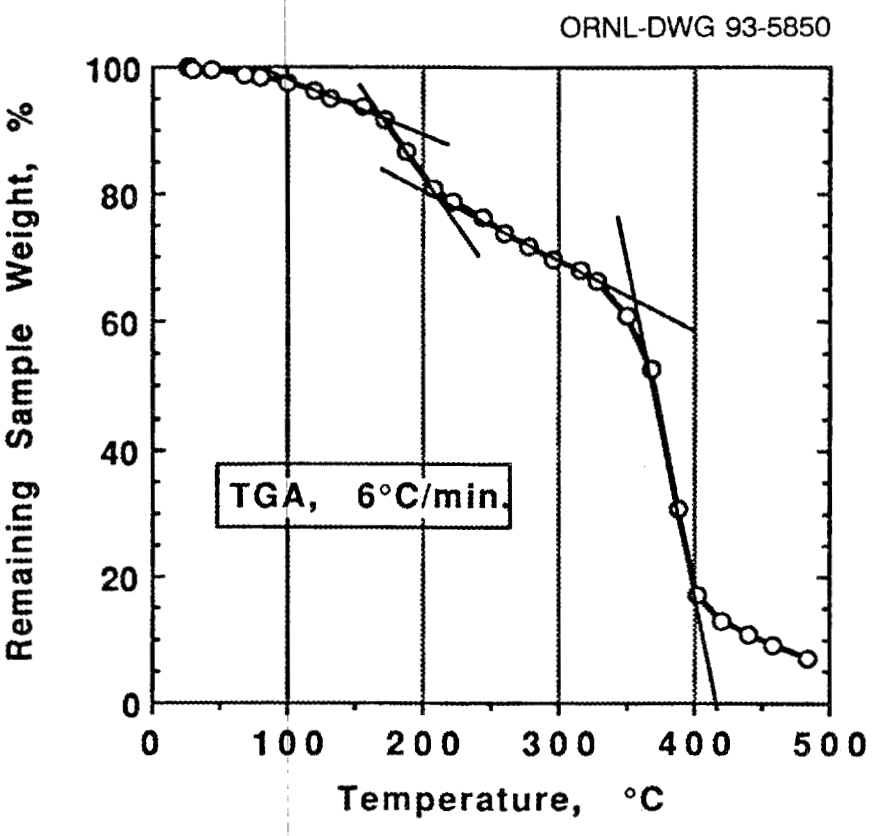

Fig. 3. Thermogravimetric analysis (TGA) of the decomposition of a dried monomer methacrylamide/polyethylene glycol (MAM/PEG) gel.

Rheology and Particle Packing of Chem- and Phys-Adsorbed, Alkylated Silicon Nitride Powders

T. Kramer and F. F. Lange (University of California)

Objective/scope

Three alcohols with extended carbon chain lengths between ≈ 1 to 2 nm were chem-adsorbed on a Si_3N_4 powder by reacting with hydroxyl surface groups at temperatures ≤ 200 °C. Slurry rheology, particle packing density and body rheology were determined for toluene and dodecane slurries formed with these chem-adsorbed powders. These same properties where determined for slurries where the alcohol was simply added, but not reacted with the powder (phys-adsorbed powders). The viscosity of chem-adsorbed slurries are shear-thinning with longer chains producing lower viscosities at a given shear rate. The relative density of powder compacts produced by pressure filtration (10 MPa) was high (~ 0.60) for octadecanol and dodecanol reacted powders, and lower (~ 0.50) for the octanol reacted powder. When a sufficient amount (> 10 times that required for chem-adsorption) of the same alcohol was simply added to the unreacted Si_3N_4 slurry system, the phys-adsorbed slurries exhibited similar rheological behavior as the chem-adsorbed slurries, but unlike chem-adsorbed slurries, their packing density was lower and their slurries were de-stabilized by water vapor. Stress relaxation experiments showed that bodies formed with the octadecanol chem-adsorbed powders where plastic after consolidation, whereas phys-adsorbed bodies were brittle (fractured before flow). All evidence suggests that the short chained alkyl groups are steric 'stabilizers' at small interparticle distances, and thus prevent the particles from making surface-surface contact in common organic liquids, i.e., they produce a short-range interparticle, repulsive potential. Chem-adsorbed molecules, but not phys-adsorbed molecules, persist during particle packing and in moist environments.

1. Introduction

It has been shown [1,2] that weakly attractive interparticle potentials can be achieved in aqueous alumina slurries by adjusting the pH to produce a highly repulsive interparticle potential (pH $\leq$ 4) and adding a large concentration of an indifferent electrolyte. When the electrolyte is added, the counterions diminish the magnitude of the repulsive, long-range electrostatic potential and produce a short-range, repulsive potential not suggested by classical Derjaguin-Landau-Verwey-Overbeek (DLVO) theory.[3] When the salt concentration exceeds a critical value, [1,2] known as the critical coagulation concentration (CCC), the initially dispersed particle network becomes attractive. Above the CCC, the yield strength of the particle network increases with salt content until a concentration where further additions have no further effect. [2] The short-range repulsive potential due to added salt has been confirmed with sapphire plates in the surface force apparatus by Ducker et al. [4] The short-range interparticle potential is currently believed to be due to a hydrated layer similar to that found for mica surfaces [5] and suspected for clay surfaces. [6]

Pressure filtration and centrifugation studies show that alumina bodies produced with slurries where particles are attractive, but non-touching exhibit high particle packing. [1,7] It appears that the short-range repulsive forces can act as a 'lubricant' to aid in the rearrangement process required for particle packing. [8] Due to the attractive nature of the interparticle potentials, bodies can be formed by centrifugation without mass segregation [9] as recently demonstrated by the processing of unique multi-layered transformation toughened composites. [10] In addition, bodies formed from coagulated slurries exhibit plastic-like body rheology [11] and can be reshaped. In many respects, coagulated slurries and the bodies they form can have rheological characteristics similar to clay systems.

Recent rheology and particle packing studies [12] with aqueous Si_3N_4 slurries exhibiting an isolectric point at pH 6 show that an indifferent electrolyte can produce similar effects as observed for alumina slurries when the Si_3N_4 surface has a net positive charge density (low pH), but not when the surface has a net negative charge density (high pH). In addition, although the short-range repulsive potentials appear to be present in the slurry state, they disappear during particle packing, viz., the saturated, Si_3N_4 bodies crack before they plastically deform.

We have considered using the steric effect of very small adsorbed molecules as a second means of producing a short-range repulsive potential. It is well known [3] that large adsorbed macromolecules can produce long-range repulsive interparticle

potentials. It is also well know that the macromolecules are much more effective when they are strongly attached, e.g., chemically bonded (chem-adsorbed), to the surface rather than weakly bonded, e.g., hydrogen bonded (phys-adsorbed). Thus, adsorbed molecules that are short enough to allow particles to be attractive due to their van der Waals potential, but sufficiently long enough to keep particles from touching and thus falling into a deep potential well, are expect to produce the weakly attractive particle network found for the salt added, alumina slurries. We chose to demonstrate this concept by using the reaction of different alcohols with -M-OH surface groups, a method patented by Iler [13] for grafting carbon chains to the surface of silica particles for lubrication applications. Since Iler's work, both methanol and ethanol were reported [13] to produce some "additional stabilization" preventing particles from coalescing or to form weak instead of hard agglomerates.

Other short, adsorbed molecules have been reported to produce effects suggesting the presence of a short-range repulsive potential. Johnson et al. [14] note that oleic acid or steric acid adsorbed onto an alumina surface do not produce stable non-aqueous dispersions but reduce the viscosity of the slurry relative to uncoated powders. Since these molecules are not long enough to produce a stable dispersion by steric stabilization, they term this the 'semi-steric effect'. They attribute this 'semi-steric effect' to a decrease in the apparent energy minimum because the bound molecules prevent the surfaces from touching and to a reduction in the effective Hamaker constant as described by the Vold model [15]. Bergström et al. [16] have shown that a series of adsorbed fatty acids that increase the steric barrier thickness from ≈ 0.7 nm to 2.5 nm, can progressively increase the maximum particle packing density. A variety of adsorbed, potential-determining counter ions (sulfate to citrate anions) are believed to produce short-range steric effects [17] responsible for decreasing the yield strength of aqueous, ZrO_2 slurries. [18]

As we show below, alcohols, both chem- and phys-adsorbed on Si_3N_4 particles, produce short-range repulsive effects in non-aqueous slurries that are proportional to their molecular length. Only the strongly bonded, chem-adsorbed molecules persist in a moist environment and during particle packing. Chem-adsorbed molecules produce high particle packing and a plastic body rheology, whereas, phys-adsorbed molecules produce a lower particle packing and a brittle body.

2. Experimental Procedure

2.1 Preparation of Chem- and Phys-adsorbed Si_3N_4 Slurries

Two silicon nitride powders, manufactured by the same company and denoted as E-3 and E-10 [a], were used in this study. Two different lots of the E-3 powder were used for different experiments. Each had a different maximum packing density, but they could not be distinguished by other properties. Nitrogen adsorption [b] and the BET equation was used to determine the surface area (5 and 14 m^2/g, for the E-3 and E-10 respectively). Both powders appeared chemically similar (viz., identical pH of the iso-electric point), the higher specific surface area of the E-10 powder was necessary for the infrared spectroscopy. The alcohols (octanol, dodecanol, and octadecanol) were used as-received. Toluene and dodecane were used either as-received or recycled after distillation.

To produce chem-adsorbed silicon nitride powder, the powder and alcohol were mixed together (with a weight ratio of 1:1) and reacted in a three-neck flask outfitted with a nitrogen supply line, a thermometer, and a gas-exit line equipped with a bubblier. During the reaction, nitrogen flowed through the flask to prevent oxidation and carry away water, the expected reaction product. The flask was heated (± 2°C) with a mantle and controller connected to a thermocouple placed between the heating mantle and the flask. The reactants were heated for 2h at temperatures between 150°C and 200°C. After cooling, the powder was rinsed with toluene to remove unreacted alcohol. Rinsing was done with a Soxhlet extractor, followed by vacuum drying at 100 °C. The second batch of E-3 powder, used for body rheology determinations, was rinsed 3 times with isopropanol to remove unreacted alcohol, centrifuged after rinsing, and dried in an oven at 60 C for 24 h.

Chem-adsorbed slurries were formed by untrasonicating [c] the alkylated powders with dodecane (or toluene) and placing them on a shaker table for at least 16 hours. Most slurries were formulated to contain 20 volume percent Si_3N_4 powder.

Phys-adsorbed slurries were prepared by simply ultrasonicating and shaking the powder-toluene (or dodecane) slurries with a given weight fraction of alcohol (based on Si_3N_4 content) without heating. For TGA and FTIR spectroscopy experiments, the phys-adsorbed slurries were also rinsed to determine if the alcohol could be remove.

Si_3N_4-dodecane slurries that did not contain either chem- or phys-adsorbed alcohols were prepared by mixing both constituents. These slurries, termed flocced, were too viscous to ultrasonicate; they were stirred with a spatula and then shaken for at least 16 hours.

The extent of reaction and the effectiveness of rinsing was evaluated by TGA[d] weight loss measurements at 5°/min. Samples (100 mg) were loaded into the platinum pan of the TGA with a counter-balance of 100 mg added so that the system was nearly

perfectly balanced. If a two-step weight loss was observed (observations suggest that phys-adsorbed alcohol desorbes at a lower temperature relative to the pyrolysis of chem-adsorbed species) the sample was re-washed before repeating the experiments. Weight loss experiments were also carried out with as-received silicon nitride powder to obtain baseline data.

2.3 Infrared Measurements

FTIR spectroscopy [e] was used to test the hypothesis that the alcohol chemically attaches to the surface during the heat treatment. A sample of the E-10 powder was reacted with octadecanol (200°C/2h) and a second sample of E-10 was simply mixed in a solution of octadecanol and toluene to phys-adsorbed the alcohol onto the surface. Both of these samples were then washed by repeated rinsing and decanting with toluene. This washing was expected to remove the phys-adsorbed but not the chem-adsorbed species. Each were prepared for the IR spectrometer by grinding the washed powders with KCl powder before consolidating them under vacuum with a bolt press; all were uniformly translucent and gave an acceptable signal in the FTIR spectrometer.

2.4 Rheological Measurements

To understand the role played by the three different chem-adsorbed carbon chains in modifying the interparticle interaction, the viscosity vs shear rate behavior of each slurry was measured in a constant stress rheometer [f]. A cone and plate geometry (diameter = 5.0 cm, angle = 0.04 rad) was chosen because the stress-range of the instrument and slurry were compatible. Measurements were performed by placing ≈ 1 ml of slurry on the bottom plate and lowering the cone into place. Preliminary tests were run to determine the proper stress range for the sample. The sample was then pre-sheared at 1000 s^{-1} for 30 s. A stress ramp (from 0 to τ to 0, where τ is the stress required to produce a shear rate of at least 1000 s^{-1}) was then applied to the sample and the rate recorded as a function of both increasing and decreasing stress. Only octadecanol, which produced the weakest particle network, was used to compare the rheology of chem- and phys-adsorbed slurries. Phys-adsorbed slurries were prepared by mixing 0.5, 1, 2, and 5 wt % of octadecanol with the Si_3N_4 (20 vol %) in dodecane. These slurries were equilibrated for at least 16 h and then remixed immediately before rheological measurements. The viscosity of the flocced slurries (no added alcohol) was too large for similar measurements.

The effect of temperature on slurry rheology was also examined. After applying a stress-loop to the slurries at room temperature, they were cooled to either 5 or 10°C

were another stress-loop was applied, and then the temperature raised to ambient for a third measurement. For some samples, the excursion to lower temperatures was repeated. Condensed water was observed on the tool during the first runs. A nitrogen purge was used to prevent condensation and a comparison made between the purged and un-purged samples.

The rheology of the consolidated bodies were determined with stress relaxation experiments were performed within a servo hydraulic mechanical testing machine [g]. Only bodies consolidated with chem- and phys-adsorbed octadecanol slurries, as well flocced slurries, were examined; the second batch of E-3 powder was used for these experiments. Details of the test are described elsewhere. [11] Because dodecane has a very low vapor pressure relative to water, unlike experiments described for water saturated, consolidated bodies, it was not necessary to contain the dodecane saturated consolidated bodies in a plastic bag to prevent evaporation during testing. After the consolidated body was placed on the bottom platen, the piston was carefully raised to bring the top portion of the consolidated body in contact with the upper platen. A small compressive load of 0.5 to 2 N was applied to the sample to ensure that both platens were in good contact with the specimen.

An experiment consisted of applying a 2% compressive strain at a relatively rapid strain rate of 2 sec^{-1}. After attaining the 2 % strain, the cross-heads were fixed and the relaxation stress was recorded with time. The stress was calculated assuming that the area of the specimen did not change during straining. Each experiment was terminated after ≈ 20 minutes. After the applied load was relaxed to zero by lifting the loading platen, a second experiment was conducted by applying a second strain of 2% to the same specimen.

2.4 Pressure Filtration

The pressure filtration device detailed elsewhere [19] was constructed of stainless steel and consisted of a cylinder with a sintered filter at one end and a movable plunger sealed to the wall with an o-ring at the other. In operation, a Teflon membrane filter (0.2 μm pores) covered the partially dense, stainless steel filter and trapped the particles. Pressure was applied with a hand-operated press [h] and consisted of an initial low-pressure segment until the plunger motion ceased (≈10 minutes) after which pressure was increased to 10 MPa. Consolidation was estimated to be complete after the pressure would remain constant for a period of 10 minutes. Immediately after the consolidated body was removed form the die cavity, its dimensions were measured and it was weighed. Bodies prepared for density measurement were dried at room

temperature in a hood. When the sample ceased to lose weight (typically 1 day), the final weight was recorded. The initial and final weights were used to calculate the particle packing density within the saturated body assuming the body consisted of two components: silicon nitride and dodecane (or toluene) with known densities.

3. Results

3.1 Extent of Reaction

Table 1 shows the results from the TGA weight loss for the E-3 powder. The chemically bound organics pyrolyzed at ~ 250°C, while phys-adsorbed organics were removed at ~ 150°C. The values of weight-loss were near the precision of the thermal analysis system and the smallest are just above the weight loss observed for the as-received powder. For this reason, the determination of the surface site density of akly chains is not accurate. However, it is clear that the alcohols with the higher molecular weights produce the largest weight loss during pyrolysis. In addition, reacted and washed powder were very hydrophobic, whereas phys-adsorbed and washed powders became hydrophilic.

Figure 1 shows the IR spectrum of E-10 powder after reaction with octadecanol. Absorption bands (2850 cm^{-1}) indicative of hydrocarbon chains of moderate to high molecular weight can be seen. For comparison, the spectrum from a phys-adsorbed and rinsed sample showed that these absorption bands are absent, indicating that phys-adsorbed alcohol is easily removed from the surface. This comparison is a strong indication that, in the reaction process, stronger chemical bonds form between the surface and the alkyl chain. [Note that the absorption bands between 2400 and 2300 cm^{-1} are the result of atmospheric CO_2.] In addition, the washed, reacted powders were strongly hydrophobic, whereas the washed, phys-adsorbed powders were hydrophilic.

3.2 Relative Density via Pressure Filtration

Table 2 shows that the molecular weight of the alcohol had a strong influence on the particle packing density produced by pressure filtration, viz., packing densities produced by either chem-adsorbed octadecanol and dodecanol were ≈ 60 % of theoretical, whereas chem-adsorbed octanol only produced a packing density of ≈ 50 %. These data suggest that a chain length for the chem-adsorbed species must > ~ 1 nm to achieve a high particle packing density.

Relative density data for chem- vs phys-adsorbed (5 weight %) octadecanol and for flocced slurries were obtained for the second lot of E-3 powder and are also shown

Table 1

Summary of thermal analysis results for various reaction products.

Alcohol	TGA weight loss (%)	Molecular weight (g/mole)	length* nm
Octadecanol	0.17	270.5	2.3
Dodecanol	0.15	186.3	1.5
Octanol	0.07	130.2	1.0
none	0.05		

* extended bond length calculated assuming a bond length of 0.154 nm and a bond angle of 110°.

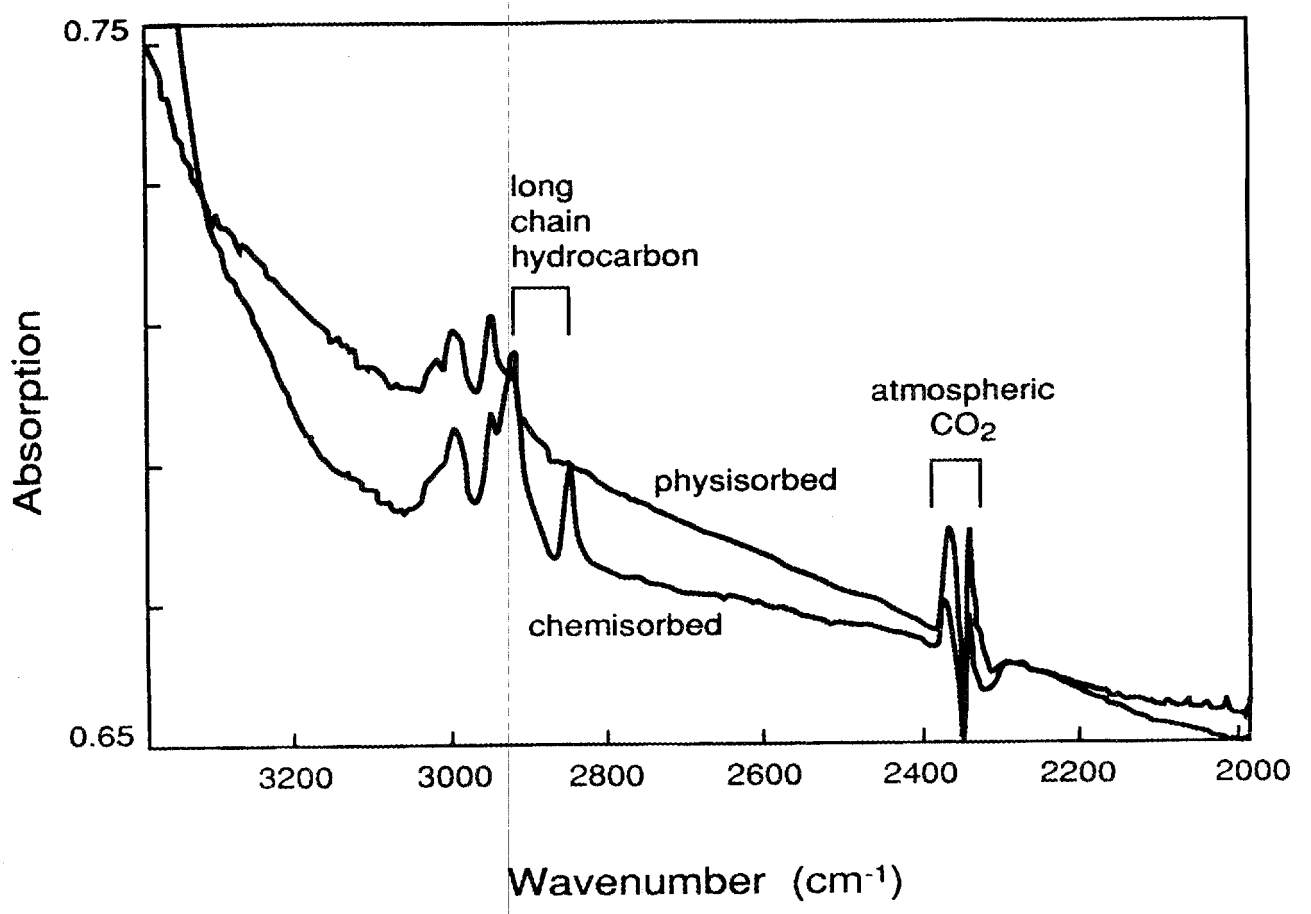

Figure 1. IR spectra of Si_3N_4 powders, one reacted with octadecanol and another simply mixed with octadecanol (5 wt %, relative to powder). Both have been repeatedly rinsed with toluene. The peak at 2850 cm^{-1} is the result of the chem-adsorbed alkyne.

Table 2
Rheology and processing results for chem- and phys-adsorbed slurries containing 20 volume % Si_3N_4 in Dodecane.

Alcohol	Chem- or Phys-Absorption	Bingham Yield Stress (Pa)	Relative Density ***
Octadecanol	chem-	2.0	60
Dodecanol	chem-	5.3	59
Octanol	chem-	80	51
Octadecanol	phys- (1%)*	20**	--
Octadecanol	phys-(2-5%)*	8	53** (5%)*
Octadecanol	chem-	2	55**
none	---	--	48**

* weight % of alcohol added relative to Si_3N_4 powder

** second lot of Si_3N_4 powder

*** Pressure Filtration, 10 MPa

in Table 2. It can be seen the relative packing density of the chem-adsorbed slurry is ≈ 5 % lower relative to the first lot of powder. In addition, the packing density of the phys-adsorbed powder is between that of the chem-adsorbed and flocced slurries of this same powder lot.

3.3 Rheological Measurements

Both toluene and dodecane produced identical results. Without any alcohol, Si_3N_4 and dodecane mixtures formed thick pastes for volume fractions examined (≥ 0.20). Namely, without either chem-absorbed alcohol or sufficient concentrations of phys-adsorbed alcohol, the Si_3N_4 particle networks were strongly attractive; their viscosity was too high to be measured with the current instrument (slippage would occur at either the cone or plate before slurry flow. Slurries with sufficient fluidity for viscosity measurements could be prepared with either chem-adsorbed or sufficient phys-adsorbed alcohols. Figure 2 shows that slurries formed with powders that were chemically reacted with the specified alcohols exhibited a shear-thinning behavior. The lower the molecular weight of the reacted alcohol, the higher the viscosity at a given shear rate. Table 2 lists the Bingham yield stress determined from this same data by extrapolating the stress vs shear rate data to zero shear rate. Note that the yield stress scales inversely with the chain-length of the reactant alcohol.

Stress vs strain–rate data for different phys-adsorbed, octadecanol-toluene slurries are shown in Fig. 3a. Similar data, illustrated as viscosity vs shear rate are shown in Fig. 3b for the second lot of E-3 powder as dodecane slurries. This data shows that the behavior of powders mixed and equilibrated with ≈ 1.5 to 5 weight % of phys-adsorbed octadecanol are similar, suggesting that the ≈ 2 weight % octadecanol is sufficient to cover the surface of the powder, and to be in equilibrium with octadecanol in solution. These figures also show that a much smaller concentration of chem-adsorbed alcohol produced a lower viscosity at any shear rate, viz., the chem-adsorbed network was much weaker relative to the phys-adsorbed network. The rheology of powders mixed and equilibrated with the 0.5 weight % octadecanol could not be measured with our instrument due to their very high viscosity.

The rheology of selected chem- and phys-adsorbed slurries were examined over the temperature range of 5 to 25°C. No significant changes were observed for chem-absorbed slurries under any condition. However, Fig. 4 shows the effect of temperature excursions on the stress vs strain–rate behavior of the phys-adsorbed toluene slurry prepared with 5 weight % octadecanol. These temperature excursions were done in air; water was observed to condense on the apparatus. As shown, the

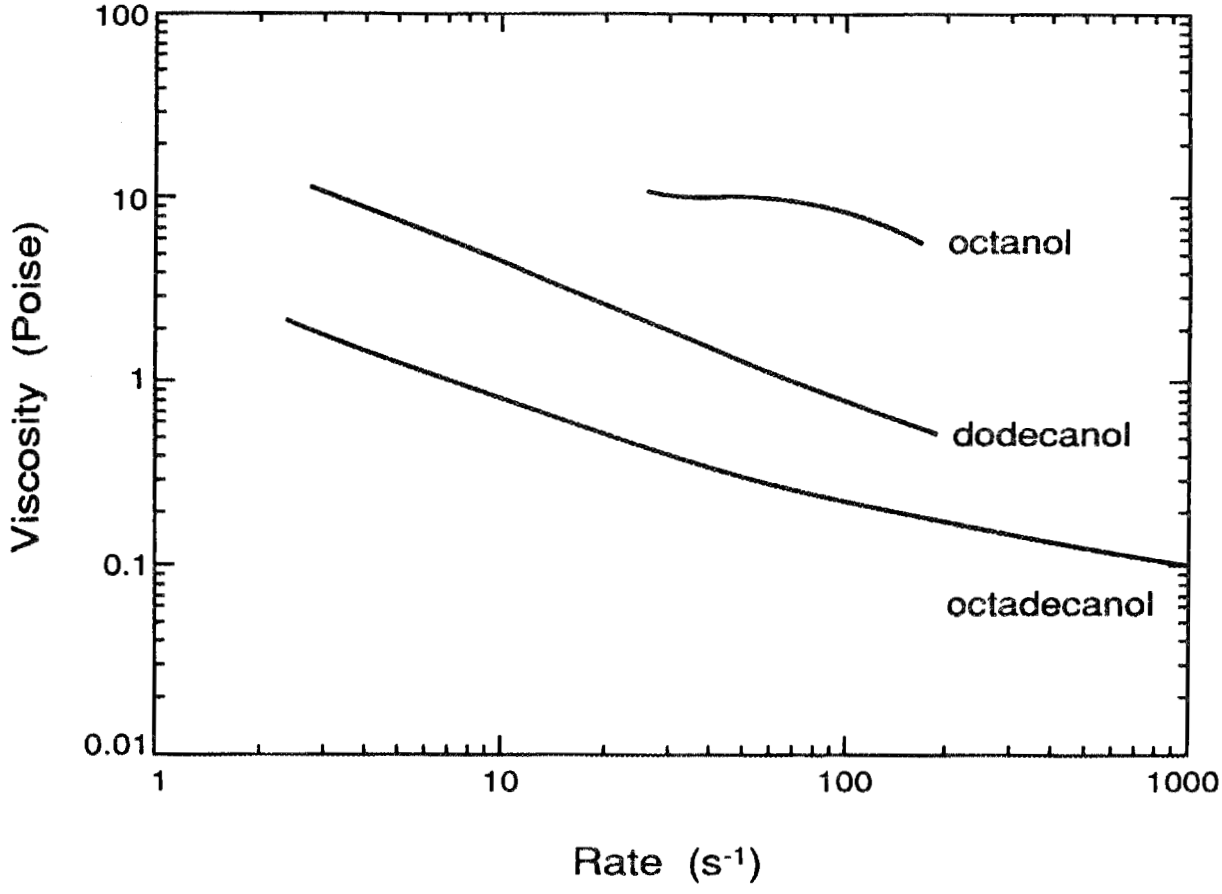

Figure 2. Viscosity of Si_3N_4-toluene slurries from alcohol-reacted powders with the labeled surface treatments.

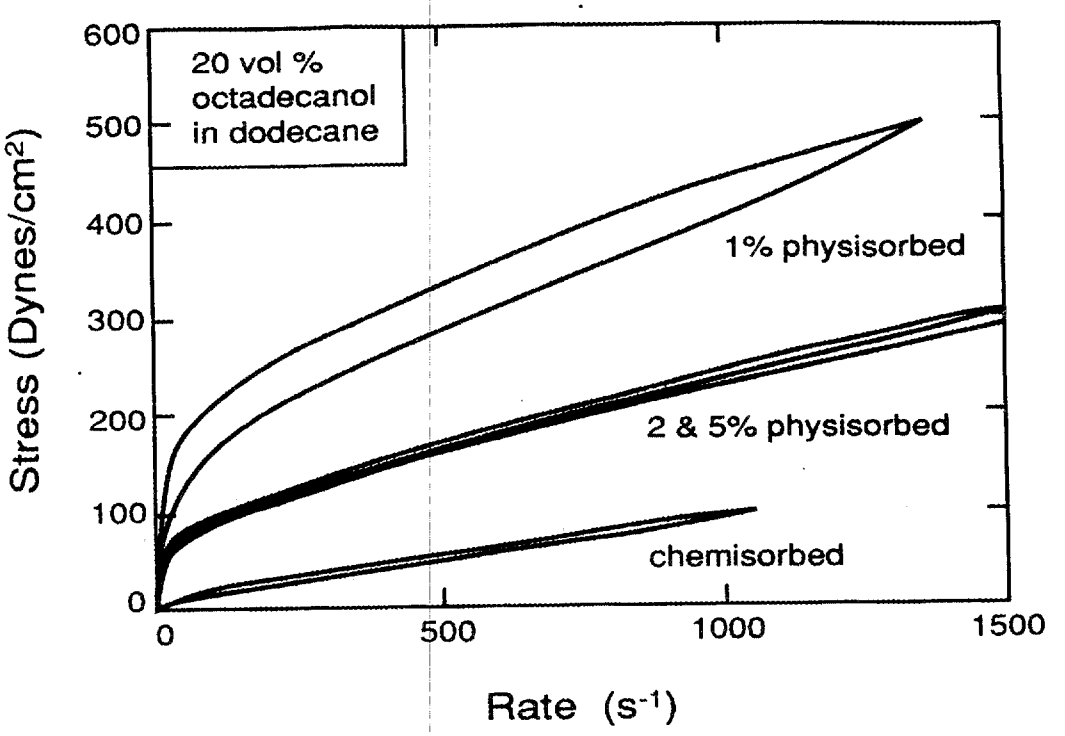

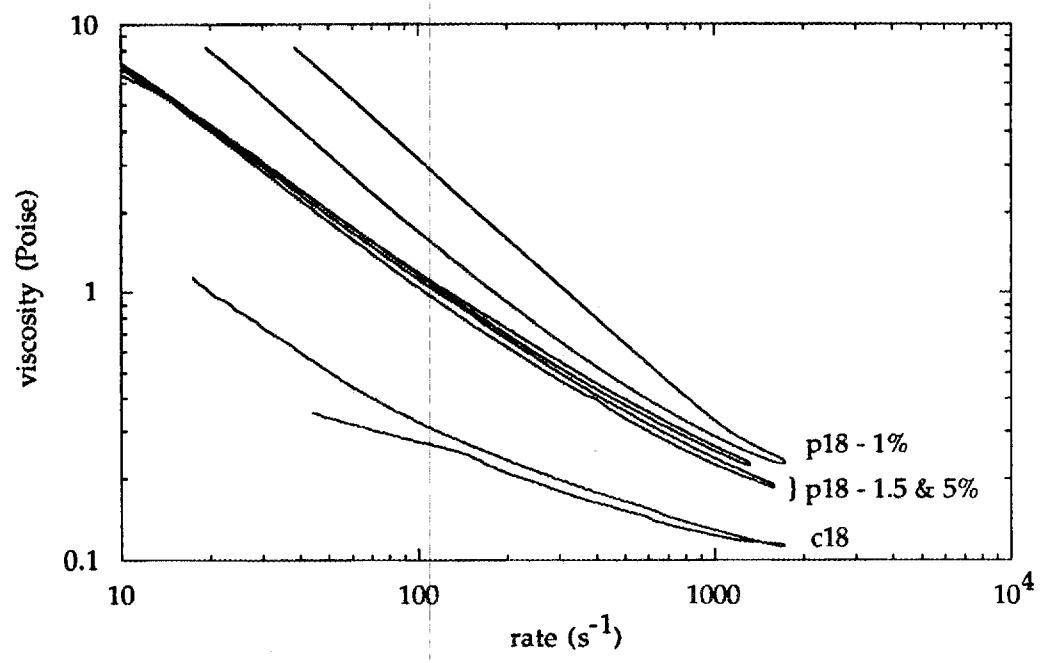

Figure 3. Rheology of Si_3N_4-dodecane slurries comparing chem- and phys-adsorbed octadecanol. a) Shear stress vs strain rate illustrating different Bingham yield stresses. b) Viscosity vs strain rate date for second lot of E-3 powder.

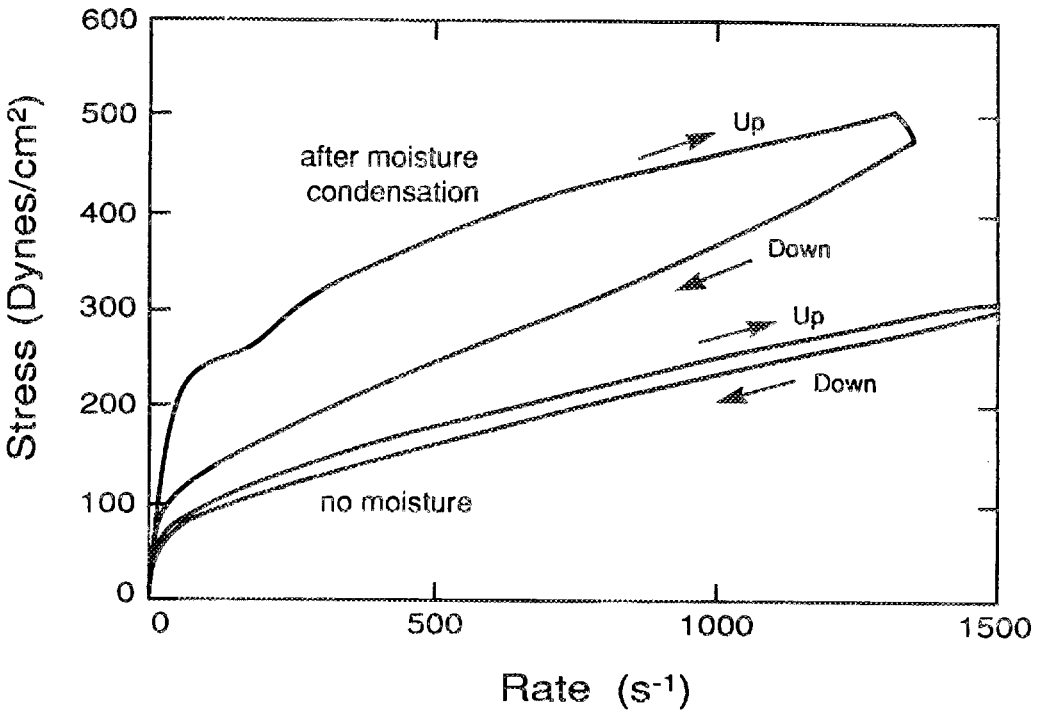

Figure 4. The effect of water adsorption on 5% phys-adsorbed powder. Lower curve is obtained prior to water exposure, upper curve illustrates change due to water exposure.

phys-adsorbed slurries were strongly affected by condensed water during these excursions. When a nitrogen purge was used to protect the samples from condensation, these changes were not observed.

Figure 5 illustrates typical stress relaxation data for consolidated bodies formed with a) chem-adsorbed octadecanol, b) 5 weight % phys-adsorbed octadecanol and c) flocced slurries formulated with the second lot of E-3 powder as dodecane slurries. As shown, bodies formed with chem-adsorbed slurries are plastic, viz., rapidly relax the applied stress. The yield stress (retained stress after an extensive relaxation period) for both phys-adsorbed and flocced bodies is a significant fraction of the applied stress required to achieve 2 % strain. The cracked body shown in Fig. 6 is typical of both the phys-adsorbed and flocced bodies observed after the stress relaxation experiment (portions of the cracked body removed), i.e., these bodies were brittle.

4. Discussion

4.1 Estimating Interparticle Potentials

To estimate the effect of adsorbing small molecules onto the surface of silicon nitride, the van der Waals potential was calculated as a function of interparticle separation distance using the methodology developed by Hough and White [20] with the optical properties of silicon nitride [21, 22] and dodecane [20]. These calculations assume that the Hamaker constants of the adsorbed species are identical to the solvent; the effective Hamaker constant for Si_3N_4 in dodecane calculated to be $A = 4 \times 10^{-20}$ J. Using the short-range approximation ($h << a$) for the van der Waals potential (E):

$$E = -\frac{A}{12}\frac{a}{h}, \qquad (1)$$

where a is the particle radius and h is the surface to surface separation distance.

Figure 7 shows a plot of this calculated potential as a function of distance from the surface for a pair of 0.4 μm diameter particles. Twice the length of octyl, dodecyl and octadecyl chains are marked on the plot, representing the separation distance where fully extended adsorbed molecules on approaching particles would begin to interact. As shown in Fig. 7, the length of each molecule is too short to produce a long-range repulsive interparticle potential, viz., the van der Waals potential is strong enough to cause the particles to be attractive before the molecules interact. With the assumptions that a) the work done by the van der Waals forces is insufficient to remove

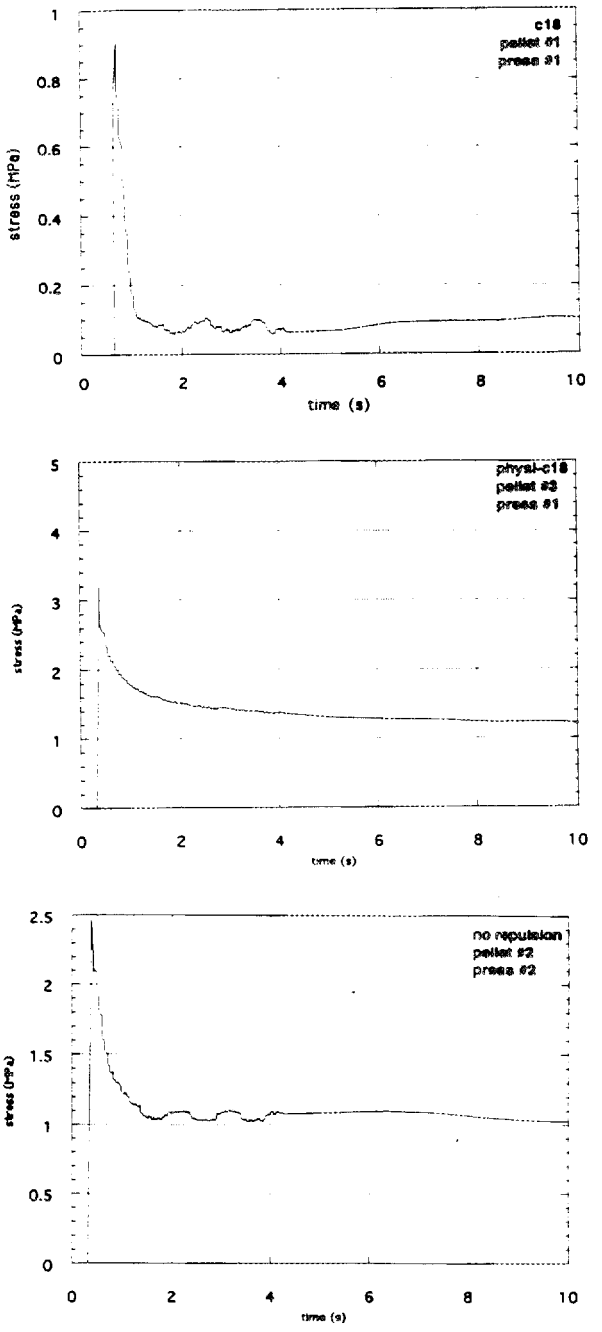

Figure 5 Stress relaxation after consolidated body was strained to 2 % for a) plastic behavior for body consolidated from chem-adsorbed, octadecanol, dodecane slurry, b) body formed with phys-adsorbed octadecanol, dodecane slurry, and c) body formed with flocced, dodecane slurry (no alcohol). Bodies in latter two figures are brittle (crack before flow-see Fig. 6).

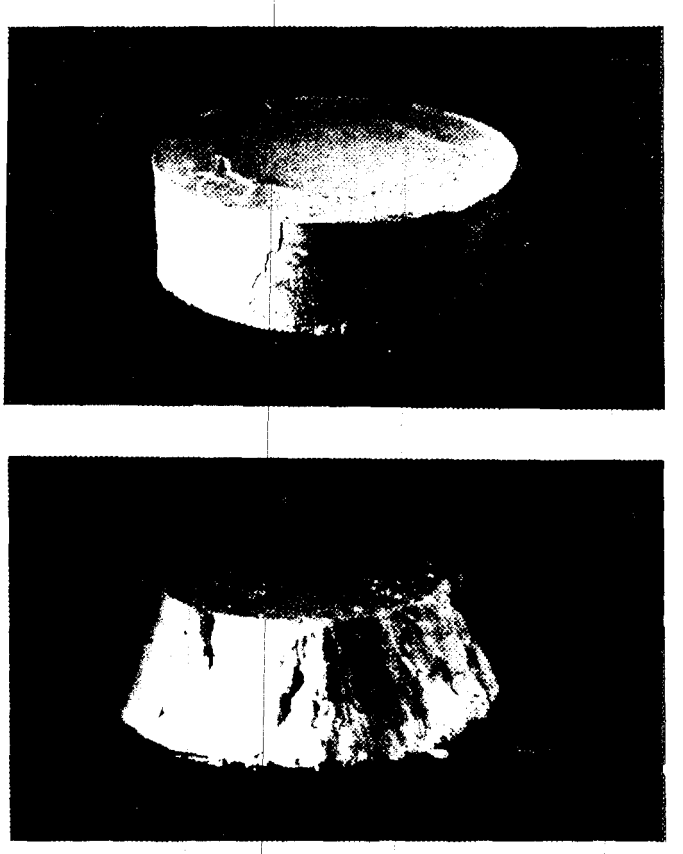

Figure 6 Cracks observed after stress-relaxation experiments in bodies produced with a) phys-adsorbed (octadecanol) and b) flocced (no alcohol), Si_3N_4-dodecane slurries. Portions of body in b) are removed to show fractured body. Both bodies are brittle, viz., fracture before flow. (Diameter of pressure filtered bodies are 25 mm).

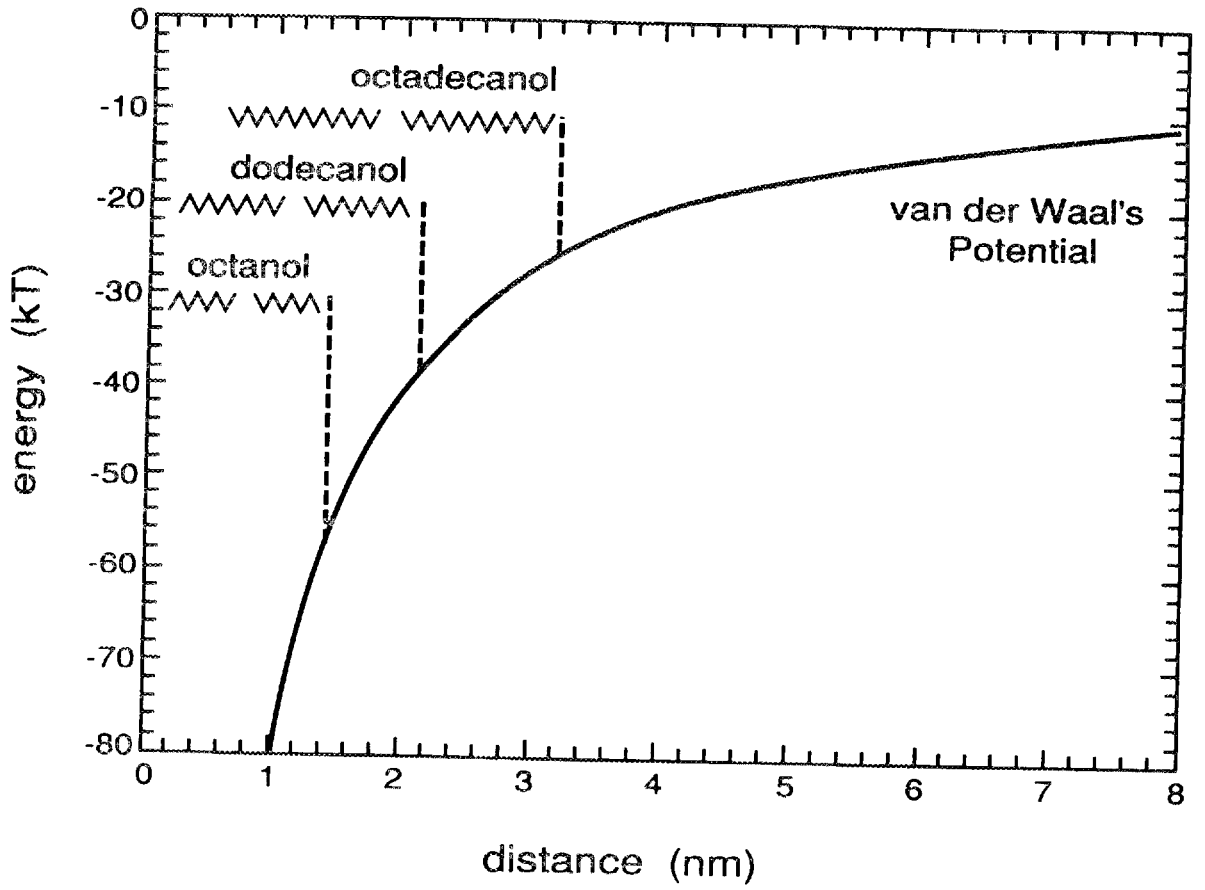

Figure 7. Interaction potential between two silicon nitride particles in dodecane as a function of their separation distance. The calculation assumes 0.5 μm spherical particle and uses the short-range approximation for van der Waals potential. The depth of the potential well due to the steric effect chem-adsorbed hydrocarbon chains studied here are shown with two extended molecules for each of the three alcohols studied.

the adsorbed molecules as the particles approach one another and b) the equilibrium particle separation distance due to the short-range repulsive potential produced by the molecules is proportional to twice the extended chain length, it is clear that for this size range of molecules, small differences in molecular chain length translates into large differences in the depth of the potential well were particle reside due to the attractive van der Waals potential.

Figure 7 suggests that adsorption of any of the alcohols studied here will produce an attractive, but non-touching particle network, where the depth of the potential well, and thus the network strength, will be inversely proportional to the molecular weight of the adsorbed organic chains. This simple model suggests that the short-range repulsive potential might be varied by changing the molecular weight of an adsorbate. Because an attractive particle network forms, it is expected that the slurries will shear thin (work is required to break apart the attractive particle network) and that the viscosity at any given shear rate will be inversely proportional to the depth of the potential well (the maximum force required to separate the particles, determined from the differential of the potential curve, increases with well depth). This expected rheological behavior is observed: all slurries are shear thinning and slurries with higher molecular weight adsorbents had lower viscosities.

4.2. Particle Packing Density vs Molecular Weight of Adsorbed Species

Both long-range and short-range repulsive forces can be effective lubricants [1,7] for the rearrangement processes required to increase the packing density with forces applied to the particle network. In effect, repulsive forces lower the coefficient of friction between particles to allow easier rearrangement. It is known that when only attractive van der Waals interparticle potentials exist, it is difficult to achieve a high particle packing density due to the strongly cohesive particle network. [19] It can be hypothesized that the coefficient of friction between particles is proportional to the depth of the potential well in which attractive particles reside. Namely, for a given particle surface morphology, the highest coefficient of friction will exist when only van der Waals interparticle potentials exist. A short-range repulsive potential, summed with the van der Waals potential will decrease the coefficient of friction in proportion to the change in depth of the potential well. With this reasoning, one can understand why particles with reacted octyl chains pack to the lowest density, viz., as suggested in Fig. 7, octyl chains are expected to result in the deepest potential well relative to the longer chains examined. They also produce the strongest attractive particle network observed through rheological measurements.

4.3. Chem- vs Phys-adsorbed Molecules

Although slurries made from chem-adsorbed and phys-adsorbed molecules show similar shear thinning behavior, larger amounts (> 2 wt %) of alcohol are required to produce the same rheological properties as observed for the chem-adsorbed slurries (< 0.2 wt %) and phys-adsorbed slurries have higher Bingham yield stresses. The chemical bond formed during the reaction makes the chem-adsorbed samples resistant to water contamination during processing. For the phys-adsorbed species, the water appears to replace the alcohol on surface sites eliminating the short-range repulsion potential. In addition since the phys-adsorbed slurries did not pack as well as the chem-adsorbed slurries, and phys-adsorbed bodies were brittle, it appears that the compressive force between particles that exists during consolidation is sufficient to 'push' away phys-adsorbed molecules.

Although our studies only used alcohols as phys-adsorbed species, other species, such as acids or amines, may provide stronger bonds with the surface and hence short-range repulsion potentials at lower concentrations. One the other hand, the polar nature of these bonds will also make them susceptible to water as observed for the phys-adsorbed alcohol studied here. The large decrease in packing density of Al_2O_3 powders with the molecular weight of adsorbed fatty acid reported by Bergström et al [16] strongly suggests that the fatty acids were also weakly bonded to the surface and could be 'pushed' away during particle packing.

5. Summary

The surfaces silicon nitride powders react with low molecular weight alcohols at moderate temperatures and reasonable times. These reacted, chem-adsorbed powders do not form stable dispersions, but form a weakly attractive particle network in liquids in which the alcohol is soluble. Rheological and packing measurements strongly suggest that the particles are not in surface to surface contact because the short chain reaction product prevents this contact in a manner similar to the well known steric effects [2] produced by much larger, adsorbed macromolecules. Namely, the short chain molecules on the surface produces a short-range repulsive potential. We propose that the depth of the potential well in which the particles reside due to the sum of the van der Waals attractive and short-range repulsive potentials is inversely proportional to the chain length (or molecular weight) of the reaction product. For this reason, the attractive, but non-touching particle network exhibits shear thinning behavior and the strength of the network, and thus the viscosity of the slurry, is inversely proportional to

the chain length of the reaction product. High particle packing is achieved during pressure filtration when the attractive network is weak, where the short-range repulsive forces act as effective 'lubricants' required for particle rearrangement. Non-reacted, phys-adsorbed molecules can also produce weakly attractive networks with in the slurry state, but phys-adsorbed molecules due not persist in moist environments and during particle packing. A minuscule amount of chem-adsorbed alcohol is needed to produce the short-range repulsive interparticle potential; the presence of a strong chemical bond with the surface are attractive for processing, viz., slurries are not effected by moisture (do not age); The chem-adsorbed alcohols have several environmental advantages, viz., they produce very smaller volumes of gas during pyrolysis and the organic liquids used in the slurry are stable and easily purified for reused. The major by-product of the powder-alcohol reaction is water.

As expected, preliminary observations show that alkylated surfaces can be produced with most ceramic powders. The similarity of the alkylated surfaces of nearly all ceramic powders is of great technological significance. Namely, discounting large differences in the Hamaker constant for different particle chemistries, the rheology and particle packing behavior of mixed powder systems are expected to behave in a similar manner described above. In addition, the attractive nature of the mixed, particle network will prevent phase segregation [9], and will thus lead to more homogeneous mixtures, especially for systems like Si_3N_4 which requires the addition of a second phase powder to achieve densification.

Acknowledgments:

This research sponsored by the U. S. Department of Energy, assistant Secretary for Conservation and Renewable Energy, Office of Transportation Technologies, as part of the Ceramic Technology Project of the Materials Development Program, under contract DE-AC05-84OR21400 with Martin Marietta Energy Systems, Inc. The UCSB contract 86X-SE807C, was monitored by Dr. D. Ray Johnson at Oak Ridge National Laboratory.

References

1. B.V. Velamakanni, J. Chang, F.F. Lange, D.S. Pearson, "New Method for Efficient Colloidal Particle Packing via Modulation of Repulsive Lubricating Hydration Forces," Langmuir 6 p1323-5 (1990).
2. J. C. Chang, F. F. Lange and D. S. Pearson, "The Viscosity and Yield Stress of Al_2O_3 Slurries Containing Large Concentrations of Electrolyte", J. Am. Ceram. Soc. (in press)
3. R.G. Horn "Surface Forces and Their Action in Ceramic Materials," J. Am. Ceramic Society 73, p1117-35 (1990).
4. W. A. Ducker, Z. Xu, J. N. Israelachili and D. R. Clarke, "The Forces between Alumina Surfaces in Salt Solutions: Non-DLVO Forces and Their Effect on Colloid Processing," to be published.
5. J. N. Israelachivili and R. M. Pashley, "Molecular Layering of Water at Surfaces and Origin of Repulsive Hydration Forces," Nature, 306 (5940) 249-50 (1983).
6. H. van Olphen, An Introduction to Clay Colloid Chemistry, p 99 John Wiley & Sons, New York, 1977.
7. J.C. Chang, F.F. Lange, D.S. Pearson and J. P. Pollinger, "Pressure Sensitivity for Particle Packing of Aqueous Al_2O_3 Slurries vs Interparticle Potential," J. Am. Ceram. Soc. (in press).
8. L. T. Kuhn, R. M. McMeeking, and F. F. Lange, "Modeling Powder Consolidation," Powders and Grains, ed. by Biarez and Gourves, pp. 331-8, Rotterdam, Balkema, (1989); also, J. Am. Ceram. Soc. 74 [3] 682-85 (1991).
9. J.C. Chang, B.V. Velamakanni, F.F. Lange, and D.S. Pearson, "Centrifugal Consolidation of Al_2O_3 and Al_2O_3/ZrO_2 Composite Slurries vs Interparticle Potentials: Particle Packing and Mass Segregation", J. Am. Ceram. Soc., 74 [9] 2201-204 (1991).
10. D. B. Marshall, J. J. Rato, and F. F. Lange, "Enhanced Fracture Toughness in Layered Microcomposites of Ce-ZrO_2 and Al_2O_3," J. Am. Ceram. Soc. J Am. Ceram.Soc., 74, 2979 (1991).
11. B.V. Velamakanni, F.F. Lange, F.C. Zok, and D.S. Pearson, "Influence of Interparticle Forces on Rheology of Consolidated Ceramic Particulate Bodies", J. Am. Ceram. Soc. (in press).
12. E. P. Luther, T. M. Kramer, F. F. Lange and D. S. Pearson, "Development of Short Range Repulsive Potentials in Aqueous Colloidal Processing of Silicon Nitride," sent to J. Am. Ceram. Soc.

13. R.K. Iler, US Patent 2,657,149 (1953) referenced p.573 in R.K. Iler, The Chemistry of Silica, Wiley-Interscience, New York, (1979).
14. R.E. Johnson, Jr and W.H. Morrison, Jr., "Ceramic Powder Dispersion in Non-aqueous Systems," Adv. in Ceramics **21** p 323-48 (1987).
15. M.J. Vold, "The Effect of Adsorption on the van der Waals Interaction of Spherical Particles," J. Colloid Science 16 p1-12 (1961).
16. L. Bergström, C. H. Schilling and I. A. Aksay, "Consolidation Behavior of Flocculated Alumina Suspensions," J. Am. Ceram. Soc.75 [12] 3305-14 (1992).
17 Y.K. Leong, D.V. Boger, P.J. Scales, T.W. Healy and R. Buscall, "Control of the Rheology of Concentrated Aqueous Colloidal Systems by Steric and Hydrophobic Forces," Chem. Com. (in press).
18. Y.K. Leoug, D.V. Boger, and D. Parris, "Surface and Rheological Properties of Zirconia Suspensions," Trans I. Chem. E. 69, Part A 381-85 (1991).
19. F.F. Lange and K.T. MIller, "Pressure Filtration: consolidation Kinetics and Mechanics," Am. Cer. Soc. Bull. 66 p1498 (1987).
20. D. B. Hough and L. R. White, "The Calculation of Hamaker Constants from Lifshitz Theory with Applications to Wetting Phenomena," Adv. in Colloid and Interface Science, 14 [1] 3-41 (1980).
21. A. Piccirillo and A. L. Gobbi, "Physical-electrical Properties of Silicon Nitride Deposited by PECVD on III-V Semiconductors," J. Electrochemical Soc. 137 [9] 3910-17 (1990).
22. Y. H. Yu, X. X. Liu, Z. W. Fang and S. C. Zou, "Optical Properties and Microstructure of Silicon Nitride Films Synthesized by Ion Beam Enhanced Deposition," Applied Surface Science 40 [1-2] 145-50 (1989).

---

a UBE Industries, Japan.

b ASAP 2000; Micromeritics; 1 Micromeritics Drive; Norcross, GA 30093.

c Sonicator W---380, Heat Systems, Ultrasonics Inc. 1938 New Highway; Farmingdale, NY 11735

d 951 Thermogravimetric Analyzer; Dupont Instruments;Concord Plaza --- Quillen Building; Wilmington, DE 19898

e FTIR 1600 series; Perkin Elmer Instruments; 761 Main Avenue; Norwalk, CT 06859.

f RSR - 8600; Rheometrics; One Possumtown Road; Piscataway, NJ 08854.

g MTS Model 850, Minneapolis, MN.

h Carver Press; Fred S. Carver, Inc.; Sub. of Sterling, Inc.; Dept. Z, Fountain Blvd.; Box 428; Menomonee Falls, WI 53051.

1.2 CERAMIC COMPOSITES

1.2.2 Silicon Nitride Matrix

Characterization of Grain Boundary Phases in Silicon Nitride Ceramics
I. M. Peterson and T. Y. Tien (The University of Michigan)

Objective/Scope

The objective of this investigation is to develop silicon nitride ceramics with high flexural strength, high fracture toughness and superior creep resistance. The fiber-like structure of the B-Si3N4 grains can be obtained by sintering the silicon nitride ceramics at higher temperature under higher nitrogen pressure. The composition of the sintering additives will affect the microstructural development, grain boundary characteristics, and hence , the mechanical properties. The grain boundary phases have never been synthesized separately and their properties have never been studied. The goal of this project is to synthesize and characterize the grain boundary phase and to understand the relationships between the nature of the grain boundary phase and the properties of silicon nitride ceramics. It is believed that with a thorough understanding of these relationships, ceramics with optimum mechanical properties can be obtained.

Glass forming compositions in the system Si,Al,Mg/N,O were selected for this study. Compsotions studied were in the compatibility triangle Si3N4, coridierite and N-phase. N phase has a composition 2Si2N2O:MgAl2O4. Both cordierite and N-phase have thermal expansion coefficients lower than that of silicon nitride.

Technical Progress

The glasses wre synthesized from the starting powders, Al2O3, Si3N4,SiO2 and MgO. They were mixed by hand with isopropyl alcohol with an agate mortar and pestle, dried, and cold pressed into pellets. The pellets were melted at temperatures between 1650°C and 1700°C, depending on the composition, for two hours under 10 atmospheres of N2. The samples were quenched by turning off the power to the furnace, and cooled to room temperature in approximately 3 hours. The compositions were verified by EPMA after firing. The presence of crystalline phases was determined by x-ray diffraction: only samples which did not show any crystalline peaks were used to determine the thermal expansion coefficient and Tg.

The thermal expansion coefficient was measured from room temperature to 1200°C using an alumina single rod dilatometer calibrated with a fused silica standard. The value of the thermal expansion coefficient form room temperature to 515°C was calculated. The Tg was determined from the dilatometer trace.

As shown in Figure 1, the thermal expansion coefficients of cordierite-based glasses with up to 10 wt % Si_3N_4 show the expected decrease in thermal expansion coefficient with increasing nitrogen content. The effect of varying the cation ratio can be seen from Figure 1 as well. For compositions with the same N/Si ratio, the addition of Si_3N_4 as the nitrogen source causes a larger decrease in the thermal expansion coefficient than the addition of N phase as the nitrogen source. When N-phase is used as a nitrogen source Mg and Al ions are added to the cordierite glass which would lower the average coordination number of the cations in the glass and partially offset the effect of the nitrogen.

The glass transition temperature shows alinear increase as the weight percent of Si_3N_4 increases, regardless of changes in the cation ratio as shown in Figure 2. The glass transition temperature for cordierite-based glasses can be fitted to an equation of the form:

$$Tg = 829.5 + 10.9\,X$$

where X is the weight percent silicon nitride added. If Tg is plotted as a function of Si/O ratio, the effect of the cation content is evident in the separation of the two thermal expansion vs composition curves. The addition of nitrogen in the form Si_3N_4 has a greater effect on Tg than the addition of the same amount of nitrogen in the form of N phase. Once again, this reflects the change in the structure of the glass with a change in cation ratio.

<u>Status of Milestones</u>
On schedule

<u>Publications</u>
None

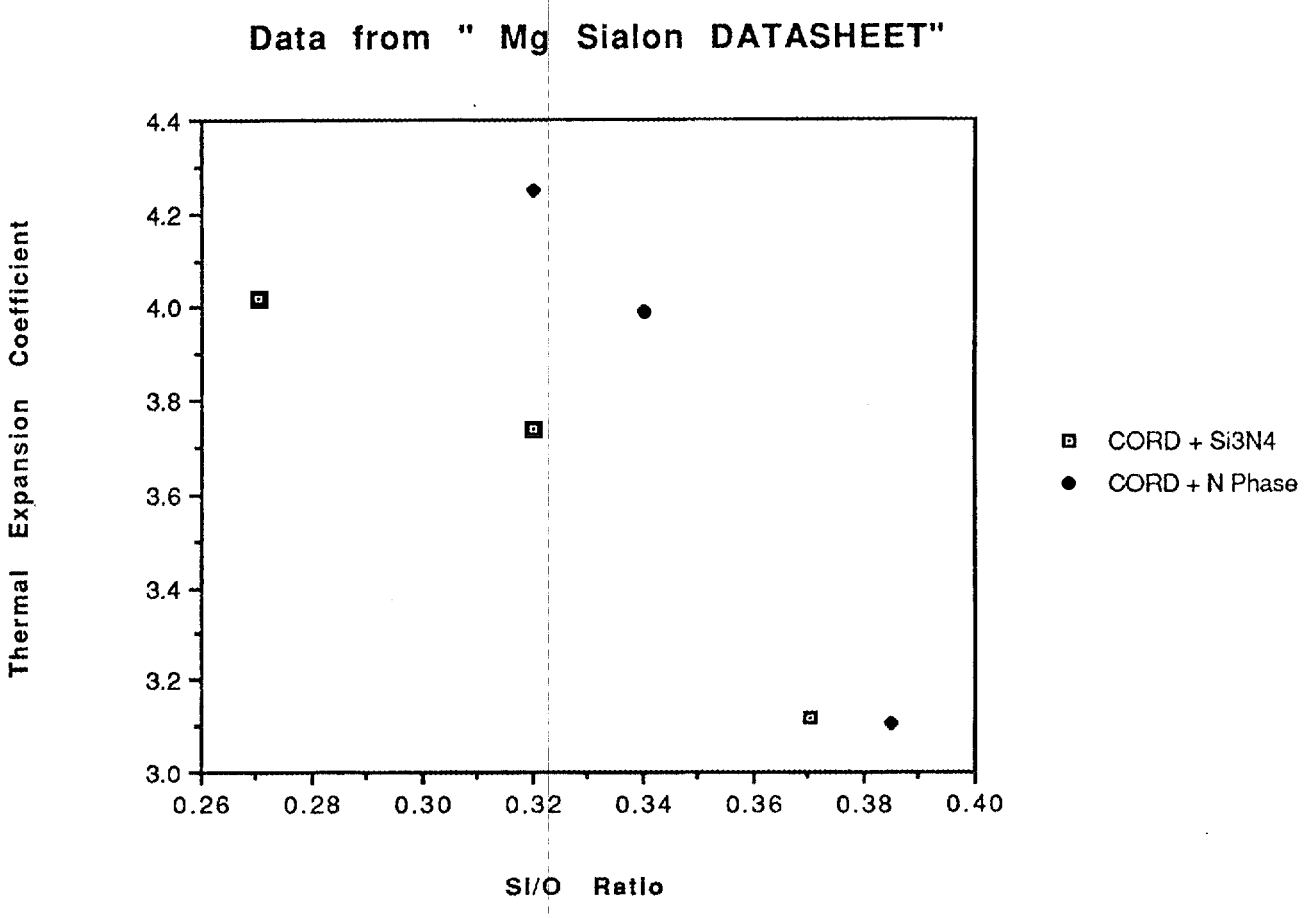
Data from " Mg Sialon DATASHEET"
Thermal Expansion Coefficient
4.4
4.2
4.0
3.8
3.6
3.4
3.2
3.0
0.26
0.28
0.30
0.32
0.34
0.36
0.38
0.40
SI/O Ratio
CORD + Si3N4
CORD + N Phase

FIGURE 1

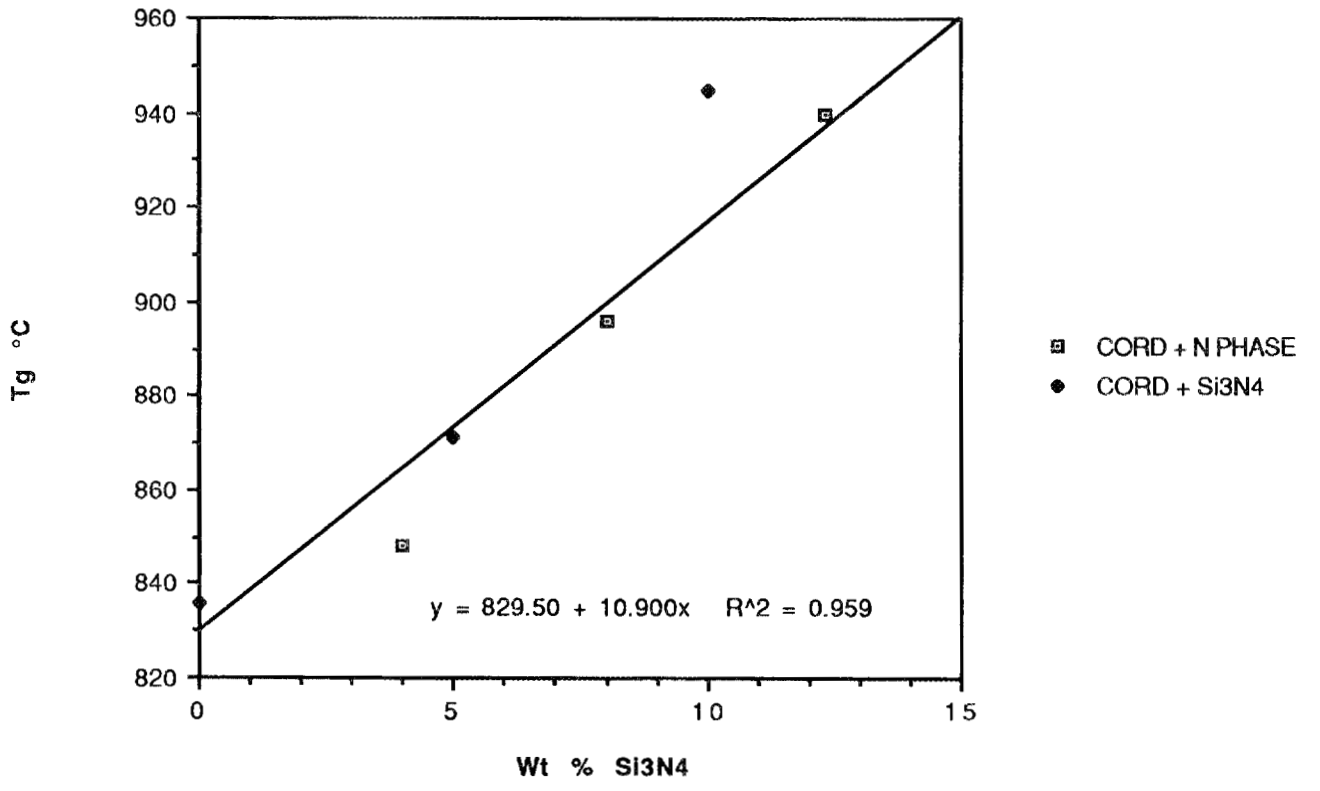

C

Figure 2 Increase in Glass Transition Temperature as a Function of Si3N4 Content

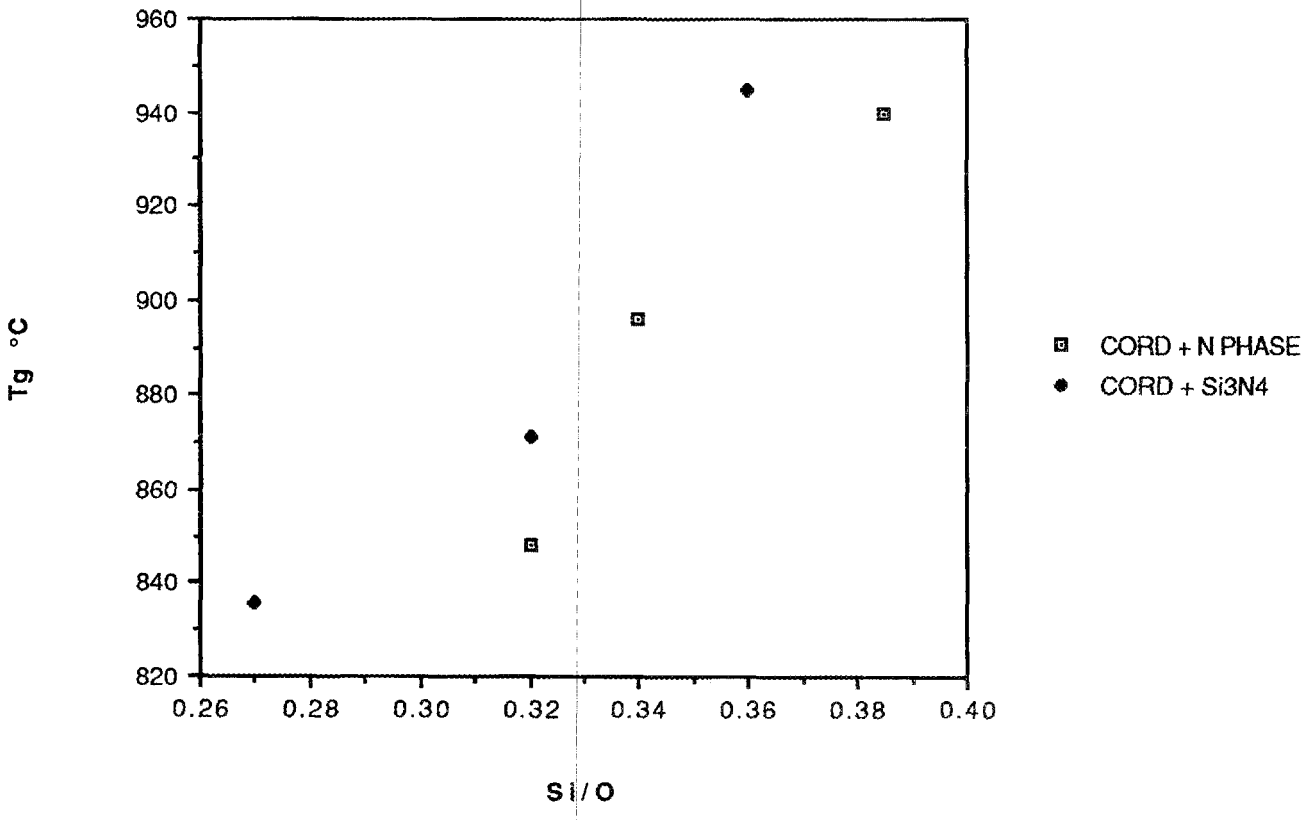

Figure 3 Increase in Glass Transition Temperature with Increasing Si/O Ratio

Optimization of Mechanical Properties of Silicon Nitride Ceramics

K. Houser, K. J. Lee, and T. Y. Tien (The University of Michigan)

Objective/Scope

The objective of this project is to develop processing techniques to obtain silicon nitride ceramics with a controlled grain morphology for optimum mechanical properties at room temperature as well as at high temperatures. Silicon nitride ceramics exhibit high flexural strengths and high fracture toughness when the microstructure contains fiber-like β-Si_3N_4 grains. Obtaining these fiber-like β-Si3N4 grains depends upon the sintering conditions and the grains' interaction with other phases present. Ideally, if the equilibrium conditions between the phases present are understood as well as the kinetics controlling the growth of these fiber-like grains, one could ultimately tailor a silicon nitride ceramic's microstructure for certain mechanical properties. This project will focus on these structure-property relationships for one composition in the Si,Al,Y/N,O system.

Technical progress

This project will be working with compositions from the β-Si_3N_4 - α'-SiAlON two-phase region along the Si_3N_4-Y_2O_3:9AlN join in the Si,Al,Y/N,O system. The α'-SiAlON phase has a composition $Y_{1/3m}Si_{12-(m+n)}Al_{m+n}N_{16-n}O_n$, which can be obtained by mixing the proper amounts of the compounds Si_3N_4, Al_2O_3, AlN, and Y_2O_3. During hot pressing, this composition was found to form a liquid phase that aided in densification during the initial stages of sintering and was later reabsorbed into the silicon nitride lattice. One objective will be to see if this transitional liquid phase sintering is possible under pressureless sintering conditions, and if the resulting microstructure contains any liquid phase at the grain boundaries. This work will be performed initially using a composition of 30wt% α'-SiAlON and 70wt% β-Si_3N_4 . Once the feasibility of pressureless sintering has been established, a controlled study of the growth of the fiber-like β-Si_3N_4 grains and the α'-SiAlON grains will be performed.

Status of Milestones

On schedule.

Publications

None.

In-Situ Reinforced Silicon Nitride

H. Yeh and J. Pollinger (Garrett Ceramic Components)
C-W. Li and J. Yamanis (Allied-Signal Research & Technology)

OBJECTIVE/SCOPE

The objective of this program is to develop compositions and processes to obtain high fracture toughness and strength for silicon nitride (Si_3N_4) based ceramic materials through microstructure control. Resulting microstructures would have elongated grains that would promote crack bridging and deflection toughening mechanisms. These types of materials known as *in situ* reinforced (ISR) Si_3N_4, are intended for application in advanced heat engine components. A significant amount of the improved mechanical properties must be retained to elevated temperatures. The properties should not substantially degrade over time and would thus allow the material to survive stress under extended exposures at high and moderate temperatures in oxidizing environments. The mechanical property goals of the program are listed below:

Modulus of Rupture at 25°C*	900 MPa (130 ksi)
Modulus of Rupture at 1200°C*	630 MPa (90 ksi)
Modulus of Rupture at 1400°C*	490 MPa (70 ksi)
Stress Rupture at 1000°C#	630 MPa (90 ksi)
Stress Rupture at 1200°C##	490 MPa (70 ksi)
Weibull Modulus+	20
Fracture Toughness, K_{Ic} at room temperature**	10 MPa$\sqrt{m}$
Maximum Use Temperature	1400°C

The technical effort is divided into two stages. The first stage shall be a refinement stage (Tasks 1 and 2) and shall focus on the effects and interactions of the chemical composition and thermal processing variables on microstructure, mechanical behavior, and oxidation resistance. In parallel, the effects of green processing on the required amount of sintering aids, room temperature strength, Weibull statistics, and critical flaws shall be assessed. The goal for this stage shall be to identify conditions which improve the baseline material and to map composition-processing-property relationships. The second stage shall be an optimization stage (Tasks 3, 4 and 5) and shall focus on the development of ISR Si_3N_4 with optimized microstructure and properties which meet or exceed the property goals and on the establishment of composition-processing-property correlations. In addition, a simulated engine component shall be fabricated in order to demonstrate process feasibility.

---

* Four point flexure using Department of Defense MIL-STD-1942 (size B) test specification

\# Stress at which sample shall survive 100 h at 1000°C.

** Measured by Chevron notch method.

\+ As determined by maximum likelihood method.

The technical effort was initiated in February 1992. During this reporting period (April-September 1992), Task 1 was completed (Milestone 122601), and Task 2 was initiated.

Technical Highlights

TASK 1 - Composition and Process Development

The objectives of this task is to determine the relationships among the variables which control the development of microstructure of the proposed *in situ* reinforced Si_3N_4. The focus is directed to the refinement of the baseline material composition (AS800) and processes which had been developed at Allied-Signal prior to the initiation of this program. The AS800 Si_3N_4 baseline composition is composed of three sintering aids (designated SA1, SA2 and SA3, present in amounts of W1, W2 and W3, expressed as weight percent of total batch mass, respectively) and a grain growth modifier (GGM present in an amount of W_m weight percent). Slip casting has been chosen as the baseline green forming process for this program instead of the cold isostatic process which had been used in the prior development work. A commercial, high purity, and fine silicon nitride powder rich in α-Si3N4 has been chosen as the baseline powder (BSN).

Effects of thermal processing, grain growth modifier, sintering aid SA3 concentration, and grain boundary crystallization on mechanical properties and oxidation behavior have been examined. Although other mechanical properties were also measured, four-point bend strength was used as the major property to evaluate the effect of processing and composition variations. In the last semi-annual report, some data were presented on the strength, toughness (short and long crack toughness) and oxidation behavior of AS800 ceramics obtained from variations in the baseline thermal processing conditions and in the amount of grain growth modifier. The data suggested that the incorporation of an initial hold period in the densification cycle improved the mechanical properties of the final ceramics. (The baseline densification cycle only comprises two hold periods, henceforth designated as intermediate and final stages, respectively.) Additional experiments were performed in this reporting period to further evaluate the effects of thermal processing and composition. Details were reported in the last three bi-monthly reports. A summary is presented below.

During Task 1, a total of twenty-six (26) batches of AS800 of varied compositions and sintering conditions were fabricated, and extensive characterizations were conducted, including strength at room and high temperatures, indentation-strength, stress-rupture testing, oxidation, and crystallization, etc. The results were used to assess the effects (or trends) of the composition and sintering conditions on final material properties.

With regard to composition effects, it was found that the baseline composition and its modifications can be sintered to full

density under a variety of sintering conditions. The resultant dense ISR silicon nitride ceramics possess good properties. Based on the properties and processing parameters, a processing window was defined which is important for the successful manufacture of engine components from this material. In the middle of Task 1, an alternate Si_3N_4 raw material, designated as ASN powder, was found to have a beneficial effect on the strength properties of the AS-800, and is commercially available. Since then ASN has then been selected as the standard Si_3N_4 powder for this program.

In the early stages of this task the critical flaws in the material were pores arising from unoptimized green processing. After slip-casting process was improved, the super-large β-Si_3N_4 grain near the tensile surface of the flexure bars became the predominant fracture origin of the material, instead of the processing pores. Therefore, one of the main directions in Task 1 has been to find ways to reduce the size and population of these super-large grains in the material without sacrificing the toughness. Although composition modifications, e.g., changing the content of the grain growth modifier, have shown some effects, it was found that the firing schedules have a much stronger impact on reducing the super-large grain size and, hence, improve the strength of the ceramic. A three stage sintering process was developed. The stages and their functions are: **initial stage**, conversion of α-Si_3N_4 to β-Si_3N_4; **intermediate stage**, densification to a density of ~92-97 theoretical and microstructure development; and **final stage**, full densification with grain-growth control. The effects of temperatures and times of the three stages were evaluated and the experimental results indicate a thermal schedule of (T_1+150°C,t_1), (T_2-25°C,t±0.5h), and (T_3-20°C,t_3-1h) generates a microstructure which imparts to the ISR ceramic excellent strength with high toughness (indentation-strength). However, it should be pointed out that these conditions are optimum for a slip-cast block having dimensions of ~2.75" x 2.75" x 1". and the composition 0.8W_3 SA3 (total sintering aids amount unchanged from that of the baseline, W_0), 0.33W_m GGM, and ASN Si_3N_4 powder. Further optimization may be required for changes in composition, silicon nitride powder, block dimensions, etc.

Oxidation behavior of AS800 was investigated at the intermediate temperature (~1000°C) and high temperatures (≥1300°C). It was found that the oxidation behavior is not only affected by composition but also on sintering schedule, GMM content, and grain boundary crystallization. Specifically, a low first-stage sintering temperature tends to degrade the intermediate temperature oxidation, a higher content of the GGM tends to degrade the high temperature oxidation resistance, and a crystallization treatment tends to reduce the weight gain at intermediate temperature and increase the weight gain at high temperatures. Notwithstanding these complications, in general samples containing W_3 of SA3 tend to show a higher weight gain after a 1300°C/100 hr treatment than the sample containing 0.8W_3 of SA3 and samples containing less than 0.8W_3 tend to show excessive weight gain after a 1000°C/100 hr oxidation heat-treatment.

Table 1 summarizes the typical properties for AS-800 materials generated in the later stage of Task 1. Note that property values are rounded numbers which represent typical properties, and specific batch to batch properties can be found in the earlier bimonthly reports. As seen, the RT Weibull modulus, 1200°C and 1400°C strength, and the 1200°C stress-rupture properties all meet the program goals, while other properties need further improvements.

TABLE 1. Typical Experimental AS800 Properties

Properties	Exp. AS800	Prog. Goals
4-pt Bend Strength (MPa)		
RT	850	900
1200°C	650	630
1400°C	550	490
Weibull	20	20
Fracture Toughness (MPa.√m)	8.5	10
Oxidation Weight Gain (mg/cm^2)		
1000°C/100 h	0.1	--
1300°C/100 h	0.4	--
Stress Rupture Life (MPa)		
1000°C/100 h	500	630
1200°C/100 h	550	490

TASK 2 - Material Property Characterization

Task 2 requires the selection of at least four compositions, based on Task 1 results, for a more comprehensive characterization, including strength, toughness, oxidation, post-oxidation strength, and crystallization behavior. In selected cases, the stress-rupture life at 1000°C and creep resistance at high temperatures shall also be evaluated. Moreover, the microstructure (2-D grain size and aspect ratio) of selected materials shall be characterized. The results will be used to guide the final optimization of the material under Task 3 - Composition and Property Optimization.

Four compositions have been selected for Task 2 and are given in Table 2. The total amount of sintering aids will be kept constant at W_0. More compositions may be included if deemed necessary. Fabrication of test specimens are under way.

Table 2. Compositions for Task 2

Composition	SA3 Content	GGM Content	Molar SA2/SA1 Ratio
1	$0.67W_3$	$0.33W_m$	M_0
2	$0.80W_3$	$0.33W_m$	M_0
3	$0.80W_3$	$0.00W_m$	M_0
4	$0.80W_3$	$0.33W_m$	$4M_0$

Examination of the limited data collected in Task 1 shows that one area which needs more attention is the effect of crystallization on the thermal and mechanical properties of the final ceramic. It has been observed that crystallization of grain boundary phase typically reduces the RT strength by ~10%. Therefore, characterization of both the as-sintered and the crystallized materials will be performed under this Task to obtain a more complete understanding.

Status of Milestones

Milestone 122601 (Refinement of baseline composition) was completed on schedule in this reporting period. The progress of all other milestones are on schedule.

Communications/Visits/Travel

C-W. Li, J. Pollinger, J. Yamanis and H. Yeh visited ORNL on July 15-16 to present an update of this program.

Problems Encountered

None

Publications

None

1.2.3 Oxide Matrix

Dispersion-Toughened Ceramic Composite

T. N. Tiegs, S. D. Nunn, P. A. Menchhofer, P. J. Jones, K. L. Ploetz,
D. W. Coffey, and C. A. Walls (Oak Ridge National Laboratory)

Objective/scope

Initially, this work involved development and characterization of SiC whisker-reinforced ceramic composites for improved mechanical performance. To date, most of the efforts involving SiC whisker-reinforced alumina, mullite, silicon nitride, and sialon have been completed. In addition, studies of whisker-growth processes were initiated to improve the mechanical properties of SiC whiskers by reducing their flaw sizes and, thereby, improving the mechanical properties of the composites. Currently, in situ acicular grain growth is being investigated to improve fracture toughness of silicon nitride materials.

Technical highlights

In-Situ Toughening of Silicon Nitride by Microstructure Development

Microstructure Development During Gas-Pressure-Sintering (GPS) - GPS is one technique used to grow elongated grain structures and obtain high-toughness silicon nitrides with refractory grain-boundary phases. Samples have been fabricated at ORNL and initial results reported previously. The refractory grain boundary phases fall into two general classifications: (1) rare-earth silicates, based on $M_2Si_2O_7$ as the crystalline intergranular phase, where M = Y, Yb, La, or Nd; and (2) grain boundary phases based on the rare-earth-oxide and nitride apatites, such as $Sr_2Y_8(SiO_4)_6O_2$, $Ba_2Y_8(SiO_4)_6O_2$, $Mg_2Y_8(SiO_4)_6O_2$, $Sr_2Nd_8(SiO_4)_6O_2$, and $Sr_2La_8(SiO_4)_6O_2$.

Samples were fabricated by turbomilling 1 to 12% rare-earth-oxide (Y_2O_3, La_2O_3, or Yb_2O_3) and 1 to 8% SiO_2 additives. The apatite materials also had SrO, MgO, or BaO added to the mixtures. Both slip-casting and cold-isostatic-pressing (CIP) have been used as the green forming method. Initial densification results were reported previously.[1]

Additional compositions containing a reduced amount of sintering aid were prepared. These specimens contain Ube E-10 silicon nitride and the appropriate sintering aid additives to form the desired crystalline intergranular phase. The compositions were formulated with 0 to 2% excess SiO_2 and contain approximately 4.3 to 8.0 equivalent % total initial oxygen. Several batches of samples were gas-pressure sintered in two-stage cycle furnace runs, and the densification results are summarized in Tables 1 and 2. Densification as a function of equivalent oxygen content for selected furnace runs is shown in Figs. 1 and 2. As shown in Fig. 1, all of the samples with rare-earth silicate grain boundary phases densified to >99% T. D. As shown in Fig. 2, samples with the rare-earth apatite grain boundary phases and having excess SiO_2 densified to >99% T. D. (samples TRSN-2, -3, and -4). However, the other samples with no excess SiO_2 densified readily only at the 1900 to 1950°C sintering conditions. Preliminary X-ray results indicate the formation of some intermediate phase formation at temperatures of 1700 to 1800°C.

Table 1. Compositions, densities, and properties of gas-pressure sintered samples.

			Density and Property Measurements						
Sample ID	Sintering aid	Composition wt % oxides	Theoretical density	Bulk density	Percent th. dens	% Open porosity	% Weight loss	Fracture strength RT*	Fracture strength 1200°C
Sintering Conditions: 1850°C 2 h 50 psi/1900°C 2 h 300 psi									
SC-281	Silicate	7.6Y4.2Si	3.25	3.24	99.7	0.09	1.86		
SC-282	Silicate	3.4Y5.3La4.1Si	3.30	3.27	99.1	0.27	1.47	672 ± 39	525 ± 25
SC-283	Silicate	10.6La4.1Si	3.34	3.32	99.5	0.05	2.17	556 ± 25	574 ± 74
SC-290	Apatite	11.2La1.8Sr3.3Si	3.37	3.34	99.1	0.01	2.06		
SC-291	Apatite	7.9Y2.7Ba3.4Si	3.29	3.02	91.9	0.15	2.34		
SC-293	Apatite	8Y1.8Sr3.4Si	3.27	3.26	99.6	0.14	2.58	730 ± 51	464 ± 34
Sintering Conditions: 1850°C 2 h 50 psi/1950°C 2 h 300 psi									
SC-281-4	Silicate	7.6Y4.2Si	3.25	3.27	100.5	0.07	3.46	471 ± 15	200 ± 122
SC-282-4	Silicate	3.4Y5.3La4.1Si	3.30	3.28	99.5	0.11	2.42	424 ± 151	490 ± 41
SC-283-4	Silicate	10.6La4.1Si	3.34	3.33	99.8	0.09	3.28	499 ± 101	555 ± 40
SC-290-4	Apatite	11.2La1.8Sr3.3Si	3.37	3.34	99.1	0.12	2.97		
SC-291-4	Apatite	7.9Y2.7Ba3.4Si	3.29	3.06	93.1	0.78	3.34	752 ± 64	375 ± 19
SC-293-4	Apatite	8Y1.8Sr3.4Si	3.27	3.29	100.5	0.41	3.50	647 ± 17	4.24 ± 30
Sintering Conditions: 1750°C 4 h 15 psi									
SC-281-5	Silicate	7.6Y4.2Si	3.25	3.10	95.4	0.02	1.99		
SC-282-5	Silicate	3.4Y5.3La4.1Si	3.30	3.21	97.2	0.03	2.25	707 ± 8	411 ± 103
SC-283-5	Silicate	10.6La4.1Si	3.34	3.30	98.8	0.08	3.11	647 ± 33	510 ± 53
SC-290-5	Apatite	11.2La1.8Sr3.3Si	3.37	3.31	98.2	0.12	3.08		
SC-291-5	Apatite	7.9Y2.7Ba3.4Si	3.29	2.55	77.6	14.82	3.99		
SC-293-5	Apatite	8Y1.8Sr3.4Si	3.27	3.20	97.9	0.00	2.19	778 ± 28	447 ± 20
Sintering Conditions: 1800°C 4 h 15 psi									
SC-281-6	Silicate	7.6Y4.2Si	3.25	3.19	98.1	0.03	2.36	578 ± 11	549 ± 11
SC-282-6	Silicate	3.4Y5.3La4.1Si	3.30	3.22	97.7	0.02	2.13	465 ± 8	456 ± 47
SC-283-6	Silicate	10.6La4.1Si	3.34	3.31	99.0	0.08	2.48	463 ± 47	546 ± 46
SC-290-6	Apatite	11.2La1.8Sr3.3Si	3.37	3.34	99.2	0.07	2.30		
SC-291-6	Apatite	7.9Y2.7Ba3.4Si	3.29	2.81	85.4	6.00	2.21		
SC-293-6	Apatite	8Y1.8Sr3.4Si	3.27	3.23	98.9	0.00	1.26	697 ± 56	475 ± 20
Sintering Conditions: 1850°C 4 h 15 psi									
SC-281-3	Silicate	7.6Y4.2Si	3.25	3.21	98.9	0.01	2.83	531 ± 37	488 ± 8
SC-282-3	Silicate	3.4Y5.3La4.1Si	3.30	3.28	99.4	0.04	3.81	745 ± 25	471 ± 9
SC-283-3	Silicate	10.6La4.1Si	3.34	3.32	99.5	0.06	na	612 ± 26	532 ± 61
SC-290-3	Apatite	11.2La1.8Sr3.3Si	3.37	3.35	99.4	0.00	na		
SC-291-3	Apatite	7.9Y2.7Ba3.4Si	3.29	2.67	81.3	13.33	6.09		
SC-293-3	Apatite	8Y1.8Sr3.4Si	3.27	3.21	98.2	0.00	3.47	543 ± 41	526 ± 49

*RT = room temperature.

Table 2. Compositions, densities, and properties of gas-pressure sintered samples. Sintering Conditions: 1850°C 2 h 50 psi 1900°C 2 h 300 psi.

Density and Property Measurements									
Sample ID		Composition wt % oxides	Theoretical density	Bulk density	Percent th. dens	% Open porosity	% Weight loss	Fracture strength RT	Fracture strength 1200°C
Sintering Conditions: 1850°C 2 h 50 psi/1900°C 2 h 300 psi									
TRSN-1-1	Standard	6Y2A1	3.27	3.25	99.3	0.11	0.23	765 ± 70	447 ± 18
TRSN-2-1	Apatite	11.2La5.5Si1.8Sr	3.36	3.35	99.8	0.03	2.39	542 ± 50	310 ± 9
TRSN-3-1	Apatite	8Y5.7Si1.8Sr	3.27	3.24	99.0	0.03	1.31	452 ± 19	258 ± 26
TRSN-4-1	Apatite	11.5Nd5.5Si1.8Sr	3.39	3.38	99.8	0.03	2.50	510 ± 9	378 ± 61
TRSN-5-1	Silicate	10.6La6.3Si	3.33	3.33	99.9	0.03	1.99	341 ± 142	525 ± 61
TRSN-6-1	Silicate	7.6Y6.5Si	3.25	3.25	100.0	0.09	2.37		
TRSN-7-1	Silicate	3.8Y5.3La6.4Si	3.30	3.29	99.8	0.00	2.90		
TRSN-8	Silicate	5.3Y3.3Si	3.24	3.22	99.3	0.00	1.31	310 ± 16	385 ± 29
TRSN-8 (bar)	Silicate	5.3Y3.3Si	3.24	3.24	99.9	0.22	2.31		
TRSN-9-1	Silicate	7.6Nd3.2Si	3.32	3.32	100.0	0.00	1.73	631 ± 80	543
TRSN-10	Silicate	7.4La3.2Si	3.29	3.29	99.9	0.00	1.48	470 ± 68	498 ± 55
TRSN-11-1	Apatite	5.6Y2.7Si1.3Sr	3.25	2.36	72.7	12.40	2.20		
TRSN-12-1	Apatite	7.9La2.7Si1.3Sr	3.32	2.80	84.3	2.04	2.71		
TRSN-13-1	Apatite	8.1Nd2.7Si1.2Sr	3.34	2.76	82.7	0.15	1.64		
TRSN-14-1	Silicate	7.8Y4.3Si	3.26	3.24	99.5	0.11	0.55	460 ± 109	370 ± 66
TRSN-15-1	Silicate	10.8La4.2Si	3.35	3.34	99.6	0.29	1.44	411 ± 55	288 ± 115
TRSN-16-1	Silicate	11.1Nd4.2Si	3.39	3.39	100.0	0.10	2.55	412 ± 102	436 ± 122
TRSN-17-1	Apatite	8.2Y3.5Si1.9Sr	3.28	2.63	80.1	7.35	1.40		
TRSN-18-1	Apatite	11.4La3.3Si1.8Sr	3.38	3.23	95.6	0.24	2.27	376 ± 40	420 ± 37
TRSN-19-1	Apatite	11.7Nd3.3Si1.8Sr	3.41	3.07	90.0	0.85	1.72		
TRSN-20-1	Silicate	9.6Y5.3Si	3.28	3.27	99.8	0.34	0.79		
SC-281-7	Silicate	7.6Y6.5Si	3.25	3.25	100.1	0.05	2.61	672 ± 32	506 ± 59
SC-282-7	Silicate	3.8Y5.3La6.4Si	3.30	3.29	99.6	0.05	2.10	712 ± 40	422 ± 157
SC-283-7	Silicate	10.6La6.4Si	3.34	3.33	99.7	0.05	2.95	767 ± 60	
SC-289-7	Apatite	8Y5.6Si1.8Sr	3.28	3.28	99.9	0.00	1.72		
SC-293-7	Apatite	8Y5.6Si1.8Sr	3.28	3.28	100.1	0.05	2.91		
Sintering Conditions: 1900°C 2 h 100 psi/1950°C 2 h 300 psi									
TRSN-1-2	Standard	6Y2Al	3.27	3.24	99.2	0.03	0.57	525 ± 79	354 ± 40
TRSN-2-2	Apatite	11.2La5.5Si1.8Sr	3.36	3.35	99.7	0.09	3.26	374 ± 54	309 ± 32
TRSN-3-2	Apatite	8Y5.7Si1.8Sr	3.27	3.27	99.9	0.22	2.26	475 ± 33	297 ± 45
TRSN-4-2	Apatite	11.5Nd5.5Si1.8Sr	3.39	3.39	99.9	0.09	na	444 ± 126	333 ± 18
TRSN-5-2	Silicate	10.6La6.3Si	3.33	3.30	99.0	0.03	2.58		
TRSN-6-2	Silicate	7.6Y6.5Si	3.25	3.25	100.1	0.00	3.35	398 ± 197	
TRSN-7-2	Silicate	3.8Y5.3La6.4Si	3.30	3.30	99.9	0.00	3.69	344 ± 113	
TRSN-8-2	Silicate	5.3Y3.3Si	3.24	3.24	100.1	0.00	1.51	503 ± 88	496 ± 6
TRSN-9-2	Silicate	7.6Nd3.2Si	3.32	3.31	99.8	0.04	1.88	379 ± 80	343 ± 24
TRSN-10-2	Silicate	7.4La3.2Si	3.29	3.29	99.9	0.04	2.42	518 ± 28	533 ± 12
TRSN-11-2	Apatite	5.6Y2.7Si1.3Sr	3.25	2.47	75.9	21.00	2.55		
TRSN-12-2	Apatite	7.9La2.7Si1.3Sr	3.32	2.94	88.5	1.25	3.04		
TRSN-13-2	Apatite	8.1Nd2.7Si1.2Sr	3.34	2.96	88.7	0.00	2.90		
TRSN-14-2	Silicate	7.8Y4.3Si	3.26	3.26	100.1	0.17	1.18	427 ± 20	291 ± 38
TRSN-15-2	Silicate	10.8La4.2Si	3.35	3.34	99.8	0.09	1.83	311 ± 133	435 ± 58
TRSN-16-2	Silicate	11.1Nd4.2Si	3.39	3.38	99.7	0.21	2.08	508	319 ± 72
TRSN-17-2	Apatite	8.2Y3.5Si1.9Sr	3.28	2.77	84.3	11.97	1.86		
TRSN-18-2	Apatite	11.4La3.3Si1.8Sr	3.38	3.35	99.1	0.06	2.26	480 ± 25	442 ± 13
TRSN-19-2	Apatite	11.7Nd3.3Si1.8Sr	3.41	3.28	96.2	0.09	2.44	320 ± 27	262 ± 160
TRSN-20-2	Silicate	9.6Y5.3Si	3.28	3.28	100.1	0.03	1.25	386 ± 23	309 ± 24

ORNL-DWG 93-5830

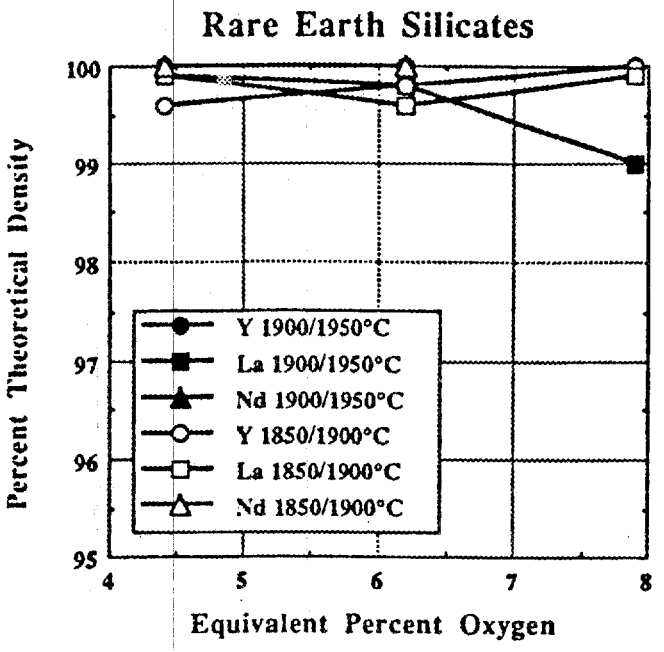

Fig. 1. Sintered density of gas-pressure sintered silicon nitride containing rare-earth-silicate sintering aids as a function of the equivalent percent oxygen in the starting composition.

ORNL-DWG 93-5831

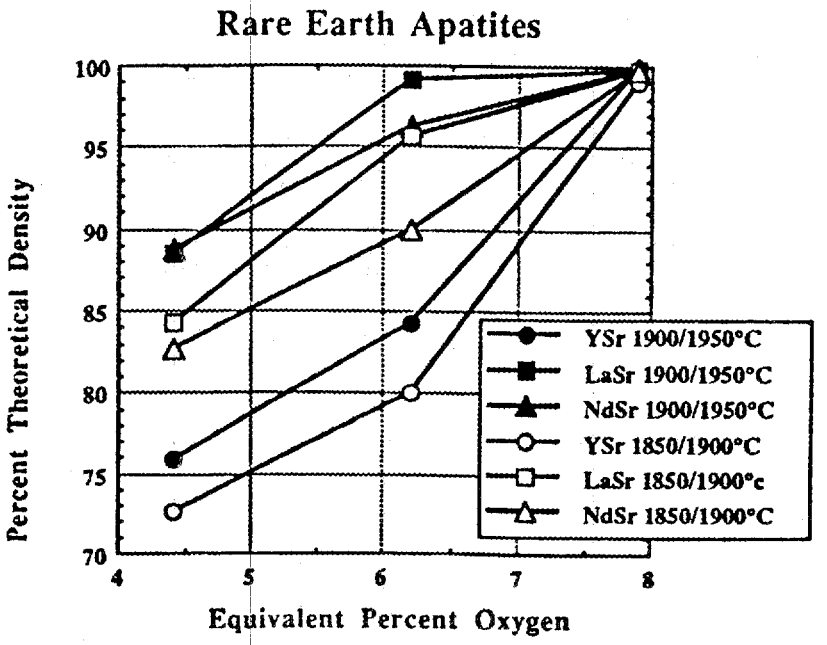

Fig. 2. Sintered density of gas-pressure sintered silicon nitride containing rare-earth-apatite sintering aids as a function of the equivalent percent oxygen in the starting compositions.

Formation of these phases is believed to decrease the amount of liquid phase present during sintering and inhibit particle rearrangement and shrinkage.

To determine the densification behavior with different sintering conditions, additional samples were fired at various conditions. The results are summarized in Tables 3 through 5. As shown, densification was quite variable among the different compositions for these GPS runs. Surprisingly, some of the compositions that densified easily in previous sintering runs at comparable temperatures, like TRSN-2 through -7, did not consistently reach high densities >95% in the present tests. These samples are currently being examined to ascertain the reasons for any anomalous behavior.

Examination of fracture surfaces by scanning electron microscopy (SEM) from sintered samples revealed significant grain growth occurred in some compositions (Figs. 3 through 5). As shown in Fig. 3, with the samples formulated to contain $La_2Si_2O_7$ as the grain boundary phase and a total initial oxygen content of 7.7 equivalent %, a duplex grain size distribution was produced. The samples formulated to contain $Sr_2Y_8(SiO_4)_6O_2$ or $Sr_2La_8(SiO_4)_6O_2$ as the grain boundary phase (Figs. 4 and 5); extensive grain growth occurred during both GPS and at lower nitrogen overpressures.

Mechanical Properties - The specimens that achieved >95% T. D. were machined into bend bars for mechanical property testing. These results are summarized in Tables 1 and 2. As shown, the flexural strengths for the TRSN samples are consistently low compared to many advanced silicon nitride materials. The major reason for this behavior appears to be the green forming technique used. The TRSN-series of samples were turbomilled, dried, screened, and CIPed. Apparently, hard agglomerates were formed in the drying steps and were carried over into the parts. The strengths are similar to other GPS samples that were isopressed.[2] Examination of fracture surfaces showed differential shrinkage around these hard agglomerates and the formation of large defects. This behavior is illustrated in Table 6 with a comparison of CIPed materials with the same composition that was slip-cast into specimens. It shows a consistently higher strength for the slip-cast materials under both identical sintering conditions (TRSN-3-1 vs. SC-293) and similar conditions. In fact, samples SC-293-5, -6, and -3 showed higher strengths even though they had lower densities than the CIPed materials. Our sample preparation had started using CIP to eliminate macro-defects, such as cracking and warping, that occurred during drying of our initial slip-cast specimens. Future samples will be prepared by both CIP and slip-casting.

Another factor affecting the strength was exaggerated grain growth experienced by some of the compositions. For example, Fig. 6 shows the large grains observed in TRSN-15-2 (Si_3N_4-10.8% La_2O_3-4.2 % SiO_2 sintered at 1900°C/2 h-1950°C/2h), which had a room-temperature strength of 311 MPa. Such large grains are well known to have detrimental effects on the strength of silicon nitride materials. Similar grain growth was observed in other compositions. Modification of the sintering cycle temperature, times, and pressures will be used to control the grain growth behavior.

During GPS, the high gas overpressures result in dissolution of nitrogen into the intergranular phases and the formation of nitrogen-rich phases. These phases are metastable at one atmosphere. There was some evidence that during the crystallization step used in the present samples (1 h hold at 1400°C and 15 psi

Table 3. Compositions and densities of gas-pressure sintered samples. Sintering Conditions: 1750°C 2 h 100 psi/1800°C 0.5 h 300 psi.

Sample ID	Sintering aid	Composition wt % oxides	Theoretical density	Bulk density	Percent th. dens	% Open porosity
TRSN-1-3	Standard	6Y2A1	3.27	2.98	91.0	2.03
TRSN-2-3	Apatite	11.2La5.5Si1.8Sr	3.36	2.74	81.5	13.71
TRSN-3-3	Apatite	8Y5.7Si1.8Sr	3.27	2.52	77.1	20.50
TRSN-4-3	Apatite	11.5Nd5.5Si1.8Sr	3.39	2.72	80.4	12.88
TRSN-5-3	Silicate	10.6La6.3Si	3.33	2.74	82.3	13.69
TRSN-6-3	Silicate	7.6Y6.5Si	3.25	2.82	86.8	2.59
TRSN-7-3	Silicate	3.8Y5.3La6.4Si	3.30	2.90	87.9	0.38
TRSN-8-3	Silicate	5.3Y3.3Si	3.24	2.63	81.0	12.61
TRSN-9-3	Silicate	7.6Nd3.2Si	3.32	2.80	84.4	7.55
TRSN-10-3	Silicate	7.4La3.2Si	3.29	2.83	85.9	6.08
TRSN-11-3	Apatite	5.6Y2.7Si1.3Sr	3.25	2.09	64.3	32.30
TRSN-12-3	Apatite	7.9La2.7Si1.3Sr	3.32	2.36	70.9	22.68
TRSN-13-3	Apatite	8.1Nd2.7Si1.2Sr	3.34	2.37	71.1	23.61
TRSN-14-3	Silicate	7.8Y4.3Si	3.26	2.60	79.8	17.44
TRSN-15-3	Silicate	10.8La4.2Si	3.35	2.67	79.6	17.46
TRSN-16-3	Silicate	11.1Nd4.2Si	3.39	2.61	77.0	17.03
TRSN-17-3	Apatite	8.2Y3.5Si1.9Sr	3.28	2.12	64.7	34.49
TRSN-18-3	Apatite	11.4La3.3Si1.8Sr	3.38	2.73	80.9	14.07
TRSN-19-3	Apatite	11.7Nd3.3Si1.8Sr	3.41	2.36	69.3	26.72
TRSN-20-3	Silicate	9.6Y5.3Si	3.28	2.83	86.4	3.28
TRSN-21-3	Apatite	10.9La5.2Si1.7Sr	3.36	2.81	83.7	7.88
TRSN-22-3	Apatite	5.8La6.5Yb5.2Si1.7Sr	3.41	2.93	86.0	4.95
TRSN-23-3	Silicate	8.8Yb3.2Si	3.36	2.77	82.6	11.74
TRSN-24-3	Silicate	4Y2.5Si	3.22	2.41	74.9	21.55
TRSN-25-3	Silicate	5.7La2.5Si	3.27	2.58	78.9	15.50
TRSN-26-3	Silicate	5.8Nd2.5Si	3.28	2.64	80.5	15.56
TRSN-27-3	Silicate	6.8Yb2.5Si	3.32	2.70	81.2	13.10

Table 4. Compositions and densities of gas-pressure sintered samples. Sintering Conditions: 1850°C 0.5 h 100 psi/1800°C 2 h 300 psi.

Sample ID	Sintering aid	Composition wt % oxides	Theoretical density	Bulk density	Percent th. dens	% Open porosity
TRSN-1-5	Standard	6Y2A1	3.27	3.06	93.7	0.65
TRSN-2-5	Apatite	11.2La5.5Si1.8Sr	3.36	3.11	92.5	0.09
TRSN-3-5	Apatite	8Y5.7Si1.8Sr	3.27	2.94	90.0	1.67
TRSN-4-5	Apatite	11.5Nd5.5Si1.8Sr	3.39	2.94	86.7	6.12
TRSN-5-5	Silicate	10.6La6.3Si	3.33	3.06	92.0	0.08
TRSN-6-5	Silicate	7.6Y6.5Si	3.25	2.94	90.3	0.03
TRSN-7-5	Silicate	3.8Y5.3La6.4Si	3.30	2.99	90.5	0.05
TRSN-8-5	Silicate	5.3Y3.3Si	3.24	2.82	87.0	5.68
TRSN-9-5	Silicate	7.6Nd3.2Si	3.32	3.01	90.6	2.24
TRSN-10-5	Silicate	7.4La3.2Si	3.29	3.00	91.2	2.19
TRSN-11-5	Apatite	5.6Y2.7Si1.3Sr	3.25	2.24	69.0	28.14
TRSN-12-5	Apatite	7.9La2.7Si1.3Sr	3.32	2.55	76.9	15.16
TRSN-13-5	Apatite	8.1Nd2.7Si1.2Sr	3.34	2.53	75.7	14.69
TRSN-14-5	Silicate	7.8Y4.3Si	3.26	2.91	89.1	1.03
TRSN-15-5	Silicate	10.8La4.2Si	3.35	3.02	90.3	2.27
TRSN-16-5	Silicate	11.1Nd4.2Si	3.39	2.77	81.6	16.07
TRSN-17-5	Apatite	8.2Y3.5Si1.9Sr	3.28	2.49	75.9	18.26
TRSN-18-5	Apatite	11.4La3.3Si1.8Sr	3.38	2.67	79.0	19.15
TRSN-19-5	Apatite	11.7Nd3.3Si1.8Sr	3.41	2.50	73.4	23.45
TRSN-20-5	Silicate	9.6Y5.3Si	3.28	2.82	86.0	8.55
TRSN-21-5	Apatite	10.9La5.2Si1.7Sr	3.36	2.97	88.4	2.83
TRSN-22-5	Apatite	5.8La6.5Yb5.2Si1.7Sr	3.41	3.09	90.6	1.00
TRSN-23-5	Silicate	8.8Yb3.2Si	3.36	3.00	89.3	2.90
TRSN-24-5	Silicate	4Y2.5Si	3.22	2.62	81.3	13.14
TRSN-25-5	Silicate	5.7La2.5Si	3.27	2.83	86.6	6.75
TRSN-26-5	Silicate	5.8Nd2.5Si	3.28	2.93	89.3	3.63
TRSN-27-5	Silicate	6.8Yb2.5Si	3.32	2.92	88.0	5.57

Table 5. Compositions and densities of gas-pressure sintered samples. Sintering Conditions: 1750°C 1 h 100 psi/1900°C 2 h 300 psi.

Sample ID	Sintering aid	Composition wt % oxides	Theoretical density	Bulk density	Percent th. dens	% Open porosity
TRSN-1-6	Standard	6Y2A1	3.27	3.07	93.9	0.00
TRSN-2-6	Apatite	11.2La5.5Si1.8Sr	3.36	3.28	97.6	0.08
TRSN-3-6	Apatite	8Y5.7Si1.8Sr	3.27	3.09	94.4	2.78
TRSN-4-6	Apatite	11.5Nd5.5Si1.8Sr	3.39	3.22	94.9	0.00
TRSN-5-6	Silicate	10.6La6.3Si	3.33	3.19	95.9	0.00
TRSN-6-6	Silicate	7.6Y6.5Si	3.25	3.17	97.4	0.00
TRSN-7-6	Silicate	3.8Y5.3La6.4Si	3.30	3.28	99.4	0.09
TRSN-8-6	Silicate	5.3Y3.3Si	3.24	3.15	97.2	-0.04
TRSN-9-6	Silicate	7.6Nd3.2Si	3.32	3.19	96.2	0.00
TRSN-10-6	Silicate	7.4La3.2Si	3.29	3.19	97.1	0.76
TRSN-11-6	Apatite	5.6Y2.7Si1.3Sr	3.25	2.31	71.0	29.36
TRSN-12-6	Apatite	7.9La2.7Si1.3Sr	3.32	2.71	81.7	8.78
TRSN-13-6	Apatite	8.1Nd2.7Si1.2Sr	3.34	2.70	80.8	1.86
TRSN-14-6	Silicate	7.8Y4.3Si	3.26	3.12	95.9	0.00
TRSN-15-6	Silicate	10.8La4.2Si	3.35	3.27	97.7	0.00
TRSN-16-6	Silicate	11.1Nd4.2Si	3.39	3.29	97.2	0.00
TRSN-17-6	Apatite	8.2Y3.5Si1.9Sr	3.28	2.60	79.1	20.48
TRSN-18-6	Apatite	11.4La3.3Si1.8Sr	3.38	3.10	91.8	1.14
TRSN-19-6	Apatite	11.7Nd3.3Si1.8Sr	3.41	2.99	87.6	2.28
TRSN-20-6	Silicate	9.6Y5.3Si	3.28	3.16	96.4	0.00
TRSN-21-6	Apatite	10.9La5.2Si1.7Sr	3.36	3.18	94.5	0.00
TRSN-22-6	Apatite	5.8La6.5Yb5.2Si1.7Sr	3.41	3.24	94.9	-0.03
TRSN-23-6	Silicate	8.8Yb3.2Si	3.36	3.29	97.9	0.00
TRSN-24-6	Silicate	4Y2.5Si	3.22	3.02	93.9	0.00
TRSN-25-6	Silicate	5.7La2.5Si	3.27	3.17	96.8	0 00
TRSN-26-6	Silicate	5.8Nd2.5Si	3.28	3.15	96.2	0.17
TRSN-27-6	Silicate	6.8Yb2.5Si	3.32	3.24	97.7	0.00

28509

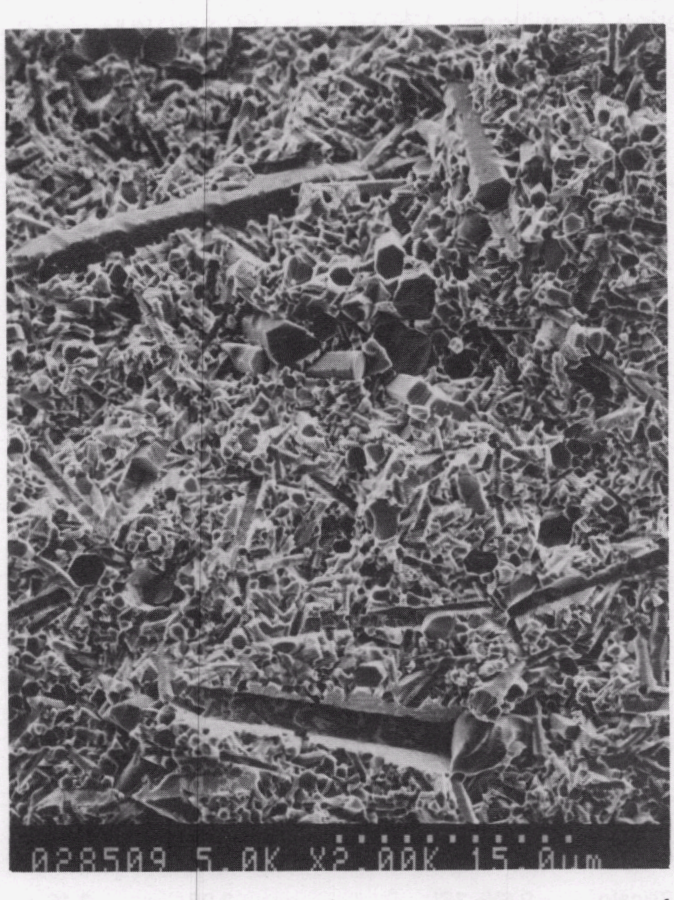

Fig. 3. Fracture surface of silicon nitride formulated to contain $La_2Si_2O_7$ as the grain boundary phase. Sintered at 0.2 MPa nitrogen at 1850°C for 4 h. Density is 99.5% T. D.

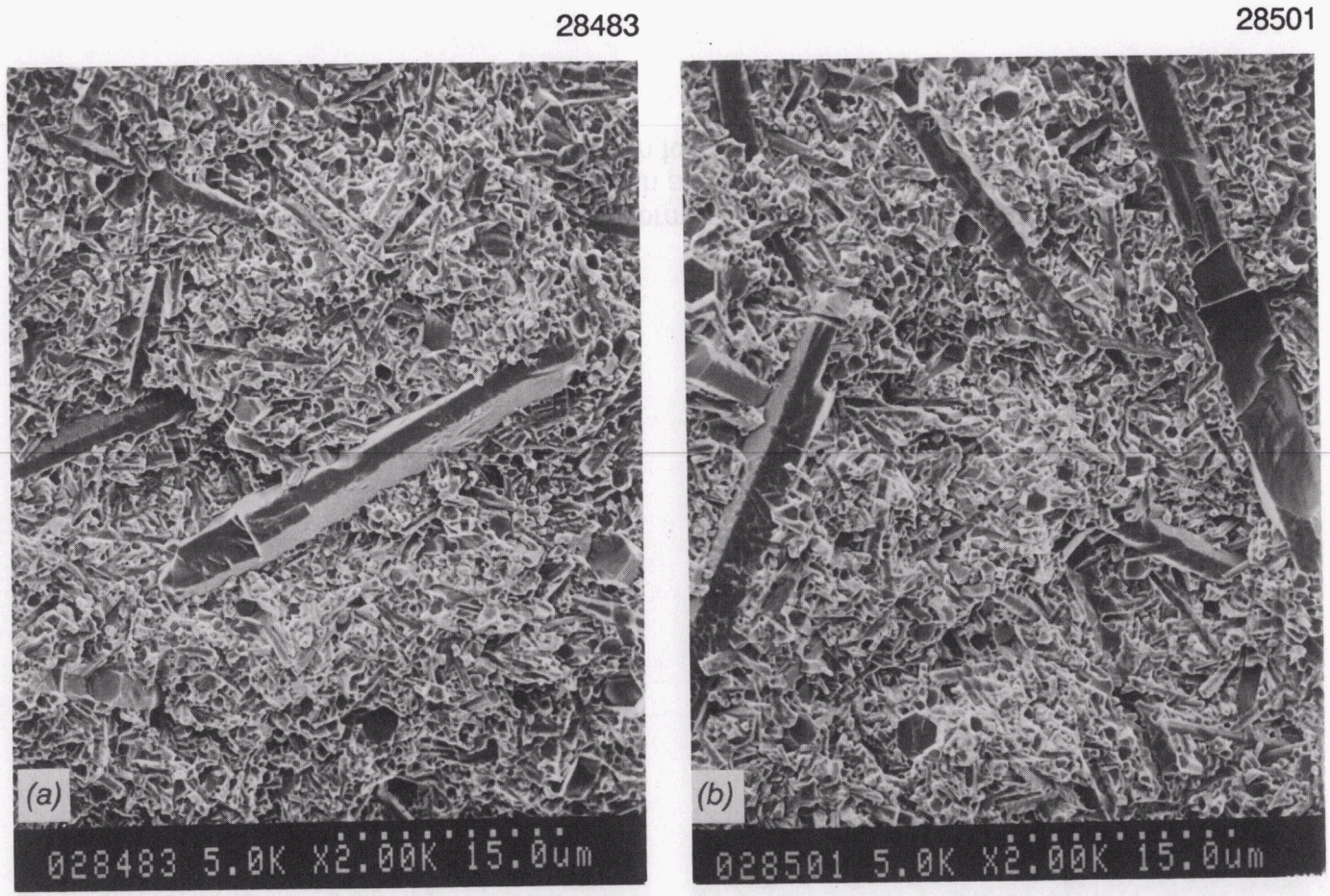

Fig. 4. Fracture surface of silicon nitride formulated to contain $Sr_2Y_8(SiO_4)_6O_2$ as the grain boundary phase: (*a*) sintered at 0.2 MPa nitrogen at 1850°C for 4 h; density is 98.2% T. D. and (*b*) sintered at 0.3 MPa nitrogen at 1850°C for 2 h followed by 2.0 MPa nitrogen at 1900°C for 2 h; density is 99.6 % T. D.

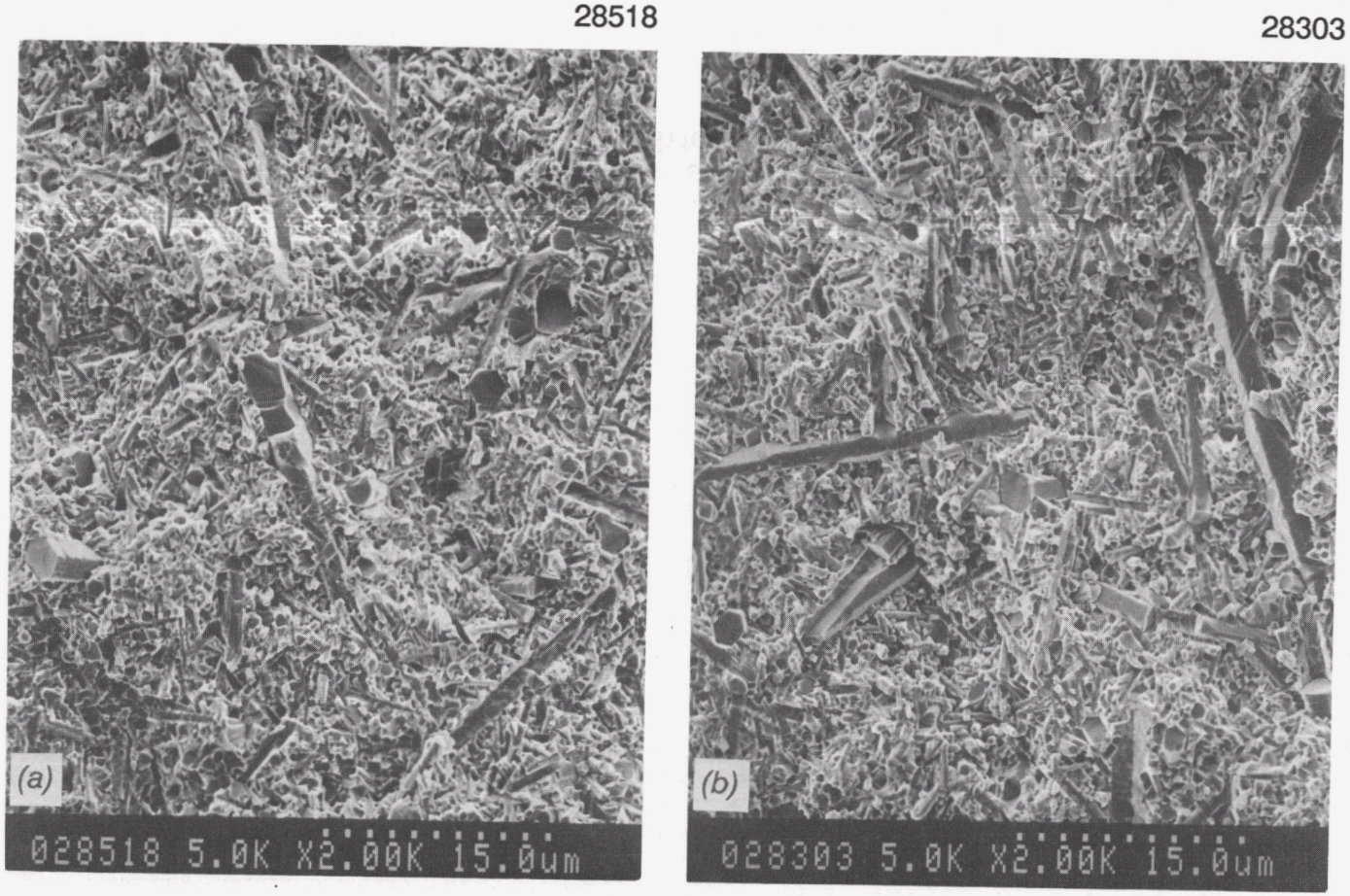

Fig. 5. Fracture surface of silicon nitride formulated to contain $Sr_2La_8(SiO_4)_6O_2$ as the grain boundary phase: (*a*) sintered at 0.2 MPa nitrogen at 1850°C for 4 h; density is 99.4% T. D. and (*b*) sintered at 0.3 MPa nitrogen at 1850°C for 2 h followed by 2.0 MPa nitrogen at 1900°C for 2 h; density is 99.1% T. D.

Table 6. Comparison of flexural strengths for cold isostatically pressed and slip-cast specimens of Si_3N_4-8% Y_2O_3-5.6 % SiO_2-1.8% SrO sintered to high density. The slip-cast specimens consistently showed higher strengths.

Sample	Density (g/cm^3)	Cold forming technique[1]	Sintering conditions (°C/h)	Flexural strength at 25°C (MPa)	Flexural strength at 1200°C (MPa)
TRSN-3-1	3.24	CIP	1850/2 1900/2	452 ± 19	258 ± 25
TRSN-3-2	3.27	CIP	1850/2 1950/2	475 ± 33	297 ± 45
SC-293	3.26	Slip-Cast	1850/2 1900/2	730 ± 51	464 ± 34
SC-293-4	3.29	Slip-Cast	1850/2 1950/2	647 ± 17	424 ± 30
SC-293-5	3.20	Slip-Cast	1750/4	778 ± 28	447 ± 20
SC-293-6	3.23	Slip-Cast	1800/4	697 ± 56	475 ± 20
SC-293-3	3.21	Slip-Cast	1850/4	730 ± 51	526 ± 49

[1]CIP = Cold-isostatically pressed.

31749

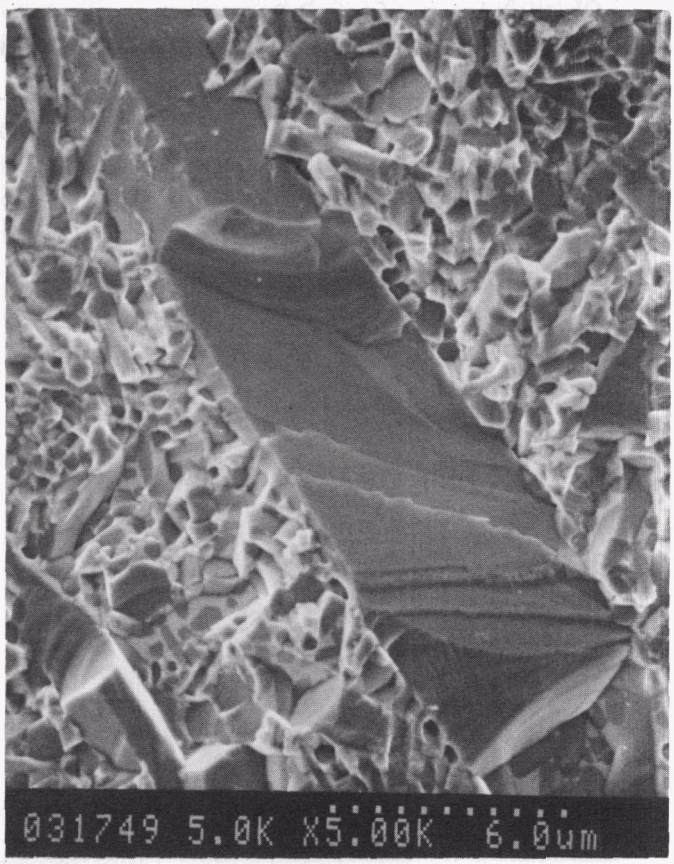

Fig. 6. Example of exaggerated grain growth in gas-pressure sintered silicon nitride. Sample TRSN-15-2.

nitrogen), excess nitrogen came out of solution and formed gas bubbles as shown in Fig. 7. Modification of the crystallization cycle temperature, times, and pressures will be systematically varied to eliminate these types of defects.

Microstructure Development - Small samples of the compositions listed above were fired to 1700 or 1800°C and held at temperature for only 15 min. Densities and $\beta/(\beta+\alpha)$ ratios were measured to determine the progress of microstructural development during the early stages of densification. The results on selected samples are given in Table 7. As shown, significant α-to-β transformation takes place in some samples, like TRSN-1, prior to densification. Generally, the lower the eutectic liquid formation temperature, the higher the α-to-β conversion as indicated in Fig. 8.

References

1. T. N. Tiegs et al, "Dispersion Toughened Ceramic Composite," pp. 158-69 in *CeramicTechnology Project Semiannual Progress Report for October 1991 through March 1992*, ORNL/TM-12133, Martin Marietta Energy Systems, Inc., Oak Ridge Natl. Lab., 1992.

31675

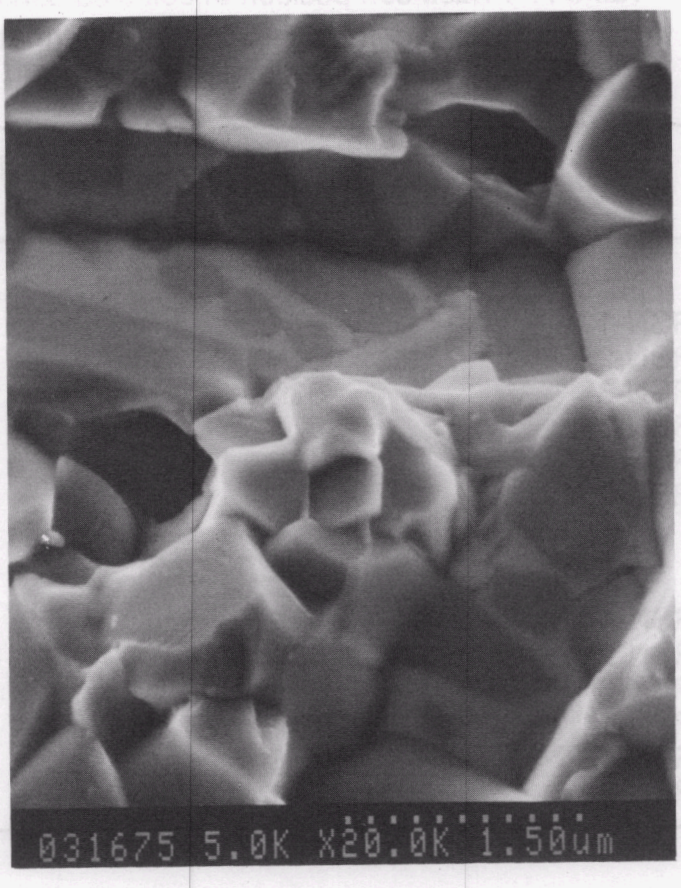

Fig. 7. Evidence of gas bubble formation in gas-pressure sintered silicon nitride. Sample TRSN-1-2.

Table 7. Phase composition of selected samples partially fired to determine α-to-ß transformation during early stages of densification.

	Density (% T. D.)	ß/(α-to-ß) Ratio
	1700°C for 15 min	
TRSN-1	77.6	41
TRSN-2	61.4	27
TRSN-3	53.2	32
TRSN-14	57.7	10
TRSN-18	48.2	16
TRSN-20	61.6	38
	1800°C for 15 min	
TRSN-1	82.2	>98
TRSN-2	68.8	90
TRSN-3	66.1	--
TRSN-14	70.2	38
TRSN-18	74.9	50
TRSN-20	74.1	--

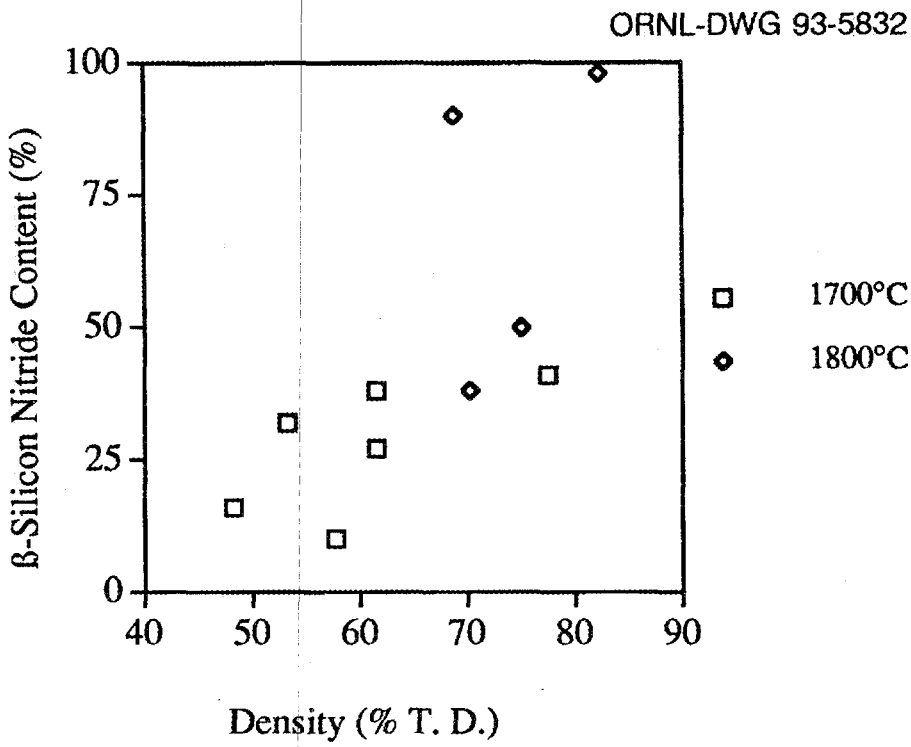

Fig. 8. ß-Silicon nitride content as a function of density.

2. E. Tani, S. Umebayashi, K. Kishi, K. Kobayashi, and M. Nishijima, "Gas-Pressure Sintering of Si_3N_4 With Concurrent Addition of Al_2O_3 and 5 wt % Rare Earth Oxide: High Fracture Toughness with Fiber-Like Structure," *Am. Ceram. Soc. Bull.* **65**(9),1311-15 (1986).

Status of milestones

Milestone 123111, "Fabricate high-toughness silicon nitride materials with elongated grain microstructures," was not completed due to previous delays in operation of the GPS.

Communications/visits/travel

S. D. Nunn attended the Annual Meeting of the American Ceramic Society from April 11-16, 1992, in Minneapolis, Minnesota.

P. A. Menchhofer attended the Annual Meeting of the American Ceramic Society from April 11-16, 1992, in Minneapolis, Minnesota.

Travel by T. N. Tiegs on September 29, 1992, to Knoxville, Tennessee, to present a seminar to the University of Tennessee Graduate Seminar entitled, "Development of Silicon Nitride Ceramics for Structural Applications."

Problems encountered

None

Publications

Draft paper written by T. N. Tiegs entitled, "Whisker Synthesis Processes," for publication in *Non-oxide Ceramic Engineering*, Van Nostrand Reinhold Publishers.

1.2.4 Silicate Matrix

Low Expansion Ceramics for Diesel Engine Applications
D. A. Hirshfeld and J. J. Brown (VPI)

Objective/Scope

Optimize the chemistry, properties, and processing of selected low thermal expansion compositions based on the zircon (NZP) and the β-eucryptite-$AlPO_4$ systems. These materials also exhibit stable properties above 1200°C. The major objective is to demonstrate fabricability and to promote commercialization of these ceramics.

Technical Highlights

Zircon (NZP) System

Three forming methods of $(Ca_{0.6},Mg_{0.4})Zr_4(PO_4)_6$ [CMZP] monolithic ceramics have been studied: 1. Hot Pressing, 2. Pressureless Sintering, and 3. Hot Isostatic Pressing (HIPping). Hot pressing was undertaken at Caterpillar, Inc. by Dr. M. H. Haselkorn. Various processing conditions were analyzed using single phase, sol-gel formed, amorphous powder. Densities were all greater than 97% of theoretical. The microstructure of the densest specimen showed minimal porosity with a grain size of 6-7μ with some grains >10μ (Figure 1). Hot pressing conditions of 5°C/min to a final temperature of 1290°C for 4 h and applying a 5600 psi pressure at the final temperature resulted in the 4 point Modulus of Rupture value of 136 MPa.

Since some of these hot pressed samples exhibited evidence of liquid phase sintering, it was theorized that sol-gel CMZP powder should be able to be cold-pressed and sintered. Following the "optimal" hot pressing conditions, sol-gel powder was pressed and fired to 1250°C for 4 h. Maximum density achieved was 85% of theoretical. Judging from the unsintered agglomerates in the microstructure, the sintering time was upped to 24 h, which increased the density to 93%. The resultant microstructure consisted of porous agglomerates with no distinct grain structure.

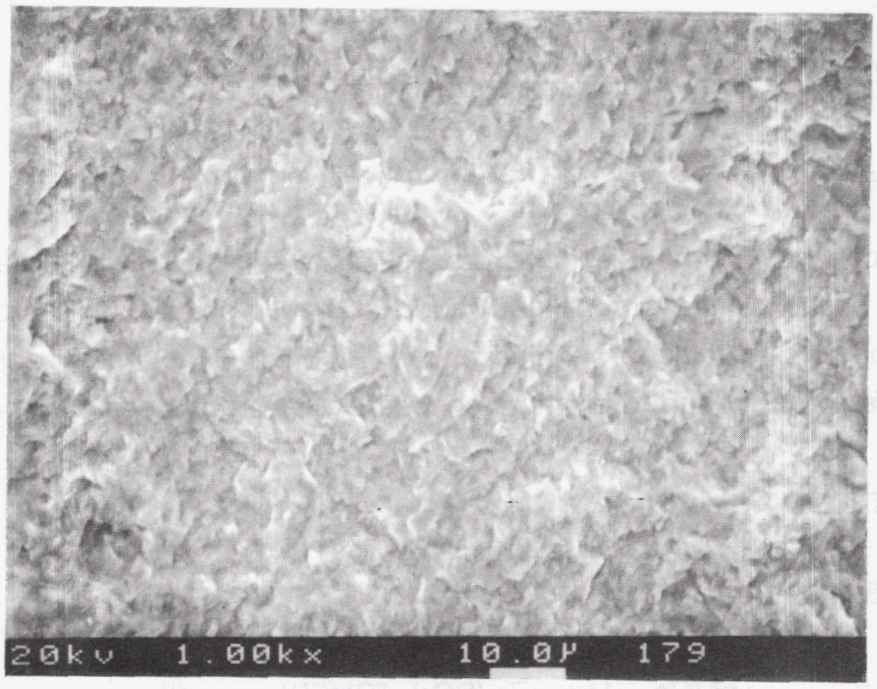

Fig. 1. Fracture Surface of Hot Pressed CMZP, fracture surface, 98% theoretical density

To enhance the sintering process and improve densification, ZnO and MgO were added to the dry amorphous powder. Agrawal and Stubican[1] reasoned that the ionic radii of Mg^{2+} and Zn^{2+} are similar to Zr^{4+} (0.86, 0.89, and 0.86Å, respectively) which may lead to improved sintering via an ionic exchange mechanism. Equally important is the liquid phase formation from the Mg and Zn phosphates which melt below the sintering temperature (about 1186 and 1000°C), aiding in densification. Table 1 shows that adding 2 wt% ZnO led to a density 96% of theoretical and 5 wt% MgO resulted in 94% theoretical density. Some porosity was visible on fracture surfaces and the grain size was 10 and 20μ, respectively, as shown in Figure 2 and 3. Figure 4 plots theoretical density against sintering aid content.

To determine if further densification was possible for flexural strength studies, HIPping of monolithic CMZP was also studied. Taguchi methods have been applied to optimize the HIPping process. Two levels of each factor were tested: HIP temperature, pressure, and

Table 1. Cold Pressing and Sintering Summary

Composition	(°C/min, °C, h)	Density	Microstructure
CMZP	5, 1250, 4	85%	unsintered agglomerates, very porous
CMZP	5, 1300, 24	93%	porous agglomerates, no grain structure
CMZP + 2wt% ZnO	10, 1200, 24	96%	relatively dense, few pores, grain size 15-20μ
CMZP + 5wt% MgO	10, 1200, 24	94%	uniform grain structure, small pores, grain size <10μ

* Cold pressure applied: 20-25 ksi

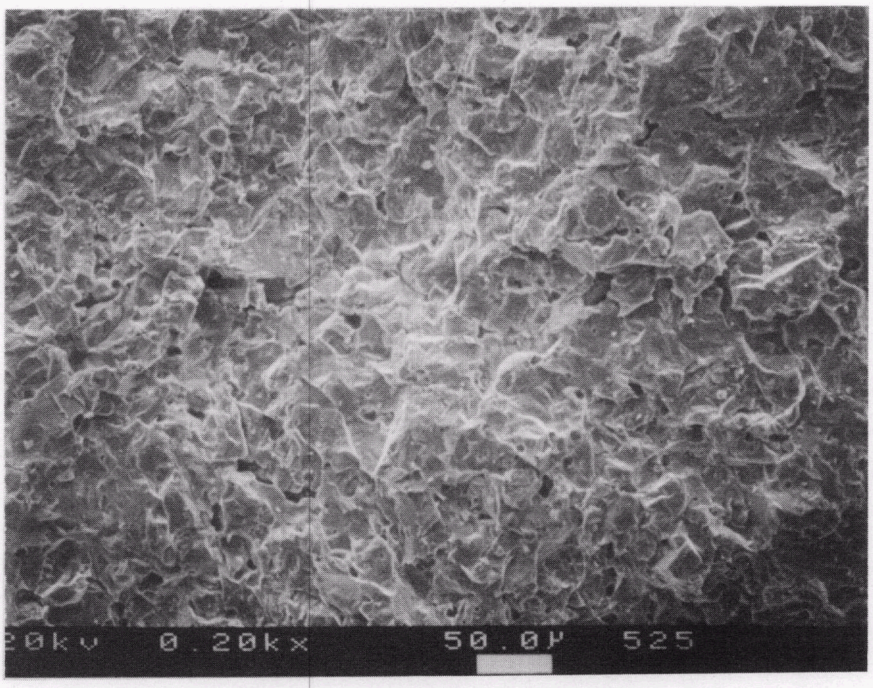

Fig. 2. Fracture surface of CMZP with 2wt% ZnO, Cold-pressed and sintered, 96% theoretical density

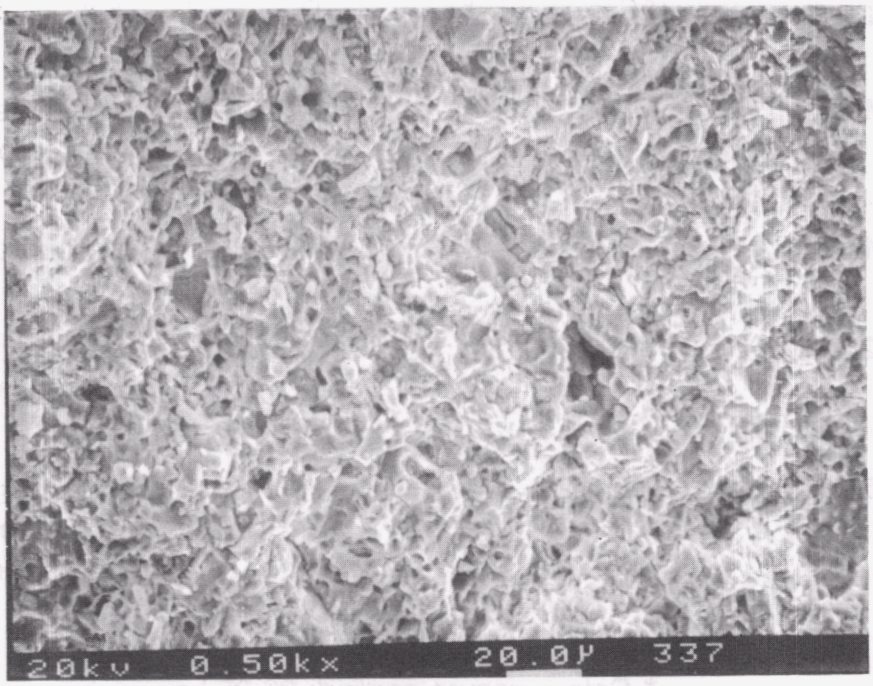

Fig. 3. Fracture surface of CMZP with 5 wt% MgO, Cold-pressed and sintered, 94% theoretical density

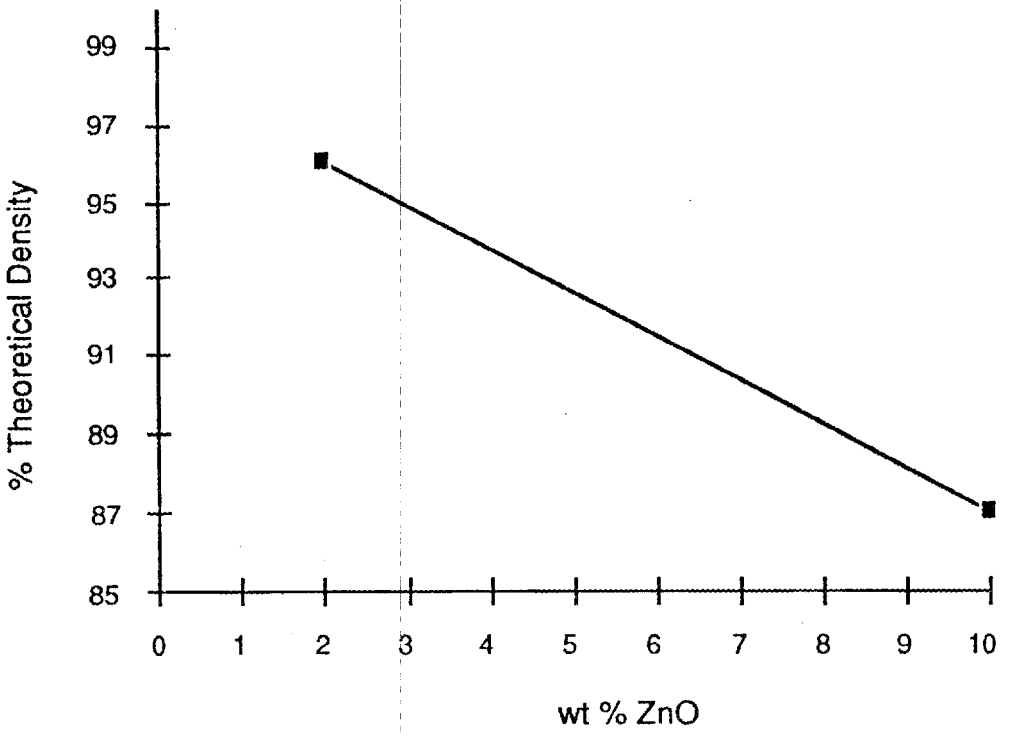

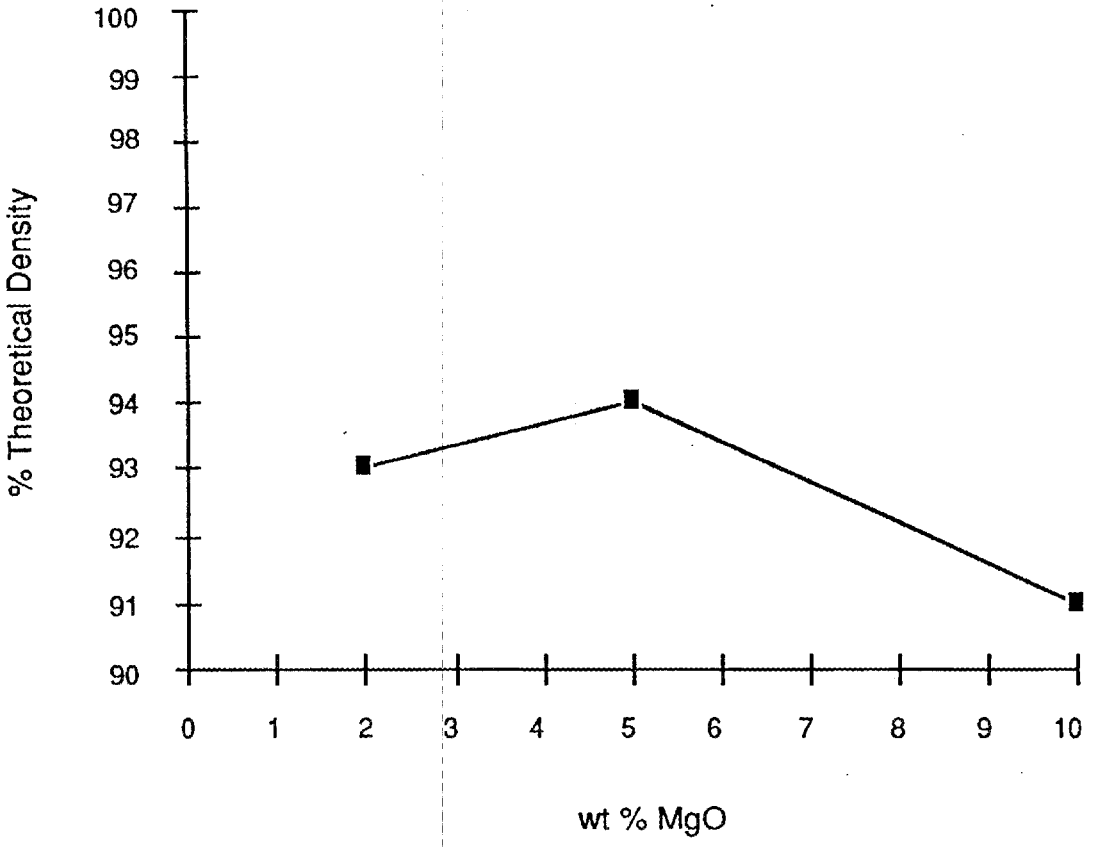

Figure 4. Density vs. Sintering Aid Content of CMZP

time. The experiment resulted in densities greater than 98% of theoretical with optimal levels at 1050°C, 15 ksi, and 30 min, as shown in Table 2. The microstructure was very dense with minimal porosity (in size and number of pores) and the grain size was approximately 2-3μ as seen in Figure 5.

Ceramic Composites

The densification of SiC whisker and chopped Nicolan-SiC fiber reinforced CMZP composites (SiCw/CMZP and SiCf/CMZP, respectively) using hot isostatic pressing (HIP) the room temperature flexural strength of SiCw/CMZP composites and the effects of whisker content and HIPping parameters on the strength were investigated. The flexural strength of SiCw/CMZP composites was found to increase with whisker content. All the SiCw/CMZP composites containing 20 vol% of whiskers HIPped at temperatures from 1030 to 1070°C exhibited flexural strengths higher than 110 MPa. The best HIPping temperature-pressure-time combination to optimize the flexural strength of SiCw/CMZP composites was determined to be 1050°C-15000 psi-0.25 h.

To prepare composite samples, sol-gel derived amorphous CMZP powders and SiC whiskers or chopped Nicolan-SiC fibers were first mixed and blended in water to obtain homogeneous mixtures. The mixtures were then air-dried and cold pressed into billets.

Table 2. Taguchi Experimental Conditions for HIPping

Processing Parameters (°C, ksi, min)	Density	Grain Structure & Size
1050, 10, 15	95.2%	very dense, 2-3μ
1050, 15, 30	98.1%	very dense, uniform structure, 2-3μ
1150, 10, 30	94.5%	bimodal grain size distribution, 2-3 & 4-5μ, slightly more porous
1150, 15, 15	93.8%	bimodal grain size distribution, 2-3 & 4-5μ, slightly more porous

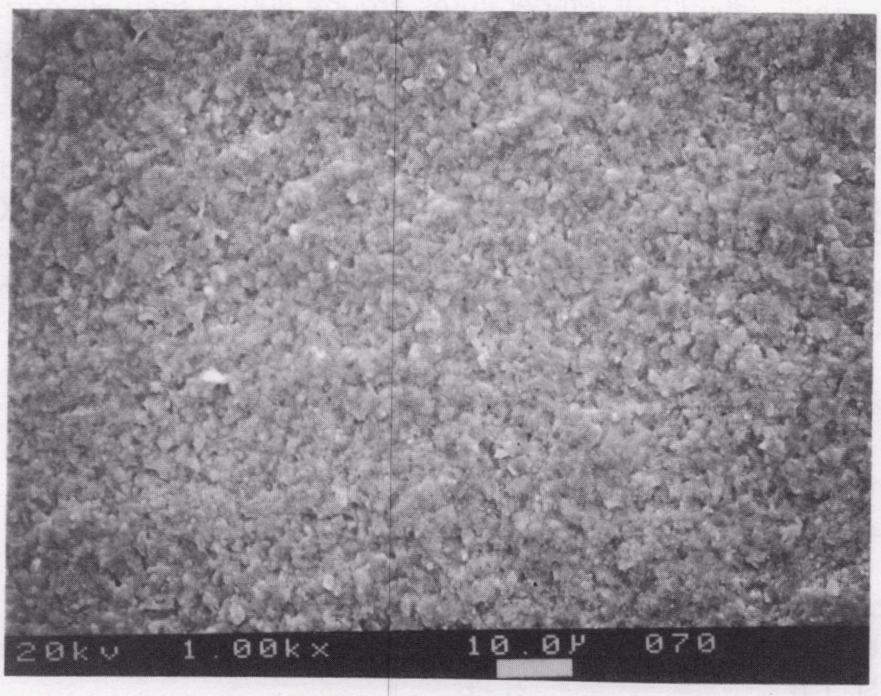

Fig. 5. Fracture surface of HIPped CMZP, 98% theoretical density

The billets were fired at 1000°C for 6 hours to remove volatiles prior to encapsulation in Pyrex glass tubes under vacuum at temperatures around 800°C then HIPped. During HIPping, the crystallization of amorphous CMZP matrix and densification of the composite take place simultaneously.

Because SiCw/CMZP is a new system, appropriate HIPping parameters could only be determined by trial-and-error. Based on experience in hot pressing SiCf/CMZP composites, HIPping experiments at temperatures between 1250 and 1400°C at pressures of 10 and 15 ksi for times between 10 minutes and 2 hours were examined as shown in Table 3.

Table 3. Densification of SiCw/CMZP Composites by HIPping

HIPping parameters (Temperature, Pressure, Time)	Porosity (%)
10 vol% whisker content:	
1280°C, 15 ksi, 1 h	3 - 4
1300°C, 15 ksi, 1 h	5 - 6
1300°C, 15 ksi, 2 h	7 - 8 (aging: 1100°C/10 h)
1350°C, 15 ksi, 0.5 h	6 - 7 (aging: 1100°C/10 h)
20 vol% whisker content:	
1250°C, 15 ksi, 10 min.	6 - 8
1280°C, 15 ksi, 1 h	10 - 12 (aging: 1100°C/10 h)
1350°C, 10/15 ksi, 0.5/0.5 h	10 - 12
1400°C, 15 ksi, 0.5 h	8 - 9

The results indicate that at the tabulated pressures, raising HIPping temperature above 1250°C and/or extending soaking time does not promote the densification. On the other hand, standard X-ray diffraction analysis (XRD) showed that in the sample, containing 20 vol% whiskers HIPped at 1250°C for 10 minutes, only SiC and CMZP phases existed, while phases other than SiC and CMZP were found in the samples with the same whisker content but HIPped at 1350°C. The results suggest that HIPping should be performed at lower temperatures and for shorter times.

To facilitate the study of the densification, Taguchi methods were used to design another group of experiments and analyze the results.[2] Examining the results of the previous experiments, the HIPping temperature (T), pressure (P), and soaking time (t) were found to significantly affect the densities. To compare their effects and consequently find desirable T-P-t combination(s) to achieve high densities for SiCw/CMZP composites, a

three factor-two level ($L_4(2^3)$) array[2] was chosen to arrange the second group of HIPping experiments with the following settings: T_1 = 1250°C, T_2 = 1150°C; P_1 = 15000 psi, P_2 = 10000 psi; t_1 = 30 min., t_2 = 15 min. The HIPping parameters and the achieved densities in this group of experiments are summarized in Table 4.

Table 4. Densification of SiCw/CMZP Composites by HIP

HIPping parameters (°C, psi, min.)	Density (%) 10 vol% whiskers	20 vol% whiskers
1250, 15000, 30	98.5	96.7
1250, 10000, 15	97.0	97.8
1150, 15000, 15	98.5	99.7
1150, 10000, 30	99.6	99.6

Analysis of the variance of density as a function of HIPping temperature, pressure, time and whisker content is shown in Table 5. It can be seen from Table 5 that of among these factors, temperature causes the largest variance in density, followed by soaking time, pressure, and whisker content in a descending order of the importance.

Table 5. Analyses of Variance in Density

Source	Degree of freedom	Variance in Density ($\%_7$)
Temperature	1	6.845
Pressure	1	0.045
Soaking time	1	0.245
Whisker content	1	0.005
Error	3	0.885
Total	7	1.399

Although densities greater than 99% were achieved by HIPping at 1150°C, analysis of the results using the Taguchi method suggests that at the tabulated pressures and times, the HIPping temperature can be lowered, and at the lower temperature(s), equal or higher densities can be achieved but the variance in density due to temperature change can be minimized. As HIPping at low temperatures can decrease processing costs and usually results in a better microstructure, a third group of experiments was designed and executed to study the densification of SiCw/CMZP composites in the temperature range of 1150 - 1050°C. (Table 6).

Table 6. Densification of CMZP/SiCw Composites by HIP

HIPping parameters (°C, psi, min.)	Density (%) 10 vol% whiskers	20 vol% whiskers
1050, 15000, 30	99.7	99.8
1050, 10000, 15	99.6	99.9
1150, 15000, 15	98.5	99.7
1150, 10000, 30	99.6	99.6

The phase composition of the eight samples was determined by standard XRD techniques and no phases other than CMZP and SiC were found. The samples were dark green in color except for those HIPped at 1050°C which were lighter. This color difference indicates that there is a possibility of a reaction between SiC and CMZP and the tendency of the reaction increases with temperature. To further explore the possibility to densify SiCw/CMZP composites by HIPping at lower temperatures, two samples with SiC whisker contents of 10 and 20 vol%, respectively, were HIPped at 1000°C at 15 ksi for 30 minutes. Although densities of >99% were achieved for the both, XRD analysis indicated that the CMZP matrix was not completely crystallized. Thus, for the tabulated pressures and times, a HIPping temperature of about 1050°C is required to form crystalline composites.

Analysis of the variance in the density as a function of HIPping and whisker content within the temperature range of 1050 - 1150°C is shown in Table 7. The most important factor affecting the density, i.e. the factor contributing the largest variance in density, is now the whisker content rather than a HIPping parameter (T, P, or t). These results indicate that HIPping at temperatures about 1050°C at pressure of 10000 to 15000 psi for 15 to 30 minutes is favorable for the densification of SiCw/CMZP composites.

Table 7. Analyses of Variance in Density

Source	Degree of freedom	Variance in Density ($\%^2$)
Temperature	1	0.281
Pressure	1	0.151
Soaking time	1	0.101
Whisker content	1	0.320
Error	3	0.142
Total	7	0.188

It is concluded from the results that: (1) using amorphous CMZP powder and SiC whisker as starting materials, nearly fully densified SiCw/CMZP composites with a desirable phase composition can be prepared by cold pressing - pre-sintering - HIPping (2) optimum densification of SiCw/CMZP composites is achieved by HIPping at about 1050°C at pressures of 10000-15000 psi for 15-30 minutes, and (3) because the density is near 100% and no longer sensitive to small changes in processing parameters, the desirable HIPping T-P-t combination(s) should be found to optimize the mechanical properties.

Based on the experience obtained from processing SiCw/CMZP composites, SiCf/CMZP composites were HIPped at temperatures from 1050 to 1250°C at pressures 10000 to 15000 psi for 15 to 30 minutes. The HIPping parameters and achieved densities for the SiCf/CMZP composites are summarized in Table 8 and indicate that the best temperature for the densification by HIPping is 1150°C.

Table 8. Densification of SiCf/CMZP Composites by HIP

Processing parameters	Density(%)	
°C, psi, min.)	10 vol% fibers	20 vol% fibers
1050, 15000, 30	97.9	98.2
1050, 10000, 15	97.6	98.1
1150, 15000, 15	98.5	98.9
1150, 10000, 30	98.0	98.5
1250, 15000, 30	97.9	97.8
1250, 10000, 15	97.7	97.3

To find the desirable HIPping T-P-t combination(s) to optimize flexural strength, SiCw/CMZP composites were prepared by HIPping at temperatures from 1030 to 1070°C at pressures from 10000 to 15000 psi for 15 to 30 minutes, and then their room temperature flexural strength was determined. Again, Taguchi methods were used in designing the experiments and analyzing the results. The HIPped samples were machined into 2-4 MOR bars according to Military Spec. 1942 B then tested following the same specifications. The processing parameters and measured strength of the samples are summarized in Table 9. All the samples listed were measured to have a density greater than 99% of theoretical and determined by standard XRD to have no phases other than CMZP and SiC.

Table 9. Flexural Strength of SiCw/CMZP Composites

Whisker content(vol%)	HIPping parameters (°C, psi, min.)	Strength values Average (MPa)
5	1030, 10000, 15	68.9±11.9
5	1050, 10000, 30	59.4±6.6
10	1050, 10000, 30	98.4±1.6
10	1070, 10000, 15	84.4±1.9
20	1030, 10000, 15	116.1±0.6
20	1030, 15000, 30	111.5±0
20	1050, 10000, 30	126.7±0.8
20	1050, 15000, 15	135.6±10.6*
20	1070, 10000, 15	120.1±7.1
20	1070, 15000, 30	119.0±5.2

Among these samples, the lowest strength value measured was 47 MPa for the sample containing 5 vol% of SiCw and HIPped at 1030°C at 10000 psi for 15 minutes, the highest is 148 MPa for the sample containing 20 vol% of SiCw and HIPped at 1050°C at 15000 psi for 15 minutes.

The flexural strength is plotted against whisker content in Figure 6 for SiCw/CMZP composites HIPped using different T-P-t combinations. It can be seen from Table 9 and Figure 6 that the flexural strength of the SiCw/CMZP composites increases with whisker content. In fact, some of the HIPped SiCw/CMZP composite samples containing 5 or 10 vol% of SiC whiskers broke during machining while all the samples with SiC whisker contents of 20 vol% survived under the same machining conditions. Furthermore, compared to monolithic CMZP hot pressed at temperatures between 1260 and 1290°C with flexural strength varying from 73 to 136.3 MPa,[3] the SiCw/CMZP composites, especially the ones containing 20 vol% of whisker, exhibited a much smaller strength variation (Table 9).

Analysis of the flexural strength of the SiCw/CMZP composites containing 20 vol% of whisker as a function of HIPping temperature, pressure, and time using Taguchi methods is summarized in Figure 7, 8 and 9. The results indicate that the best HIPping T-P-t combination to optimize the flexural strength of the SiCw/CMZP composites is 1050°C-15000 psi-15 min.

β-Eucryptite-$AlPO_4$ System

The mechanical properties of modified β-eucryptite glass ceramics [96%$(Li_{0.4},Ca_{0.05})Al(Si_{0.75},P_{0.5})O_{4.5}$, 4% TiO_2] are improved through the formation of in-situ

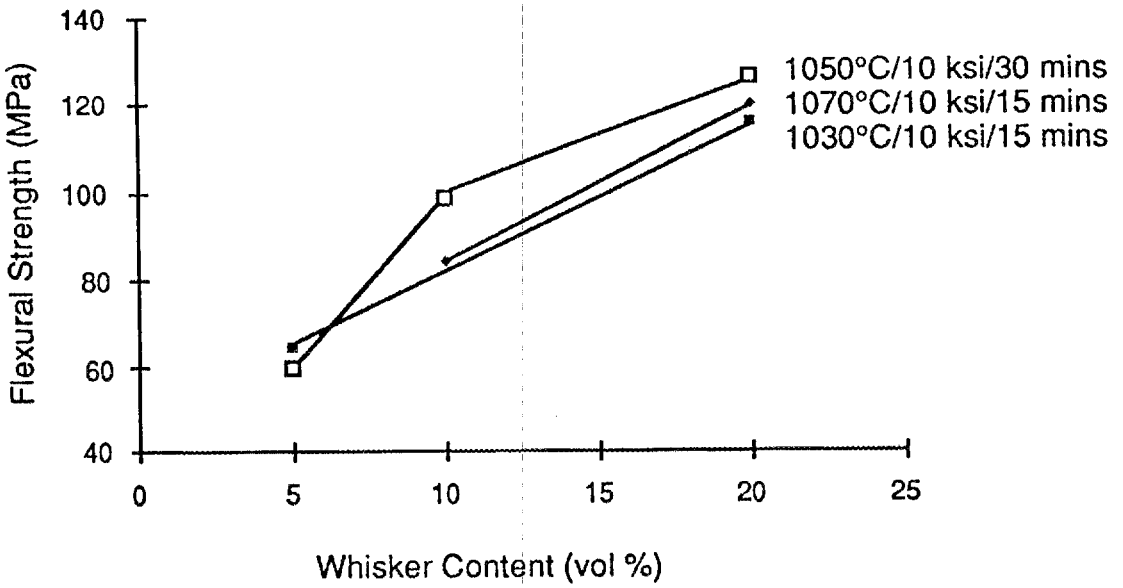

Fig. 6. Flexural strength of SiCw/CMZP composites found under different HIPping conditions

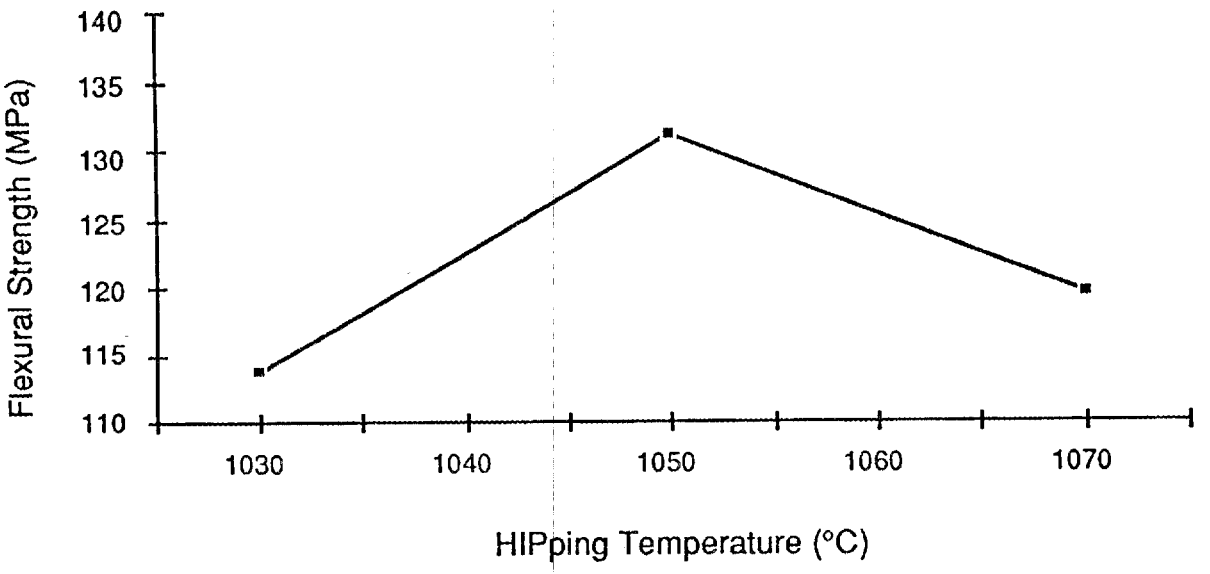

Fig. 7. Flexural strength of 20 wt% SiCw/CMZP composites as a function of HIPping temperature

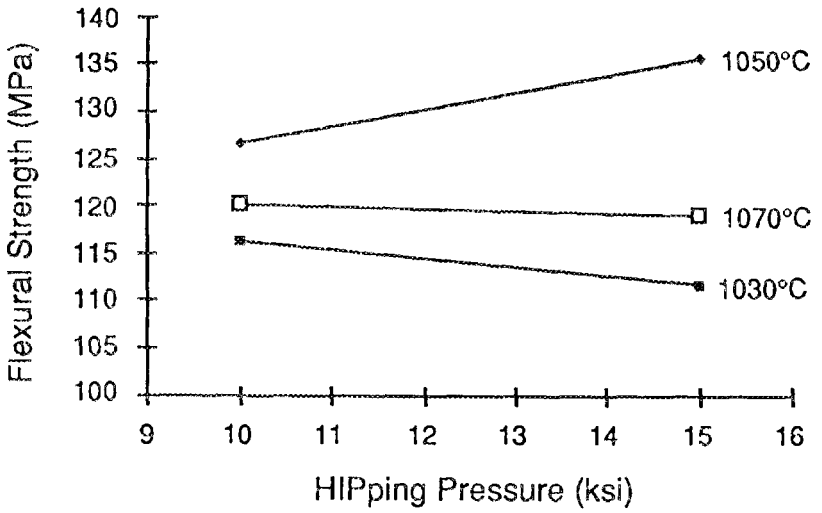

Fig. 8. Flexural strength of 20 wt% SiCw/CMZP composites as a function of HIPping pressure

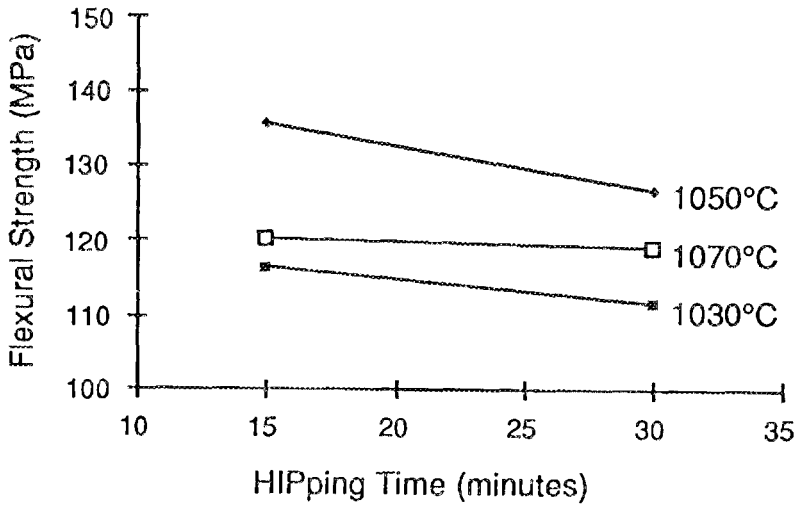

Fig. 9. Flexural strength of 20 wt% SiCw/CMZP composites as a function of HIPping time

TiO_2 whiskers as summarized in Table 10.

Table 10. Mechanical properties of $AlPO_4$ modified β-eucryptite glass-ceramics

Crystallization Heat Treatment	Elastic Modulus (GPa)	MOR (MPa)	K_{IC} (Mpa•√m)
original glass	62±9*	66±5	1.1±0.03
850°C, 2h**	67±8	81±12	--
950°C, 10h**	68±13	72±19	1.2±0.07
1040°C, 20h***	85±8	134±13	1.6±0.04

*95% confidence intervals shown
**Glass-ceramics without TiO_2 whisker precipitation
***Glass-ceramic with TiO_2 whisker precipitation

Strengthening of the in situ TiO_2-reinforced $AlPO_4$ modified β-eucryptite glass-ceramic matrix composite is attributed to three factors:

(1) Precipitation of TiO_2 whiskers which are stiffer (E=283 GPa)[4] and stronger (over 300 MPa)[5] whiskers than the $AlPO_4$ modified β-eucryptite glass-ceramic matrix.

(2) Average aspect ratio of the precipitated TiO_2 whiskers is 28, which is much greater than the critical aspect ratio (l/d=8) which is determined from an empirical equation developed by Termonia[6] where E_w is the elastic modulus of the TiO_2 whisker (E_w

$$\left(\frac{l}{d}\right)_c = \frac{2E_w}{E_m}$$

= 283 GPa) and E_m is the elastic modulus of the $AlPO_4$ modified β-eucryptite glass-ceramic (E_m = 67 GPa).

(3) No whisker pull-outs were observed on the fracture surface of the in situ composite, indicating strong interfacial bonding between the whisker and the matrix.

The increase in elastic modulus of $AlPO_4$-modified β-eucryptite glass-ceramic from 67 GPa

to 85 GPa is attributed to TiO_2 whiskers which have a high elastic modulus (283 GPa).

The modulus of the randomly oriented TiO_2 whisker-reinforced composite can be estimated using an empirical equation[7]

$$E_c = \frac{3}{8}E_L + \frac{5}{8}E_T$$

where E_L and E_T are the longitudinal and transverse moduli, respectively. These moduli can be calculated using the Halpin-Tasi equations[8]

$$\frac{E_L}{E_m} = \frac{1 + 2\left(\frac{l}{d}\right)\eta_L V_w}{1 - \eta_L V_w}$$

and

$$\frac{E_T}{E_m} = \frac{1 + 2\eta_T V_w}{1 - \eta_T V_w}$$

where

$$\eta_L = \frac{(E_w/E_m) - 1}{(E_w/E_m) + 2(l/d)}$$

and

$$\eta_T = \frac{(E_w/E_m) - 1}{(E_w/E_m) + 2}$$

The glass-ceramic heat treated at 1040°C for 20 h contains about 12 vol% of randomly oriented TiO_2 whiskers with average aspect ratios of 28. Using E_w = 283 GPa, E_m = 67 GPa, V_w = 0.12, and (l/d) = 28 in the Halpin-Tsai equations., the modulus is calculated as E_c = 84 GPa which confirms the value (85 GPa) measured experimentally.

Fracture toughness, K_{IC} measured by the indentation method using a 9.8 N load was increased with the formation of TiO_2 whiskers. The indented surface observations revealed that crack deflection and crack branching by the TiO_2 whiskers may contribute

to improving fracture toughness of this composite (Figure 10). The degree of crack deflection is governed by residual stresses around the whiskers which arise due to a thermal expansion mismatch and the interfacial bonding strength between the whiskers and the matrix. The bulk coefficient of thermal expansion of TiO_2 is approximately 7.3 x 10^{-6}/°C which is much larger than that of modified β-eucryptite (less than 0.4 x 10^{-6}/°C). Khaund et al.[9] have shown that localized stress concentrations, i.e., those resulting from expansion mismatch, may increase the crack tip stress intensity factor and thus result in a lowering of the applied stress required to propagate cracks. In order to examine the residual stress effect on the fracture toughness, an experimental study was conducted where samples were quenched in air or water.

Samples of modified β-eucryptite glass were heat treated at 740°C for 1 h and at 1040°C for 20 h to allow in situ growth of TiO_2 whiskers, then cut into blocks (4 x 5x 15 mm) and polished. To introduce different levels of residual stress, the blocks were quenched from 400°C, 600°C, 800°C, and 1000°C into either air or water at 25°C. Critical fracture toughness, K_{IC}, was determined by indentation using 8 indents with a 9.8 N load.

As shown in Table 11, air quenching has no effect on the K_{IC} values. However, there was a decrease in the average fracture toughness with water quenching, with a significant decrease noted for the sample quenched from 800°C. This sample exhibited localized regions of microcracking. The sample quenched from 1000°C into water exhibited more severe localized microcracking and a higher value of K_{IC}, possibly due to microcrack toughening.

No change in the K_{IC} value with air quenching indicates that the actual residual stresses due to thermal expansion mismatch in the given fabrication conditions (cooling from the in situ composite fabrication temperature in a furnace with 60°C/h cooling rate) do not affect fracture toughness value. Therefore, crack deflection around the whisker is governed by bonding between the whisker and the matrix. Strong interfacial bonding between the TiO_2 whisker and the glass-ceramic matrix acts effectively in this composite to improve strength of the material but does not affect fracture toughness significantly.

References

1. D.K. Agrawal and V.S. Stubican, "Synthesis and Sintering of $Ca_{0.5}Zr_2P_3O_{12}$ - A Low Thermal Expansion Material," *Mat. Res. Bull.* 20 [2], 99-106 (1985)

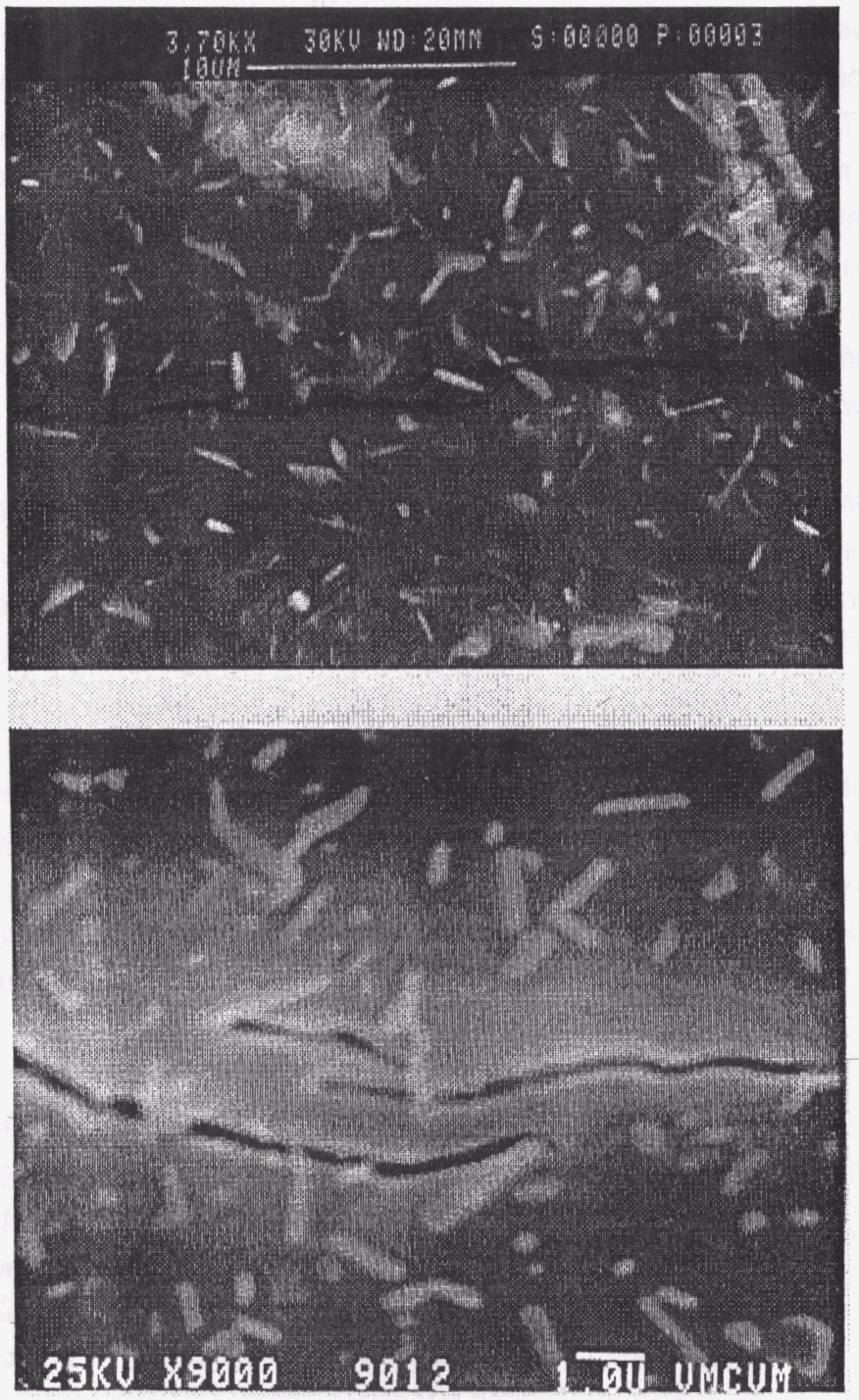

Fig. 10. Scanning electron micrographs showing indentation crack propagation in an in situ TiO_2 whisker-reinforced modified β-eucryptite glass-ceramic

Table 11. Fracture toughness of TiO_2 whisker reinforced modified β-eucryptite glass-ceramic as a function of quench temperature and condition

Quench Temp. (°C)	Quench Condition	K_{IC} (Mpa•√m)	Crack Formation
0	--	1.64±0.04*	no
400	air	1.68±0.08	no
	water	1.44±0.05	no
600	air	1.64±0.12	no
	water	1.42±0.06	no
800	air	1.64±0.06	no
	water	1.19±0.06	localized
1000	air	1.67±0.10	no
	water	1.59±0.10	more severe than 800°C

*95% confidence interval

2. G.Taguchi and Y.Wu, "Introduction to Off-Line Quality Control", Central Japan Quality Control Association, Japan, (1985)

3. D.A.Hirschfeld and J.J.Brown, "Low Expansion Ceramics for Diesel Engine Applications", Semiannual Progress Report for the Period October 1, 1991 through May 31, 1992

4. S. Musikant, *What Every Engineer Should Know about Ceramics*, pp. 104-5, Dekker, New York, 1991

5. H.P. Kirchner, and R. M. Grover, "Strength-Anisotrophy-Grain Size Relations in Ceramic Oxides," *J. Am. Ceram. Soc.*, **Vol.** 53 [5], pp. 232-236 (1970)

6. Y. Termonia, "Theoretical Study of the Stress Transfer in Single Fiber Composite," *J. Mat. Sci.*, **Vol.** 22, pp. 504-8 (1987)

7. B.D. Agrawal and L.J. Broutman, Analysis and Performance of Fiber Composite, Wiley, New York, 1980; pp.71-103

8. J.C. Halpin and S.W. Tsai, "Effect of an Environmental Factors on Composite Materials," AFML-TR67-423, (1969)

9. A.K. Khaund, V.D. Kistic, and P.S. Nicholoson, "Influence of Elastic and Thermal Mismatch on the local Crack-Driving Force in Brittle Composites," *J. Mat. Sci.*, **Vol** 12, pp.2269-73 (1977).

Status of Milestones

A nine month no cost extension has been granted to allow completion of the evaluation of mechanical properties of the ceramics and composites.

Communications/Visits/Travel

Dr. D. A. Hirschfeld and Mr. W. S. Russ visited Dr. Michael Haselkorn at Caterpillar Corp., Peoria, IL on April 2, 1992, to discuss hot pressing of CMZP.

Drs. J. J. Brown and D. A. Hirschfeld attended the Low Expansion Ceramics Workshop in Knoxville, TN on April 30, 1992, and presented a paper on "Research in Low Expansion Ceramics at Virginia Tech."

Dr. D. A. Hirschfeld presented a paper entitled "NZP Ceramics - High Temperature Heat Resistant Materials" at the 11th Annual High Technology R&D Trade Fair, Arlington, VA, May 18, 1992.

Dr. D. A. Hirschfeld presented a seminar entitled "Development of New Low Expansion Ceramics: CMZP and Modified β-Eucryptite" at Benet Labs, U. S. Army Armament, Munitions and Chemical Command, Watervliet, NY, on July 16, 1992.

Mr. K. H. Lee and Dr. D. A. Hirschfeld attended the Fourth Symposium on Nucleation and Crystallization in Glasses and Liquids at the Glass and Optical Materials Meeting, August 16-19, in Stone Mountain, GA. Mr. Lee presented a paper entitled "In-Situ Reinforced Glass-Ceramic in the Lithia-Alumina-Silica System."

Problems Encountered

None

Figure 11 Status of milestones

	1991					1992							
Milestone	O	N	D	J	F	M	A	M	J	J	A	S	*
2.4.1													O
2.4.2			Completed										O
2.4.3													B
2.4.4													B
2.4.5			Completed										O
2.4.6													B
2.4.7			Completed										O
2.4.8													B

• On, Ahead of, or Behind Schedule

Publications

On April 7, 1992, U. S. Patent No. 5,102,836, "Ceramic Materials with Low Thermal Conductivity and Low Coefficients of Thermal Expansion" was granted to J. Brown, D. Hirschfeld, D. Liu, Y. Yang, T. Li, R. Swanson, and J. Kim.

Two patent disclosures were filed with Virginia Tech Intellectual Properties on July 9, 1992:

1. "Processing of NZP Ceramic Foam with Superfine Open Cell Structure" by T.K. Li, D.A. Hirschfeld, and J. J. Brown, Jr.
2. "CMZP Coatings" by T.K. Li, D.A. Hirschfeld, and J.J. Brown

One patent accepted by patent examiner to be issued in March, 1993:

1. "An In-Situ Whisker Reinforced Glass-Ceramic" by J.J. Brown, D.A. Hirschfeld, and K.H. Lee.

1.3 THERMAL AND WEAR COATINGS

Fabrication and Testing of Corrosion-Resistant Coatings
D. P. Stinton and D. W. Graham (Oak Ridge National Laboratory)

Objective/scope

Sodium corrosion of SiC and Si_3N_4 components in gas turbine engines is a potentially serious problem. The outer surfaces of SiC and Si_3N_4 parts oxidize at high temperatures to form an SiO_2 layer that inhibits further oxidation. However, sodium that is present in high-temperature combustion atmospheres reacts with the SiO_2 layer, such that it is no longer protective. The objective of this program is to develop a coating that will protect the underlying SiC or Si_3N_4 from sodium corrosion and provide simultaneous oxidation protection. To evaluate the behavior of potential materials such as stabilized ZrO_2 or HfO_2, TiO_2, $Al_2O_3 \cdot TiO_2$, and Ta_2O_5 in sodium-containing atmospheres, the corrosion resistance of hot-pressed samples of these materials will first be evaluated. A chemical vapor deposition (CVD) process will be developed for the application of the most promising coatings. The effect of the combustion environment upon coating characteristics such as microstructure, strength, adherence, and other properties will then be evaluated.

Technical highlights

The development of oxide coatings to protect SiC or Si_3N_4 heat engine components from sodium corrosion continued this period. Processing conditions were systematically explored to optimize the morphology of Ta_2O_5 coatings and minimize the porosity or voids present in the coating. Even though coatings consisted of large columnar grains that do not grow completely together, the coatings exhibited very good adherence since no spalling was observed even after rapid cooling from the coating temperature. Coated SiC samples were corrosion tested by applying 10 to 20 mg/cm^2 of sodium sulfate to the surface of a Ta_2O_5-coated specimen and annealing at 1000°C for 100 h. Observation of the annealed samples by optical and scanning electron microscopy revealed no visible reaction between the sodium sulfate and the Ta_2O_5. Examination of the materials by X-ray diffraction (XRD) showed that the Ta_2O_5 was unaffected by the exposure to sodium sulfate. A technical publication was completed that describes the development of corrosion-resistant oxide coatings. The paper entitled "Chemical Vapor Deposition of Ta_2O_5 Corrosion Resistant Coatings," written by D. W. Graham and D. P. Stinton, was submitted for publication in the *Proceedings of the 1992 Coatings for Advanced Heat Engines Workshop*, Monterey, California, August 1992.

The development of a CVD process for the application of $ZrTiO_4$ coatings was initiated this period. $ZrTiO_4$ was selected because of its potential corrosion resistance and its very low coefficient of thermal expansion that closely matches the thermal expansion of Si_3N_4. $ZrTiO_4$ coatings will be deposited by separately chlorinating Zr and Ti metal to form $ZrCl_4$ and $TiCl_4$ and reacting those gases with oxygen in a hot-wall tube furnace. The initial experiments identified processing conditions for the application of ZrO_2 coatings. Examination of coated samples by XRD determined that a powdery monoclinic ZrO_2 coating was deposited. Similar experiments were utilized to determine processing conditions for the application of TiO_2 coatings. After combining the two processes, experiments will be initiated to determine processing conditions for the application of $ZrTiO_4$ coatings.

Development of Adherent Coatings to Reduce Contact Stress Damage of Ceramics

V. K. Sarin (Boston University)

Objective/Scope

The development of oxidation/corrosion resistant, high toughness, adherent coating configurations for silicon based ceramic substrates for use in advanced gas turbine engines.

Technical Progress

Al_2O_3 coatings have been successfully grown on Si_3N_4 substrates in a reactor geometry that is also suitable for depositing SiO_2. Several difficulties were encountered in trying to deposit Al_2O_3 in the same reactor geometry. As was previously reported SiO_2 coatings had been deposited on Si_3N_4 using Tetraethoxysilane $[Si(OC_2H_5)_4]$ as the source at 800°C and 50 torr pressure. Growth rates were typically in the range of 1 μm per hour. Process parameters used for depositing Al_2O_3 were varied within the range established for SiO_2. The reactor geometry and process parameters had to be adjusted so as to accommodate both SiO_2 and Al_2O_3 coatings. In-situ formed $AlCl_3$, and H_2O formed by the water-gas-shift reaction of H_2 and CO_2 were used as the reactants in formation of Al_2O_3. Figure 1 shows an SEM micrograph of Al_2O_3 coating on Si_3N_4 grown at 900°C and 50 torr pressure. The growth rates were in the order of 0.5 μm per hour. Adherence of these coatings is being evaluated, to help in optimizing the process parameters.

Al_2O_3 coatings have also been grown on SiO_2 coated Si_3N_4 samples. Figure 2 shows a 3 μm thick SiO_2 coating on Si_3N_4. Figure 3 shows a 1 μm thick Al_2O_3 coating on the SiO_2 coated Si_3N_4 substrate. Investigative studies are being made to extend this to produce Al_2O_3-SiO_2 laminated coatings.

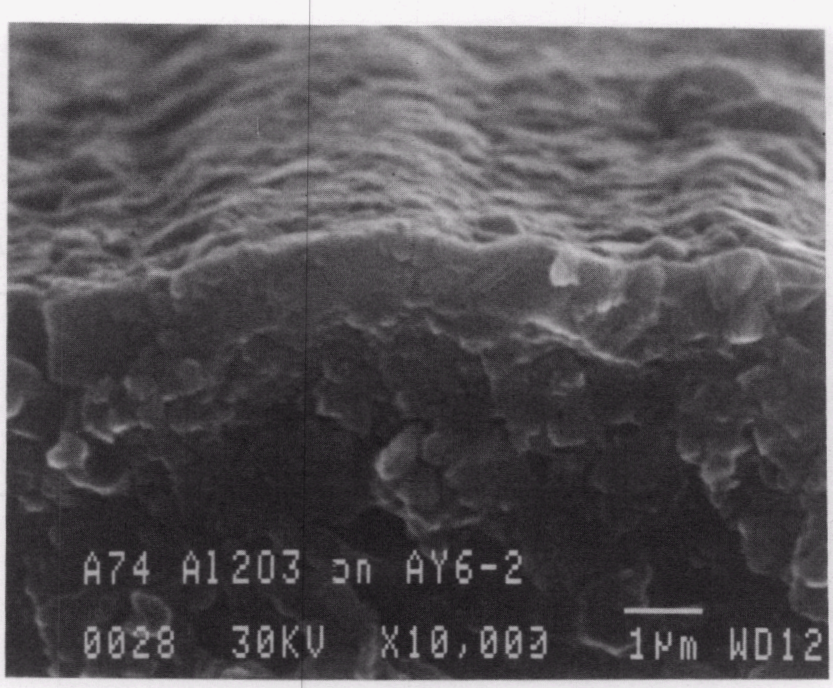

Figure 1: SEM micrograph of Al_2O_3 coating grown on Si_3N_4

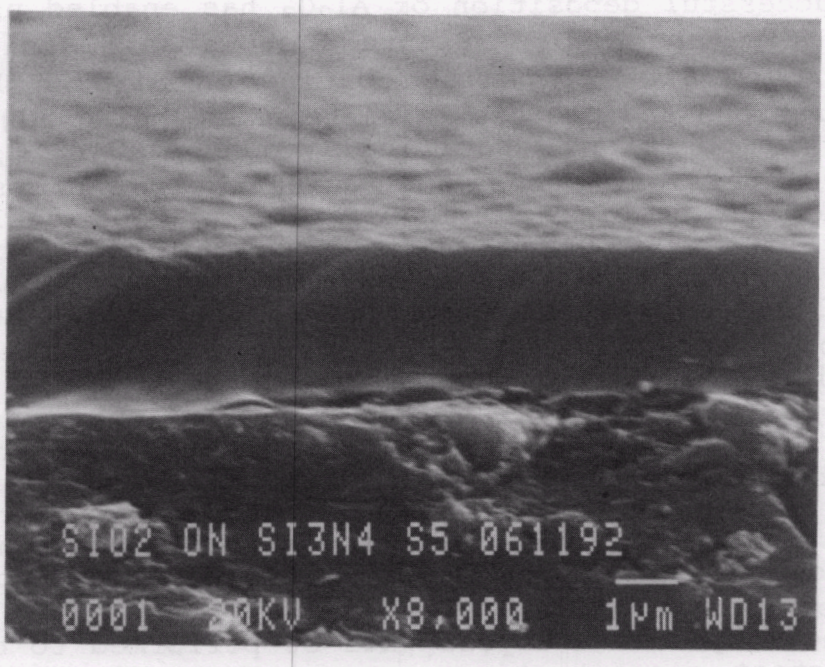

Figure 2: SEM micrograph of SiO_2 coating grown on Si_3N_4

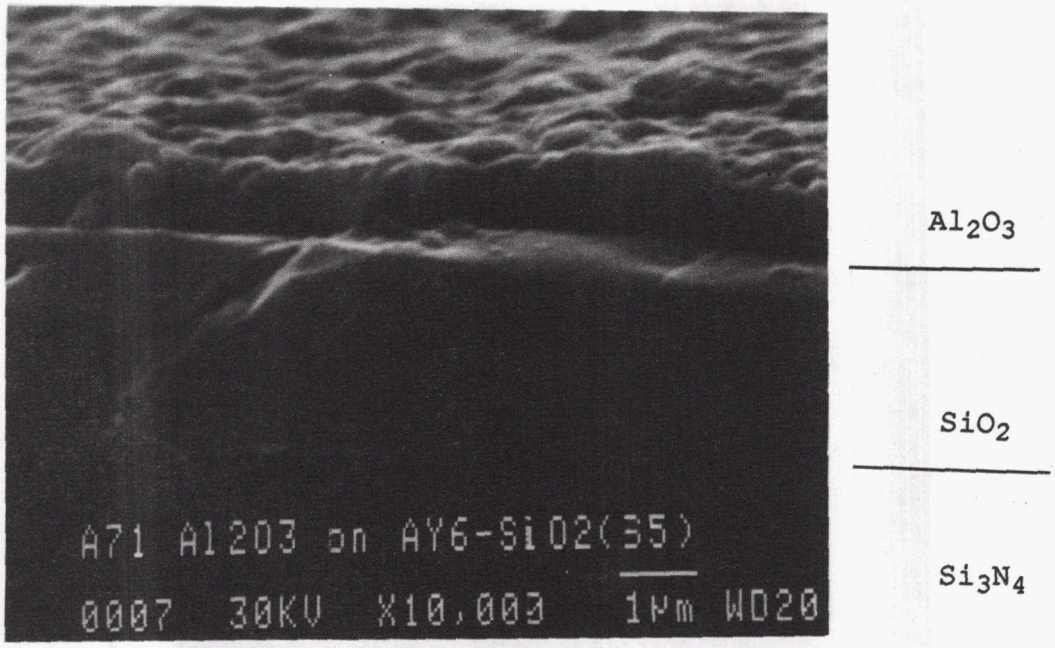

Figure 3: SEM micrograph of Al_2O_3 coating grown on SiO_2 coated Si_3N_4

Successful deposition of Al_2O_3 has enabled us to co-deposit SiO_2 and Al_2O_3. Figure 4 shows an SEM micrograph of the Al_2O_3/SiO_2 composite coating on Si_3N_4. Reactant concentrations and process parameters are being adjusted to control composition, specifically the Al_2O_3/SiO_2 ratio. Energy Dispersion Spectra and Quantitative Analysis were performed to determine these ratios. The acceleration voltage of the filament in the scanning microscope was selected so as to reduce the influence of substrate material. To verify this effect Al_2O_3 coatings have been grown on WC-Co substrates. Figure 5 shows the energy dispersion spectra of Al_2O_3 coating grown on WC-Co. As can be seen, only Al in the coating and Au in the conductive coating were detected. This confirms the fact that the substrate material had no effect on the energy dispersion spectra at the chosen filament voltage. A variety of process conditions have been investigated to find their influence on the Al_2O_3/SiO_2 ratio in these composite coatings.

Thermodynamic analysis will be performed to optimize the reactant concentrations, pressures, and temperatures that would produce coatings with the required stoichiometry.

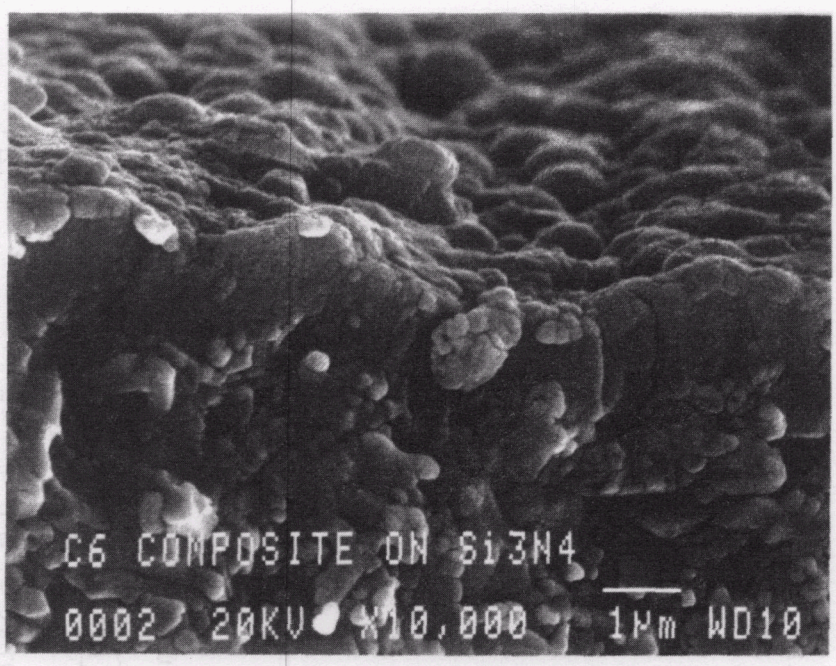

Figure 4: SEM micrograph of Al_2O_3/SiO_2 composite coating grown on Si_3N_4

Figures 6, 7, and 8 show the energy dispersion spectra and quantitative analysis performed on three samples that were grown with increasing amounts of Tetraethoxysilane, the source used for depositing SiO_2. The reactants participating in the formation of Al_2O_3 were kept constant through these experiments. The relative proportions of the constituent elements in the coating were calculated by normalizing the atomic percent to 100. The gold present in the spectra is the thin conductive coating on the samples. The increase in silicon content in the coatings from Figures 6 to 8 is very evident from the spectra. The Al:Si ratio is approximately 5:1 in figure 6, versus 3:2 in figure 8. Temperature gradient from the wall to the center of the CVD reactor is also seen to have an effect on the composition of the composite coating. Figures 8, 9, and 10 show the spectra taken from one end to the other on a sample placed radially in the reactor. Experiments are being conducted to further evaluate this effect. The difference in temperature ΔT between two points at the same level in the reactor can be related to the change in the composition of the coating.

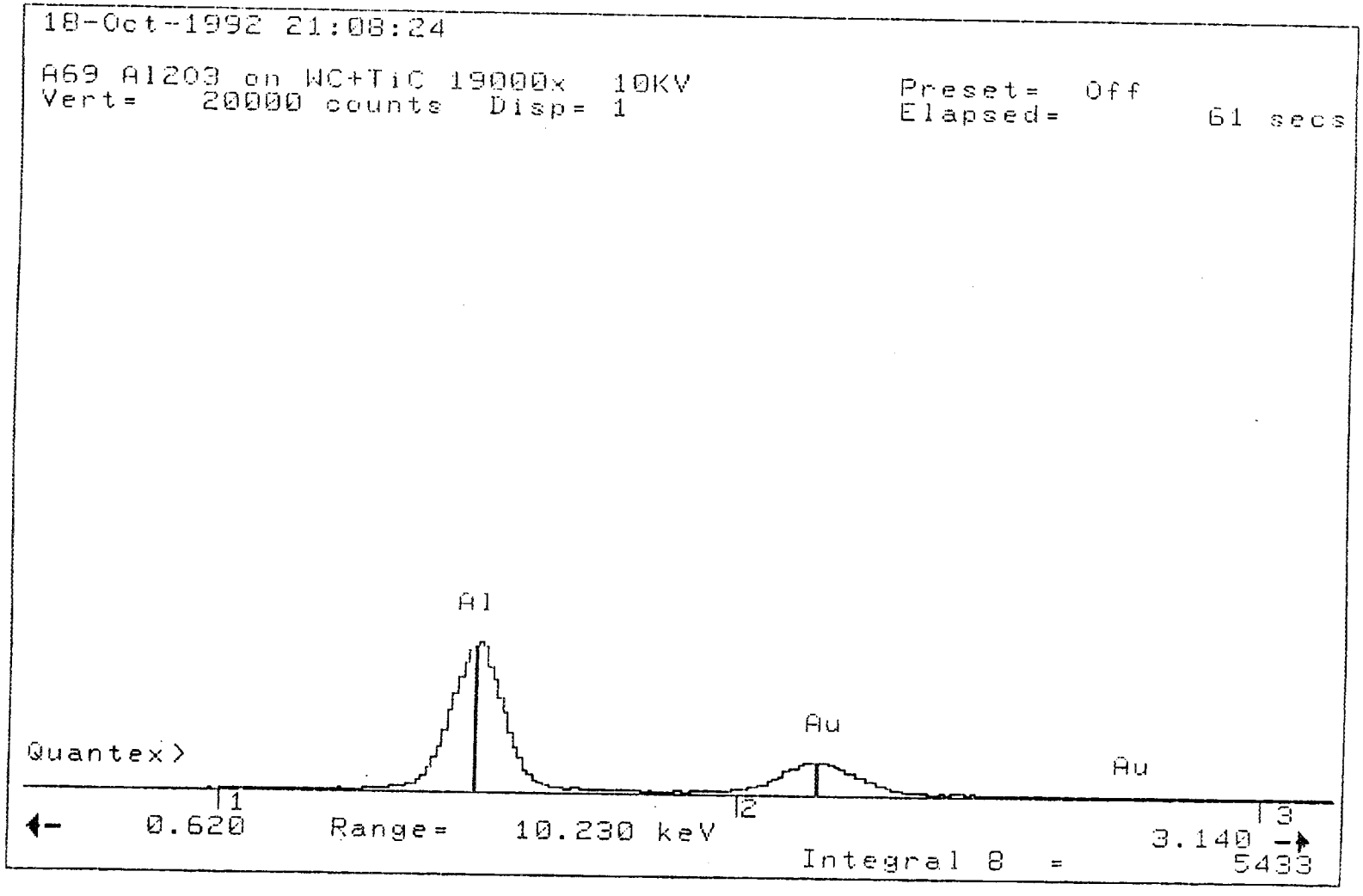

Figure 5: Energy Dispersion Spectra and Quantitative Analysis performed on Al2O3 coating on WC-Co substrate

12-Sep-1992 15:38:12

C5b
Vert= 5000 counts Disp= 1

Preset= 60 secs
Elapsed= 60 secs

Quantex>

STANDARDLESS EDS ANALYSIS
(ZAF CORRECTIONS VIA MAGIC V)

ELEMENT & LINE	WEIGHT PERCENT	ATOMIC PERCENT*	PRECISION 2 SIGMA	K-RATIO**	ITER
Al KA	39.77	72.53	0.19	0.4681	
Si KA	8.27	14.49	0.09	0.0917	
Au MA	51.96	12.98	0.58	0.4402	4
TOTAL	100.00				

*NOTE: ATOMIC PERCENT is normalized to 100

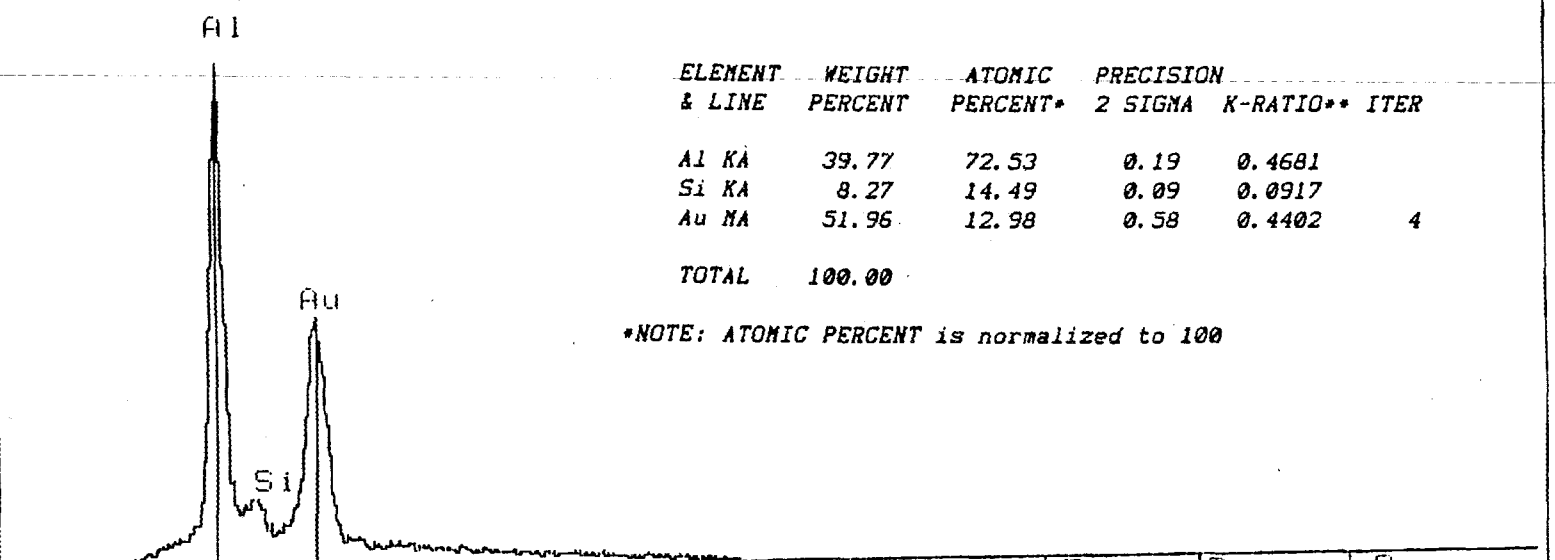

Figure 6: Energy Dispersion Spectra and Quantitative Analysis performed on composite coating with low Si content

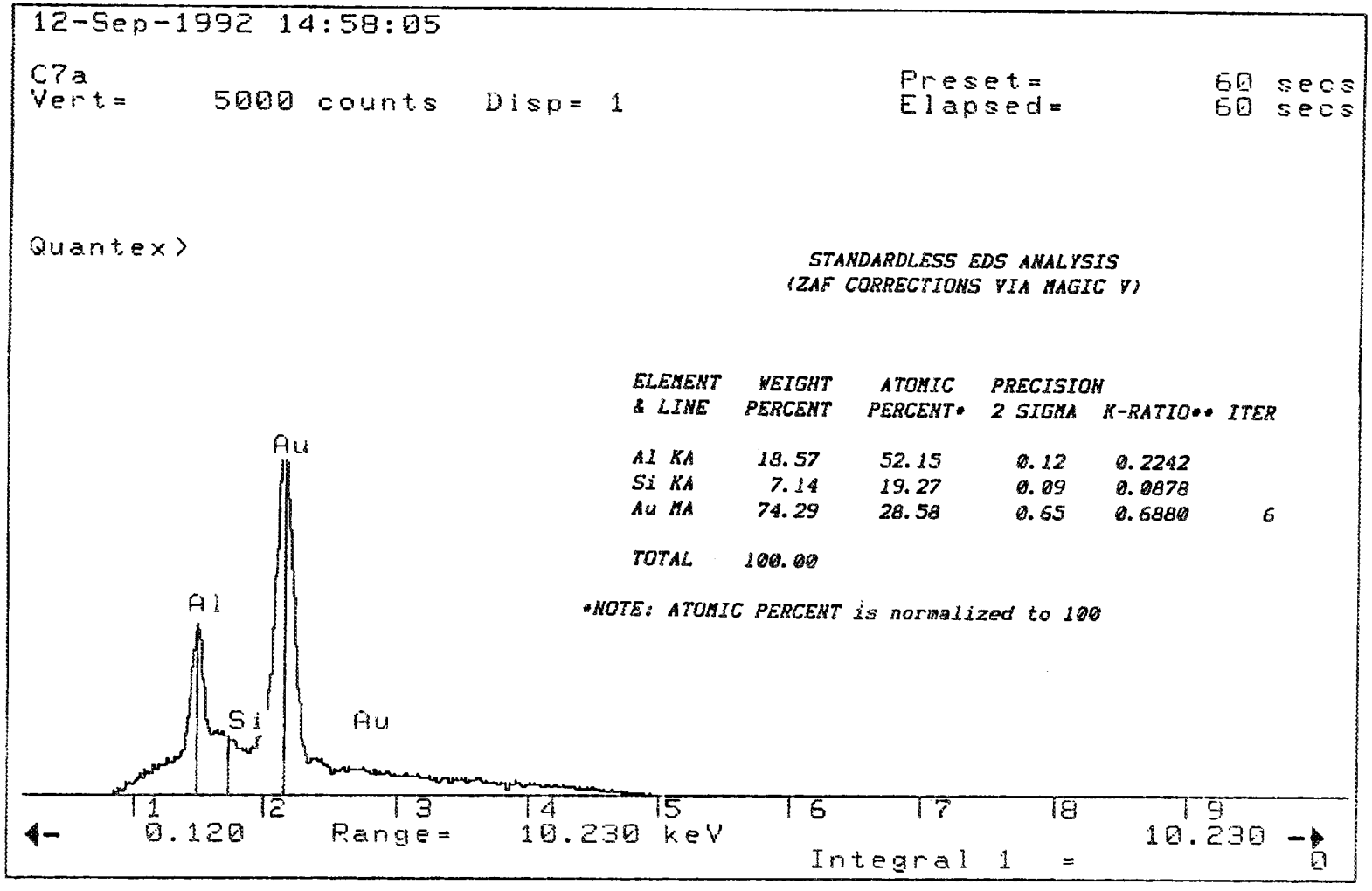

Figure 7: Energy Dispersion Spectra and Quantitative Analysis performed on composite coating with medium Si content

12-Sep-1992 15:08:54

C6
Vert= 5000 counts Disp= 1

Preset= 60 secs
Elapsed= 60 secs

STANDARDLESS EDS ANALYSIS
(ZAF CORRECTIONS VIA MAGIC V)

ELEMENT & LINE	WEIGHT PERCENT	ATOMIC PERCENT*	PRECISION 2 SIGMA	K-RATIO**	ITER
Al KA	15.78	44.01	0.12	0.1903	
Si KA	10.36	27.77	0.11	0.1282	
Au MA	73.86	28.22	0.69	0.6815	6
TOTAL	100.00				

*NOTE: ATOMIC PERCENT is normalized to 100

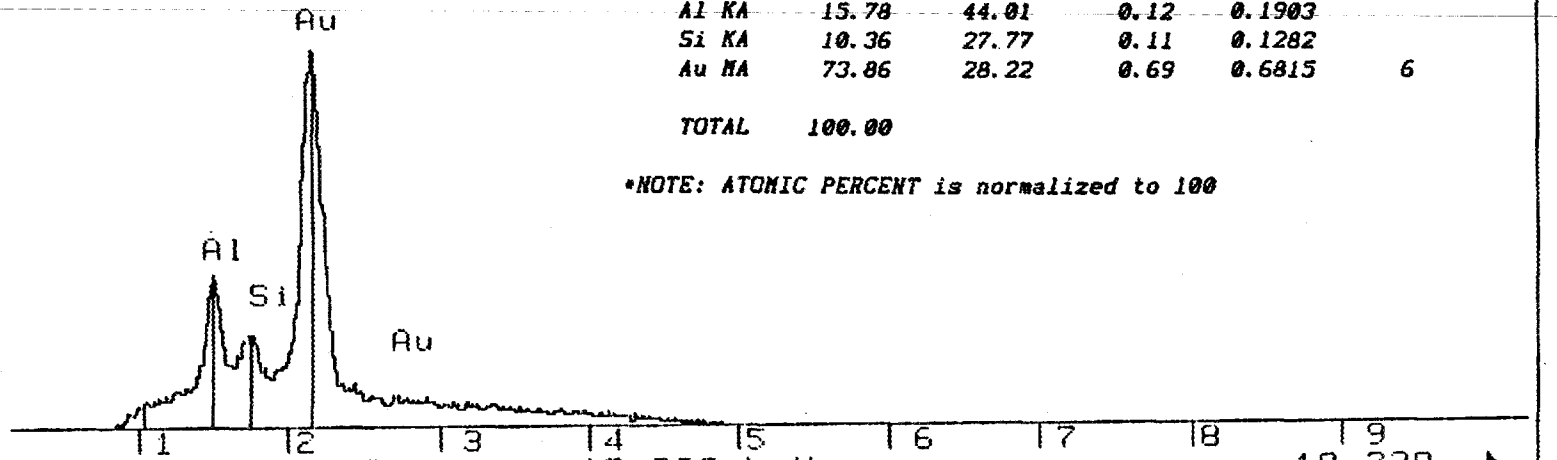

Figure 8: Energy Dispersion Spectra and Quantitative Analysis performed on composite coating with high Si content close to the center of the reactor

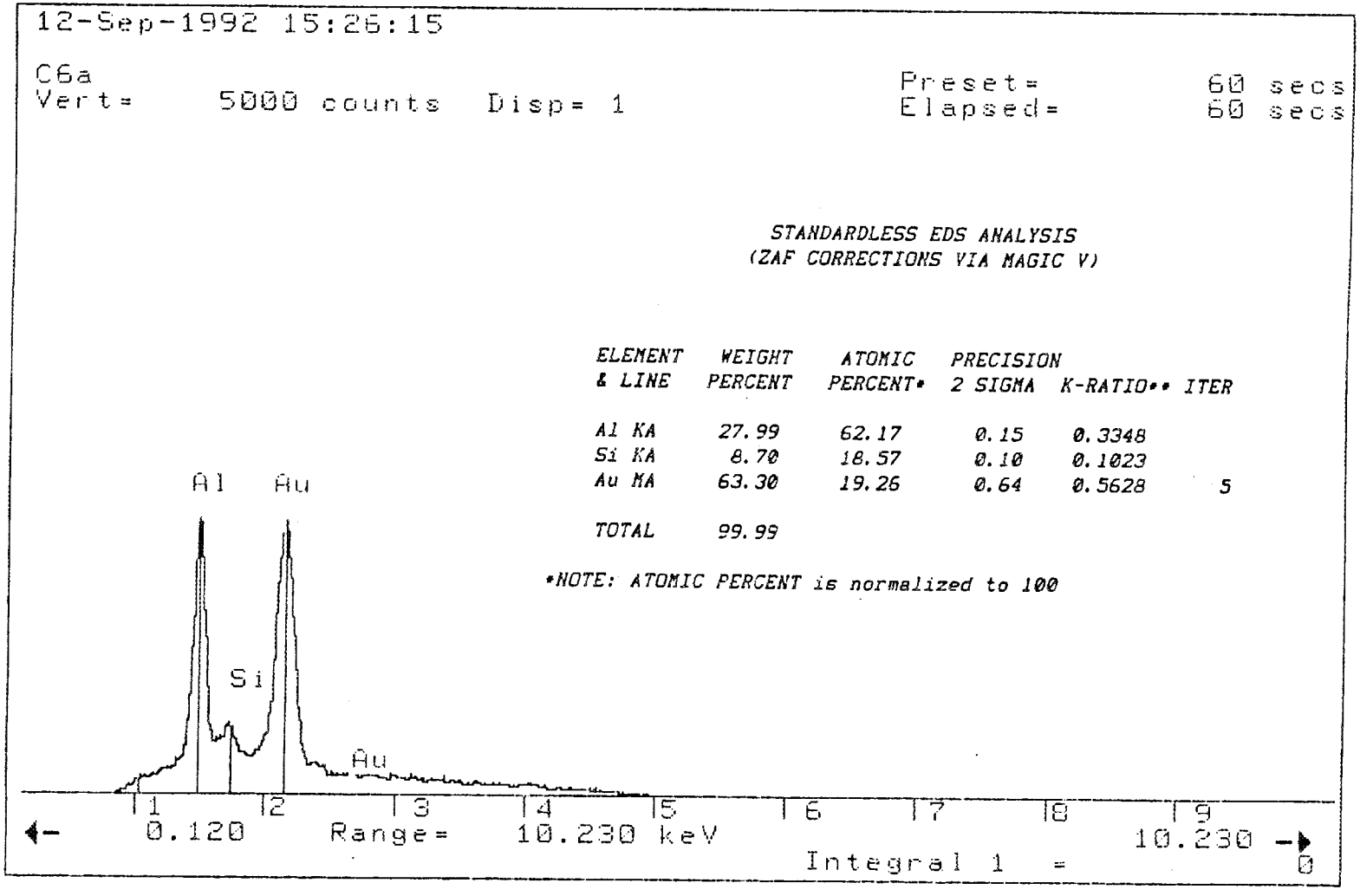

Figure 9: Energy Dispersion Spectra and Quantitative Analysis performed on composite coating away from the center of the reactor.

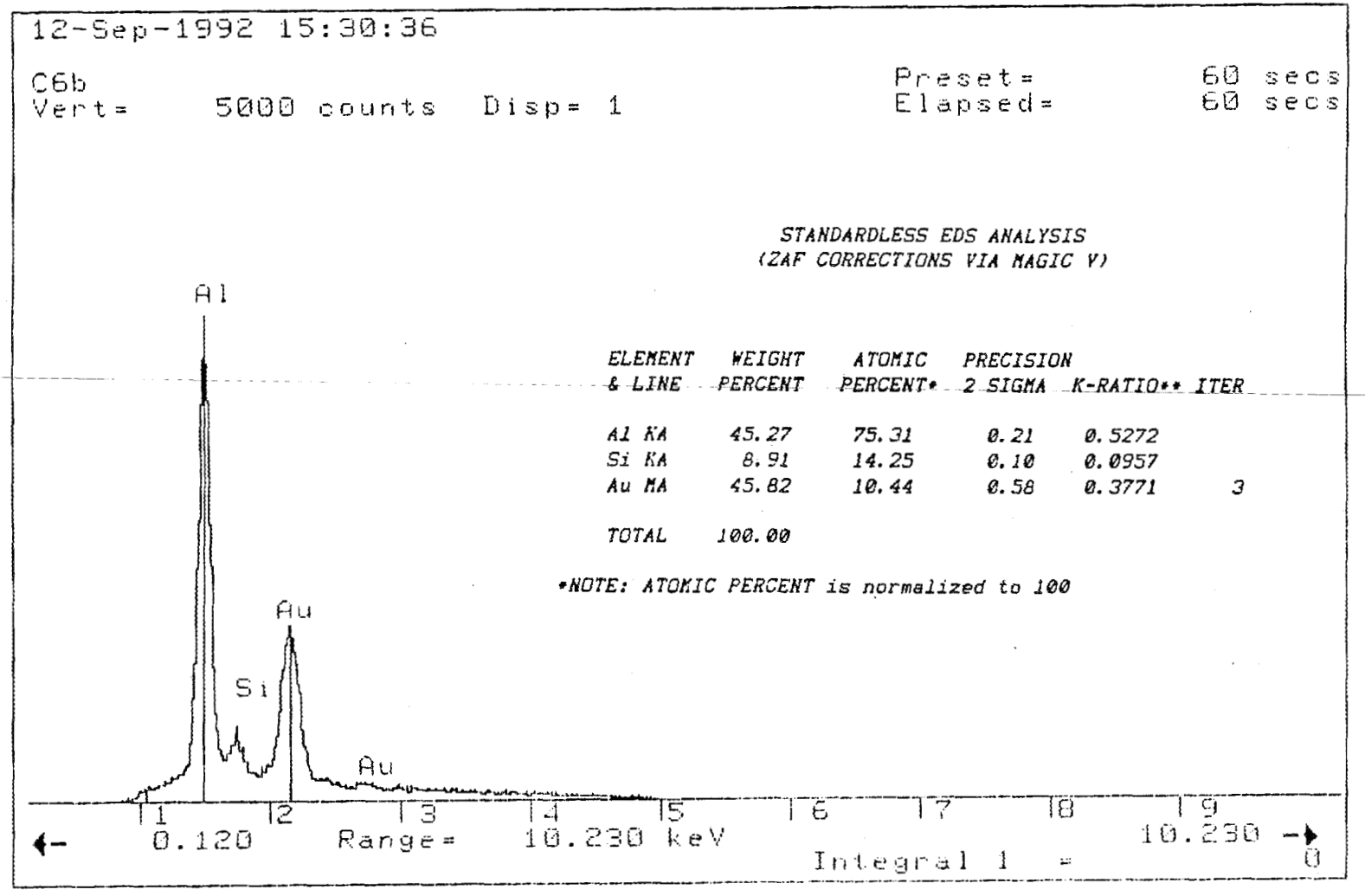

Figure 10: Energy Dispersion Spectra and Quantitative Analysis performed on composite coating close to the reactor wall.

A new process controller manufactured by MKS Instruments has been added to the system. This controller would enable us to accurately control the reaction and source temperatures, gas flow rates, and chamber pressures. This system also allows the user to run the process from a preset "recipe" providing consistency between experiments. This controller is a valuable asset in deposing composite/ laminated coatings with gradually changing compositions from inner to the outer layer of the coating.

Status of Milestones

	Schedule	Status
Deposition of chemically graded SiO_2 coatings on Si_3N_4 substrates.	6/92	On Schedule
Composite Al_2O_3/SiO_2 coatings on SiO_2 coated substrates.	12/92	On Schedule
Development of the complete coating configuration for contact stress, oxidation, and corrosion resistance evaluation.	6/93	On Schedule

Wear-Resistant Coatings

M. H. Haselkorn (Caterpillar Inc.)

Objective/Scope

The goal of this technical program is to develop wear-resistant coatings for piston ring and cylinder liner components for low heat-loss diesel engines.

Friction and wear screening in Phase I identified plasma sprayed high carbon iron-molybdenum and chromia-silica coatings as candidate piston ring wear coatings. Plasma sprayed chromia-silica and high carbon iron-molybdenum coatings, as well as, a low temperature arc vapor deposited (LTAVD) chrome nitride coating were identified as candidate cylinder liner wear coatings. The cast iron porcelain enamel coatings exhibited unsatisfactory wear rates because of porosity in the coating.

The three main technical tasks for Phase II are further optimization of the LTAVD chrome nitride and cast iron porcelain enamel wear coatings and the process scale-up of wear-resistant plasma coatings for cylinder liners.

The optimization of the LTAVD chrome nitride coating involves the development of an adherent 15 micron thick coating which meets the friction and wear goals of this program. The cast iron porcelain enamel process optimization centers on developing a CIPE composition with a minimum of porosity. The process scale-up of the plasma coatings will first develop I.D. plasma spray parameters for coating cylinder liners. Next, simulated cylinder liner specimens will be coated and the friction and wear properties of these coatings be determined using reciprocating friction and wear testing using both new and "used" engine oil.

Technical Progress

Phase II Task 1 Optimization of LTAVD Chrome Nitride Coating

In Phase I, a 3-5 micron thick low temperature arc vapor deposited (LTAVD) chrome nitride coating was applied to cast iron substrates which met the friction and wear goals of the contract. However, wear curves generated showed that even with wear coefficients of less than 10-8 mm3/N-m, a 5-micron thick coating will not meet commercial diesel engine durability requirements. The wear curves showed a 15-micron thick LTAVD chrome nitride coating is needed to meet these durability requirements. For this reason, the overall goal of this task is the development of a 15 micron thick, adherent chrome nitride coating which can be applied to the inner diameter of cast iron cylinder liners. This task was divided into four subtasks:

1. Optimization of LTAVD chrome nitride coating parameters,

2. Development of a 15-micron thick LTAVD chrome nitride coating containing an intermediate layer,

3. Determination of the effect of single vs. multiple alternative layers on the adherence of 15-micron thick LTAVD chrome nitride coatings, and

4. Friction and wear characterization of selected 15-micron thick LTAVD chrome nitride coating systems.

The LTAVD chrome nitride coating development has been completed. Only nitrogen partial pressure and substrate cleaning procedures had any significant effect on the LTAVD chrome nitride coating adherence or microhardness. Incorporating a chromium or a layered titanium/titanium nitride intermediate coating in combination with either a 15-micron thick chromium nitride or a 15-micron thick "layered" coating (consisting of alternating layers of chromium and chromium nitride) resulted in LTAVD chrome nitride coating systems which had excellent physical appearances, hardnesses and adhered well to a cast iron substrate. In addition, these coating systems were able to withstand both up and down-cycle thermal shock testing from room temperature and 650 C.

Upon completion of the thermal shock and adherence testing, three LTAVD chrome nitride coating systems were selected and applied to cast iron Hohman A-6 rub shoes. These shoes will be evaluated for friction and wear running against a plasma-sprayed, high carbon iron-molybdeum coated disk. The three LTAVD chrome nitride coating systems selected were:

1. 15-micron thick chrome nitride top coat over a chromium intermediate layer (System 1),

2. 15-micron thick top coat consisting of alternating chrome nitride and chromium layers over a chromium intermediate layer, (System 2), and

3. 15-micron thick top coat consisting of alternating chrome nitride and chromium layers over a layered titanium and titanium nitride intermediate layer (System 3).

Table 1 lists the results of the friction and wear characterization of the three LTAVD chrome nitride coating systems.

TABLE 1
Friction and Wear Test Results
After 1000 Minutes of Testing at 350 C, Lubricated

LTAVD Chrome Nitride Coating System	Average Shoe Wear Rate (mm3/N-m)	Average Disk Wear Rate (mm3/N-m)
System 1	3.0xE-8	1.6xE-5
System 2	No measurable wear	7.6xE-6
	No measurable wear	4.2xE-6

These friction and wear results showed that after 1000 hours of running against a plasma sprayed high carbon iron molybdenum counterface, under lubricated conditions at 350 C, all three LTAVD chrome nitride systems had average wear coefficients which meet the goals of this program.

While the LTAVD chrome nitride shoes meet the wear goals of the contract the high carbon iron-molybdenum disk exhibited wear rates which did not meet the contract's goals. However, the high wear coefficients of the plasma sprayed high carbon iron-molybdenum disks were caused by the lubricant charring during the test and forming hard carbon particles. These particles then became trapped at the rub shoe/disk interface and galled the surface of the plasma sprayed high carbon iron-molybdenum disk.

Using the results of thermal shock tests, and the friction and wear characterization, along with an estimate of the production costs for application for each chrome nitride coating system as a guide, Systems 1and 2 were selected for further process development.

Phase II Task 2--
Process Scale-Up Of Wear Resistant Plasma Coatings for Cylinder Liners

The overall objective of this task is the optimization of inner diameter plasma spray gun parameters for both the chromia-silica composite and high carbon iron-molybdenum blend powders. Statistical experiments were designed and run to determine the effect of primary gas flow, current, voltage, spray bias, deposition efficiency.

The results of these experiments were then used to build a predictive equation to select three sets of I.D. plasma spray gun coating parameters for both the chromia-silica and high carbon iron-molybdenum powders. The coating parameters selected by the model will produce the optimum plasma spray coating microstructures and hardnesses along with the highest coating deposition efficiencies. Three sets of Hohman A-6 conforming rub shoes were plasma sprayed with each powder using an I.D. plasma spray gun with the spray parameters selected by the model (Sets 1-3). The counterfaces run against these shoes were disks plasma sprayed with the opposite powder; i.e., high carbon iron-molybdenum shoes ran against chromia-silica disks.

Table 2 contains the results of the Hohman A-6 friction and wear characterization of the I.D. plasma spray coatings. The initial test results show that the I.D. plasma spray parameters selected for either powder will result in average wear coefficients between 10^{-8} and 10^{-9} mm3/n-m for both the rub shoes and disks.

TABLE 2
Friction and Wear Characterization
I.D. Plasma Spray Coating Optimization

Powder ---- I.D. Spray Parameter	Disk Coating	Average Wear Coeff.(mm3/N-m) Shoes	Disk
Chromia-silica ---- Set 2	high carbon iron-molybdenum	1.2xe-9	6.0xe-8
Chromia-silica ---- Set 3	high carbon iron-molybdenum	3.0xe-9	8.0xe-8
High carbon iron-Mo — Set 1	chromia-silica	1.1Xe-8	2.0Xe-9

Another part of the process scale-up task involved determining methods for cost-effectively finish machining the plasma sprayed coatings applied to the I.D. of a cylinder liner. Norton's Ceramic Machining Technology Centerwas selected to do the initial machining studies. A fully programmable Huffman HS-75R, 5-axis, CNC grinder was used for these machining studies. Norton rotated the machine head 90 degrees and built a special chuck to enable the Huffman to do surface grinding.

Norton has completed all the machining and has returned the specimens to Caterpillar. The initial results of this machining study were:

1. Best surface finish was achieved with 15-micron diamond grit, irrespective of the bond type,

2. Increasing depth of cut or diamond grit size increased material removal rates,

3. Reducing feed rates with 15-micron diamond grit in a vitreous bonded wheel and large depth of cut resulted in the best surface finish with the highest material removal rates.

Thick Thermal Barrier Coating (TTBC) Systems for Low Heat Rejection Diesel Engines

M. B. Beardsley (Caterpillar Inc.)

Objective/scope

The objective of this program is to advance the fundamental understanding of thick thermal barrier coating systems for application to low heat rejection diesel engine combustion chambers. Areas of TTBC technology that will be examined include powder characteristics and chemistry; bond coat composition; coating design, microstructure, and thickness as they affect properties, durability, and reliability; and TTBC "aging" effects (microstructural and property changes) under diesel engine operating conditions.

Technical progress

TTBC POWDERS

Fifteen TTBC ceramic powders have been acquired to evaluate different chemistries, different manufacturing methods, lot-to-lot variations, different suppliers and varying impurity levels, Table 1. The results of the powder characterization for chemistry, particle size distribution, surface area, crystallographic phases, apparent density and Hall flow are shown in Tables 2 to 6.

In the chemical analysis it can be seen that the three spray dried and sintered materials to be used in the impurity study (lots 34850, 34992, and 34993) range from low levels of alumina and silica (34992), low alumina and mid-level silica (34850), and high alumina and silica (34993). The chemistries of the HOSP (proprietary Metco process), spray dried, spray dried and sintered, fused and crushed, and sol gel materials also show slightly differing ranges of impurities reflecting the differing manufacturing methods.

The particle size distributions of the fifteen materials show small variations in the mean and major size ranges. Small variations in the "fines" content of the materials may be present and will be evaluated if major differences in spraying characteristics of the powders are evident.

The surface area of the powders does show a wide range even for similarly manufactured powders (lots 34850, 34992, 34993 and lots 34243, 34302, 34547). This may be the major factor in powder "lot-to-lot" variations. The high surface area of the sol gel material was unexpected. Examination of the powder by scanning electron microscopy (SEM) showed that the sol gel particles consisted of porous spherical shells enclosing balls of the material, Figure 1. Thus the surface inside the balls is included in the surface area.

The crystallographic phase analyses of the materials were done using a peak intensity ratio method. This method is an industry standard used for fully reacted yttria-zirconia

Table 1 Powders acquired for evaluation of different powder characteristics

MATERIAL	MFG METHOD	SUPPLIER	LOT NO
8% Yttria-Zirconia	HOSP	METCO	34547-1
20% Yttria-Zirconia	Spray Dried	METCO	34108-2
24% Ceria-Zirconia	HOSP	METCO	34209-3
Calcium Titanate	Spray Dried	METCO	34849-4
Mullite	Fused & Crushed	METCO	34542-5
DIFFERENT MANUFACTURING METHODS			
8% Yttria-Zirconia	Sprayed Dried	METCO	32678-6
8% Yttria-Zirconia	Spray Dried & Sintered	METCO	34850-7
8% Yttria-Zirconia	Fused & Crushed	Norton	281-8
8% Yttria-Zirconia	SOL GEL	METCO	34440-9
DIFFERENT SUPPLIERS			
8% Yttria-Zirconia	Sprayed/Compact/Sintered	Zircoa	39073-10
8% Yttria-Zirconia	Spray Dried & Sintered	MET TECH	1081MP-11
LOT-TO-LOT VARIATIONS			
8% Yttria-Zirconia	HOSP	METCO	34143-12
8% Yttria-Zirconia	HOSP	METCO	34301-13
IMPURITIES			
8% Yttria-Zirconia	Spray Dried & Sintered	METCO	34992-14
8% Yttria-Zirconia	Spray Dried & Sintered	METCO	34993-15

Table 2. Chemistries of the TTBC powders

MATERIAL	LOT NO.	Al_2O_3	CaO	Fe_2O_3	HfO_2	MgO	SiO_2	TiO_2	Th+V	Y_2O_3	CeO_2	ZrO_2	Na_2O
8% Yttria-Zirconia-HOSP	34547	<.01	<.01	<.01	1.73	<.01	<.01	0.09	<.01	7.98	<.01	90.21	0.27
20% Yttria-Zirconia-S/D	34108	0.06	0.03	<.01	1.51	<0.01	0.16	0.07	0.03	19.34	<.01	77.40	0.08
24% Ceria-Zirconia-HOSP	34209	<.01	0.07	0.02	1.27	0.04	0.04	0.08	<.01	2.42	25.12	70.84	0.15
Calcium Titanate-S/D	34849	0.21	40.90	0.06		0.23	0.43	57.54	<.01	<.01	<.01	0.09	0.18
Mullite-F/C	34542	74.34	0.03	0.01		<0.01	25.32	<.01	<.01	<.01	<.01	0.01	.37
8% Yttria-Zirconia-S/D	32678	0.27	.13	.06	1.79	<0.01	0.72	.10	<.01	7.34	<.01	89.44	0.10
8% Yttria-Zirconia-S/D-S	34850	0.01	0.01	0.01	1.74	<0.01	0.16	0.04	<0.01	7.60	<0.01	90.21	.29
8% Yttria-Zirconia-F/C	281	0.03	0.04	<0.01	1.64	<.01	<.01	0.20	<.01	7.46	<.01	90.63	.08
8% Yttria-Zirconia-Sol Gel	34440	<.01	<.01	<.01	1.58	<.01	<.01	0.06	<.01	7.37	<.01	90.99	0.18
8% Yttria-Zirconia-S/C-S	39073	0.08	0.18	0.11	1.81	<.01	<.01	<.01	.04	7.50	<.01	90.21	.03
8% Yttria-Zirconia-S/D-S	1081MP	0.01	<.01	0.02	1.84	<.01	0.22	.08	.01	7.47	.01	90.21	0.16
8% Yttria-Zirconia-HOSP	34143	<.01	<.01	0.04	1.67	<.01	<.01	0.10	<0.01	7.77	<.01	90.42	0.11
8% Yttria-Zirconia-HOSP	34302	<.01	<.01	<.01	1.63	0.03	0.03	0.13	<.01	7.58	<.01	90.51	0.22
8% Yttria-Zirconia-S/D-S	34992	<.01	<.01	0.03	1.65	<.01	<.01	0.14	<.01	7.20	<.01	90.98	0.22
8% Yttria-Zirconia-S/D-S	34993	0.26	0.13	0.05	1.76	<.01	0.69	0.10	0.01	7.01	0.01	89.99	0.24

*34849 - P_2O_5 = 0.32

Table 3 Particle Size Distribution of Selected TTBC Powders

MATERIAL	LOT NO.	MEAN DIA. MICRON	10%	50%	90%
			MICRON		
8% YSZ-HOSP	34547	56.76	20.37	50.87	103.78
20% YSZ-S/D	34108	74.15	30.16	66.36	124.11
24% CSZ-HOSP	34209	56.92	22.12	50.92	103.15
$CaTO_5$	34829	75.61	39.23	67.09	119.88
Mullite	34542	96.22	52.32	94.38	147.98
8% YSZ-S/D	32678	67.00	29.41	60.67	113.90
8% YSZ-S/D-S	34850	62.82	27.95	56.54	108.70
8% YSZ-F/C	281	70.01	32.07	64.08	117.43
8% YSZ-Sol Gel	34440	62.59	33.62	57.22	101.93
8% YSZ-S/C-S	39073	68.30	34.74	63.83	110.45
8% YSZ-S/D-S	1081MP	60.42	29.01	54.95	102.47
8% YSZ-HOSP	34143	59.90	25.23	54.08	105.31
8% YSZ-HOSP	34302	56.32	22.85	49.65	102.46
8% YSZ-S/D-S	34992	59.91	26.08	53.84	104.87
8% YSZ-S/D-S	34993	60.67	26.50	55.08	104.66

Table 4 BET Surface Area Analyses of TTBC Powders

MATERIAL	LOT NUMBER	SINGLE POINT M^2/g	BET M^2/g
8% YSZ-HOSP	34547	0.3346	0.3461
20% YSZ-S/D	34108	1.9386	2.0047
24% CSZ-HOSP	34209	0.2994	0.3031
$CaTO_5$	34829	2.2343	2.3069
Mullite	34542	0.1833	0.1440
8% YSZ-S/D	32678	3.6373	3.7554
8% YSZ-S/D-S	34850	1.0337	1.0640
8% YSZ-F/C	281	0.0623	0.0442
8% YSZ-Sol Gel	34440	4.1542	4.2505
8% YSZ-S/C-S	39073	0.1715	0.1307
8% YSZ-S/D-S	1081MP	0.3071	0.3155
8% YSZ-HOSP	34143	0.2559	0.2664
8% YSZ-HOSP	34302	0.2671	0.2790
8% YSZ-S/D-S	34992	0.7742	0.7970
8% YSZ-S/D-S	34993	0.2544	0.2706

Table 5 X-ray Diffraction Analyses of TTBC Powders

MATERIAL	LOT NO.	% CUBIC & TETRAGONAL ZIRCONIA	% MONOCLINIC ZIRCONIA	% YTTRIA
8% YSZ-HOSP	34547	91.1	8.9	ND
20% YSZ-S/D	34108	*		
24% CSZ-HOSP	34209	93.8	6.2	ND
$CaTO_5$ -S/D	34829	100% Calcium Titanate		
Mullite-F/C	34542	*		
8% YSZ-S/D	32678			
8% YSZ-S/D-S	34850	63.5	36.5	ND
8% YSZ-F/C	281	100	ND	ND
8% YSZ-Sol Gel	34440	100	ND	ND
8% YSZ-S/C-S	39073	85.7	14.3	ND
8% YSZ-S/D-S	1081MP	62.5	37.5	ND
8% YSZ-HOSP	34143	91.3	8.7	ND
8% YSZ-HOSP	34302	93.0	7.0	ND
8% YSZ-S/D-S	34992	73.5	26.5	ND
8% YSZ-S/D-S	34993	70.1	29.9	ND

Table 6 Apparent Density and Hall Flow of TTBC Powders

MATERIAL	LOT NUMBER	HALL FLOW (SEC)	APPARENT DENSITY (g/cc)
8% YSZ-HOSP	34547	77.9	2.27
20% YSZ-S/D	34108	47.3	1.52
24% CSZ-HOSP	34209	34.1	2.40
$CaTO_5$	34829	117.4	1.05
Mullite	34542	71.6	1.16
8% YSZ-S/D	32678	52.2	1.44
8% YSZ-S/D-S	34850	*	1.10
8% YSZ-F/C	281	45.1	2.55
8% YSZ-Sol Gel	34440	39.2	1.72
8% YSZ-S/C-S	39073	*	1.84
8% YSZ-S/D-S	1081MP	40.3	2.00
8% YSZ-HOSP	34143	51.3	2.27
8% YSZ-HOSP	34302	81.7	2.26
8% YSZ-S/D-S	34992	*	1.97
8% YSZ-S/D-S	34993	46.3	1.76

* MATERIAL DID NOT FLOW

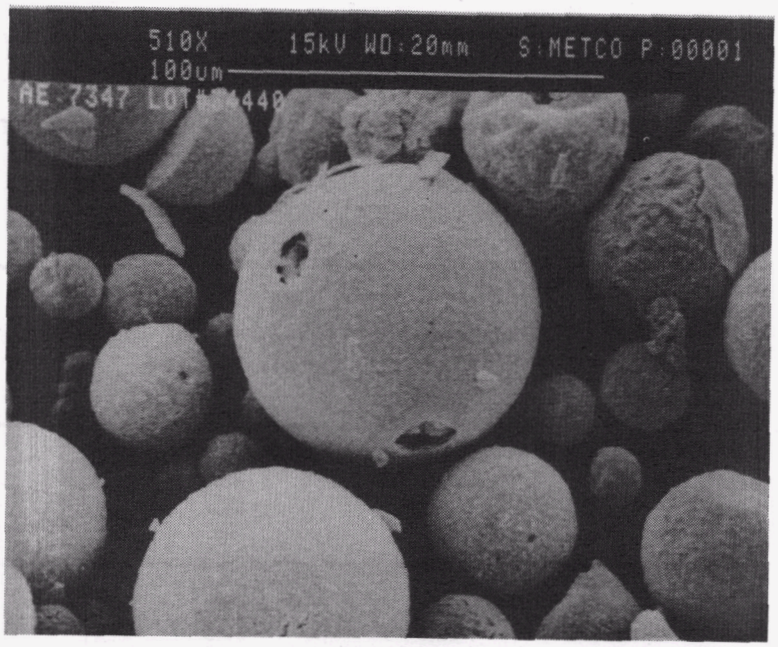

Figure 1 SEM photograph of the sol gel produced 8% yttria-zirconia showing the porous spherical shell enclosing a spongy mass.

materials. When used for the spray dried yttria-zirconia materials, this method gave twice the yttria content from the chemical analysis. A review of this method is being performed at Metco to determine why this occurred.

The apparent density of the materials fall as expected from the particle size and chemistry of the materials. The lack of flow for lots 34850, 39073, and 34992 is unexpected since no feeding problems were encountered during spraying of these materials. This may indicate that the Hall flow is not a useful measurement for plasma powders.

Each of the 15 materials has been sprayed using 36 parameters selected by a design of experiments (DOE) to determine the effects of primary gas (Ar and N_2), primary gas flow rate, secondary gas flow rate (H_2), arc current, powder feed rate, carrier gas flow rate, and spraying distance. The deposition efficiency, density, and thermal conductivity of the resulting coatings are being measured. A coating with a high deposition efficiency and low thermal conductivity is desired from an economic stand point. Data to date has shown that as the deposition efficiency increases the thermal conductivity also increases, Figure 2. An optimum combination of thermal conductivity and deposition efficiency will be sought in follow-on experiments and deposition parameters will be chosen for making coating specimens for full characterization.

BOND COATS

Oxidation studies of four bond coat materials and two graded materials produced using air plasma spraying (APS) and high velocity oxy-fuel (HVOF) processes have been completed. The nickel-based bond coat alloys studied were Ni-20%Cr, Ni-5%Al, Ni-20%Cr-6%Al and Ni-17%Cr-6%Al-0.5%Y. Graded materials were made from mixtures of

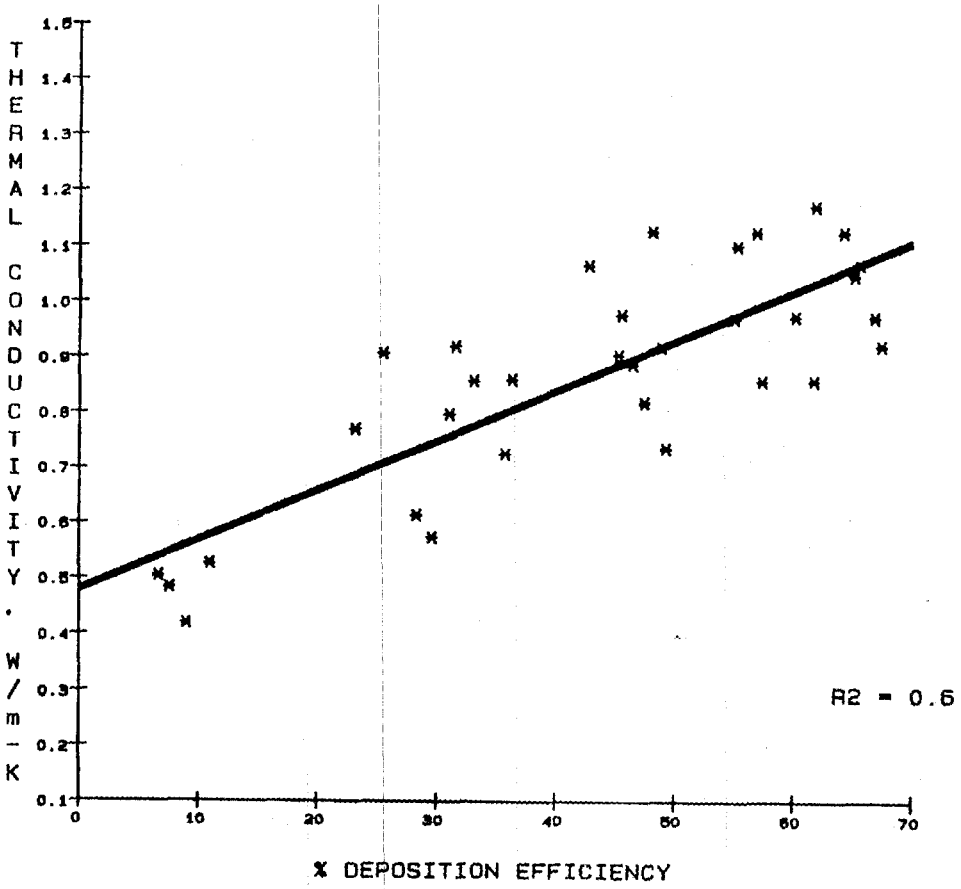

Figure 2 Thermal conductivity plotted versus deposition efficiency for lot 34547 showing decreasing deposition efficiency with decreasing thermal conductivity.

the Ni-20Cr-6Al bond coat and an 8% yttria-zirconia ceramic and from a mixture of a 316 type stainless steel and an 8% yttria-zirconia. The test coupons were obtained from free-standing deposits. The particle size, chemistry, phase analysis, and SEM particle morphology of the materials were determined similar to that for the TTBC powders.

Oxidation tests were conducted for 100 hours at 400 C, 600 C, and 800 C in flowing air with 29% humidity. The specimens were not given any post-spray surface treatment. The specific weight gains were measured following the oxidation tests. Metallographic examination, using optical microscopy, and x-ray diffraction studies of the oxidized coupons were conducted.

The specific weight gain results indicated that of the four bond materials, NiCrAl and NiCrAlY exhibited the best oxidation resistance, but the test temperature is also a major factor, Figure 3. For bond coat temperatures below 500 C, the NiCr bond coat would have similar oxidation resistance as the NiCrAl and NiCrAlY bond coats. The NiCr, NiCrAl, and NiCrAlY materials were chosen to be further characterized.

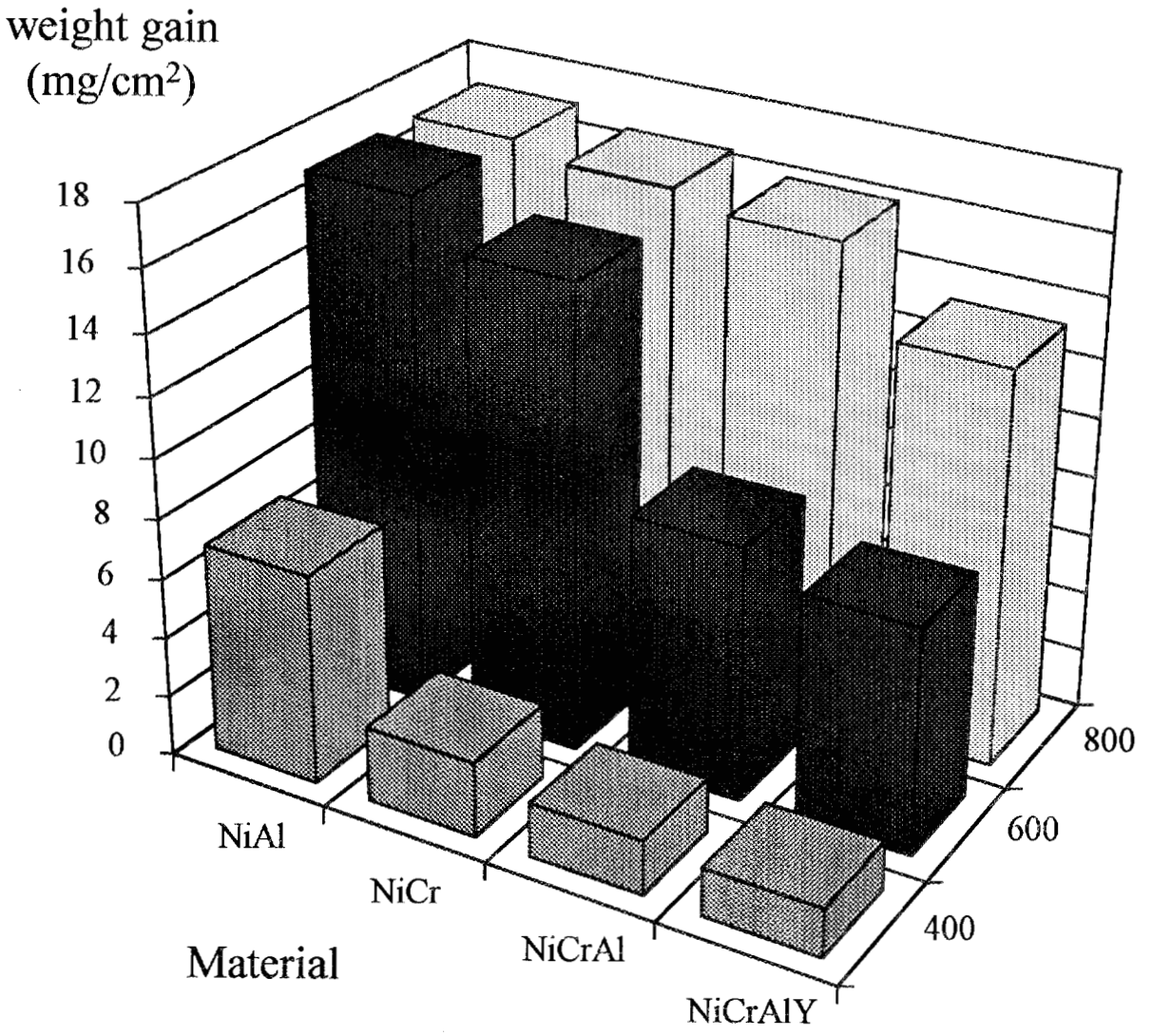

Figure 3 Weight gain of four potential bond coating materials versus three exposure temperatures (°C) for 100 hours.

The NiCrAl and 8% yttria-zirconia materials showed increased oxidation when sprayed as a mixture, Figure 4. The higher the ceramic content, the higher was the oxidation rate. This is caused by the increased surface area of the coating due to the introduction of porosity when the ceramic is added. This is also shown in comparing the HVOF to the APS coating of the 100% NiCrAl which has a lower porosity then the APS coatings and lower oxidation. The graded coatings produced with the HVOF process did not contain the same ratio of metal to ceramic as the starting powders. The ceramic does not melt in the oxygen-propylene flame and therefore has to be physically captured in the molten metal phase resulting in a low ceramic phase content. HVOF is therefore not a good method for producing graded coatings. The APS produced coatings showed a nearly equal metal to ceramic ratio as the starting powders.

Stainless steel, type 316, sprayed with the HVOF process had better oxidation resistance than the APS produced coating and is comparable to the NiCrAl APS produced coating, Figure 5. (Note that the results shown in Figure 3 were obtained from a different run of the oxidation test while the results in Figures 4 and 5 were from the same run of the oxidation test. The differences in the NiCrAl results from Figure 3 to Figure 4 are due to run-to-run variations. The results in Figures 4 and 5 may be compared since they were run at the same time.) Due to the good oxidation resistance of the HVOF stainless steel, it will be further characterized as a bond coating material.

The APS produced graded stainless steel materials show higher oxidation rates than the NiCrAl graded material. However, it is not known if this higher oxidation rate would cause a problem. Further characterization of the stainless steel graded materials is planned as well as additional testing of a 400 Series stainless steel and an additional 300 Series stainless (type 347).

A nickel aluminide (Ni_3Al) wire was obtained from ORNL and sprayed using a single-wire arc plasma under ambient atmospheric conditions. The hardness of the as-received wire was 541 DPH and the coating hardness was 243 DPH. X-ray diffraction indicated that the coating was virtually "pure" nickel. Oxidation of the aluminum from the alloy occurred during spraying. Similar results have been obtained by other investigators when spraying nickel aluminides in a air. (Ref. 1) A nickel aluminide powder (INMET 310) has been obtained from Metallamics, Traverse City, MI, and will be sprayed using vacuum plasma spraying to determine if a nickel aluminide phase can be maintained.

DESIGN, DEPOSITION, AND CHARACTERIZATION

Selection of the parameters for spraying the fifteen TTBC powders is awaiting the results of the optimization for deposition efficiency and thermal conductivity. Spraying of bond coatings for characterization of the NiCr, NiCrAl, NiCrAlY, and stainless steel materials is underway.

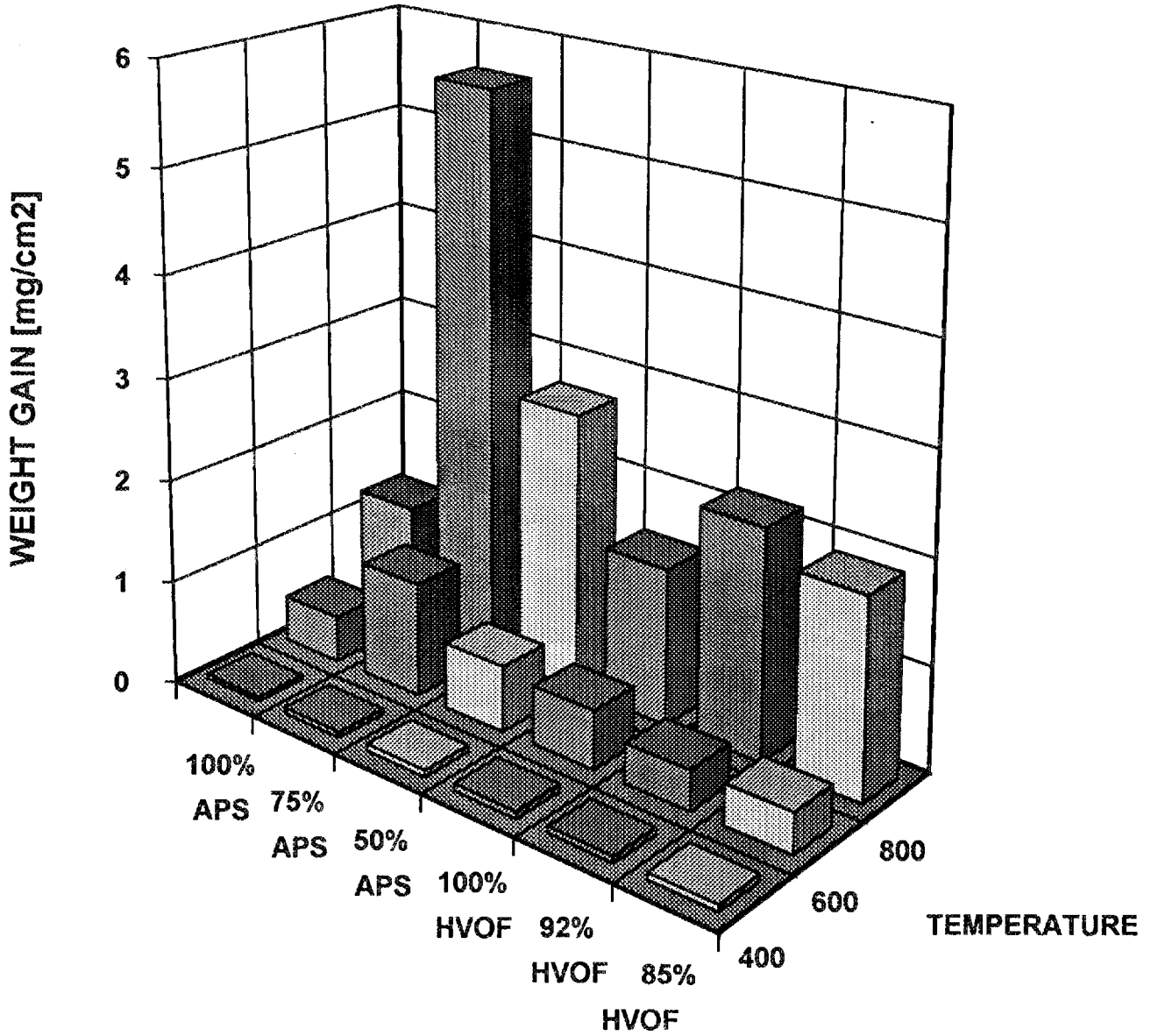

Figure 4 Weight gain of graded NiCrAl and 8% yttria-zirconia verses three exposure temperatures (°C) for 100 hours. The percentages are the metal content with the balance being ceramic. Note the low ceramic content of the HVOF coatings which were sprayed with the same powder compositions as the APS coatings.

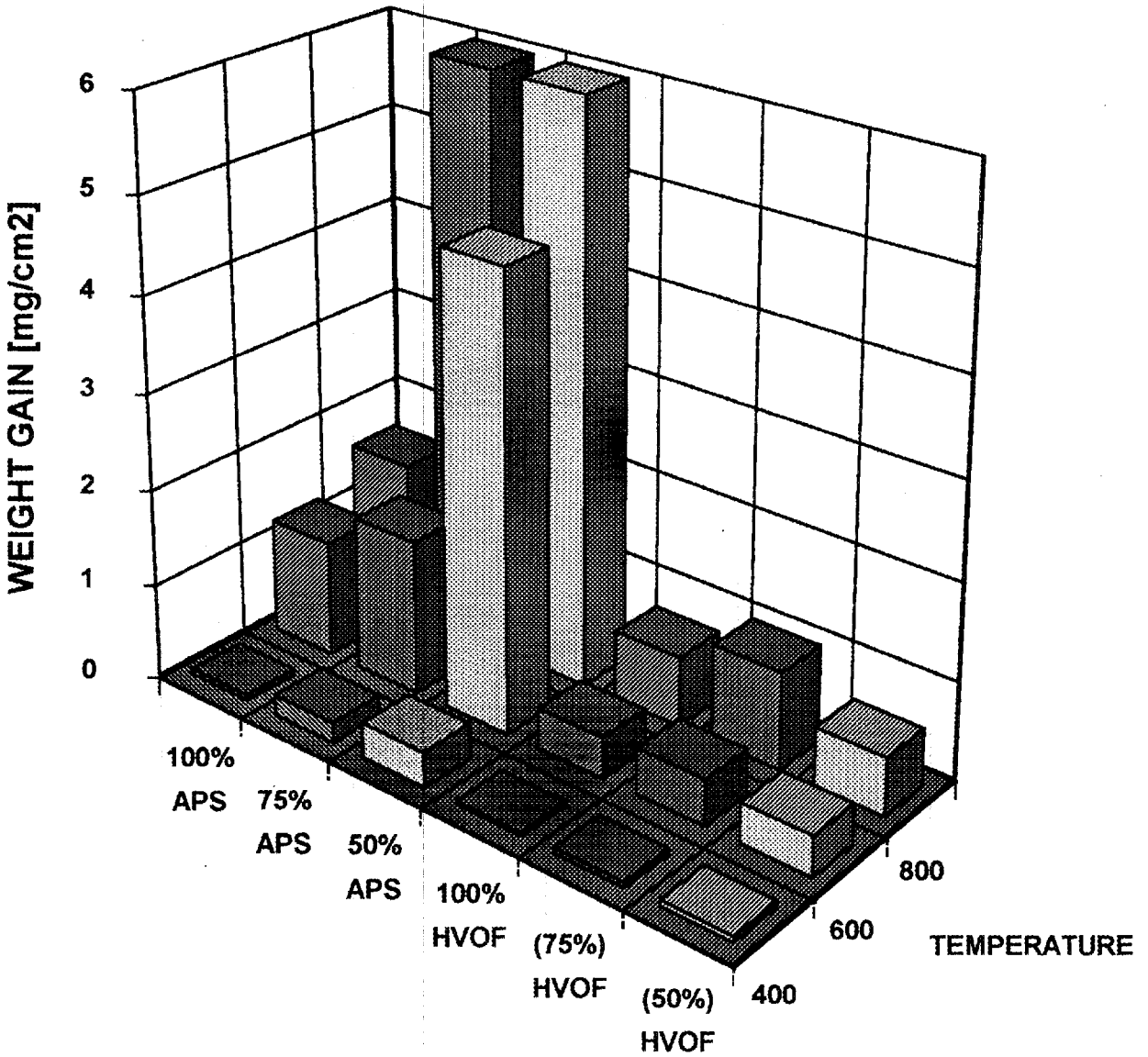

Figure 5 Weight gain of graded 316 type stainless steel and 8% yttria-zirconia verses three exposure temperatures (°C) for 100 hours. The percentages are of the metal with the balance the ceramic. The HVOF percentage are the starting powder compositions not the coating compositions which were much lower in ceramic.

DURABILITY/RELIABILITY

Development of an axial fatigue test to determine the high cycle fatigue behavior of TTBCs has been underway at the University of Illinois. A fatigue test apparatus has been designed and initial test work performed with it which demonstrates the ability to provide a routine method of axial testing of coatings. The test fixture replaces the normal load frame and fixtures used to transmit the hydraulic oil loading to the sample with the TTBC specimen itself, Figure 6.

The TTBC specimen is a composite metal/coating with stainless steel ends, Figure 7. The coating is sprayed onto the mild steel center and the specimen is then machined. After machining, the specimen is placed in an acid bath which etches the mild steel away leaving the TTBC attached to the stainless steel ends. Plugs are then installed in the ends and the composite specimen is loaded in the test fixture where the hydraulic oil pressurizes each end to apply the load. Since oil transmits the load, bending loads are minimized.

A TTBC coating has been tested at room temperature using this method and the resulting stress-life curve is shown in Figure 8. This data matches previous fatigue data for this material obtained in 4-point bending, but long life data was obtained with this test method. In addition to the room temperature data, specimens have recently been tested at 800 C with surprising results. At high temperature, the TTBC exhibits much higher fatigue strength, Figure 9. This behavior is not understood at this time. It does indicate the need for additional testing to cover the temperature range (300 to 800 C) that the coatings will experience.

Reference

S. Sampath, et al., "Plasma Sprayed Ni-Al Coatings", Surface Engineering, 1989, Vol. 5, No. 4, pg. 293-298.

Status of milestones

All milestones are on schedule.

Publications

1. M.B. Beardsley, "Material Development of Thick Thermal Barrier Coating (TTBC) Systems for Low Heat Rejection Diesel Engines", to be published in proceeding to The 1992 Coatings for Advanced Heat Engines Workshop, Monterey, CA.

2. C. Berndt, et al., "Bond Coats for Thick Thermal Barrier Coatings", to be published in proceedings to The 1992 Coatings for Advanced Heat Engines Workshop, Monterey, CA.

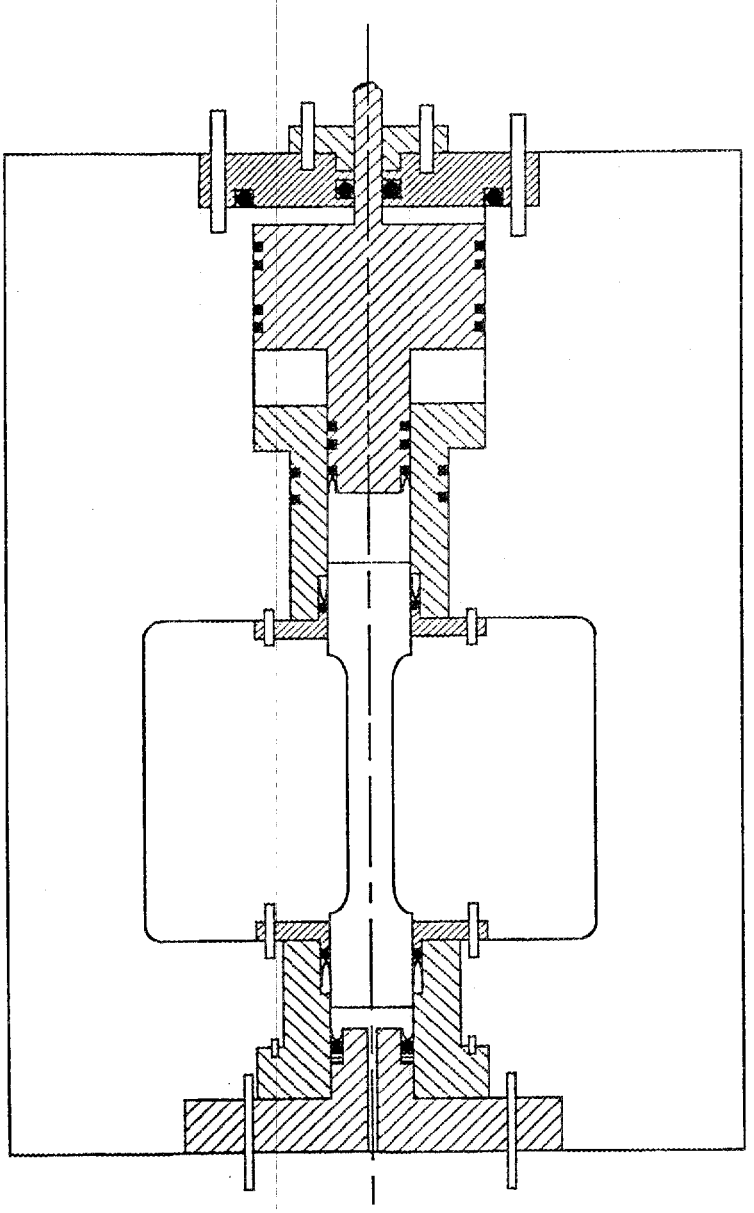

Figure 6 Schematic of the test apparatus used to determine the compressive fatigue strength of TTBC materials. Note that oil is used to load the specimen ends which minimizes bending loads in the TTBC material.

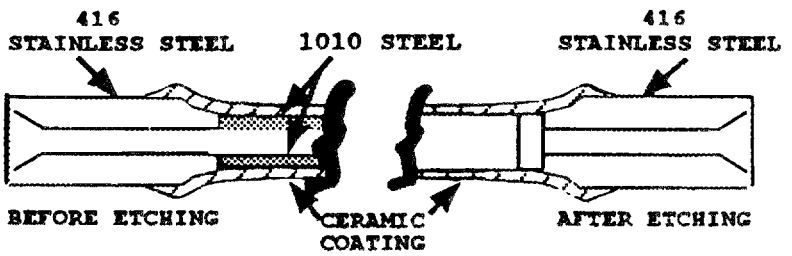

Figure 7 Schematic of the composite metal/ceramic specimen used to determine the fatigue response of TTBC materials. The specimen is approximately 125 mm long.

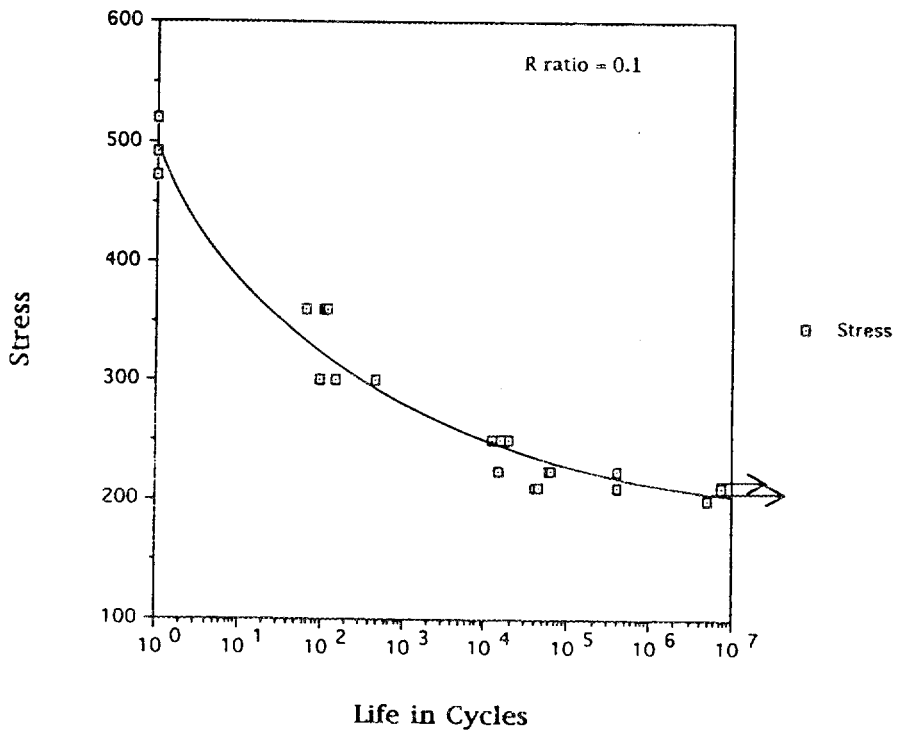

Figure 8 Room temperature fatigue data for a TTBC ceramic showing a significant reduction in strength with cycles.

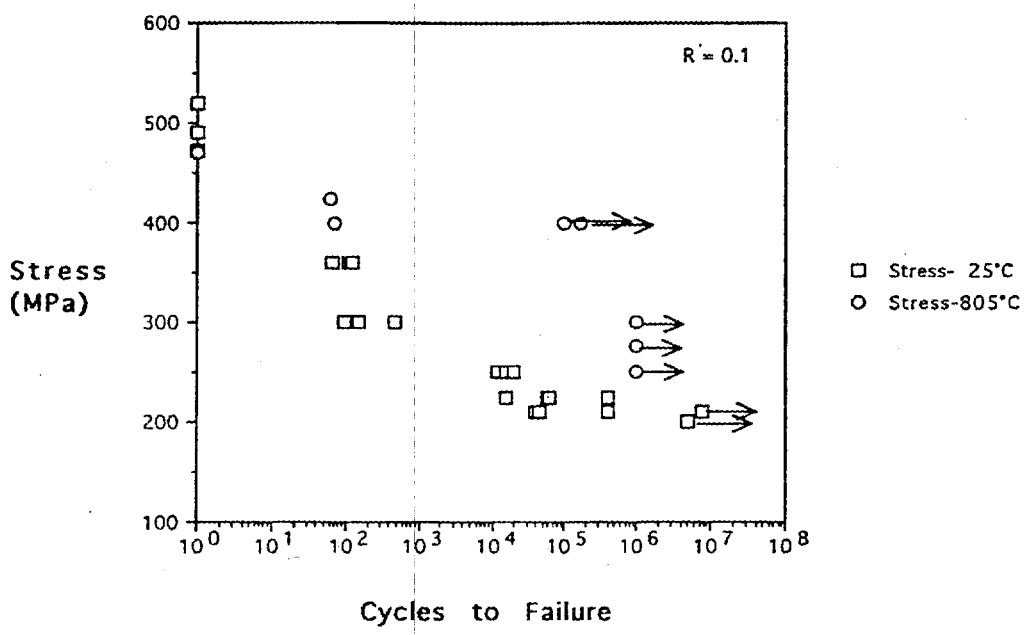

Figure 9 The TTBC materials fatigue behavior is shown compared to the room temperature data shown in Figure 8. Note that at the higher temperature, the TTBC exhibits increased fatigue strength.

1.4 JOINING

1.4.1 Ceramic-Metal Joints

Joining of Ceramics for Heat Engine Applications
M. L. Santella (Oak Ridge National Laboratory)

Objective/scope

The objective of this task is to develop strong, reliable joints containing ceramic components for applications in advanced heat engines. The overall emphasis of this task is on studying the brazing characteristics of silicon nitride and silicon carbide. The techniques of direct brazing, as well as vapor coating ceramics to circumvent wetting problems, will be applied to these materials. The specific areas of emphasis for this activity during FY 1992 will be on: (1) continuing the study of high-temperature brazing of silicon nitride and the effects of thermal aging on joint strength and (2) initiating a study of the brazing characteristics of sintered α-SiC.

Technical highlights

Si_3N_4 brazing: Several braze joints were made of Ti-vapor-coated SN220 Si_3N_4 by vacuum brazing at 1130°C with Au-25Ni-25Pd wt % filler metal. These joints and some monolithic SN220 were prepared into test bars for creep testing. Testing is expected to begin during the next reporting period.

Also, some PY6 Si_3N_4 billets, acquired from GTE, were prepared into specimens for a variety of experiments aimed at examining the materials systems they developed in more detail, optimizing brazing conditions, and ultimately improving the mechanical properties of PY6-to-metal joints similar to those developed under the GTE joining subcontract. Preliminary experiments were done to evaluate both the wetting characteristics of the SK-1 and SK-2 braze filler metals developed by GTE Laboratories and the characteristics of these alloys for producing braze joints of PY6-to PY6, PY6-to-Incoloy, and Incoloy-to-Incoloy. The experiments were done in vacuum at either 1100 or 1200°C, and selected specimens were prepared for metallographic analysis.

The wetting experiments were done by placing small pieces (4 x 4 mm) of the SK-1 and SK-2 alloys on either Ti-vapor-coated PY-6 or Incoloy 909 and holding them at temperature for 20 min. On the Ti-vapor-coated PY-6, both filler metals appeared to only partially melt at 1100°C, while melting appeared to be complete at 1200°C. These observations loosely agree with the melting behavior reported by GTE where liquidus temperatures were given as 1260°C for SK-1 and 1270°C for SK-2. The lower melting temperature observed in the wetting experiment could have resulted from reaction of the filler metals with the Si_3N_4 substrate. On the Ti-vapor-coated PY-6 at 1200°C, the wetting angles of the alloys were in the range of 10 to 20°, and there was no indication of undesirable chemical reaction. Neither alloy melted completely on Incoloy 909. These results indicate that the SK-1 and SK-2 filler metals reacted with the substrate materials and that the reactions influenced the melting and brazing characteristics of the alloys. Nevertheless, both alloys showed good adherence to both substrates, even in conditions where partial melting occurred.

Based on the wetting experiments, it was expected that acceptable joints of PY-6-to-PY-6 would be obtained but that joints of PY-6-to-Incoloy 909 and Incoloy 909-to-Incoloy 909 would be more difficult to achieve. This was not the case. Joints of

PY-6-to-PY-6 bonded reasonably well and had very good exterior appearance, but they contained large unbonded regions after brazing at both 1100 and 1200°C. No bonding could be obtained in joints of PY-6-to-Incoloy 909. In these joints, the filler metals adhered to the Incoloy 909 but not to the Ti-vapor-coated PY-6. Acceptable joints of Incoloy 909-to-Incoloy 909 were obtained at both brazing temperatures even though the wetting experiments indicated that melting was incomplete in both cases. The results of the brazing experiments suggest that there is no inherent difficulty in the bonding of these filler metals to Incoloy 909. On the other hand, they also suggest that reactions between the filler metals and the Ti-vapor-coated PY-6 occur, which are detrimental to forming an acceptable bond. Metallographic examination of these joints is proceeding.

Also, the package developed by GTE for analyzing the stress state of ceramic-to-metal joints and their behavior under applied loads was transferred to computers at ORNL and set up for general use. A license for the ABAQUS software was purchased, and this finite element analysis program was installed on an IBM RISC 6000 workstation. The ABAQUS portion of the analysis of ceramic-to-metal joints by GTE was rerun to verify its operation. Work to run the full analysis, including the treatment of failure using CARES, is continuing.

Simultaneous to establishing a capability to use the GTE analysis, an intensive effort was undertaken to analyze the stresses in a diesel engine glow plug tip using ABAQUS and to predict how well the glow plug would perform in service. The present glow plug design is based on a ceramic rod being press fit into the end of a metallic tube. However, it was decided to consider a glow plug with a brazed rather than a press-fit tip in order to provide for better electrical conductivity and mechanical integrity. The general geometry of this part was similar to the shaft joint analyzed under the GTE joining subcontract, and it was decided to try to apply their work to the glow plug problem. The analysis was run after adjusting the part geometries to approximate those of the glow plug and assuming a bonding temperature of 830°C. The material properties used for the plug tip were those of PY-6 Si_3N_4 because the properties of the actual glow plug material were not readily available. An overall view of the maximum principal stress distribution in the part after cooling to room temperature is shown in Fig. 1. The ceramic plug tip is situated inside a metal tube, and a vertical axis of symmetry is assumed. Figure 1 shows that bonding produces large stresses in both the ceramic tip and the metal tube. A detailed view of the region experiencing the highest stresses is shown in Fig. 2. Residual stresses in the range of 200 to 300 MPa are predicted in the ceramic at the edge of the joint region. Residual stresses up to 500 MPa are predicted in the metal tube. Further analysis of this and similar ceramic-to-metal joints is planned. These results suggest that producing such a joint may be problematic unless further refinements of the joint design and materials selection processes are considered.

Status of milestones

141111 Complete metallographic analysis of reactions of high-temperature braze filler metals with silicon nitride. On schedule: December 31, 1992.

Publications

M. L. Santella, "A Review of Techniques for Joining Advanced Ceramics," *Ceram. Bull.* **71**(6), 947-54 (1992).

YP17344

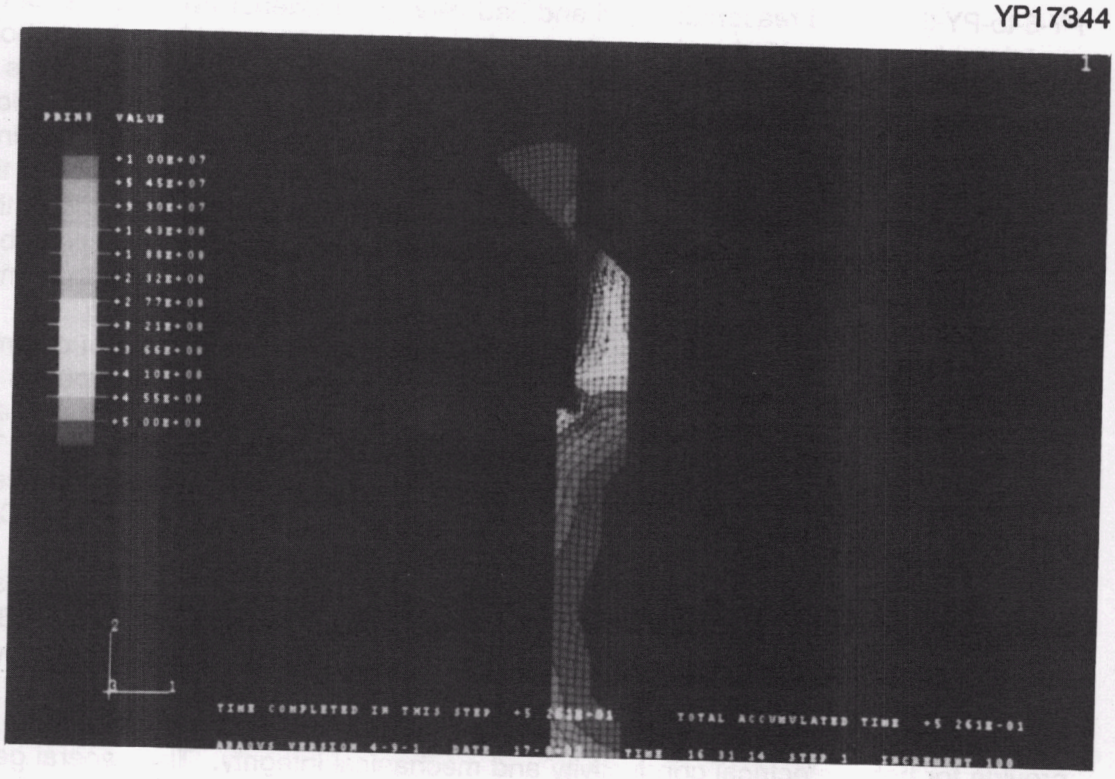

Fig. 1. Overall view of distribution of maximum principal stress in simulated design of a brazed diesel glow plug. Ceramic tip is on top; metal tube is on bottom. A vertical axis of symmetry is assumed.

YP17345

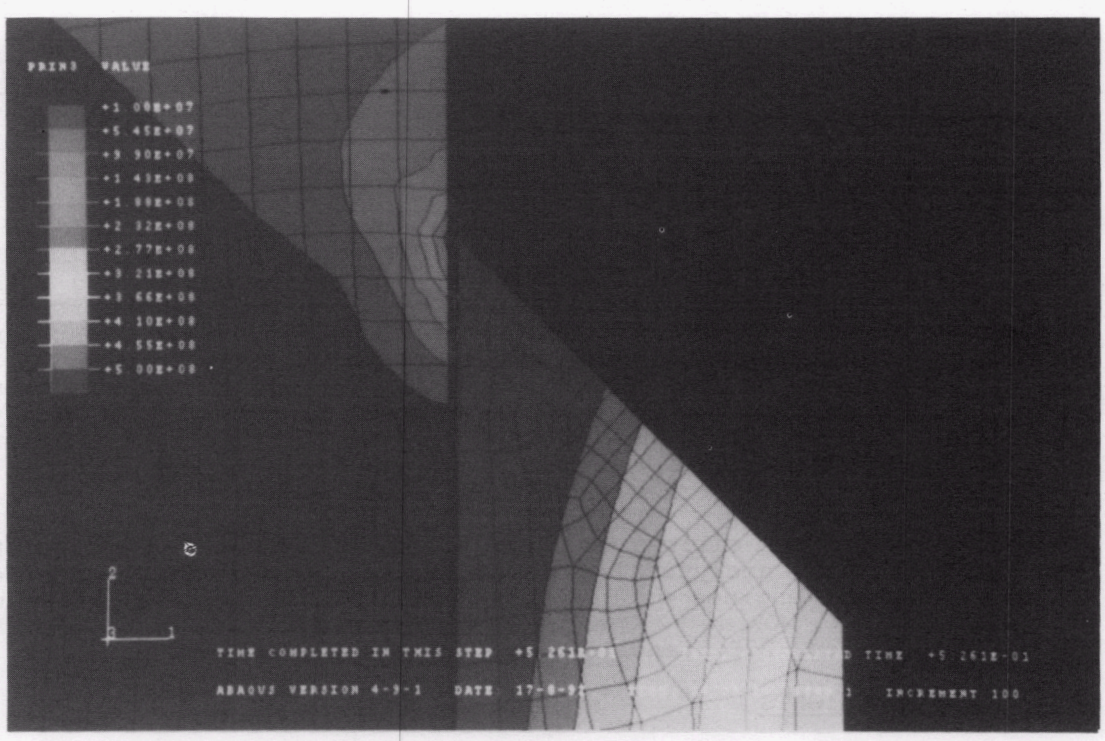

Fig. 2. Detail view of maximum principal stress distribution showing very high residual stresses are produced when the part is cooled from the bonding temperature of 830° C to room temperature.

1.4.2 Ceramic-Ceramic Joints

Analytical and Experimental Evaluation of Joining Silicon Carbide to Silicon Carbide and Silicon Nitride to Silicon Nitride for Advanced Heat Engine Applications Phase II

G. J. Sundberg, J. A. Wade, and C. S. White (Norton Company)

OBJECTIVE/SCOPE

Joins of hot isostatically pressed (HIP'ed) Si_3N_4-4wt% Y_2O_3 (NCX-5100 family) and sintered Beta-SiC (NCX-4500) were developed during Phase I of the contract and were demonstrated to have mechanical properties attractive for advanced heat engine applications.[1] An experimental database was developed for both materials based upon limited MOR and buttonhead tensile tests. Within the limitations of this database, analytical/numerical models were developed for prediction of join reliability. The purpose of this program is to develop joining technologies for HIP'ed Si_3N_4 with 4wt% Y_2O_3 and for a siliconized SiC (NT-230) for various geometries including: butt joins, curved joins and shaft to disk joins. In addition, more extensive mechanical characterization of silicon nitride joins to enhance the predictive capabilities of the analytical/numerical models for structural components in advanced heat engines will be provided. Mechanical evaluation will be performed by: MOR at 22°C and 1370°C, stress rupture at 1370°C, high temperature creep, 22°C tensile testing and spin tests.

TECHNICAL/HIGHLIGHTS

Si_3N_4 Butt Joints - Creep Resistance (Task 1.1)

The objective of this task is to evaluate the creep resistance of parent (unjoined) and joined material. The examples of the data, presented below, are work in progress and illustrate the methodology for evaluating creep resistance of joined materials. Testing is currently underway on the parent (unjoined) specimens to determine if creep behavior differs from the joined specimens.

Experimental Procedure - Twenty joined NCX-5101 specimens have been tensile creep tested according to the conditions summarized in Table 1. The specimen status after creep evaluation has been noted as the time to failure or suspension with the corresponding location of the failure when appropriate for each of the creep conditions. Table 1 will be discussed in detail later in the report.

A laser extensometry system was used to measure and store the displacement of four flags upon each tensile creep specimen (Figure 1). The relative displacement between any two flags has been used to calculate the strain of different segments of the gage section. Creep data is reported for a specific flag couple. For example, the creep of the parent material (segments D1-2 and D3-4) and the join (segment D2-3) may be calculated independently or the combined creep of the parent material and the join (segment D1-4) may be determined. In this manner, creep strain as a function of time has been plotted to compare the creep of the joined interlayer and the parent material at varying temperature and applied stress.

The theta projection curve (Equation 1) is fitted to the creep curve to obtain theta parameters. Theta projection is a convenient way to express the experimental strain as a function of time for the entire creep test. The four theta parameters have been generated for each of the experimentally derived strain versus time curves by fitting equation 1 to the test data using the simplex method (Table 2). Theta, θ_i, are

Research sponsored by the U.S. Department of Energy, Assistant Secretary for Conservation and Renewable Energy, Office of Transportation Technologies, as part of the Ceramic Technology Project of the Materials Development Program, under contract DE-AC05-84OR21400 with Martin Marietta Energy Systems, Inc.

Table 1: Joined NCX-5100 Silicon Nitride Creep Specimen Summary

Temperature (C)	Stress (MPa)	Specimen	Strain Rate (1-4) (1/hours)	Test Time (hours)	Status at Test Completion	Failure Location
1400	100	19-2	1.78E-05	475	suspended	
1400	100	19-4	1.83E-05	444	suspended	
1400	120	20-1	2.43E-05	202	failed	join
1400	120	20-2	2.19E-05	449	suspended	
1400	120	20-3	2.01E-05	384	failed	transition
1370	120	19-1	8.90E-06	475	suspended	
1370	120	17-8	1.13E-05	601	failed	transition
1370	120	19-7	8.26E-06	669	suspended	
1370	150	17-1	4.03E-05	93	failed	join
1370	150	17-4	Primary	24	failed	transition
1300	175	20-7	2.97E-06	819	suspended	
1300	175	20-8	1.27E-06	1100	suspended	
1300	200	17-5	1.20E-05	233	failed	transition
1300	225	17-6	4.93E-05	54	failed	transition
1300	225	20-5	4.11E-05	43	suspended	
1250	225	19-8	1.09E-06	1692	suspended	
1250	225	19-9	1.65E-06	507	failed	transition
1250	250	19-6	2.69E-06	890	failed	join
1250	250	20-4	Primary	8	failed	transition
1250	250	20-6	2.25E-06	936	suspended	

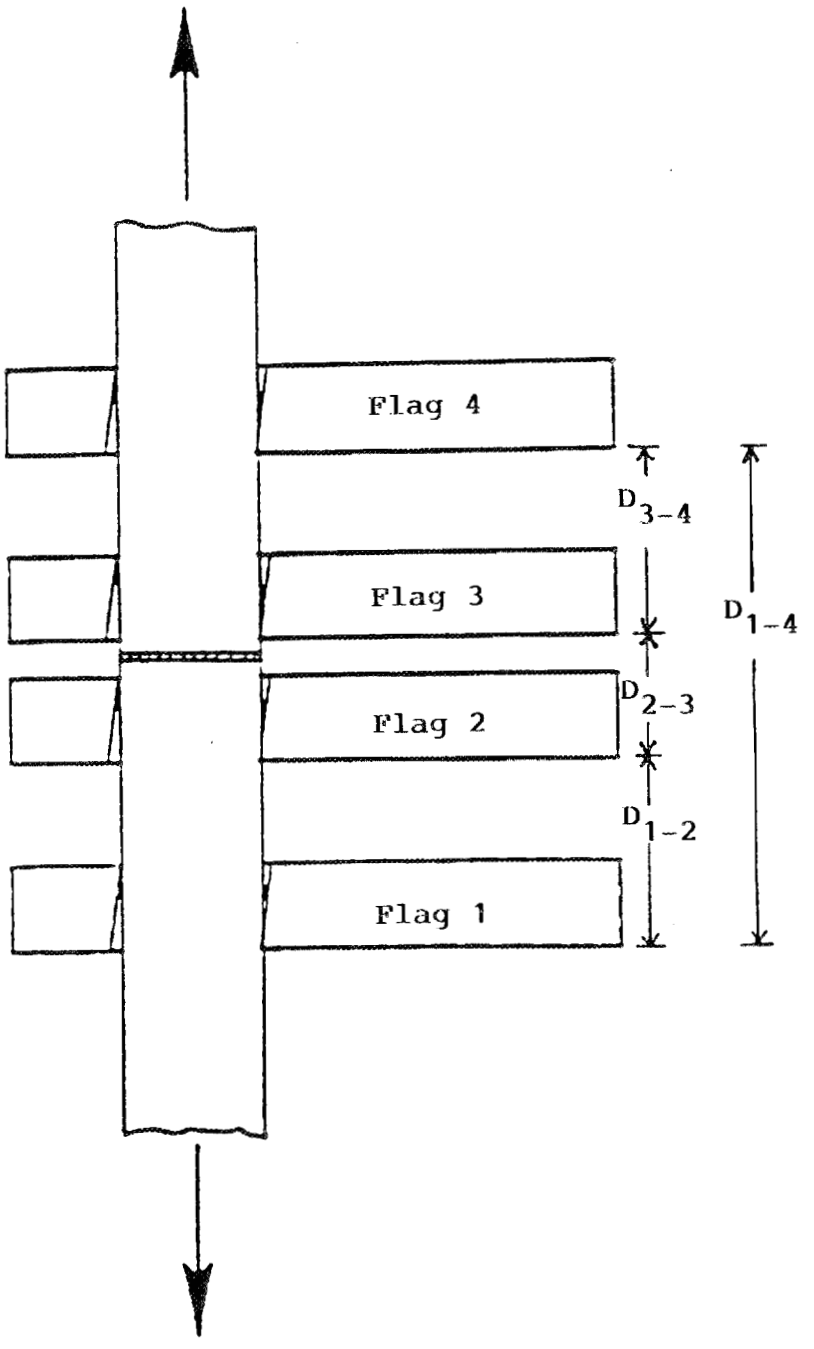

Figure 1: Extensometer Flag Arrangement

Table 2: Joined NCX-5100 Silicon Nitride Theta Projection Values

Data Set	Stress (MPa)	Temperature (C)	θ1	θ2	θ3	θ4
17-1	150	1370	6.612E-04	0.129	1.881	2.144E-05
17-5	200	1300	2.209E-03	2.150E-02	0.917	1.149E-05
17-8	120	1370	4.232E-03	1.363E-02	1.922	6.245E-06
19-1	120	1370	2.637E-03	3.271E-02	2.528	4.146E-06
19-2	100	1400	3.475E-03	2.045E-02	2.702	7.064E-06
19-4	100	1400	4.688E-03	3.690E-02	1.62	1.295E-05
19-6	250	1250	2.606E-03	7.347E-03	4.347	5.988E-07
19-7	120	1370	2.203E-03	1.143E-02	3.48	2.508E-06
19-8	225	1250	1.129E-03	3.640E-03	1.278	7.458E-07
19-9	225	1250	1.575E-03	3.581E-02	7.266	3.415E-07
20-1	120	1400	2.304E-03	5.712E-02	7.796	3.488E-06
20-2	120	1400	2.271E-03	1.683E-02	4.236	5.115E-06
20-3	120	1400	3.236E-03	2.653E-02	2.861	7.416E-06
20-5	225	1300	6.218E-04	3.594E-02	0.888	3.556E-05
20-6	250	1250	2.129E-03	1.047E-02	6.326	3.781E-07
20-7	175	1300	3.194E-03	0.131	2.826	1.334E-06
20-8	175	1300	3.401E-03	3.080E-03	5.609	6.903E-08

constants that define creep behavior[2]. The remaining task involves fitting individual theta values to a bilinear equation of stress and temperature. When completed, this will give a complete representation of the creep versus time curves using only 16 parameters.

$$\epsilon_{creep} = \theta_1 \ (1-e^{-\theta_2 t}) + \theta_3 \ (e^{\theta_4 t}-1) \qquad (1)$$

Results - Variations in strain at test termination and primary creep rate were observed between most of the specimens tested under like conditions. Furthermore, strain variations were observed along the gauge length within a given specimen. The strain variation within specimens was greatest between segments D1,2;D3,4 which contained only the parent material without the join interlayer. The percent difference of strain at test termination between opposing halves of the parent material typically ranged between 5% to 57%.

The data acquisition method was reviewed to ensure apparent strain variation was not an artifact induced by systematic error. No detectable temperature gradient was measured in the furnace hot zone at the creep gage section when monitored with thermocouples. The high and low strain measurements for creep specimens were randomly oriented at the upper and lower ends of the creep specimen. The strain of the center segment (D2,3) and the overall gauge length (D1,4) represented the creep of the join interlayer and the entire aggregate joined body, respectively, and correlated well with the weighted average of the measured creep segments (Figure 2). These findings confirm the measured strain variation to be an actual behavior difference and not an artifact from data acquisition.

Preliminary results have indicated inherent creep strain variability does exist within the NCX-5100 unjoined controls (Figure 3). However, the creep strain variability was independent of position within the gage section. The difference in overall strain between the two parent halves of the joined specimen was possibly attributed to the joining procedure itself.

Optical fractography of failed creep specimens revealed origins primarily at the surface at the stress riser in the transition zone. Three of twelve creep specimens failed at the join (Table 1). Several failed specimens were fractured and analyzed with SEM. Initial analysis of micrographs showed the primary creep mechanism to be cavitation at two grain junctions (Figure 4) and wedge cracking at the triple junctions. A more detailed analysis is underway.

None of the creep data, for tests as long as 1,692 hours, exhibited tertiary behavior for the joined silicon nitride when using a classical creep interpretation.[3] The lack of creep curve divergence from the constant slope of the secondary regime supports this conclusion. However, theta projection convention defines the secondary regime as the sum of primary and tertiary creep behavior.[2] Theta projection will be used later to extrapolate tertiary creep over a limited time interval from the creep data generated to date.

Since none of the creep tests completed to date display stage three (or tertiary) behavior, it is felt that the stage 2 (or steady state) creep rate is the most important. In this reporting period the focus has been on modeling the steady state creep. Twenty NCX-5101 specimens have been tested in phase II of the contract. Three of these specimens failed prior to stage 2 but there are also 6 specimens from phase I of the contract that displayed steady state behavior. The steady

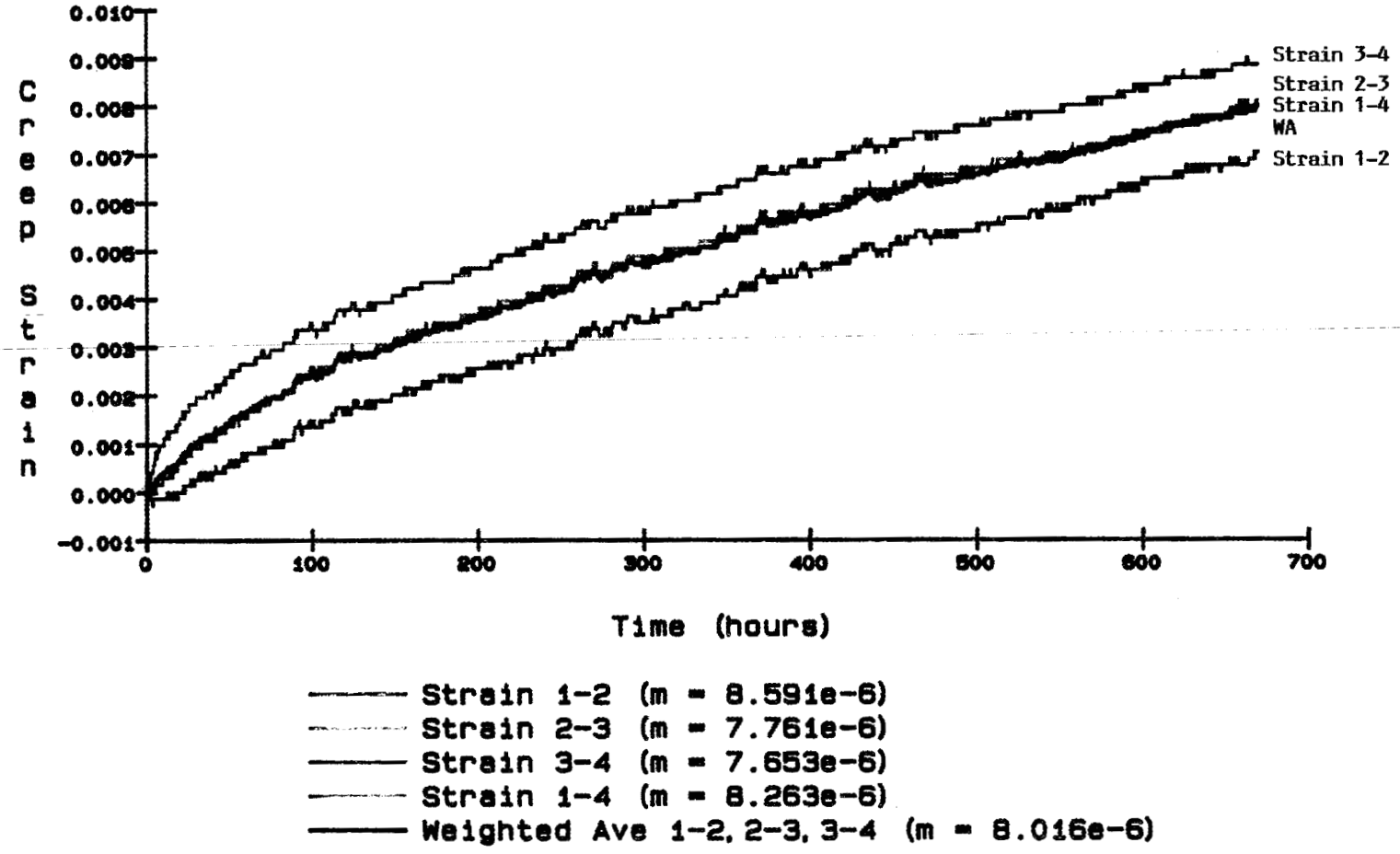

Figure 2: Creep Strain As A Function Of Time For Silicon Nitride Butt Join #19-7 at 1370°C And 120MPa. Test Suspended After 670 Hours.

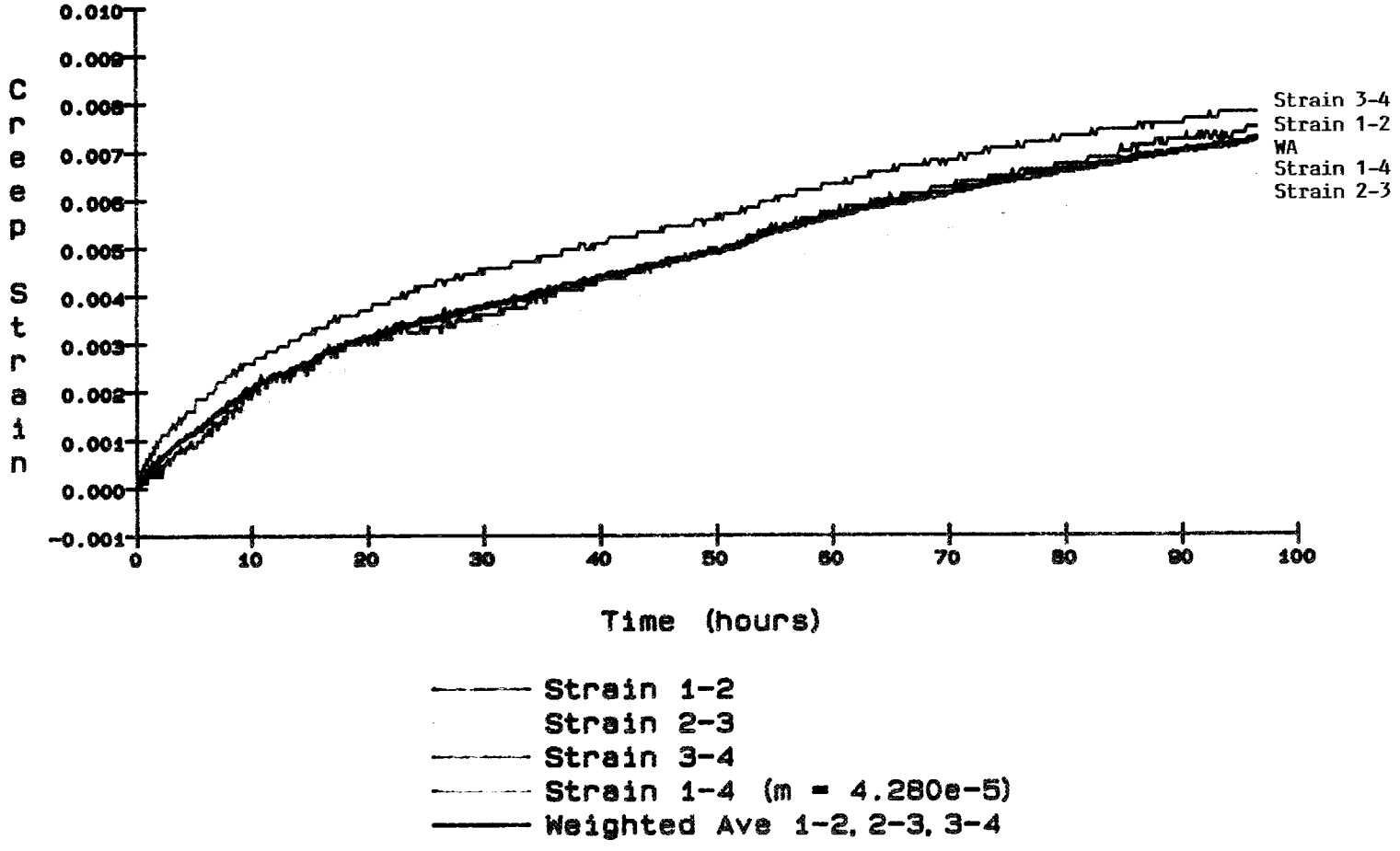

Figure 3: Creep Strain As A Function Of Time For Silicon Nitride Unjoined Control #46-2 At 1400°C and 100 MPa. Test Still In Progress.

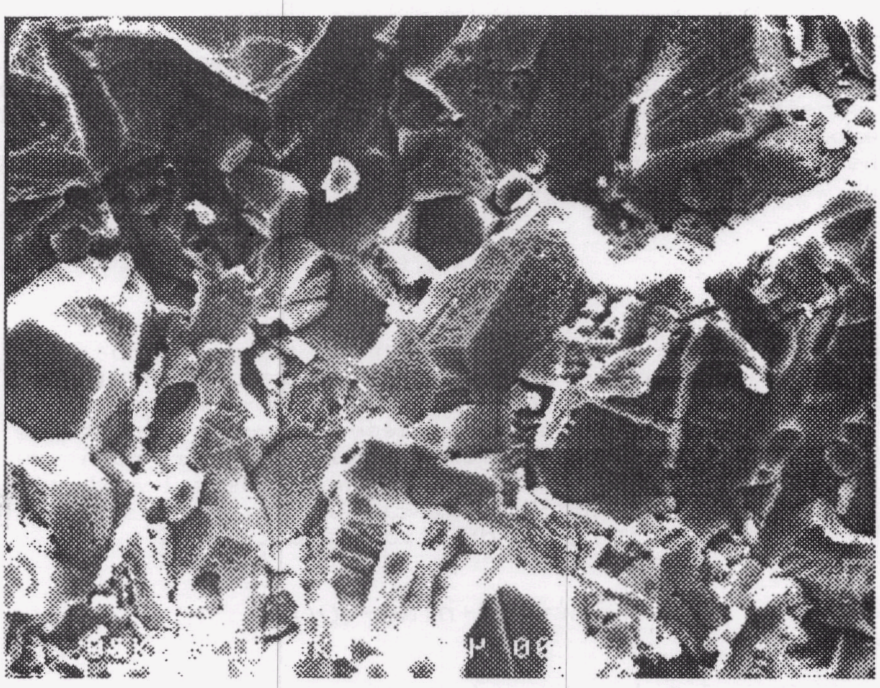

A) 10,000X

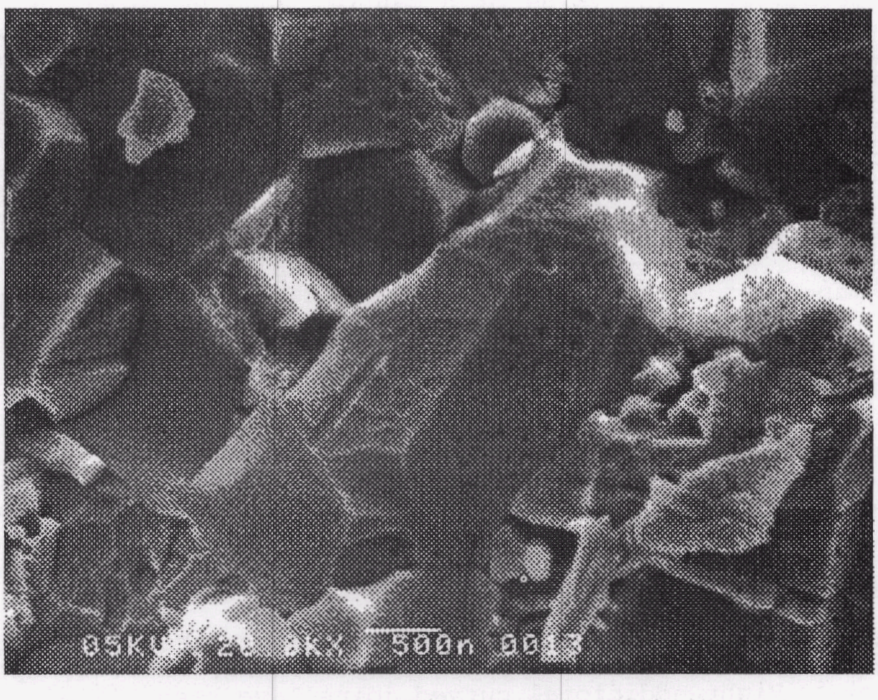

B) 20,000X

Figure 4: NCX-5100 Silicon Nitride Joined Tensile Specimen After Creep Testing Exhibiting Cavitation

state creep strain rate was calculated for these 24 specimens by fitting a line using the least squares method to the quasi-linear, stage 2 region of the experimental curves. The strain rates for the phase II experiments are shown in Table 1. The secondary creep rate exhibits a greater sensitivity to stress at lower temperatures, as indicated by the stress exponent, n (Figure 5).

The first attempt at modeling the steady state creep rate involved using the well known Arrhenius dependence:

$$\dot{\epsilon}=A\sigma^{n}e^{(-Q/RT)} \tag{2}$$

Here, $\dot{\epsilon}$ is the steady state strain rate, A and n are material constants, σ is the applied stress, Q is the activation energy for creep, R is the universal gas constant, and T is the absolute temperature. This equation, and its variations, has received wide acceptance for high temperature creep behavior in the literature for both ceramics and metals. Consequently, the efficacy of the classical Arrhenius approach was evaluated for the experimental creep data. Consider the natural logarithm of the equation 2 to graphically determine Q.

$$\ln\dot{\epsilon}=\ln A+n\ln\sigma-(Q/RT) \tag{3}$$

The value of Q was determined from plotting $\ln(\dot{\epsilon})$ versus 1/T at constant stress (Figures 6 and 7). The values of Q were determined to be 650 kJ/mole and 1397 kJ/mole for constant stresses of 120MPa and 225 MPa, respectively. The value of n can be found by plotting $\ln(\dot{\epsilon}e^{(Q/RT)})$ against $\ln(\sigma)$ using Q of 650 kJ/mole. The temperature dependent creep strain rate can be used to plot all of the experimental creep data with the slope of the best fit line giving n (Figure 8). Note the considerable scatter from the best fit line. This suggests the Arrhenius form may not be the best way to model the NCX-5101 material. The variation of the activation energy with stress shown on Figures 6 and 7 implies that it may be important to include an explicit stress term in the activation energy. Alternative models will be considered during the next reporting period as well as modeling of the primary creep region.

The strain rate versus failure time is plotted in Figure 9 to show the Monkman-Grant correlation for joined NCX-5100 and is represented mathematically as:

$$\dot{\epsilon}_s^{\beta}\ t_f = C \tag{4}$$

The Monkman-Grant parameters β and C are 1.012 and 2.670e-3, respectively, assuming that the relationship of equation 2 is valid. Note that the strain rate is in hours^{-1} and the time to failure is in hours.

<u>Si_3N_4 Curved Joint - Development</u> (Task 1.2)

Initial join development trials have demonstrated the effectiveness of the joining technique utilized during Joining, Phase I, upon curved geometries.[4] Eight additional curved joins have been HIP'ed to theoretical density to provide sufficient quantity of flexure specimens to statistically evaluate the mechanical properties of joins made with type A, B and variations of these slip interlayers. Four types of aqueous slips made with dispersed NCX-5101 powder were used to form the join interlayers (A, B, C and D). The aqueous slips although applied

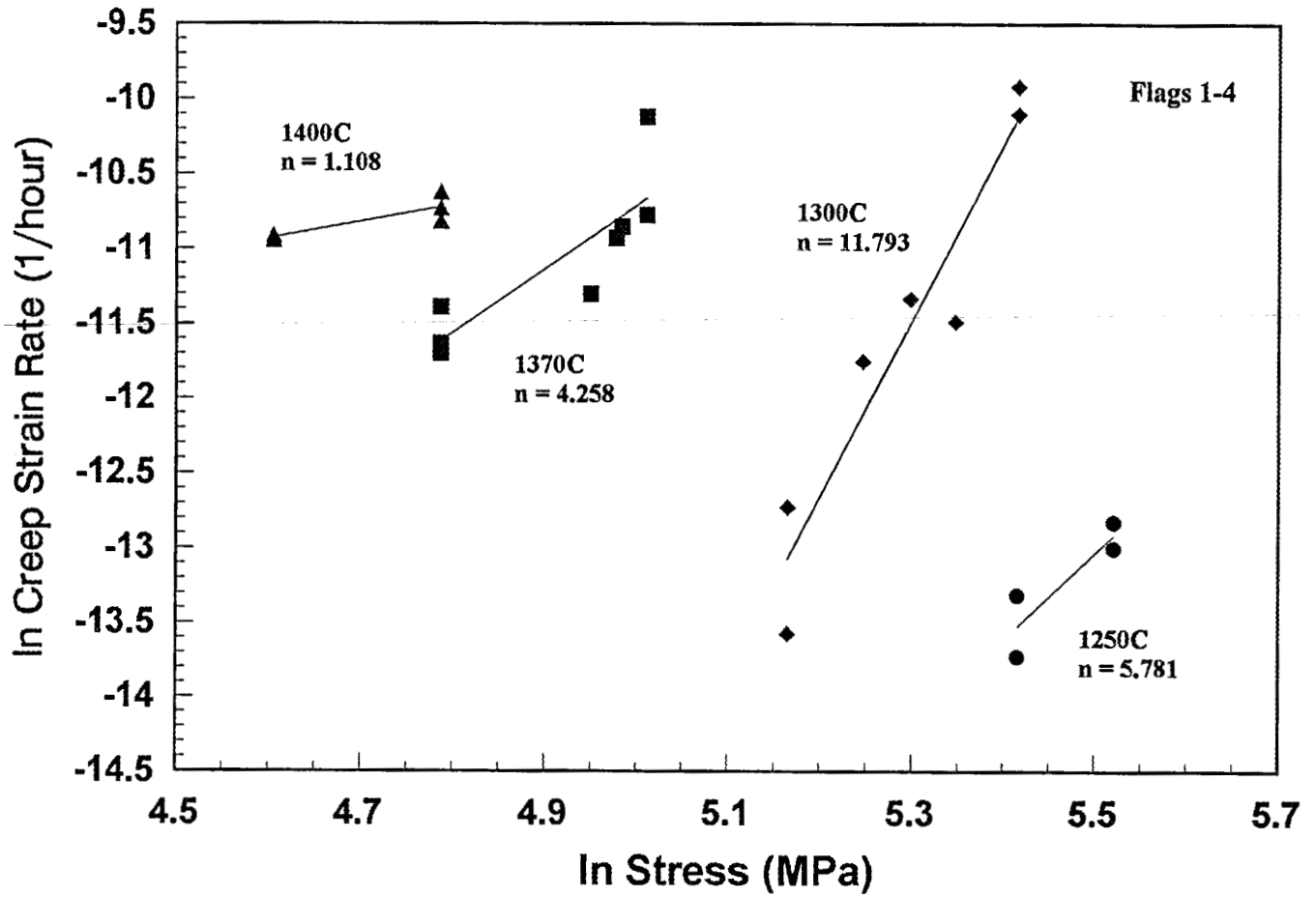

Figure 5: Determination Of The Stress Exponent (n) For NCX-5100 As A Function Of Temperature

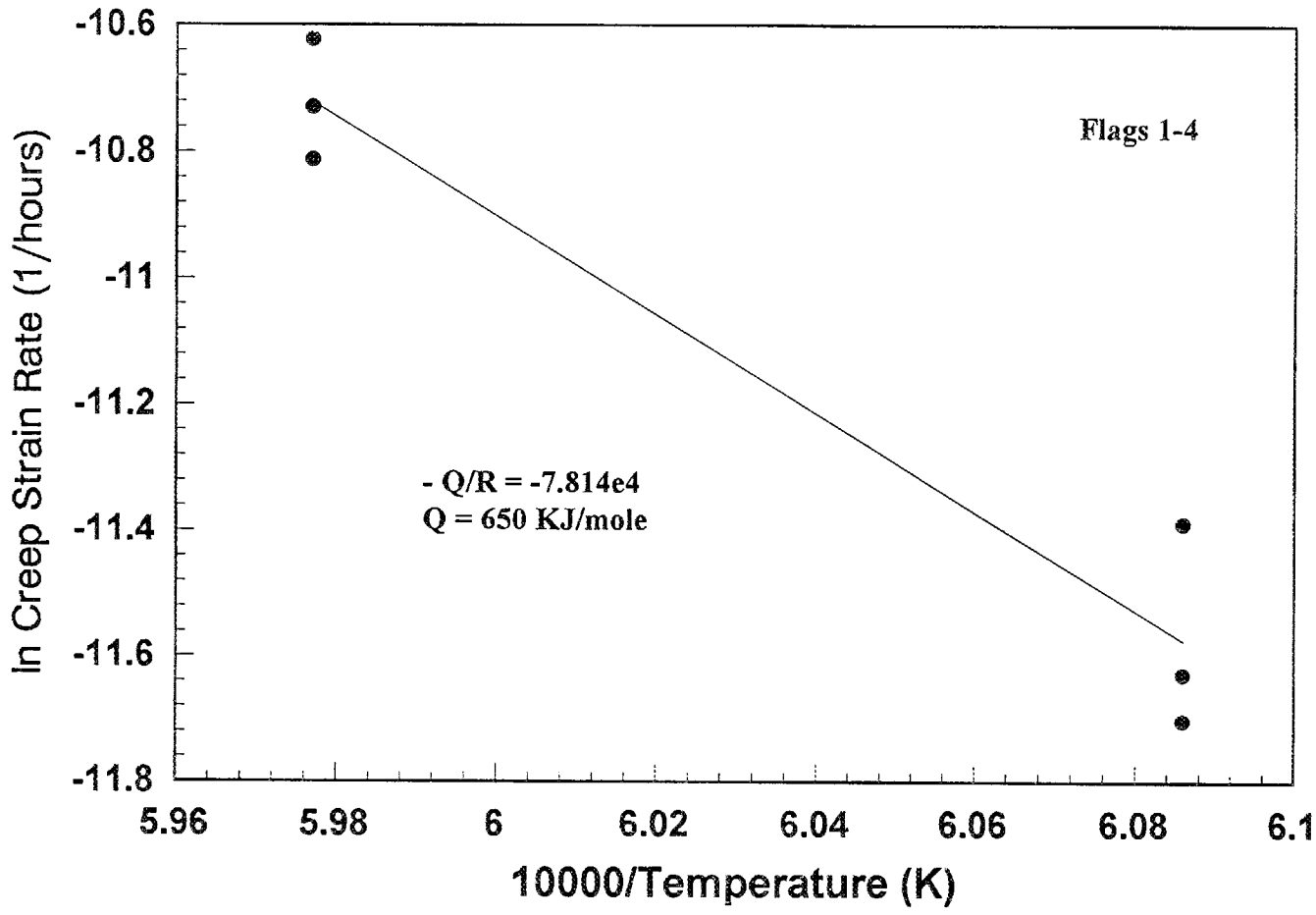

Figure 6: Determination Of The Joined Silicon Nitride Creep Activation Energy (Q) For Stress Of 120MPa

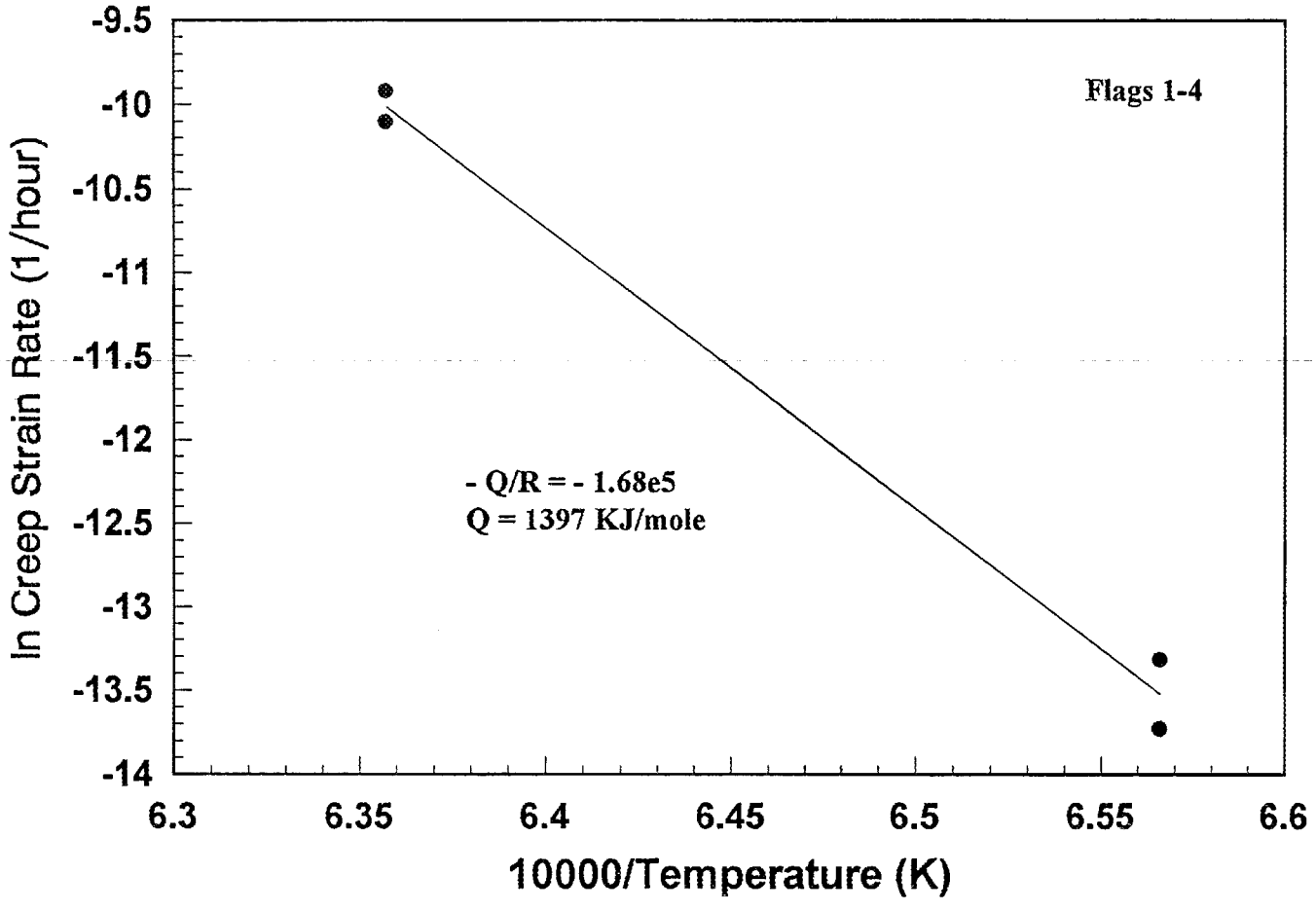

Figure 7: Determination Of The Joined Silicon Nitride Creep Activation Energy (Q) For Stress Of 225MPa

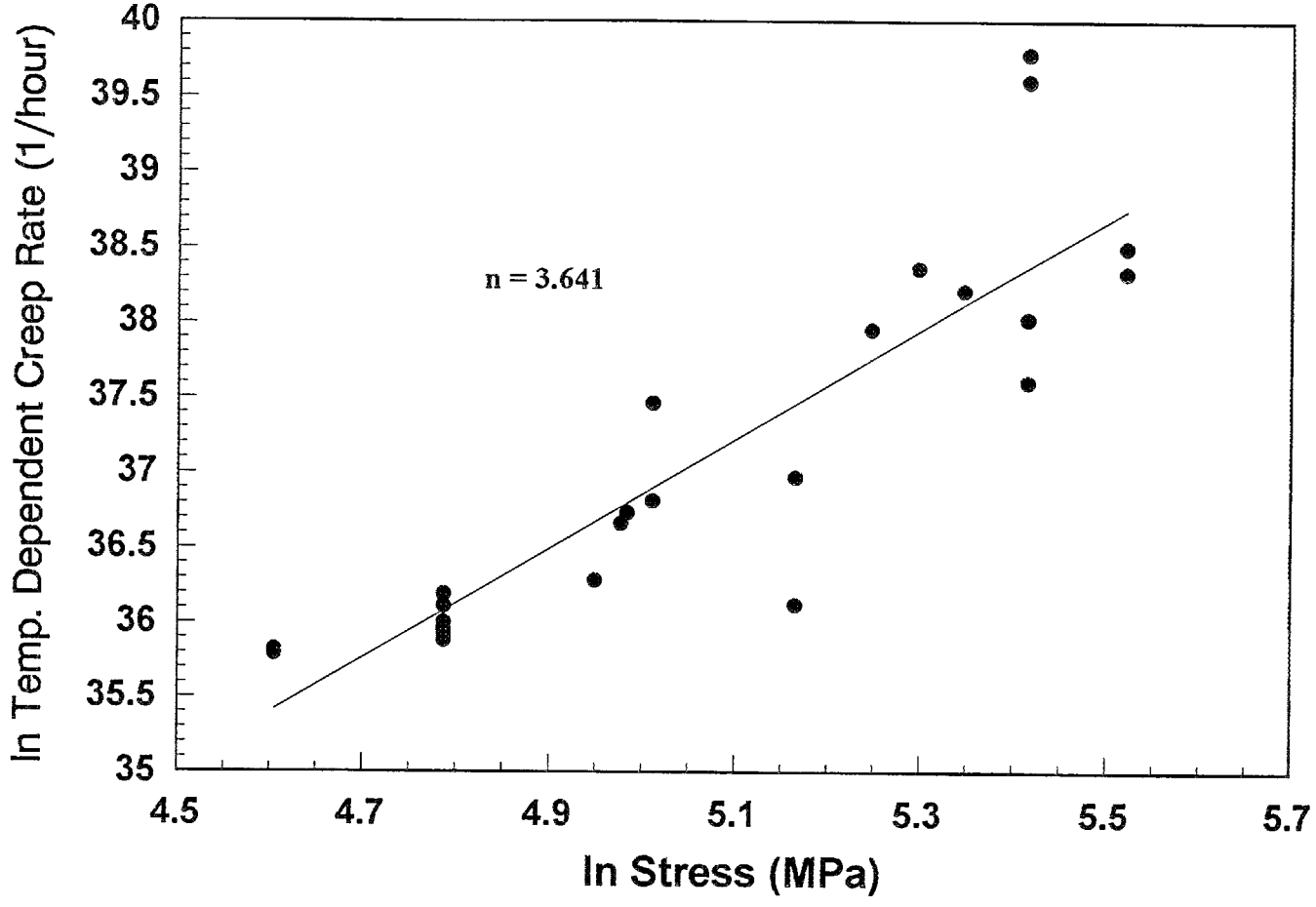

Figure 8: Determination Of The Joined Silicon Nitride Creep Stress Exponent (n)

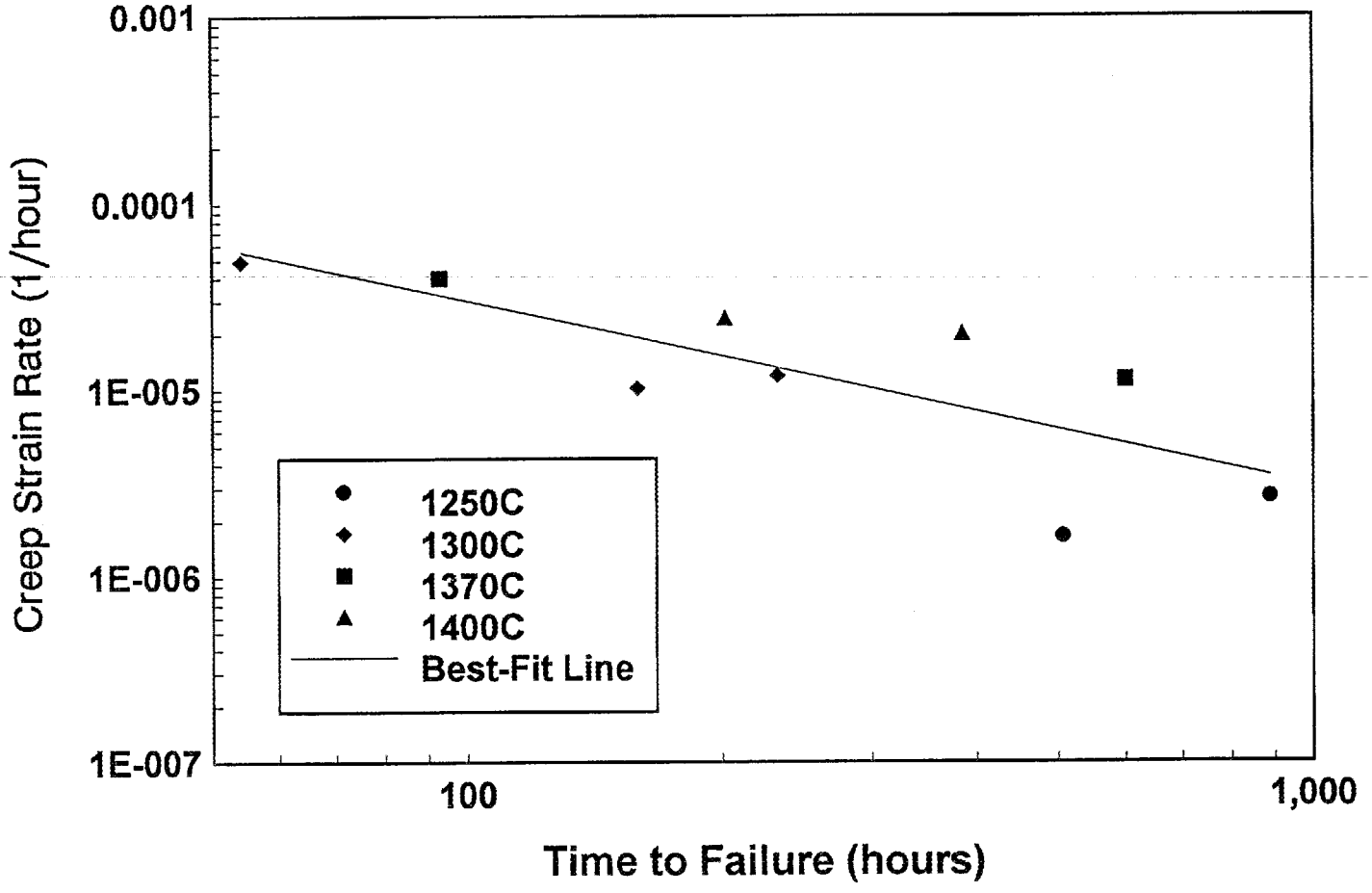

Figure 9: Monkman-Grant Relationship For Flags 1-4

similarly, differ in the method of preparation and the pre-conditioning of the green silicon nitride billets prior to joining. The type A slip and method of application was formerly used for Joining, Phase I mechanical characterization and analytical modeling[1]; and Task 1.1 of Joining, Phase II. Ground join sections indicate that incomplete densification of the near external surface of the join interlayer (~1mm depth) was not controlled by application of a varying amounts of slip to the external join seam. No apparent trend of incomplete densification of the near external surface of the joins with the type of slip interlayer was noted as with earlier work.[2] More work will be required to address this limitation of the joining method.

Mechanical Testing - **Room Temperature Fast Fracture:** Mechanical evaluation of the final iteration of silicon nitride curved join development is summarized in Table 3. While certain disk joins have visible join lines the failures do not often originate at the join. Joins 11 and 13 had the highest frequency of join failures with incomplete join interlayer closure during hot isostatic pressing as the primary cause. A statistical comparison of data sets using a non-parametric Robust analysis found no difference between most of the flexure strengths at the 95% confidence level. Joins 15 and 16, made with slip D, showed a significantly greater room temperature strength and weibull modulus relative to the other join types, complete join closure and an absence of failures originating in the join interlayer. The type D slip will be used for the remainder of silicon nitride joining on this contract.

1370°C Fast Fracture: Results from 1370°C temperature fast fracture of MIL STD 1942A, Specimen A type bars for the second iteration of curved join development are shown in Table 4. There were no statistically significant differences of 1370°C strength as a function of slip type. The joins made with types B and D slips demonstrated an absence of failure initiating within the join at 1370°C and gave the best high temperature strength. The high temperature performance and the room temperature properties for type D joins supports selection of type D joins for the remainder of the contract.

Siliconized SiC Butt Joint - Joint Development (Task 2.1A)

Siliconized silicon carbide and pre-sintered un-siliconized silicon carbide billets were manufactured during this reporting period. Microfocus x-radiography was used to ensure only billets without structural defects were to be used for the contract. The faces to be joined were ground flat prior to joining.

Attempts were made to join NT-230 silicon carbide butt joins. The two approaches were to join siliconized (dense) to siliconized materials and unsiliconized to unsiliconized materials with slip interlayers. The joins formed with slip interlayers were subsequently sintered and siliconized. There was a silicon enrichment at the join interface with both joining approaches that resulted in a join of much lower strength than the parent materials. Joins made from the initial unsiliconized materials exhibited a join interlayer with such pronounced silicon enrichment and strength degradation that the join interlayer was incapable of withstanding stress of grinding causing fracture of the join interlayer. Macrostructure of the join interlayer was comprised of silicon carbide honeycomb cells predominantly filled with silicon (Figure 10). Microstructure inside of cells incompletely filled with silicon exhibited a poorly bonded silicon carbide network at the join interlayer (Figure 11).

Mil Std. 1942MR B geometry flexure specimens were ground from the joins made with the initial siliconized materials with the join interlayer plane located at the center of the flexure specimens

Table 3: Silicon Nitride Curved Join Development Room Temperature Flexure Data (Task 1.2)

Disk Number	Interlayer Slip	Specimens Tested	Mean Strength (Mpa)	Std. Dev. (Mpa)	Min. Strength (Mpa)	Join Failures	Join Non Closure	Weibull Modulus
10	A	11	765	103	593	1	0	9.5
11	A	11	572	228	193	4	3	2.9
12	C	11	738	159	276	0	0	6.7
13	C	11	745	214	262	4	2	5
15	D	11	855	76	676	0	0	14.9
16	D	11	793	55	710	0	0	14.2
17	B	11	793	62	717	0	0	11.7
18	B	11	765	110	448	1	0	12.1

Table 4: Silicon Nitride Curved Join Development 1370°C Flexure Data (Task 1.2)

Disk Number	Interlayer Slip	Specimens Tested	Mean Strength (Mpa)	Std. Dev. (Mpa)	Min Strength (Mpa)	Join Failures	Weibull Modulus
10	A	7	530	40	462	0	14.6
11	A	7	455	110	186	2	6.4
12	C	7	524	41	455	1	17.5
13	C	7	448	131	131	1	5
15	D	7	524	48	462	0	12.1
16	D	7	538	35	469	0	16.1
17	B	7	538	41	462	0	13.2
18	B	7	531	28	503	0	19.8

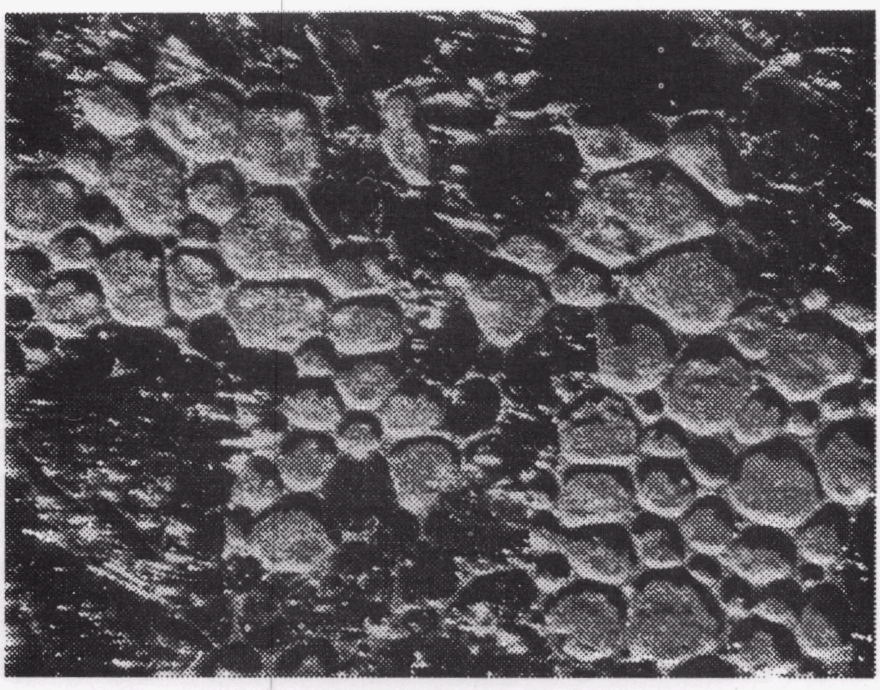

A) 12X

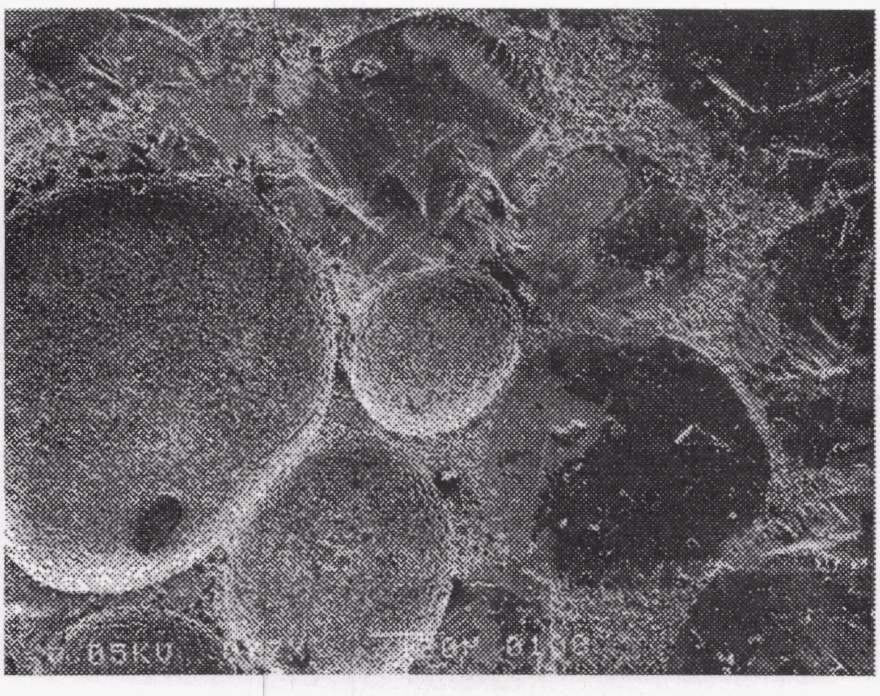

B) 27X

Figure 10: Macrostructure Of Join Interlayer For Join Made With Initial Unsiliconized Silicon Carbide Parent Material

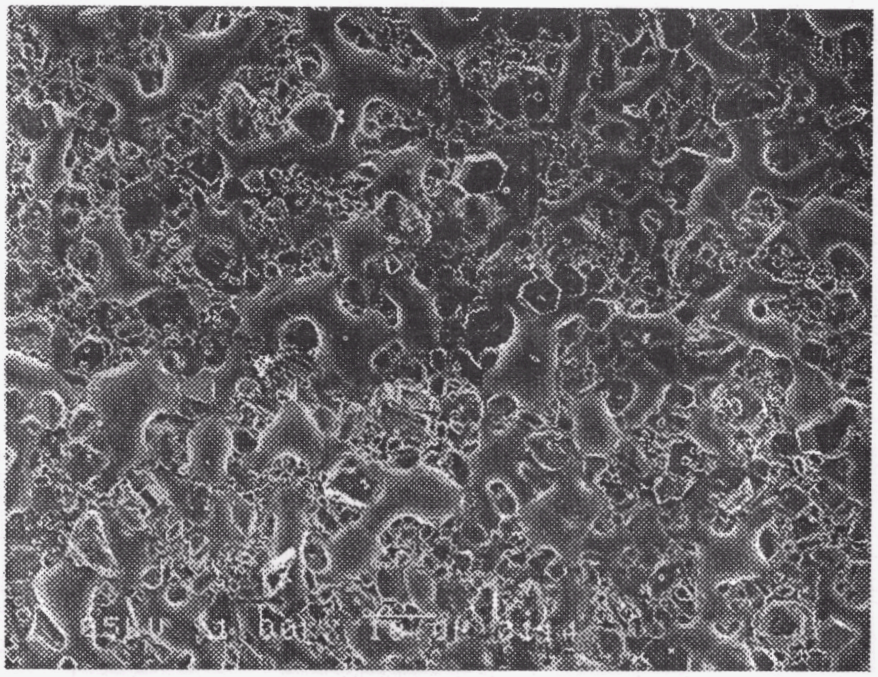

A) 1,000X

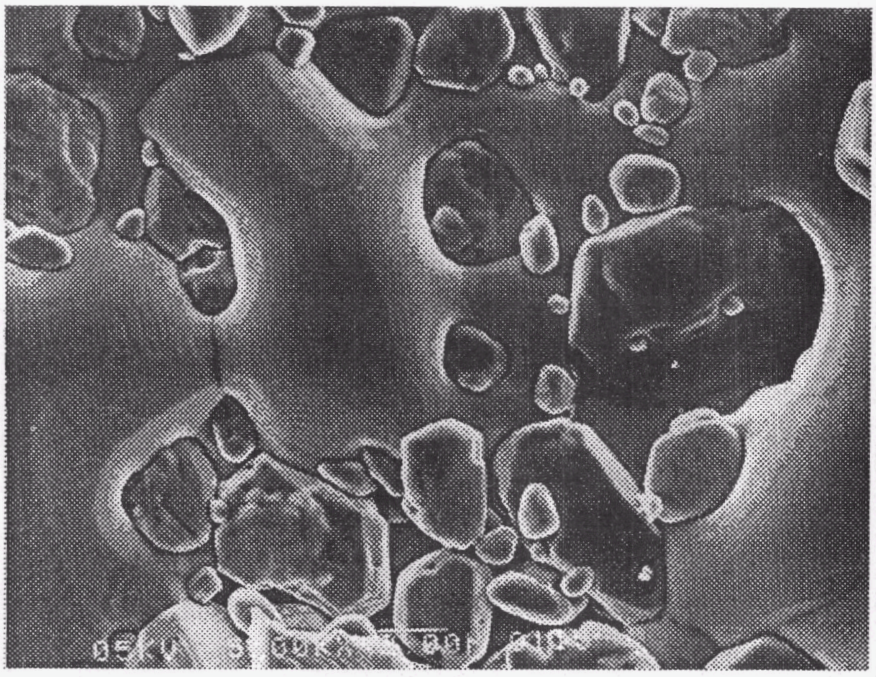

B) 5,000X

Figure 11: Microstructure Of Join Interlayer For Join Made With Initial Unsiliconized Silicon Carbide Parent Material

perpendicular to the length. Mean flexure strength of the joins was 222MPa with a standard deviation of 41MPa as compared to a mean flexure strength of the unjoined control body of 410MPa. All failure originated within the join interlayer at sites of porosity and/or silicon enrichment (Figure 12).

Additional silicon carbide joining work is underway to decrease excessive silicon enrichment at the join interlayer.

STATUS OF MILESTONES

The due dates for Tasks 2.1A, 2.1B, and 2.2 have been modified due to delayed silicon carbide billet manufacture. The modified completion dates are as follows.

2.1A	Siliconized SiC Butt Joint - Joint Development	(12/31/92)
2.1B	Siliconized SiC Butt Joint - Creep Resistance	(8/31/93)
2.2	Siliconized SiC Curved Joint - Joint Development	(4/31/93)

All other milestones remain on schedule.

COMMUNICATIONS/VISITS/TRAVEL

None.

PROBLEMS ENCOUNTERED

See Status of Milestones section.

PUBLICATIONS

None.

ACKNOWLEDGEMENTS

The authors wish to acknowledge Mr. L.D. Ton and Mr. A.M. Vartabedian for valued contributions to the success of this program.

REFERENCES

1. M.R. Foley, G.A. Rossi, G.J. Sundberg, J.A. Wade, F.J. Wu, *Analytical and Experimental Evaluation of Joining Silicon Carbide to Silicon Carbide and Silicon Nitride For Advanced Heat Engine Applications, Final Report, Subcontract 86X-SB045C*, Norton Company, September 30, 1991, 56-86.

2. B. Wilshire, *Rate Controlling Processes During Creep of Ceramics*, Science of Ceramics, Vol. 14, Proc. Conf., Canterbury, U.K., 1987.

3. H.E. Evans, "Mechanisms of Creep Failure" Elsevier Applied Science Publishers LTD., NY, 1984.

4. G.J. Sundberg, J.A. Wade, F.J. Wu, *Analytical and Experimental Evaluation of Joining Silicon Carbide to Silicon Carbide and Silicon Nitride to Silicon Nitride for Advanced Heat Engine Applications, Phase II, Semi-Annual Report, Subcontract 86X-SB045C*, February 1992 to March 1992, Norton Company, Northboro, MA.

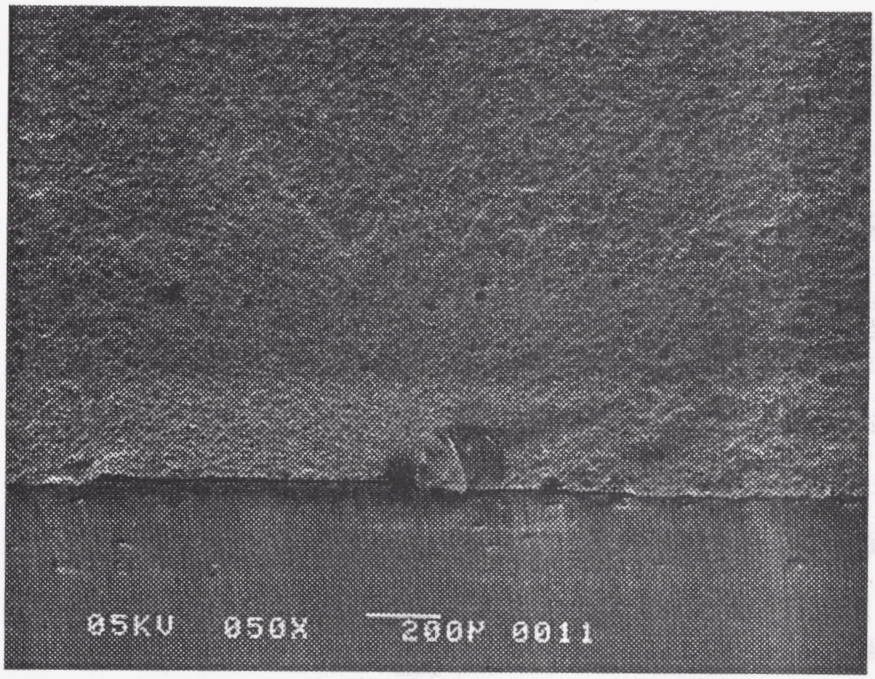

A) 50X

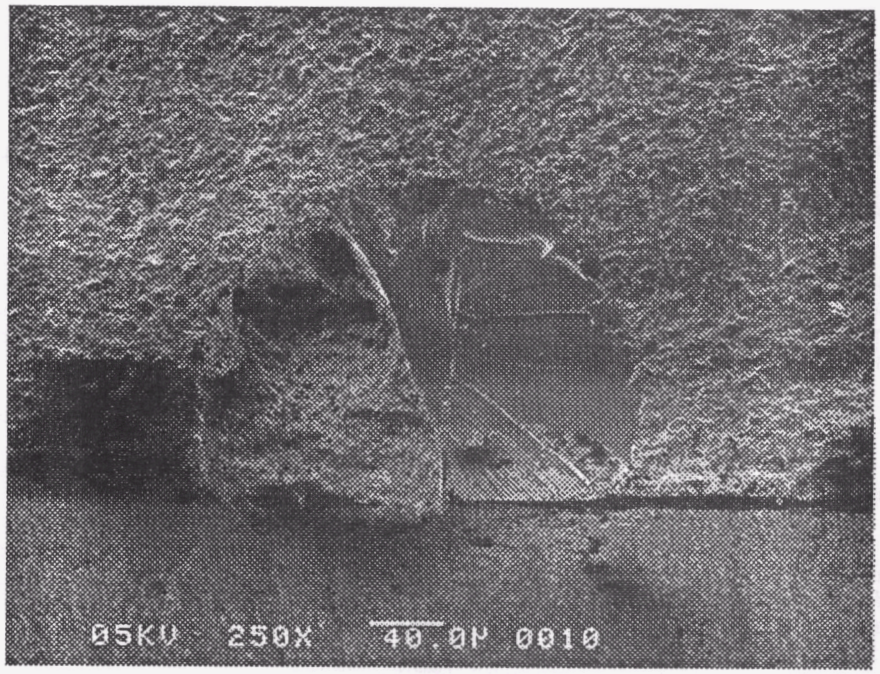

B) 250X

Figure 12: Fracture Origin Within Join Interlayer For Join Made With Initial Siliconized Silicon Carbide

2.0 MATERIALS DESIGN METHODOLOGY

INTRODUCTION

This portion of the project is identified as project element 2 within the work breakdown structure (WBS). It contains two subelements: (1) Modeling, (2) Contact Interfaces, and (3) New Concepts. The subelements include macromodeling and micromodeling of ceramic microstructures, properties of static and dynamic interfaces between ceramics and between ceramics and alloys, and advanced statistical and design approaches for describing mechanical behavior and for employing ceramics in structural design.

The major objectives of research in Materials Design Methodology elements include determining analytical techniques for predicting structural ceramic mechanical behavior from mechanical properties and microstructure, tribological behavior at high temperatures, and improved methods for describing the fracture statistics of structural ceramics. Success in meeting these objectives will provide U.S. companies with methods for optimizing mechanical properties through microstructural control, for predicting and controlling interfacial bonding and minimizing interfacial friction, and for developing a properly descriptive statistical data base for their structural ceramics.

2.2 CONTACT INTERFACES

2.2.1 Static Interfaces

Elastic Properties and Adherence of Thin Films and Coatings
Debra Joslin (The University of Tennessee)

Objective/Scope

The objective of this research is the examination of the effects of ion bombardment on the structure of thin ceramic films on ceramic substrates. The material combinations will include oxide films that have (a) no solid solubility, (b) limited solid solubility, and (c) complete solid solubility with the substrate material (also an oxide). Techniques for determination of elastic and plastic properties of thin films or coatings on ceramic substrates and for the determination of the strength of the bond between the film and substrate, which are currently being developed, will be used to determine the hardness, elastic modulus, and adherence of each material combination. The main testing techniques will be the ultra-low load microindentation tester (Nanoindenter), and thermal cycling tests.

Technical Highlights

During this report period, oxide films (Cr_2O_3 or ZrO_2) were grown on sapphire (Al_2O_3) to thicknesses of approximately 80 nm by rf sputter deposition. These samples were implanted at room temperature with 475 keV Kr ions to fluences of 5×10^{16} and 8×10^{16} ions-cm^{-2}. The energy was chosen such that the maximum energy deposition occurs at the film/substrate interface. To retain a portion of unimplanted film, an area of each sample was masked during the implantation. Rutherford backscattering spectroscopy (RBS) was performed on each of the samples to look for mixing of the film and the Al_2O_3.

Approximately 45% of the films had been sputtered away during the implantation, thus no mixing could be distinguished in the RBS spectra. Depth profiling using x-ray photoelectron spectroscopy (XPS) was performed to determine whether any mixing took place.

From the XPS data, it was determined that, in the unimplanted portion of the ZrO_2/Al_2O_3 specimens, the Zr is present as ZrO_2, the Al is present as Al_2O_3, and the film/substrate interface is sharp. The film/substrate interface from the implanted sample (8×10^{16} Kr/cm^2) is not sharp. The Zr is at first present as ZrO_2, and then as metallic Zr. The Al shows similar behavior. The depth of the mixed region is approximately 180 nm. The Cr_2O_3/Al_2O_3 sample implanted under the same conditions showed a sharp interface similar to the unimplanted portion of the sample.

Also during this period, analytical electron microscopy was performed on cross section samples of ZrO_2 films grown on c- axis sapphire (Al_2O_3). Four conditions were examined: unimplanted; implanted at room temperature with 340 keV Cr to a fluence of 4×10^{16} ions-cm^{-2}; implanted at 900°C with 340 keV Cr (4×10^{16} ions-cm^{-2}); and implanted at room temperature with 475 keV Kr ions to a fluence of 1×10^{17} ions-cm^{-2}. Each of the samples was ground to a thickness of about 500 mm, dimpled to a thickness of around 30 mm, and then ion milled to electron transparency via ion milling with Ar ions. The samples were milled at liquid nitrogen temperature at 6 kV and 1 mA current (0.5 mA per gun).

The unimplanted specimen appeared to have a sharp interface between the ZrO_2 and the Al_2O_3. The sample implanted with Cr at room temperature was amorphous in the region below the ZrO_2 film; the amorphous layer was about 3-4 nm thick. The Zr did not appear to extend past the amorphous layer. However, the Cr range was approximately 20 nm past the original film/substrate interface, and the straggle was ± 20 nm. The presence of Cr at the interface was confirmed via energy dispersive analysis (EDS). The presence of Zr in this layer was also confirmed. The sample implanted with Cr at elevated temperature showed no evidence of an amorphous region. It is known that defects in Al_2O_3 are mobile at 900∞C; during the implantation, recrystallization could occur. The sample implanted with Kr at room temperature showed a region of Al_2O_3 just below the interface between the ZrO_2 film and the Al_2O_3 substrate which was either of different orientation or crystal structure than the c-axis substrate. This region was about 3 nm thick. The range of the implanted Kr is about 40 nm past the original film/substrate interface, and the straggle is around 20 nm. Analysis by EDS showed that the new layer in the Al_2O_3 contained no Kr, but did contain Zr. Evidence exists in the literature [1] for amorphization of sapphire by Zr implantation. There may be a threshold Zr concentration below which the sapphire does not go completely amorphous, or the amorphous region may be stabilized by the presence of the implanted Cr.

Status of Milestones

N/A

Communications/Visits/Travel

None

Problems Encountered

None

Publications

None

2.2.2 Dynamic Interfaces

Development of Standard Test Methods for Evaluating the Wear Performance of Ceramics

P. J. Blau (Oak Ridge National Laboratory)

Objective/scope

The goal of this effort is to improve consistency in reporting ceramic wear data by helping to develop one or more standard test methods for quantitatively determining the wear resistance of structural ceramics in reciprocating sliding, a type of motion that is experienced by several types of automotive and truck engine wear parts. ORNL is working with the American Society for Testing and Materials (ASTM) in meeting this objective. Wear-test development normally falls within the scope of ASTM's G-2 Committee on "Wear and Erosion," and in 1990, P. J. Blau was appointed chairman of a newly established Task Group G02.40.07, "Reciprocating Sliding Wear Testing," within the G-2 Committee. This report describes activities within the Task Group.

Technical highlights

During this period, we (1) submitted a draft reciprocating wear test standard to ASTM subcommittee G-2.40 on "Non-abrasive Wear" for comment and review and (2) continued to lead a round-robin testing program of unlubricated wear tests using tool steel and silicon nitride materials as test specimens.

Status of the Draft Standard-A draft standard entitled "Reciprocating Sliding Wear of Ceramic and Metallic Materials," written in the prescribed ASTM form and style, was presented to the subcommittee chairman for "Non-Abrasive Wear." He recommended the draft be distributed for informal comment prior to balloting. ASTM sent out copies of the draft, and as a result, nine letters containing detailed comments have been received at ORNL. Based on these comments, the initial draft will be revised, and ASTM will send out a formal subcommittee ballot of the revised draft so that results can be received prior to the next ASTM G-2 meeting on December 10-11, 1992.

Progress of the Round-Robin Program-Two types of materials were selected for the round-robin testing program: a tool steel wear couple and a silicon nitride wear couple. Each test kit contained specimen materials enough for four tests per material type, a set of instructions (testing protocol), forms to use for reporting raw data, and a special clamp to hold the ball specimens.

The following six participants, in addition to ORNL, completed the tests and returned the specimens:

Howard Hawthorne, National Research Council of Canada
Glenn Elliott, Caterpillar Tech Center
Peter Vernia, General Motors Research and Envir. Staff
Ken Budinsky, Eastman Kodak Company
Alex Alliston-Greiner, Cameron-Plint (United Kingdom)
Carlton Rowe, Mobil Research

The eighth participant, Cummins Engine Company, has not yet returned the specimens or data sheets. Except for Kodak, all participants had reciprocating test machines made by Cameron-Plint.

An ASTM software package, specifically designed to analyze round-robin test data (per ASTM E 691) was used to compute the statistics of the following quantities, recorded for each test:

1. beginning friction coefficient,
2. steady-state friction coefficient,
3. range in friction coefficient at steady state,
4. diameter of the wear scar on the ball specimen,
5. wear volume loss of the ball (based on scar diameter),
6. weight change of the flat specimen, and
7. volume loss of the flat specimen from stylus profiling.

Running these seven parameters through the computer analysis indicated significant variations in the test results between labs. The repeatability of results (i.e., comparing runs within the same lab) was, however, generally good. In light of the spread in lab-to-lab data ("reproducibility"), a letter containing a detailed FAX questionnaire was sent to participants to learn more about their specific machines (age and model), their methods of calibration, and their specimen handling procedures. It is expected that the additional information will help pin-point sources of discrepancies and may lead to a tightening of the control of key variables in the draft standard.

Future plans

During the next period, we will investigate the sources of scatter in the round-robin test data, revise the draft standard, and present results at the ASTM committee meeting in Miami, Florida, in December 1992.

References

None.

Status of milestones

222204 - Submit first draft of wear test standard to ASTM. Completed.

Communications/visits/travel

P. J. Blau attended the ASTM G-2 Committee meeting in Louisville, Kentucky, on June 17-19, 1992. A workshop on the subject of specimen cleaning methods preceded the committee meeting (see citation, below).

Problems encountered

Results of the first round-robin test series had unacceptable scatter. Sources of this variability are being investigated. One of the participants did not complete tests in time.

The ASTM E 691 standard requires a minimum of six participants, so this situation did not affect the validity of the statistical analysis. It was, however, unfortunate that a larger set of test data was not available from this initial test series.

Publications/presentations

P. J. Blau, R. L. Jackson, and C. S. Yust, "Specimen Cleaning Effects on the Friction Break-in Behavior in Sliding Wear Tests," was presented at the ASTM G-2 Committee's Workshop on Selection and Use of Specimen Cleaning Methods for Wear Testing, Louisville, Kentucky, June 17, 1992.

2.3 NEW CONCEPTS

Advanced Statistical Concepts of Fracture in Brittle Materials
C. A. Johnson and W. T. Tucker (General Electric Corporate Research and Development)

Objective/Scope

The design and application of reliable load-bearing structural components from ceramic materials require a detailed understanding of the statistical nature of fracture in brittle materials. The overall objective of this program is to advance the current understanding of fracture statistics, especially in the following four areas:

- Optimum testing plans and data analysis techniques.
- Consequences of time-dependent crack growth on the evolution of initial flaw distributions.
- Confidence and tolerance bounds on predictions that use the Weibull distribution function.
- Strength distributions in multiaxial stress fields.

The studies are being carried out largely by analytical and computer simulation techniques. Actual fracture data are then used as appropriate to confirm and demonstrate the resulting data analysis techniques.

Technical Highlights

Work during this reporting period continued on generalized tests of goodness-of-fit for the size-scaled Weibull distribution. Quantitative tests of goodness-of-fit are helpful in judging applicability of the distribution and validity of resulting estimates of strength and probability of failure. Effort on goodness-of-fit tests has concentrated on variations of the Kolmogorov-Smirnov (K-S) test. The previous semi-annual report described a common misuse of conventional tables of the critical K-S statistic, described the use of Monte Carlo simulations to create more appropriate tables, and demonstrated the modified K-S tests on actual Class I strength data (no pooling of data, single specimen size and geometry).

Most of the previous effort was aimed at Class I analyses of strengths where all specimens are tested in the same specimen size and loading geometry. Work during this reporting period concentrated on goodness-of-fit testing of Class IV problems, where fracture data from multiple specimen sizes and geometries are pooled together to better characterize the underlying strength distribution. There are at least five aspects of goodness-of-fit of Class IV data that can be tested.

- Material homogeneity between subgroups — compare to assumed uniformity
- Variability in strengths within subgroups — compare to Weibull model
- Specimen size effects between subgroups — compare to Weibull model
- Stress distribution effects between subgroups — compare to Weibull model
- Overall behavior — compare to Weibull model

Work is continuing on development and validation of K-S and other approaches to evaluate each of these aspects of goodness-of-fit in Class IV problems and to handle the associated inference problems that arise from use of simultaneous statistical tests.

In addition, effort has continued on the ASTM Standard Practice entitled "Reporting Uniaxial Strength Data and Estimating Weibull Distribution Parameters For Advanced Ceramics." This standard is a jointly defined and written document with S. Duffy of NASA Lewis Research Center and G. Quinn of NIST that defines standardized methods of data analysis and reporting. The standard is limited to Class I analysis of specimens or components that are primarily subjected to uniaxial stress states (it does not include multiaxial probabilistic approaches). The standard includes maximum likelihood estimation of Weibull distribution parameters for materials that are controlled by multiple concurrent (competing) flaw populations using censored data analysis techniques. In addition, for data sets that include a single active flaw population, the standard practice outlines methods to correct for bias errors and to calculate confidence intervals on distribution parameters. The standard has recently been submitted to ASTM for balloting.

Status of Milestones

On schedule.

Publications

None.

3.0 DATA BASE AND LIFE PREDICTION

INTRODUCTION

This portion of the project is identified as project element 3 within the work breakdown structure (WBS). It contains five subelements, including (1) Structural Qualification, (2) Time-Dependent Behavior, (3) Environmental Effects, (4) Fracture Mechanics, and (5) Nondestructive Evaluation (NDE) Development. Work in the Structural Qualification subelement includes proof testing, correlations with NDE results and microstructure, and application to components. Work in the Time-Dependent Behavior subelement includes studies of fatigue and creep in structural ceramics at high temperatures. Research in the Environmental Effects subelement includes study of the long-term effects of oxidation, corrosion, and erosion on the mechanical properties and microstructures of structural ceramics. Work in the Fracture Mechanics subelement includes development of techniques for measuring the tensile strength and creep resistance of ceramic materials at high temperatures, and testing ceramic materials at high temperatures under uniaxial tension. Work in the NDE Development subelement is directed at identifying approaches for quantitative determination of conditions in ceramics that affect their structural performance.

Major objectives of research in the Data Base and Life Prediction project element are understanding and application of predictive models for structural ceramic mechanical reliability, measurement techniques for long-term mechanical property behavior in structural ceramics, and physical understanding of time-dependent mechanical failure. Success in meeting these objectives will provide U.S. companies with the tools needed for accurately predicting the mechanical reliability of ceramic heat engine components, including the effects of applied stress, time, temperature, and atmosphere on the critical ceramic properties.

3.1 STRUCTURAL QUALIFICATION

Microstructural Analysis of Structural Ceramics

B. J. Hockey and S. M. Wiederhorn
(National Institute of Standards and Technology)

Objective/Scope

The objective of this part of the program is to identify mechanisms of failure in structural ceramics subjected to mechanical loads at elevated test temperatures. Of particular interest is the damage that accumulates in structural ceramics as a consequence of high temperature exposure to stresses normally present in heat engines.

Design criteria for the use of ceramics at low temperature differ from those at high temperature. At low temperature ceramics are elastic and brittle; failure is controlled by a distribution of flaws arising from processing or machining operations, and the largest flaw determines the strength or lifetime of a component. By contrast, at high temperature where ceramics are viscoelastic, failure occurs as a consequence of accumulated, or distributed damage in the form of small cavities or cracks that are generated by the creep process. This damage effectively reduces the cross-section of the component and increases the stress that must be supported. Such increases in stress are autocatalytic, since they increase the rate of damage and eventually lead to failure as a consequence of loss in cross section. When this happens, the individual flaw loses its importance as a determinant of component lifetime. Lifetime now depends on the total amount of damage that has occurred as a consequence of the creep process. The total damage is now the important factor controlling lifetime.

Recent studies of high temperature failure of the non-oxide ceramics intended for use for heat engines indicates that for long term usage, damage accumulation will be the primary cause of specimen failure. Mechanical defects, if present in these materials, are healed or removed by high temperature exposure so that they have little influence on long term lifetime at elevated temperature. In this situation, lifetime can be determined by characterizing the damage and the rate of damage accumulation in the material at elevated temperatures. In ceramic materials such as silicon nitride and SiAlON, such characterization required high resolution analyses because of the fine grain size of these materials: hence the need for transmission electron microscopy as an adjunct to the mechanical testing of ceramics for high temperature applications is apparent.

In this project, the creep and creep-rupture behavior of several ceramic materials will be correlated with microstructural damage that occurs as a function of creep strain and rupture time. Materials to be studied include: SiAlON; hot-pressed silicon nitride; sintered silicon carbide. This project will be coordinated with WBS 3.4.1.3, Tensile Creep Testing, with the ultimate goal of developing a test methodology for assuring the reliability of structural ceramics for high temperature applications.

Technical Highlights

A study was made of the accumulated cavity damage produced in Norton/TRW NT-154 silicon nitride by tensile creep. The total cavity volume was found to scale directly with creep strain. In addition, it was found that two types of cavities are produced: one being discrete, ellipsoidal-shaped grain boundary cavities; the other being large (0.5 to 1.0 micron), "pore-like" cavities. At a given temperature, the relative extent of these two types of cavities appears to depend on the applied stress. At high stresses, the formation of grain boundary cavities is favored, and this leads to creep rupture at relatively low strains. At low stresses, the formation of large, pore-like cavities is favored, and this leads to a significant decrease in the density of the material with increasing strain. Thus even at low stresses,where low creep rates are realized, creep lifetime should ultimately be limited by the progressive decrease in material density with increased strain.

Experimental Technique

Various techniques were used to characterize the nature and extent of cavitation damage produced in a commercial grade of Norton/TRW NT-154 silicon nitride after tensile creep. These included: precision density measurement; low angle neutron scattering (SANDS); low angle X-ray scattering (SAXS); and analytical transmission electron microscopy (ATEM). They were applied to samples crept to failure at temperatures from 1370 to 1430°C at various applied stresses. Creep lifetimes ranged from 18 to over 1500 hours.

Results and Discussion

During the past six months, a study was made of accumulated cavity damage produced in a recent version of Norton/TRW NT-154. Various characterization techniques were employed. These included precision density measurement, small angle neutron scattering (SANDS), small angle X-ray scattering (SAXS), as well as analytical transmission electron microscopy (ATEM). This effort was prompted not only by a need to assess the use of these techniques, but by tensile creep test results which showed an improved creep behavior relative to an earlier version of NT-154. In brief results from density measurement, SANDS, and SAXS showed that accumulated cavity volume scaled with creep strain. Moreover, results from SAXS, in particular, indicated that most of the cavity volume is associated with cavities having dimensions of 600 nm and larger. In contrast, previous ATEM results on the earlier NT-154 had identified discrete, ellipsoidal shaped grain boundary cavities having a maximum dimension of about 300 nm as the primary form of cavitation; cavities of larger dimensions were thought to be inherent porosity. Recent ATEM results, obtained not only on the improved NT-154 but by reexamination of the earlier version, require that this description of cavity damage in NT-154 be modified. These new results confirm that tensile creep results in the formation of large-scale, 500 to 1000 nm, cavities, Figure 1, and that

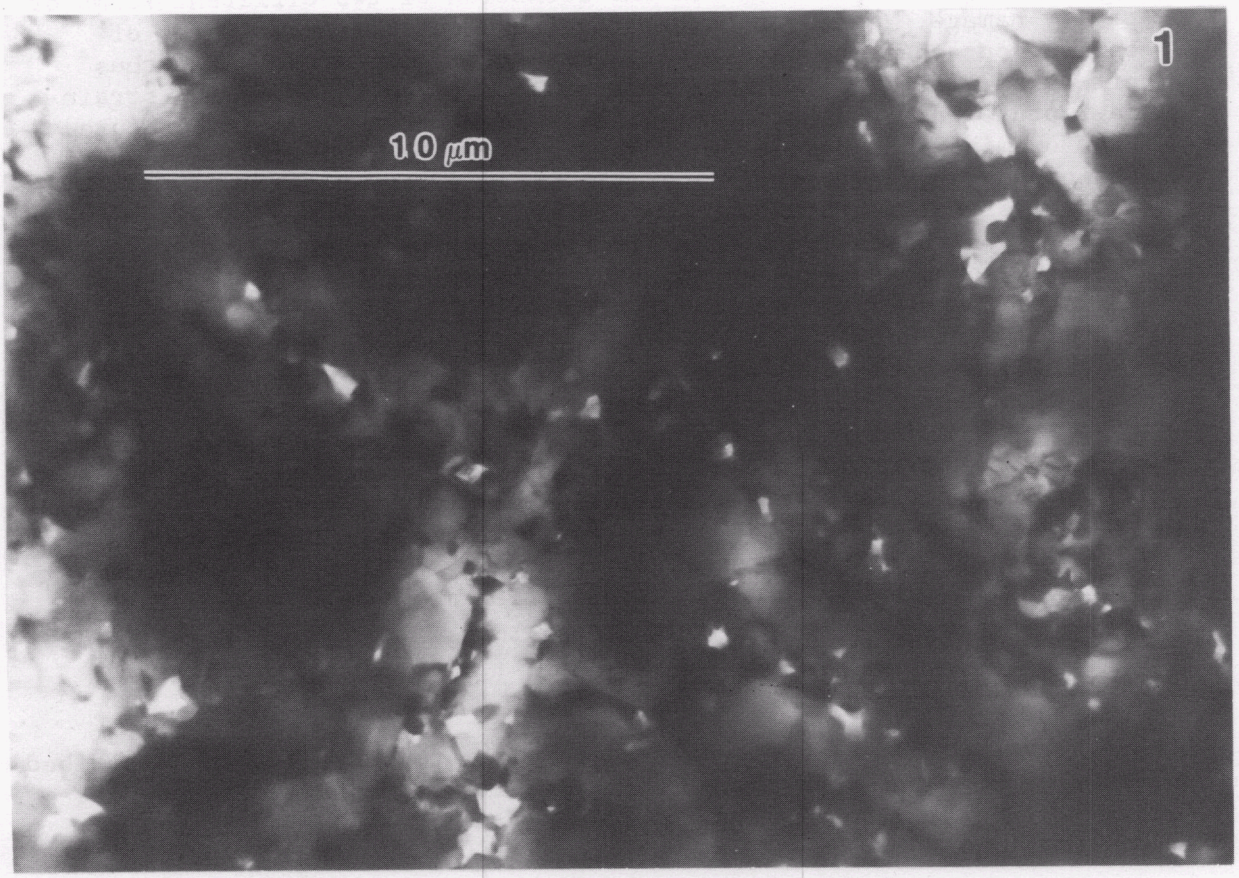

Figure 1. Large-scale view showing representative density and distribution of large (0.5 to 1.0 micron), "pore-like" cavities produced in NT-154 at high creep strains.

the density of these large cavities appears to increase with increasing strain. Individually, these cavities are found within multi-grain junctions separating relatively large silicon nitride grains and effectively resemble inherent porosity in this material, Figure 2. As such, this form of cavitation appears to involve the dissolution and subsequent redeposition of small second phase "grains" -and possibly small silicon nitride grains - normally found within these regions. As before, crept samples of the improved NT-154 also contained ellipsoidal grain boundary cavities, Figure 3, and it appears that creep results in the formation of two different forms of cavity damage. Based on comparative results, these two forms of cavitation appear to have a different stress dependence, and thus effect on lifetime. In this regard, both creep lifetime and strain-to-rupture increase with decreasing stress for a given temperature. From examination, samples that fail rapidly at high stresses contain grain boundary cavities (Figure 3), but show little or no evidence of the larger multi-grain junction cavities. Conversely, samples tested under low stresses, such that lifetimes in excess of 1000 hours are realized, exhibit high densities of large multi-junction cavities (Figures 1 and 2) and relatively low densities of widely scattered grain boundary cavities. At intermediate stresses, significant densities of both forms of cavities are found. While further work is needed to determine the stress dependence of grain boundary cavitation - present results indicate a possible initial increase in density and size with increasing stress - grain boundary cavitation appears responsible for failure at relatively high stress levels. Multi-grain junction cavitation, which increases the porosity of the material, clearly contributes to creep failure at intermediate stresses and, importantly, should ultimately limit lifetime even at negligible stress levels.

Status of Milestones

Work on GTE PY-6 was delayed in order to carry out the described study on Norton/TRW NT-154. Otherwise, milestones are on schedule.

Publications

1. "Effect of Microstructure on the Creep of Siliconized Silicon Carbide", B.J. Hockey and S.M. Wiederhorn, J. Am. Ceram. Soc. 75, 1822-30 (1992).

2. "The Effect of Microstructure on the Tensile Creep/Creep Rupture of Silicon Nitride", B.J. Hockey and S.M. Wiederhorn, accepted for presentation - Material Research Society 1992 Fall Meeting, Nov. 30-Dec. 4, 1992.

References

None

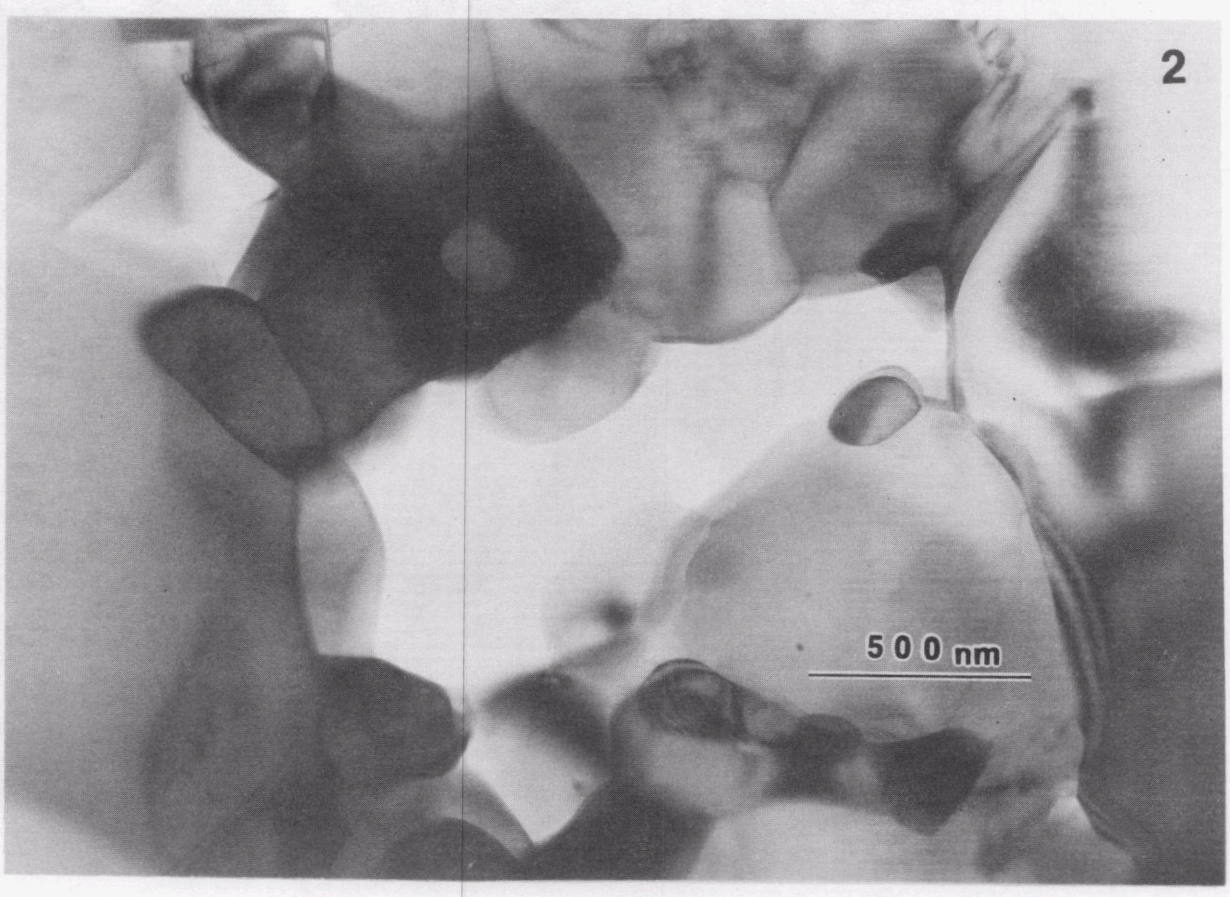

Figure 2. Detailed view of large, "pore-like" cavity produced after prolonged creep. Typically, these cavities form within regions containing clusters of small silicon nitride and secondary phase grains.

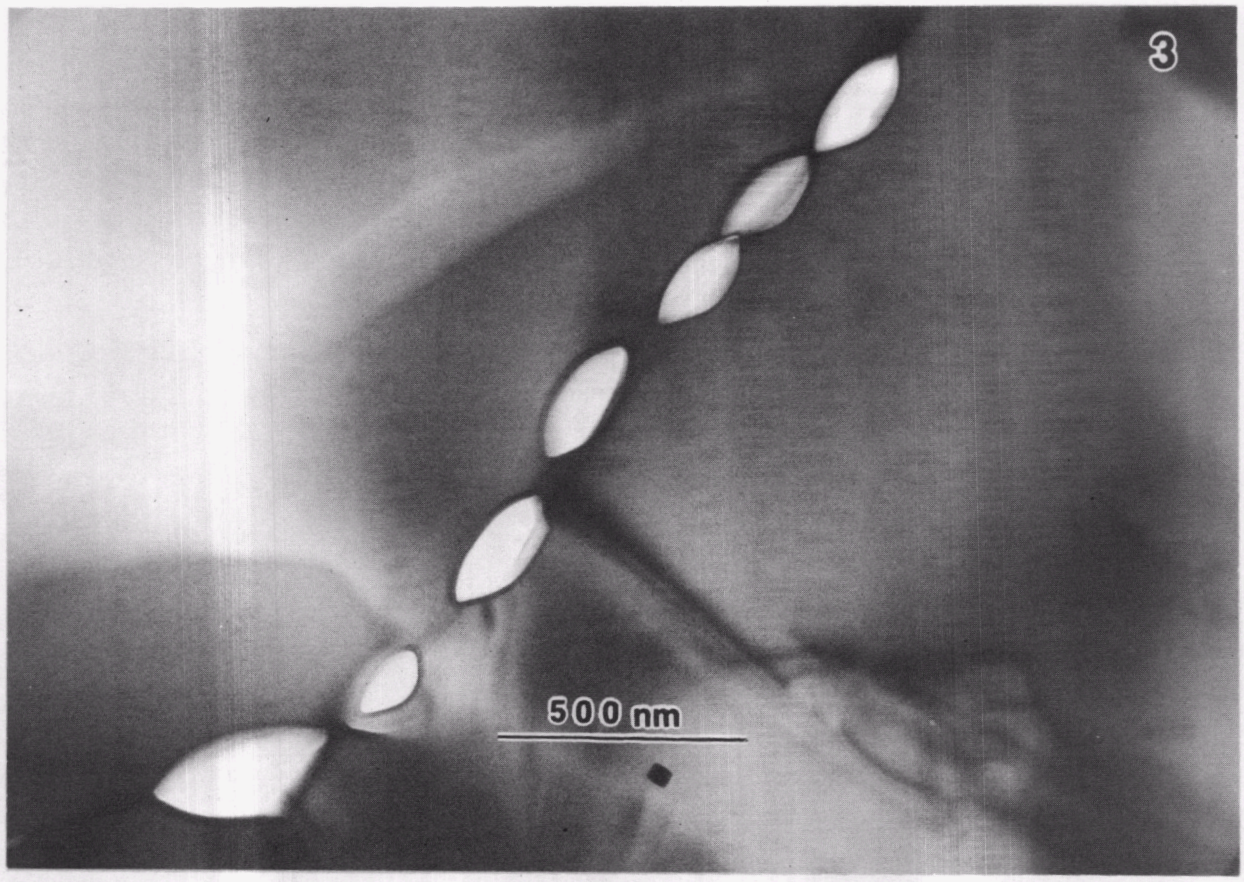

Figure 3. Representative view of ellipsoidal-shaped grain boundary cavities typically produced in NT-154 by tensile creep.

Mechanical Properties and Microstructural Characterization of Si_3N_4 Ceramics

K. L. More, T.A. Nolan, and L.F. Allard (Oak Ridge National Laboratory)

Objective/scope

The objective of the research is to use analytical and high-resolution electron microscopy to characterize the microstructure of Norton Si_3N_4 ceramic materials following mechanical strength (tensile) testing at elevated temperatures in air. This work represents a collaboration with several institutions including Norton/TRW (R. L. Yeckley), the University of Dayton (N. L. Hecht), and Allied-Signal Aerospace Co. (M. N. Menon). In addition to characterization work performed on various silicon nitride materials, microstructural characterization of silicon carbide fibrils manufactured by Carborundum is also under way.

Technical highlights

The material under investigation, NT-154, is a hot-pressed Si_3N_4 supplied by Norton containing 4.0 wt % Y_2O_3 intentionally added as a sintering aid. The material was annealed to crystallize the grain boundary phase as part of the Norton processing procedure. The microstructure of NT-154 is composed of Si_3N_4 grains having a "bimodal" distribution of grain sizes. Clusters of extremely small Si_3N_4 grains, usually < 0.2 mm, are surrounded by larger, usually acicular, Si_3N_4 grains, > 0.5 mm in size, with many >> 1 mm. X-ray diffraction reveals that the Si_3N_4 is typically β-phase, but some specimens contain as much as 10% residual α-phase. Transmission electron microscopy (TEM) reveals that most of the compounds associated with the sintering aid are crystalline and localized in pockets. X-ray and electron diffraction and energy dispersive x-ray elemental analysis (EDS) show the primary grain boundary phases to be α-$Y_2Si_2O_7$ (JCPDF 38-223) and $Y_5(SiO_4)_3N$ (JCPDF 33-1459). Finally, and most importantly, high-resolution TEM reveals that Si_3N_4 grains are separated by a yttrium-containing amorphous film of from 0.5- to 1.5-nm thickness. The present work is aimed at improving the understanding of the mechanisms of creep at the microstructural level. It has been reported previously that NT-154 (and several other Si_3N_4 ceramic materials) accommodate creep by the formation and growth of two distinct classes of voids. One class results from the opening of triple- point or multi-grain junctions, or the growth of pre-existing voids at these sites. These voids are most frequently seen in regions where small β-grains and secondary phases associated with the sintering aids predominate. The other class of voids form in the amorphous phase between β-grains and propagate into the β-grains via solution-reprecipitation mechanisms. These voids have a distinctive lenticular shape and are typically seen only after extended exposure to tensile stress at high temperature.

Analysis of voids formed in several suites of samples of NT-154 mechanically tested as part of several High Temperature Materials Laboratory (HTML) user projects is under way. Typical examples of both classes of voids are shown in the scanning electron microscopy (SEM) and TEM micrographs comprising Fig. 1. Triple-point voids are marked as "A" and lenticular voids as "B." Lenticular voids are observed to form preferentially on grain boundaries normal to the stress axis. Void size decreases and number increases with decreasing test temperature. Lenticular voids are typically smaller but more numerous than triple-point voids. Future work will address the quantification of void size

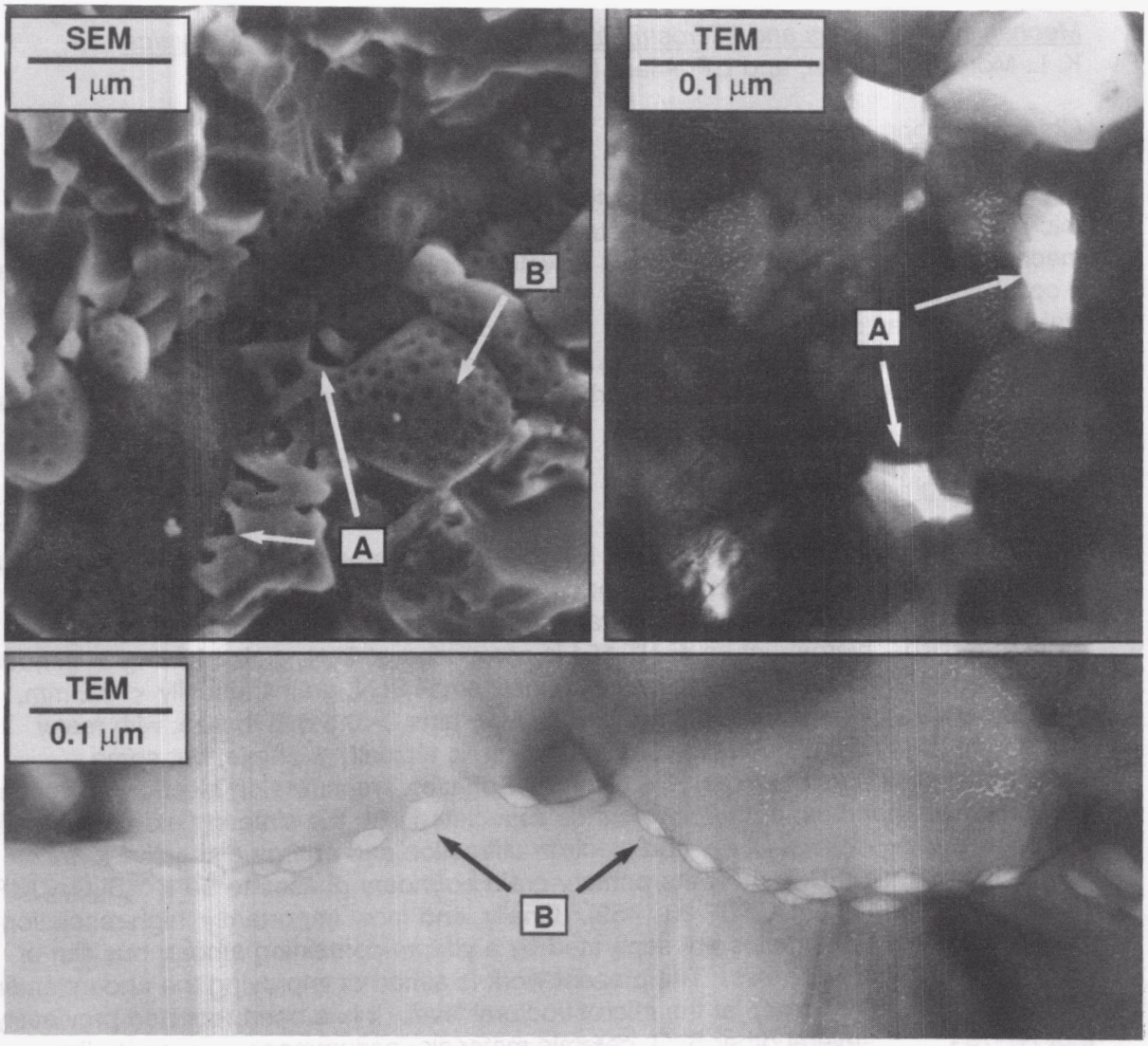

Fig. 1. Examples of typical triple-point (A) and lenticular two-grain-junction voids (B) in high-temperature tensile creep tested NT-154 Si_3N_4. Lenticular voids are often quite numerous and comprise up to one-half of the surface of some interfaces. The fracture surface shown in the scanning electron microscopy view was produced after failure and is roughly parallel to the original fracture surface.

and number with test conditions for several populations of tested NT-154 specimens that are now available.

Silicon carbide fibrils are being produced by Carborundum Company, Niagara Falls, New York. These fibrils are being grown by a vapor-liquid-solid (VLS) process that is based on a process developed originally by Los Alamos National Laboratory; Carborundum Co. is developing scale-up technology for this process under a Fossil Energy contract. Methods for the TEM characterization of these fibrils are being developed as part of the Ceramic Technology Project (CTP), and the actual characterization including TEM, SEM, and other methods is being performed as an HTML User Program project. It is desired to grow smooth, single-crystal fibrils that will be suitable for making tows that can be fabricated into ceramic composites. For production of such tows, fibrils on the order of 5 to 10 μm in diameter and with aspect ratios of 1000 to 1 or greater are needed. Fibrils having these dimensions have recently been produced and are currently being characterized by SEM and TEM. Figure 2 shows an SEM image of one variety of SiC fibrils currently under study. These fibrils have a rounded, triangular cross section, as seen in the inset. It is of interest to determine both the surface crystallography and internal microstructure of these fibrils.

In much past work, both at ORNL and in outside research efforts, SiC "whiskers" grown by various processes including the VLS process, have been characterized by SEM and TEM techniques. TEM analysis is usually conducted on whiskers that are sufficiently thin to transmit electrons, i.e. those which range from 0.1 to 0.5 μm thick, so that the internal microstructure can be revealed. The fibrils being investigated in the present study are much too thick for electron penetration, and thus a method was needed to prepare both longitudinal and cross sections of the fibrils to produce the required electron-transparent thin sections.

Ceramic specimens for TEM work are typically prepared by ion beam milling methods, in which thin slices of the ceramic are "dimpled" to a thickness of 20 mm or so and subsequently milled to perforation using energetic argon ions. The edges of the hole so produced electron transparent areas suitable for microanalysis. There are typically few problems with making such sections from bulk ceramic specimens; however, fibers must first be embedded in a matrix before thin sections (especially cross sections) can be obtained. It was found that epoxy materials were not satisfactory for embedding SiC fibrils because the epoxy thinned preferentially to the SiC material, and thin sections could not be obtained. Satisfactory sections have recently been obtained, however, by first producing a ceramic composite containing the fibrils, using the technique of chemical vapor infiltration (CVI) pioneered at ORNL[1]. A section of a tow was retained in a suitable position of the reaction chamber in a CVI run that was depositing silicon carbide. The resulting composite was then sliced to produce both longitudinal and cross sections. Figure 3 shows a low-magnification image of the microstructure of a longitudinal specimen. The fibril and the CVI SiC are seen to be uniformly thin, permitting the entire microstructure of the composite to be examined. Images of several such fibrils have been obtained, and all fibrils initially examined show a nearly perfect β-SiC structure, with only a few stacking defects present on non-basal {111} planes in the structure. Figure 4 is a higher magnification image of the interface between the fibril and the CVI SiC.

In summary, the CVI process to produce a bulk ceramic composite from which longitudinal and cross sections of large-diameter SiC can be successfully produced has been demonstrated. Work is under way using this technique to systematically characterize a suite of samples of SiC fibrils being produced by Carborundum Co.

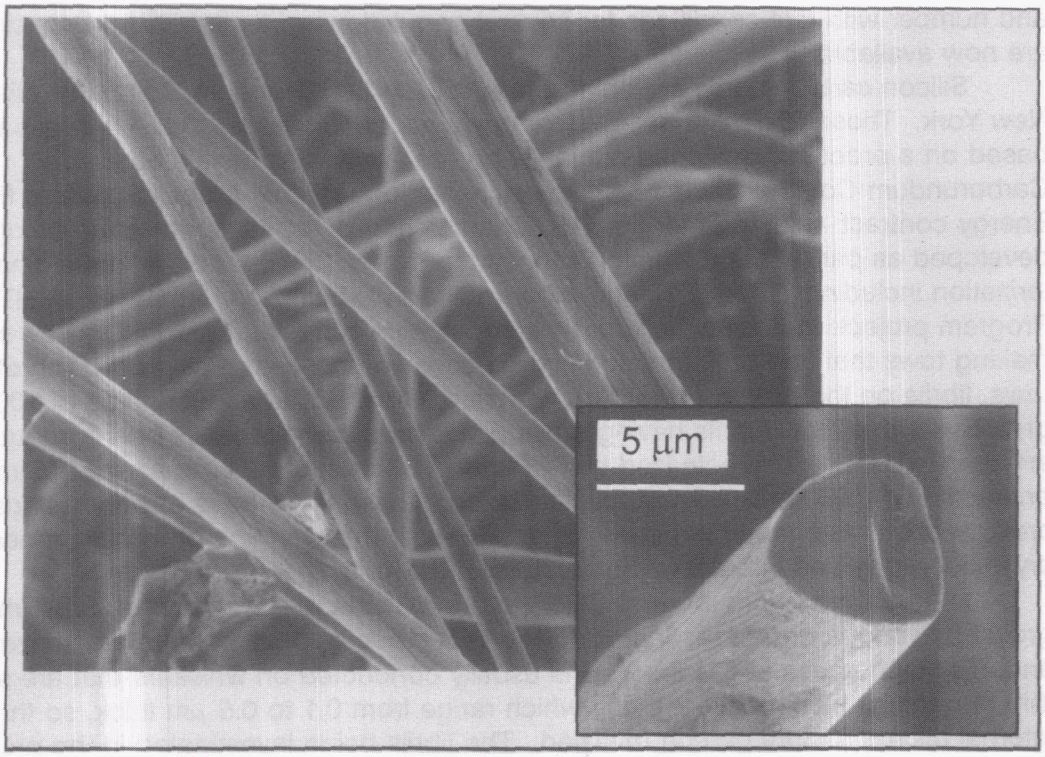

Fig. 2. SiC fibrils grown by vapor-liquid-solid process show uniform diameters and relatively smooth surfaces. Fibrils have rounded, triangular cross section as seen in the inset.

References

1. T. M. Besmann, B. W. Sheldon, R. A. Lowden, and D. P. Stinton, "Vapor-Phase Fabrication and Properties of Continuous-Filament Ceramic Composites," *Science* **253**, 1104-9, September 1991.

Status of milestones

Program on schedule.

Communications/visits/travel

1. K. L. More, D. A. Koester, and R. F. Davis, "Microstructural Characterization of a Creep-Deformed SiC Whisker-Reinforced Si_3N_4 Composite," presented at the Frontiers of Electron Microscopy in Materials Science Meeting, May 21, 1990, Oak Brook, Ill. Published in *Ultramicroscopy*.

2. K. L. More, D. A. Koester, and R. F. Davis, "The Role of Interfaces in the Creep-Deformation of a SiC Whisker-Reinforced Si_3N_4 Composite," presented at the International Congress for Electron Microscopy, August 17-22, 1990, Seattle, Wash. Published in conference proceedings.

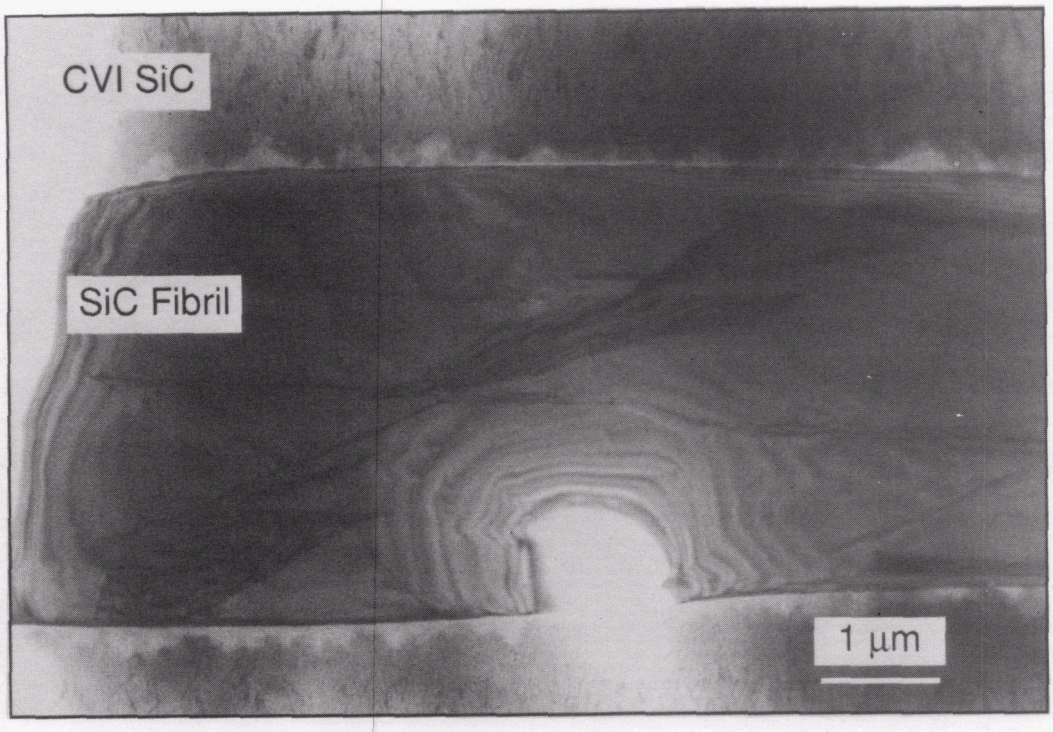

Fig. 3. Longitudinal thin section of large-diameter SiC fibril in chemical vapor infiltration SiC matrix, showing uniform thickness over large region of fibril and surrounding matrix. Stacking faults and dislocations are seen in the fibril microstructure.

3. D. A. Koester, K. L. More, and R. F. Davis, "Steady-State Creep of Hot-Pressed SiC Whisker-Reinforced Silicon Nitride," presented at the U.S.-Japan Seminar on Processing, Microstructure, Development, and Properties of Advanced Ceramics and Their Composites, Tokyo, Japan, August 20-22, 1990.

4. K. L. More, D. A. Koester, and R. F. Davis, "Creep Behavior of a SiC Whisker-Reinforced Si_3N_4 Composite in Air and Nitrogen," presented at the 2nd International Ceramic Science and Technology Congress, Orlando, Fla., November 12-15, 1990.

5. K. L. More, D. A. Koester, and R. F. Davis, "Creep of a SiC Whisker-Reinforced Silicon Nitride in Compression and Bending," presented at the 15th Annual Conference on Composites and Advanced Ceramics, Cocoa Beach, Fla., January 13-16, 1991.

6. K. L. More, "Defect Characterization in a CVD α-Si_3N_4," presented at the 93rd Annual Meeting of the American Ceramic Society, Cincinnati, Ohio, April 28 - May 2, 1991.

7. T. A. Nolan, L. F. Allard, D. W. Coffey, M. K. Ferber, and K. L. More, "Microstructural Characterization of Tensile and Flexural Creep Deformation and Fatigue in a Si_3N_4 Ceramic," ibid.

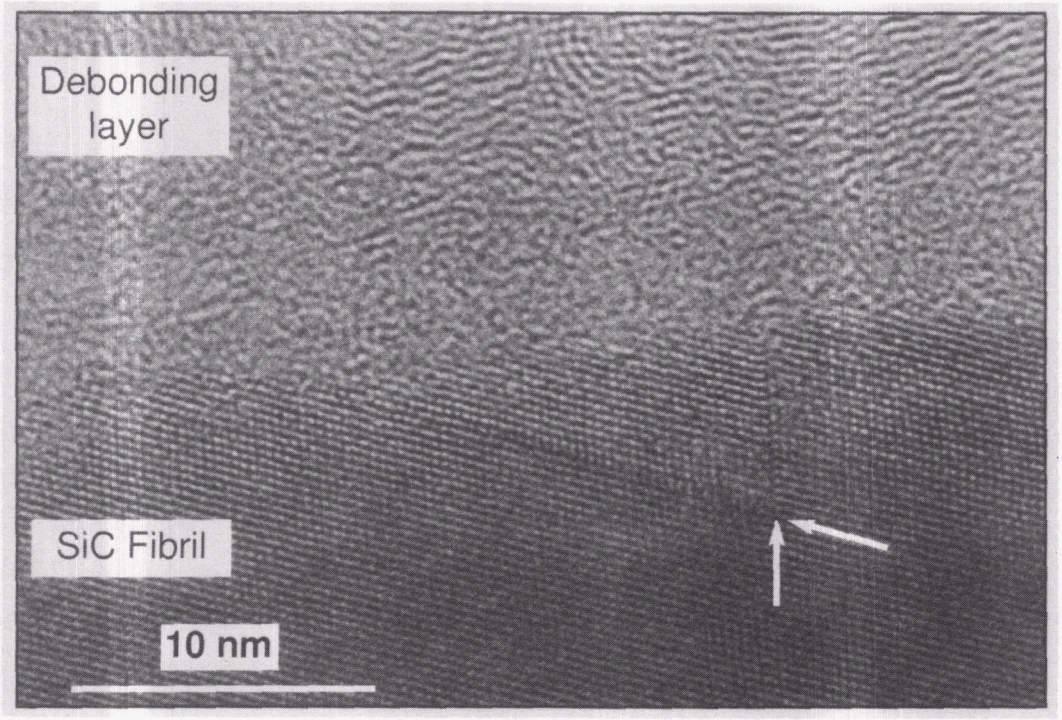

Fig. 4. High-resolution image of interface between SiC fibril and a partially graphitized "debonding" layer produced during the chemical vapor infiltration deposition process. Two intersecting stacking faults seen edge-on are arrowed.

8. K. L. More, "Defect Characterization in a CVD α-Si_3N_4," presented at the 49th Annual Meeting of the Electron Microscopy Society of America, San Jose, Calif., August 5-9, 1991. Published in conference proceedings.

9. D. A. Koester, K. L. More, and R. F. Davis, "Steady-State Creep of Hot-Pressed SiC Whisker-Reinforced Silicon Nitride," presented at the 1st Canadian International Composites Conference and Exhibition, Montreal, Canada, September 4-6, 1991. To be published in conference proceedings.

10. K. L. More, D. A. Koester, and R. F. Davis, "Microstructural Analysis and Mechanisms of Deformation of Hot-Pressed SiC Whisker-Reinforced Silicon Nitride," presented at the 1st International Symposium on the Science of Engineering Ceramics, Osaka, Japan, October 14-18, 1991. To be published in conference proceedings.

11. K. L. More, "Defect Characterization in CVD a-Si3N4," presented at ASM Materials Week '92, Chicago, Ill., November 2-5, 1992.

Problems encountered

None

Publications

1. K. L. More, D. A. Koester, and R. F. Davis, "Microstructural Characterization of a Creep-Deformed SiC Whisker-Reinforced Si_3N_4 Composite," *Ultramicroscopy* **37**, 263 (1991).

2. K. L. More, D. A. Koester, and R. F. Davis, "The Role of Interfaces in the Creep-Deformation of a SiC Whisker-Reinforced Si_3N_4 Composite," p. 382 in *Electron Microscopy 1990*, Vol. 4, ed., L. D. Peachey and D. B. Williams, San Francisco Press, San Francisco, Calif., 1990.

3. D. A. Koester, K. L. More, and R. F. Davis, "Deformation and Microstructural Changes in SiC Whisker-Reinforced Si_3N_4 Composites," *J. Mater. Res.* **6** (12), 2735 (1991).

4. K. L. More, "Defect Characterization in a CVD α-Si_3N_4," p.936 in *Proceedings of the 49th Annual Meeting of the Electron Microscopy Society of America*, ed. G. W. Bailey, San Francisco Press, San Francisco, Calif., 1991.

5. D. A. Koester, K. L. More, and R. F. Davis, "The High Temperature Creep of a SiC Whisker-Reinforced Si_3N_4 in an Air Ambient," submitted to *J. Mater. Res.*

6. T. A. Nolan, L. F. Allard, D. W. Coffey, C. R. Hubbard, and R. A. Padgett, "Microstructure and Crystallography of Titanium Nitride Whiskers Grown by a VLS Process," *J. Am. Ceram. Soc.* **74** (11), 2769 (1991).

Project Data Base

B. L. Keyes (Oak Ridge National Laboratory)

Objective/scope

The objective of this task is to develop a comprehensive computer data base containing the experimental data on properties of ceramic materials generated in the total effort. This computer system should provide a convenient and efficient mechanism for the compilation and distribution of the large amounts of data involved. The data base will be available in electronic form to all project participants. In addition, periodic hard-copy summaries of the data, including graphical representation and tabulation of raw data, will be issued to provide convenient information sources for project participants.

Technical highlights

The Ceramic Technology Project (CTP) data base presently contains 7466 test results on 27 different types of tests, 596 material characterizations, 13 lubricant characterizations, 101 coating characterizations, and 2290 associated records containing various metadata. A more detailed description of test result records is shown in Table 1.

Data base personnel upgraded the dBASE IV program used to manage the data base to version 1.5 in July 1992. This update contains enhanced programming commands, including some basic input routines that accept mouse input. Differences between versions 1.1 and 1.5 were otherwise very subtle, at least for the purposes of this data base.

Work on the computerized interface for the data base began on June 2, 1992. Initial planning efforts involved development of a flowchart and menu screens on paper to facilitate the actual programming process. This interface should help the user locate and extract the necessary information for the data base files with a minimum knowledge of the system. No elaborate calculation and/or graphic capabilities will be included in the interface, since such functions are beyond the original scope of the program. Once extracted to subset files, the user may use whatever software desired for further processing.

The primary function modules have been written in dBASE IV programming language and are in initial stages of testing. Access to the data will be available through material-based queries, property-based queries, or by browsing selected files. Browsed files will not be linked automatically to related files due to the nature of the browse command in this programming language. Queries based on processing properties and other attributes will be added in the future. All retrieved information (other than the browsed files) will contain the associated notes, test background details, material characterizations, chemistries, and other items stored in the data base that pertain to the data requested.

Extended plans for the interface call for a simple working interface composed of several primary-function modules at first, then adding more sophistication in steps. This method should produce better quality improvements as time and funding permit. As dBASE options improve, the new capabilities will be incorporated into the interface.

During construction of the query modules, a decision was made to improve the method of storing ceramic processing information in the data base. Accessing the processing information via searches was confounding, confusing, and difficult using the

Table 1. Ceramic Technology Project data base summary as of September 30, 1992

Material class	Brazed specimens					Creep	Cyclic fatigue	Density	Dynamic fatigue	Elasticity
	MOR 4[a]	Shear str.	Toughness	Torsion	Tor fatigue					
Alumina							15	5	9	28
Alumina + reinforcing fibers								7		
Alumina + zirconia										
Mullite										2
Mullite + reinforcing fibers										11
Silicon carbide		12					17	10	23	15
Silicon nitride	87	48		15	7	131	36	28	76	24
Silicon nitride + reinforcing fibers							15	2	14	16
Zirconia	241	58	43				51	158		119
Zirconia + reinforcing fibers										
Other				6				4		
Totals	328	118	43	21	7	131	134	214	122	215

Material class	Fracture toughness	Hardness	Interrupted fatigue	MOR[a] 3-Pt bend	MOR[a] 4-Pt bend	Oxidation rate	Poisson's ratio	Shear modulus	Tensile	Stress rupture
Alumina	39	4			418				15	13
Alumina + reinforcing fibers	39				144				11	
Alumina + zirconia					7					
Mullite	1			1	4					
Mullite + reinforcing fibers	12			9	20					
Silicon carbide	30	27			254				81	4
Silicon nitride	109	112		10	1157	1	2	1	216	63
Silicon nitride + reinforcing fibers	53				144	3	17	16	50	
Zirconia	377	24	239		1613				16	20
Zirconia + reinforcing fibers					2					
Other	2	39			61					
Totals	662	206	239	20	3824	4	19	17	389	100

[a]MOR = modulus of rupture.

Table 1. (Continued)

Material class	Thermal conductivity	Thermal contraction	Thermal diffusivity	Thermal expansion	Thermal shock	Torsion	X-Ray diffraction	Material char.	Chemistry
Alumina	3			1	2			20	14
Alumina + reinforcing fibers	34		18	4	6			102	
Alumina + zirconia		23		21				7	
Mullite								2	
Mullite + reinforcing fibers								35	
Silicon carbide				23			17	11	57
Silicon nitride	23		23	44		3	49	155	7
Silicon nitride + reinforcing fibers	9		17	14				57	
Zirconia							72	51	44
Zirconia + reinforcing fibers								5	
Other				35		4		36	17
Totals	69	23	58	142	8	7	138	481	139

Material class	Wear resistance	Coatings	Lubricants	
Alumina based	9	3		
Alumina + reinforcing fibers	1			
Silicon carbide	3			
Silicon nitride	22			
Chromia based	98	20		
Zirconia based	13	16		
Enamels	5	10		
Other	126	53	13	
Totals	277	102	13	
Grand total (characterization data)				596
Grand total (test data only)				7466

data as they are currently stored. The actual searching process now requires scanning large amounts of data to extract only a few key words. Data base personnel hope to separate these key words into special fields to speed up the searches and reduce programmer/user wear.

One solution to the material processing information problem would be to add a detailed processing information data base to this task. The present format allows storage of general processing information for each material in brief notes, which is probably adequate for most users. However, much of the CTP is involved with experimental materials and experimental processes. Rather than lose such valuable information, data base personnel decided to try to preserve the processing parameters for future reference. This data base will be linked to the test results data base via material name and batch code. No proprietary information will be stored for security reasons. In such cases, only owner-allowable information will be included.

Data base personnel now have the dBASE runtime modules available to software developers on a royalty-free basis. These modules eliminate the need for data base users who have IBM-compatible computers to have their own full copy of dBASE IV installed. These modules will be sent to requestors with the interface when it is completed. Efforts are under way to locate a similar product for the Macintosh version of Foxbase.

Much of the past year was spent upgrading and updating the data base and working on the interface, so significant amounts of new information were lacking. The recent release of numerous program reports for the project provided the remedy to this dilemma. Time was taken to process as much of the data as possible.

The report is now complete and includes information on a variety of ceramics but concentrates more on silicon nitride-based ceramics than any other class. More creep, dynamic fatigue, and crack growth-related testing is being performed now, and that is reflected in the report. Since these data are produced for different studies, this report also includes a brief description of each program that contributed information for the report.

B. L. Keyes attended the ASTM Spring E-49 Committee on computerized materials data bases held in Pittsburgh, Pennsylvania in mid-May 1992. The E-49.01.05 task group on material designations of ceramics is working on a document to provide data base builders with guidelines on how to describe and define specific ceramics in a computerized data base. This document will be presented to the C-28 committee on ceramics later this year for their input and suggestions.

Status of milestones

All previous data base summary reports are now in publication. Due to miscommunication problems, the reports were held up earlier in the year and missed the June 1992 publication date originally planned. The September 1992 data base summary is now complete through first draft and should go to reviewers in the next few days. Completion of this document took a little longer than originally planned because of work on the computerized interface that could not be stopped at the planned time and because of the publication of huge amounts of data at a time that it was badly needed for the report.

Publications

The Ceramic Technology for Advanced Heat Engines Project Database: September 1990 Summary Report is in publication.

The Ceramic Technology for Advanced Heat Engines Project Database: March 1990 Summary Report is in publication.

The Ceramic Technology for Advanced Heat Engines Project Database: September 1991 Summary Report is in publication.

The Ceramic Technology for Advanced Heat Engines Project Database: September 1992 Summary Report is complete through first draft form.

3.2 TIME-DEPENDENT BEHAVIOR

Fracture Behavior of Toughened Ceramics

H. T. Lin, P. F. Becher, and W. H. Warwick (Oak Ridge National Laboratory)

Objective/scope

Whisker-reinforced ceramics, particulate phase composites, and ceramics with reinforcing grain structures offer important advantages for heat engine applications. Chief among these is the improved fracture toughness that can be achieved by appropriate design of microstructural and material parameters. Previous studies show that these materials often exhibit substantial improvements in damage, thermal shock, and slow crack growth resistances. However, design of such systems must also consider those factors influencing their performance at elevated temperatures.

In response to these needs, studies are conducted to determine the mechanical properties (e.g., creep, delayed failure, strength, and toughness) at elevated temperatures for these toughened ceramics. Particular emphasis is placed on understanding how microstructure and composition influence the mechanical performance at elevated temperatures and the stability of these properties for extended periods at these temperatures. The knowledge gained from these studies provides input on how to modify materials to optimize their mechanical properties for the temperature ranges of interest.

Technical highlights

The long-term high-temperature mechanical reliability of silicon nitride ceramics in an oxidizing environment is governed by the presence of secondary viscous phases that were introduced by the addition of oxide additives. Flexural creep studies on *in situ* reinforced silicon nitride ceramics hot-pressed with various combinations of SrO, La_2O_3, Al_2O_3, and Y_2O_3 additives were, therefore, conducted to provide an understanding on the influence of the secondary viscous phases, i.e., silicate or apatite phases, on the creep rates and controlling mechanisms. The *in situ* reinforced Si_3N_4 ceramics with elongated microstructure were fabricated under the work breakdown structure (WBS) Element 1.2.3.1 (Dispersion-Toughened Ceramic Composite). The creep properties in flexure of Si_3N_4 materials containing 2 wt % Al_2O_3-6 wt % Y_2O_3 (2Al6Y), 2 wt % SrO-6 wt % Y_2O_3 (2Sr6Y), 2 wt % Al_2O_3-3 wt % Y_2O_3-4 wt % La_2O_3 (2Al3Y4La) and 2 wt % Al_2O_3-8 wt % La_2O_3 (2Al8La) were characterized at temperatures of 1200 and 1300°C under selected stress levels in air during this reporting period.

1. Creep Behavior of In Situ Reinforced Si_3N_4 Ceramics

Figure 1 shows the creep rate versus applied stress curves for *in situ* reinforced silicon nitride ceramics with 2Al6Y and 2Sr6Y sintering additive systems at 1200 and 1300°C in air under applied stresses from 75 to 400 MPa. The creep data indicate that the 2Sr6Y materials exhibit lower creep rates (6×10^{-10} to 2×10^{-9} s^{-1}) at temperatures of 1200 and 1300°C. The low creep rate (good creep resistance) of 2Sr6Y materials is corroborated by the good strength retention to high temperatures.[1] The stress exponent of creep rate of 2Sr6Y material is about one at these two test temperatures. For ceramic

ORNL-DWG 93-5845

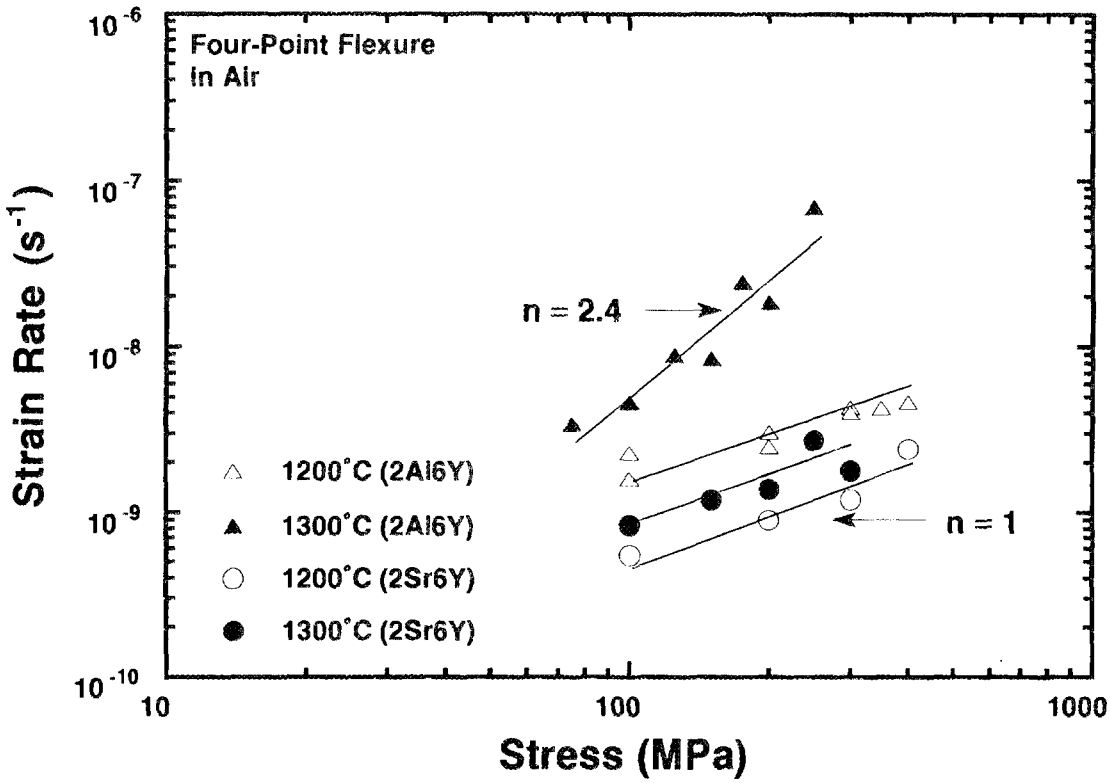

Fig. 1. Strain rate versus stress curves for self-reinforced Si_3N_4 ceramics with elongated grain microstructure.

materials containing viscous phases, the stress exponent of one is generally attributed to viscous or diffusional creep mechanism. On the other hand, the 2Al6Y material reveals the creep rates which are 4 to 25 times higher than silicon nitride material containing 2Sr6Y additive. In addition, the 2Al6Y material reveals a substantial increase in creep rates (approximately an order of magnitude) at 1300°C at stress levels >150 MPa and a higher stress exponent (n = 2.4) as compared with the creep results at 1200°C (n = 1). The flexural strength results[1] show that the 2Al6Y materials exhibit a substantial strength loss (40 to 60%) at temperatures >1200°C which reflects the poor creep resistance. The increase in both creep rate and stress exponent in 2Al6Y containing silicon nitride material at 1300°C is associated with enhanced creep damage, and oxidation reaction as confirmed by the scanning electron microscopy (SEM) examinations.

Figure 2 shows the creep results at 1200°C in air for Si_3N_4 materials hot-pressed with 2Al3Y4La and 2Al8La additive systems. The creep results of material with the 2Sr6Y additive are included for comparison. The creep data reveal that, in spite of the similarity in strength behavior between 2Al3Y4La- and 2Al8La-containing materials at temperatures ≤1200°C, the material with the 2Al8La additive exhibits creep rates that are two to four times lower than those of the 2Al3Y4La-containing material under the stress range employed. The regression analysis of the creep rate versus stress curves also shows that both materials exhibit the same stress exponent (n = 2) indicating similar creep-controlling

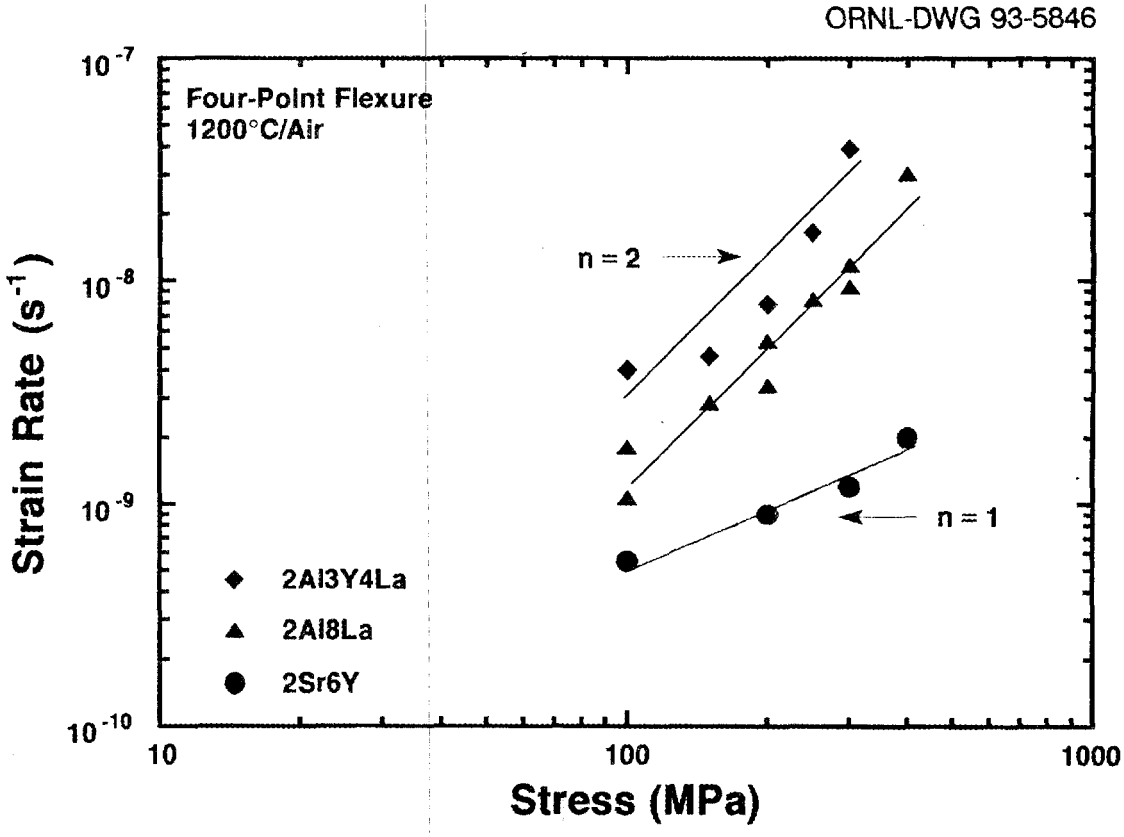

Fig. 2. Strain rate versus stress curves of self-reinforced Si_3N_4 ceramics with elongated grain microstructure.

mechanisms. At the same time, the creep results (Fig. 2) show that the alumina-containing materials (i.e., either with 2Al8La or 2Al3Y4La sintering additive) exhibit creep rates that are approximately one order of magnitude higher than those of the material with 2Sr6Y additive. The higher creep rates and stress exponents in these two alumina-containing silicon nitride materials at 1200°C are again to be associated with much extensive creep cavitation.

The higher creep rates observed in Si_3N_4 material containing oxide additives that include Al_2O_3 could arise from their low eutectic temperatures of secondary phases. The eutectic temperature for the Al-La-Si-O-N system is estimated to be approximately 1230°C and that of Al-Y-Si-O-N is about 1280°C (refs. 3-5). The addition of the Y_2O_3 to the system of Al-La-Si-O-N will further reduce the eutectic temperature leading to the observed low creep resistance for the 2Al3Y4La-containing material. An accurate measurement of the eutectic temperature for the Sr-Y-Si-O-N system is not available but is estimated to be between 1350 and 1400°C (refs. 3,4,6). This higher eutectic temperature in 2Sr6Y material would result in higher creep resistance than the materials employing oxide additives that include Al_2O_3. Furthermore, both the X-ray and transmission electron microscopy (TEM) results indicate that the secondary phases present in Al_2O_3-containing materials remain amorphous, whereas the one in 2Sr6Y material devitrifies during creep. The devitrification of glassy phase increases the viscosity of the secondary phase and further reduces the

creep rate. The higher stress exponent obtained for Si_3N_4 ceramics with Al_2O_3 additions is attributed to a strong contribution of cavitation to the creep strain. This is evidenced by the higher number density of creep cavities in a region near tensile surface. The uncrystallized glassy phases also provide a fast diffusion path of mass transport for oxidation resulting in enhanced oxidation reaction (damage) as observed by SEM examinations. The poor creep performance accompanied by the lower oxidation resistance exhibited by the alumina-containing Si_3N_4 materials is reflected in their significant reduction (28 to 36%) in strength between room temperature and 1200° C (ref. 1).

2. Stress State Effect on Creep Behavior of Al_2O_3 and Al_2O_3-SiC_w

During this reporting period, the tensile creep response of a polycrystalline fine-grained alumina at 1200° C in air was determined. This experiment provides an understanding of the effect of the applied stress state on the creep rate and controlling mechanisms of ceramic materials. When cavitation dominates the creep process for the same temperature, applied stress level, and atmosphere, the creep rates are found to decrease when going from tensile to flexural to compressive loading. These effects are critical in designing materials with improved elevated-temperature performance. Therefore, a data base for the comparison of creep response in compression, flexure, and tension is also being developed for silicon nitride ceramics.

The tensile creep system is equipped with an optical-based extensometer system and can resolve displacements to an accuracy of greater than ± 1 μm at temperatures up to 1600° C in ambient air. The tensile creep specimen geometry is that of a flat, dogbone shape that is loaded through SiC pins. In the tensile creep tests conducted to date, the system has performed remarkably well. An initial problem with fracture of the upper SiC pullrod, due to impact loading, upon fracture of the tensile specimen was solved by a modification to the knife-edge alignment couplings.

Figure 3 shows creep data for single-phase, fine-grained alumina (2 μm in diameter) in compression, flexure, and tension at 1200° C at stress levels from 25 to 150 MPa. Creep data in flexure and compression have been reported previously.[6] The results indicate that the applied stress state has little influence on the creep rate for this ceramic under the stress range employed. A regression analysis of the creep rate versus stress curve yields a stress exponent of two, which is also independent of the stress state, indicative of the same creep-governing mechanism. The creep stress exponent of two obtained for polycrystalline fine-grained alumina is attributed to the creep mechanism of grain boundary sliding, which is evident from observations of alumina grain offset and rotation and formation of cavities at triple grain junctions. It was noted that the creep damage (cavitation) was observed for all of the applied stress states under the stress ranges employed. In fact, an insensitivity of the creep rate and stress exponent to the applied stress states of tension, flexure, and compression at temperatures between 1200 and 1300° C has also been observed in polycrystalline fine-grained alumina without grain boundary phases.[7,8]

Status of milestones

On schedule

ORNL-DWG 93-5847

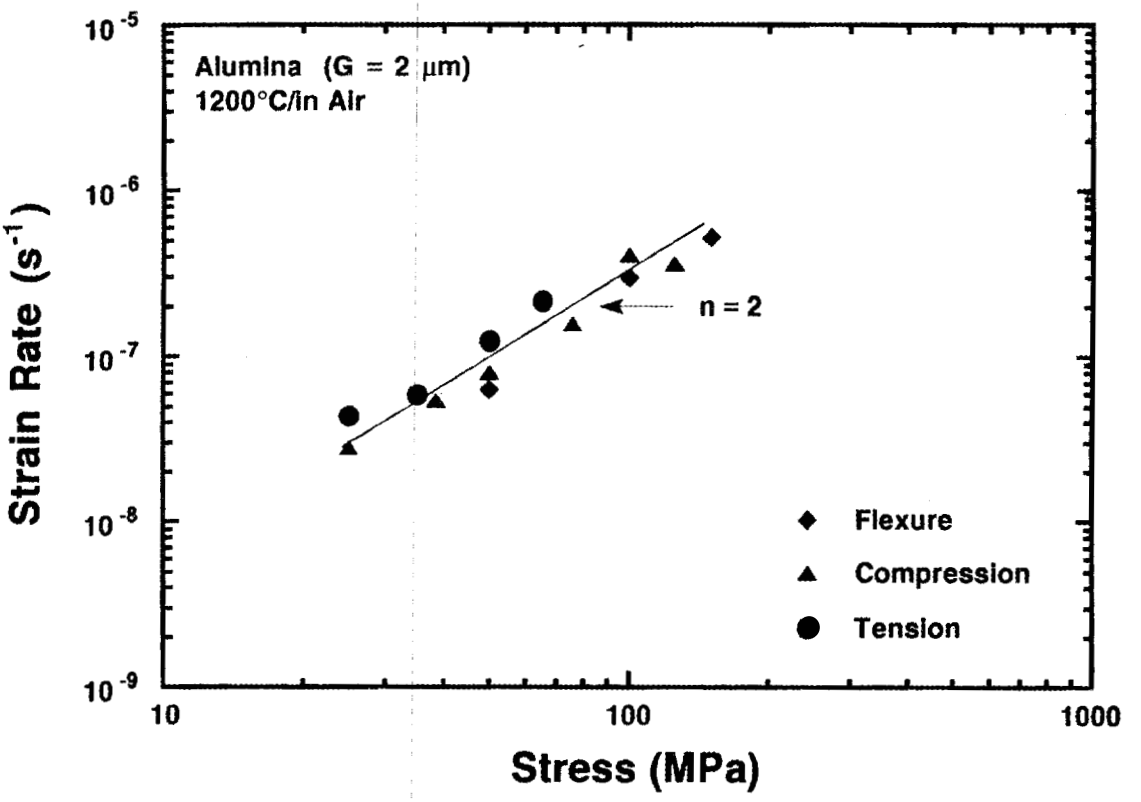

Fig. 3. Strain rate versus stress curve for polycrystalline fine-grained alumina tested at 1200°C under various stress states.

Publications

H. T. Lin and P. F. Becher, "Grain Sise Effect on the Creep Deformation of Alumina-SiC Composites," submitted to *J. Am. Ceram. Soc.*

References

1. H. T. Lin, P. F. Becher, and W. H. Warwick, "Fracture Behavior of Toughened Ceramics," pp. 265-70 in *Ceramic Technology Project Semiannual Progress Report*, ORNL/TM-11984, Martin Marietta Energy Systems, Inc., Oak Ridge Natl. Lab., March 1992.

2. D. P. Thompson, "Alternative Grain-Boundary Phases for Heat-Treated Si_3N_4 and β'-Sialon Ceramics," *Proc. Br. Ceram. Soc.* **45**, 1-13 (1990).

3. *Phase Diagrams for Ceramics, 1969 Supplement*, The American Ceramic Society, Inc., Columbus, Ohio, 1969.

4. M. Ohashi, S. Kanzaki, and H. Tabata, "Effect of Additives on Some Properties of Silicon Oxynitride Ceramics," *J. Mater. Sci.* **26**, 2608-14 (1991).

5. T. N. Tiegs, Martin Marietta Energy Systems, Inc., Oak Ridge Natl. Lab., personal communication.

6. H. T. Lin, P. F. Becher, and W. H. Warwick, "Fracture Behavior of Toughened Ceramics," pp. 265-70 in *Ceramic Technology Project Semiannual Progress Report*, ORNL/TM-11984, Martin Marietta Energy Systems, Inc., Oak Ridge Natl. Lab., 1991.

7. A. G. Robertson, D. S. Wilkinson, and C. H. Cáceres, "Creep and Creep Fracture in Hot-Pressed Alumina," *J. Am. Ceram. Soc.* **74**[5], 915-21 (1991).

8. S. M. Wiederhorn, National Institute of Standards and Technology, Gaithersburg, Md., personal communication.

Cyclic Fatigue of Toughened Ceramics

K. C. Liu, C. O. Stevens, and C. R. Brinkman (Oak Ridge National Laboratory)

Objective/scope

The objective of this task is to develop, design, fabricate, and demonstrate the capability to perform tension-tension dynamic fatigue testing on a uniaxially loaded ceramic specimen at elevated temperatures. Three areas of research have been identified as the main thrust of this task: (1) design, fabrication, and demonstration of a load train column which truly aligns with the line of specimen loading; (2) development of a simple specimen grip that can effectively link the load train and test specimen without complicating the specimen geometry and, hence, minimize the cost of the test specimen; and (3) design and analysis of a specimen for tensile cyclic fatigue testing.

Technical progress

Cyclic fatigue of SiC whisker-reinforced Al_2O_3 matrix composite

Cyclic fatigue tests were performed on SiC_w/Al_2O_3 at 1200° C. Test parameters and results obtained to date are summarized in Table 1, and data (open symbols) are plotted in Fig. 1. Monolithic fatigue data[1] (filled symbols) are also included for comparison. The arrow indicates the test was discontinued at the indicated number of cycles with no specimen failure. The fatigue curve shown in Fig. 1 was determined visually; therefore, it must be regarded as an approximation. Although the number of test data is limited, the test results suggest that the 1200° C fatigue behavior of monolithic Al_2O_3 and that of SiC_w/Al_2O_3 are about the same. The addition of SiC whiskers apparently did not enhance the fatigue resistance of the composite material at 1200° C. This is significantly different compared to the room-temperature situation, reported previously,[2] in that the high-cycle fatigue strength of the composite material was found to be about double compared to that of monolithic alumina.

Pronounced ratchetting, i.e., accumulation of strain in small incremental steps due to cyclic loading, was observed at every level of cyclic stresses used in the testing of the composite material. It is speculated that the enhancement of fatigue resistance observed at room temperature by the presence of SiC whiskers may have been negated by the strain ratchetting. However, it remains unknown at this time whether the same ratchetting behavior was detected in cyclic fatigue testing of monolithic material at 1200° C or not. The average value of elastic modulus was determined to be 218 GPa at 1200° C.

Creep Testing of NT-154 Si_3N_4

Experimental efforts were continued on creep testing of NT-154 Si_3N_4. All specimens tested were annealed at 1370° C for 150 h. Activities that occurred during this reporting period are as follows.

Creep behavior at 1250° C

Specimen 20-56: The test is continuing at 1250° C under a constant stress of 175 MPa. A total of about 0.78% strain has been accumulated after 12,000 h (1 year and

Table 1. Results of cyclic fatigue of SiC whisker-reinforced Alumina tested at 1200° C

Specimen	Maximum stress (MPa)	Cycles to failure
4	160	27
5	137.8	107
6	104	638
7	70.3	22,248

Note: Tests were performed using a triangular waveform with a stressing rate of 21,000 MPa/min.

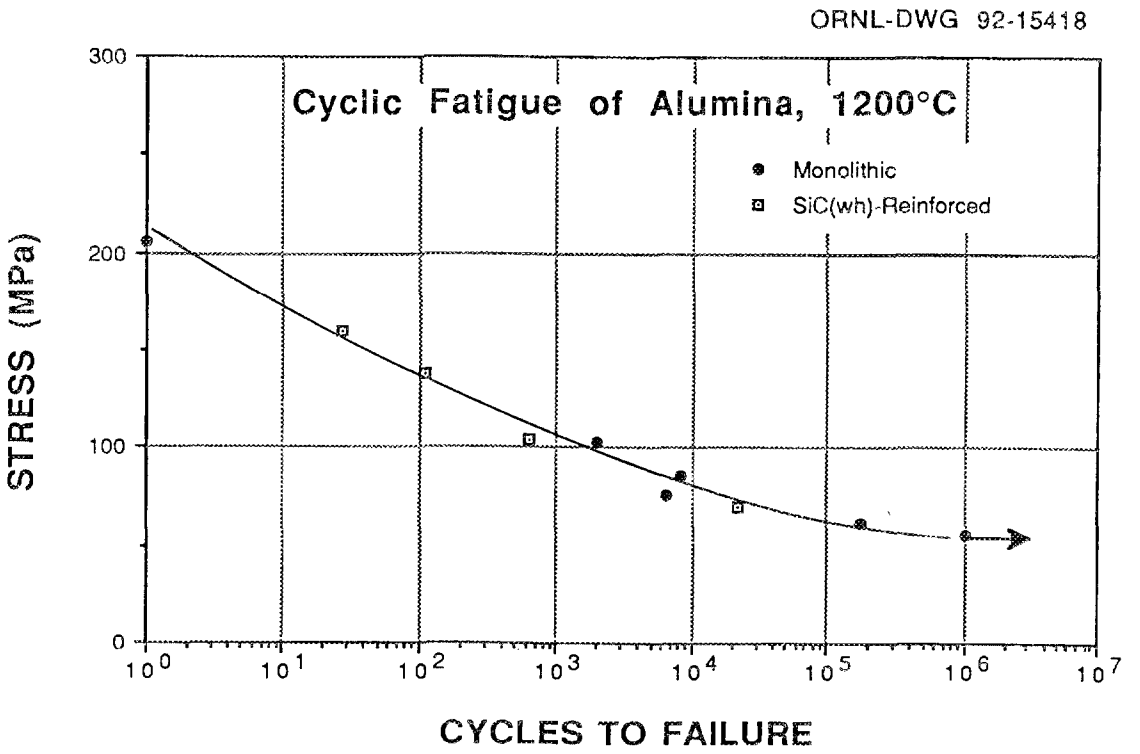

Fig. 1. Cyclic fatigue behavior of monolithic Al_2O_3 and SiC whisker-reinforced Al_2O_3 matrix composite materials tested at 1200° C.

4.5 months) of testing to date, as shown in Fig. 2. The test was interrupted twice, the first time due to a thermocouple failure at t = 5211 h and the second time due to a general power outage at t = 9600 h. Other than showing a brief period of transient creep occurring immediately following reloading, the specimen behaved as if no interruption had taken place. The measured creep rate was reasonably steady at a value of about 7.52 x 10^{-11} s^{-1} for the last 2000 h of testing.

Specimen 20-00: The test is continuing at 1250° C under a constant stress of 150 MPa. Test results are shown in Fig. 3. The specimen accumulated a total of about 0.374% strain after 8400 h of testing. Restarting of the test at t = 1745 h due to a power failure and again at t = 6100 h did not appear to have changed the subsequent creep behavior.

Specimen 20-32: Test results obtained to date are shown in Fig. 4. Since the inception of the test, the applied stress has been decreased in three steps to 150 MPa. For the purpose of comparison with test results of specimen 20-00, which is currently being tested under the same condition, the specimen was kept steady at 150 MPa for about 1650 h since the last partial unloading. Generally, creep rate decreased immediately following the partial unloading but gradually increased to the levels as if the specimen had been tested with no prior strain history. An examination shows that both specimens are currently deforming at the same creep rate of 7.22 x 10^{-11} s^{-1}.

Creep behavior at 1370° C

Specimen 19-44: The specimen failed after 3728 h of testing at 1370° C under an applied stress of 75 MPa. Test results are plotted in Fig. 5. This specimen exhibited a short transient creep range followed by a fairly long range of steady-state creep up to t = 1300 h. Therefore, the creep behavior was thought to be more consistent with that of specimens made from lot-"CP." However, the creep rate decelerated rapidly after t > 2000 h, showing a creep rate of about 7 x 10^{-10} s^{-1} during the last 500 h of testing. The decrease in creep rate changed the creep behavior exhibited during the last half of its creep life to be consistent with that of specimens with a prefix of lot number "20."

In summary, observations based on data obtained to date indicate that the creep behavior of NT-154 at elevated temperatures was consistent and reasonably predictable provided that the material was annealed and obtained from the same lot.

Creep Testing of GN-10 Si_3N_4

Specimen 89340-2-4: This specimen was tested at 1250° C under an applied stress of 75 MPa. This is the first of three supplemental tests designed to obtain the information about the minimum creep rates at the low-stress end of the test spectrum, to aid in determining the stress exponent for GN-10. The test was interrupted by fracture at the specimen shank due to surface contamination after 2260 h of testing. The creep curve of this specimen is shown in Fig. 6. The minimum creep rate was determined to be 4.64 x 10^{-10} s^{-1}, which combined with data obtained previously, gives a value of the stress exponent of about four.

Specimen 89367-1-1: This is the second of the three supplemental tests. The test is currently ongoing at 1300° C under an applied stress of 50 MPa. A total of about 2.4% creep strain has been accumulated after 2600 h of testing, as shown in Fig. 7. Although the test was interrupted twice due to power failure, the creep behavior appeared

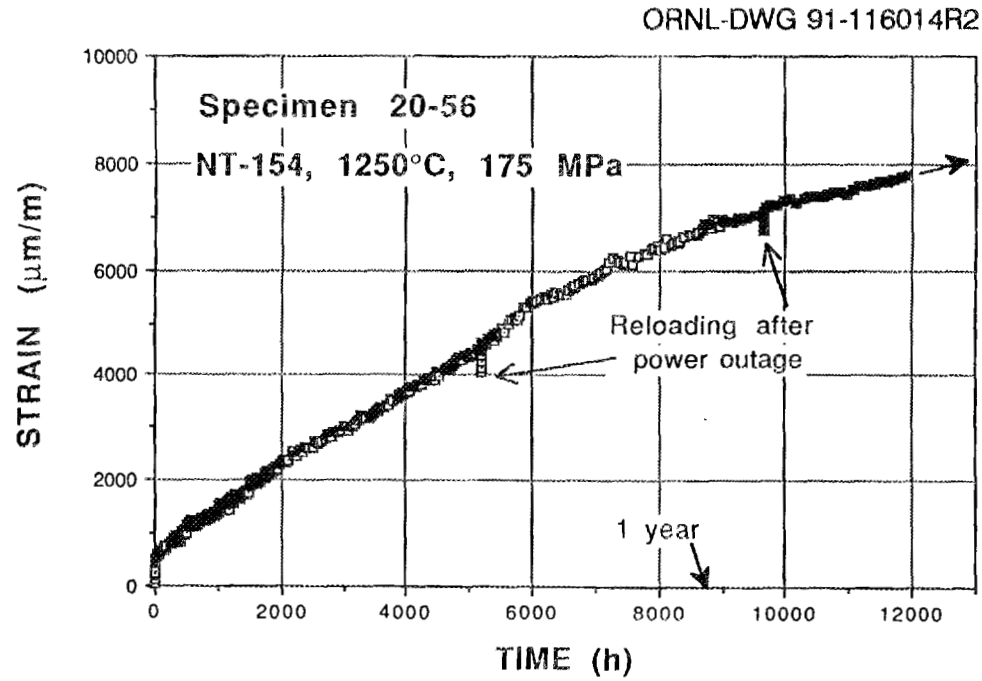

Fig. 2. Creep curve of NT-154 Si_3N_4 (specimen 20-56) tested at 1250°C under an applied stress of 175 MPa.

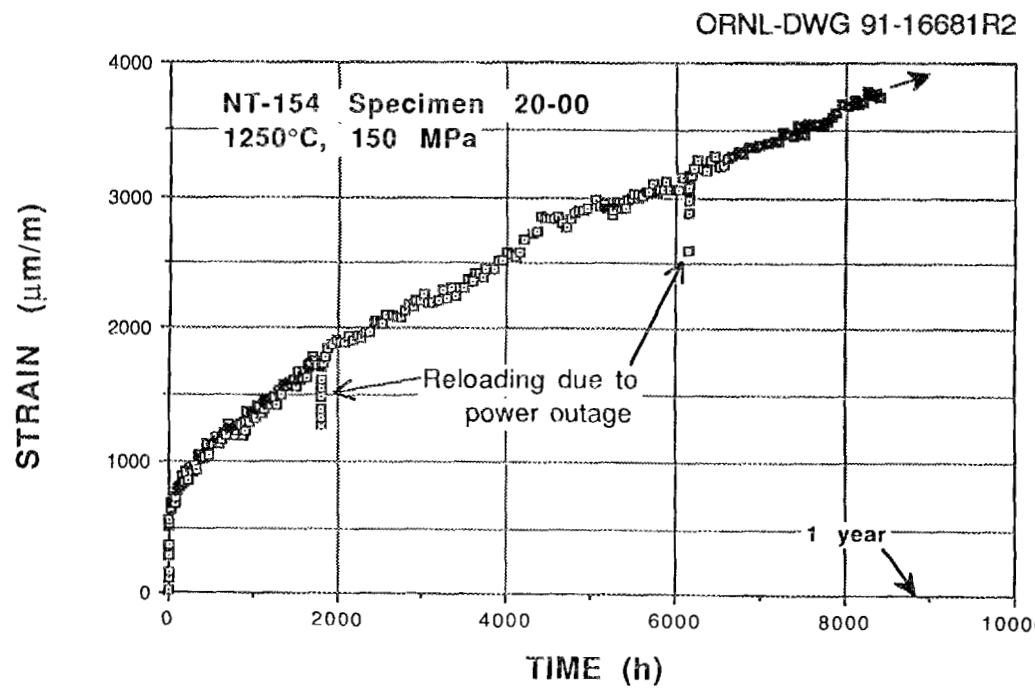

Fig. 3. Creep curve of NT-154 Si_3N_4 (specimen 20-00) tested at 1250°C under an applied stress of 150 MPa.

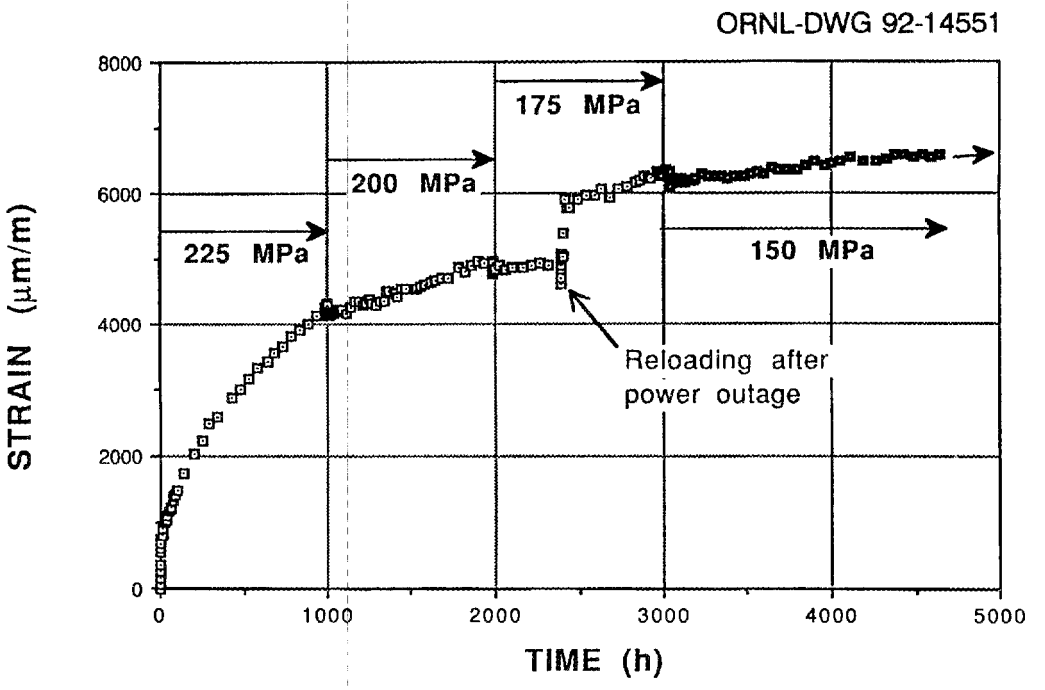

Fig. 4 Creep curve of NT-154 Si_3N_4 (specimen 20-32) tested at 1250°C under step-down loading conditions. The specimen was tested initially at 225 MPa followed by partial unloading in steps of 25 MPa at an interval of 1000 h. Since the last partial unloading at t = 3000 h, the applied stress was kept constant at 150 MPa.

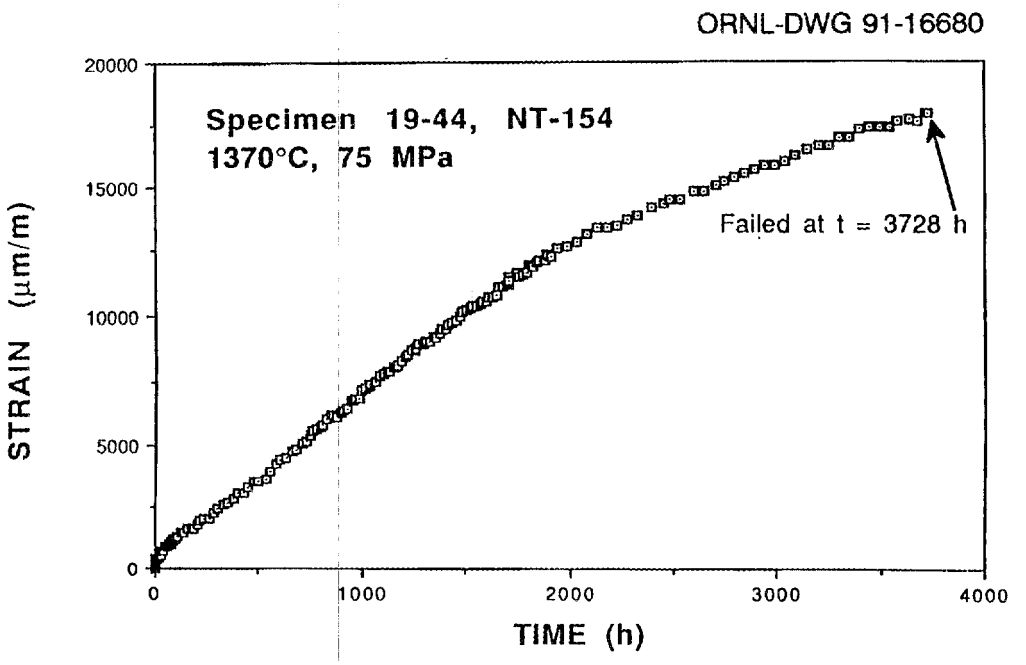

Fig. 5. Creep curve of NT-154 Si_3N_4 (specimen 19-44) tested at 1370°C under an applied stress of 75 MPa.

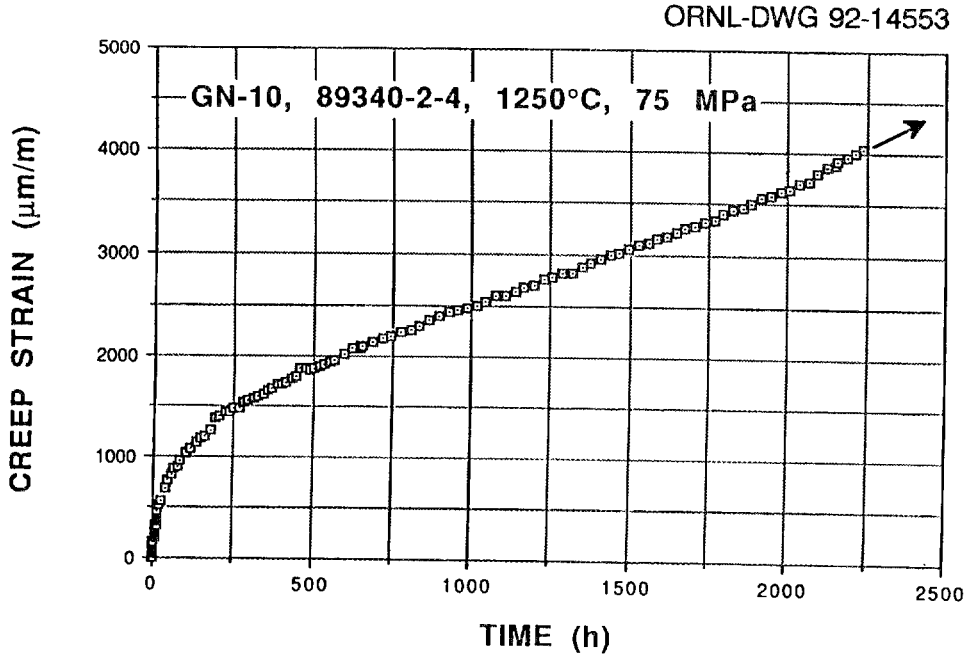

Fig. 6. Creep curve of GN-10 Si_3N_4 tested at 1250°C under an applied stress of 75 MPa. The test was interrupted by fracture at specimen shank due to surface contamination after 2260 h of testing.

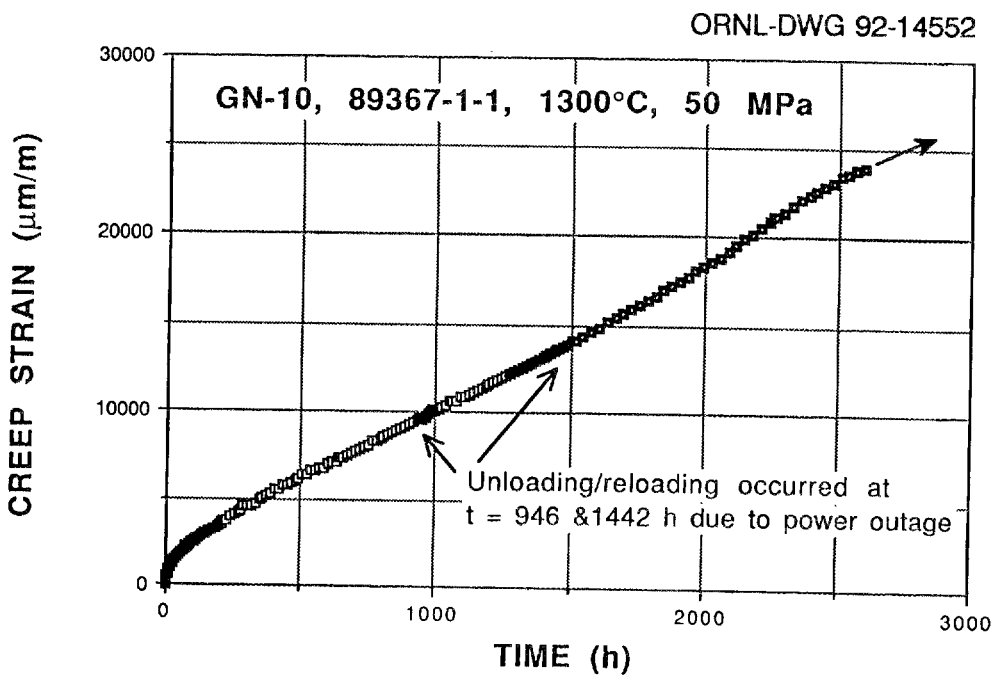

Fig. 7. Creep curve of GN-10 Si_3N_4 tested at 1300°C under an applied stress of 50 MPa. Although the test was interrupted twice due to power failure, the creep behavior appeared unchanged before and after the interruptions.

unchanged before and after the interruptions. After completing the initial transient creep, the specimen exhibited a long period of steady-state creep at a creep rate of 2.27 x 10^{-9} s^{-1}. The creep rate increased slightly after 2000 h of testing. However, no tertiary creep was indicated following an additional 600 h of testing.

Creep Behavior of Microwave-Annealed (M-A) SNW-1000 Si_3N_4

Creep behavior of microwave-annealed, sintered Si_3N_4 was investigated. Specimens numbered as MA-1 to -6 were annealed at 1400°C for 20 h in batches of three specimens each and those numbered as MA-7 to -10 at 1500°C for 20 h in a single batch.

Specimen MA-1: This specimen was tested at 1200°C under a stress of 140 MPa and failed after about 3000 h of testing, as shown in Fig. 8. Comparison with unannealed data obtained at 1200°C/138 MPa by North Carolina A&T State University[3] indicates that microwave annealing was beneficial to the material. The creep resistance was enhanced by a factor of 6 to 7 in terms of creep rate and by an order of magnitude in terms of time to fracture. Although not shown here, the creep curve of an unannealed specimen tested under 90 MPa and that of this specimen are about the same in shape and size. This implies that the creep load capacity of the M-A specimen is 50% better than that of the unannealed. The test was interrupted once at t = 1585 h due to a power outage. A sharp rise in transient creep was exhibited immediately following reloading to the original test condition. However, the strain recovery following the brief transient creep virtually cancelled the strain riser.

Specimen MA-2: This is the second M-A specimen that was initially tested at 1200°C under 160 MPa, as shown in Fig. 9. The applied stress was increased to 180 and 200 MPa after 1025 and 2210 h of testing, respectively. The specimen failed after 47 h of testing at 200 MPa. A cursory comparison of Figs. 9 and 10 will show that this specimen was significantly more creep resistant than specimen MA-1 by a factor of five in terms of creep rate. Exact reasons for the contradictory behavior, showing the 160 MPa creep curve falling far below the 140 MPa curve, although not unusual behavior for ceramic materials in creep, is not known at this time until a more detailed investigation is completed. However, it is speculated that the variation in heat flux due to waveguide bias may be the cause of the inconsistency in creep behavior. The sensitivity of creep behavior relative to the annealing position in the microwave oven and the morphology of microstructure are being investigated to clarify the apparent contradictory results. Interesting to note that brief strain riser and strain recovery periods were observed also immediately following reloading due to a power outage at t = 630 h.

Advanced Turbine Technology Applications Project Tensile Rupture/Creep Testing

Tensile rupture characterization tests (Task 2) for NT-154 specimens were completed. Test parameters and test results are summarized in Tables 2 through 4, and data are shown in Fig. 10. Data with an asterisk, shown in Fig. 10, indicate the specimens failed prematurely due to the large internal defects. Because these defective specimens were received from the supplier with numbers beginning at 33 and continuing in sequence, they were suspected of being made from the same contaminated lot. Therefore, the data points were censored and not included in the regression analysis. Data points with a horizontal arrow attached indicate the specimens did not fail after 150 h of testing, and the stress-rupture tests were discontinued thereafter. Residual tensile strengths were

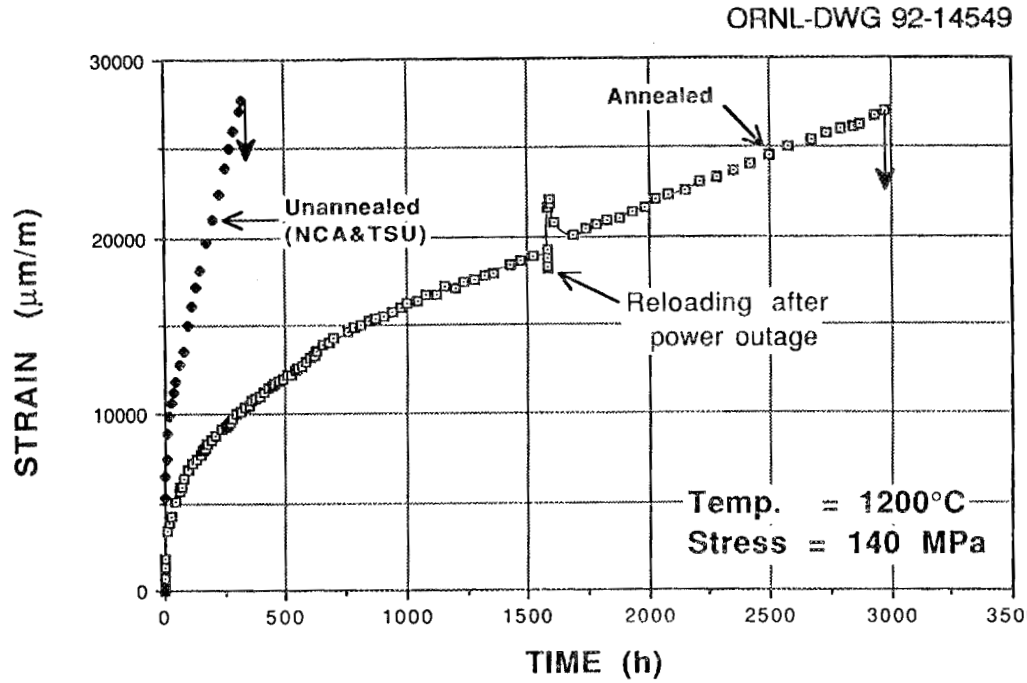

Fig. 8. Creep curve of microwave-annealed (1400°C/20 h) sintered Si_3N_4 (GTE SNW-1000) tested at 1200°C under a constant stress of 140 MPa is compared with that of an unannealed specimen tested at 1200°C/138 MPa. Results show that the annealing can significantly enhance the creep resistance of the material.

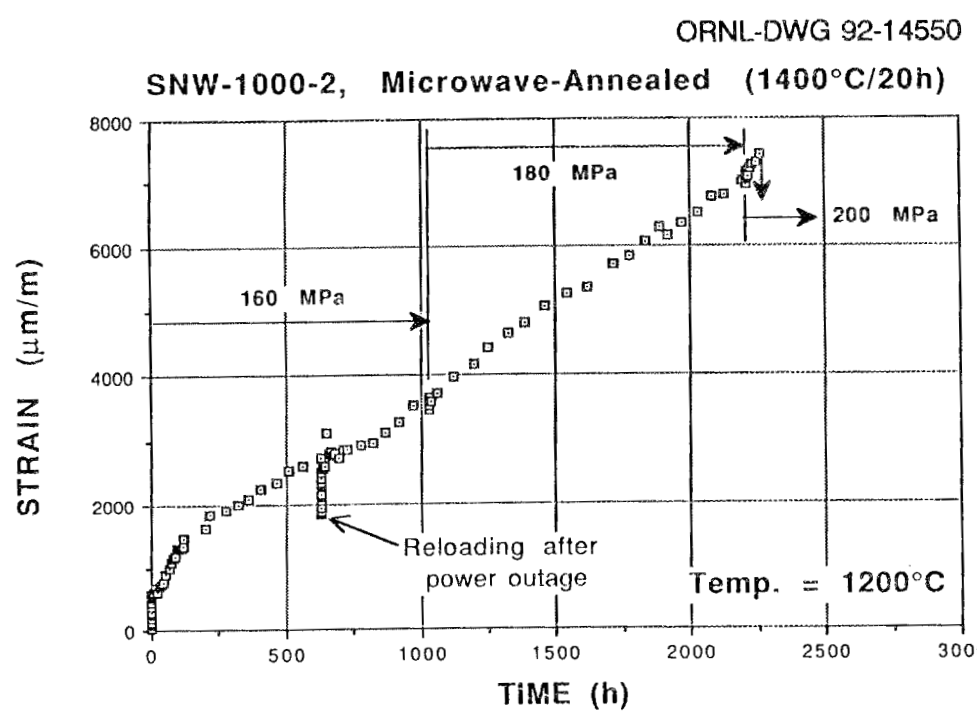

Fig. 9. Creep curve of microwave-annealed (1400°C/20 h) sintered Si_3N_4 tested at 1200°C under step-up loading conditions as indicated. The annealed specimen sustained a stress of 200 MPa for 47 h. Contrastingly, an unannealed specimen was reported[3] to have failed in fast fracture under a stress of 196 MPa.

ORNL-DWG 92-15419

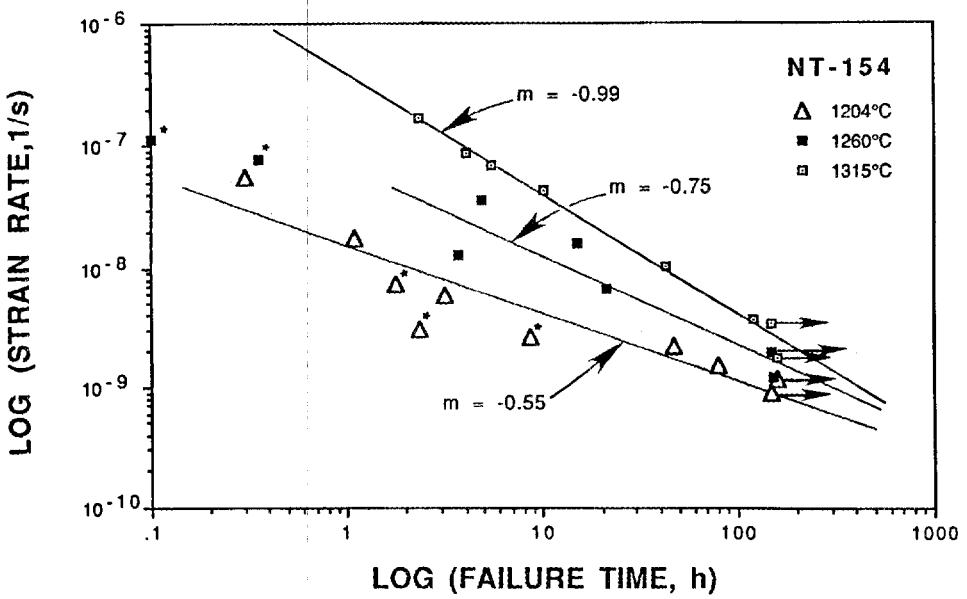

Fig. 10. Creep-rupture data for NT-154 show that the Monkman-Grant relationship is dependent on temperature. Data with an asterisk (*) are not included in the linear regression analyses.

Table 2. ATTAP stress-rupture test matrix for NT-154 Si_3N_4 at 1204° C (2200° F)

Stress (ksi)	Specimen	Minimum creep rate (m/m s^{-1})	Time to rupture (h)	Creep strain at failure (%)
	NTC-09	8.9 E-10	> 150	0.837
50	NTC-42	1.02 E-8	0.91[a]	0.0127
	-	-	-	-
	NTC-32	1.14 E-9	> 159.7	0.154
52.5	NTC-33	5.56 E-8	0.3[a]	0.0096
	NTC-34	3.02 E-9	2.31[a]	0.0157
	NTC-10	2.18 E-9	47.45	0.099
	NTC-15	1.49 E-9	80.8	0.069
55	NTC-14	7.19 E-9	1.75[a]	0.01
	NTC-16	2.55 E-9	8.6[a]	0.017
	NTC-17	8.77 E-10	> 150	0.083
	NTC-35	-	Failed at 54 ksi[a]	
57.5	NTC-36	-	Failed at 54.9 ksi[a]	
	NTC-37	-	0.075[a]	-
	NTC-20	5.89 E-9	3.1	0.02
60	NTC-22	1.77 E-8	1.1	0.077
	-	-	-	-

[a]Fracture initiated from a large internal flaw; the rupture lifetime indicated may not be valid.

Table 3. ATTAP stress-rupture test matrix for NT-154 Si_3N_4 at 1260° C (2300° F)

Stress (ksi)	Specimen	Minimum creep rate (m/m s^{-1})	Time to rupture (h)	Creep strain at failure (%)
45	NTC-12	1.92 E-9	> 150	0.155
	NTC-13	1.2 E-9	151	0.218
	NTC-44	1.29 E-8	16.67[a]	0.132
47.5	NTC-27	6.45 E-9	21.2	0.086
	NTC-38	7.65 E-8	0.35[b]	0.0096
	NTC-40	1.12 E-7	0.1[b]	0.0041
50	NTC-07	3.58 E-8	4.9	0.073
	NTC-08	1.59 E-8	15	0.108
	NTC-23	1.27 E-8	3.7	0.035

[a]Fracture initiated from a large inclusion near specimen surface outside the gage section; the rupture lifetime indicated may not be valid.

[b]Fracture initiated from an internal flaw; the rupture lifetime indicated may not be valid.

Table 4. ATTAP stress-rupture test matrix for NT-154 Si_3N_4 at 1315° C (2400° F)

Stress (ksi)	Specimen	Minimum creep rate (m/m s^{-1})	Time to rupture (h)	Creep strain at failure (%)
35	NTC-18	3.36 E-9	> 150	0.330
	NTC-19	1.74 E-9	> 159	0.437
	NTC-25	3.65 E-9	121.3	0.471
37.5	NTC-26	4.27 E-8	10.15	0.280
	NTC-29	1.03 E-7	42.9	0.453
	-	-	-	-
40	NTC-05	7.04 E-8	5.41	0.189
	NTC-06	1.7 E-7	2.34	0.162
	NTC-24	8.68 E-8	4	0.203

determined subsequently at room temperature for the specimens surviving the 150 h testing.

The distribution of the rupture data indicates that a single-line Monkman-Grant relationship can not appropriately represent the data collectively. This observation is inconsistent with the finding reported earlier by the National Institute of Standards and Technology (NIST),[4] using a limited data base in which all of the rupture data for NT-154 fell on a single curve regardless of stress and temperature. Contrastingly, the ORNL rupture data are somewhat independent of stress but are a function of temperature as indicated by three linear curves determined by the least-squares method.

Tensile rupture characterization tests (Task 2) for GN-10 specimens were performed. A total of nine specimens was tested. Test parameters and test results are summarized in Table 5, and data are shown in Fig. 11.

In contrast to the behavior exhibited by NT-154, the distribution of the rupture data for GN-10 indicates that a single-line Monkman-Grant relationship can represent the data collectively, regardless of temperature and applied stress. The above information has been transmitted to Garrett Auxiliary Power Division (GAPD).

Status of Patent Application

A patent application entitled, "Apparatus for Tensile Testing Plate-type Ceramic Specimens," was filed with the U.S. Patent Office in July 1992.

Important Findings and Observations

Preliminary test data, although limited, show that microwave annealing can significantly increase the creep resistance of sintered Si_3N_4.

Status of Milestones

1. Completed a technical report covering results of the acoustic emission study on cyclic fatigue behavior of ceramic and ceramic composite materials by July 31, 1992 (Milestone 321415).

2. Completed exploratory creep-fatigue interaction tests on NT-154 Si_3N_4 by June 30, 1992 (Milestone 321508).

3. Completed a draft report describing results of creep-fatigue interaction tests on NT-154 Si_3N_4 by September 30, 1992 (Milestone 321509).

Publications

1. J. L. Ding, K. C. Liu, and C. R. Brinkman, "Development of a High Temperature Deformation and Life Prediction Model for Advanced Silicon Nitride Ceramics," was submitted to *J. Am. Ceram. Soc.*

2. K. C. Liu and J. L. Ding, "A Mechanical Extensometer for High Temperature Tensile Testing of Ceramics," was submitted to *J. Test. Eval.*

Table 5. ATTAP stress-rupture test matrix for GN-10 Si_3N_4 at various temperatures

Stress (ksi)	Specimen	Minimum creep rate (m/m s^{-1})	Time to rupture (h)	Creep strain at failure (%)
		1204°C (2200°F)		
30	E-2	1.54 E-8	> 57.35	0.633
	F-2	3.5 E-8	41.16	0.871
	-	-	-	-
32.5	F-3	1.34 E-7	9.92	0.513
	F-4	1.24 E-7	13.55[b]	0.662
	-	-	-	-
35	G-2	4.37 E-8	23.48	0.493
		1260°C (2300°F)		
22.5	E-3	6.51 E-8	20.76	0.879
	F-1	1.65 E-7	12.65	1.191
25	G-3	1.05 E-7	13.78	0.74
		1315°C (2400°F)		
15	E-1	9.69 E-8	18.4	1.101

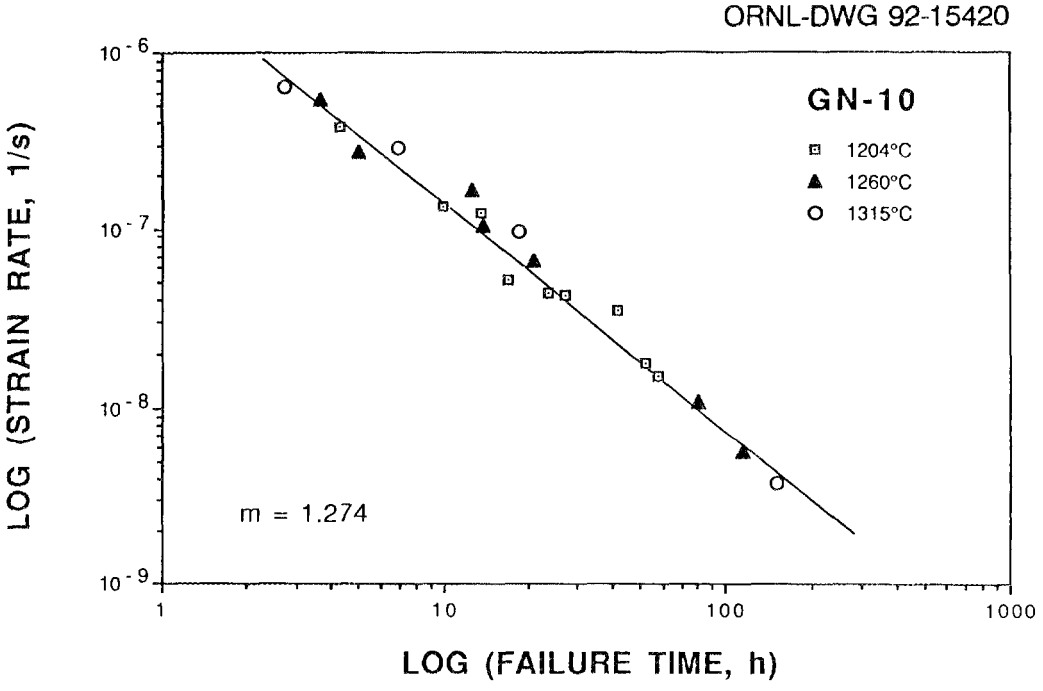

Fig. 11. Creep-rupture data for GN-10 show that the Monkman-Grant relationship is independent of stress and temperature and can be represented by a single linear line.

References

1. C.-K. J. Lin, "Fatigue of Alumina at Room and High Temperatures," p. 62, Report No. 155/UILU-ENG 91-3601, University of Illinois at Urbana-Champaign, October 1991.

2. K. C. Liu, C. O. Stevens, and C. R. Brinkman, "Tensile and Cyclic Fatigue Properties of SiC whisker-Reinforced Al_2O_3," in *Proceedings of the First Canadian International Composites Conference*, Quebec, Canada, September 4-6, 1991 (in press).

3. J. Sankar, A. D. Kelkar, V. S. Avva, and Jun Gao, "Testing and Evaluation of Advanced Ceramics at High Temperature in Uniaxial Tension," pp. 396-403 in *Ceramic Technology for Advanced Heat Engines Project Semiannual Progress Report for April 1990 through September 1990*, ORNL/TM-11719, Martin Marietta Energy Systems, Inc., Oak Ridge Natl. Lab., December 1990.

4. S. M. Wiederhorn, R. Krause, and D. C. Cranmer, "Tensile Creep Testing of Structural Ceramics," pp. 273-80 in *Proceedings of the Annual Automotive Technology Development Contractors' Coordination Meeting*, Dearborn, Michigan, October 28-31, 1991, Society of Automotive Engineers, Inc., Warrendale, Pa, June 1992.

Rotor Data Base Generation

M. K. Ferber, M. G. Jenkins, C.-K. Lin, A. A. Wereszczak, and
K. Breder (Oak Ridge National Laboratory)

Objective/scope

The goal of the proposed research program is to systematically study the tensile strength of a silicon nitride ceramic as a function of temperature and time in an air environment. Initial tests will be aimed at measuring the statistical parameters characterizing the strength distribution of three samples types (two tensile specimens and one flexure specimen). The resulting data will be used to examine the applicability of current statistical models as well as sample geometries for determining the strength distribution.

In the second phase of testing, stress-rupture data will be generated by measuring fatigue life at a constant stress. The time-dependent deformation will also be monitored during testing so that the extent of high-temperature creep may be ascertained. Tested samples will be thoroughly characterized using established ceramographic, scanning electron microscopy (SEM), and transmission electron microscopy (TEM) techniques. A major goal of this effort will be to better understand the microstructural aspects of high-temperature failure including:

1. extent of slow crack growth (SCG),
2. evolution of cavitation-induced damage and fracture,
3. transition between brittle crack extension and cavitation-induced growth, and
4. crack blunting.

The resulting stress-rupture data will be used to examine the applicability of a generalized fatigue-life (SCG) model. If necessary, model refinements will be implemented to account for both crack blunting and creep damage effects. Insights obtained from the characterization studies will be crucial for this modification process. Once a satisfactory model is developed, separate stress-rupture (confirmatory) experiments will be performed to examine the model's predictive capability. Consequently, the data generated in this program will not only provide a critically needed base for component utilization in automotive gas turbines but also facilitate the development of a design methodology for high-temperature structural ceramics.

Technical progress

Studies of the high-temperature mechanical properties of a high-performance silicon nitride (PY6)* were continued this reporting period. The PY6 was fabricated by first isopressing the silicon nitride powder and densification aid of 6 wt % yttria to form the green body and then hot isostatic pressing (HIP) to complete the sintering process. The microstructure typically consists of 1- to 6-μm-long acicular grains surrounded by nominally equiaxed grains 0.1 to 1.0 μm in diameter. This morphology leads to a relatively dense microstructure. The silicon nitride grains, which are generally in the form of β-Si_3N_4, are separated by relatively thin layers of an amorphous yttrium silicate. The

*PY6 silicon nitride, GTE Laboratories, Inc., Waltham, Massachusetts.

intergranular phase is also present in the triple points as a crystalline yttrium silicate. The exact phase composition of these intergranular compounds depends upon the HIP conditions.

As reported previously,[1] the evolution of creep damage (primarily in the form of grain boundary cavities) in PY6 silicon nitride was studied by periodically measuring the elastic modulus, E, during creep testing at 1370°C. Data were generated for this study, as well as related investigations of PY6, using button-head tensile specimens (gage section of 6.35-mm-gage diameter and 35-mm-gage length) fabricated from as-received isopressed and HIPed rods 160 mm long and 22 mm in diameter. Based upon the studies of Suresh and Brockenbrough,[2] E should be sensitive to this level of creep damage generally decreasing relative to the starting value, E_o, as the creep damage accumulation increases. In the present study, measurement of E involved the periodic application (~24-h interval) of an unload/load cycle to the statically loaded specimen continued at the intervals until specimen failure. Values of E were calculated from the slopes of the resulting stress-strain curves generated by first unloading the specimen to 10 to 20% of the static, creep stress, σ_a, and then reloading back to σ_a. Generally, E tended to decrease with increasing time to ~85 to 90% of E_o and remaining stable at that level until specimen failure. However, an unexpected effect of this cycling was to increase the fatigue life over that measured under "no cycle" conditions. The relative increase in fatigue life, t_f (cycled)/t_f (not cycled), was dependent upon the number of cycles applied prior to failure with the total strain to failure for the "cycled" tests tending to be greater than that for the "no cycle" tests.

In order to better characterize the effect of cyclic loading upon the fatigue characteristics of the PY6 material, a series of low-cycle fatigue tests at 1150, 1260, and 1370°C were initiated. The baseline static fatigue characteristics at each temperature were established from dynamic fatigue tensile tests in which the fracture strength, σ_f, was measured as a function of stressing rate, $d\sigma/dt$. Results from these tests are shown in Fig. 1. The parameter, N, in this figure represents the fatigue exponent in the expression,

$$\sigma_f = A\,(d\sigma/dt)^{1/(N+1)}\,, \tag{1}$$

where A is a constant. When failure is controlled by slow crack growth, N should be equal to the value determined from static fatigue tests. In this case, N is calculated from the expression,

$$t_f = B\,(\sigma_a/\sigma'_o)^N\,, \tag{2}$$

where σ_a is the applied stress, σ'_o is a normalizing parameter (=1 MPa), and B is a constant.

In Fig. 1, the dynamic fatigue data measured at 1260 and 1370°C reveal a transition in fatigue behavior as the stressing rate decreased to $<10^{-1}$ MPa/s. As shown in Fig. 2, this transition approximately corresponds to generation of large nonlinear strains preceding failure. In the low-stressing-rate regime at 1370°C, the fatigue exponents are comparable (N = 4 to 6) for the two highest temperatures. Based upon static stress data,[3] this value of N is consistent with creep-controlled fatigue. This has been confirmed by SEM studies which show that grain boundary cavitation occurs at stressing rates of $\leq 10^{-2}$ MPa/s and below. In the high-stressing-rate regime, the N values are much larger

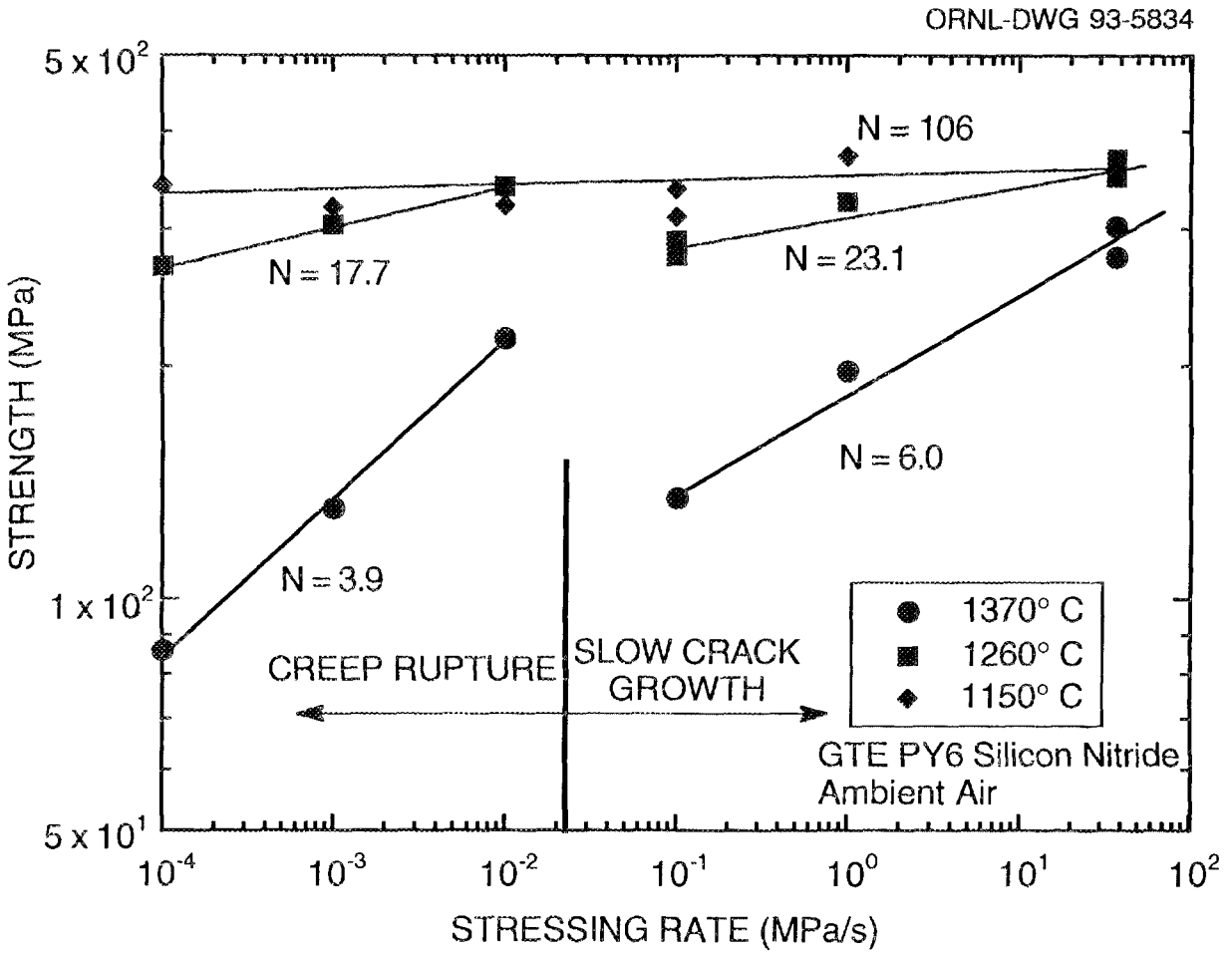

Fig. 1. Dynamic fatigue data for the PY6 silicon nitride generated at 1260 and 1370°C revealed two distinct fatigue regions. No change in failure mode was indicated for the 1150°C data.

indicating a change in failure mechanism related possibly to SCG of a single flaw. This transition is in agreement with static fatigue results.[3]

The dynamic fatigue data can be used estimate the static fatigue failure times, t_{fest}, using the expression,

$$t_{fest} = t_{fd}/(N+1), \tag{3}$$

where t_{fd} is the failure time for the dynamic fatigue test. For this calculation, the failure stress in dynamic loading is assumed to be equal to the effective applied stress in the static fatigue test. Figure 3 compares the fatigue life characteristics determined from Eq. 3 with those measured in ref. 3.

The values of t_{fest} calculated from the low-stressing-rate regimes at 1260 and 1370°C represent a reasonable extension of the static fatigue data. In the case of the high-stressing-rate regions, the corresponding σ_a versus t_{fest} curves are shifted to much lower

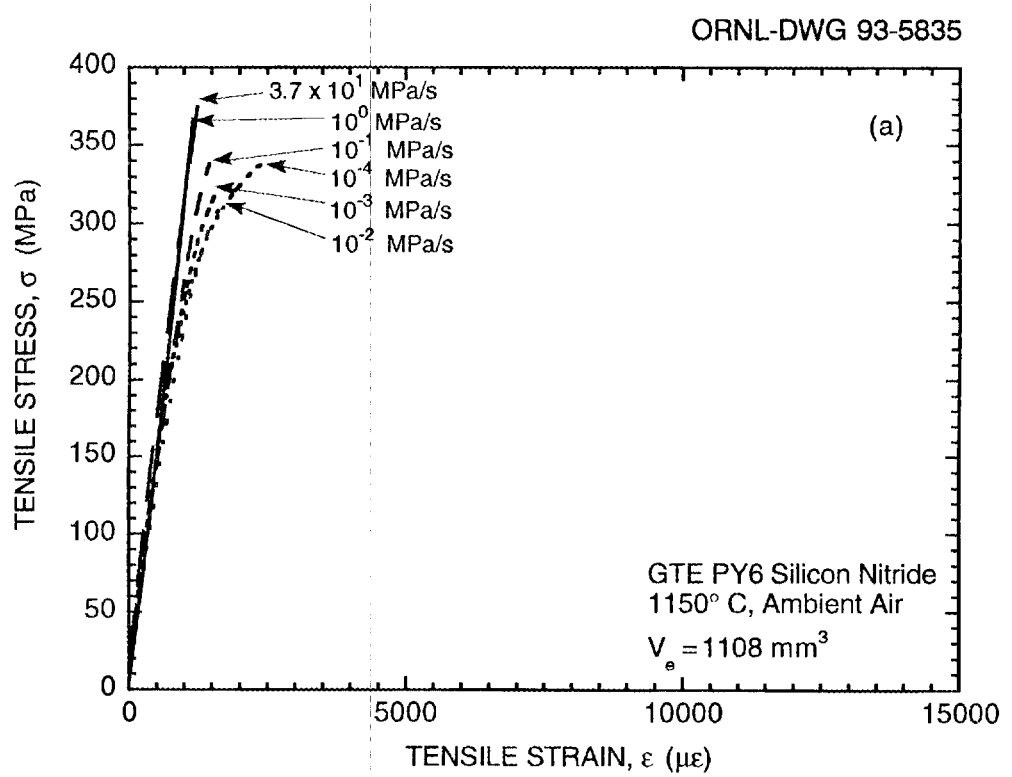

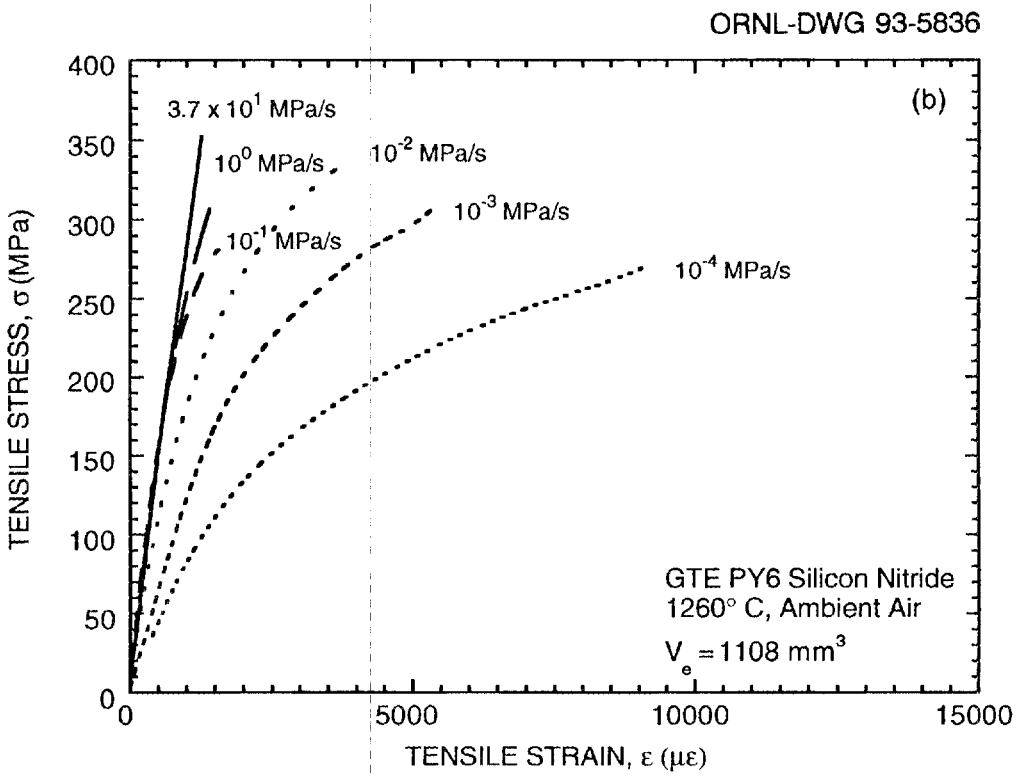

Fig. 2. Stress-strain curves associated with dynamic fatigue tests indicated that the change in failure mechanism was accompanied by the generation of large nonlinear strains preceding failure.

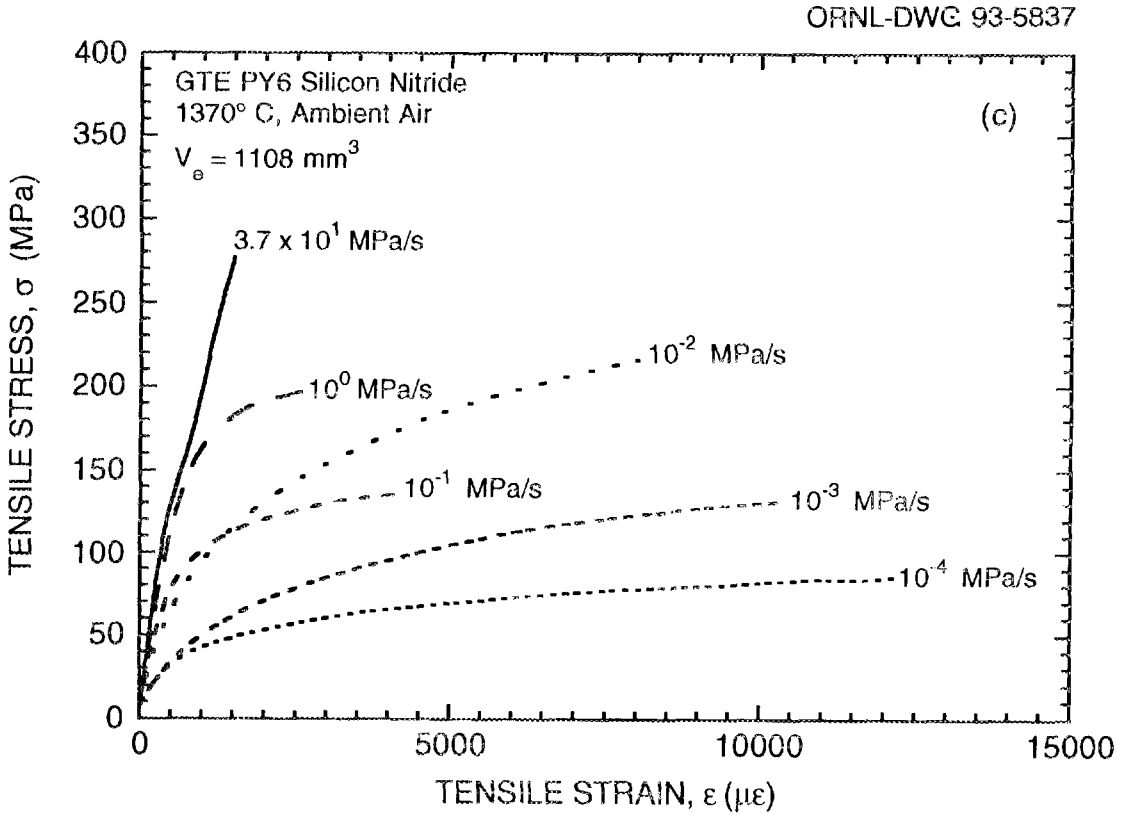

Fig. 2. Continued.

fatigue lives consistent with the change in failure mechanism. Although the calculation of t_{fest} is based on a somewhat simplified analysis, the comparisons shown in Fig. 3 illustrate the utility of the dynamic technique for the study of high-temperature failure modes.

Cyclic fatigue tests were conducted under constant frequency and stress amplitude conditions as shown in Fig. 4. Three wave forms were used [trapezoidal at 0.1 Hz (0.5-s ramp and 4.5-s dwell), triangular at 0.1 Hz, and sinusoidal at 10 Hz] at consistent stress ratios of R = 0.1 and maximum stresses ranging from 75 MPa to 332 MPa over the temperature range of 1150 to 1370°C. Specimens that did not fail in a runout time of 1000 h were fast-fractured at room temperature to determine the retained strength. Except in a few cases where strain was monitored continuously during the test, strain was recorded only at discrete intervals during the cyclic tests due to the uncertainty of leaving the contacting, mechanical extensometer against the specimen for the entire test. Therefore, the bulk of the cyclic fatigue information consisted of cycles (or total time) to failure under given maximum stresses in addition to records of the periodic stress-strain curves.

Figures 5*(a)* through *(c)* show stress-rupture results as log-log plots of maximum stress versus time to failure for static, dynamic, and cyclic fatigue tests at 1150, 1260, and 1370°C, respectively. For simplicity, the time to failure is the actual time to failure since no failure mechanism, such as SCG, needs to be assumed a priori. Maximum stress for the static tests is the constant stress applied until failure of the specimen. For the

ORNL-DWG 93-5838

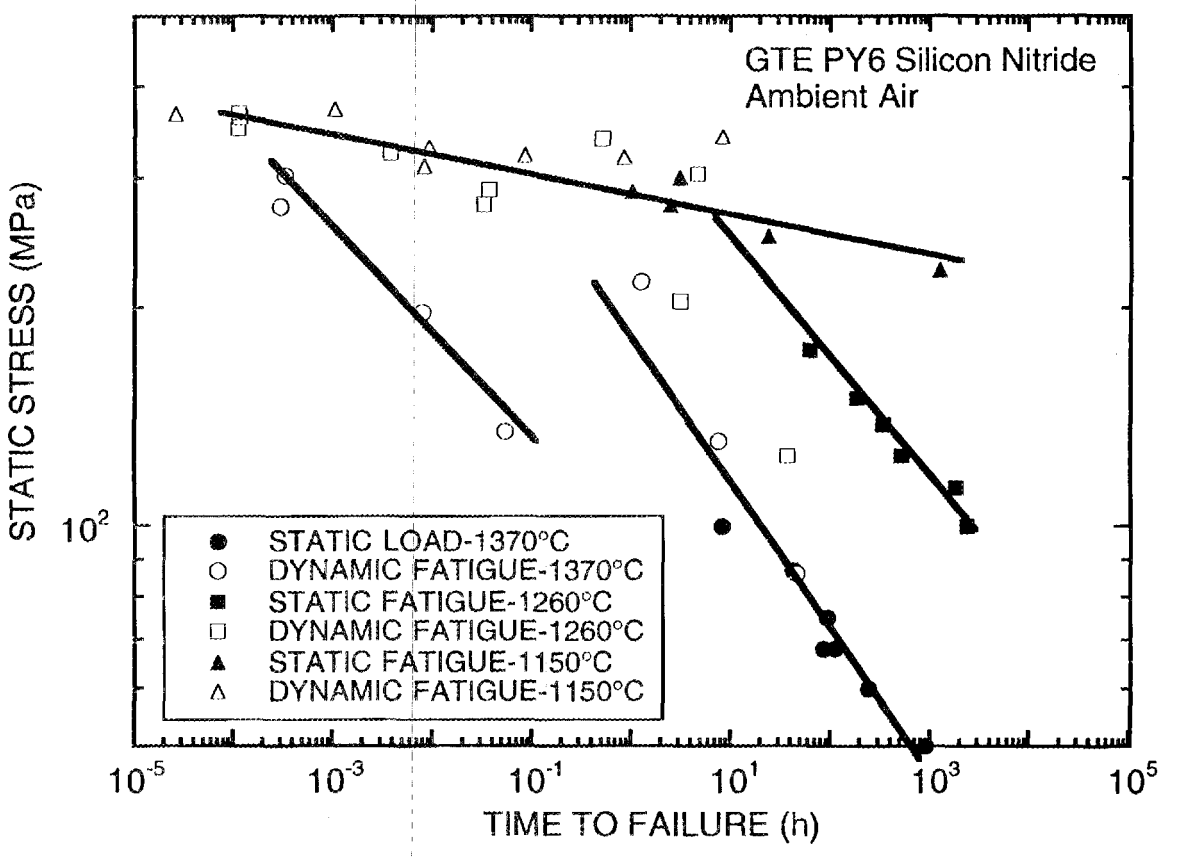

Fig. 3. The static fatigue data generated at 1260 and 1370°C (ref. 2) were in good agreement with fatigue lives predicted from the low-stressing-rate dynamic fatigue data.

dynamic tests, maximum stress corresponds to the failure stress at the particular stressing rate. Maximum stress under cyclic loading is the maximum applied stress during each stress cycle. Also shown on each plot for each data point is the classification of each failure origin where the first letter designates the type of failure damage (C is creep/ environmental damage and D is inherent defect), and the second letter designates the location of the failure origin (S is surface, NS is near surface, and V is volume).

In Fig. 5*(a)* for the 1150°C tests, the data points apparently scatter about the indicated single curve (N ≈ 58) implying that all failures originate from a similar SCG mechanism as previously identified for PY6 at this temperature.[3] Also in agreement with an SCG mechanism, all the identified failure damage types were defects located either at the surface or in the volume. In Fig. 5*(b)* for the 1260°C tests, the data points tend to fall into two distributions. A nearly horizontal line (N ≈ 56) tends to fit all the failures for dynamic and cyclic tests with failure damage in all cases attributed to defects located at the surface or in the volume. The results for the static fatigue tests group around a line of sharply decreasing slope (N ≈ 7) with all failure damage in all cases attributed to creep/ environmental damage originating at the surface. In Fig. 5*(c)* for the 1370°C tests, the

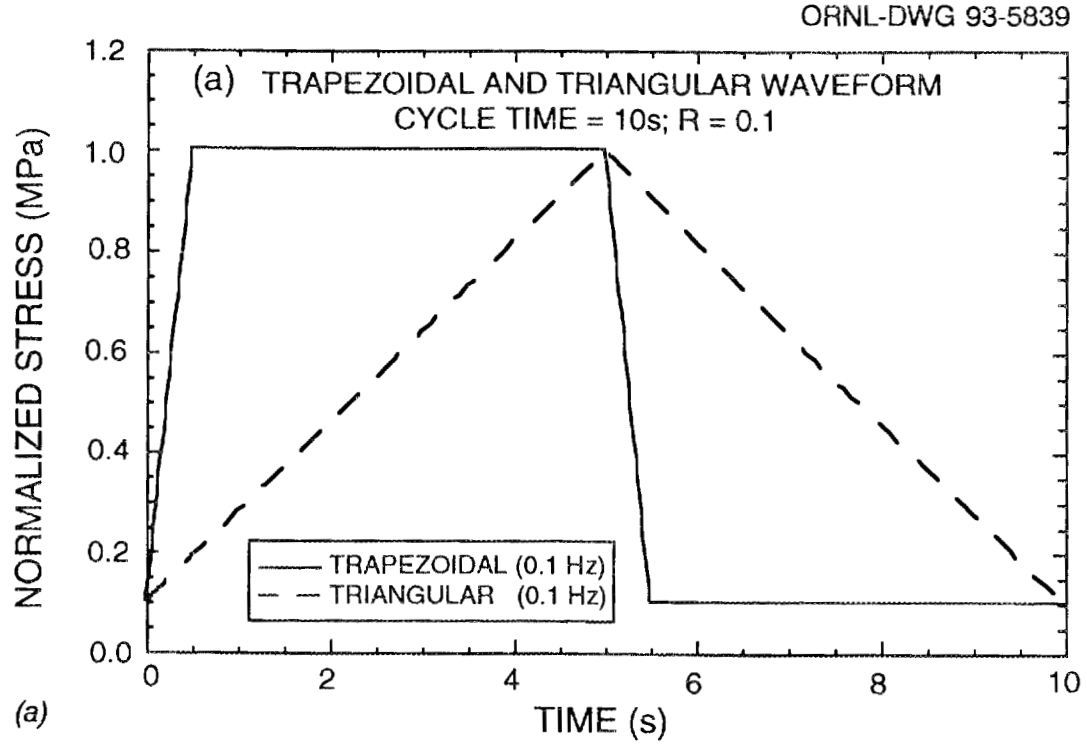

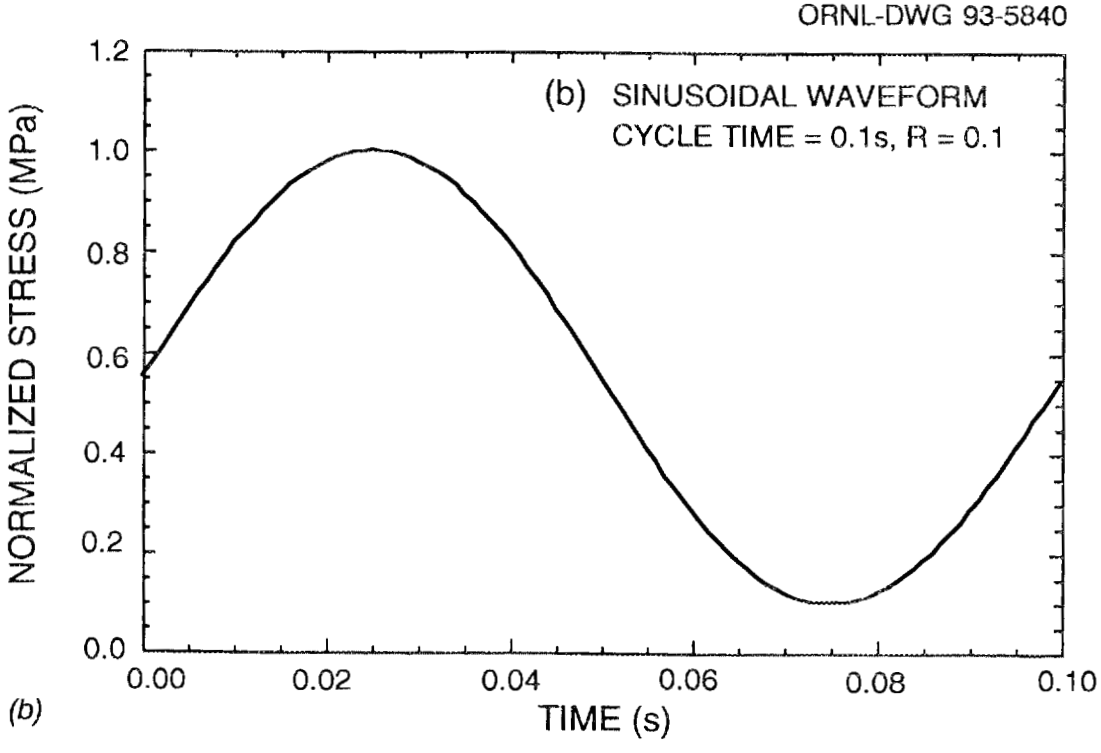

Fig. 4. Three wave forms were utilized for the cyclic fatigue tests: *(a)* trapezoidal and triangular wave forms and *(b)* sinusoidal wave form.

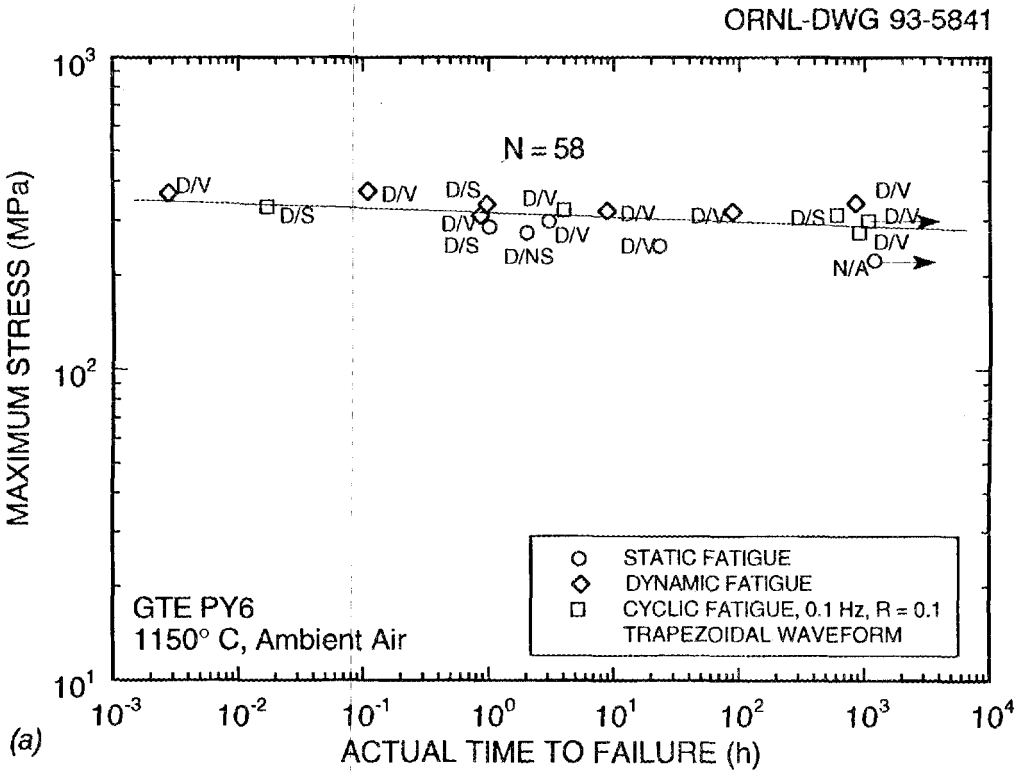

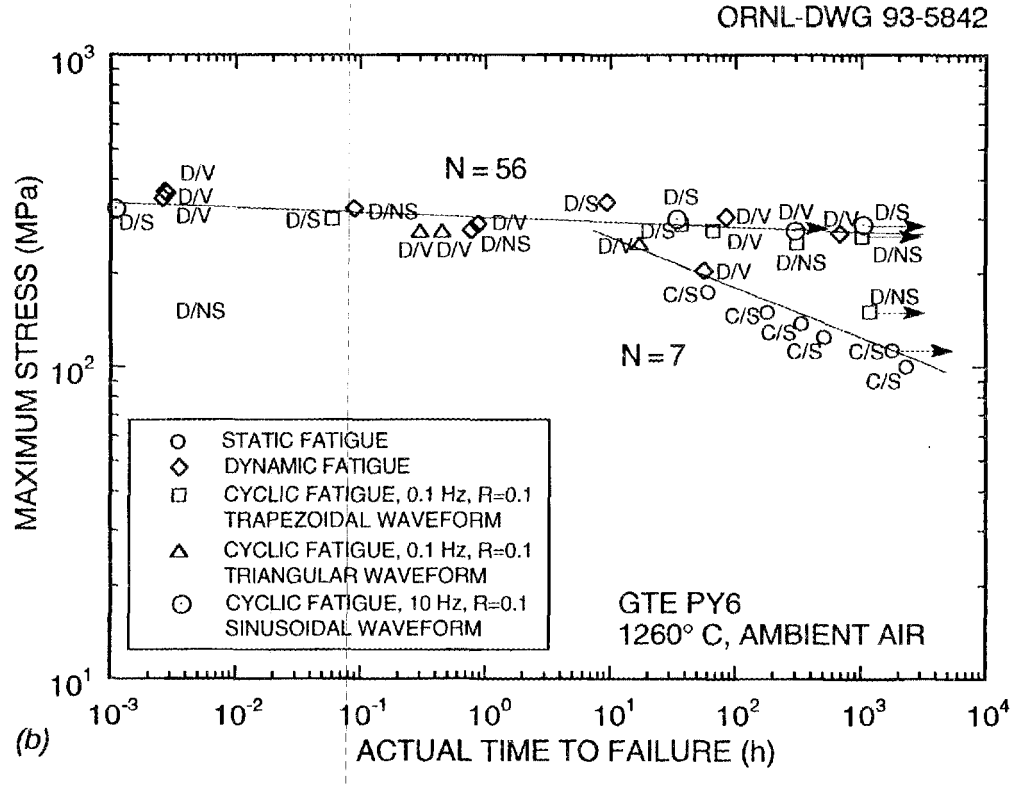

Fig. 5. The tensile stress-time to failure relations for PY6 silicon nitride at: *(a)* 1150°C, *(b)* 1260°C, and *(c)* 1370°C indicated that as the temperature increased, the failure mode changed from that controlled by intrinsic defects to that controlled by the evolution of creep damage.

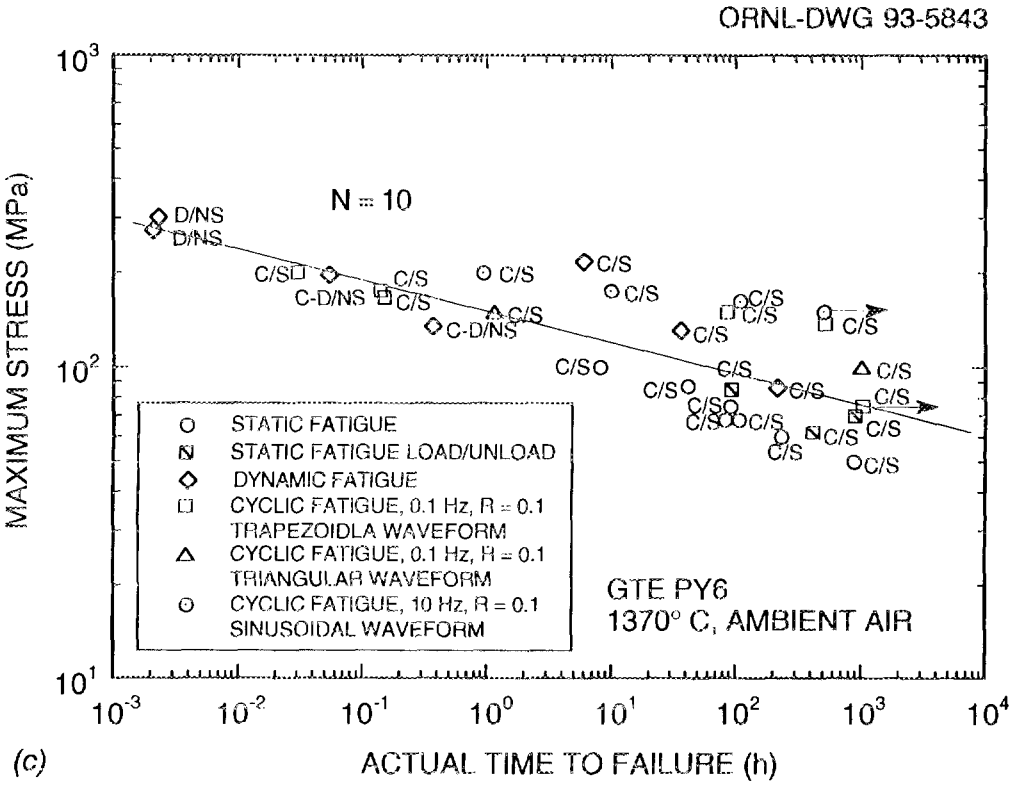

Fig. 5. Continued.

data points again tend to scatter around the indicated single curve (N ≈ 10) indicating a similar failure mechanism for all the tests. However, in this case, all the failure damage, except two at very short failure times, was classified as creep/environmental with origins at or near the surface.

The stress-rupture and failure origin results shown in Fig. 5*(a)* for 1150°C are consistent with an SCG failure mechanism hence implying that no cyclic fatigue effect is operative. Given the limited range of factors for effective time (2 to 22), the trends for failure times are evident using actual time rather than assuming a potentially confusing effective time approach. For the results of Fig. 5*(b)* at 1260°C, a different picture emerges in which static loading appears to be detrimental to the times to failure. For example, at 10^3 h, maximum cyclic stresses of 250 to 275 MPa can be sustained with failures originating from defect damage, whereas static stresses of only 113 to 125 MPa can be sustained with failures occurring from creep/environmental damage originating at the surface. In this, the loading-unloading of the cyclic tests appears to interrupt the creep/environmental damage nucleation and accumulation process, thus allowing greater stresses to be sustained for similar failure times. Failures must then originate from inherent defects rather than from the accumulation of the creep/environmental damage. Such a hypothesis is supported by SEM fractography. Creep/environmentally assisted cavitation damage is much more evident in the static test than the cyclic. The results shown in Fig. 5*(c)* for 1370°C do not show a strong tendency of apparent "enhanced" cyclic fatigue resistance as might be expected based on the results at 1260°C.

Identification of the majority of failure origins as creep/environmental damage originating from the surface suggests that rapid oxidation damage previously cited in PY6 at this temperature[3] is masking the "enhanced" cyclic fatigue resistance. Instead, accelerated failures from the surface are not as strongly interrupted by the loading/unloading as at 1260° C.

Such "enhanced" cyclic fatigue resistance has been noted previously in studies cited by Ohji et al.[4] An intriguing aspect of the work of Ohji et al. involved the relation of the "yield" (point of nonlinearity of the stress-strain behavior under a monotonic testing rate) stress under various testing rates to the cyclic fatigue behavior under various frequencies and stresses. Ohji et al. speculated that this "yield" stress denotes the stress above which damage accumulation mechanisms such as grain boundary sliding and cavitation are promoted. Therefore, cyclic loading at a maximum stress less than the "yield" stress at that particular testing rate would produce "enhanced" cyclic fatigue resistance. Preliminary efforts in the present investigation have shown promise in the application of this concept to understanding the fatigue behavior of PY6 with future work in this area continuing.

Additional studies during this reporting period focused on the examination of the effect of environment upon the dynamic fatigue characteristics of PY6. As shown in Fig. 6, the PY6 specimens tested in ambient air were quite susceptible to creep rupture as reflected by the significant loss in strength with decreasing stressing rate. The fatigue exponent, N, was 10, which is comparable to the static stress results. Exact agreement is

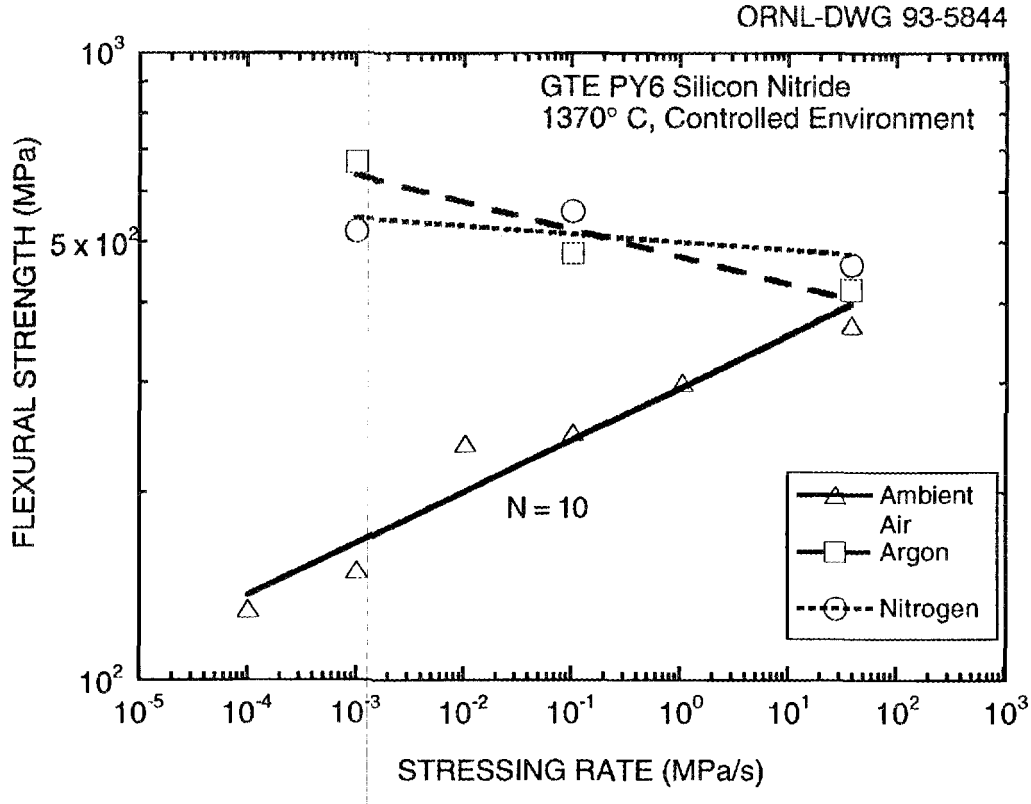

Fig. 6. The dependence of flexure strength upon stressing rate was strongly dependent upon test environment.

not expected due to effects of stress redistribution in the flexure specimens. Examination of the fracture surfaces for specimens tested at the lower stressing rates also revealed a creep damage zone similar to that observed for the creep-rupture results conducted under static, tensile stresses. When similar tests were conducted in nitrogen or argon, no creep-rupture effects were observed. In fact, the PY6 specimens exhibited a slight increase in strength with decreasing stressing rate. This trend may have been due to stress redistribution effects arising from creep, evidence of which was provided by the observed non-linearity in the load-displacement plots. Therefore, the major effect of testing in argon or nitrogen was to eliminate the evolution of the creep/environmental damage zone, which was ultimately responsible for creep rupture for specimens tested in air.

Status of milestones

None

Communications/visitors/travel

1. During a visit by S. M. Wiederhorn from the National Institute of Standards and Technology (NIST) in September 1992, discussions were held concerning the creep/fatigue measurements being conducted as part of their Ceramic Technology Project effort.

Problems encountered

None

Publications

1. C.-K. J. Lin, M. G. Jenkins, and M. K. Ferber, "Evaluation of Tensile Static, Dynamic, and Cyclic Fatigue Behaviour for a HIPed Silicon Nitride at Elevated Temperatures," to be published in *Proceedings of the Symposium on Silicon Nitride Ceramics—Scientific and Technological Advances*, 1992 Materials Research Society Fall Meeting, Boston, Massachusetts, November 1992.

2. M. G. Jenkins, M. K. Ferber, and C.-K. J. Lin, "Apparent Enhanced Fatigue Resistance Under Cyclic Tensile Loading for a HIPed Silicon Nitride," submitted to *J. Am. Ceram. Soc.*, October 1992.

3. C.-K. J. Lin, M. G. Jenkins, and M. K. Ferber, "Tensile Dynamic and Static Fatigue Relations for a HIPed Silicon Nitride at Elevated Temperatures," accepted for publication by *J. Eur. Ceram. Soc.*, October 1992.

References

1. M. K. Ferber and M. G. Jenkins, "Rotor Data Base Generation," to be published in Ceramic Technology Project Semiannual Progress Report for October 1991 through March 1992, ORNL Technical Memorandum, Martin Marietta Energy Systems, Inc., Oak Ridge Natl. Lab., 1992

2. S. S. Suresh and J. R. Brockenbrough, "A Theory for Creep by Interfacial Flaw Growth in Ceramics and Ceramic Composites," *Acta Metall. Mater.* **38** (1), 55-68 (1990).

3. M. K. Ferber and M. G. Jenkins, "Evaluation of the Strength and Creep-Fatigue Behaviour of a HIPed Silicon Nitride," *J. Amer. Ceram. Soc.* **75** (9), 2453-62 (1992).

4. T. Ohji, Y. Yamauchi, W. Kanematsu, and S. Ito, "Cyclic Fatigue Strength of Engineering Ceramics at High Temperatures," *Nippon Seramikkusu Kyokai Gakujutsu Ronbunshi* **98** (10), 1063-69 (1990).

TOUGHENED CERAMICS LIFE PREDICTION

Jonathan A. Salem and Sung R. Choi (NASA Lewis Research Center)

Objective/Scope

The purpose of this research is to understand the room temperature and high temperature [≤ 1370°C (2500°F)] behavior of toughened ceramics as the basis for developing a life prediction methodology. A major objective is to understand the relationship between microstructure and mechanical behavior within the bounds of a limited number of materials. A second major objective is to determine the behavior as a function of time and temperature. Specifically, the room temperature and elevated strength and reliability, the fracture toughness, slow crack growth and the creep behavior will be determined for the as-manufactured material. The same properties will also be evaluated after long-time exposure to various high temperature isothermal and cyclic environments. These results will provide input for parallel materials development and design methodology programs. Resultant design codes will be verified.

Technical Highlights

There are several ways of determining fatigue parameters. Dynamic, static or cyclic fatigue loading can be applied to smooth specimens or to precracked fracture mechanics specimens in which the crack velocity measurements are made directly. A considerable number of studies have been carried out to characterize fatigue behavior of silicon nitride ceramics using the testing methods mentioned above [1-7]. Although the reported results agree to some degree, there remains uncertainty and disagreement among the testing methodologies, depending on test materials and even on researchers.

In this study, high temperature fatigue behavior of a hot-pressed silicon nitride was determined at 1200 and 1300°C in air using three different loading conditions: dynamic and static loading for flexure beam specimens and static loading for dog-bone-shaped uniaxial tensile specimens. Finite element analysis was carried out for the tensile specimens to obtain stress distributions and to assure the appropriateness of the specimen configurations designed. The material was chosen because it exhibited moderate fatigue susceptibilities at high temperatures, enabling the comparison of fatigue lifetime prediction results from various testing methods.

EXPERIMENTAL METHOD

Material

The material used in this study was a hot-pressed silicon nitride

containing 8% Y_2O_3, fabricated in 1979 by Norton Company. The room temperature basic physical and mechanical properties of the material are shown in Table 1. The material exhibited a slightly bimodal grain structure of large elongated and fine equiaxed grains. This bimodal grain structure resulted in a high fracture toughness ($K_{IC} \approx 7$ MPa$\sqrt{m}$) as well as a rising R-curve [8], typical to most in-situ toughened silicon nitrides with elongated grain structure.

Table 1. Physical and mechanical properties of NCX 34 silicon nitride at room temperature [8, 9]

Young's[1] Modulus E(GPa)	Hardness[2] H (GPa)	Density[3] (g/cm^3)	Fracture Toughness[4] K_{IC}(MPa$\sqrt{m}$)	RT Strength[5] (MPa)
296	14.5±0.6	3.37	6.90±0.56	805±50

Notes:
1. By strain gaging
2. By Vicker's microhardness indenter
3. By buoyancy method
4. By SEPB method
5. Specimens with 6.35 mm by 3.17 mm in width and height, respectively; 9.525/19.05 mm in inner and outer spans in four-point flexure [9].

Test Procedures

Dynamic and static fatigue testing for the as- machined flexure beam specimens was conducted in ambient air at 1200 and 1300°C using a SiC four-point bend fixture in an electromechanical testing machine. The inner and outer span of the test fixture were 10 mm and 30 mm, respectively. The nominal dimensions of the rectangular test specimens were 3 mm by 7 mm by 35 mm, respectively, in height, width, and length. Four loading rates of 4.2 to 4200 N/min were used in the dynamic fatigue testing, resulting in the corresponding stressing rates of 2 to 2000 MPa/min. Stress levels applied in the static fatigue tests were 250 to 500 MPa at 1200°C, and 75 to 400 MPa at 1300°C, respectively. The number of the test specimens in the dynamic fatigue testing was four at each loading rate per temperature; whereas, the number of the test specimens in the static fatigue testing was 14 and 25, respectively, at 1200 and 1300°C. Each test specimen was preloaded with 20 N to maintain good alignment relative to the test fixture, and held at the test temperature for 20 min prior to testing.

The tensile fatigue behavior was investigated at temperatures of 1200 and 1300°C in air. The dog-bone-shaped tensile test specimens, similar to those used in creep testing measurements by Wiederhorn et al. [10], were utilized for this testing. A test specimen with strain gages attached is shown in Fig. 1. The dimensions of the test specimens were 2.5 mm by 2.5 mm by 20 mm in cross section and gage length, respectively. To minimize the degree of misalignment of the tensile test specimen, the loading pin holes of each test specimen were tapered toward the center so that load was applied to the center of the specimen, as suggested by Carrol et al [11]. With this tapered pin hole configuration and careful specimen mounting, it was possible to achieve less than two percent misalignment at a stress of 150 MPa.

The tensile specimens were preloaded with 35 N at room temperature and heated to the test temperature. Each test specimen was kept at the test temperature for about 20 min prior to applying the full test load. The testing was conducted in dead weight creep machines. A total of 15 test specimens were used at 1200°C with a nominal applied load range of 80 to 200 MPa; whereas, at 1300°C a total of 16 were used with applied stresses from 50 to 100 MPa. A finite element analysis of the test

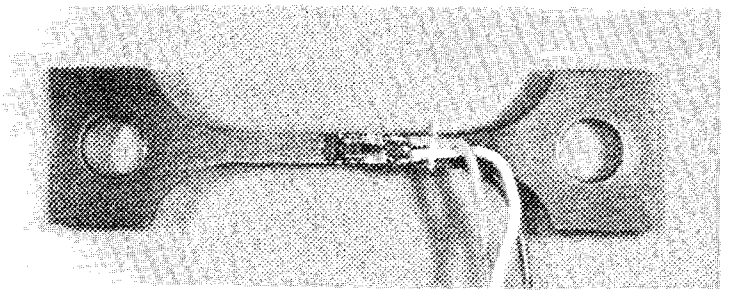

Figure 1. A dog-bone-shaped tensile test specimen with strain gages attached.

specimen has shown that high stress, similar in magnitude to those occurring in the gage section, occurred around the loading pin hole due to the stress concentration. Hence, particular care was taken to minimize the possibility of machining-induced damage around the tapered pin-hole. Every pin hole was carefully diamond polished with a specially designed hand tool. Also, all the surfaces and edges of each as-machined test specimen were carefully hand-sanded to minimize any machining damage.

Finite Element Analysis of Tensile Specimens

The finite element model for the tensile test specimen consisted of 1040 HEX/20 element with a total of 5747 nodes. The model was analyzed using the MSC/NASTRAN finite element package. Linear static analysis was employed, with one eighth symmetry for simplicity. The specimen was loaded such that a specified uniform uniaxial tensile stress was present in the gage section. Three FORCE cards were used to apply the load. The load was applied to the one side of one element through the thickness. Since HEX/20 elements were used for the analysis, the load was divided into four parts. The outer nodes of the element received one part of the load each and the center node received two parts of the load. This load scheme was used to remain consistent with the element shape function formulations employed for the 20 node element [12].

Typical stress contours thus obtained are shown in Fig. 2, where σ_{zz} (principal stress along the specimen length) is plotted for one eighth symmetry of the specimen. This figure indicates that the maximum stress is present both at the gage section and at the pin hole (in the nine o'clock direction) due to the stress concentration. Note that the stresses in the neck region are always lower than that occurring in the gage section. Although the maximum stress occurs at the pin hole as well as at the gage section, the probability of failure is considerably higher at the gage section than at the pin hole since the volume or surface area stressed under the maximum stress is much greater at the gage section than

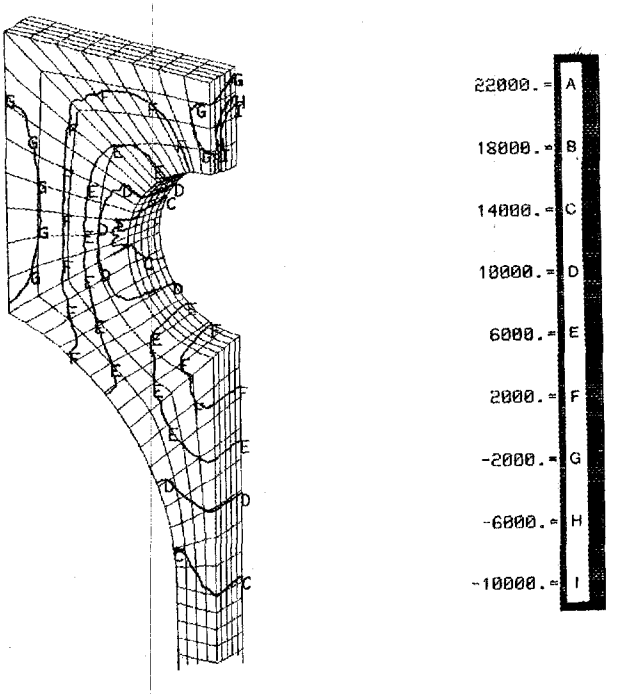

Figure 2. Contours of principal stress along specimen length obtained from finite element analysis (one eighth symmetry).

at the pin hole. However, every attempt was made to minimize machining-induced damage.

RESULTS AND DISCUSSION

For most ceramics and glasses, slow crack growth can be expressed by the empirical relation

$$v = A\ [K_I/K_{IC}]^n \tag{1}$$

where A and n are the fatigue parameters associated with material and environment, K_I is the mode I stress intensity factor, and K_{IC} is fracture toughness. For dynamic fatigue testing which employs constant loading ($\dot{P}$) or constant stressing rate ($\dot{\sigma}$), the corresponding fatigue strength, σ_f, is expressed [13]

$$\sigma_f = [B\ (n+1)\ S_i^{n-2}]^{1/n+1}\ \dot{\sigma}^{1/n+1} \tag{2}$$

where $B = 2/[AY^2(n-2)K_{IC}^{n-2}]$ with Y being crack geometry factor and S_i is the inert strength. The fatigue constants n, B and A can be obtained from the intercept and slope, respectively, of the linear fit of Log σ_f versus Log $\dot{\sigma}$. In the same way, for static fatigue testing where constant stress is applied, the time to failure (t_{fs}) can be derived easily in terms of applied stress (σ) as follows [1]

$$t_{fs} = [B\ S_i^{n-2}]\ \sigma^{-n} \tag{3}$$

Likewise, static fatigue parameters B and n can be evaluated by a linear regression analysis of the static fatigue curve when time to failure (Log t_{fs}) is plotted against applied stress (Log σ). However, it should be noted that there are several statistical approaches to estimate the fatigue parameters from dynamic and static fatigue data [14]. Currently, statistical approaches such as the median value, the bivariant and trivariant analyses are being developed and reviewed at NASA LeRC for incorporation in the CARES-Life code.

The relationship in fatigue life between dynamic and static fatigue is [15]

$$t_{fs} = t_{fd}/(n+1) \tag{4}$$

where t_{fd} is the time to failure in dynamic fatigue, which corresponds to $t_{fd} = \sigma_f/\dot{\sigma}$. By substituting t_{fs} in Eq. (4) into Eq. (3) with $\sigma = \sigma_f$, the dynamic fatigue curve can be converted into an equivalent static fatigue curve as follows:

$$t_{fd} = \alpha\ \sigma_f^{-n} \tag{5}$$

where α is the value associated with B, n and S_i.

Dynamic and Static Fatigue in Bending

A summary of the dynamic fatigue results at 1200 and 1300°C in air is presented in Fig. 3. The solid lines in the figure represent the best-fit lines based on Eq. (2). The decrease in fatigue strength with decreasing stressing rate, which represents fatigue susceptibility, was evident at both temperatures. The fatigue parameter (n) was determined to be n = 16.0 and 15.0 at 1200 and 1300°C, respectively, from a linear regression of Log σ_f versus Log $\dot{\sigma}$. Fractographic analysis of the failure surfaces revealed the presence of slow crack growth zones at the lower stressing rates, while no appreciable slow crack growth was obtained at higher stress rates.

The results obtained from the static fatigue tests at 1200 and 1300°C in air are shown in Fig. 4. The arrow marks in the figure represent the specimens that did not break before about 600 hr. Also, the solid lines in the figure represent the best-fit lines based on Eq. (3). The fatigue constant n was evaluated to be n = 20.7 and 15.0 at 1200 and 1300°C, respectively. The fatigue constant n = 15-21 thus obtained agrees reasonably well with the value of n = 15-16 determined from the dynamic fatigue testing. A value of n = 12 was reported previously, obtained from static fatigue with MOR bars at 1400°C in air [16].

It is important to note that appreciable creep deformation occurred for the specimens subjected at 1300°C to the lowest stressing rate in the

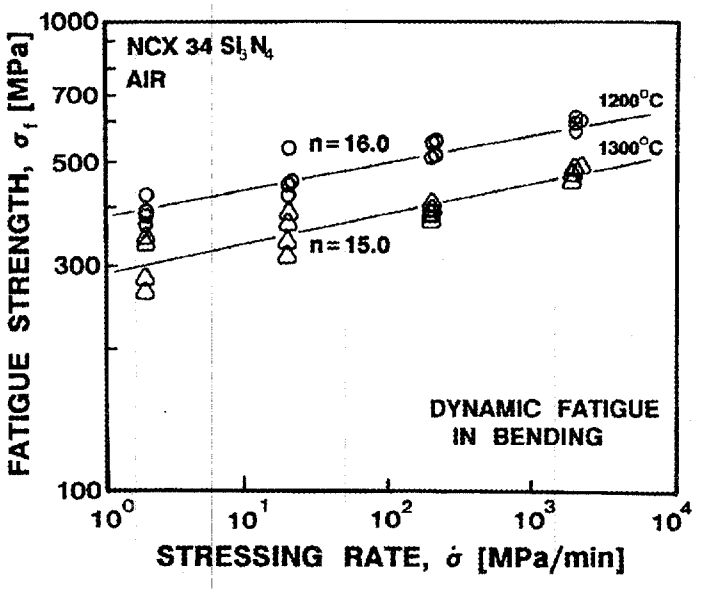

Figure 3. Results of dynamic fatigue testing in bending of NCX 34 silicon nitride at 1200 and 1300°C in air.

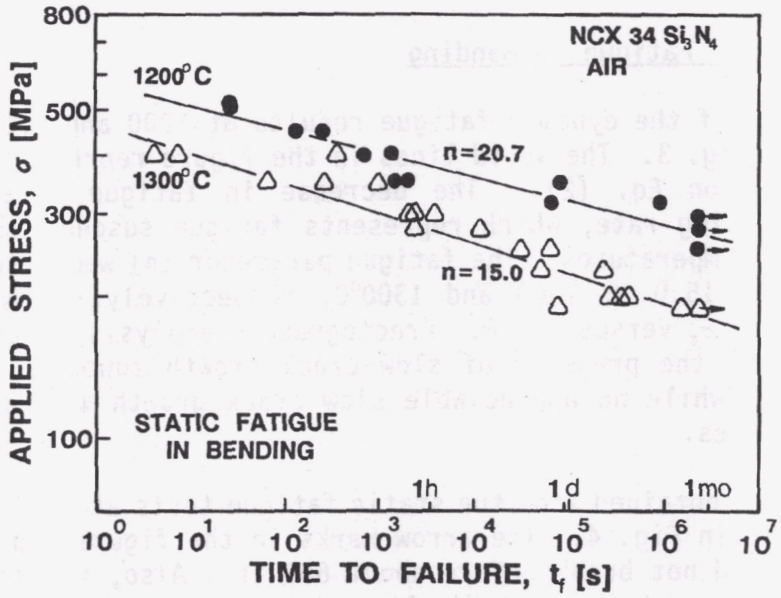

Figure 4. Results of static fatigue testing in bending of NCX 34 silicon nitride at 1200 and 1300°C in air.

dynamic fatigue testing and to the lowest applied stress in the static fatigue testing. Fracture surfaces of the specimens tested at different stressing rates or applied stresses showed that slow crack growth zones dominate failure as stressing rate or applied stress decreases. One complication evident from the fractography is the shape of the crack developed, especially in the specimens subjected to long time to failure. The cracks, though initially half-pennies in configuration, develop into corner and straight-through cracks as the crack size approaches the specimen size, as shown in Fig. 5. This may affect the values of the

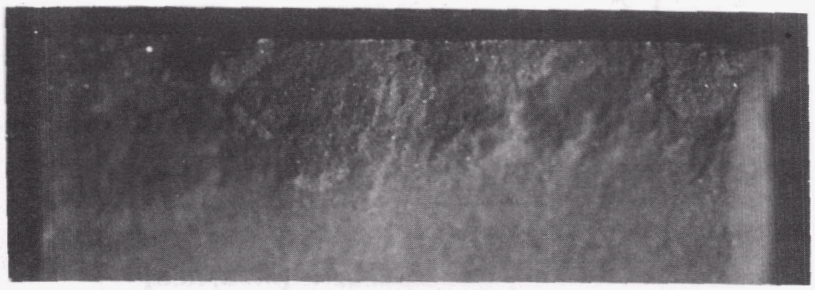

Figure 5. Fracture surface of a specimen subjected to static fatigue in bending; σ = 190 MPa and t_f = 456 hr.

measured fatigue parameters, due to changes in crack geometry and net section stress. Further, enhanced creep at high temperature can result in neutral axis shift attributed to asymmetric creep behavior between the compression and tension sides of a flexure beam specimen [17]. This neutral axis shift may affect the stress distribution and possibly change the fatigue parameters.

Static Fatigue in Tension

Some of the uniaxial tensile specimens failed from the loading pin holes. This undesirable pin-hole failure was found to be associated with machining damage, which was minimized later by careful hand polishing with diamond compound around the tapered pin holes. Another undesirable failure associated with machining damage occurred at the intersection of the straight gage section and the radius of curvature of the neck region, where a small surface discontinuity (damage) existed. The typical gage section and intersection failures are shown in Fig. 6. This neck region failure was also minimized by careful hand polishing around the intersections with SiC sand paper.

A summary of the uniaxial tensile fatigue results obtained at 1200 and 1300°C in air is presented in Fig. 7. The solid lines in the figure represent the best-fit lines obtained by a linear regression analysis of Log t_f versus Log σ. It should be noted that specimens failed from the pin holes and neck region (marked with vertical arrows) were excluded in the regression analysis. The fatigue parameter n was determined to be n = 10.0 and 10.6 at 1200 and 1300°C, respectively. This fatigue parameter of $n \approx 10$ is somewhat lower than that ($n \approx 15$-21) from the dynamic and static

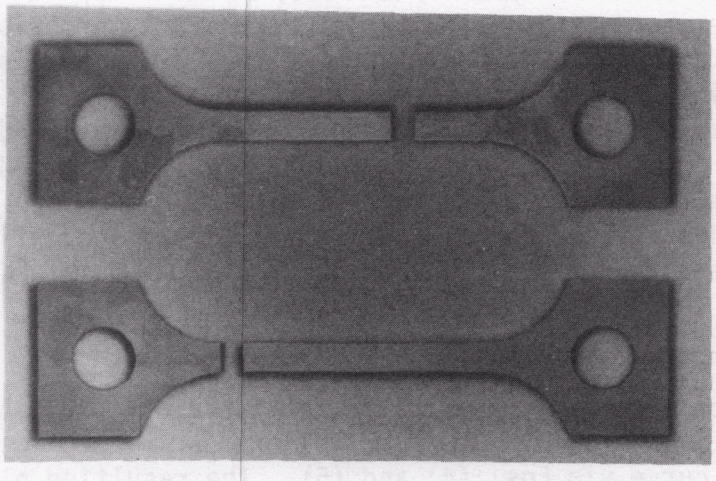

Figure 6. Fractured uniaxial tensile test specimens: (a) desirable gage section failure; (b) undesirable neck region failure.

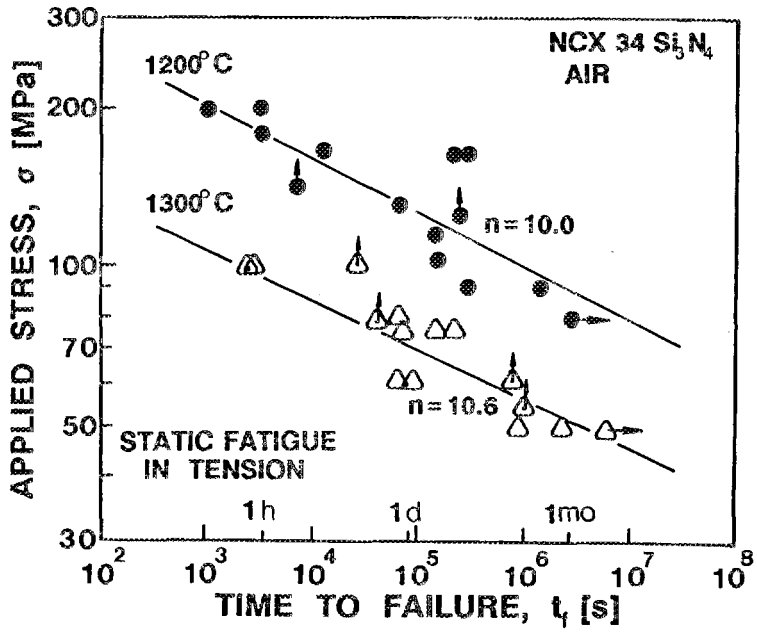

Figure 7. Results of static fatigue testing in uniaxial tension of NCX 34 silicon nitride at 1200 and 1300°C in air.

fatigue testing with the flexure beam specimens. By contrast, the parameter of $n \approx 10$ determined for the smooth (as-machined) specimens is higher than the value of $n = 5.2$ obtained for the uniaxial tensile specimens with Knoop indent cracks by Henager and Johns [18].

At high applied stress, failure was usually (but not always clearly) associated with slow crack growth; whereas, at lower applied stress creep-induced failure was dominant. Multiple creep crack formation in the gage section was typically observed for the specimens failed at lower stresses. Fig. 8 shows the fracture surfaces of specimens failed at two different applied stresses of $\sigma = 100$ and 50 MPa. The formation of a dominant crack is evident for the specimen failed at 100 MPa with $t_f = 42$ min (volume failure). However, a clear fracture origin was not readily discernable from the specimen failed at 50 MPa with $t_f = 682$ hr, suggesting that crack coalescence associated with creep damage caused specimen failure.

Comparison of Fatigue Parameters

Comparison of dynamic and static fatigue behavior in bending can be evaluated by converting the dynamic fatigue data into a corresponding static fatigue curve via Eqs. (4) and (5). The resulting plots are shown in Fig. 9, where the converted dynamic fatigue data are compared with the static fatigue data. Also included in the figure are the data obtained

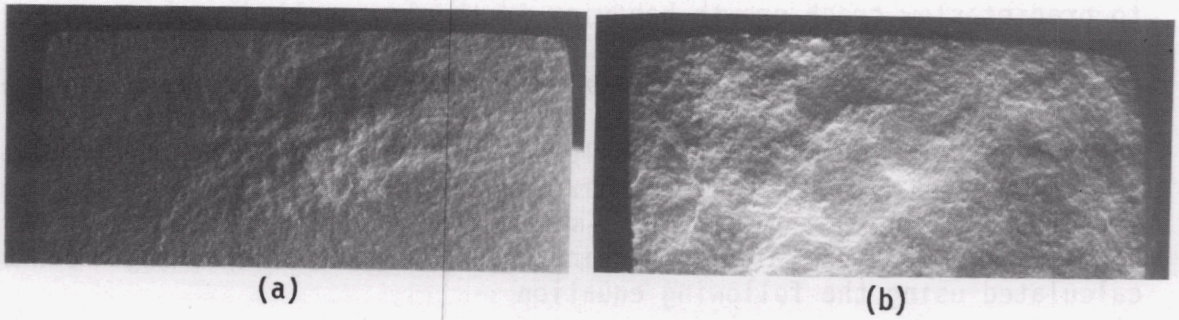

Figure 8. Fracture surfaces of specimens subjected to static fatigue in uniaxial tension: (a) σ = 100 MPa; t_f = 42 min; (b) σ = 50 MPa; t_f = 682 h.

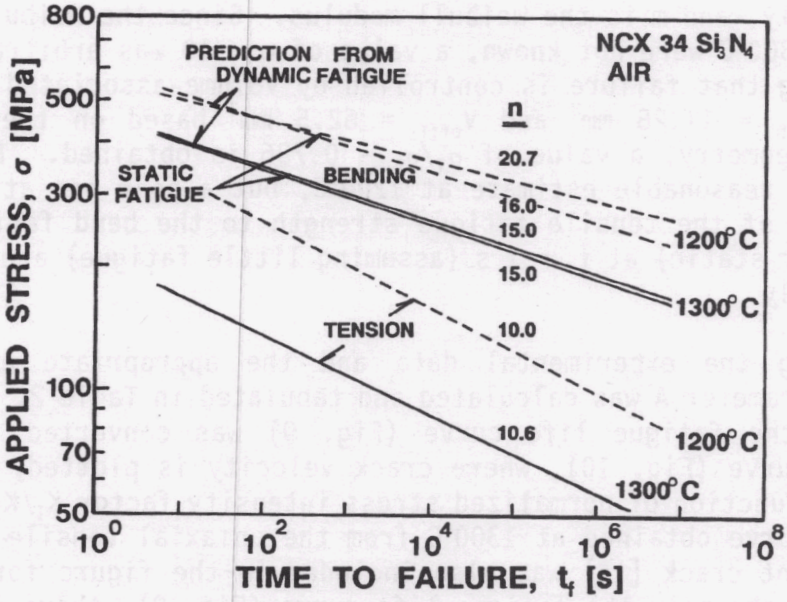

Figure 9. Comparison of fatigue life curves obtained from dynamic and static bend fatigue and tensile static fatigue for NCX 34 silicon nitride at 1200 and 1300°C in air.

from the uniaxial tensile fatigue testing.

Overall agreement between dynamic and static fatigue in bending is reasonably good, notwithstanding a little variation, especially at 1200°C. Therefore, based on these results it is possible to obtain slow crack growth parameters from either static or dynamic fatigue testing techniques, as observed previously for Ceralloy 147A silicon nitride [19]. The dynamic fatigue testing is preferable since the time to failure is

shorter in dynamic fatigue than in static fatigue. However, care should be taken when an extrapolation based on the dynamic fatigue data is made to predict slow crack growth behavior in the low applied stress regime.

The difference between the tensile static fatigue and the dynamic or static bend fatigue is much larger as seen in Fig. 9. The difference in fatigue strength between the tensile and bend loading is probably due to the difference in effective volume or surface area between the two specimen configurations (dog-bone-shaped tensile specimens and flexure beam specimens). The ratio of bending strength to tensile strength can be calculated using the following equation

$$\sigma_T/\sigma_B = [A_{effB}/A_{effT}]^{1/m} \quad \text{or}$$

$$= [V_{effB}/V_{effT}]^{1/m} \tag{6}$$

where A_{eff} and V_{eff} are effective surface area and effective volume, respectively, and m is the Weibull modulus. Since the Weibull modulus at 1200 and 1300°C were not known, a value of $m \approx 10$ was arbitrarily chosen. By assuming that failure is controlled by volume-associated failure, and taking $V_{effB} = 11.28$ mm^3 and $V_{effT} = 62.5$ mm^3 based on the fixture and specimen geometry, a value of $\sigma_T/\sigma_B = 0.786$ is obtained. This ratio of 0.786 is a reasonable estimate at 1200°C, but a poor one at 1300°C since the ratios of the tensile fatigue strength to the bend fatigue strength (dynamic or static) at $t_f = 1$ s (assuming little fatigue) are 0.7 and 0.4, respectively.

Using the experimental data and the appropriate equation, the fatigue parameter A was calculated and tabulated in Table 2. By using the A value, the fatigue life curve (Fig. 9) was converted into a crack velocity curve (Fig. 10), where crack velocity is plotted, based on Eq. (1), as a function of normalized stress intensity factor K_I/K_{IC}. The crack velocity curve obtained at 1300°C from the uniaxial tensile fatigue with Knoop indent crack [18] was also included in the figure for comparison. As already shown in the fatigue life curve (Fig. 9), there is reasonably good agreement between the dynamic and static fatigue in bending, but a large discrepancy between the uniaxial tension and bend fatigue data. Fig. 10 also shows that in uniaxial tensile loading the fatigue susceptibility of the indent cracks was much greater than that of the smooth, as observed previously for the GN-10 silicon nitride material at 1200°C [5].

The difference in fatigue susceptibility of smooth and knoop precracked specimens may be due to the nature of the cracks used or the method of parameter estimation: The dynamic and static methods determine parameters empirically from stress and time-to-failure data that results from inherent defects that develop into cracks, grow and cause failure; whereas fracture mechanics methods, such as the knoop indent, attempt to directly observe and track the length of an initially sharp, well

Table 2. Summary of fatigue parameters of NCX 34 silicon nitride at 1200 and 1300°C in air.

Loading and geometry	Temperature (°C)	n	B (MPa^2min)	A (m/min)
Dynamic in Bending	1200 1300	16.0 15.0	14.702 10.269	0.194 0.300
Static in Bending	1200 1300	20.7 15.0	11.148 11.697	0.191 0.262
Static in Tension	1200 1300	10.0 10.6	16.242 11.126	0.319 0.417
Static in Tension with indent cracks [18]	1300	5.2	-	-

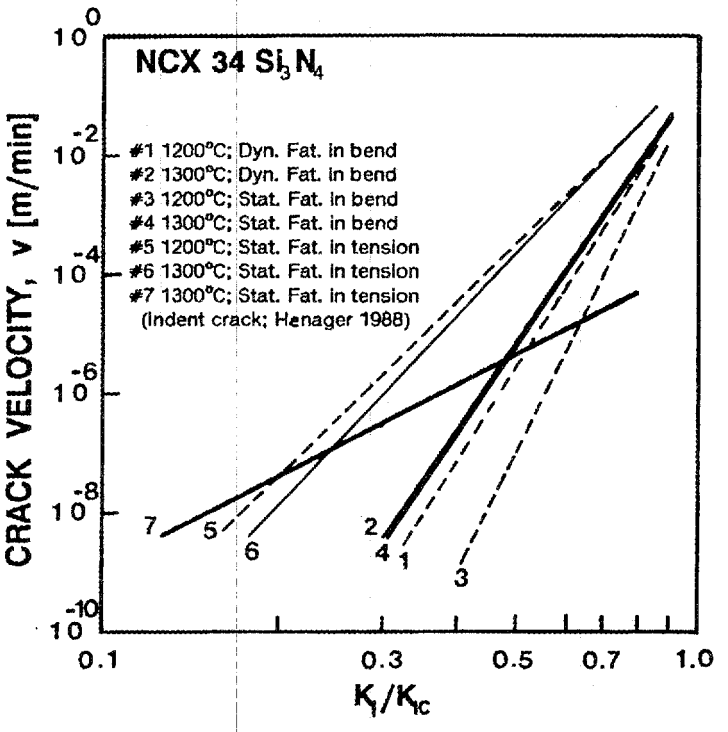

Figure 10. Summary of crack velocity curves obtained from different testing methods for NCX 34 silicon nitride at 1200 and 1300°C in air.

developed crack.

These results indicates that there is no unique fatigue testing methodology, implying that a variety of fatigue loading cycles, specimen configurations and flaw systems should be used to thoroughly characterize fatigue behavior of ceramic components that will have multiaxial stresses. One of the important results obtain from this fatigue testing study is that the dog-bone-shaped tensile specimens that have been used primarily in creep studies of ceramics can be applied to high-temperature tensile fatigue life (stress rupture) testing.

CONCLUSIONS

(1). The high-temperature fatigue parameters determined from dynamic and static fatigue bend data are in good agreement. Fatigue parameters were n = 15 to 20.

(2). A discrepancy exists between bend (dynamic or static) fatigue and uniaxial tensile fatigue, resulting in more fatigue susceptibility for uniaxial tension.

(3). Creep-associated failure became dominant as applied stress or stressing rate decreased. In this case, neutral axis shift via asymmetric creep deformation may have affected the stress distribution of flexure specimens, and presumably changed the fatigue parameters, which were based on an elastic stress solution. The use of tensile specimens is thus strongly preferable in this case.

(4). Fatigue behavior should be evaluated with a variety of stress states, loading cycles and flaw (inherent or artificial) configurations to ensure accurate life prediction parameters.

REFERENCES

[1] Ritter, J. E., "Engineering Design and Fatigue Failure of Brittle Materials," pp 661-686 in Fracture Mechanics of Ceramics, Vol. 4, Bract, R. C., Hasselman, D. P. H., and Lange, F. F. Eds., Plenum Publishing Co., NY, 1978.

[2] Trantina, G. G., "Strength and Life Prediction for Hot-Pressed Silicon Nitride," Journal of American Ceramic Society, Vol. 62, 1979, pp 377-380.

[3] Govila, R. K., "Uniaxial Tensile and Flexural Stress Rupture Strength of Hot-Pressed Si_3N_4," Journal of American Ceramic Society, Vol. 65, 1982, pp 15-21.

[4] Quinn, G. D., and Quinn, J. B., "Slow Crack Growth in Hot-Pressed Silicon Nitride," pp 603-636 in Fracture Mechanics of Ceramics, Vol. 6, Bract, R. C., et al. Eds., Plenum Press, NY, 1983.

[5] Choi, S. R., and Salem, J. A., "Comparison of Dynamic Fatigue Behavior Between SiC Whisker-Reinforced Composite and Monolithic Silicon Nitrides," NASA TM 103707, NASA Lewis Research Center, Cleveland, OH, 1991.

[6] Chuck, L., McCullum, D. E., Hecht, N. L., and Goodrich, S. M., "High-Temperature Tension-Tension Cyclic Fatigue for a Hipped Silicon Nitride," Ceramic Engineering and Science Proceedings, Vol 12, 1991, pp 1509-1523.

[7] Evans, A. G., and Wiederhorn, S. M., "Crack Propagation and Failure Prediction in Silicon Nitride at Elevated Temperatures," Journal of Materials Science, Vol. 9, 1974, pp 270-278.

[8] Salem J. A., and Choi, S. R., Bimonthly Progress Report, CTAHE Project, W.B.S. Element 3.2.1.7. 11-12/1991.

[9] Sanders, W. A., unpublished work, NASA Lewis Research Center.

[10] Wiederhorn, S. M., Roberts, D. E., Chuang, T.-Z., and Chuck, L., "Damage-Enhanced Creep in a Siliconized Silicon Carbide: Phenomenology," Journal of American Ceramic Society, Vol. 71, 1988, pp 602-608.

[11] Carrol, D. F., Wiederhorn, S. M., and Roberts, D. E., "Technique for Tensile Creep Testing of Ceramics,"Journal of American Ceramic Society, Vol. 72, 1989, pp 1610-1614.

[12] Bathe, K. J., Finite Element Procedures in Engineering Analysis, Prentice-Hall, Englewood Cliffs, NJ, 1982.

[13] Evans, A. G., "Slow Crack Growth in Brittle Materials under Dynamic Loading Conditions," International Journal of Fracture, Vol. 10, 1974, pp 1699-1705.

[14] Jakus, K., Coyne, D. C., and Ratter, J. E., "Analysis of Fatigue Data for Lifetime Prediction for Ceramic Materials," Journal of Materials Science, Vol. 13, 1978, pp 2071-2080.

[15] Davidge, R. W., McLaren, J. R., and Tappin, G., "Strength-Probability-Time (SPT) Relationship in Ceramics," Journal of Materials Science, Vol. 8, 1973, pp 1699-1705.

[16] Larsen, D. C., and Adams, J. W., "Property Screening and Evaluation of Ceramic Turbine Materials," AFWAL-TR-83-4141, Wright Aeronautical Laboratories, Wright-Patterson AFB, OH, 1984.

[17] Chuang, T.-J., and Wiederhorn, S. M., "Damage-Enhanced Creep in a Siliconized Silicon Carbide: Mechanics of Deformation," Journal of American Ceramic Society, Vol. 71, 1988, pp 595-601.

[18] Henager, C. H., and Jones, R. H., "Environmental Effects Slow Crack Growth in Silicon Nitride," Ceramic Engineering and Science Proceedings

[19] Salem, J. A., and Choi, S. R., Ceramic Technology Project Semiannual Progress Report for April 1991 through September 1991, pp 305-319, ORNL/TM-11984, Oak Ridge National Laboratory, 1992.

Status of Milestones

Milestone are on time.

Publications

J.A. Salem, J.L. Shannon, Jr., and M.G. Jenkins, "Some Observations in Fracture Toughness and Fatigue Testing with Chevron-Notch Specimens," in Chevron-Notch Fracture Test Experience, ASTM STP 1172, K.R. Brown and F.I. Baratta, Eds., 1993.

Life Prediction Methodology

P. K. Khandelwal (Allison Gas Turbine Division, General Motors Corporation)

Objective/Scope

The objective of this project is to develop and demonstrate the necessary nondestructive examination (NDE) technology, materials data base, and design methodology for predicting useful life of structural ceramic components of advanced heat engines. The analytical methodology will be demonstrated through confirmatory testing of ceramic components subject to thermal-mechanical loading conditions similar to those anticipated to occur in actual vehicular service. The project addresses fast fracture, slow crack growth, creep, and oxidation failure modes.

Technical Highlights

Data Base Development

Flexural Testing

The oxidation testing was completed during this reporting period. Information was generated for a temperature range between 1000°C to 1400°C from 1 to 500 hours in static air using the Type-B (3 x 4x 50 mm) modulus-of-rupture (MOR) specimens. Figure 1 shows that the oxide layer thickness increases as a function of temperature and time. The rate of oxidation is accelerates above 1200°C after 500 hours. This may be due to the presence of impurities such iron, calcium, etc. which increase the diffusion rates of various species. Fractographic analysis revealed very few pits on the surface of the specimens. X-ray diffraction analysis of typical specimens has been completed. Preliminary analysis has shown the presence of SiO_2, alpha and beta $Y_2Si_2O_7$, and $10Y_2O_3.9SiO_2.Si_3N_4$ phases depending on the time and temperature conditions. Further analysis of the data is in progress.

The effect of inert (Argon) environment as function of time (10 and 110 hours) and temperature (1000°C, 1200°C, 1400°C) on the MOR strength was studied at ORNL under an User agreement. The work was directed by Dr. M. Ferber at ORNL. The average measured strength after 10 and 110 hours exposure at 1000C was 833.28 MPa and 954.34 MPa, respectively. The average measured strength at 1200°C after exposure of 10 and 110 hours was 674.51 MPa and 817.12 MPa, respectively. The average measured strength at 1400°C after exposure of 10 and 110 hours was 701.17 MPa and 670.93 MPa, respectively. Scanning electron microscopy (SEM) analysis of typical specimens, conducted at ORNL as User, indicated that surface or near surface flaws generally controlled the strength.

Slow Crack Growth

Dynamic fatigue studies were conducted to determine the slow crack growth (SCG) parameter "N" both at 1200°C and 1400°C. Figure 2 shows that the PY6 hip'ed silicon nitride material degrades relatively slowly with N=33 at 1200°C and N=16 at 1400°C. SEM analysis of these specimens is in progress. Dynamic fatigue studies are also being conducted both in air and argon at ORNL-HTML under the direction of Dr. M. Ferber.

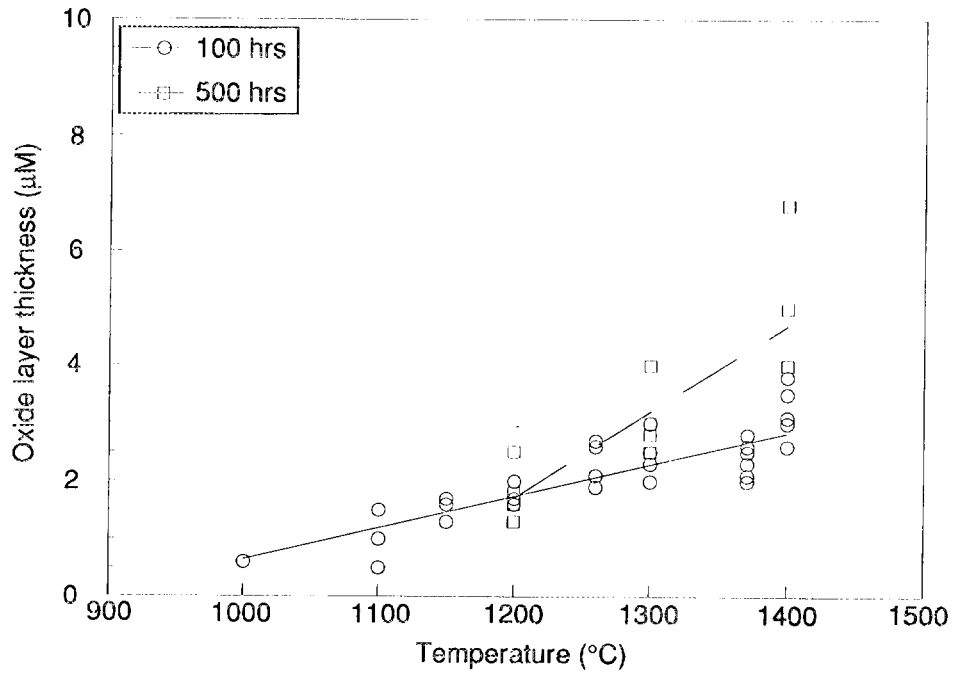

Figure 1. Oxidation behavior of injection molder HIPed silicon nitride PY6 in air.

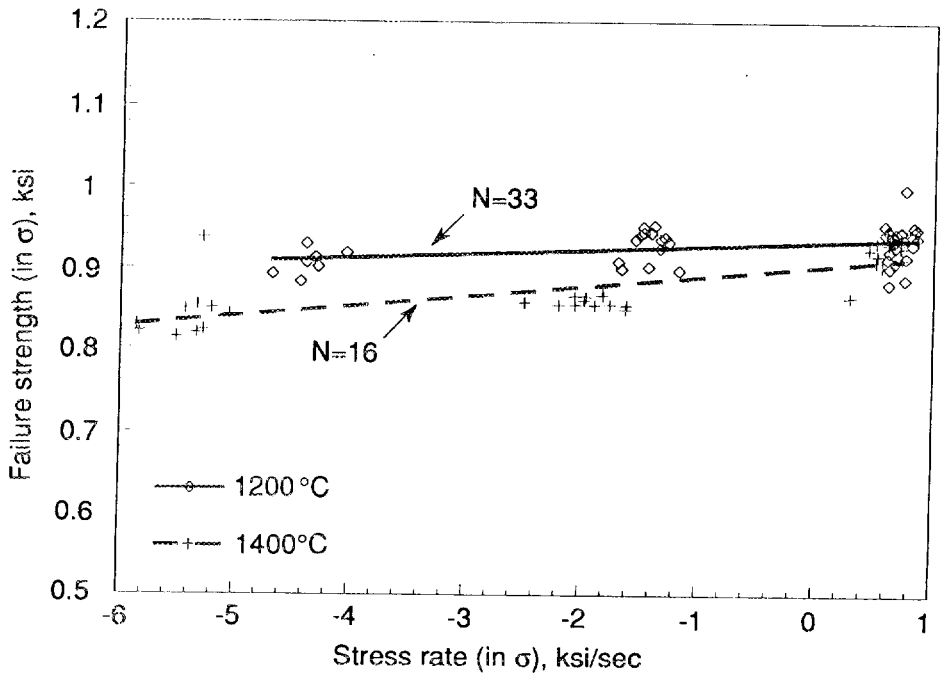

Figure 2. Dynamic fatigue behavior of PY6 material at elevated temperatures.

Fracture Toughness (K_{Ic})

Fracture toughness of the PY6 hip'ed silicon nitride was measured using chevron notch (both in 3 point and 4 point loading configuration), controlled flaw, and diametral compression disk methods to compare the measured values by various techniques. Chevron notch specimens were fabricated using the standard MOR bar 3 x 4 x 50 mm in dimensions. The notch testing was conducted at two laboratories (1) Oak Ridge National Laboratory (ORNL) in 3-point loading with a span of 40mm at 10 micron/min stroke speed (2) NASA-Lewis Research Center in 4-point loading with a outer span of 40mm and inner span of 20mm at 50 micron/min stroke speed. Both the loading conditions resulted in stable crack extension. Table I summarizes the results of the measured room temperature fracture toughness by various techniques. The calculated K_{Ic} obtained by the different methods was within $\pm$5% of each other.

Fracture toughness was measured at elevated temperatures up to 1400°C at ORNL using the chevron-notch method as described in Figure 3. The average K_{Ic} value decreased up to 1200°C to about 4.8 MPa$\sqrt{m}$ from the room temperature value of 6.4 MPa$\sqrt{m}$, but increased back to 6.4 MPa$\sqrt{m}$ both at 1300°C and 1400°C. This is believed to be due to creep and viscous softening of the grain boundary phase. Fractographic analysis is currently in progress to identify the failure mechanisms.

Uniaxial Tensile Testing (Button-Head)

Fast fracture uniaxial tensile testing of button-head specimens continued during this reporting period at Southern Research Institute (SoRI) at elevated temperatures. One hundred seventy (170) specimens have been tested to date at a loading rate of 600 KSI/Min (69 MPa/Sec). The average measured strength as a function of temperature is depicted in Figure 4. The measured room temperature strength is 59.2 KSI (408.2 MPa) which is statistically similar to the strength at 1000°C, 1200°C, and 1300°C. The strength, however, degraded at 1100°C to 48.3 KSI (MPa) and 44.3 KSI (305.4 MPa) at 1400°C. The majority of the specimens failed from volume defects which contain isolated or distributed iron or iron based compounds at the fracture controlling sites. Tensile testing is continuing at elevated temperatures at SoRI to develop a statistical data base.

Table I.
Comparison of room temperature fracture toughness (K_{Ic}) of PY6 HIP'ED silicon nitride.

METHOD	K_{Ic},(MPa$\sqrt{m}$)
Chevron Notch[1]	6.4
Chevron Notch[2]	6.8
Diametral Compression[3]	6.4
Controlled Flaw (Vicker's)[3]	
Microindentation	5.97
Strength	6.7

1 - Oak Ridge National Laboratory (ORNL)
2 - NASA-Lewis Research Center
3 - Battelle Research Laboratory, Columbus, Ohio

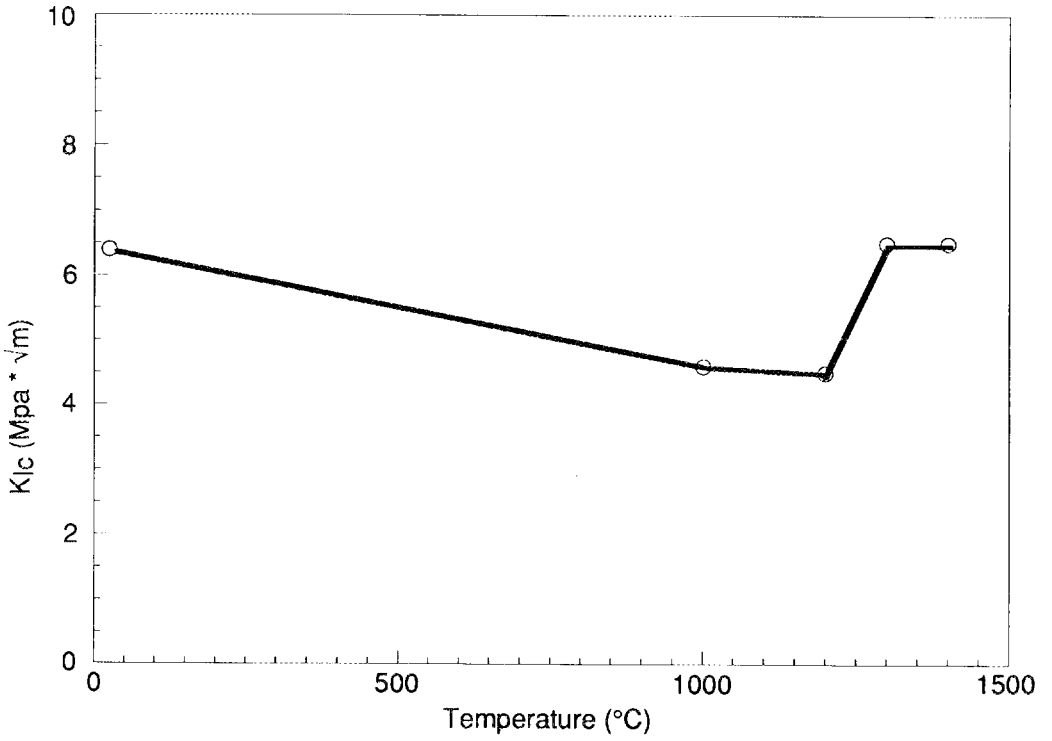

Figure 3. Elevated temperature fracture toughness of PY6 material using chevron-notch method.

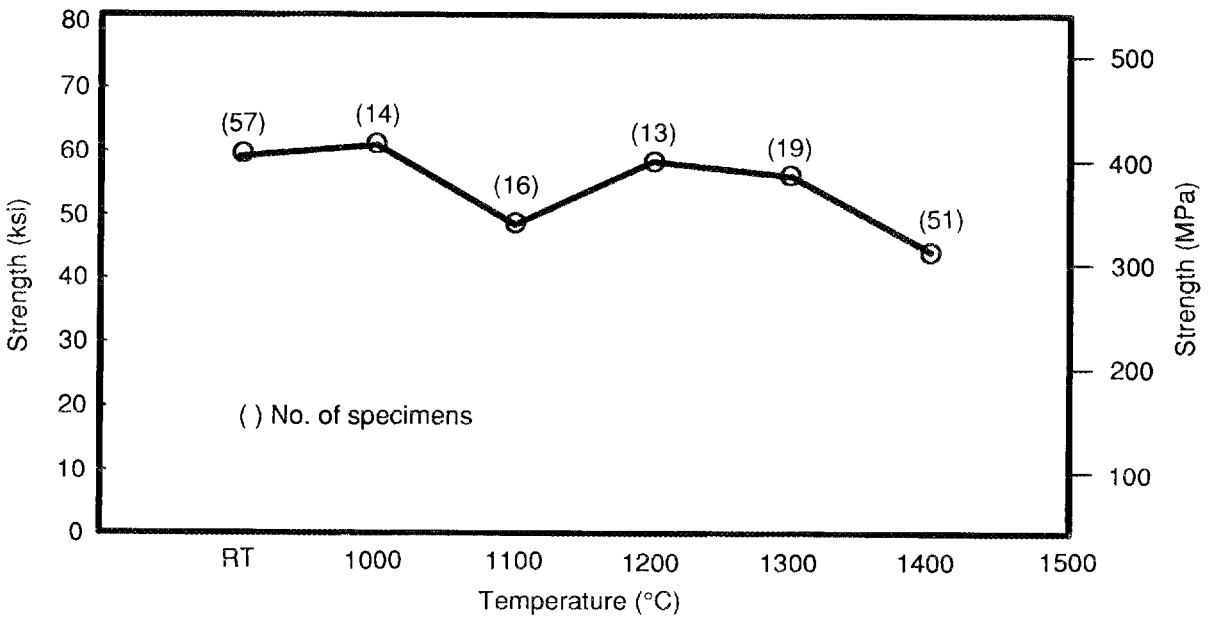

Figure 4. Uniaxial tensile strength of PY6 material as function of temperature using the button-head specimens.

Tensile creep and creep rupture behavior of button-head specimens between 1200 to 1400°C continued to be studied at SoRI during this reporting period. The results obtained to date are summarized in Table II. Experimental data indicates that the PY6 material may have stress rupture life of 100 hours or more (1) between 1200 to 1260°C at an applied stress of 175 MPa or less (2) at 1370°C at an applied stress of 95 MPa or less and (3) at 1400°C at an applied stress of about 75 MPa. A limited number of specimens are being tested to assess the scatter in the stress rupture life of the material. Scanning electron microscopy (SEM) continues to show void formation due to creep rupture phenomenon between 1300 and 1400°C. Both SEM and transmission electron microscopy (TEM) analysis is continuing at Oak Ridge National Laboratories (ORNL) under a User agreement with the High Temperature Materials Laboratory (HTML). Further testing and SEM analysis is also continuing at SoRI to better understand the creep behavior of this material.

Table II.
Summary of creep behavior of HIPed PY6 material.

SPECIMEN NUMBER	TEST TEMP °C	APPLIED STRESS (MPa)	TIME TO FAILURE t_f (HRS)	TOTAL STRAIN TO FAILURE $X10^{-6}$IN/IN
341A	1200	125	240.0*	530
635B	1200	150	232.0*	2710
517B	1200	160	360.0*	1730
636A	1200	175	389.0*	1240
454B	1200	177	0.008**	--
452A	1200	178	0.733	--
629A	1200	181	291.0***	--
514A	1200	185	0.009	610
448A	1200	190	0.159	140
460A	1200	200	2.06	1650
454A	1200	221	0.008	--
463B	1200	225	0.55	1650
453A	1200	250	0.48	1750
90A	1200	290	266.0**	1570
533B	1260	125	721.0***	--
488B	1260	150	0.82	490
515A	1260	175	1154.0*	3380
463A	1260	175	364.0	2010
486A	1260	177	26.24	1060
528A	1260	180	0.475	850
456A	1260	185	0.205	990

* Test stopped. Did not fail.
** Failed during loading.
** Clip-on flags slipped during test.
*** Temperature overshoot. Test stopped.

Table II. (cont).

SPECIMEN NUMBER	TEST TEMP °C	APPLIED STERSS (MPa)	TIME TO FAILURE t_f (HRS)	TOTAL STRAIN TO FAILURE $X10^{-6}$IN/IN
626B	1300	150	473.0*	3200
634B	1300	151	624.0*	2750
626A	1300	173	0.003*	--
491B	1300	175	0.003	740
188B	1300	175	772.0	5490
457B	1300	176	0.364	1130
514B	1300	178	0.826	1230
341B	1300	180	3.32	1710
343	1300	185	0.97	1930
77A	1300	200	0.69	1250
334B	1300	249	0.23	1670
201A	1300	275	0.0125	1100
464A	1370	66	617.0***	--
522B	1370	71	287.0	1470
84B	1370	74	287.0	7010
80A	1370	75	387.0	--
457A	1370	79	0.003 --	--
55A	1370	86	0.006	1470
521B	1370	91	106.0*	--
522A	1370	95	146.0*	480
535B	1370	95	74.0*	1340
490B	1370	100	0.61	1300
524A	1370	105	8.13	3770
192B	1400	75	844.0	10190
523B	1400	86	4.5	1160
195B	1400	100	12.97	3100
530B	1400	110	2.89	1310
171A	1400	125	1.96	2960
60A	1400	150	0.025	1380
340A	1400	175	0.016	1310
621A	1427	70	14.74****	--
525B	1500	90	0.84****	2350

* Test stopped. Did not fail.
** Failed during loading.
*** Clip-on flags slipped during test.
**** Temperature overshoot. Test stopped.

Nondestructive Evaluation (NDE)

Reference standards with volume holes were designed and fabricated to assess both the detectability and spatial resolution in various types of specimens. Both counter-bore and laser drilled holes were machined in MOR bars, rectangular 15 mm thick billets, and cylindrical button-head specimens. The specimens are currently being evaluated using microfocus x-ray, ultrasonic microscopy, and computer tomography. Ultrasonic imaging detected 500 micron diameter holes 13.5 mm below the surface using a 25 MHz flat broadband transducer. A similar specimen with 25 to 500 micron diameter (D) holes drilled at various diameters apart (1D, 2D, 3D, 5D) from each other was investigated using ultrasonic tomography at the Mayo Clinic, Rochester at 10 MHz frequency. The reconstructed image showed that individual 100 micron flaws were detected.

X-ray computed tomography studies were conducted at Chalk River Nuclear Laboratory, Canada using volumetrically dispersed iron inclusions of 100 micron size in a button-head cylindrical specimen. Four CT scans were measured, with image noise of 2%, 1.5%, 0.9%, and 0.6%. The average density values measured from these scans were, respectively, 3.32, 3.31, 3.30, and 3.30 gms/cc. Some distributed defects (density fluctuations) were detected which represent the varying number of inclusions in a voxel. The pattern of these density variations were observed in all the scans. One tensile specimen with no intentional defect was also examined. Three scans were measured, with image noise of 2%, 1.5%, and 1%. The average density values measured from these scans were 3.27, 3.26, and 3.26gm/cc., respectively. No distributed defects (i.e., long-range density gradients or clusters of defects) were detected; however, small, 1 to 3 pixel size defects were present, which might represent point defects (i.e, defects smaller than the pixel size). Based on these results, it is concluded that presence of iron inclusions changes the density by 1 to 2%. Further studies are continuing at Chalk River.

Analytical Methodology

The analysis during this reporting period focused on the reduction of the fast fracture data. Using the CARES program, Weibull constants were calculated for Surface, Table III, and Volume, Table IV, failures of MOR bar and button head (BH) tensile specimens.

Table III.
Surface Weibull constants.

MOR BARS		BH TENSILE SPECIMENS		
Temp C	$\sigma°$ (MPa)	m	$\sigma°$ (MPa)	m
20	652.3	6.34	804.5	4.93
1000	659.4	10.69	623.5	8.84
1100	527.3	13.93	440.7	5.55
1200	530.7	9.49	502.4	5.80
1300	517.1	13.03	538.0	6.37
1400	402.1	10.60	436.4	15.3

Table IV.
Volume Weibull constants.

	MOR BARS		BH TENSILE SPECIMEN	
Temp °C	σ° (MPa)	m	σ° (MPa)	m
1000			297.2	6.68
1000	508.9	14.06	250.4	4.38
1100			238.3	5.35
1200	390.5	11.21	349.4	9.98
1300	356.5	11.72	308.6	8.90
1400	341.7	13.45	206.3	4.99

The MOR bars typically had effective areas of about 0.97 square centimeters (0.15 square inches), and effective volumes of 0.0098 cubic centimeters (0.0006 cubic inches). The tensile specimens had areas of 8.38 square centimeters (1.30 square inches) and volumes of 0.98 cubic centimeters (0.60 cubic inches.) This means that the ratio of volume to area is eleven times greater in the tensile specimens than in the MOR bars. Not surprisingly, the test data shows that surface failures are far more common in MOR bars, Table V, while volume failures are more common in tensile specimens.

Based on the Weibull parameters generated from the MOR bars, an expected percentage of surface failures can be calculated for the tensile specimens, Table VI. The calculated and actual numbers appear to agree well at temperatures of 1200°C and 1300°C, but not at 1000°C and 1400°C. No values can be calculated at room temperature and 1100°C due to insufficient volume failures in the MOR bars.

Weibull constants from the MOR bars have been normalized to the tensile specimen effective areas and volumes, and plotted with the tensile data. Representative plots are shown in Figures 5 and 6. When the normalization is made, the probabilities of failure for the MOR bars are greater.

Table V.
Percent surface failures in MOR and tensile specimens.

	MOR BARS		BH TENSILE SPECIMEN	
TEMP C	# FAIL-URES	% SUR-FACE	# FAIL-URES	% SUR-FACE
20	80	100.0	66	6.1
1000	20	80.0	14	14.3
1100	20	95.0	16	43.8
1200	88	83.0	13	46.2
1300	32	78.1	19	21.1
1400	80	93.8	33	12.1

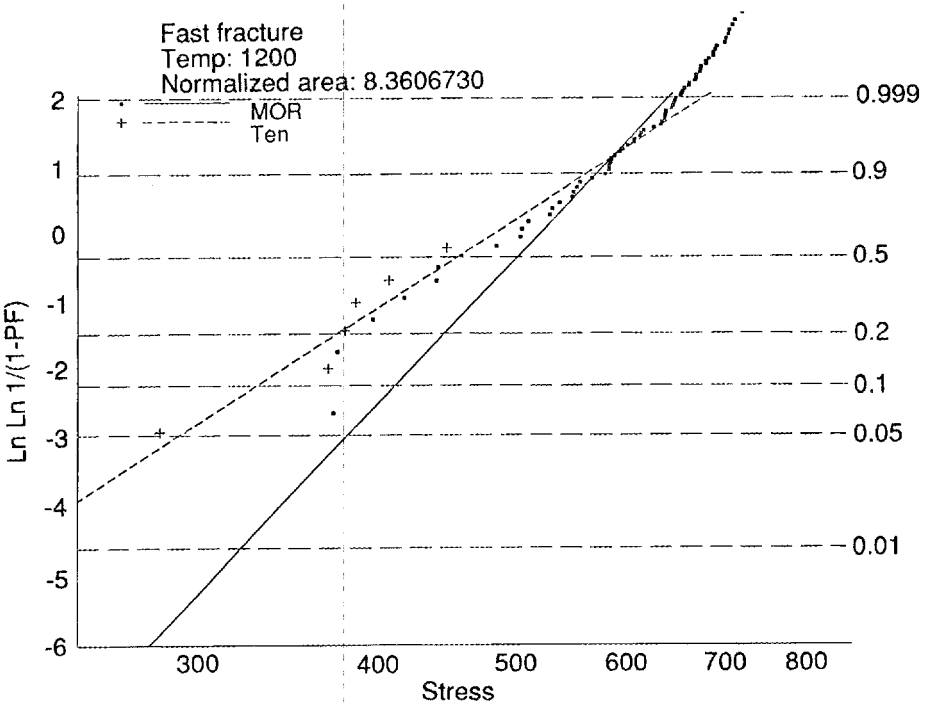

Figure 5. Weibull distribution of surface area normalized strengthof MOR and tensile specimens.

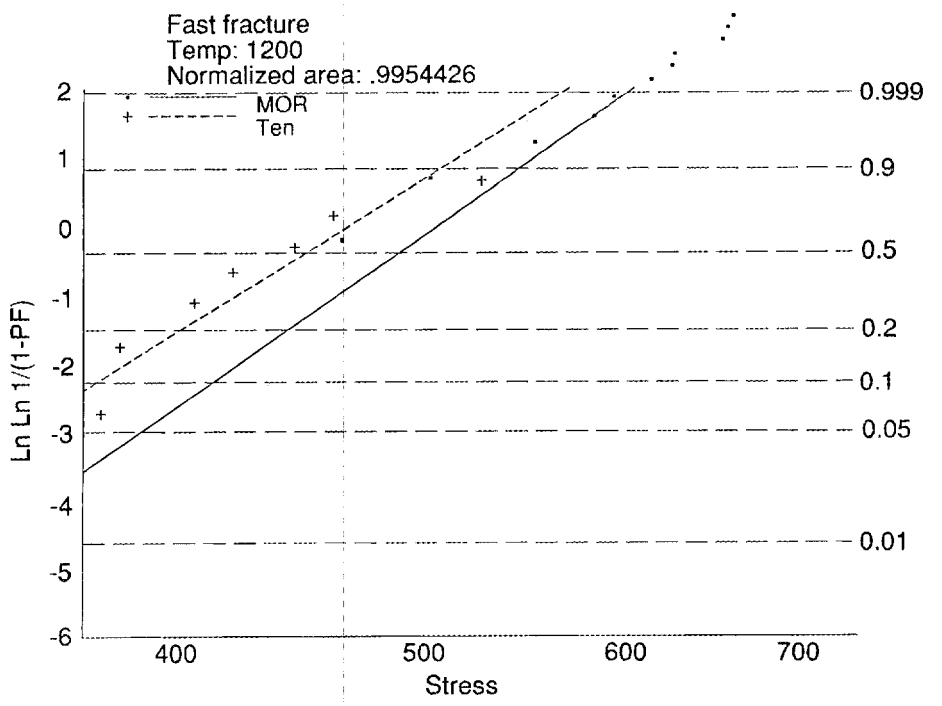

Figure 6. Weibull distribution of volume normalized strengthof MOR and tensile specimens.

Table VI.
Comparison of experimental and calculated surface failures in tensile specimens.

TEMP °C	ACTUAL % SURFACE FAILURES	CALCULATED % SURFACE FAILURES
20	6.1	--
1000	14.3	41.3
1100	43.8	--
1200	46.2	43.6
1300	21.1	19.0
1400	12.1	71.3

Because of this, many of the MOR points are very high on this plot. Generally, it appears that the MOR bars exhibit better properties than the tensile specimens, even after corrections are made for the effective volumes and areas.

Status of Milestones

322201: Computer Implementation of Initial Failure Models - Complete
322202: Initiation of MOR Testing - Complete
322203: Initiation of Tensile Testing - Complete
322204: Initiation of Biaxial Testing - Complete
322205: Confirmatory Testing discontinued because of the poor quality spin disks received from GTE
322206: Completion of All Specimen Testing - Scheduled completion, May 93
322207: Finalization/Verification of Computer Code - Scheduled completion August 1993
322208: Draft Final Report - Scheduled completion, October 1993
322209: Final Report - Scheduled completion, December 1993

Publications

A paper entitled, "Fracture Toughness of a Hip'ed Silicon Nitride at Elevated Temperatures" by A. A. Wereszczak, M. G. Jenkins, R. R. Sanders, and P. K. Khandelwal has been accepted for presentation at the Annual Conference on Composites and Advanced Ceramics to be held at Cocoa Beach, Florida on January 10-15, 1993.

Life Prediction Methodology

J. Cuccio (Garrett Auxiliary Power Division, Allied-Signal Aerospace Company)

Objective/Scope

Garrett Auxiliary Power Division (GAPD) has defined a program to develop the methodology required to adequately predict the useful life of ceramic components used in advanced heat engines. GAPD's approach to ceramic life prediction consists of comprehensive testing of various specimen geometries under both uniaxial and multiaxial loads at different environmental conditions to determine the strength-controlling flaw distributions and to identify various failure mechanisms. This information will be used to develop the flaw distribution statistical models and material behavior models for fast fracture, slow crack growth, creep deformation, and oxidation. As sub-routines, these models will be integrated with stress and thermal analyses into a failure risk integration analytical tool to predict the life of ceramic components. The methodology developed will be verified (for completeness and accuracy) by analytically predicting the life of several ceramic components and testing these components under stress and temperature conditions encountered in ceramic turbine engines.

Technical Highlights

Material Testing and Analysis
H. Fang, N. Menon, and T. Strangman

Material Testing

All the required test and confirmatory NT154 silicon nitride specimens have been obtained from Norton/TRW Ceramics (NTC), and were processed under identical conditions and finish machined and heat treated by NTC. Selected specimens were notched and precracked for testing. All specimens were subjected to visual inspection, laser marking, and NDE (which may include fluorescent penetrant, radiography, ultrasonic inspection, and computed tomography) before testing. Table 1 summarizes the specimens and their current status.

Tensile Creep and Slow Crack Growth Testing

GAPD completed continuing tensile creep and tensile slow crack growth testing as a User at the ORNL High Temperature Materials Laboratory (ORNL-HTML) under the direction of Drs. M.G. Jenkins and M.K. Ferber of the Mechanical Properties User Center. The specimens are of the ORNL cylindrical buttonhead geometry with a 6.35 mm diameter by 35 mm length gage section. The specimens are loaded in uniaxial tension in Instron screw-driven machines using the ORNL/Instron Supergrips. Instron extensometers with SiC probes are being used to monitor the strain deformation of the gage sections during testing.

One hundred and twenty-five specimens have been tested at temperatures between 982C to 1400C. Table 2 summarizes the test temperature, load, time to failure, and strain to failure data for 114 of these specimens.

Specimens are being examined with the scanning electron microscope (SEM). The gage sections of the specimens were partially notched in the transverse plane, i.e., parallel to the fracture surface, and then broken in a low-energy mode to create a clean fracture surface. The quantity and size of the cavities appear to increase as a function of test time and temperature. Characterization of the fracture origins is in progress.

TABLE 1. ORNL LIFE PREDICTION CERAMIC TEST SPECIMEN STATUS

Type of Test	Specimen Size	Surface Machining Direction	Specimen Status
4-Point Bend	MIL-STD-A	Longitudinal	Testing Completed
4-Point Bend	MIL-STD-B	Longitudinal	Testing Completed
4-Point Bend	MIL-STD-B	Transverse	Testing Completed
4-Point Bend	MIL-STD-B	45 degrees	Testing Completed
4-Point Bend	0.35 x 0.72 x 6 in	Longitudinal	Testing Completed
Chevron Notch	--	--	Testing Completed
Diametral Compression	--	--	Ready for Testing
Plate Bending	--	--	In Testing
Tensile Fast Fracture	--	--	Testing Completed
Tensile Stress Rupture (S/R)	--	--	Testing Completed
Pre-cracked Tension/Torsion	--	--	Testing Completed
Unnotched Tension/Torsion	--	--	Ready for Testing
Notched Tensile (Fast Fracture and S/R)	--	--	In Testing
Rectangular Flaw Growth	--	--	In Testing
Spin Disk	--	--	In Testing

8491(07)-1

TABLE 2. SUMMARY OF PRELIMINARY TENSILE CREEP TEST RESULTS

Specimen ID	Test Temp., C	Applied Stress σ_0, MPa	Time to Failure t_f, hrs	Total Strain to Failure ε_f, $\mu\varepsilon$
3-29	1400	150	80	16,350
1-21	1400	140	96	18,270
1-10	1400	130	192	21,930
2-125	1400	130	139	16,500
1-4	1400	125	341	22,820
2-114	1400	110	411	24,570
2-68	1400	100	462	25,800
2-123	1400	90	476*	15,110
2-35	1400	85	597*	14,970
2-55	1371	210	1.4	3,510
1-9	1371	190	68	10,920
1-6	1371	180	62	13,450
3-32	1371	180	64	12,430
2-118	1371	180	28	9,280
2-140	1371	180	25	8,960
2-60	1371	180	19	8,580
1-8	1371	180	14	8,440
2-91	1371	180	8.6	7,510
1-7	1371	180	6.8	6,600
2-116	1371	180	6.8	6,370
2-34	1371	180	5.6	5,700
3-69	1371	180	1.8	4,060
1-19	1371	180	1.6	4,380
1-16	1371	180	0.84	3,750
2-72	1371	180	0.24	2,390
2-69	1371	180	0.24	1,620
2-109	1371	180	0.14	1,880
1-20	1371	160	209	14,410
2-126	1371	155	24	7,790
2-113	1371	150	208	17,210
2-134	1371	150	171	15,420
3-33	1371	150	75	11,060
3-50	1371	145	443	19,355

*Test stopped.
**Failed during loading
> = Ongoing test
Uniaxial tension, gage section 6.35 mm diameter, 35 mm length.

8491(07)-2-1

TABLE 2. SUMMARY OF PRELIMINARY TENSILE CREEP TEST RESULTS (Contd)

Specimen ID	Test Temp., C	Applied Stress σ_0, MPa	Time to Failure t_f, hrs	Total Strain to Failure ε_f, $\mu\varepsilon$
2-120	1371	145	385	20,420
2-7	1371	145	373	18,940
1-12	1371	145	368	20,460
2-92	1371	145	368	19,400
2-63	1371	145	293	17,670
1-13	1371	145	266	18,900
3-35	1371	145	236	17,470
2-57	1371	145	364	20,200
2-136	1371	145	122	15,020
2-162	1371	145	117	17,200
2-101	1371	145	112	14,170
1-17	1371	145	111	13,840
2-50	1371	145	90	15,470
2-46	1371	145	73	11,930
2-45	1371	145	57	11,170
2-124	1371	140	586	21,250
2-117	1371	135	587	18,780
2-130	1371	135	280	18,450
2-119	1371	130	588	21,230
2-121	1371	125	728	16,950
1-2	1315	250	24	3,640
1-24	1315	240	2.9	2,360
2-64	1315	235	52	6,960
2-111	1315	232.5	297	10,660
2-37	1315	230	244	10,870
2-112	1315	230	168	9,100
2-128	1315	227.5	20	5,260
1-15	1315	225	675*	10,300
1-11	1295	375	0.35	2,230
1-23	1295	300	0.40	790
2-66	1295	200	530*	--
2-102	1260	325	1.2	1,420
2-142	1260	305	46	4,640
1-36	1260	300	0.35	5,150
3-44	1260	295	560	8,190

*Test stopped.
**Failed during loading
> = Ongoing test
Uniaxial tension, gage section 6.35 mm diameter, 35 mm length.

8491(07)-2-2

TABLE 2. SUMMARY OF PRELIMINARY TENSILE CREEP TEST RESULTS (Contd)

Specimen ID	Test Temp., C	Applied Stress σ_0, MPa	Time to Failure t_f, hrs	Total Strain to Failure ε_f, $\mu\varepsilon$
2-145	1260	285	379	6,910
3-112	1260	275	474*	6,960
3-89	1260	275	31	2,690
1-46	1260	275	6.1	1,130
3-120	1260	250	838*	7,430
2-56	1204	415	1.3	1,430
3-73	1204	400	1.1	--
3-121	1204	385	501*	--
3-75	1204	375	252	3,370
3-48	1204	375	>200	--
3-118	1204	375	>95	>3,240
3-116	1204	375	>95	>2,770
2-149	1204	375	66	2,690
3-54	1204	375	43	2,060
3-66	1204	375	24	1,980
3-34	1204	375	19	1,830
2-146	1204	375	12	1,500
2-164	1204	375	0.84	1,250
2-72	1204	375	0.5	--
2-28	1204	350	612*	5,190
2-71	1204	350	2.3	1,330
3-39	1204	345	636	--
2-30	1204	340	566	--
3-37	1204	340	177	3,550
2-36	1204	337	593*	3,800
3-19	1204	335	469	4,420
2-74	1204	325	68	2,900
2-31	1204	315	594*	3,630
1-3	1204	300	517*	1,580
3-41	1149	450	7.0	--
2-47	1149	450	0.08	1,490
2-75	1149	445	0.02	--
2-32	1149	440	376	--
3-31	1149	435	594*	--
3-109	1149	425	509*	--
2-62	1149	425	32	1,640
2-61	1149	425	**	--

*Test stopped.
**Failed during loading
> = Ongoing test
Uniaxial tension, gage section 6.35 mm diameter, 35 mm length.

8491(07)-2-3

TABLE 2. SUMMARY OF PRELIMINARY TENSILE CREEP TEST RESULTS (Contd)

Specimen ID	Test Temp., C	Applied Stress σ_0, MPa	Time to Failure t_f, hrs	Total Strain to Failure ε_f, $\mu\varepsilon$
2-70	982	475	21	--
2-38	982	470	512*	--
2-73	982	465	**	--
2-51	982	465	**	--
2-54	982	460	602*	--
2-44	982	460	**	--
3-18	982	455	808*	--
3-27	982	455	336	--
3-40	982	450	631*	--

*Test stopped.
**Failed during loading
> = Ongoing test
Uniaxial tension, gage section 6.35 mm diameter, 35 mm length.

8491(07)-2-4

Specimen Testing Milestone

The Specimen Testing Milestone has been successfully completed. All flexure testing, tensile fast fracture testing, chevron notch fracture toughness (KIC) testing, and notched tension-torsion (KI/KIII) testing was completed. Details of the testing are described below.

Flexure Testing

The following numbers and sizes of flexure bars were tested: 60 MIL-A (1.5 x 2 x 25 mm), 500 MIL-B (3 x 4 x 50 mm), and 100 GAPD E-Size (18 x 9 x 152 mm). All the bars were tested in four-point bending at room temperature and, for 180 randomly selected MIL-B bars, at 980, 1148, 1204, 1260, 1315, and 1371C (1800, 2000, 2100, 2200, 2300, 2400, and 2500F). Test results are plotted in Figure 1. As an example of the data, the average flexure strength of longitudinally machined MIL-B bars is 916 ±164 MPa (standard deviation) at room temperature, 670 ±26 MPa at 1204C, and 630 ±26 MPa at 1371C. Strain gaged NT154 flexure bars were used to check the fixture setup and to verify acceptable bending for the MIL-B and E-size bar test fixtures. The 500 MIL-B bars tested also included 180 oxidation study specimens and 80 specimens with different surface machining directions (transverse and 45 degrees). The test results are shown in Figure 2.

Chevron Notched Fracture Toughness Bars

Fracture toughness (KIC) was measured at the same seven temperatures at which the flexure tests were conducted. Seventy long-beam, chevron notched specimens of 5.08 x 6.35 x 6.35 mm dimension were used. The specimens were tested in a special hot-pressed SiC fixture at 0.0005 in/min. crosshead speed. The test data is plotted in Figure 3. Ten specimens were tested at each temperature, but only data from specimens showing stable crack growth (as indicated by the load deflection curves) was included. The average KIC was 5.0 ±1.25 MPa · $m^{1/2}$ at room temperature, 6.14 ±0.19 MPa · $m^{1/2}$ at 1204C, increasing to a maximum of 6.37 ±0.08 MPa · $m^{1/2}$ at 1148C, then decreasing to 5.79 ±0.46 MPa · $m^{1/2}$ at 1371C.

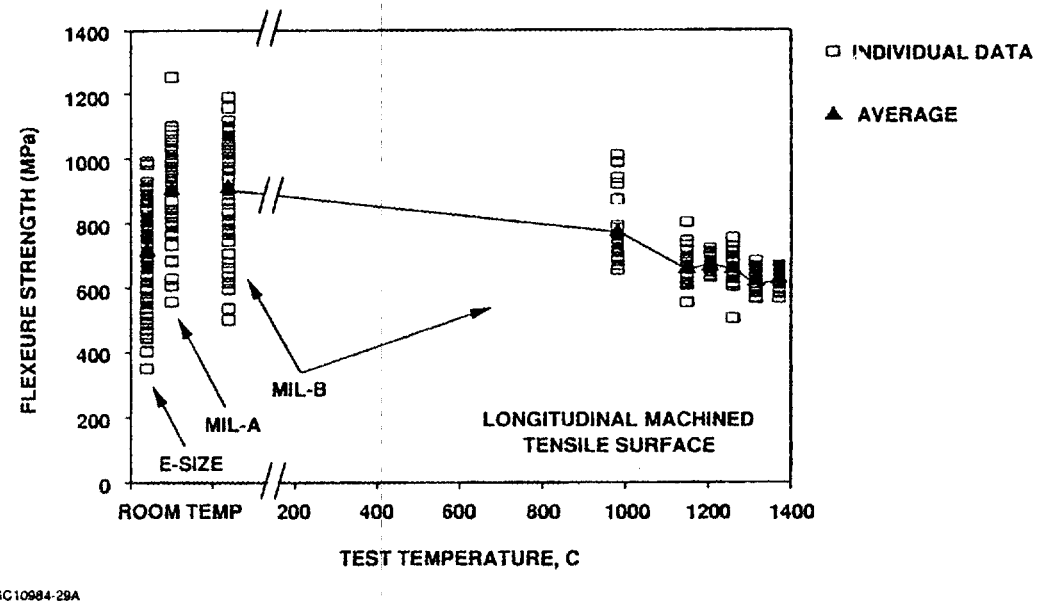

Figure 1. Four-Point Flexure Test Results.

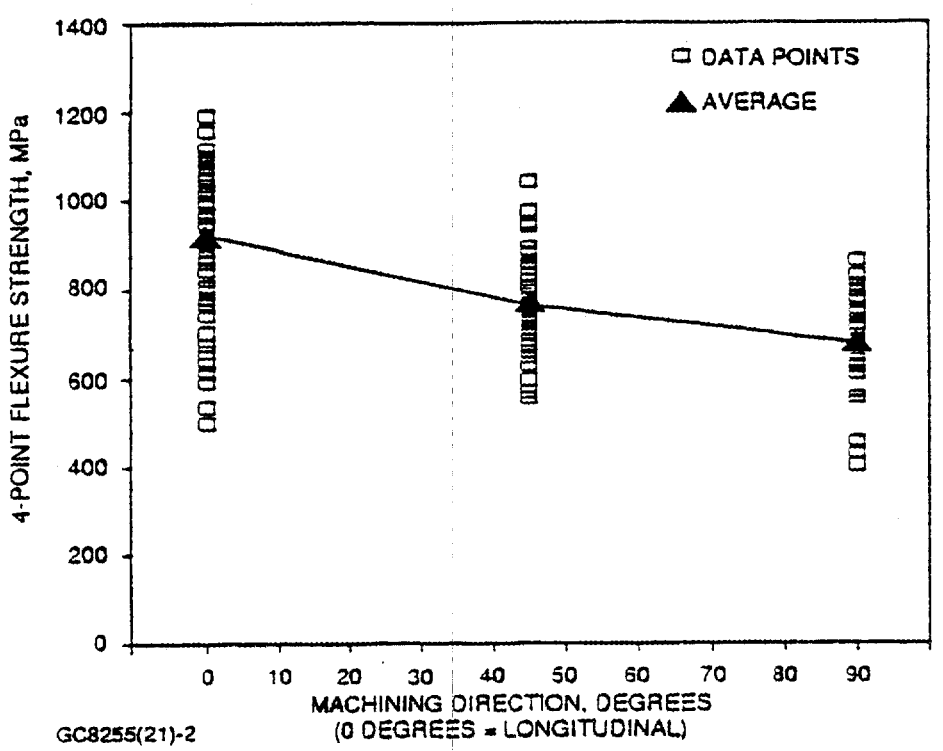

Figure 2. Dependence Of Flexure Strength On Surface Machining Direction.

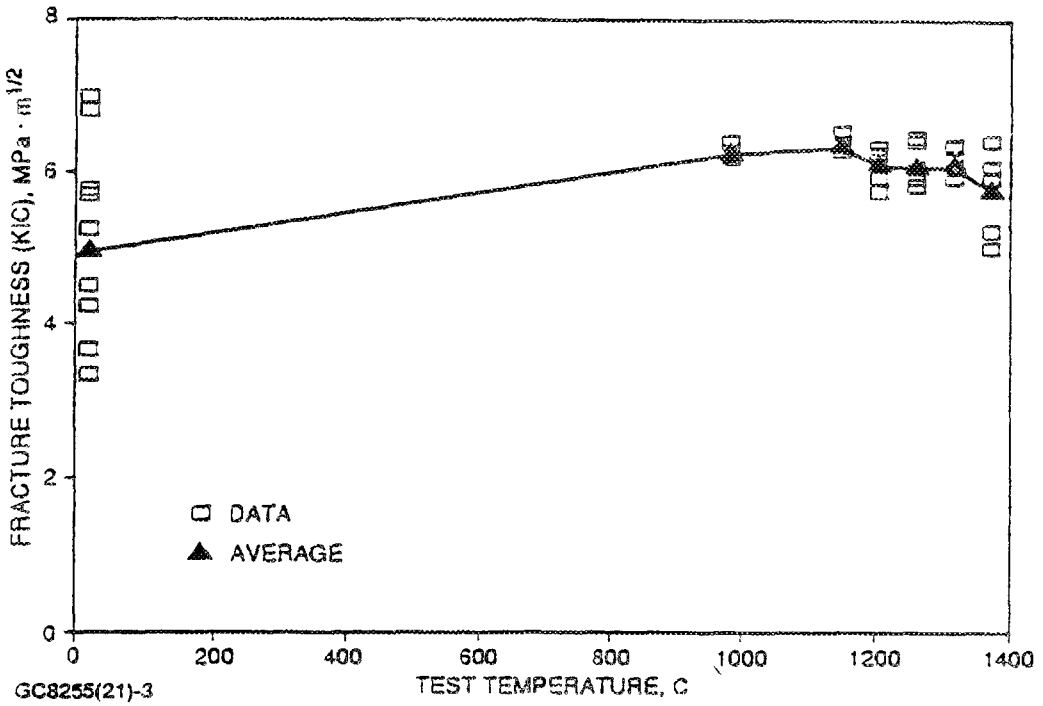

Figure 3. Fracture Toughness (KIC) Test Results.

Tensile Fast Fracture

A total of 125 specimens were tested in tensile fast fracture. One hundred specimens were tested at room temperature, five at 1148C, and twenty at 1204C. The ORNL buttonhead specimen geometry of 6.35 mm gage diameter and 165 mm length was used. Identical Instron test machine and self-aligning Supergrips used by GAPD in the International Energy Agency (IEA) round-robin tensile testing were used for these tests. Test procedures were developed from GAPD's IEA and IR&D strain gaged tensile specimen testing experience to minimize bending and avoid buttonhead failures. The results are shown in Figure 4. Data showed that the average tensile strength is 762 ±112 MPa at room temperature, 559 ±37 MPa at 1148C, and 500 ±69 MPa at 1204C. The lowest strength specimen failed at room temperature at 336 MPa. Scanning electron micrograph of the fracture origin, as shown in Figure 5, indicated failure originated from a surface inclusion containing aluminum. New annealed copper collets were used for each test and there were no buttonhead failures.

Notched Tension/Torsion

Notched tension/torsion tests to evaluate room temperature mode I/mode III (KI/KIII) fracture toughness were completed by Dr. Subra Suresh at Brown University, Providence, Rhode Island, under subcontract to GAPD. The specimens were 115 x 19 mm dia. cylinders circumferentially notched and cyclic compression fatigue precracked in the middle. It was demonstrated for the first time in this work that stable cyclic compression fatigue precracks, 100 microns or more in depth, can be introduced in Si_3N_4.

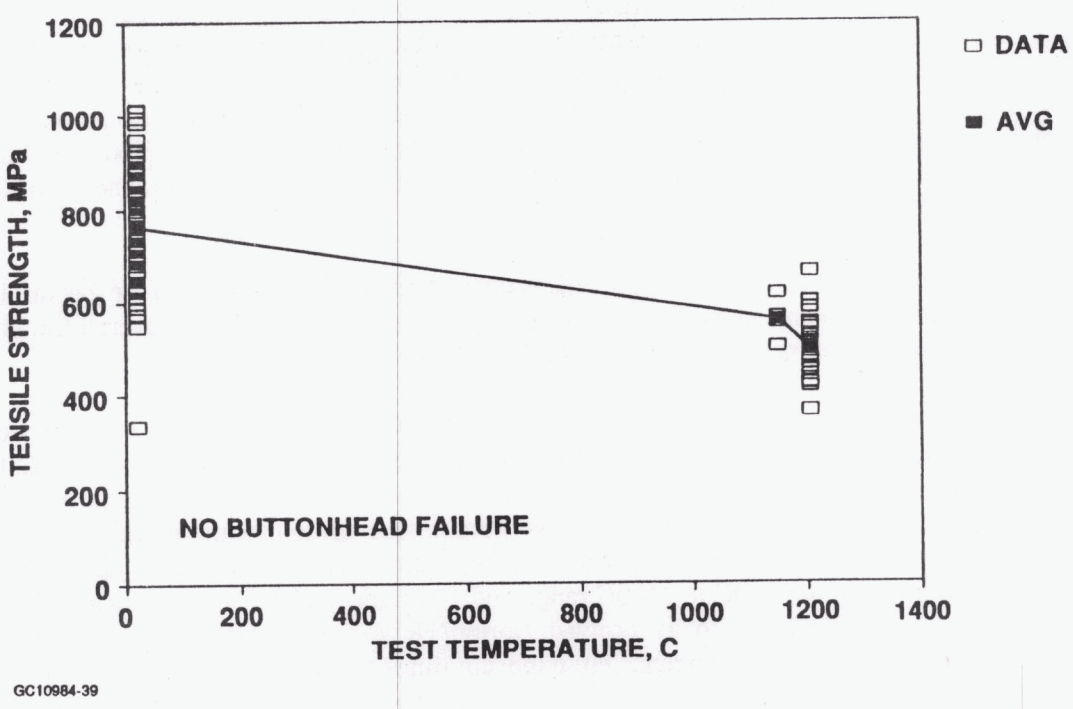

Figure 4. Tensile Stength Of NT154 ORNL Buttonhead Tensile Specimen.

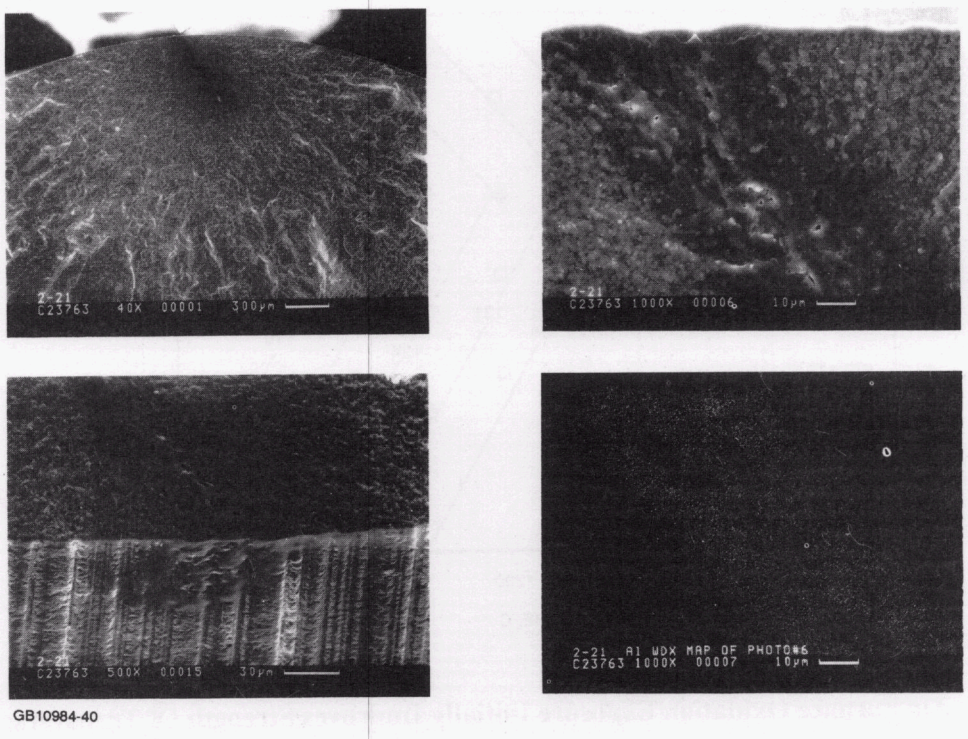

Figure 5. Lowest Strength (336 MPa) Specimen Failed From Surface Al Inclusion.

An Instron Model 1322 servohydraulic biaxial testing machine was used for the KI/KIII fracture testing. Three special tension/torsion specimens were strain gaged to verify proper equipment alignment. More than 20 specimens were successfully tested at room temperature to obtain a complete fracture envelope spanning from pure mode I (tension) to pure mode III (torsion) with in-between data corresponding to combined tension/torsion conditions. The pure mode I fracture toughness (KIC) data generated in this work is comparable to the long-beam, chevron notched KIC results generated at GAPD.

The surface strength of silicon nitride components is dependent upon the severity of the gas turbine oxidation environment, which can modify critical surface flaws. Consequently, the overall Ceramic Life Prediction Model must include the effects of oxidation on the strength of NT154.

In this oxidation testing program, 180 MIL-STD-B size transverse machined flexure test bars were exposed to a static air furnace environment at temperatures in the range of 980C to 1400C for times in the range of 1 to 1000 hours. The distribution of test specimens is shown by the symbols in Figure 6. Following exposure, the specimens were tested in four-point bending at room temperature. Test results are shown as lines of relative strength in Figure 6. Unexpectedly, exposures of 100 hours in the 980C to 1100C range and 10 hours at 1200C resulted in significant improvement in strength, relative to as-received Norton/TRW heat-treated specimens; average specimen strength increased by 38 percent. For exposure times less than or equal to 100 hours in the 1100C to 1400C temperature range, specimen strength decreased, which was expected. The results in Figure 6 also show unusual behavior for exposures longer than 100 hours in the 1100C to 1400C temperature range; the average specimen strength increased with additional exposure time.

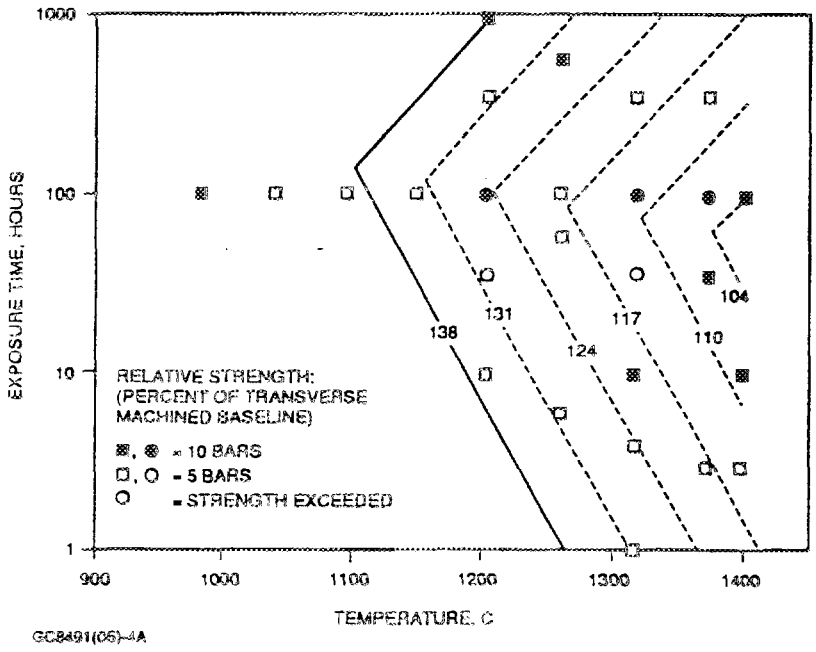

Figure 6. **Air Furnace Oxidation Exposure Initially Improves Strength Of Transverse Machined Specimens.**

Increased specimen strength following exposures greater than 100 hours at temperatures over 1100C has not been previously observed in cyclic oxidation exposures in the Mach 0.3 burner rig ceramic durability tests conducted by GAPD under DOE/NASA Contract No. DEN3-27. The effects of static air furnace and cyclic burner rig exposures at 1260C (2300F) are compared in Figure 7. Up to exposure times of 100 hours, the slopes of the room temperature strength lines (rate of strength decrease) are similar for both types of exposure tests. However, in the cyclic oxidation environment (burner rig tests), the strength continued to decline for exposures longer than 100 hours.

Flexure test data for exposure times less than or equal to 100 hours has been modeled as a function of time and temperature. The resulting relationship is shown in Figures 8 and 9. Figure 8 illustrates the relationship based on all of the data.

Fracture in the as-received specimens, which were heat treated by Norton/TRW, typically initiated in the chamfered edge of the specimen. Only seven percent of the as-received transverse machined specimens failed on the tensile surface. This result implies that machining damage was more severe on the chamfer than the transverse machined surface.

Exposure to the high temperature oxidizing environment reduced the severity of the chamfer damage; i.e., over 80 percent of the environmentally exposed specimens failed on the tensile surface. When specimens associated with chamfer failure are eliminated from the database, scatter in the data is reduced as shown in Figure 9.

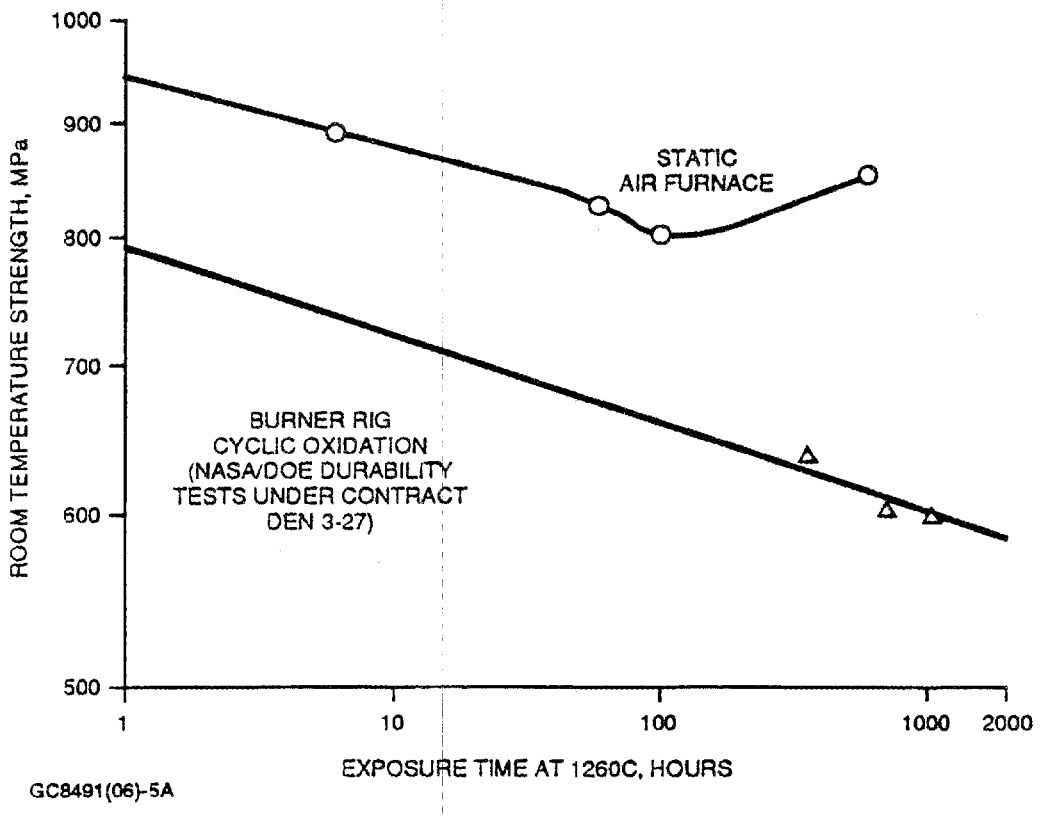

Figure 7. Specimen Strength Declined In Cyclic Oxidation (Burner Rig) Testing.

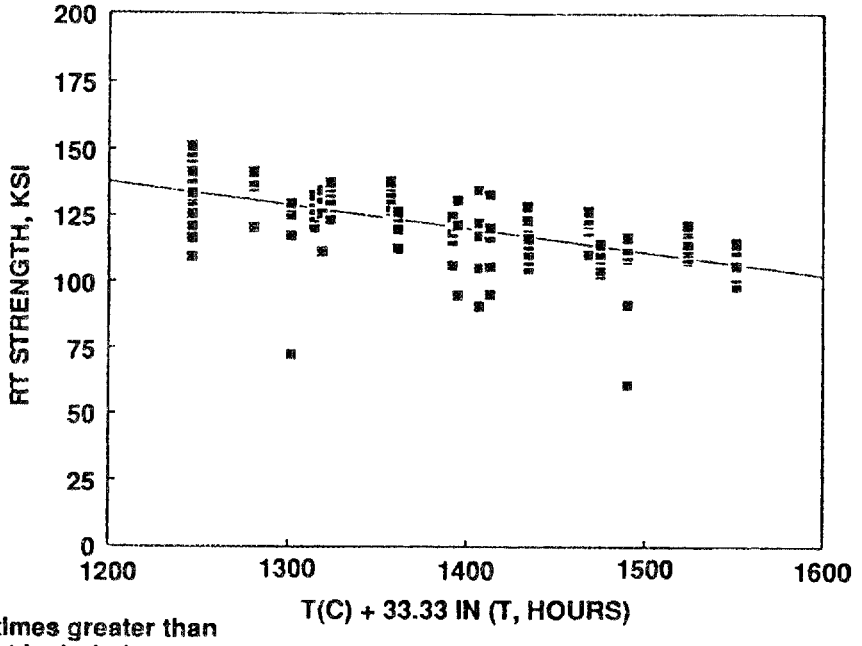

Note: data for times greater than 100 hours is not included.

GC10984-35

Figure 8. Room Temperature Flexure Strength Is A Function Of Exposure Temperature And Time.

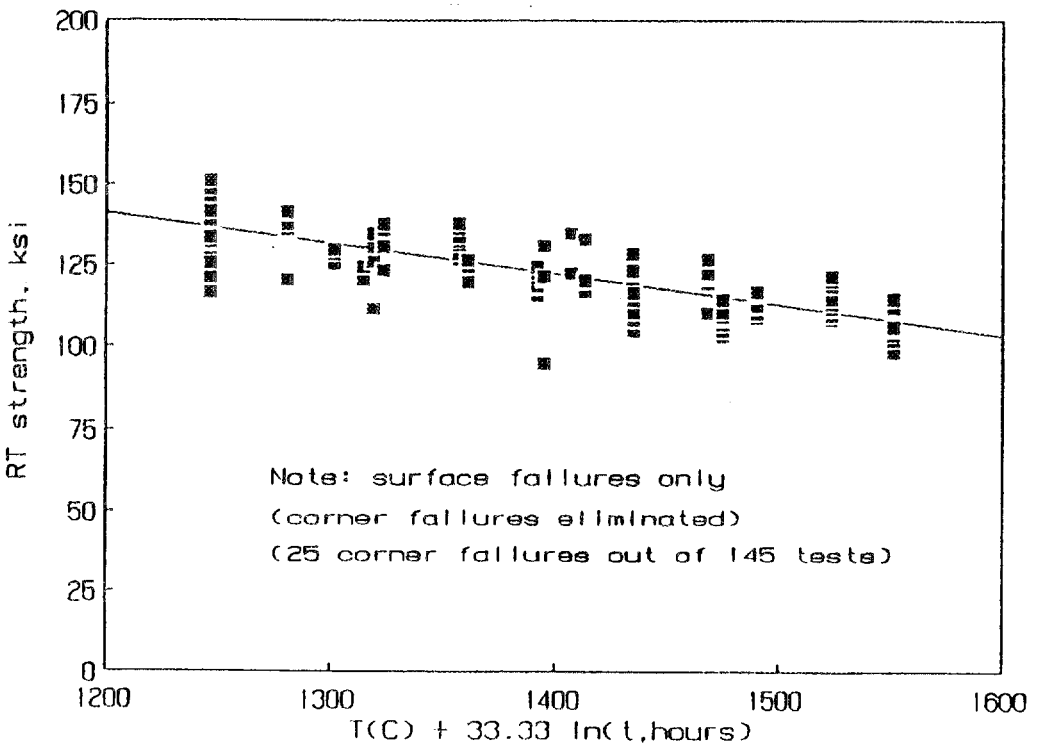

Figure 9. Censoring Chamfer Failures Reduces Data Scatter.

Fracture surfaces were examined on the SEM to determine the thickness of the oxidation affected layer. It was found that growth of the oxidation-affected layer of these specimens followed logarithmic instead of the parabolic growth behavior (Figure 10). WDX dot maps indicated that oxygen was typically present as a gradient in the surface of the silicone nitride (Figure 11). WDX analysis also indicated that the concentration of nitrogen in the oxidation affected zone remained high -- almost to the level present below the oxidation-affected zone.

Reasons for oxidation to increase the strength of transverse machined NT154, relative to as-received material, have not been established. However, we speculate that oxidation may be producing a large residual compressive stress in the machined surface layer, because conversion of silicon nitride to silicon oxynitride or silica involves a large volume increase. If this reaction occurs within machining microcracks and grain boundaries, the volume increase will be constrained by strong silicon nitride grains, producing compressive stresses in the plane of the surface.

Oxygen diffusion down machining microcracks and grain boundaries is consistent with the observed logarithmic growth of the oxidation-affected surface layer; i.e., it increases the growth rate at short times. It should also be noted that oxygen diffusion through silica and silicon oxynitride is strongly dependent on the temperature-dependent lattice spacing. Compressive stresses can inhibit thermal expansion or silica and/or silicon oxynitride lattices. Consequently, oxide growth induced compressive stresses may contribute to logarithmic oxidation by slowing growth at longer times.

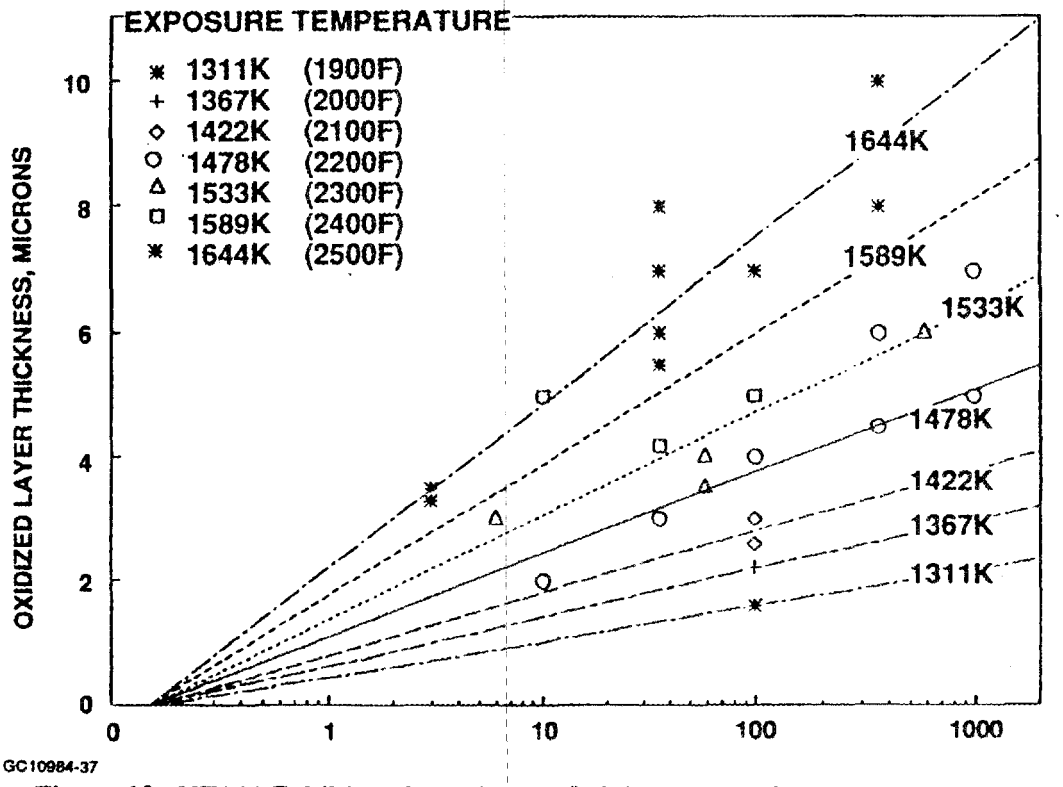

Figure 10. NT154 Exhibited Logarithmic Oxidized Layer Growth Below 2500F.

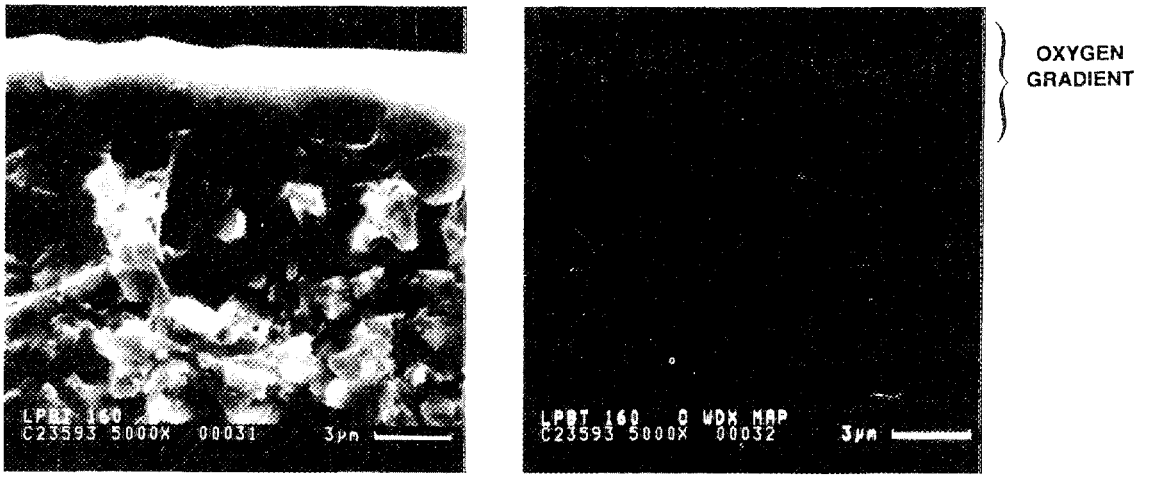

SEM PHOTOGRAPH

WDX OXYGEN MAP

EXPOSURE: 1260C/100 HOURS/AIR
POST-EXPOSURE RT STRENGTH = 920 MPA

GB10984-35

Figure 11. Oxidation Is Not A Plane Front Process.

Data Analysis and Methodology Development
A. Peralta, P. Brehm, J. Song, J. Cuccio, and D. Wu

GAPD's efforts to develop statistical analysis tools for ceramic component design are continuing. Under the Data Analysis area, extensive efforts have gone into bias correction of censored data and into developing tools for component multifailure mode reliability and design stress level confidence limit predictions. Under the multiaxial integration area, the efforts have gone into developing efficient subroutines for the volume and surface failure modes multiaxial integration kernel, and into the derivation of closed form solutions of the multiaxial integration kernel wherever possible.

The Data Analysis accomplishments include the evaluation of the bootstrap methods used for bias correction for censored data. Difficulties encountered with this approach were addressed, and to isolate the conditions under which this method fails to correct for bias, seven different simulations and bias correction analyses were performed. The results are summarized in Table 3. Case 1 is the baseline case. The shaded areas for other cases indicate the deviations from the baseline case. Results from case 1 and case 7 are also given in plots (Figures 12 through 15). The titles mean the following:

"Number of Rejects" is the number of times when a simulated specimen set contained no volume failures. In general, these data sets were replaced. If 200 data sets were rejected for any simulated σ_0, m case, the σ_0, m simulation was discarded.

TABLE 3. SUMMARY OF EVALUATION RESULTS ON BIAS CORRECTION WITH BOOTSTRAP

3 Case No.	Number of Specimens	Number of Failure Modes	Percent of Volume Failure	Number of Rejects	No ML Convergence	Successful Simulations	Specimen Size	Failure Mode	Parameters in Simulation		$D(\sigma_O)$		D(m)		Reduced Bias
									m	σ_O	Biased	Unbiased	Biased	Unbiased	
1	36	2	~13	423	116	100	4-POINTC	V	21.79	37.1	0.057	0.189	0.066	0.170	NO
						X99	3-POINTA	S	14.96	42.0	0.074	0.027	0.195	0.095	
2	100	2	~14	0	0	100	SAME	V	21.79	37.1	0.050	0.12	0.05	0.09	NO
						X100		S	14.96	42.0	0.110	0.11	0.08	0.05	
3	36	2	~13	2295	1104	300	SAME	V	21.79	37.1	0.1318	0.1861	0.1325	0.1029	NO
						X297		S	14.96	42.0	0.0656	0.0422	0.1145	0.0437	
4	36	2	~5	3455	811	100	SAME	V	21.79	39.5	0.1319	0.1660	0.1769	0.1485	NO
						X96		S	14.96	42.0	0.0698	0.1073	0.0565	0.1023	
5	36	2	~5	3533	174	100	SAME	V	15.79	37.1	0.322	0.189	0.153	0.109	YES
						X98		S	14.96	42.0	0.136	0.086	0.165	0.091	
6	36	2	~12	553	205	100	4-POINTC	V	21.79	37.1	0.150	0.120	0.180	0.08	YES
						X100		S	14.96	42.0	0.070	0.040	0.120	0.10	
7	36	2	~12	5275	1968	300	4-POINTC	V	21.79	37.1	0.158	0.084	0.157	0.047	YES
						X300		S	14.96	42.0	0.085	0.039	0.141	0.032	
8	36	2	~5	2906	58	100	4-POINTC	V	10.0	33.0	0.11	0.09	0.19	0.17	YES
						X100	3-POINTA	S	14.96	42.0	0.12	0.06	0.19	0.05	
9	36	2	~50	0	0	100	4-POINTC	V	21.79	33.5	0.08	0.14	0.10	0.11	NO
						X100	3-POINTA	S	14.96	42.0	0.10	0.13	0.10	0.11	

8491(07)-3

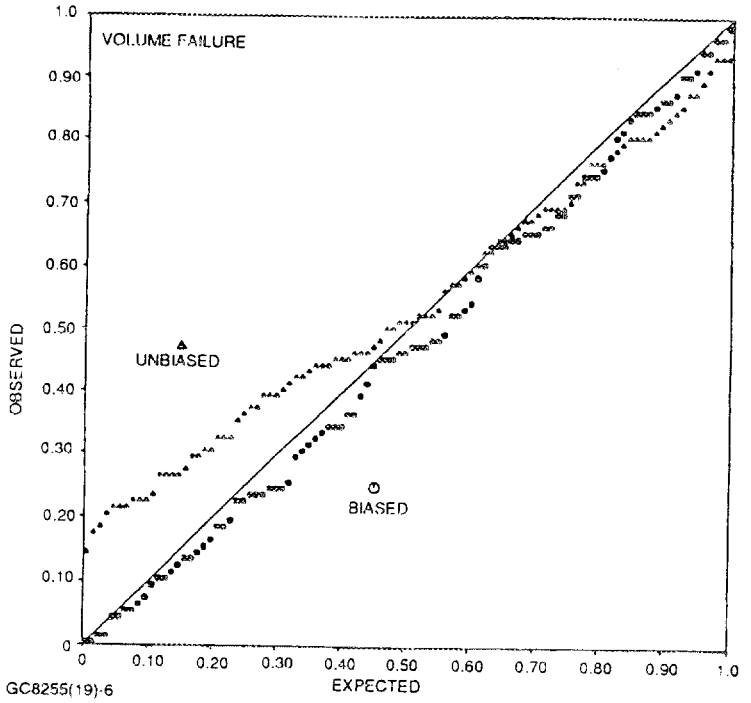

Figure 12. **Comparison Of Biased And Unbiased Estimates Of Weibull Modulus (Baseline - Case 1 - Volume Failure).**

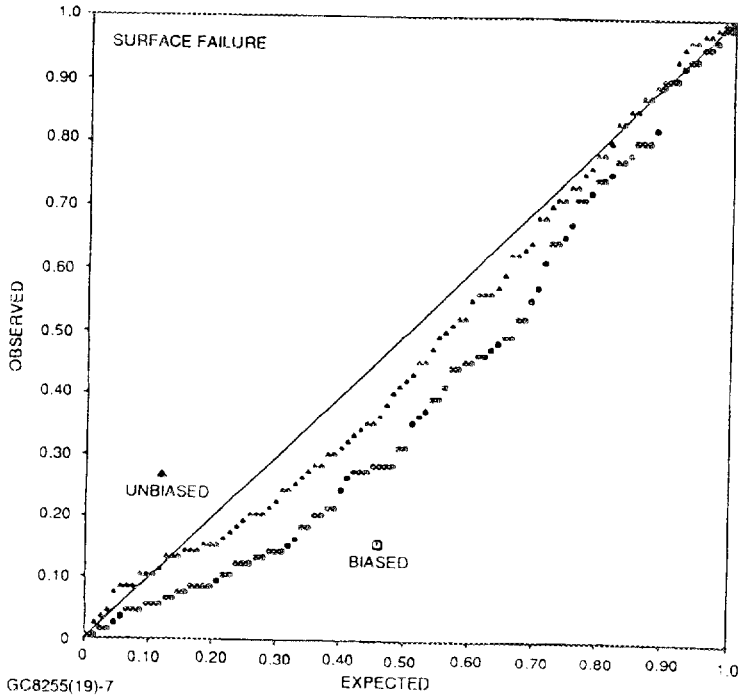

Figure 13. **Comparison of Biased and Unbiased Estimates Of Weibull Modulus (Baseline - Case 1 - Surface Failure).**

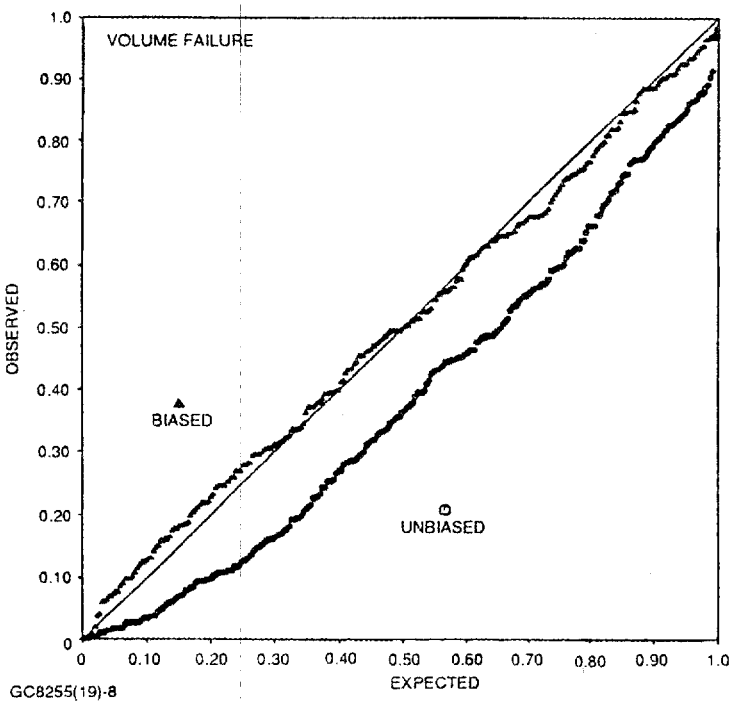

Figure 14. **Comparison Of Biased And Unbiased Estimates Of Weibull Modulus (Case 7 - Volume Failure).**

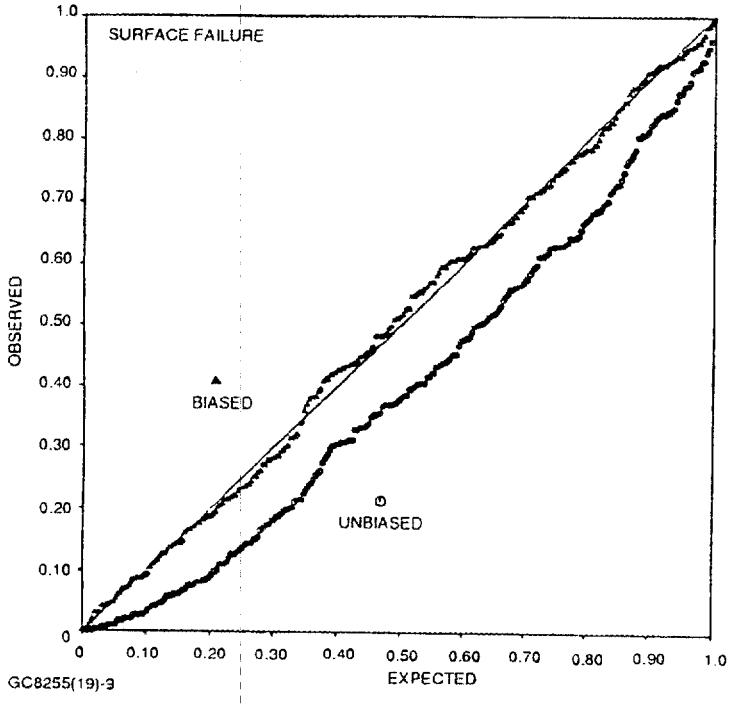

Figure 15. **Comparison of Biased and Unbiased Estimates Of Weibull Modulus (Case 7 - Surface Failure).**

"No ML Convergence" refers to the number of times when the program generated an acceptable set of specimens (at least one volume failure) and it was not able to find maximum Weibull parameter estimates. In general these data sets were replaced. If 80 data sets for any $\hat{\sigma}_0$, $\hat{m}$ could not be solved, the $\hat{\sigma}_0$, $\hat{m}$ simulation was discarded.

The first number under "Successful Simulation" refers to simulations based on the "true" values of σ_0, m. The second number refers to the number of $\hat{\sigma}_0$, $\hat{m}$ values for which successful $\tilde{\sigma}_0$, $\tilde{m}$ simulations were generated, i.e., for which "number of rejects" did not exceed 200 and for which "No ML Convergence" did not exceed 80.

In Table 3, "D" stands for the maximum discrepancy between expected probability of failure and observed probability of failure (Figure 12). The biasing was judged to be acceptable if D for the unbiased results was less than D for the biased results.

The results indicate that the invariant used in bias correction for $\hat{\sigma}_0$, $\hat{m}$ may not hold for censored data. If this is proven, a new invariant will be needed for censored data, or other means will need to be explored for bias correction.

Component multifailure mode reliability and design stress level confidence limit predictions are also in progress. The approach for these two variables follows the same line, and focus to date has been in the reliability confidence limit prediction. The probability of failure, or its complement the reliability, of a component at a stress level Z, with possible failure modes 1, 2, and 3, is given by equation [1]. By defining the variables given by equations [2] through [4], equation [1] can be written as in equation [5].

$$P_f(Z) = 1 - \exp - \left\{ I_{1C}V_{1C}\left(\frac{Z}{\sigma_{o1}}\right)^{m_1} + I_{2C}V_{2C}\left(\frac{Z}{\sigma_{o2}}\right)^{m_2} + I_{3C}V_{3C}\left(\frac{Z}{\sigma_{o3}}\right)^{m_3} \right\} \qquad [1]$$

$$p = P_f(Z) \qquad [2]$$

$$\gamma = \ln\left(\frac{1}{1-p}\right) \qquad [3]$$

$$\gamma_i = I_{ic}V_{ic}\left(\frac{Z}{\sigma_{oi}}\right)^{m_i} \qquad [4]$$

$$\gamma = \gamma_1 + \gamma_2 + \gamma_3 \qquad [5]$$

The confidence limits are derived from the solution of equation [6], where $W(\gamma)$ is the likelihood ratio function and l(.) is the loglikelihood function. But, [6] must be solved with the constraint given by equation [5].

$$W(\gamma)=\left[l\left(\hat{m}_1,\hat{m}_2,\hat{m}_3,\hat{\gamma},\hat{\sigma}_{o2},\hat{\sigma}_{o3}\right)-l\left(\hat{m}_{1\gamma},\hat{m}_{2\gamma},\hat{m}_{3\gamma},\hat{\gamma},\hat{\sigma}_{o2\gamma},\hat{\sigma}_{o3\gamma}\right)\right] \qquad [6]$$

$$\text{where} \quad W(\gamma)=\frac{\chi^2_{1,\alpha}}{2} \qquad [7]$$

The method of Lagrange multipliers was chosen to solve the constrained problem. The Lagrangian, equation [8], is formed and its derivatives computed and set to zero, equation [9]. The equations obtained from [9] and equation [6] provide a set of simultaneous equations which are solved for the unknowns γ, m_i, σ_{Oi}.

$$L=l+\lambda\left(\gamma-\gamma_1-\gamma_2-\gamma_3\right) \qquad [8]$$

$$\frac{\partial L}{\partial \gamma_i}\equiv\frac{\partial L}{\partial m_i}\equiv 0 \qquad [9]$$

The solution involving a positive value of λ is easily found, and provides an upper confidence bound on the predicted reliability. For negative values of λ, which provides the lower confidence bounds, the solution is multivalued and difficult to obtain.

The method thus far has been successful in finding both upper and lower reliability confidence bounds for data sets with a single failure mode. These result agree with previous single failure mode derivations of the likelihood ratio and bootstrap solutions. A good agreement has been observed with bootstrap solutions for the upper bound of multiple failure modes. Solutions for the lower bound for multiple failure modes are difficult to obtain; successful solutions have shown good agreement with bootstrap solutions. These positive results indicate that the theoretical derivation is correct. The successful solutions include a few points within a limited stress range for a data set with only two failure modes, which was accomplished with an iterative approach. A second solution include a data set with three failure modes and two specimen types, which was accomplished by using a method based on a formulation entailing two searches in 1-dimensional space and one search in n-dimensional space, where n is the number of failure modes.

In the risk integration development effort a number of numerical integration methods were evaluated for the multiaxial integration kernel:

$$\int_0^{\pi/2}\int_0^{2\pi} w(\phi,\psi)\cos\phi\, d\phi\, d\psi \qquad [10]$$

where $w(\phi,\psi)$ is the effective stress failure theory formulation raised to the Weibull modulus power.

A Gaussian integration scheme over the intervals 0 to $\pi/2$, 0 to $\pi/2$, (times 4) was compared to a combined trapezoidal and Simpson integration over the intervals 0 to π (where periodicity enhances the trapezoidal method), 0 to $\pi/2$ (times 2). For integrals with known closed form solutions, none of which include shear effects in the definition of the effective stress, the two methods were roughly equivalent. The Gaussian method achieved the correct solutions (to machine accuracy) with slightly fewer integration points than the other method. For integrals without known solutions, especially those of failure theories with shear effects, both methods converged to the same answer, but the Gaussian method achieve 7 to 8 "correct " digits faster than the trapezoidal/Simpson method. It has therefore been decided to implement the Gaussian method for the multiaxial integration. The selection of the Gaussian integration scheme can also be justified based on the premise that Gaussian integration schemes integrate polynomials exactly and in general the failure theories have a polynomial form, even more so when they are raised to the power of the Weibull modulus. A decision was also made to implement the Gaussian integration scheme for the spatial integration, whether it be surface or volume space.

From the above study, computer subroutines for volume and surface failure modes have been written and evaluated for accuracy. The solutions from the subroutines have been compared to closed form solutions of the Evans multiaxial integration function I(m), equations [11] and [12] for volume and surface respectively.

$$I_v(m) = \frac{1}{4\pi V}\iiint_V \int_{-\frac{\pi}{2}}^{\frac{\pi}{2}}\int_0^{2\pi} \sigma_E^m(x, y, z, \phi, \psi)\cos\phi\, d\psi\, d\phi\, dV \qquad [11]$$

$$I_S(m) = \frac{1}{2\pi S}\iint_S \int_0^{2\pi} \sigma_E^m(x, y, \theta)\, d\theta\, dS \qquad [12]$$

And for a maximum normal stress criterion, equation [13] for volume failure mode and equation [14] for surface failure mode.

$$\sigma_E = \sigma_1 \ell_1^2 + \sigma_2 \ell_2^2 + \sigma_3 \ell_3^2 \qquad [13]$$

where:

$\ell_1 = \cos\phi\cos\psi$

$\ell_2 = \cos\phi\sin\psi$

$\ell_3 = \sin\phi$

$\sigma_1, \sigma_2, \sigma_3$ = the principal stresses

$$\sigma_E = \sigma_1\ell_1^2 + \sigma_2\ell_2^2 \qquad [14]$$

where:

$\ell_1 = \cos\theta$

$\ell_2 = \sin\theta$

The subroutines were then evaluated using several finite element solutions, and they compared well with the closed-form solutions. The closed-form solutions for the multiaxial factor I(m) can only be calculated for special cases of stress distributions and Weibull slope. The case where m is an integer is presented below for several cases. For the case when m = n + 0.5 and n is an integer, a closed-form solution was also computed, but is not presented here.

The closed-form solutions used are the following:

A. Volume failure mode:

I. Uniform equitriaxial state of stress:

$$\mathrm{I}(m) = 1 \qquad [15]$$

II. Uniform equibiaxial state of stress for integer m:

$$I(m) = \frac{2m}{2m+1}\cdot\frac{2m-2}{2m-1}\cdot\frac{2m-4}{2m-3}\cdots\frac{2m-(2m-2)}{2m-(2m-3)} \qquad [16]$$

III. Uniform uniaxial state of stress for integer m:

$$\mathrm{I}(m) = \frac{1}{2m+1} \qquad [17]$$

IV. Beam in pure bending for integer m:

$$\mathrm{I}(m) = \frac{1}{2(2m+1)(m+1)} \qquad [18]$$

Exact closed-form solutions for the three- and four-point bending specimens are not straightforward, and were therefore not computed. Instead, a calculation was performed assuming that there is no shear stress present along the span of the specimen but still having the same bending stress distribution. The solutions are as follows:

V. Beam three-point bending specimen, integer m:

$$I(m) = \frac{1}{2(2m + 1)(m + 1)^2} \qquad [19]$$

VI. Beam four-point bending specimen, integer m. (a is the inner span, b the outer span):

$$I(m) = \frac{\left(\frac{a}{b}m + 1\right)}{2(2m + 1)(m + 1)^2} \qquad [20]$$

B. Area failure mode:

I. Uniform equibiaxial state of stress:

$$I(m) = 1 \qquad [21]$$

II. Uniform uniaxial state of stress and integer m:

$$I(m) = \frac{2m\text{-}1}{2m} \cdot \frac{2m\text{-}3}{2m\text{-}2} \cdot \frac{2m\text{-}5}{2m\text{-}4} \cdots \frac{2m\text{-}(2m\text{-}1)}{2m\text{-}(2m\text{-}2)} \qquad [22]$$

III. Beam in pure bending and integer m (w is the width, h the height of the specimen).

$$I(m) = \left\{\frac{2m - 1}{2m} \cdot \frac{2m - 3}{2m - 2} \cdot \frac{2m - 5}{2m - 4} \cdots \frac{2m - (2m - 1)}{2m - (2m - 2)}\right\} \frac{1}{2(w + h)} \left[\frac{2(m + 1)\, w + h}{2(m + 1)}\right] \qquad [23]$$

Subsequent work will focus on combining the multiaxial integration routines into a single code that can be used to evaluate component reliability and to compute specimen I(m). The I(m) value is used in the computation of the Weibull parameter estimates. The closed form solutions for I(m) are needed to write a self-standing code for data analysis such as CERAMIC.

REFERENCES:

A.G. Evans, "A General Approach for the Statistically analysis of Multiaxial fracture, "J. Am. Ceram. Soc., 61, 7-8, pp. 302-308 (1978).

NDE Methods Development and Application
J. Wade and B. Meade

All test specimen and confirmatory specimen inspections were completed during the last six months. Tables 4 and 5 summarize the inspections performed on the test specimens and confirmatory test specimens respectively.

Radiographic inspection procedures of the spin disks were modified to provide additional fixturing and blocking and reduce inspection times by approximately 30 percent. These modifications included the use of double film exposure techniques. For thicker cross sections, higher speed films were effectively used while maintaining the 2-1T minimum radiographic sensitivity. Digital enhancement of radiographic film is underway and has proven beneficial to film evaluation. Figure 16 shows an example of improved detection of high density inclusions in a seeded specimen. Selection of radiographic films for enhancement is underway.

A computer tomography study was conducted to determine whether the resolution varied toward the outside of the reconstruction area. The detection standard was imaged in multiple locations to duplicate the conditions of the center and the outside diameter of the spin disk. The smallest hole visible in the center and the outside reconstruction field was 0.2 mm. However, the 0.2 mm hole was more difficult to see toward the outside of the reconstruction field because image noise increases. Figure 17 shows the difference between the inner diameter and outer diameter reconstruction fields.

Data review and correlation for all NDE data are underway. Comparisons of acoustic microscopy data from test specimens show a variation in the material appearance from specimen to specimen for volume data at the same depth. This variation has been observed in the spin disks and the large volume flexure bars (E-size); however, the spin disks seem to have more variation than the E-size flexure bars even when data are compared at the same depths. Very few of the spin disks exhibited few or no internal indications, while many E-size flexure bars had few or no indications. Figure 18 shows typical variations observed in the spin disk images. Preliminary review of radiographic data for the same test specimens does not show a similar trend in the radiographic inspection data.

To facilitate data correlation, the data from each technique are being reviewed and summarized in a tabular format for each inspection method prior to correlation with other NDE methods and destructive data. This effort is nearing completion for tensile rod data and is in progress for all other data.

<u>Status of Milestones</u>

Specimen testing milestone has been completed.

TABLE 4. NONDESTRUCTIVE EVALUATION OF ALL SPECIMENS IS COMPLETE

Specimen	No. of Specimens				
		Acoustic Microscopy			
	FPI	Surface	Internal	RT	CT
MIL-A Flexure	60	NR	NR	60	NR
MIL-B Flexure	520	520	NR	520	NR
Large Flexure	100	100	30	100	12
Chevron Notch	70	NR	NR	70	NR
Diametral Compression	72	NR	NR	72	NR
Tensile Fast Fracture	125	125	NR	125	20
Tensile Stress Rupture	130	100	NR	100	NR
Notched Tension/Torsion	20	NR	NR	20	NR
NR = Not Required					

8491(07)-4A

TABLE 5. NDE OF CONFIRMATORY TEST SPECIMENS COMPLETE

Specimen	No. of Specimens				
		Acoustic Microscopy			
	FPI	Surface	Internal	RT	CT
Rectangular Flaw Growth	12	6	NR	12	0
Plate Bending	40	20	NR	40	0
Unnotched Tension/Torsion	40	40	NR	40	20
Notched Tensile	60	NR	NR	NR	NR
Spin Disk	41	8	8	41	12
NR = Not Required					

8491(07)-5A

Communications/Visits/Travel

Drs. W. Tucker and C. Johnson of General Electric Corporate Research and Development visited GAPD October 19-21, 1992 for a semiannual review of progress in data analysis and methodology development.

Problems Encountered

None.

Publications

A technical paper, copublished by GAPD and General Electric Corporation (GE), entitled "Calibration and Measurement of Resolution in Ultrasonic Images" was presented by Dr. D. Sturges of the GE Aircraft Engines Division, Engine Support Operations, at the Internal Conference on Monitoring and Predictive Maintenance of Plants and Structures, sponsored by the Italian Society for Nondestructive Testing on May 21, 1992 in Fierenzi, Italy. The paper discusses the use of high-frequency ultrasonic inspection standards for acoustic microscopy and the requirements for calibrating such systems. Portions of the paper describe joint development work performed by GAPD and GE under the ORNL Ceramic Life Prediction program.

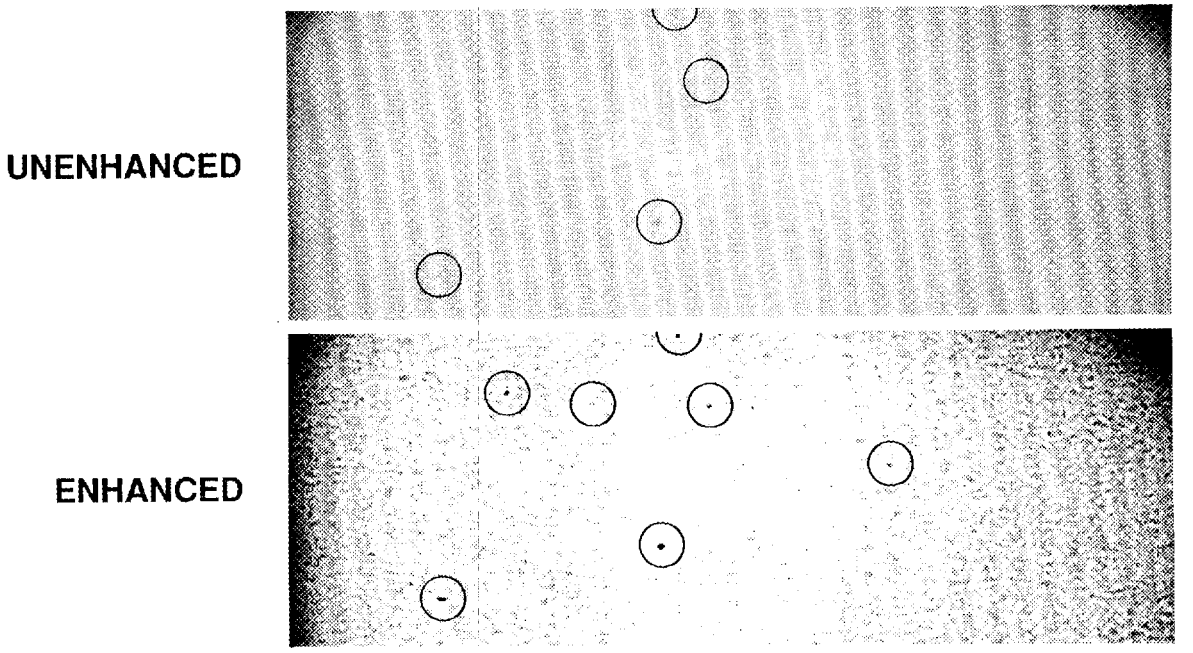

GB10825-16

Figure 16. Digital Enhancement Improves Image Contrast.

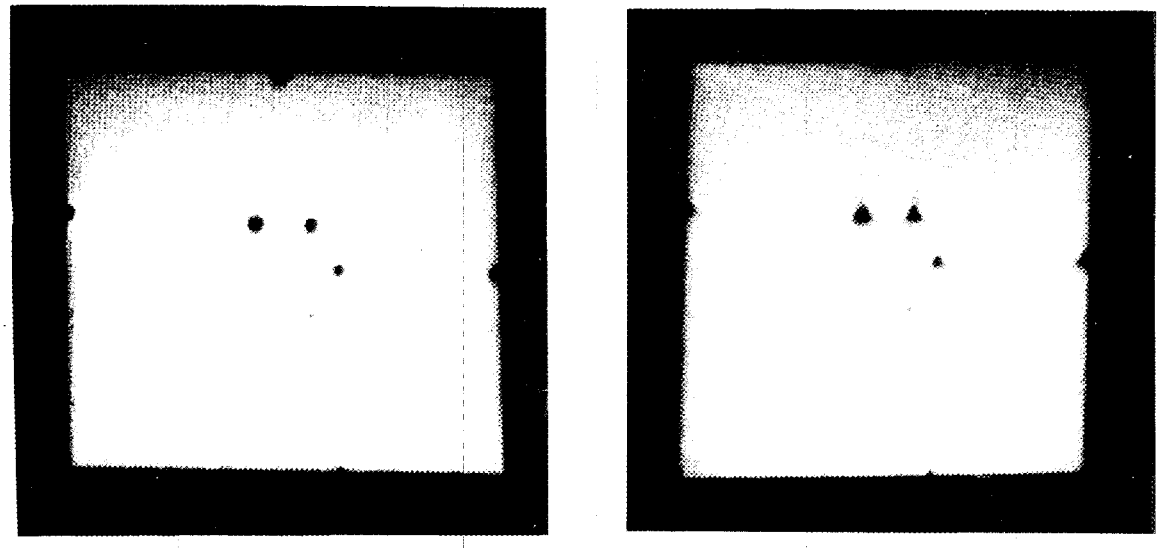

GB10984-19

Figure 17. CT Reconstruction Of Center Field Versus Outside Diameter Field Evaluated.

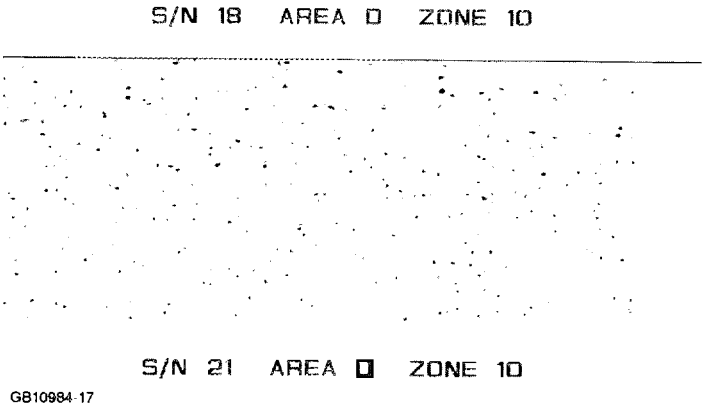

Figure 18. **Spin Disks Exhibit Large Variation in Acoustic Microscopy Inspection.**

3.3 ENVIRONMENTAL EFFECTS

Environmental Effects in Toughened Ceramics
Norman L. Hecht (University of Dayton)

Objective/scope

Since December 1984, the University of Dayton has been involved in a five-phase project to investigate the effects of environment on the mechanical behavior of commercially available ceramics being considered for heat engine applications. In the first phase of this project, the effects of environment on the mechanical behavior of transformation-toughened ZrO_2 ceramics were investigated. In the second phase, two Si_3N_4 ceramics (GTE PY6 and Norton/TRW XL144) and one SiC ceramic (Hexoloy SA) were evaluated. In the third phase, the tensile, flexural, and fatigue strength of three SiC and six Si_3N_4 ceramics were evaluated at temperatures ranging from 20 to 1400°C. Microstructure, chemistry, and physical properties were also investigated. In the fourth phase, the flexural strength and fatigue behavior of two additional Si_3N_4 ceramics (Kyocera SN-260 and Garrett GN-10) were investigated. In addition, the fatigue behavior of one Si_3N_4 ceramic (Norton/TRW NT-154) was investigated. Efforts to study the tension/compression cyclic fatigue behavior of NT-154 have been delayed because of problems with the Instron test fixture. In phase five, three newly developed SiC and three newly developed Si_3N_4 ceramics are being investigated. In addition, the effects of different machining processes on the mechanical behavior of selected SiC/Si_3N_4 ceramics will be studied.

During the past six months (April 1992 through September 1992), Norton/TRW NT-164, Si_3N_4 (β Si_3N_4 with 4% Y_2O_3), was investigated. In addition, modification of the tension/compression test system was continued and the flexural stress rupture of GN10 and NT-230 were measured.

Technical progress

Flexural strength, tensile strength, elastic modulus, hardness, density, coefficient of thermal expansion, and fracture toughness for NT-164 were evaluated. Flexural stress rupture of NT-230 (following MIL STD-1942) was measured at 1350°C using stress values of 237 and 305 MPa. In addition, the flexural stress rupture of GN-10 was also measured at temperatures of 1300°C and 1350°C using stress values of 465, 300, and 274 MPa.

The flexural strength measurements were made using Instron Universal Testing Machines (Model 1123) following MIL-STD-1942(MR). Elevated temperature measurements were conducted in ATS model #3320 high-temperature furnaces. Flexural strengths were measured on test specimens with nominal dimensions of 3 x 4 x 50 mm with all surfaces ground to a 16-microinch finish [MIL-STD-1942(MR) specimen size B]. The long edges of the tensile surface were beveled to minimize edge failures. Flexural strength was measured using four-point bend test fixtures, and the test specimens were loaded at machine

*Research sponsored by the U.S. Department of Energy, Assistant Secretary for Conservation and Renewable Energy, Office of Transportation Systems, as part of the Ceramic Technology for Advanced Heat Engines Project of the Advanced Materials Development Program under Contract DE-AC05-840R21400 with Martin Marietta Energy Systems, Inc., Work Breakdown Structure Subelement 3.3.1.4.

crosshead speeds of 0.004, 0.0004, and 0.00004 cm/sec (0.1, 0.01, 0.001 in/min). The bend fixtures for all measurements were made of SiC. The four-point bend fixtures have an outer span of 40 mm and an inner span of 20 mm. Flexural stress rupture was conducted following MIL-STD-1942 at 1300°C and 1350°C from 237 to 527 MPa for exposures up to 120 hours.

Tensile strengths were measured using cylindrical buttonhead specimens in an Instron Corporation Universal testing machine Model 1361 with "Super Grip" specimen holders and an Instron short furnace. Tensile strength tests of NT-164 were conducted at 20°C and 1350°C using crosshead rates of 0.004 and 0.00004 cm/s. In addition, the tensile stress rupture of two specimens was evaluated at 1350°C.

The following analysis and physical property measurements were also made:

- Fracture origins were determined by optical microscopy (Nikon Epiphot) and SEM (JEOL/SM-80 with EG&G Ortec System 5000 Microanalysis System).
- The microstructure and chemistry of the candidate materials were also studied. Polished specimens were plasma etched and viewed by optical microscopy and by scanning electron microscopy.
- Thermal expansion was measured from 20°C to 1370°C using a Theta Industries Dilatronic II (Model 6024).
- The elastic modulus was measured from 20°C to 1350°C using a Grindo-Sonic (Model MR35T) Transient Impulse/Elastic Modulus apparatus.
- The hardness of the candidate materials was measured by a Vickers micro-indent hardness tester. Fracture toughness was measured by the controlled flaw method using an indent load of 500g.

The results of the flexural strength testing for NT-164 are presented in Table 1.

Table 1. Flexural Strength Measurement of NT-164 Si_3N_4

Temp. (°C)	Loading Rate (cm/s)	Flexure Strength (MPa)	Coefficient of Variation (%)	Failure Initiation Site+
20	0.004	1093 ± 97	9	8 surf, 1 edge, 1 undetermined
20	0.00004	925 ± 59	6	5 edge
1250	0.004	757 ± 67	9	9 surf , 1 edge
1250	0.00004	676 ± 51	8	5 surf
1350	0.004	785 ± 31	4	10 surf
1350	0.0004	747 ± 38	5	4 surf, 1 edge
1350	0.00004	654 ± 9	1	4 surf, l edge

*coefficient of variance (std dev/strength x 100)%
+surf - surface

Flexural strength measured for NT-164 is plotted as a function of temperature in Figure 1. A significant decrease in flexural strength for NT-164 was observed at the slowest stressing rate at 20°C, 1250°C, and 1350°C. The decrease in strength at the slower stress rates would suggest susceptibility to creep at 1250°C and 1350°C. Slow stress rate strength decrease at 20°C is usually attributed to moisture induced stress corrosion. However, every NT-164 specimen in the set tested at 20°C and 0.00004 cm/s failed at edge initiation sites, and this mode of failure may be responsible for the decrease observed. The NT-164 material is also subject to a decrease in strength with increasing temperature. A 20 to 30% decrease was observed from 20°C to 1350°C.

Comparison of the flexural strength of NT-164 with NT-154 is plotted in Figures 2a and 2b. As shown in Figures 2a and 2b, the flexural strength of NT-164 ranged from 14 to 25% higher than measured for NT-154. The higher strength of NT-164 prevails at both the rapid and slower stressing rate conditions.

The results of the tensile strengths measured for NT-164 are presented in Table 2 and plotted as a function of temperature in Figure 3. Comparison of the tensile strengths of NT-164 with NT-154 are plotted in Figures 4a and 4b.

Table 2a. Tensile Strength Measurement of NT-164 Si_3N_4

Temp.	Loading Rate (cm/s)	Strength (MPa)	Failure Situation Site
20	0.004	700	2 volume; 1 @ pore; 1 @ inclusion*
	0.00004	546	1 volume @ pore
1350	0.004	567	1 volume @ inclusion; 1 surface
	0.00004	388	2 surface

Table 2b. Tensile Stress Rupture at 1350°C

Stress (MPa)	Time to Failure (min)	Fracture Origins
284	77	surface
379	6	surface

*EDXA of inclusions showed the following metallic elements; Mn, Cr, Ni and Fe (in order of increasing percentage).

As shown in Figures 4a and 4b, the NT-164 has higher tensile strength than NT-154 at both rapid and slow stressing rate. However, NT-164 is also susceptible to high temperature (1350°C) creep. The stress rupture behavior appears similar to that observed for NT-154. However, the data is very limited. The results of the flexural stress rupture testing for NT-164 are presented in Table 3. As shown in Table 3 a number of the flexural specimens were subject to deformation (bending). Typical deformation obtained for NT-164 specimens are shown in Figures 5a and 5b. As shown in Table 3 the flexural stress rupture displayed the same degree of variation as was found for the tensile stress rupture.

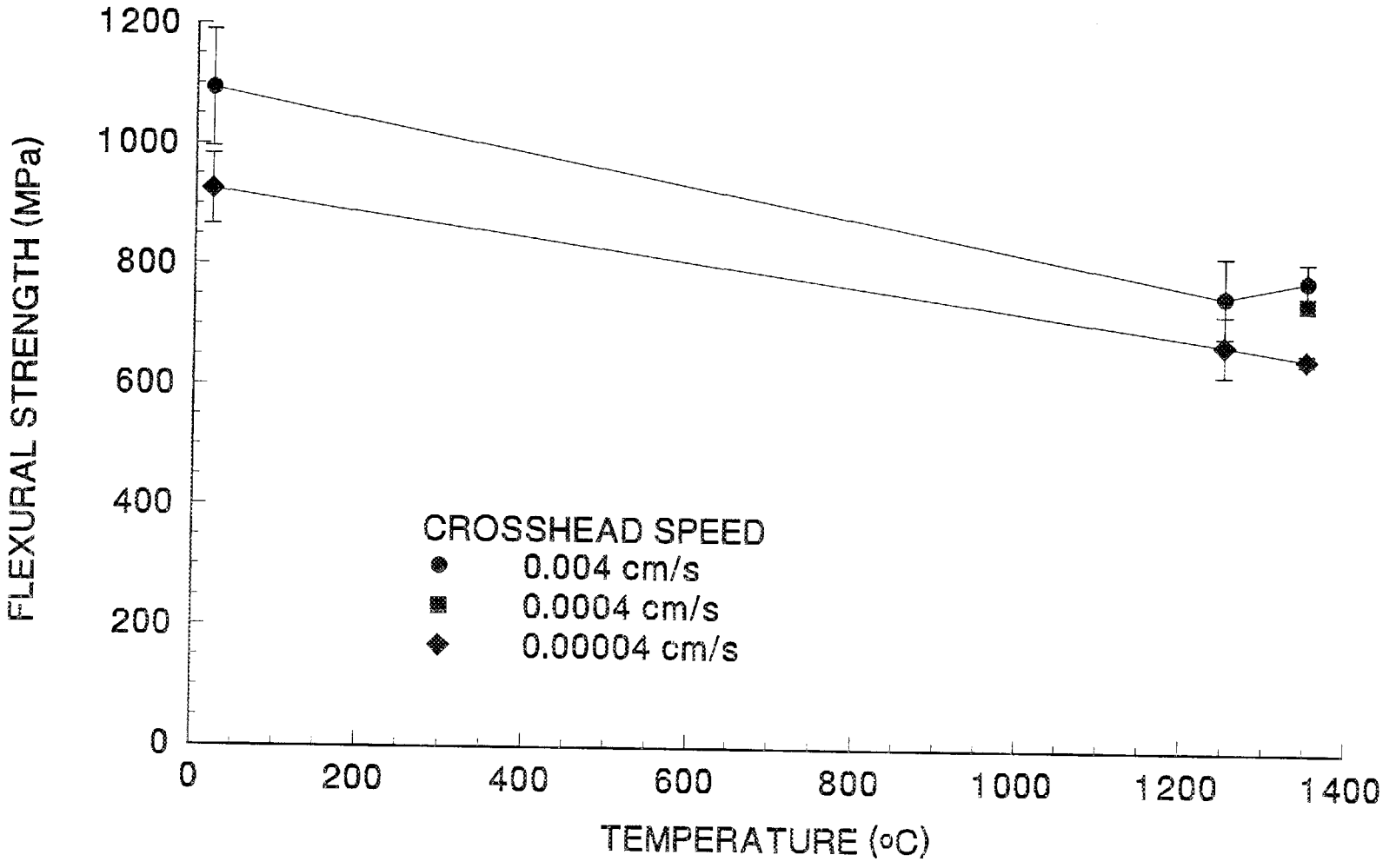

Figure 1. Flexural strength of Norton/TRW NT-164 Si_3N_4.

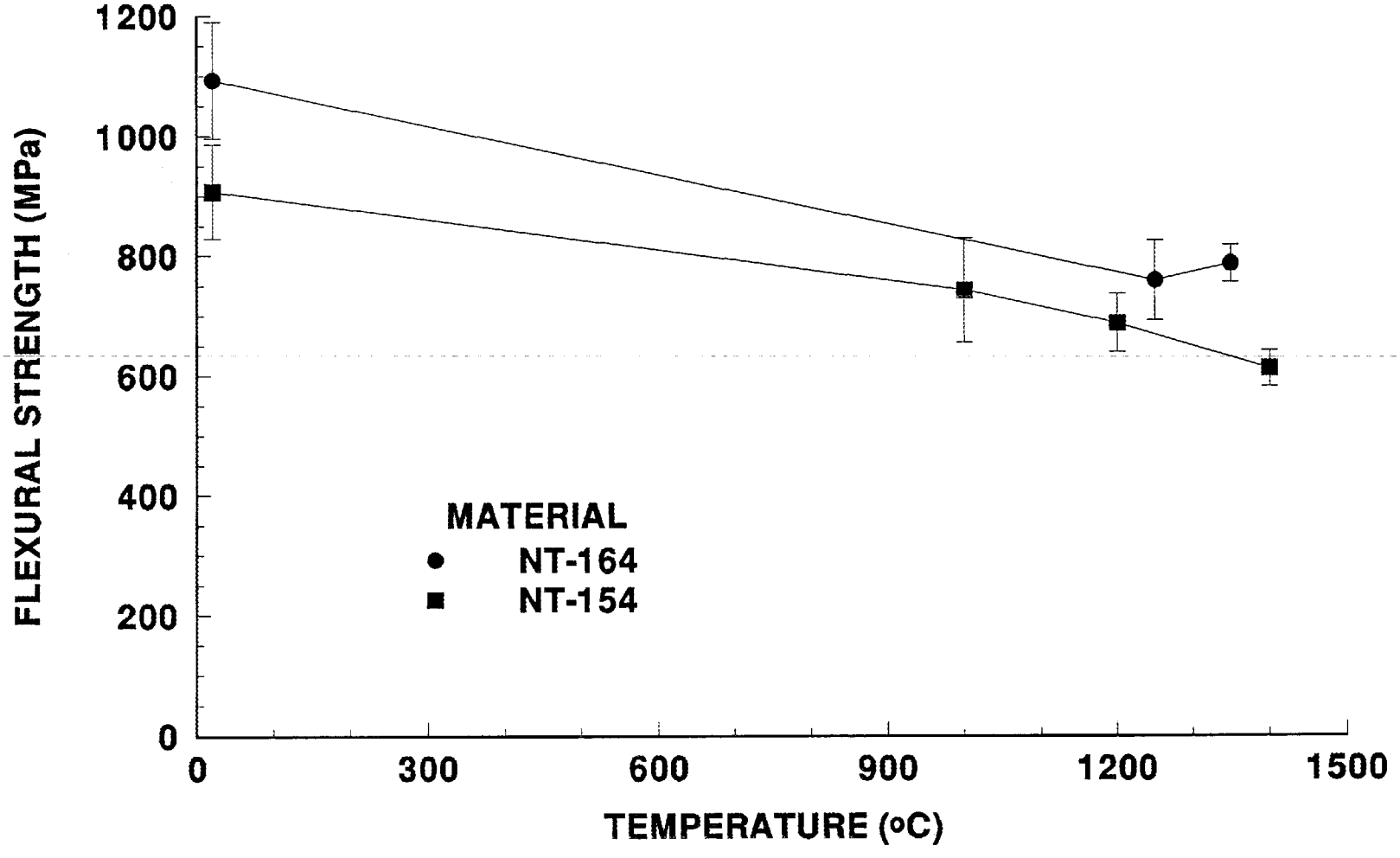

Figure 2a. Comparison of Norton/TRW silicon nitrides (crosshead speed 0.004 cm/s).

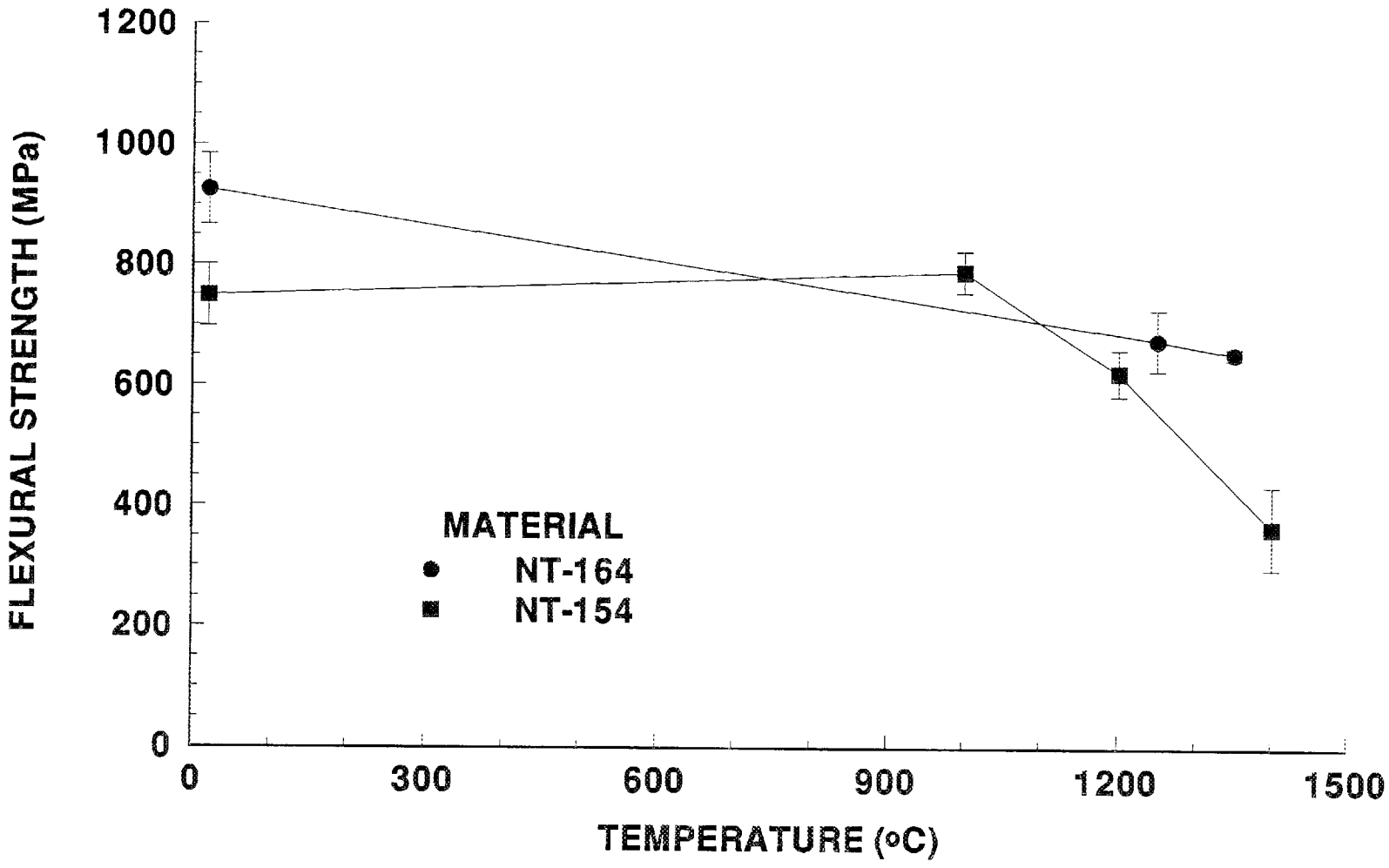

Figure 2b. Comparison of Norton/TRW silicon nitrides (crosshead speed 0.00004 cm/s).

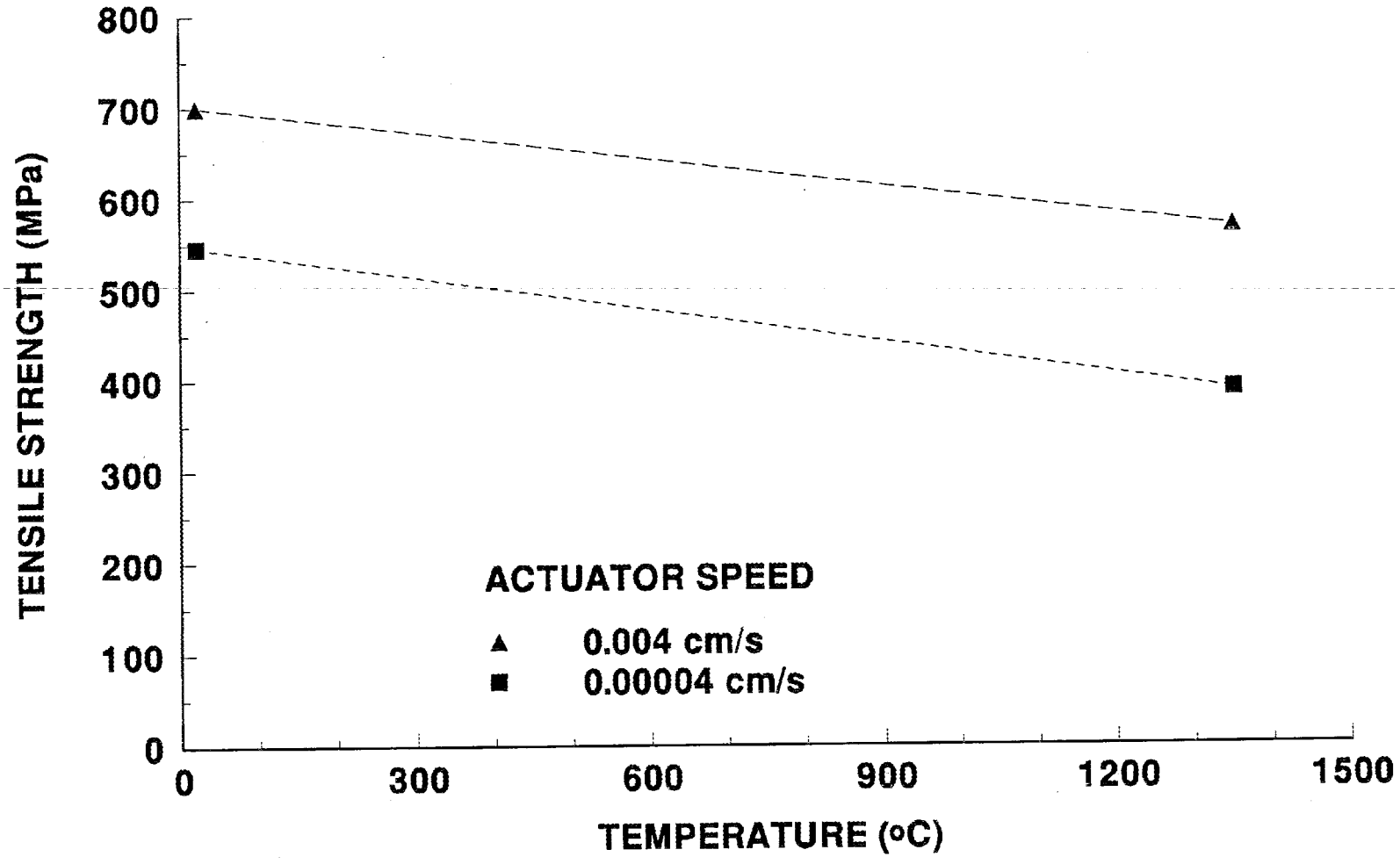

Figure 3. Tensile strength of Norton/TRW NT-164.

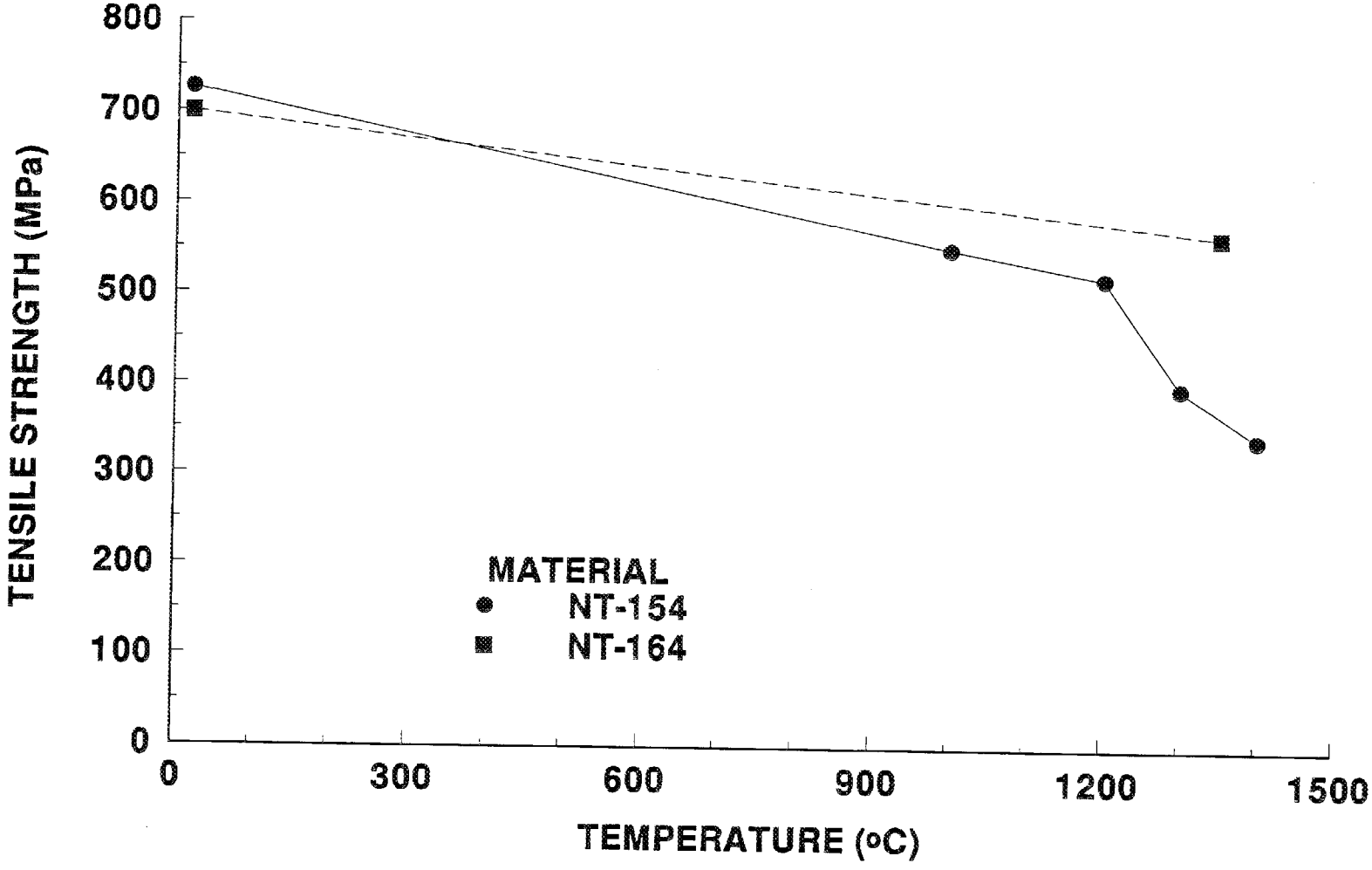

Figure 4a. Comparison of Norton/TRW silicon nitrides (actuator speed 0.004 cm/s).

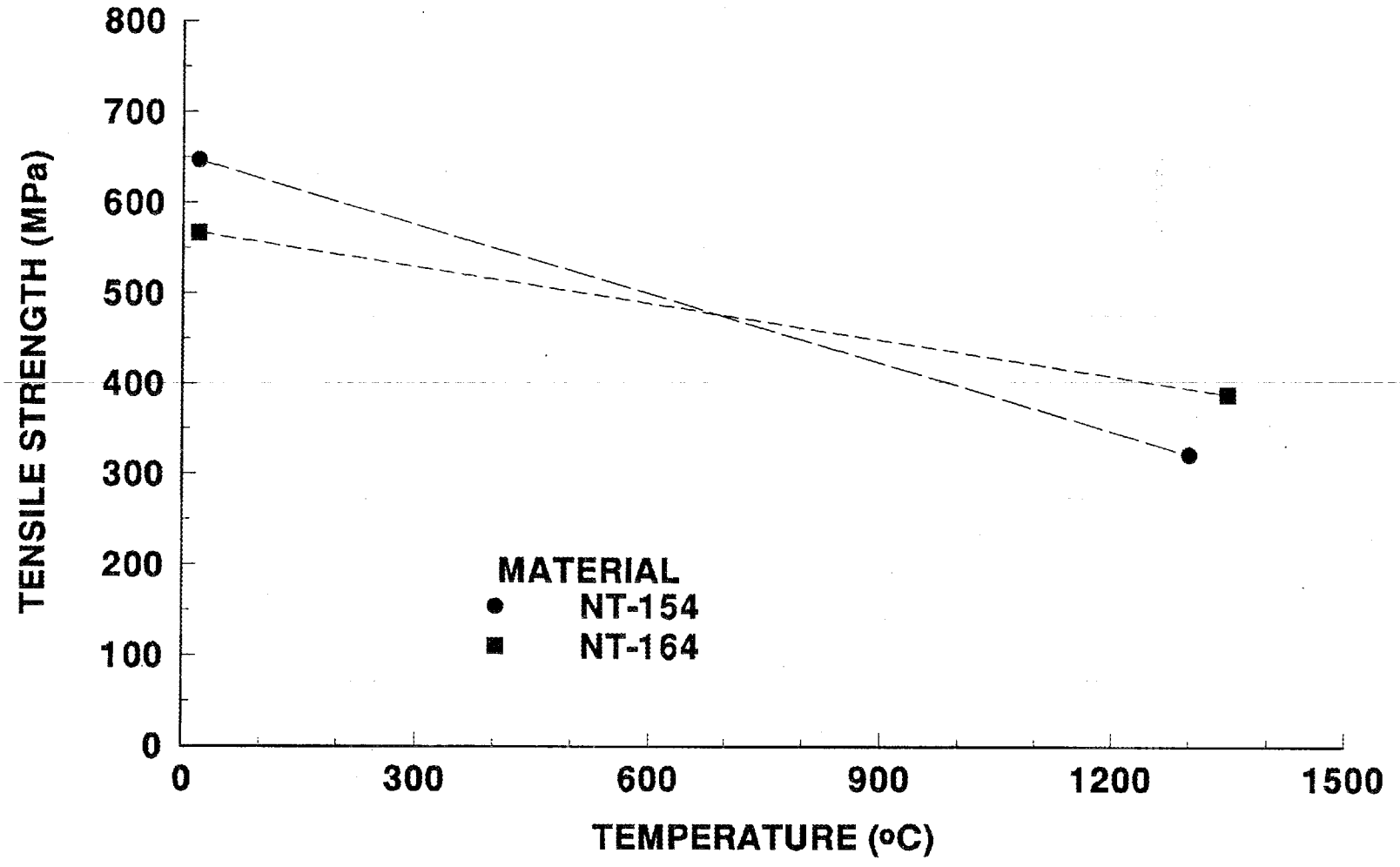

Figure 4b. Comparison of Norton/TRW silicon nitrides (actuator speed 0.00004 cm/s).

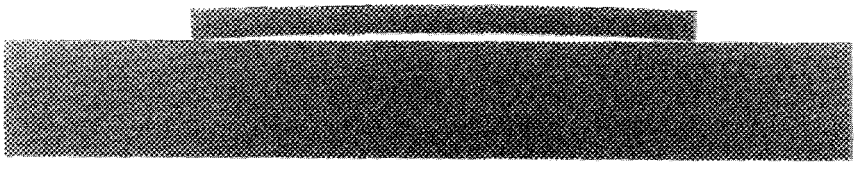

Silicon Nitride, NT-164

a) flexural static fatigue, 1350°C/102.7 hrs., specimen #83

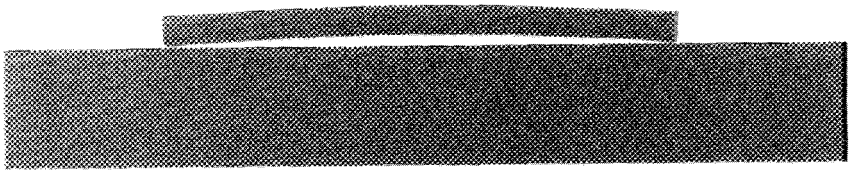

Silicon Nitride, NT-164

b) flexural static fatigue, 1350°C/108.7 hrs, specimen #79

Figures 5a and b. Typical flexural stress rupture deformation for two NT-164 specimens.

Table 3. Flexural Strength Rupture of NT-164

Number	Temp. °C	Stress (MPa)	Time (hrs)	Comments+
76	1350	527	u[x]	surface flaw
77	1350	527	5.3	surface flaw
78	1350	385	3.7	spec def*
79	1350	385	108.7	surface flaw
80	1350	385	0.65	surface flaw
81	1350	385	1.05	surface flaw
82	1350	385	0.4	edge flaw
83	1350	261	102.7	spec def*
84	1350	261	102	spec def*
13	1350	261	102	spec def*

+comments denote failure origin
*spec def = specimen deformation (bending)
[x]u = unknown

A summary of the physical properties measured for NT-164 are presented in Table 4. Micrographs of NT-164 fractured tensile specimens are shown in Figure 6. The EDAX spectrum obtained for the inclusions shown in specimen #9 (Figure 6) is shown in Figure 7. Micrographs of NT-164 fractured flexural specimens are shown in Figure 8. Specimen #12 was found to have an inclusion and blister (bubble) on its surface. Micrographs showing specimen #12 and the blister and inclusion at high magnification are presented in Figure 9. EDAX spectra for both the blister and inclusion are presented in Figure 10. The micrographs obtained for NT-164 specimens tested in flexural stress rupture are presented in Figure 11. These micrographs provide better insight into the fracture behavior of these ceramics.

Table 4. Summary of Property Measurement Results of NT-164

Average Young's Modulus (GPA)	
20°C	306.1
1000°C	295.7
1250°C	291.7
1350°C	290.6
Density (g/cc)	3.1%
Average Hardness (kg/mm^2)	1891*
Coefficient of Thermal Expansion (10^{-6}mm/cm in/°C)	4.93
Fracture Toughness (MPa • m$^{1/2}$)	4

*500 g load

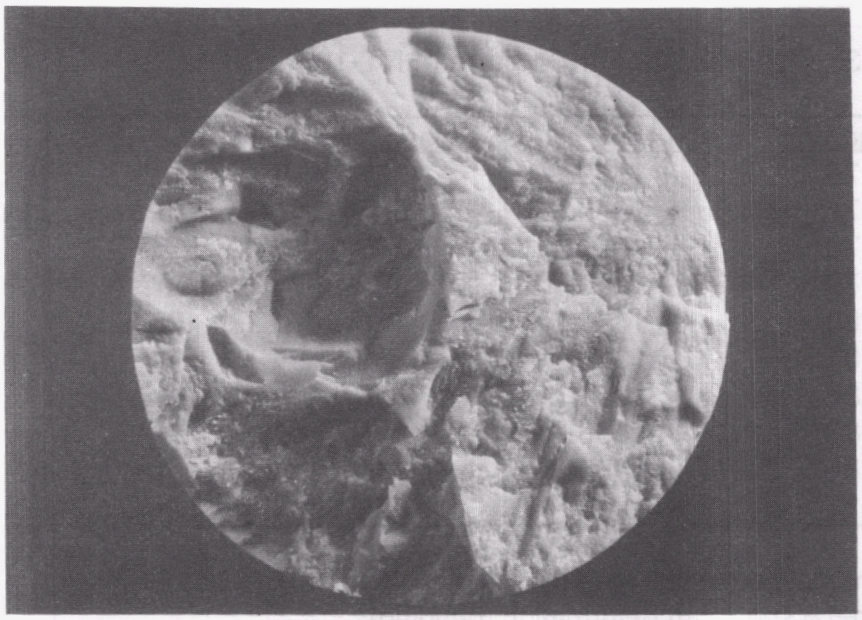

a) specimen #13 tested at 20°C at 0.004 cm/s crosshead speed

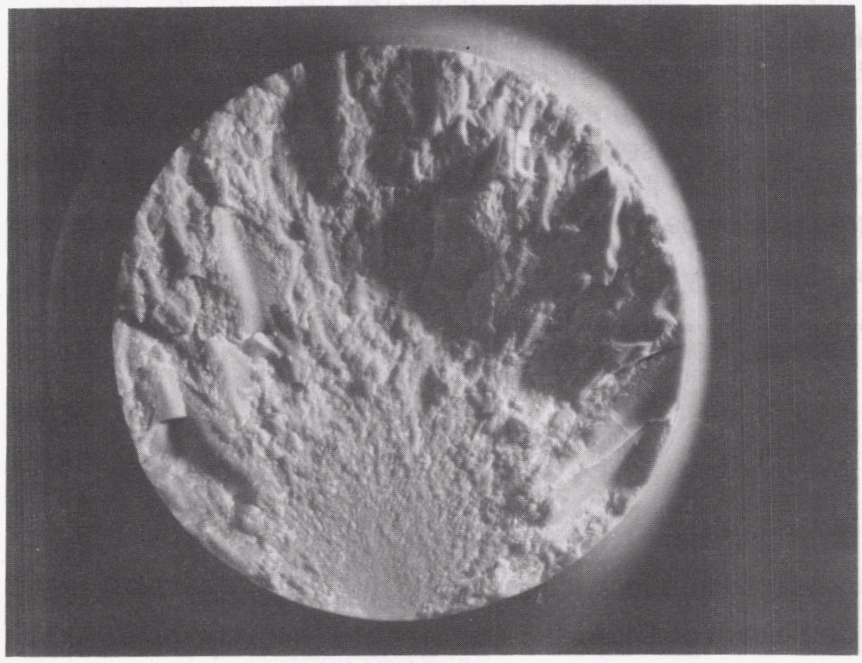

b) specimen #12 tested at 20°C at 0.00004 cm/s crosshead speed

Figures 6a and b. Micrographs of NT-164 fractured tensile specimen (12X).

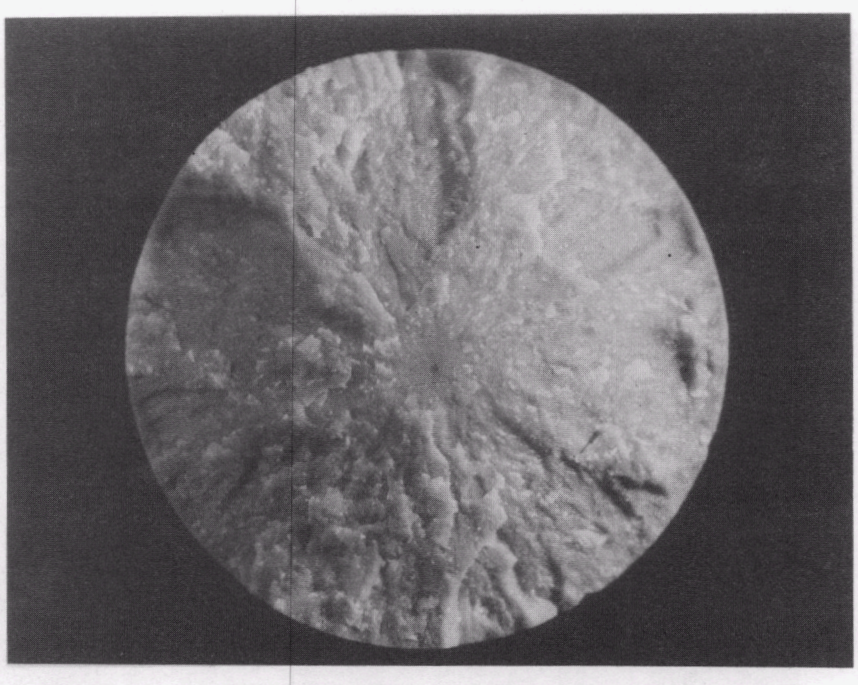

c) specimen #9 tested at 1350°C at 0.004 cm/s crosshead speed

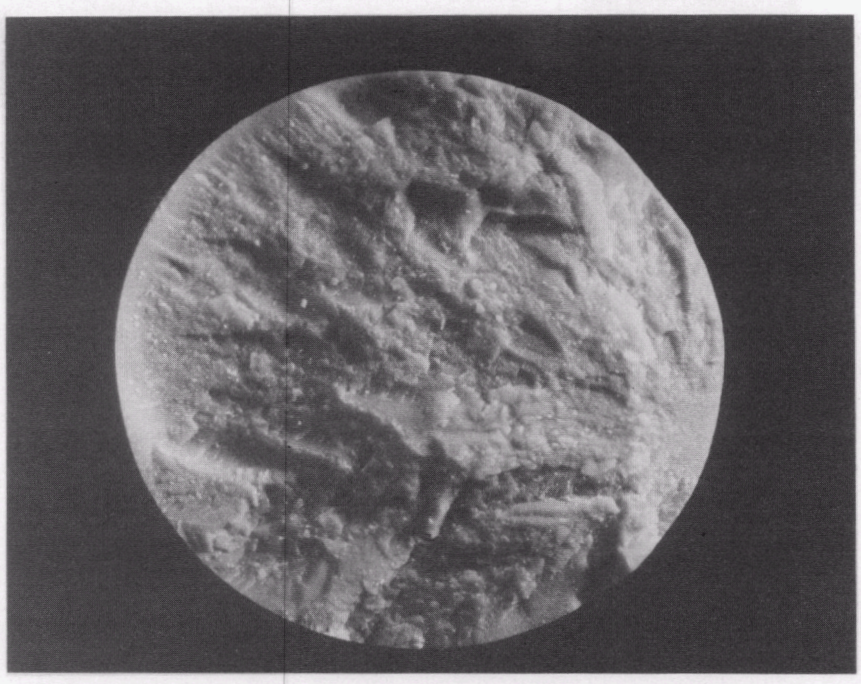

d) specimen #15 tested at 1350°C at 0.00004 cm/s crosshead speed

Figures 6c and d. Micrographs of NT-164 fractured tensile specimen (12X).

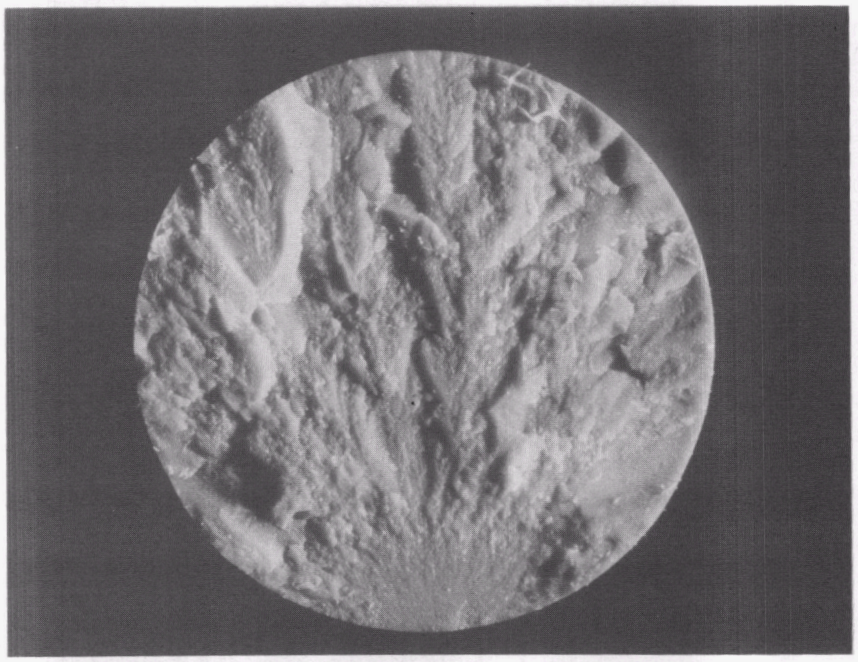

e) specimen #5 tested in tensile stress rupture
at 1350°C at a stress of 284 MPa

Figure 6e. Micrograph of NT-164 fractured tensile specimen (12X).

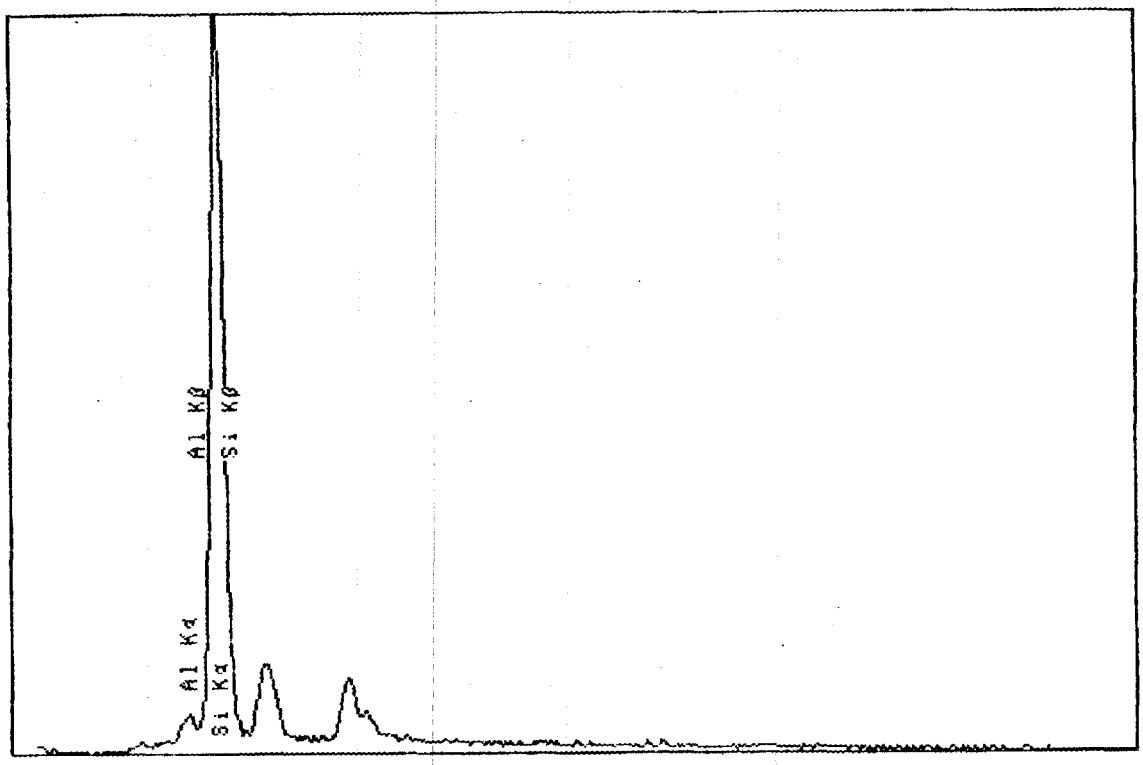

Figure 7. EDAX spectrum of inclusion in NT-164, specimen #9.

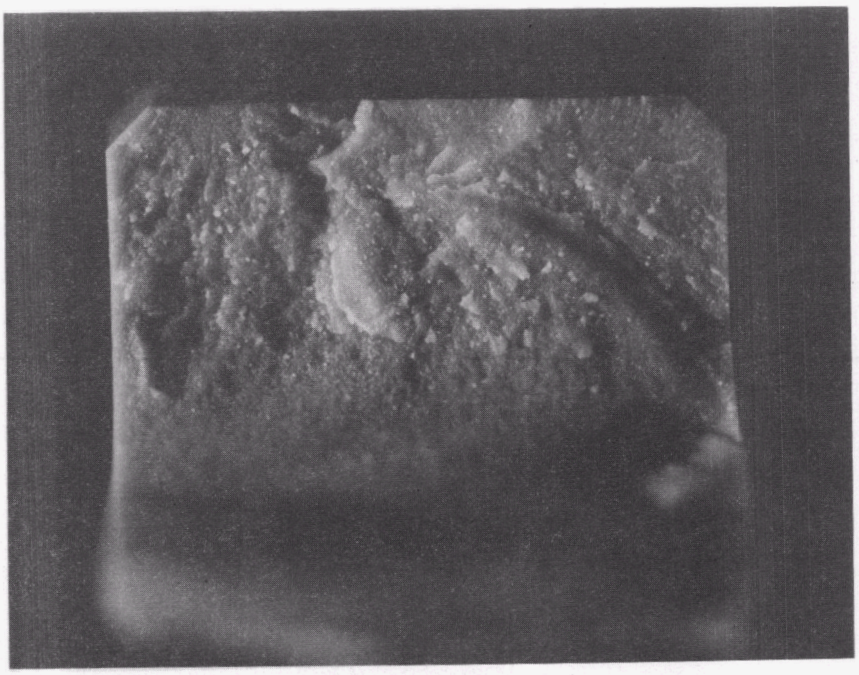

a) specimen #72 tested at 1250°C at 0.00004 cm/s crosshead speed

b) specimen #5 tested at 1350°C at 0.004 cm/s crosshead speed

Figures 8a and b. Micrographs of NT-164 fractured flexural specimens (20X).

c) specimen #20 tested at 1350°C at 0.0004 cm/s crosshead speed

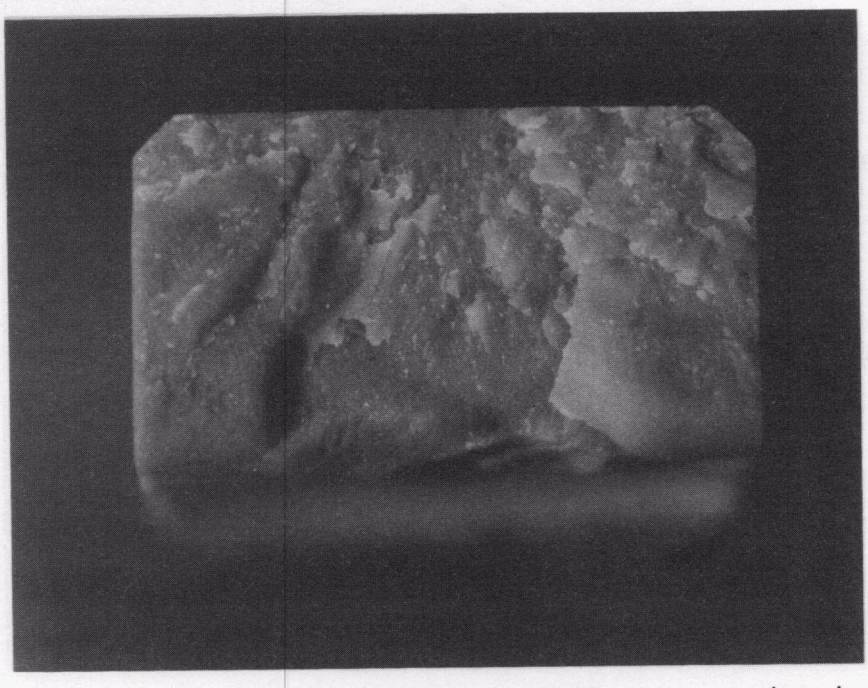

d) specimen #12 tested at 1350°C at 0.00004 cm/s crosshead speed

Figures 8c and d. Micrographs of NT-164 fractured flexural specimens (20X)

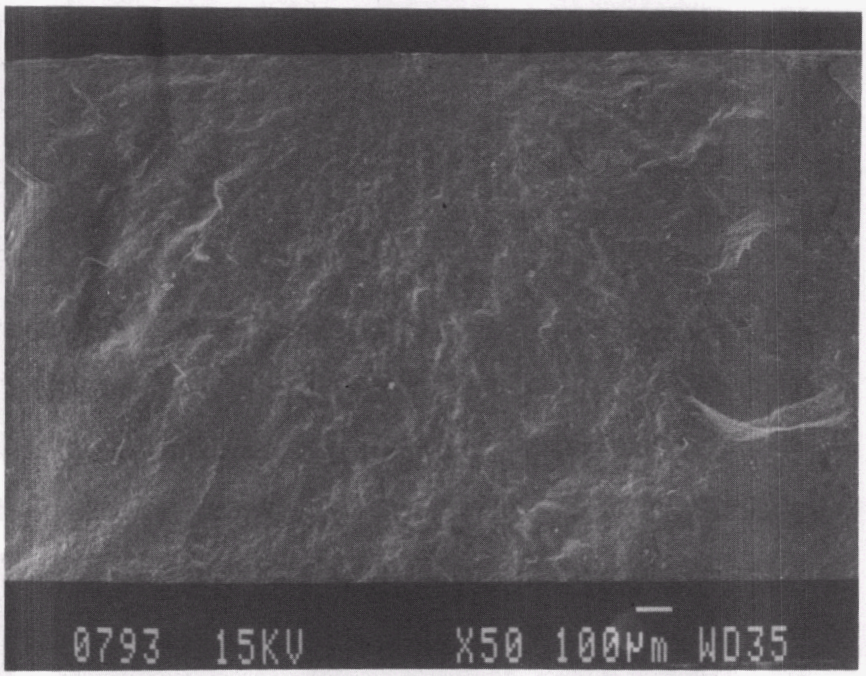

e) specimen #12 tested at 1350°C at 0.00004 cm/s crosshead speed (50X)

Figure 8e. Micrograph of NT-164 fractured flexural specimen (50X).

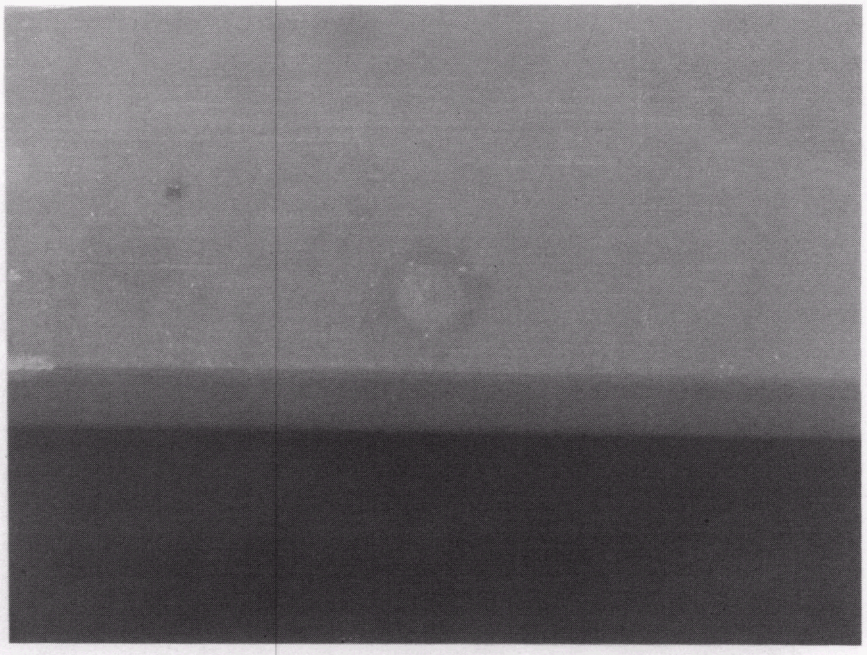

a) blister and inclusion (30X)

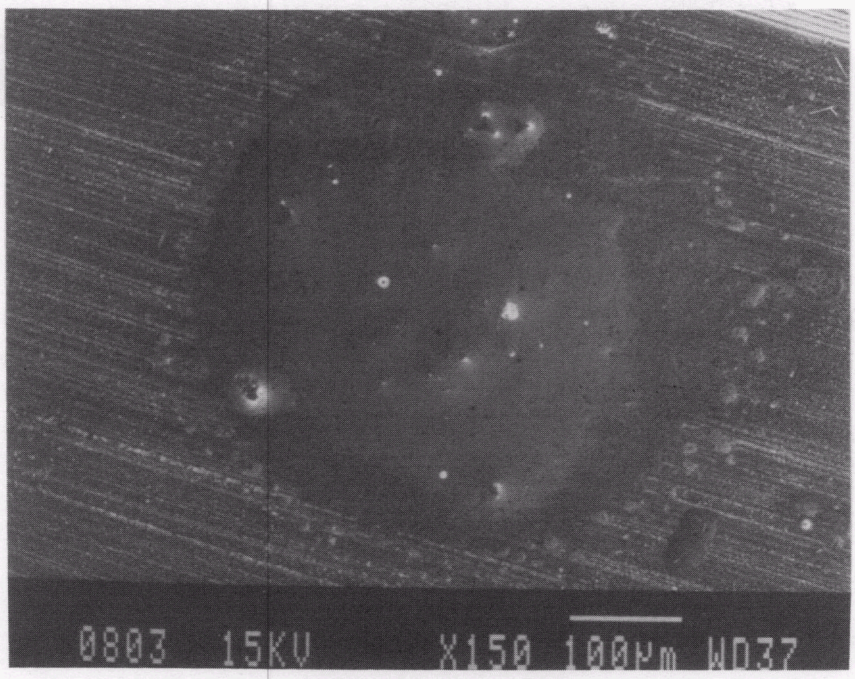

b) blister (150X)

Figures 9a and b. Micrographs of the blister and inclusion found on the surface of NT-164, specimen #12.

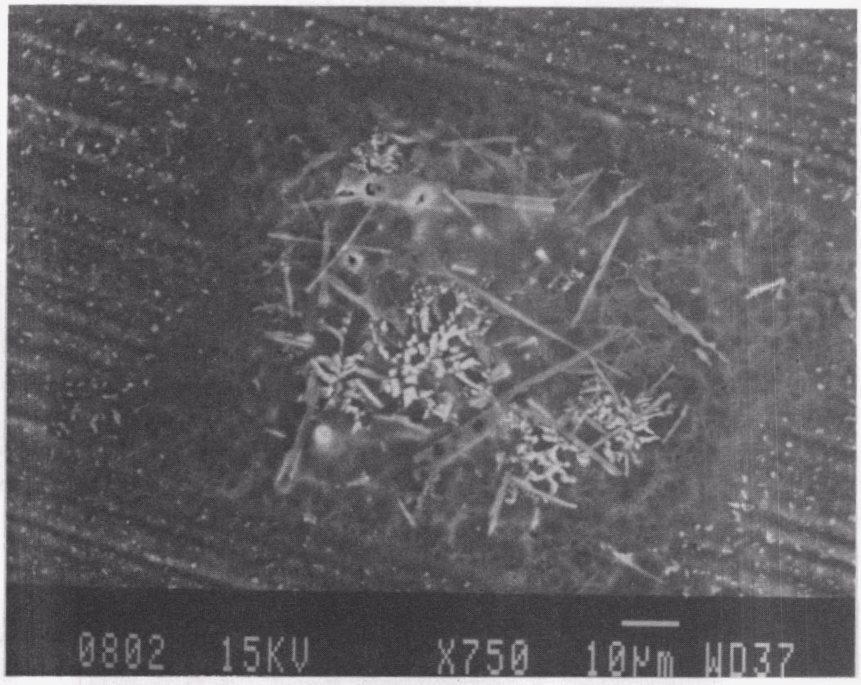

c) inclusion (750X)

Figure 9c. Micrograph of inclusion found on the surface of NT-164, specimen #12.

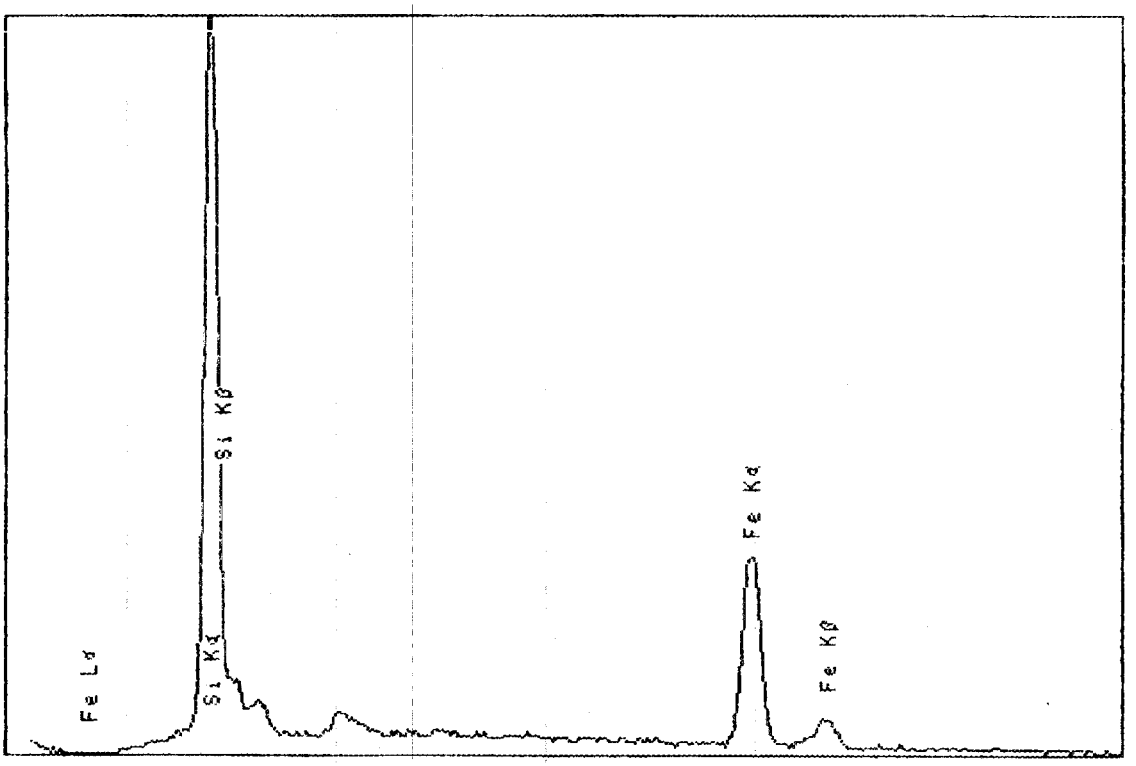

a) inclusion spectrum on specimen surface

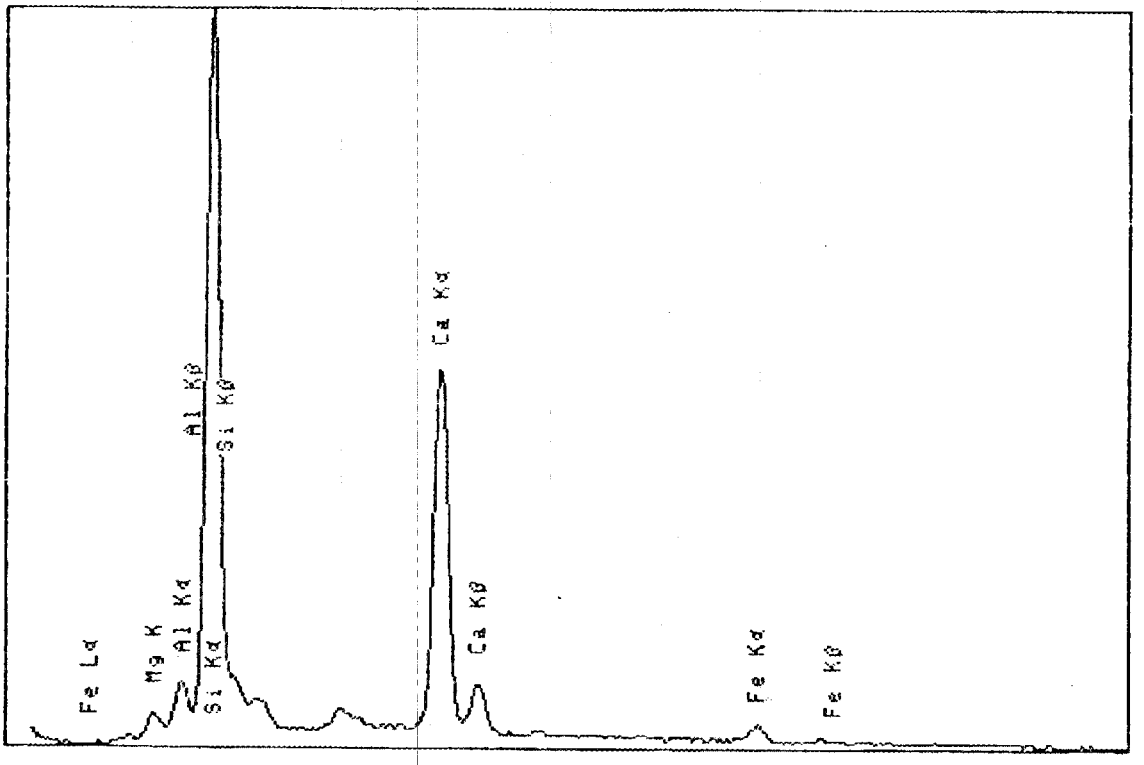

b) blister spectrum on specimen surface

Figures 10a and b. NT-164, specimen #12.

a) specimen #81 tested at 1350°C at 385 MPa (20X)

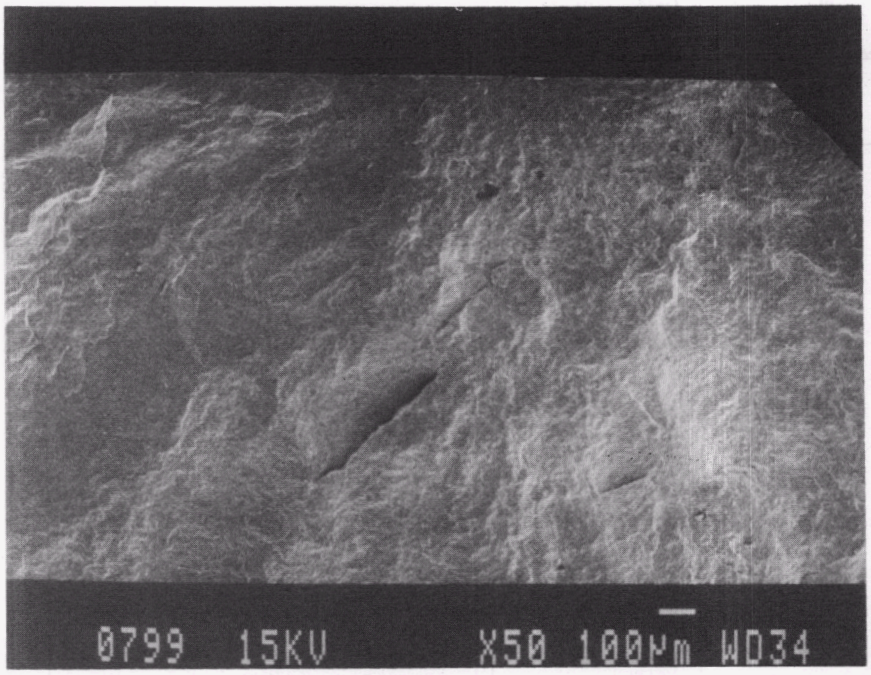

b) specimen #81 tested at 1350°C at 385 MPa (50X)

Figures 11a and b. Micrographs of NT-164 specimens tested in flexural stress rupture.

The results for the flexural stress rupture testing of GN-10 and NT-230 are presented in Tables 5 and 6.

Table 5. Flexural Stress Rupture of GN-10¤

Number	Temp. °C	Stress (MPa)	Time (hrs)	Comments+
31	1350	465	3.2	-
32	1350	465	32.6	surface flaw
33	1350	300	7.0	edge
34	1350	300	7.3	edge
35	1350	274	5.4	pitting
36	1350	274	112.8	spec def*
37	1300	274	104.3	spec def*
38	1300	274	14.7	spec def*
39	1300	274	104.9	spec def*
40	1300	274	23.2	spec def*

¤specimens were severely oxidized
+comments denote failure origin
*spec def = specimen deformation (bending)

Table 6. Flexural Stress Rupture of NT-230

Number	Temp. °C	Stress (MPa)	Time (hrs)	Comments
60	1350	237	116.8	Bent* (defl.-.112 mm)
61	1350	237	116.8	Bent* (defl.-.106 mm)
63	1350	305	163	Bent* (defl.-.169 mm)
64	1350	305	163	Bent* (defl.-.164 mm)
65	1350	305	106.3	Bent* (defl.-.191 mm)
66	1350	305	30	Surface Failure at Pit
67	1350	237	118.6	Bent* (defl.-.187 mm)
68	1350	237	118.6	Bent* (defl.-.174 mm)
69	1350	237	120.2	Bent* (defl.-.163 mm)

*Nine of the 10 specimens deformed (bent). The degree of deflection (defl.) was measurec for each bent specimen.

During this reporting period the resistance to pest oxidation was evaluated at 850°C, 900°C, and 950°C for four Si_3N_4. Both as-received and surface ground specimens of NT-154, PY6, GN-10, and SN-260 Si_3N_4 were weighed after 50, 100, 150, 200, and 250 hour exposures at temperature. The percent weight change as a function of time and temperature for all four Si_3N_4 ceramics is presented in Tables 7a-c. As shown in Tables 7a-c only the SN-260 showed any evidence of low temperature oxidation effects. The surface ground samples showed greater susceptibility to oxidation effects.

Status of milestones

Milestones 331415 and 331416 are in progress.

Table 7a. Pest Oxidation Effects

PEST OXIDATION STUDY 850°C

UDRI CONTROL NUMBER: SMG-92-1-44

Material	Specimen Number	Condition	% Weight Change @ 0 hrs.	% Weight Change @ 50 hrs.	% Weight Change @ 100 hrs.	% Weight Change @ 150 hrs.	% Weight Change @ 200 hrs.	% Weight Change @ 250 hrs.
NT-154	10	As Received	XX	0.016	0.008	0.008	-0.008	-0.008
NT-154	35	Ground	XX	0.000	-0.011	0.000	-0.023	-0.023
PY-6	75	As Received	XX	0.008	0.008	0.008	-0.024	0.000
PY-6	63	Ground	XX	0.000	-0.011	0.011	-0.011	0.011
GN-10	8	As Received	XX	0.000	-0.010	0.020	-0.010	0.000
GN-10	58	Ground	XX	0.031	0.041	0.062	0.031	0.041
SN-260	16	As Received	XX	0.092	0.172	0.368	0.655	0.816
SN-260	33	Ground	XX	0.083	0.156	0.250	0.344	0.490

Table 7b. Pest Oxidation Effects

PEST OXIDATION STUDY 900°C

UDRI CONTROL NUMBER: SMG-92-1-45

Material	Specimen Number	Condition	% Weight Change @ 0 hrs.	% Weight Change @ 50 hrs.	% Weight Change @ 100 hrs.	% Weight Change @ 150 hrs.	% Weight Change @ 200 hrs.	% Weight Change @ 250 hrs.
NT-154	5	As Received	XX	0.000	0.000	-0.011	-0.011	-0.011
NT-154	33	Ground	XX	0.011	-0.011	-0.011	-0.077	0.000
PY-6	72	As Received	XX	-0.009	-0.028	-0.038	-0.056	-0.019
PY-6	62	Ground	XX	-0.011	-0.044	-0.044	-0.066	-0.022
GN-10	5	As Received	XX	0.018	0.018	0.000	-0.027	-0.018
GN-10	57	Ground	XX	0.033	0.011	0.000	0.011	-0.011
SN-260	15	As Received	XX	0.075	1.544	0.000	0.015	0.105
SN-260	32	Ground	XX	0.986	1.143	1.248	1.311	1.626

Table 7c. Pest Oxidation Effects

PEST OXIDATION STUDY 950°C

UDRI CONTROL NUMBER: SMG-92-1-45

Material	Specimen Number	Condition	% Weight Change @ 0 hrs.	% Weight Change @ 50 hrs.	% Weight Change @ 100 hrs.	% Weight Change @ 150 hrs.	% Weight Change @ 200 hrs.	% Weight Change @ 250 hrs.
NT-154	2	As Received	XX	0.000	-0.020	-0.041	-0.010	0.000
NT-154	31	Ground	XX	-0.033	-0.055	-0.088	-0.055	-0.033
PY-6	71	As Received	XX	0.033	0.008	-0.016	0.000	0.008
PY-6	61	Ground	XX	0.000	-0.022	-0.065	0.043	-0.011
GN-10	1	As Received	XX	0.035	0.017	-0.026	0.000	0.035
GN-10	56	Ground	XX	0.021	0.010	-0.021	0.021	0.042
SN-260	14	As Received	XX	0.086	0.238	0.432	0.843	1.113
SN-260	31	Ground	XX	0.922	1.163	1.247	1.351	1.477

3.4 FRACTURE MECHANICS

Testing and Evaluation of Advanced Ceramics at High Temperature in Uniaxial Tension

J. Sankar, A. D. Kelkar, and S. Krishnaraj
(North Carolina A&T State University)

Objective/Scope

The objective of this research is to test and evaluate the mechanical behavior of a sintered Si_3N_4 in uniaxial tension at temperatures upto 1200^0 C. The emphasis of this effort in the current year is to analyze the influence of precycling on the creep behavior and the tensile strength of GTE SNW-1000 at 1200^0 C, and to compare these results with previously obtained creep data for the same material. This effort also includes micro-structural/microchemical analysis of the fracture surfaces using scanning electron microscopy(SEM) and energy dispersive spectral analysis(EDS).

Technical Progress

All investigations were performed at 1200^0 C in uniaxial tension.

1. Investigate the effect of precycling on the creep behavior(specimens 1 and 2).
2. Investigate the effect of precycling and creep loading on the residual tensile strength(specimen 3).
3. Investigate the effect of precycling on the residual tensile strength(specimen 4-11).

Test Procedure: Virgin specimens 1 through 3 were creep tested in uniaxial tension at 1200^0 C immediately following the uniaxial fatigue loading at the same temperature. Specimens 1 and 2 were cycled using a constant amplitude triangular waveform. Load was applied in tension with maximum stresses of $50\%\sigma_f$(70 MPa) and $70\%\sigma_f$(98 MPa) of the material at 1200^0 C respectively. σ_f is the fatigue strength of SNW-1000 at 1200^0 C, which is 140 MPa (Liu et al., 1987).

Specimen 3 was cycled from low(50%) to high(70%) stress levels in steps. This method of loading is called "coaxing". This specimen which was cyclically loaded in coaxing mode, was not tested until failure in creep. Instead, after 290 hours of creep testing, it was tested in tension at a stressing rate of 450 MPa/min to find its residual tensile strength.

Eight(8) virgin specimens(specimens 4 through 11) were precycled in four different levels of tension-tension loading patterns at 1200^0 C. Two(2) specimens were cycled in tension in each pattern, the conditions being maximum stresses of $25\%\sigma_f$(35 MPa), $50\%\sigma_f$(70 MPa), and $70\%\sigma_f$(98 MPa) at 1200^0 C. The last two specimens(10 and 11) were coaxed from low(50%) to high(70%) stress levels in steps. All the eight(8) samples, after cycling were pulled in tension at 1200^0 C at a stressing rate of 450 MPa/min. This was done to see the effect of precycling on the strength of the silicon nitride material.

COMMON FATIGUE LOADING PARAMETERS FOR ALL TESTS:

Tension-tension cyclic triangular waveform
Frequency: 0.5 Hz
Cycles: 50,000
Temperature: 1200 ^{0}C
R-Ratio(min. stress/max. stress): 0.1
Maximum stress: Varying percentages of the fatigue strength of the material at 1200 ^{0}C.
(Available data from ORNL: Fatigue strength of SNW-1000 at 1200 ^{0}C = 140 MPa.)

CREEP LOADING CONDITIONS:

Uniaxial constant tensile load
Temperature: 1200 ^{0}C
Load: 161 MPa(70% tensile strength of SNW-1000 at 1200 ^{0}C
(Available data: Average tensile strength of SNW-1000 at 1200 ^{0}C = 230 MPa)

TENSILE LOADING CONDITIONS:

Uniaxial tensile load at a stressing rate of 450 MPa/min.
Temperature: 1200^0 C

Test Results and Discussions:

Cyclic loading prior to creep loading in specimens 1 through 3 resulted in low primary creep strain curves as well as lower steady state creep rates (Figure 1.) as compared to the plain creep curves(Fig 2.), which was reported earlier (Sankar et al., 1991). A comparison of the three creep curves (Figure 1.) which were precycled at different stress levels and pattern, showed that coaxed precycled specimen(#3) yielded the least primary creep strain amongst the precycled specimens. From the current results, it can be shown that coaxing enhances the creep resistance of the material. The specimen, which was not tested until failure in creep(specimen 3), when tested in tension at a stressing rate of 450 MPa/min immediately following the creep, yielded the maximum residual tensile strength(580 MPa). This strength value is even higher than the average room temperature tensile strength(492 MPa)(Vaidyanathan et al., 1987) for this material.

The results of residual tensile strength of the SNW-1000 after just precycling is shown in Figure 3. The average residual tensile strengths obtained in different fatigue conditions is compared(Figure 4.) with those of the monotonic tension tests performed earlier at room temperature and 1200^0 C. From these results, it can be seen that the cyclic loading at 1200^0 C had improved the strength of the material considerably.

Further, the strength improvement seems to take fuller effect at higher fatigue

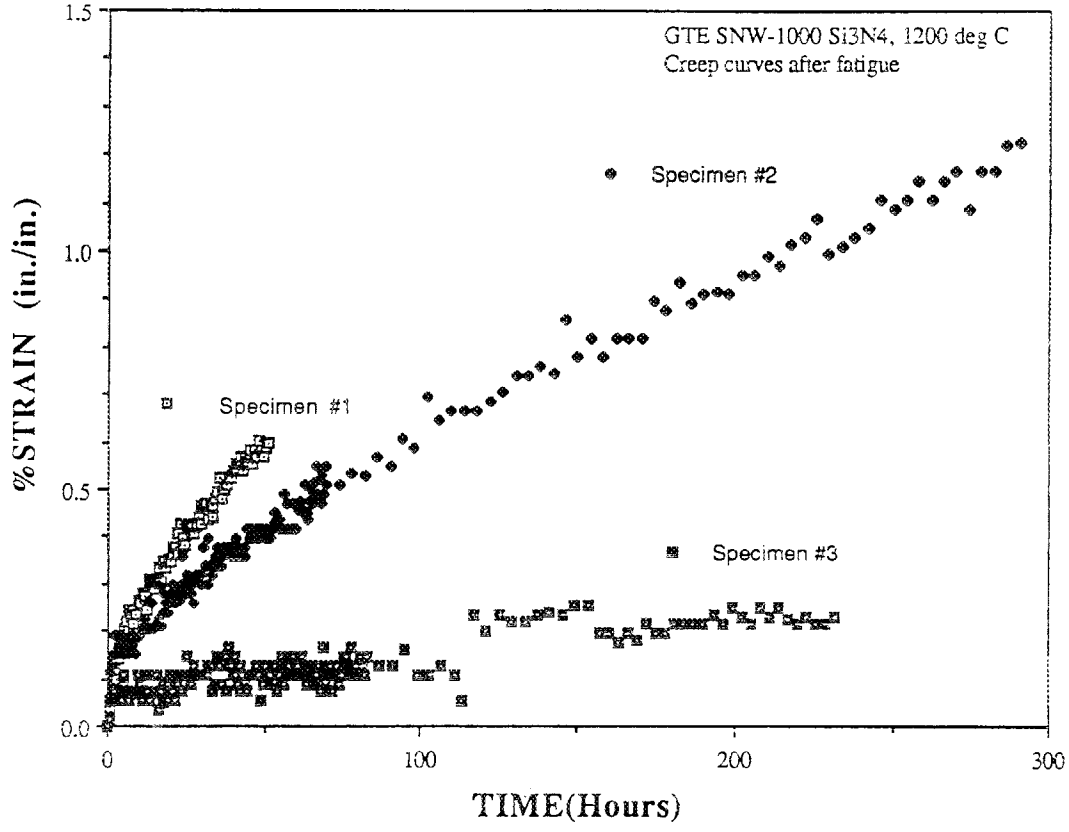

Figure 1. Creep curves for precycled specimens

Specimen #1: 50,000 cycles @50%(70 MPa) fatigue strength, R-ratio = 0.1, and creep at 70%(161 MPa) T.S
Specimen #2: 50,000 cycles @70%(98 MPa) fatigue strength, R-ratio = 0.1, and creep at 70%(161 MPa) T.S
Specimen #3: 50,000 cycles coaxing fatigue from 50% to 70% fatigue strength, R-ratio = 0.1, & creep @70%(161 MPa) T.S

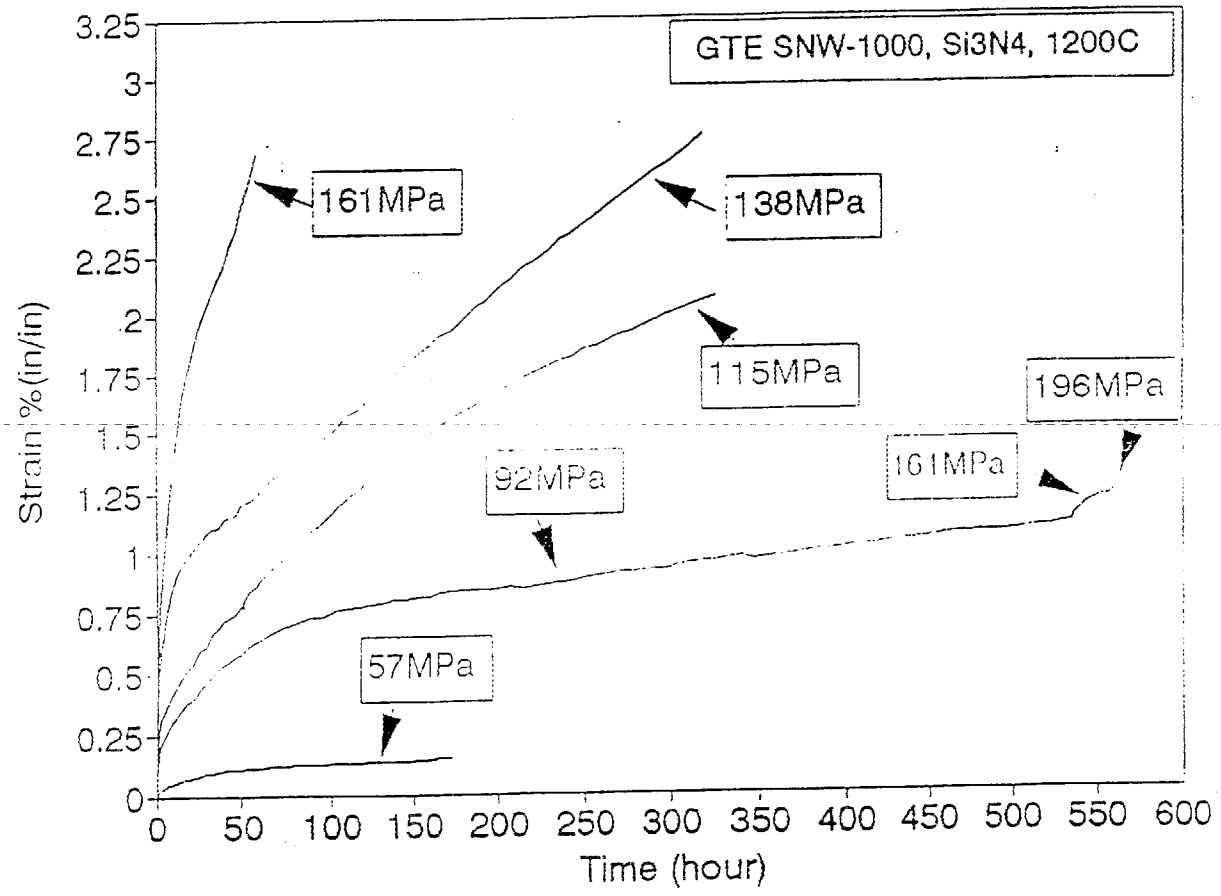

Fig. 2. Strain vs time for five specimens tested at 1200 deg C

Test Temperature: 1200^0 C
Fatigue Endurance Limit σ_{FL} = 140 MPa at 1200^0 C (ORNL data)
Pure Tensile Strength σ_{TS} = 230 MPa at 1200^0 C (ORNL data)
X denotes the test conditions.

SPEC #	FATIGUE LOADING PATTERNS 50,000 cycles, 0.5 Hz, R-ratio = 0.1				CREEP $70\%\sigma_{TS}$ constant loading	RESIDUAL TENSILE STRENGTH, MPa. 450 MPa/min stressing rate.	AVERAGE RESIDUAL TENSILE STRENGTH, MPa
	$25\%\sigma_{FL}$	$50\%\sigma_{FL}$	$70\%\sigma_{FL}$	50/60/70 COAXING			
1.		X			X		
2.			X		X		
3.				X	X	580.0	
4.	X					334.0	371.5
5.	X					409.0	
6.		X				460.0	505.0
7.		X				550.0	
8.			X			345.0	451.5
9.			X			558.0	
10.				X		481.0	501
11.				X		521.0	

Figure 3. Fatigue/Creep/Tensile loading patterns and the residual strengths of GTE SNW-1000 sintered silicon nitride

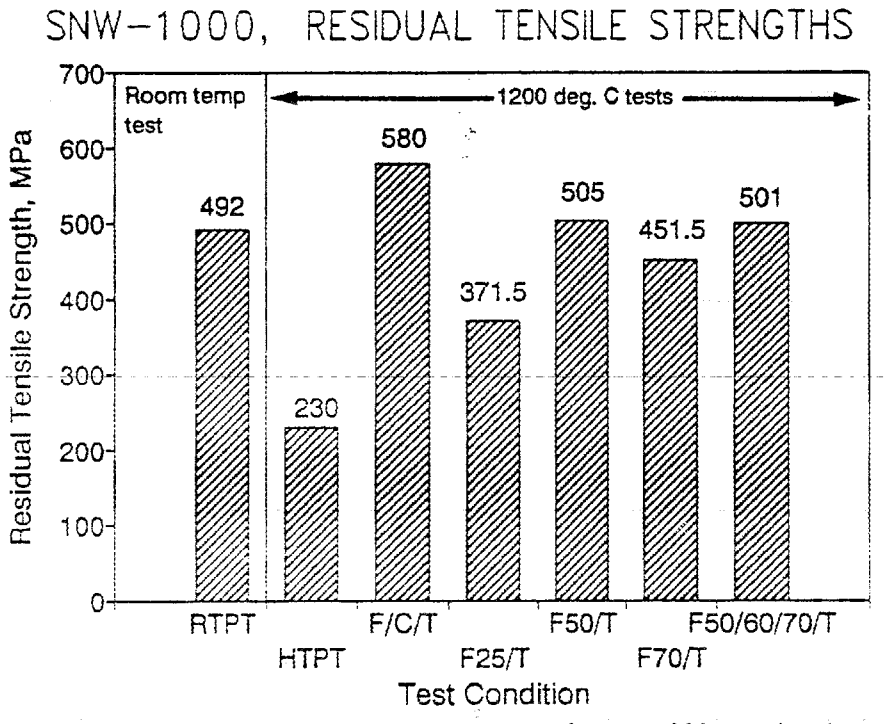

Figure 4. Comparison of the residual tensile strengths of SNW-1000 tested under various conditions.

RTPT: Room temperature and pure tension. All other tests were conducted at 1200^0 C.
HTPT: High temperature(1200^0 C) and pure tension
F/C/T: 50000 cycles coaxing fatigue from 50% to 70% fatigue strength, R-ratio = 0.1, creep at 70%(161 MPa)T.S, and pure tension
F25/T: 50000 cycles fatigue at 25%(35 MPa) fatigue strength, R-ratio = 0.1, and pure tension
F50/T: 50000 cycles fatigue at 50%(70 MPa) fatigue strength, R-ratio = 0.1, and pure tension
F70/T: 50000 cycles fatigue at 70%(98 MPa) fatigue strength, R-ratio = 0.1, and pure tension
F50/60/70/T: 50000 cycles coaxing fatigue from 50% to 70% fatigue strength, R-ratio = 0.1, and pure tension

stresses than lower(25%σ_f). It is quite possible that there is a threshold stress above which the effect would be more pronounced. Further, in this investigation no efforts were made to understand the effect of the number of cycles, frequency etc. More detailed work needs to be done in this phase of research to understand clearly these effects.

Mechanical behavior of Silicon Nitride is known to be influenced by the crystalline structure of the grain boundary material (Liu et al., 1990). Liu et al., have also mentioned that information gained from previous studies(Cinibulk, M. K., et al., 1990, and Lee, W. E., et al., 1988) suggests that amorphous intergranular phase of silicon nitride can be devitrified by thermal annealing in the high temperature range above 1350^0 C or by low stress cyclic loading at an appropriate temperature.

From the present results, it can be said that the improvement in the strength of the material could probably be due to the transformation of the intergranular glassy phase to a stronger crystallized phase. The reason that specimen 3 exhibited the maximum strength could be due to the fact that creep process comparable to thermal annealing, in addition to precycling process, aided in crystallization. This again is only a possible reasoning, but more detailed microscopy work has to be done to clarify these effects.

The microstructural analysis of these specimens is in progress to further determine the causes for the improvement in the strength of the material.

Status of Milestones

On schedule

Communications/Visitors/Travel

None

Problems Encountered

None

Publications & Presentations

None

References

1. Cinibulk, M. K., Thomas, G., and Johnson, S. M., "Grain-Boundary-Phase Crystallization and Strength of Silicon Nitride with a YSiAlON Glass," *Journal of American Ceramic Society*, pp. 1606-1612, vol. 73, No. 6, 1990.
2. Lee, W. E., Drummond III, C. H., Hilmas, G. E., Kiser, J. D., and Sanders, W.

A., "Microstructural Evolution on Crystallizing the Glassy Phase in a 6 wt % Y_2O_3-Si_3N_4 Ceramics," *Ceramic Engineering Science Proceedings*, pp. 1355-1366, vol. 9, Nos. 9-10, 1988.

3. Liu, K. C., and Brinkman, C. R., "Dynamic Tensile Cyclic Fatigue of Silicon Nitride", *Proceedings of the Twenty-Fifth Automotive Technology Development Contractors' Coordination Meeting*, P-209, pp. 189-197, Society of Automotive Engineers, Warrendale, PA, (1987).

4. Liu, K. C., Stevens, C. O., and Brinkman, C. R., "Tensile Creep Behavior and Cyclic Fatigue/Creep Interaction of Hot-Isostatically Pressed Silicon Nitride", *Proceedings of the Annual Automotive Technology Development Contractors' Coordination Meeting*, P-243, pp. 213-220, Society of Automotive Engineers, Warrendale, PA, (1990).

5. Sankar, J., Kelkar, A. D., Vaidyanathan, R., and Gao, J., "Creep testing of SNW-1000 sintered silicon nitride", *Proceedings of the Twenty-ninth Automotive Technology Development Contractors' Coordination Meeting*, P-256, pp. 293-305, Society of Automotive Engineers, Warrendale, PA, (1991).

6. Vaidyanathan, R., Sankar, J., and Avva, V. S., "Testing and Evaluation of Silicon Nitride in Uniaxial Tension at Room Temperature", *Proceedings of the Twenty-Fifth Automotive Technology Development Contractors' Coordination Meeting*, P-209, pp. 175-186, Society of Automotive Engineers, Warrendale, PA, (1987).

Standard Tensile Test Development

S. M. Wiederhorn, R. F. Krause, Jr., and D. E. Roberts
(National Institute of Standards and Technology)

Objective/Scope:

This project is concerned with the development of test equipment and procedures for measuring the tensile strength and creep resistance of ceramic materials at elevated temperatures. Inexpensive techniques for measuring the creep behavior and strength of structural ceramics have been developed and are being used to characterize the mechanical behavior of these materials. The ultimate goal of the project is to help develop a data base and a test methodology for the structural design of heat engines for vehicular applications.

Technical Highlights:

During the past six months, we expanded our studies on the creep and creep rupture of on PY6, a grade of silicon nitride containing ≈6 wght. % Y_2O_3. This work is being performed in collaboration with Pramod Khandelwal of Allison Gas Turbine. To date, 33 specimens have been tested in creep; 21 of these were tested to failure yielding creep rupture data. In addition, tensile strengths were measured on 22 specimens in the temperature range 1100 to 1400°C. These data will be part of a data base to compare materials manufactured by different companies.

Experimental Techniques:

Both the specimen design and the test apparatus used in this tensile creep study are described in reference [1]. This apparatus utilized flat dog-bone shaped samples to which SiC "flags" are attached to define the gauge length. Relative displacements of the flags are continuously monitored during each test either by means of a long range telescope, or by means of a laser extensometer. Gauge lengths measured by the telescope are accurate to ± 2 μm, whereas gauge lengths measured by the laser are accurate to ± 1 μm. To assure thermal stability, specimens were heated at the test temperature for approximately 20 hours before testing. Tests were made over a temperature range of 1200°C to 1400°C and a stress range ≈70 to ≈200 MPa. For most tests, the applied stress was maintained until the specimen failed. In this way, both the creep and creep rupture behavior of the material could be characterized.

Tensile strength data were also collected on flat dogbone specimens, which were from the same series of material as those used in the creep studies. Strength data were collected at loading rates of ≈0.06 and ≈6.00 MPa/s. The test temperature ranged from 1000°C to 1400°C. After heating to temperature, specimens were held for a two hour period to assure thermal equilibrium before testing. Specimens loaded at ≈6.00 MPa/s required about 30 seconds for failure, whereas those loaded at ≈0.06 MPa/s required approximately 30 minutes. As was

observed earlier by Hecht et al. [2] this difference in rate of loading leads to a significant difference in strength.

Results:

The strength data collected at 6 MPa/s are compared in figure 1 with similar data collected at Oak Ridge National Laboratory (ORNL) and at Allison Gas Turbine. These data were also obtained at high rates of loading. As can be seen, strength measurements at the three laboratories were consistent. Within the temperature range 900°C to 1400°C, the strength of PY6 ranged from about 400 MPa to about 350 MPa. As shown earlier, this strength depends on the loading rate during the test. At lower rates of loading, the strength is considerably lower, as shown in figure 2. At lower rates of loading, creep damage accumulation and subcritical crack growth reduce the strength. A thorough study of this regime of behavior requires the use of creep rupture techniques. Results of creep and creep rupture studies are given below.

Creep data obtained to date are summarized in figure 3. Over the data range 1250°C to 1400°C, the data fit a consistent set of curves with a shift in the data due to both applied stress and temperature. The data obtained at 1200°C seems to fit a curve with a different stress and temperature dependence than the rest of the data. This change of behavior is consistent with that reported by Ferber and Jenkins [3] in an earlier study of this material. These authors attributed the change in behavior to a change in failure mode, from cavitation and damage accumulation to crack growth.

The stress and temperature dependence of the creep behavior were determined by expressing the logarithm of the strain rate, $\dot{\varepsilon}$, as the sum of the inverse absolute temperature, 1/T, and the logarithm of the applied stress, σ, for the entire data set.

$$\log_{10}(\dot{\varepsilon}) = A + n \cdot \log_{10}(\sigma) + 0.434 \cdot \Delta H/RT \qquad (1)$$

Where n is the stress exponent, ΔH is the apparent activation energy and R is the universal gas constant. A least squares analysis of the data over the temperature range 1250°C to 1400°C yielded a stress exponent of ≈8.7 and an apparent activation energy of ≈1350 kJ/mol for this material. The constant A has a value of 17.67 when σ is expressed in MPa. Both of these values differ slightly from those reported earlier by Ferber and Jenkins [3], 5 and 1102 kJ/mol, respectively. The difference is sufficient that at 1260°C the creep rate from the Ferber and Jenkins data was approximately two orders of magnitude faster than that in this study. At 1370, the creep rate was only a factor of approximately 5 faster. The difference between the tow sets of data are a consequence of the fact that different lots of materials were studied at the two laboratories. Comparison of our data with that from Allison Gas Turbine suggests that the creep rate from the two laboratories were essentially identical. The data from Allison Gas Turbine and The National Institute of Standards and Technology (NIST) were obtained on the same lot of material.

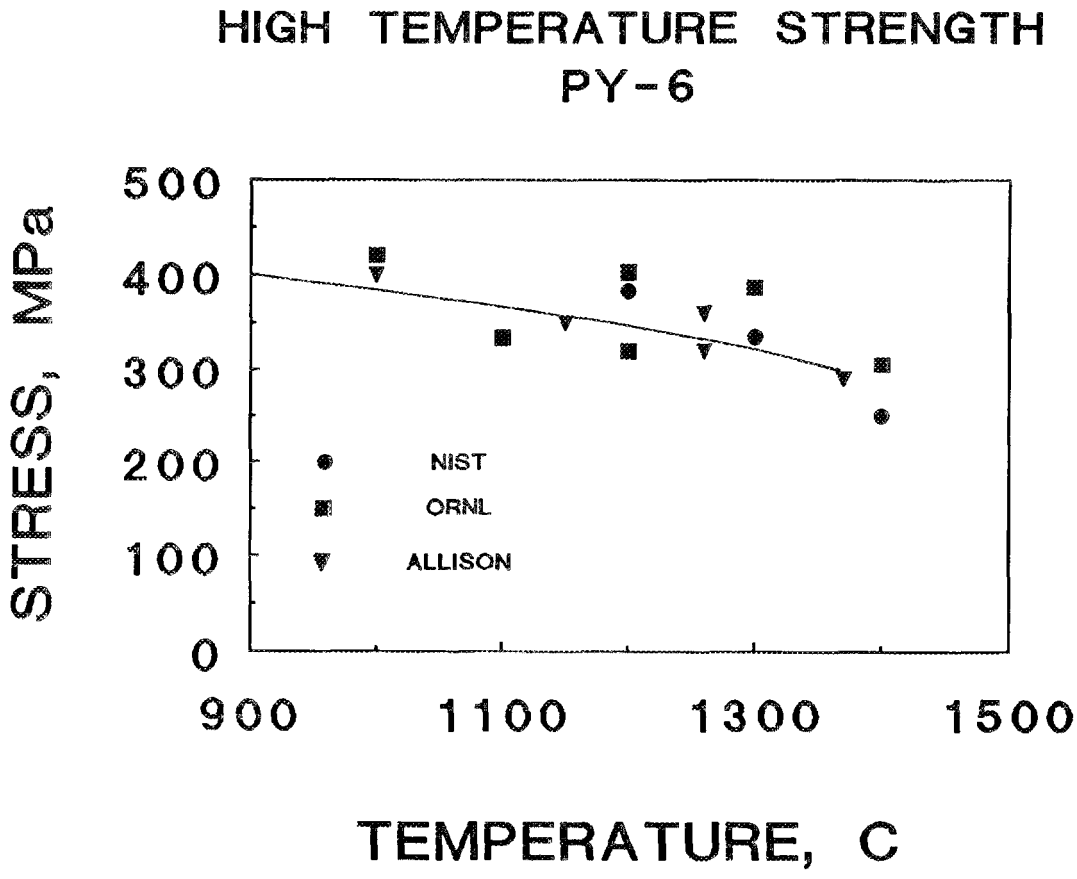

1. A comparison of tensile strength measurements on PY6 made in this study with those made by Ferber and Jenkins [3] and Pramod K. Khandelwal [5].

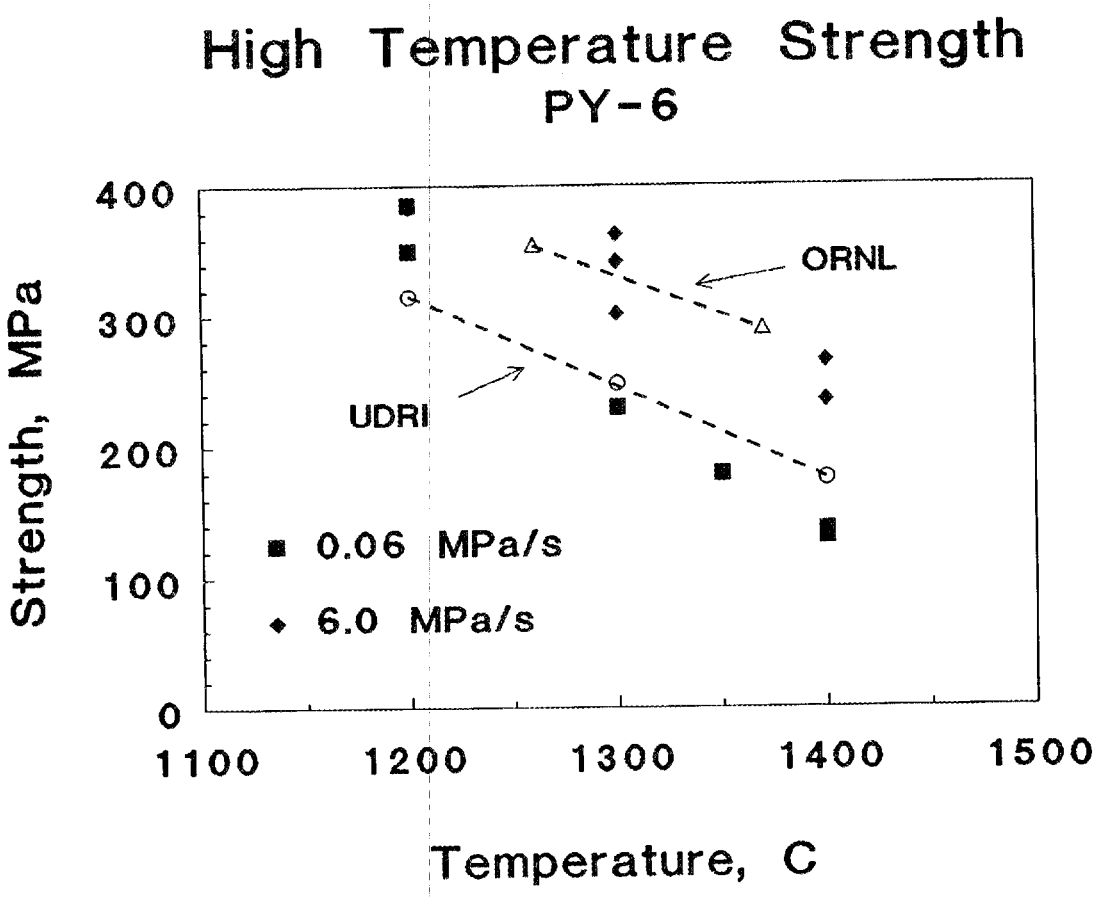

2. A comparison of tensile strength measurements on PY6 made in this study with those made by Ferber and Jenkins [3] and Hecht et al. [2].

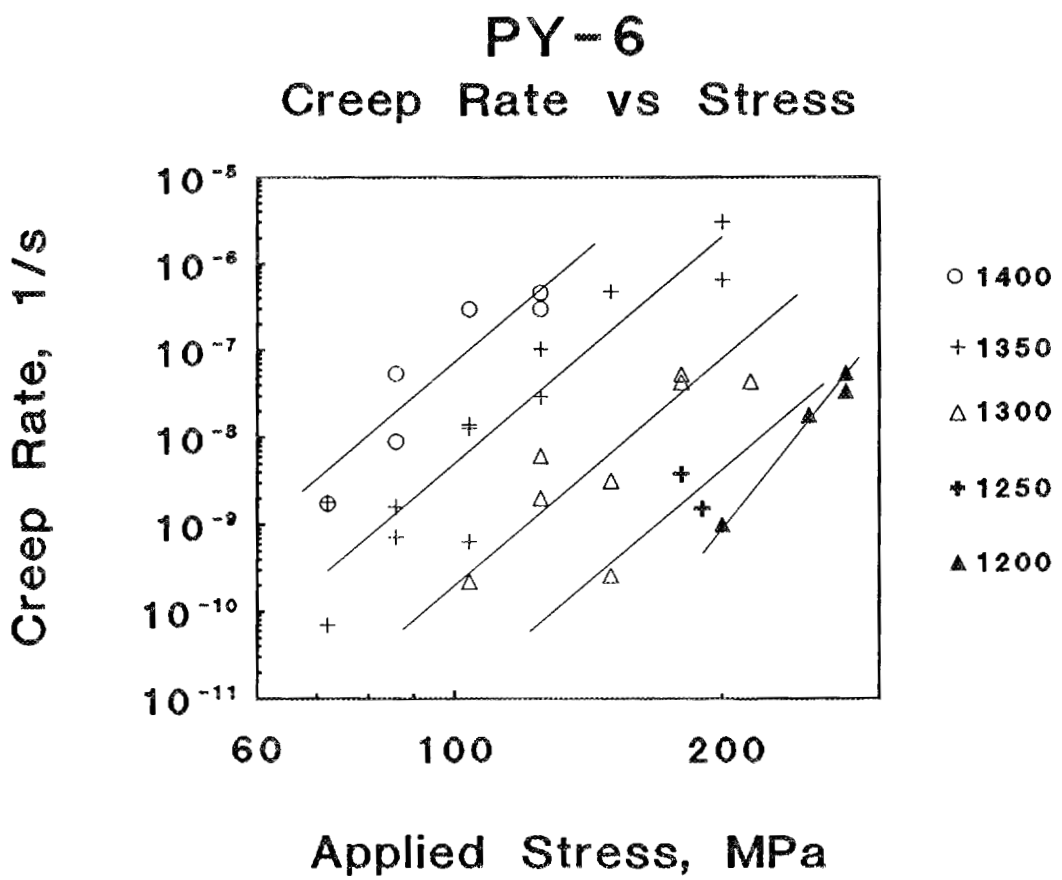

3. Summary of creep data for PY6. From 1200°C to 1400°C the data follow a Norton type equation modified by a Boltzman factor, see equation 1.

Graphical representations of the data for the PY6 are given in figures 4 and 5. In figure 4 the data are temperature compensated to show the stress dependence of the data, whereas in figure 5 the data are stress compensated to illustrate the temperature dependence of the data. For both figures, the data tend to cluster about straight lines, suggesting that the functionality assumed in equation 1 provides a reasonable fit of the minimum creep rate.

Creep rupture data are presented in figure 6 in the form of a Monkman-Grant plot,

$$t_f = t_o \cdot \dot{\varepsilon}^m, \qquad (2)$$

where t_f is the time to failure, and $\dot{\varepsilon}$ is the creep rate. The temperatures for each data point are identified by the plotting symbol. Despite the range of temperature, all of the data seem to fall around a common curve, suggesting that the lifetime of this material at elevated temperature is determined entirely by the creep rate. The data from this study lie on a curve with a slope of approximately -1. The fact that all of the data tend to cluster about a single line indicates that this curve can be used for purposes of lifetime prediction independent of temperature and applied stress.

The creep rupture data collected in this study on PY6 have been compared in figure 6 with data collected at Oak Ridge National Laboratories by Ferber and Jenkins [3], and with data collected by Pramod K. Khandelwal of Allison Gas Turbine. The data by Khandelwal were collected on a much larger specimen with a circular cross section. The data by Ferber and Jenkins were also collected on a larger round specimen. Differences among these three plots are not statistically significant, which is meaningful as the creep-rupture data were collected by three different techniques. Apparently, creep rupture data on this material can be represented by the same Monkman-Grant plot regardless of material lot, or test technique.

Discussion:

Creep and creep rupture data have now been obtained on PY6 at three different laboratories, The National Institute of Standards and Technology, Oak Ridge National Laboratory and Allison Gas Turbine. The creep and creep rupture data from the three laboratories can be compared by following the methodology recommended in reference 4. By substituting equation 1 into equation 2, the following equation is obtained [4]:

$$t_f = A \cdot t_o \cdot \dot{\varepsilon}_o{}^m \cdot \sigma^{n \cdot m} \cdot \exp(-m \cdot \Delta H/R \cdot T) \qquad (3)$$

This equation gives the time to failure as a function of stress and temperature. The equation depends on the operating failure mechanism, as both the activation energy and the stress exponent depend on failure mechanism. Equation 3 was evaluated from the data collected at The

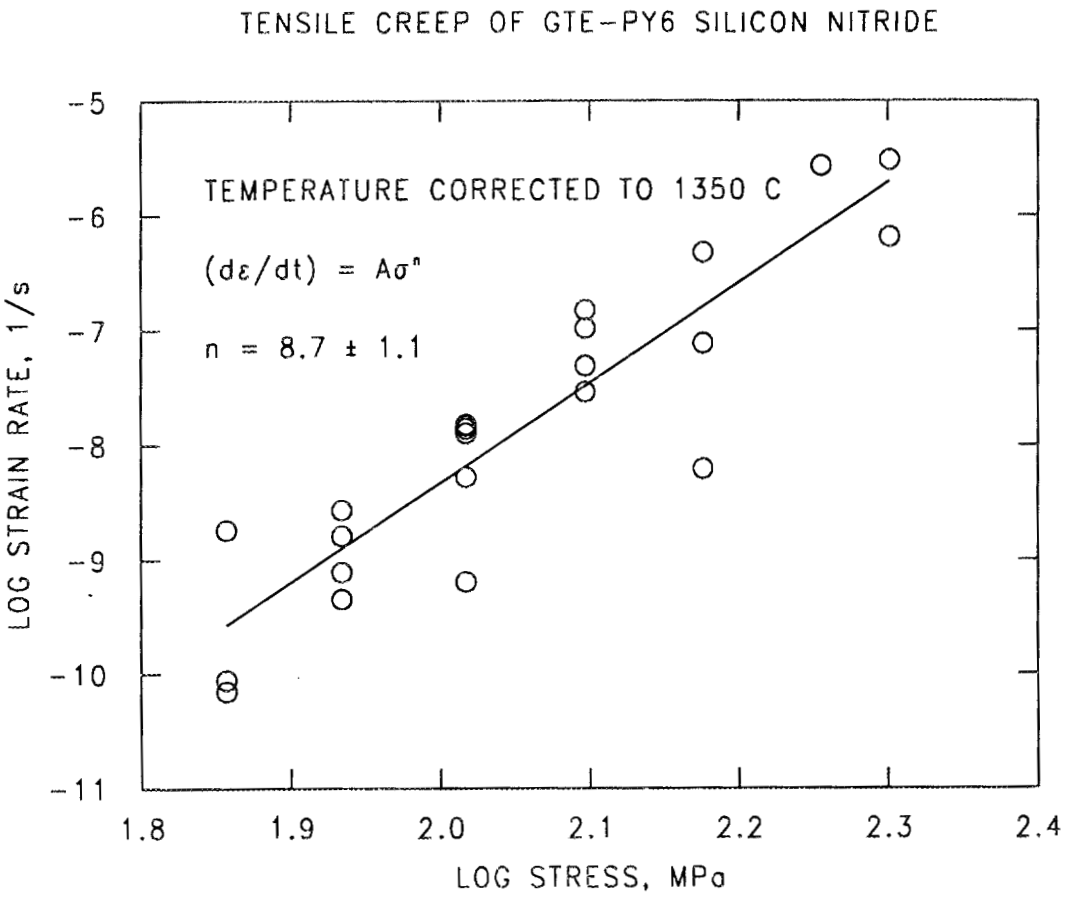

4. Stress dependence of the creep rate. The data have been temperature compensated using equation 1 so that more of the creep data could be used to obtain the stress exponent.

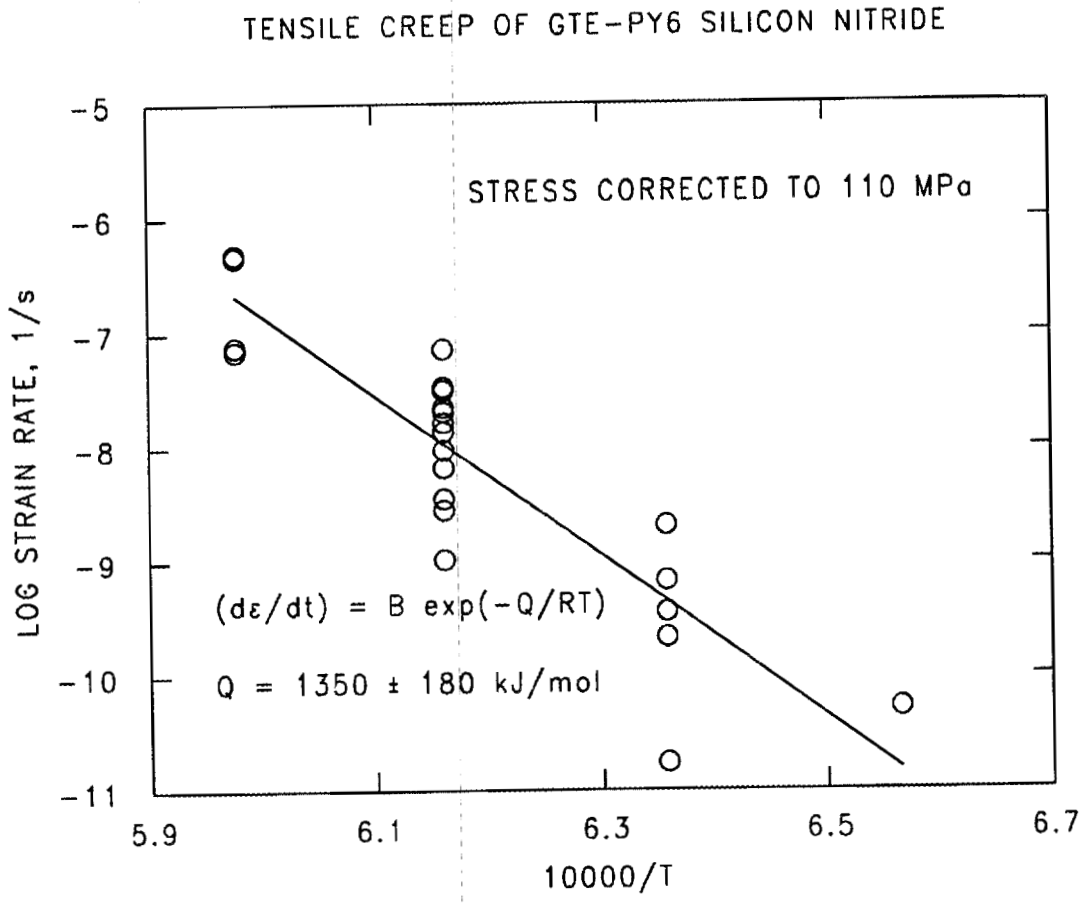

5. Temperature dependence of the creep rate. The data have been stress compensated using equation 1 so that more of the creep data could be used to obtain the apparent activation energy.

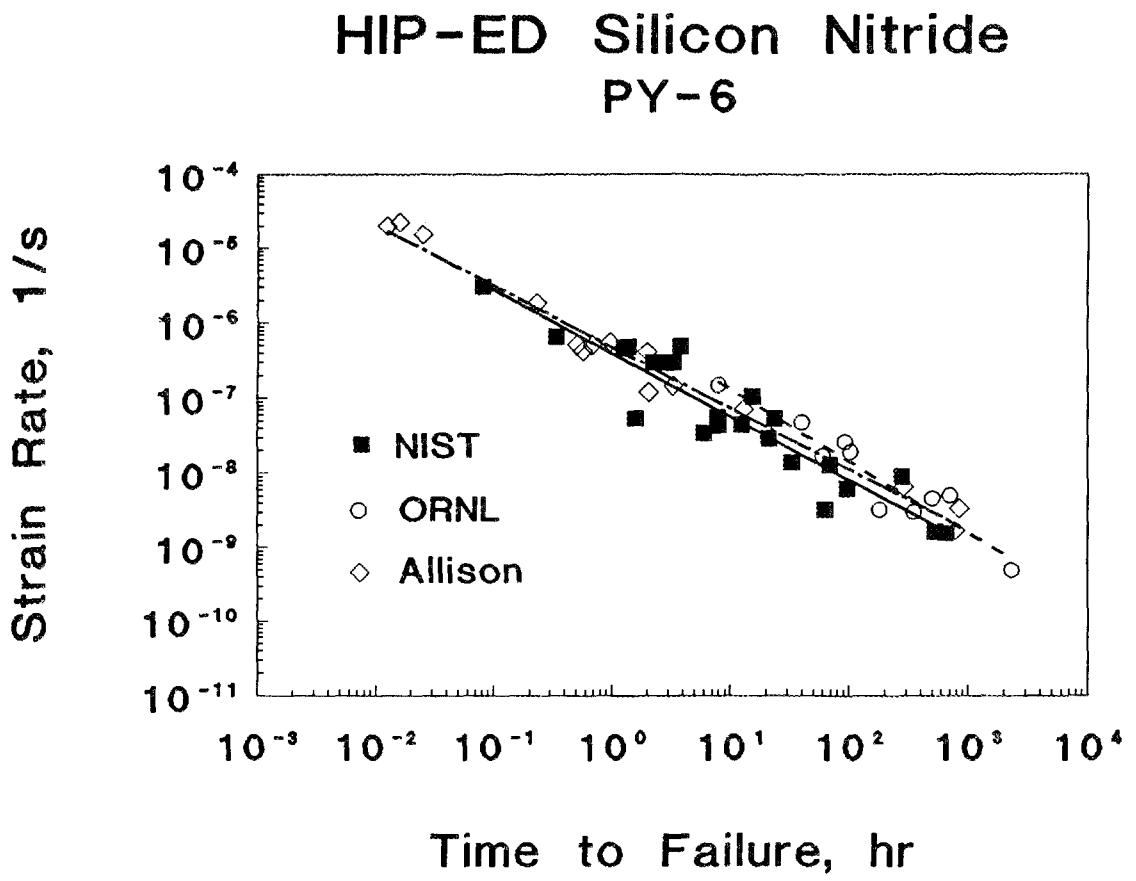

6. Creep rupture data presented in the form of a Monkman-Grant plot. The data collected in this study are compared with those collected by Ferber and Jenkins [3] and Pramod Khandelwal [5]. These three plots are statistically indistinguishable.

National Institute of Standards and Technology. The time-to-failure, t_f, calculated from equation 3 was then compared with the measured times to failure from all three laboratories. In figure 7, this estimate of the time-to-failure is compared with data obtained at The National Institute of Standards and Technology and at Allison Gas Turbine. The straight line in figure represents equal measured and predicted lifetimes. It is not a least squares fit of the data. As can be seen, both sets of data lie slightly above this line, which means that the failure times occur slightly sooner than predicted. Both sets of data are intermingled, and are indistinguishable statistically. As both sets of data were obtained on the same lot of material, the result implies that test geometry does not have a major influence on creep and creep rupture results for silicon nitride.

A comparison of the data from Oak Ridge National Laboratories with those from The National Institute of Standards and Technology is given in figure 8. For short failure times <100 hr, the ORNL data lies on the outer fringe of the NIST data at about an order of magnitude above the predicted line. For long failure times, ≈1000 hr, the ORNL data lies about two orders of magnitude above the predicted line. The ORNL data is internally more consistent than those from the other two laboratories. Since creep rupture data from all three laboratories can be represented by the same Monkman-Grant plot, the difference between the ORNL and NIST data is primarily a consequence of the difference in the creep behavior. Indeed, a comparison of the creep data from these two laboratories indicates a substantially higher creep rate for ORNL data. These results imply that differences in material lot can have a major effect on creep and creep rupture data.

Status of Milestones:

All milestones are on schedule.

Publications:

None.

References:

1. D.F. Carroll, S.M. Wiederhorn and D.E. Roberts, "Technique for Tensile Creep Testing of Ceramics," J. Am. Ceram. Soc., 72, 1610-14 (1989).

2. N.L. Hecht, S.M. Goodrich, L. Chuck, and D.E. McCullum, "Effects of the Environment on the Mechanical Behavior of Ceramics," Proceedings of the Annual Automotive Technology Development Contractors' Coordination Meeting, P-243, Dearborn, MI, October 22-25, 1990, Society of Automotive Engineers, Inc., 4007 Commonwealth Drive, Warrendale, PA 15096-0001, pp. 199-212.

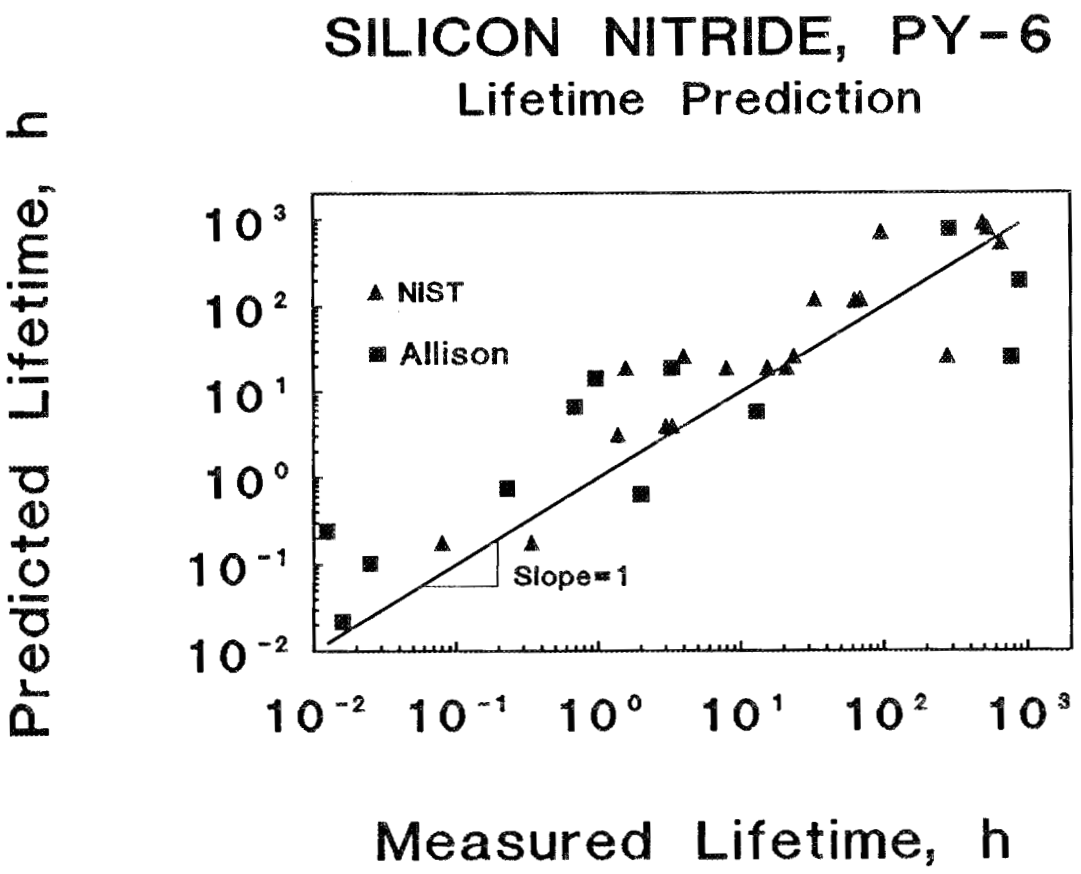

7. A comparison of predicted and measured lifetime for the National Institute of Standards and Technology and Allison Gas Turbine. The predicted lifetimes were based on the creep and creep rupture data obtained at NIST. The Allison and NIST data are statistically indistinguishable. The Allison and NIST data were obtained on the same powder lot of PY6.

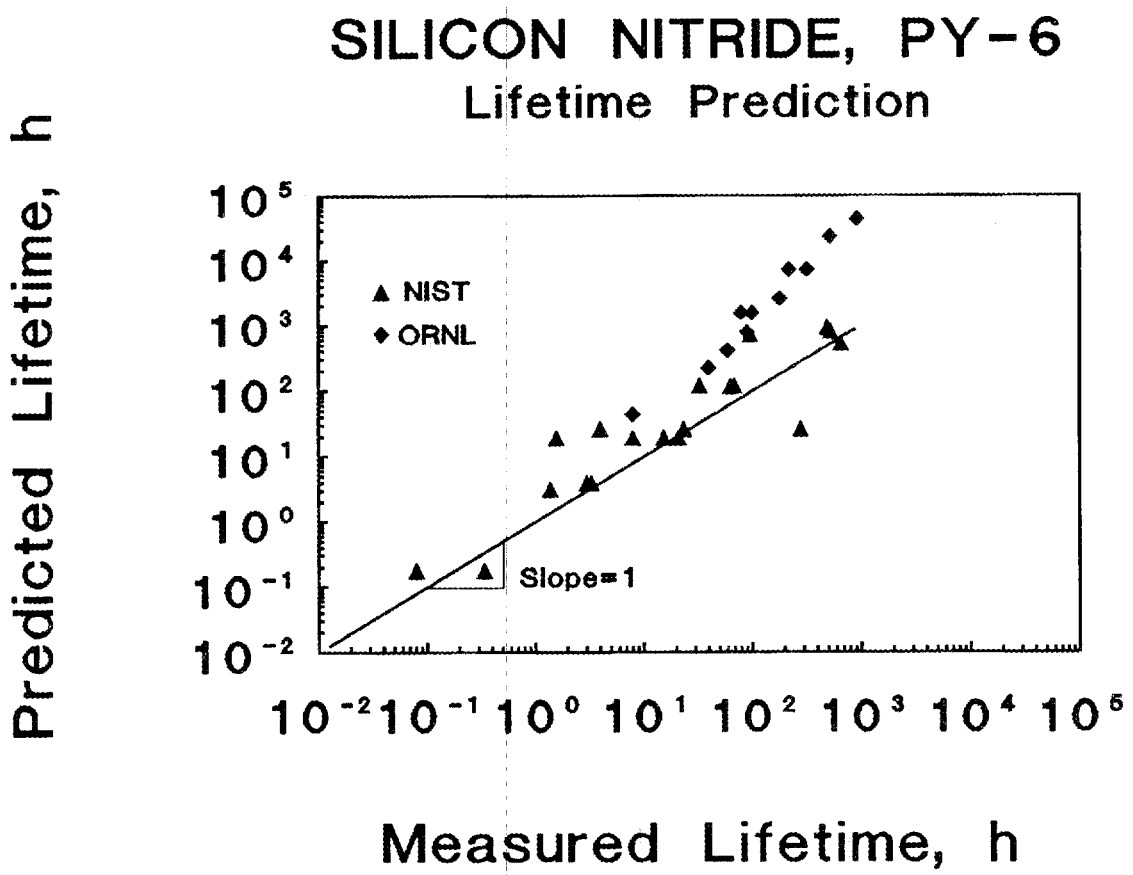

8. A comparison of predicted and measured lifetime for the National Institute of Standards and Technology and Oak Ridge National Laboratories data. The predicted lifetimes were based on the creep and creep rupture data obtained at NIST. Significant deviation from the NIST data are observed as lifetimes exceed ≈100 h. The NIST data and ONRL data were collected on different powder lots of PY6.

3. M.K. Ferber and M.G. Jenkins, "Evaluation of the Elevated-Temperature mechanical Reliability of a HIP-ed Silicon Nitride," J. Am. Ceram. Soc., 75[9] 2453-62 (1992).

4. D. C. Cranmer, B. J. Hockey, S. M. Wiederhorn and R. Yeckley, "Creep and Creep-Rupture of HIP-ed Si_3N_4," Ceram. and Eng. Sci. Proc. 12[9-10] 1862-1872 (1991)

5. Pramod K. Khandelwal, pp. 176-179 in Ceramic Technology Project Bimonthly Technical Progress Report, DOE Office of Transportation Technologies, April - May 1992

Development of a Fracture Toughness Microprobe

G. M. Pharr and D.S. Harding (Rice University)

Objective/scope

The objective of this study is to develop a technique for measuring fracture toughness in thin films and small volumes on a spatially resolved basis using the Mechanical Properties Microprobe at ORNL (MPM or Nanoindenter). The MPM is currently used to measure both hardness and elastic modulus with a spatial resolution of better than 1 μm. Once developed, the technique will be useful in probing toughness at the scale of the microstructure and thus in establishing important relations between microstructure and fracture behavior.

Technical progress

The method we are pursuing is based on the cracking which occurs when brittle materials are indented by a sharp indenter, such as a Vickers diamond. The indentation cracking method has been developed by several investigators over the last 15 years. A critical review of its predictive capabilities when applied to a wide variety of ceramics and glasses has shown that it is accurate to about 40%.

The basis of the method is to compute the fracture toughness, K_c, from the length of the cracks, c, through the semi-theoretical relation

$$K_c = \alpha \left(\frac{E}{H}\right)^{1/2} \left(\frac{P}{c^{3/2}}\right) \qquad (1)$$

Here, α is an empirically determined geometric constant (for a Vickers indenter, its value is about 0.016), P is the indentation load, and E and H are the elastic modulus and hardness of the material, respectively. One attractive feature of applying this method with the MPM is that, in addition to being able to produce very small indentations with very precise positioning, the load-displacement data provided by the instrument can be used to establish the local modulus and hardness. Since a knowledge of both these quantities is needed for the computation of toughness, the MPM potentially provides a simple and convenient means for obtaining *all* the data needed to measure toughness on a spatially resolved basis.

In applying the indentation cracking method in the nanoindentation regime, a significant problem is encountered in that there are distinct threshold loads below which indentation cracking does not occur. For the Berkovich indenter, i.e., that used most often in nanoindentation experiments, threshold loads in most ceramics are relatively high. In fact, they are usually greater than the 12 gram maximum load capability of the Nanoindenter. Early in this research, we demonstrated that this problem can be overcome in a simple

manner by changing the indenter geometry, and we have since shown that a three sided indenter with the geometry of the corner of a cube is quite effective in achieving this goal. Every ceramic material we have tested, including several new materials investigated in the last 6 months, cracks at loads of less than 1 gram (some as low as 0.1 gram), and this has paved the way for implementation of the method to micron and sub-micron indentations.

For the past year we have been testing a variety of ceramic materials to determine how well the indentation cracking methods works at low loads, how universally applicable it may be, and what the value of the geometric constant α is for the cube corner indenter. We have also studied the low load cracking behavior of the Vickers and Berkovich indenters, since very little is actually known about the cracking thresholds for these indenters, particularly the Berkovich. The materials on which we concentrated originally were soda-lime glass, fused quartz, pyrex glass, sapphire, silicon, and silicon nitride (NC132), the behavior of which is documented in a previous semiannual report. The work showed that Eqn.1 appears to work well for the cube corner indenter, even when the materials are indented in the micron to submicron range. The value of the constant α is about 0.032.

During the last 6 months, indentation testing with the Vickers, Berkovich, and cube-corner indenters continued with emphasis on obtaining and indenting new materials to expand the data set and further examine the applicability and universality of the method. Cube-corner diamond indentations were made in the Nanoindenter in the load range 0.01-10 grams, and indentations at higher loads (up to 1000 grams) were made in a microhardness tester with the Berkovich, Vickers and cube corner indenters. The new materials included spinel (2 orientations), germanium, the glass-ceramic Robax®, Pyroceram 9606 and 9658, and the silicon carbides Hexoloy® SA and ST. All of the nanoindentations were carefully imaged in a high resolution SEM, and the photomicrographs are currently being analyzed to determine indentation sizes, crack lengths, and threshold loads for indentation cracking. Once this analysis is complete, a final assessment of the applicability of the method will be made.

One new observation concerns the morphology of cracks in small-grained polycrystalline materials such as the silicon carbides. When the grain size and the indentation size are about the same (approximately 1 μm in this study), there is a tendency for indentation cracks to follow grain boundary paths, and this often results in the removal of grains in the vicinity of the indentation. Clearly, crack length measurements are not possible when this happens, but it is doubtful that a toughness derived from such a measurement would be meaningful anyway. Thus, as in the case of indentation toughness testing using microindentation techniques, measurement of toughness in the nanoindentation regime may be possible only when the indentation size is much greater than or much less than the grain size.

Further examination of acoustic emission during nanoindentation revealed that thresholds for cracking cannot be accurately determined using the equipment available to us, due to ambiguities in identifying the nature of the event giving rise to the acoustic emission signal. Further progress in this

area will require more sophisticated equipment capable of distinguishing amongst the various acoustic emission events which occur during indentation.

Status of milestones

All milestones are proceeding on schedule.

Publications

A paper entitled "Measurement of Fracture Toughness in Thin Films and Small Volumes Using Nanoindentation Methods" by G.M. Pharr, D.S. Harding, and W.C. Oliver was submitted and accepted for publication in the Proceedings of the NATO Advanced Study Institute on Mechanical Properties and Deformation Behavior of Materials Having Ultra-Fine Microstructures, Praia Do Porto Novo, Portugal (July 1992).

3.5 NONDESTRUCTIVE EVALUATION DEVELOPMENT

Nondestructive Characterization
D. J. McGuire (Oak Ridge National Laboratory)

Objective/Scope

The purpose of this program is to conduct nondestructive evaluation (NDE) development directed at identifying approaches for quantitative determination of conditions (including both properties and flaws) in ceramics that affect the structural performance. Those materials that have been seriously considered for application in advanced heat engines are all brittle materials whose fracture is affected by structural features whose dimensions are on the order of the dimensions of their microstructure. This work seeks to characterize those features using high-frequency ultrasonics and radiography to detect, size, and locate critical flaws and to measure nondestructively the elastic properties of the host material.

Technical progress

Ultrasonics - W. A. Simpson, Jr., and K. V. Cook

Since upgrading our ceramics data acquisition system, we have been examining various flaw standards in order to determine the ultimate flaw detection sensitivity of the new hardware. We have several standards that contain seeded voids having diameters as small as 25 μm; these voids were marginally recordable with the old system. The presence of still smaller flaws could be seen in the A-scan presentation, even though they could not be recorded. With the new 8-bit digitizer, these voids can be recorded with a comfortable gain reserve, and still smaller flaws are now recordable.

The smallest standards available to us were laser-drilled holes in silicon nitride modulus of rupture (MOR) bars. Since these standards are surface breaking, the appropriate ultrasonic technique for detecting them would be high-frequency acoustic surface waves. These waves are generated by a high numerical aperture ultrasonic transducer, which produces a radially propagating surface wave ideally suited for detecting cracks in any orientation (conventional surface-wave evaluation uses angle-beam generation of the surface wave and is sensitive only to cracks whose plane is perpendicular to the direction of propagation of the wave). The standards examined were 20-μm-diam by 20-μm-deep and 10-μm-diam by 10-μm-deep laser-drilled holes. These holes were not flat-bottomed; all tapered to a point at the bottom of the hole. The transducer used was a nominal 50-MHz center-frequency unit.

Figure 1 shows a contrast-enhanced image of the 20-μm hole, which is the "bulls-eye" feature near the center of the scan. The semicircular features above and below the hole are caused by drops of paint that were placed on the bar to locate the drilled hole. The horizontal, dark striations in the figure are caused by surface grinding marks. When the hole is exactly centered in the ultrasonic beam, there is a small increase in the amplitude of the surface wave; hence, the center of the image is bright. When the hole is within the diameter of the beam at the sample surface but is not centered, however, the amplitude of the surface wave is decreased. This is the reason for the alternating light and dark rings. Note that the hole is easily detected and imaged.

YP13368

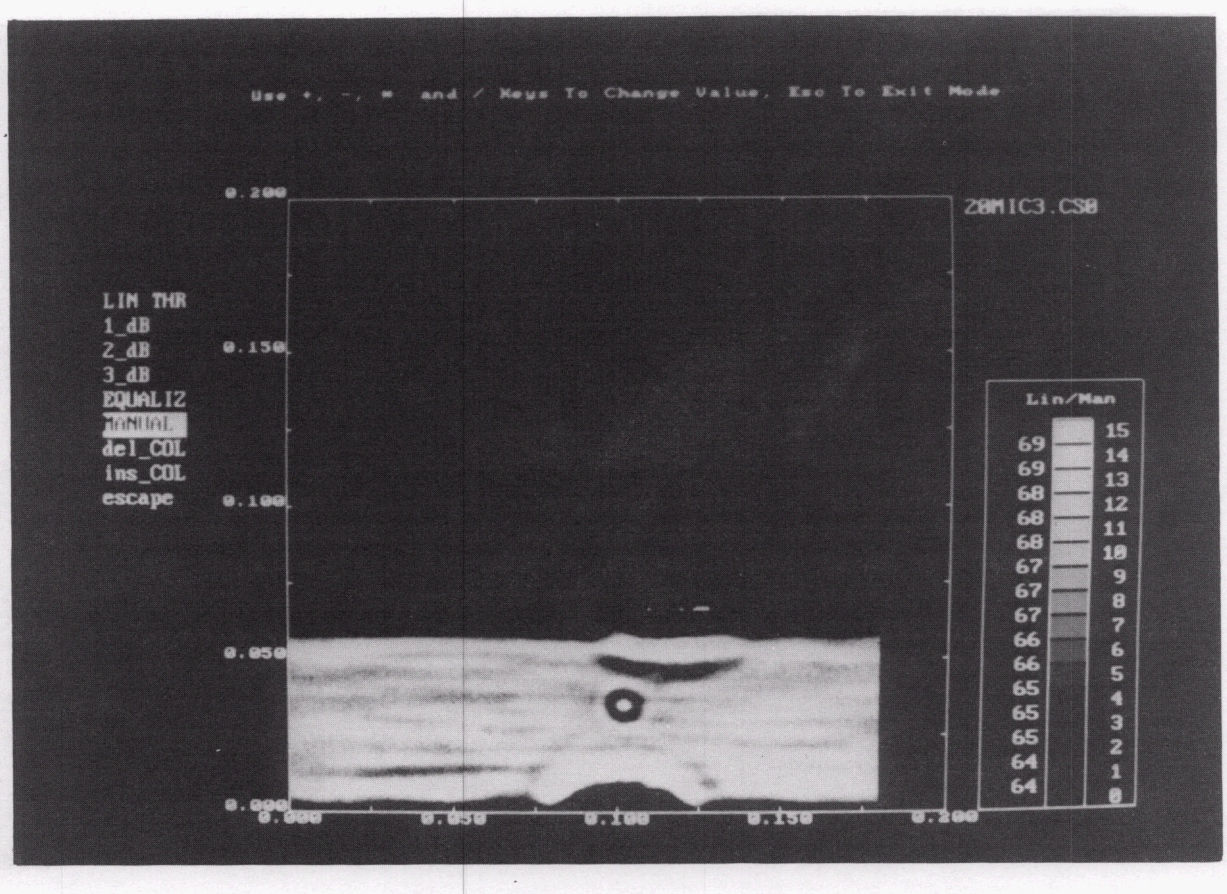

Fig. 1. Contrast-enhanced ultrasonic image ("bulls-eye" feature) of a 20-μm-diam by 20-μm-deep laser-drilled hole in silicon nitride.

Figure 2 shows the contrast-enhanced image of the 10-μm hole, which is the small, dark, circular feature just below the semicircular image of the single drop of paint used to locate the hole. This hole is less than one-twelfth of a wavelength in both diameter and depth and indicates the excellent amplitude sensitivity of the new hardware.

Of continuing interest in ceramic processing is the effect of surface preparation on in-service strength. It is known that grinding or machining introduces surface damage (cracking), which may lead to rapid failure of the specimen if the affected surface is placed in tension. According to accepted practice, the damage incurred is "removed" by fine grinding and/or polishing the machined surface. However, recent studies of fracture strength have suggested that, for some ceramics, fine grinding or polishing not only fails to solve the problem but may actually exacerbate it. We have been interested in investigating this result nondestructively and have recently been able to cooperate with other participants in the Ceramic Technology Project (CTP) who have made available suitable samples. As high-frequency surface acoustic waves are maximally sensitive to surface and near-surface flaws (cracks, voids, etc.), they are ideally suited to detection of machining damage.

YP13365

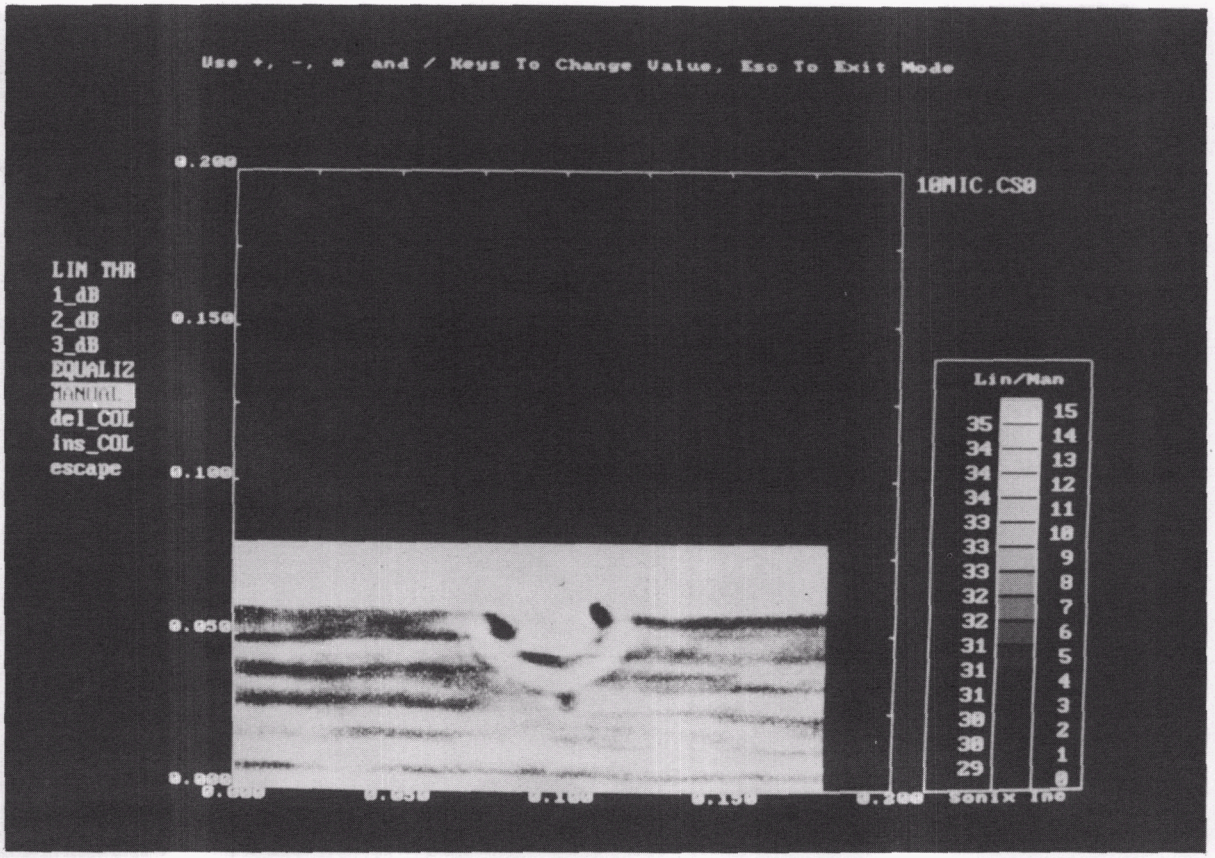

Fig. 2. Contrast-enhanced ultrasonic image (small black spot) of a 10-μm-diam by 10-μm-deep laser-drilled hole in silicon nitride.

We first obtained samples of four different ceramics (monolithic alumina, silicon carbide, silicon nitride, and whisker-toughened alumina). These samples had been rough ground, fine ground, and polished on one edge while the other edge remained in the as-sawn condition. Each edge was evaluated with high-frequency surface acoustic waves with the frequency, gain, and transducer focus set to provide sufficient sensitivity to detect cracks that were 10 μm or more deep and at least 10 μm long. Figure 3 shows the surface-wave result obtained on the as-sawn edge of the monolithic alumina. A few indications of subsurface damage can be seen (most notably at the upper right of the scanned area), but the sample, which had a density of better than 99% of the theoretical value, was remarkably free of flaws. The sample was also examined using visible microscopy, and no damage could be detected.

Figure 4 shows the surface-wave result obtained on the polished edge of the monolithic alumina. Note the much higher density and relatively larger size of the damage indications. Because of the translucency of alumina, it was possible to light the sample from the side and observe the subsurface damage optically. The large indications near the lower right and upper center of the scanned area appear to be conchoidal fractures

YP15265

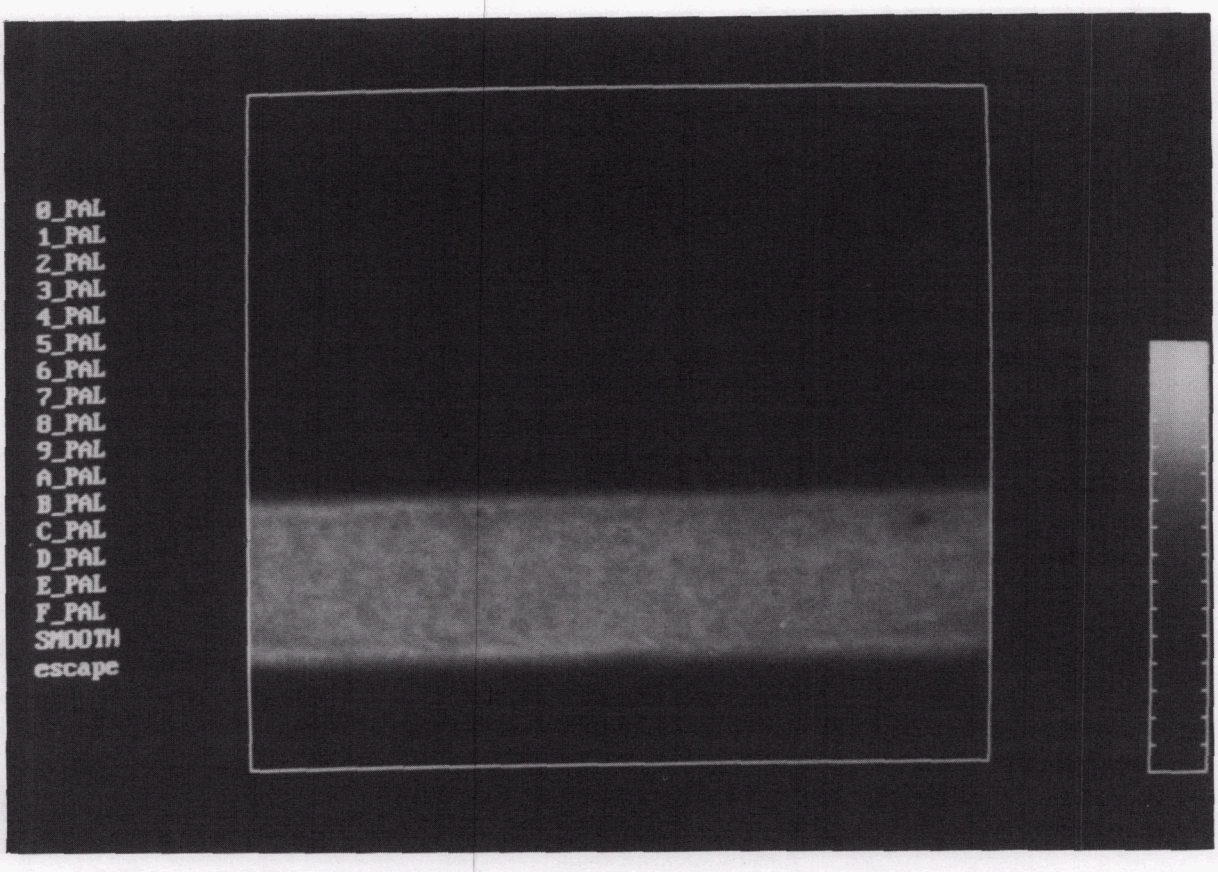

Fig. 3. Surface acoustic-wave image of the as-sawn edge of a monolithic alumina.

just below the surface. Separation of the fractured region appeared imminent. No surface damage could be seen optically.

Both the silicon carbide and silicon nitride samples exhibited very fine cracks parallel to the grinding direction on the polished surface, but the damage was much less severe than for the alumina. In addition, there was virtually no difference in the as-sawn and polished edges for the silicon carbide. The as-sawn edge of the silicon nitride sample was too rough for analysis at the frequencies used in this study.

Figure 5 shows the surface-wave result obtained on the polished edge of the whisker-toughened alumina. No damage could be detected. The very faint striations running horizontally along the surface do not appear to be very small cracks, nor could they be detected optically. Both acoustically and optically, the polished surface of the toughened alumina was, by far, the most homogeneous of the four materials. The whisker-toughened alumina thus appears to have much higher resistance to machining damage than any of the materials studied.

Although the above results are suggestive, we had no way of knowing whether the damage observed on the polished edges was present before fine grinding and polishing. Accordingly, we requested and obtained samples containing one as-sawn edge and one rough-ground edge. The condition of the latter edge was then monitored as successive

YP15264

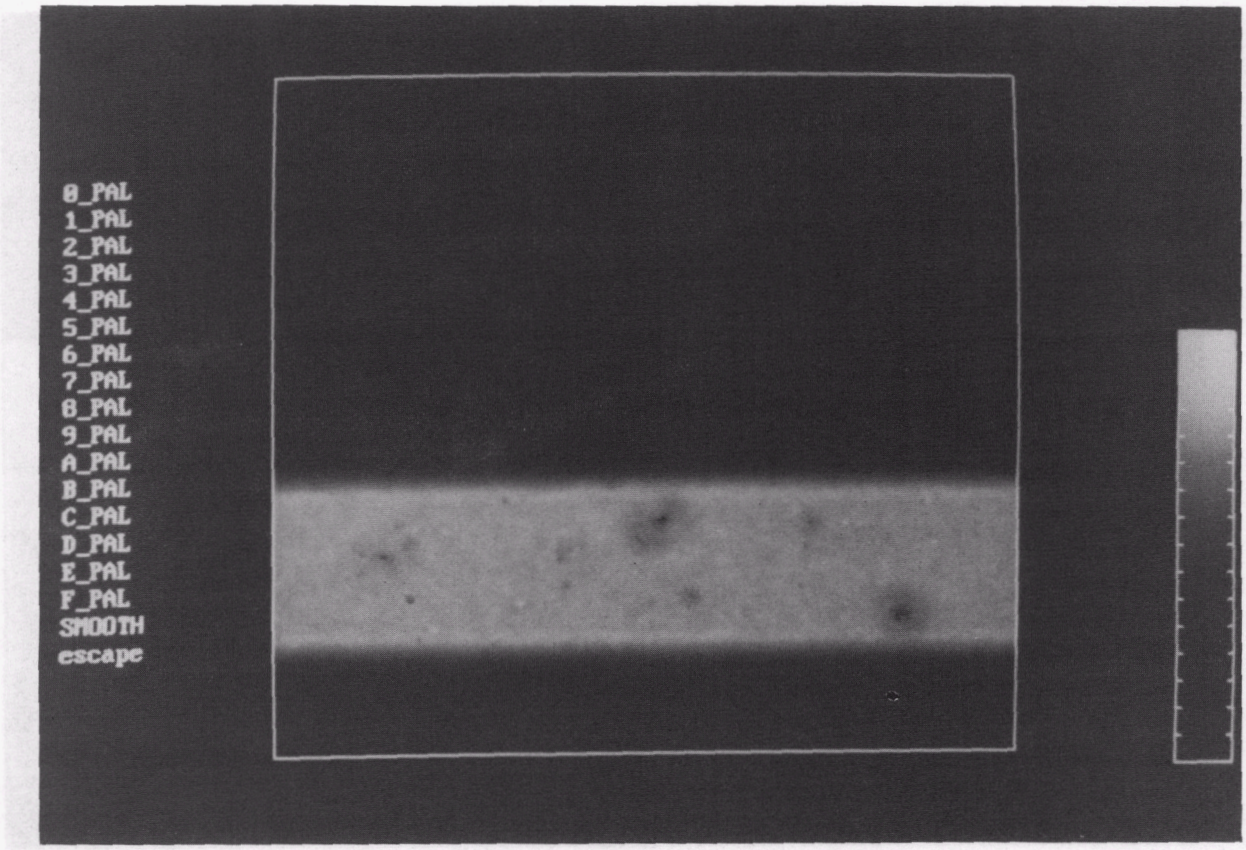

Fig. 4. Surface acoustic-wave image of the polished edge of a monolithic alumina.

stages of fine grinding and polishing were undertaken. The materials studied were a Coors AD-85 and a McDanel AD-998 monolithic alumina, a Carborundum alpha silicon carbide, and a Cercom PAD-AS 30W whisker-toughened alumina.

The materials were scanned using a 50-MHz, radially propagating ultrasonic surface wave. The transducer height and electronic gating were adjusted to provide the greatest sensitivity, which from previous studies on the selected materials should be sufficient to detect voids or cracks that are 10 μm or more deep. All samples were scanned using a 25-μm step size, which for the test conditions selected would guarantee at least 10 "hits" on a flaw of the minimum detectable size. Each sample was scanned in sections 0.4 in. (101 mm) long to ensure full coverage at the chosen step size. The system gain reserve was about 12 dB for all of the materials under consideration.

The as-sawn surface of each of the four materials was remarkably free of cracklike indications. A few examples of relatively severe subsurface damage were noted, but, in general, the surfaces were quite uniform. The one exception was the AD-85 sample, which exhibited numerous subsurface voidlike indications. In fact, the relatively low density of this material generated so many indications that the surface condition was effectively masked at each stage of surface preparation. In other words, the polished surface looked identical to the as-sawn surface ultrasonically. Accordingly, while the

YP15263

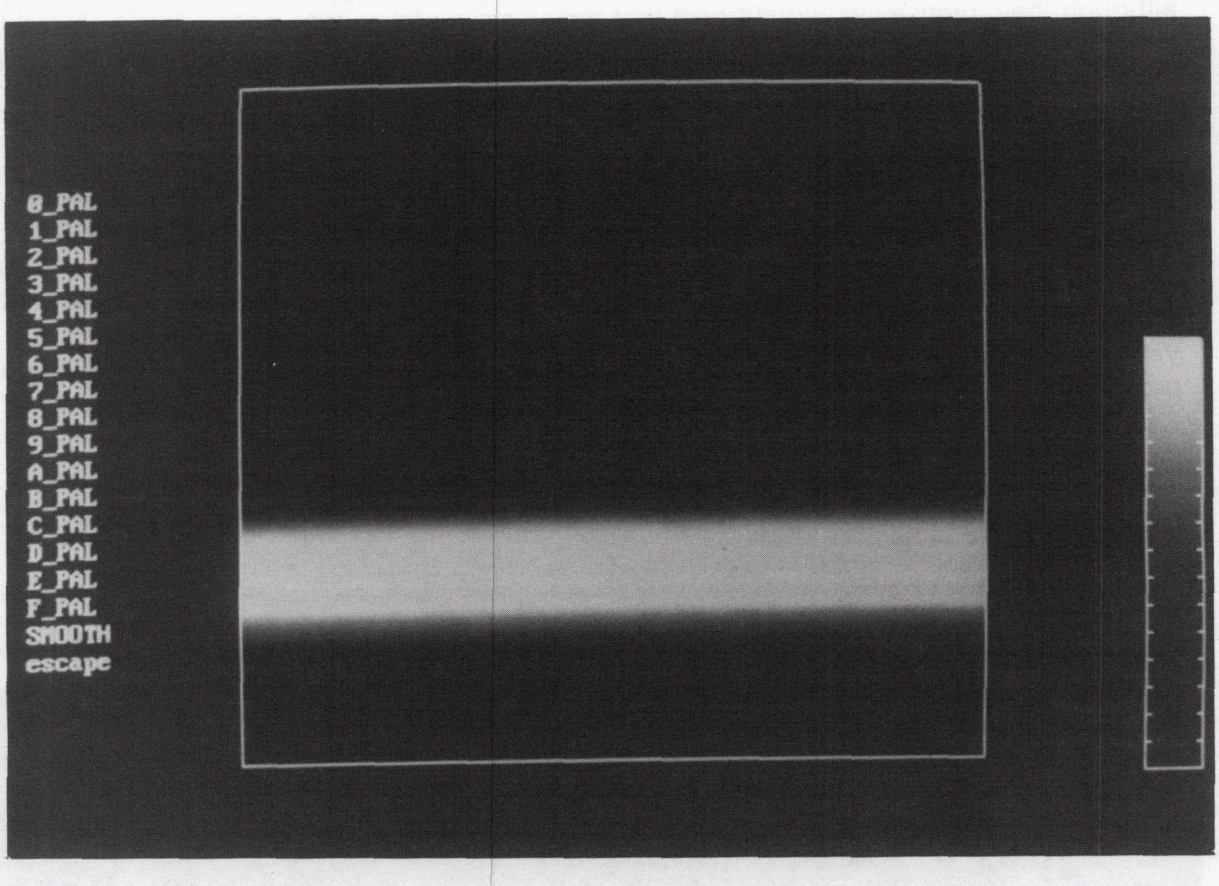

Fig. 5. Surface acoustic-wave image of the polished edge of a whisker-toughened alumina.

AD-85 material was characterized for each step of the surface preparation, the ultrasonic results did not change, and thus no further discussion of this material will be given.

The rough-ground surfaces of the three remaining materials exhibited numerous fine cracklike indications that revealed the grinding direction. Some of these indications could be matched with surface scratches by visible microscopy, but the intensity of indication suggests that some subsurface cracking probably accompanied the rough grinding. No other indications were detected in the silicon carbide; however, several very strong subsurface indications were noted in the AD-998 material. No surface features at the location of the ultrasonic indication could be seen under visible microscopy, but by strongly side-lighting the sample, which is translucent, the detected features could be seen. All were near-surface flaws that appeared to be small conchoidal fractures. A single subsurface indication was detected in the whisker-toughened alumina.

Unfortunately, the amount of material removed during the fine grinding step was excessive; i.e., it exceeded the depth of penetration of the ultrasonic surface wave. Therefore, the volume interrogated by the surface wave included material not seen in the earlier scans. For both the silicon carbide and whisker-reinforced alumina samples, faint

grinding marks (which were not residuals of the rough grinding) were still detectable although their intensity would suggest that they were merely surface scratches induced by the grinding. No other indications were noted. For the AD-998 sample, however, several new subsurface flaws could be seen in addition to the grinding marks. As before, these appeared to be small fractures initiated by the grinding forces.

The most interesting results were obtained following the polishing step. The small amount of material removed guarantees that the volume that was inspected is essentially that examined following fine grinding. For the silicon carbide and whisker-reinforced alumina, the ultrasonic results yielded a completely featureless image; i.e., no flaws of any kind were detected. For the AD-998 alumina, however, a very intense new indication and several smaller new ones were detected where nothing was found after fine grinding. Visible microscopy using intense side lighting revealed a subsurface fracture that was not present before polishing. These results are shown in Figs. 6 (after fine grinding) and 7 (after polishing). A section approximately 6 mm long was removed from the left end of the sample before polishing to form an archive specimen; thus, the end of the sample evident in Fig. 7 is missing in Fig. 6. The faint vertical striations seen in Fig. 6 are the marks left by fine grinding; the dark circular area at the right of Fig. 2 is the new fracture.

YP15691

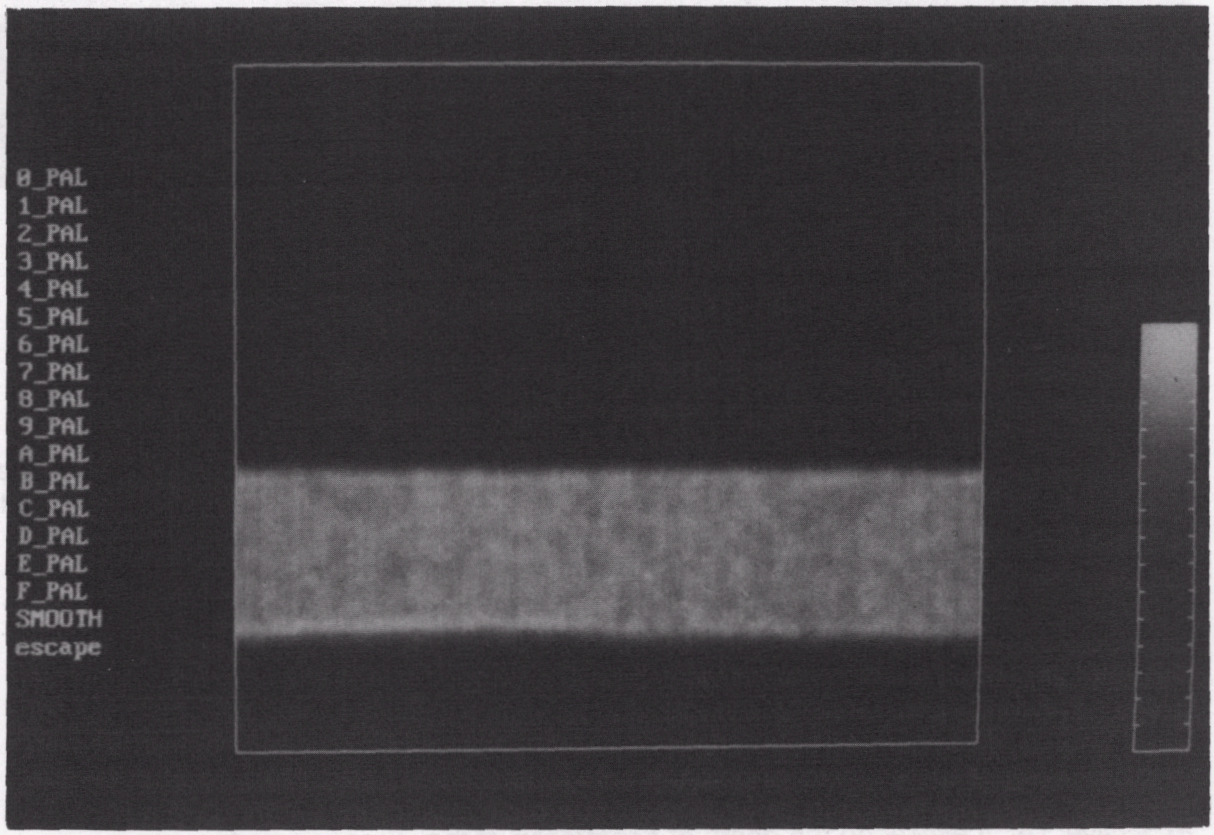

Fig. 6. Surface acoustic-wave image of an AD-998 alumina after fine grinding.

YP15690

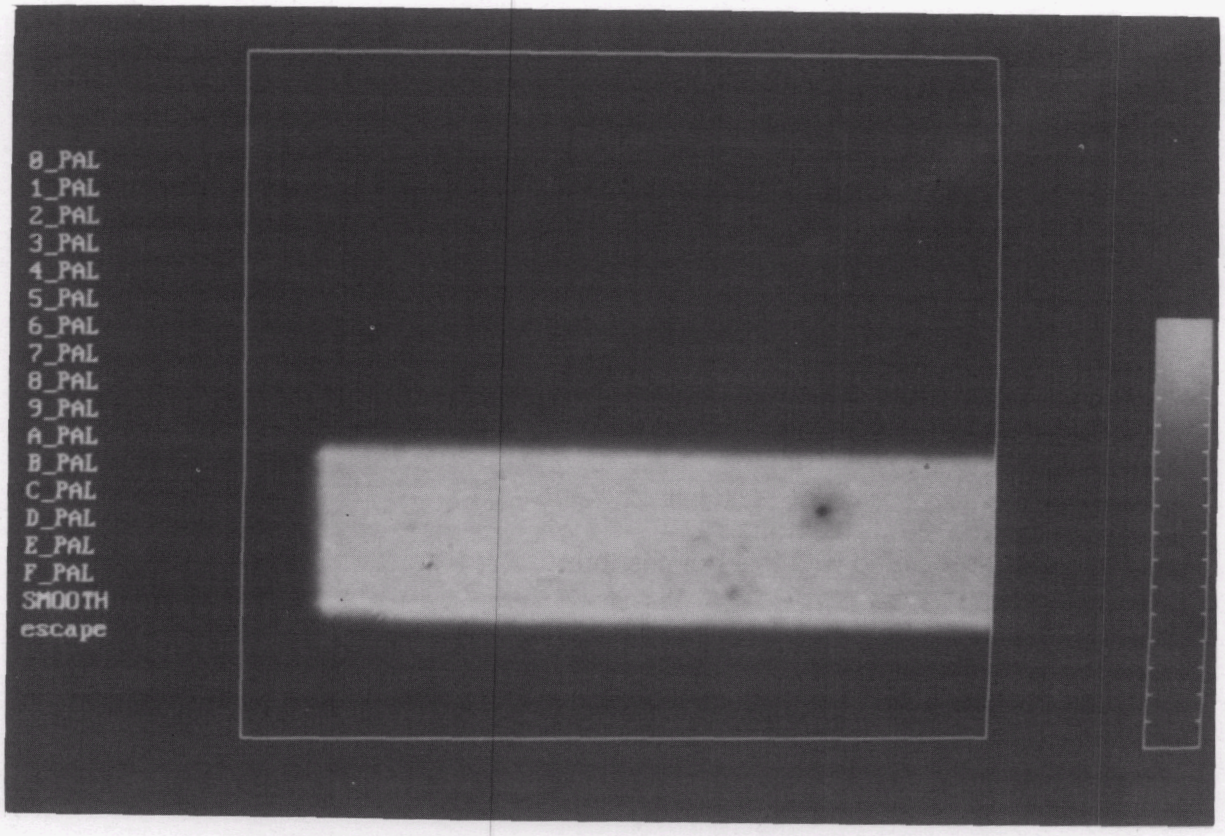

Fig. 7. Surface acoustic-wave image of part of the region shown in Fig. 6 after polishing. The dark circular indication is a new subsurface fracture that occurred during polishing.

Although this study was limited to a single example of each of four structural ceramics, the results suggest that silicon carbide and whisker-reinforced alumina may benefit from post-saw surface preparation, while AD-998 alumina appears to incur additional damage after each successive step of surface conditioning. We would like to expand these studies to a wider selection of materials with a statistically significant number of samples for each material if a suitable source can be found.

We continued to work on extending our synthetic aperture capability to nonplanar (i.e., cylindrical) samples. Software for implementing the processing algorithms has been written for the new geometry. However, our current systems do not have the capability of scanning cylindrical samples. We are currently examining the possibility of constructing a stepping motor-driven addition to our primary high-frequency ceramic evaluation system. Several designs for such an addition have been proposed, but none are clearly superior within our budget constraints.

Of considerable interest in synthetic aperture processing is the response to a flaw that is not located at the "focal point" of the aperture. We showed previously that the phase dependence across the synthetic aperture for a flaw at the focus is given by:

$$\Phi(n) = \exp[ik(n\delta x)^2/r_0] \quad , \tag{1}$$

where k is the wave vector of the ultrasonic radiation, r_0 is the flaw depth, δx is step size in the aperture, and n is the aperture point under consideration. This phase is summed coherently for each aperture point. If the flaw does not lie at the focal point of the aperture but is displaced laterally and in depth, there will be a phase error associated with each point of the aperture. This error may be found as follows. Let the displacement of the flaw be given by x_0 laterally and by δr in depth. The distance from the aperture point to the flaw is thus

$$r = [(r_0-\delta r)^2 + (x_0-n\delta x)^2]^{1/2} \quad . \tag{2}$$

Assume first that the flaw is located in the plane of focus, i.e., δr is zero. Expanding the square root term by the binomial theorem and retaining only the first terms,

$$r = r_0\{1 + \tfrac{1}{2}[(x_0-n\delta x)/r_0]^2\} \quad . \tag{3}$$

The phase shift associated with this point is thus

$$\Phi(n) = \exp[ik(x_0-n\delta x)^2/r_0] \quad . \tag{4}$$

Comparing this result with the first equation above, the phase error at each aperture point is

$$\delta\Phi(n) = (kx_0^2/r_0) - (2kx_0\delta x/r_0) \quad . \tag{5}$$

The first term is constant across the aperture and is unimportant to the coherent sum. When the aperture signals are summed, however, the second term contributes a response given by:

$$\Phi = \sum \exp(-i2kx_0\delta x/r_0) \quad , \tag{6}$$

where the summation is from -N/2 to N/2, and N+1 is the number of aperture points (our algorithms always assume equal numbers of points on either side of the aperture center). From the well-known fact that

$$(1-x)^{-1} = \sum x^n \quad , \tag{7}$$

where the summation is from 0 to ∞, it is easy to show that

$$\sum x^n = (1-x^N)/(1-x) \quad , \tag{8}$$

where the summation is from 0 to N-1; thus, the summation above for Φ becomes:

$$\Phi = \sin[(N+1)z]/\sin(z) \quad , \tag{9}$$

where $z = kx_0\delta x/r_0$. This result is recognizable as the response due to multiple-slit interference or as the Fourier transform of N+1 identical signals.[1] Thus, the response of a

laterally miscentered flaw may be easily estimated, and the resolution of the aperture is seen to improve as the aperture size increases, which is expected.

For a flaw displaced in depth but centered laterally, the error term that is coherently summed (aside from a term that is constant across the aperture) is:

$$\Phi = \sum \exp\{-ik\delta r(n\delta x)^2/[r_0(r_0+\delta r)]\} \quad , \tag{10}$$

which has the form of the sum for a flaw at the focal point of an aperture focused at the depth $r_0(1+r_0/\delta r)$. Note that this depth goes to infinity as δr goes to zero; thus, the error summation reduces to zero as δr vanishes.

We continued work on synthetic-aperture technology for ceramic evaluation. We have now written software to allow processing of two-dimensional data acquired by a commercial B-scan package running on a 386-based personal computer. The package was designed to permit bi-directional scanning of a sample, but we found that the accuracy of the scan bridge was not sufficient for synthetic aperture use; the phase error associated with positional inaccuracies of the transducer destroyed the coherence of the synthetic-aperture data. However, the commercial software can be run in a uni-directional mode (where the forces on the transducer are the same for each scan line), and the phase error incurred in this mode is much less than for bi-directional scanning. The maximum sample rate for the current B-scan software is 100 MHz, which restricts us to relatively low-frequency (<25 MHz) testing. However, a new release of the commercial software, which permits equivalent-time sampling at rates up to 3200 MHz, should be available shortly.

We are currently evaluating several commercial, very high-frequency (1 to 2 GHz) acoustic microscopes for surface and near-surface characterization of structural ceramics. In this frequency range, resolutions of less than 1 μm are possible, and the high sensitivity to surface-wave velocity allows individual grains (because they are anisotropic and have random orientations) as well as intergranular and transgranular cracking to be observed. We have also seen examples of the imaging of induced (by diamond pyramid indentation) and residual stress and of the concentration of stress around the tip of a crack. We expect to finish writing the specification for such a system within a month with delivery sometime within the first quarter of the year.

Computed Tomography (CT) - B. E. Foster

Four silicon nitride spin disks (115 × 13 mm with a shaft 48 × 13 mm) have been received for inspection with both film radiography and tomography. These disks (identified as 36, 37, 40, and 41) are part of those fabricated by GTE for Allison that had been rejected because of visible cracking on the surface. Film radiography shows numerous cracks through the 13-mm thickness. Some of the cracking as detected with tomography is throughout the 13-mm thickness. Figures 8, 9, 10, and 11 show a 0.25-mm-thick CT slice through the diameter and 1 mm from the surface of each sample. Several cracks of various lengths are evident in each figure. The dark spot at the 9 o'clock position on Fig. 10 is a void caused by a missing surface chip. Many of the cracks have a width about 25 μm.

In conjunction with attendance at the ASME Code week in San Antonio, Texas, visits were made to Scientific Measurement Systems in Austin on May 4, 8, and 11, 1992. The purpose was to evaluate the use of area detectors with our present Scientific

YP14574

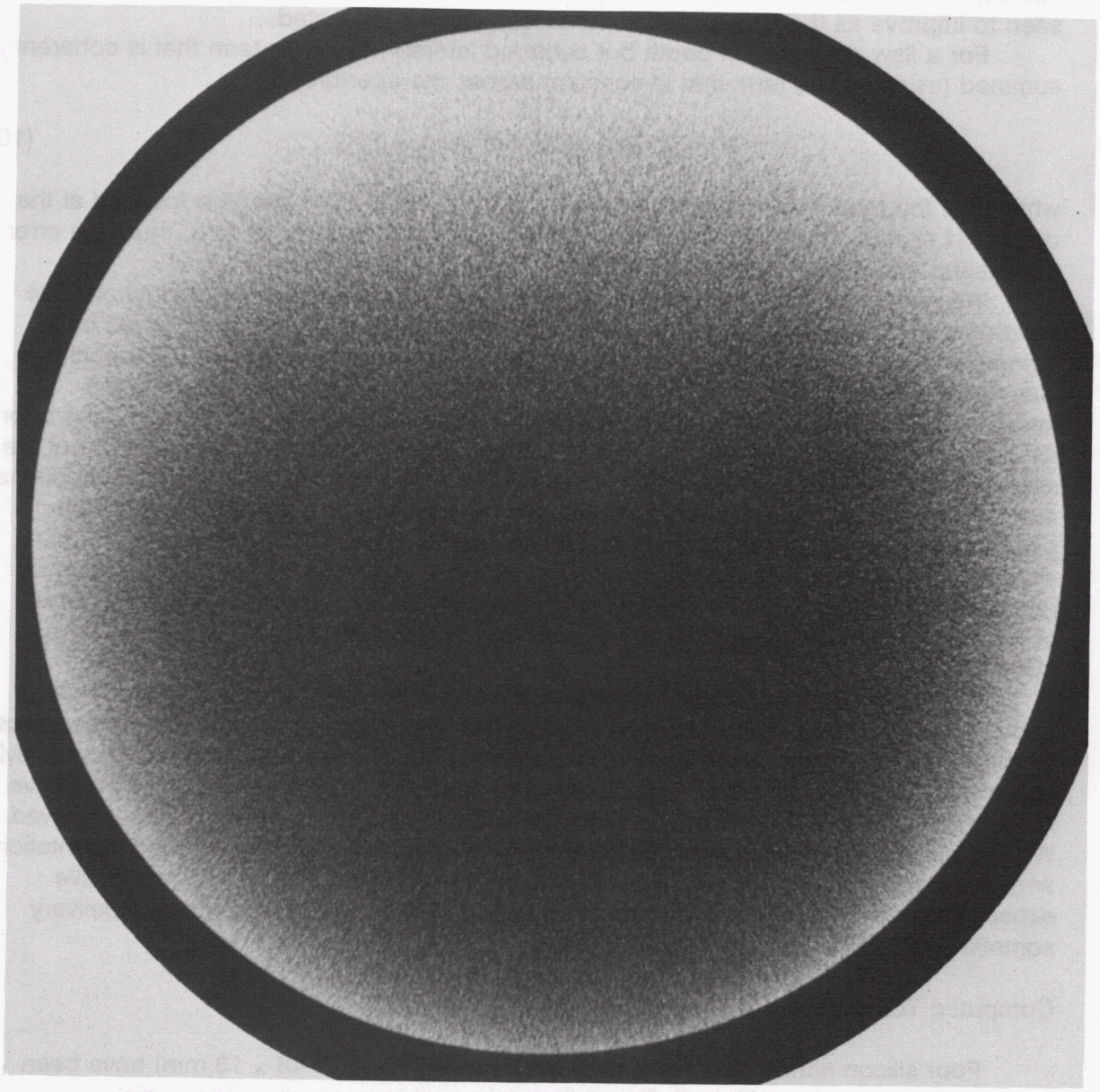

Fig. 8. CT slice through the diameter of sample 41.

YP14572

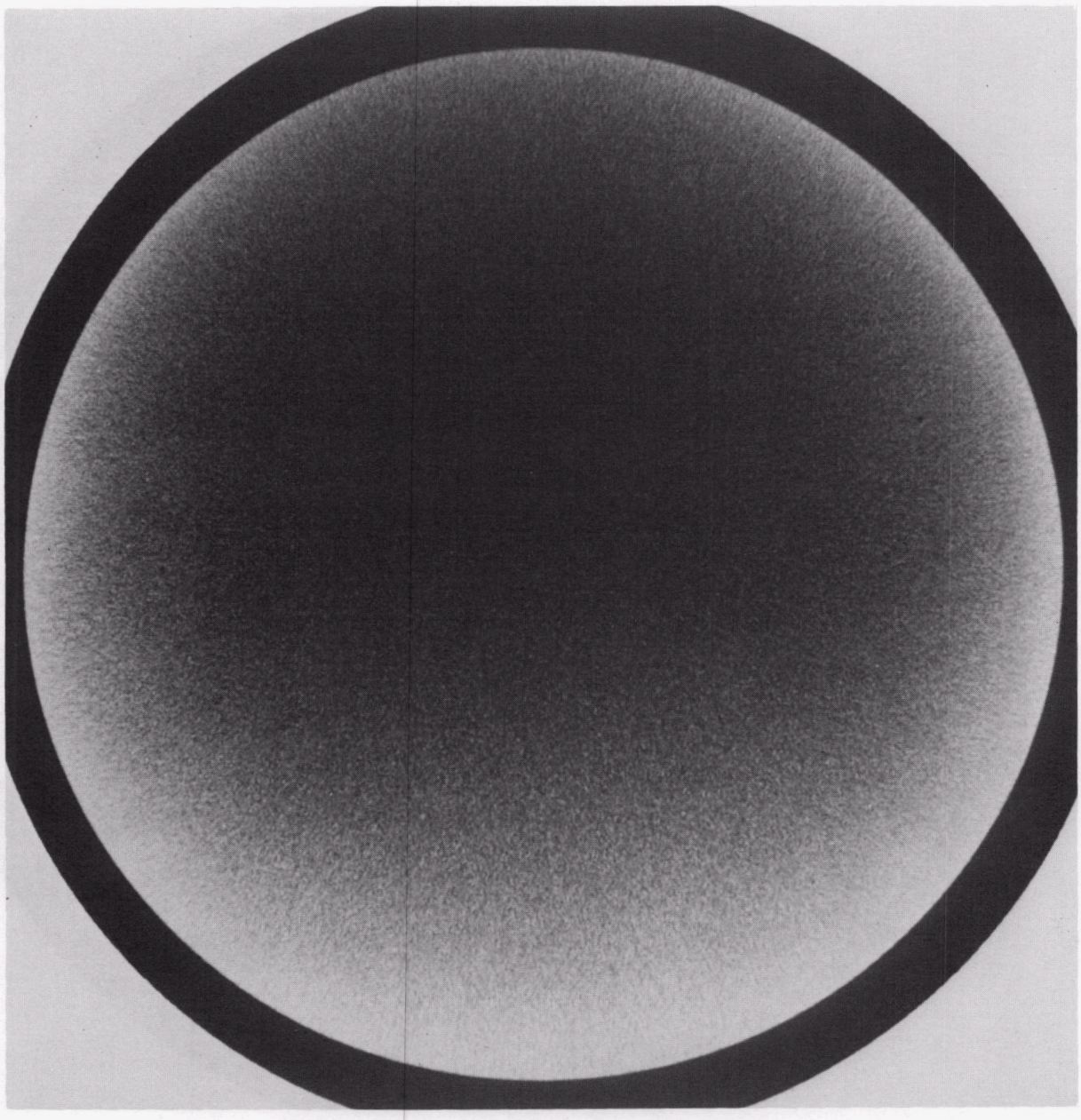

Fig. 9. CT slice through the diameter of sample 40.

YP14571

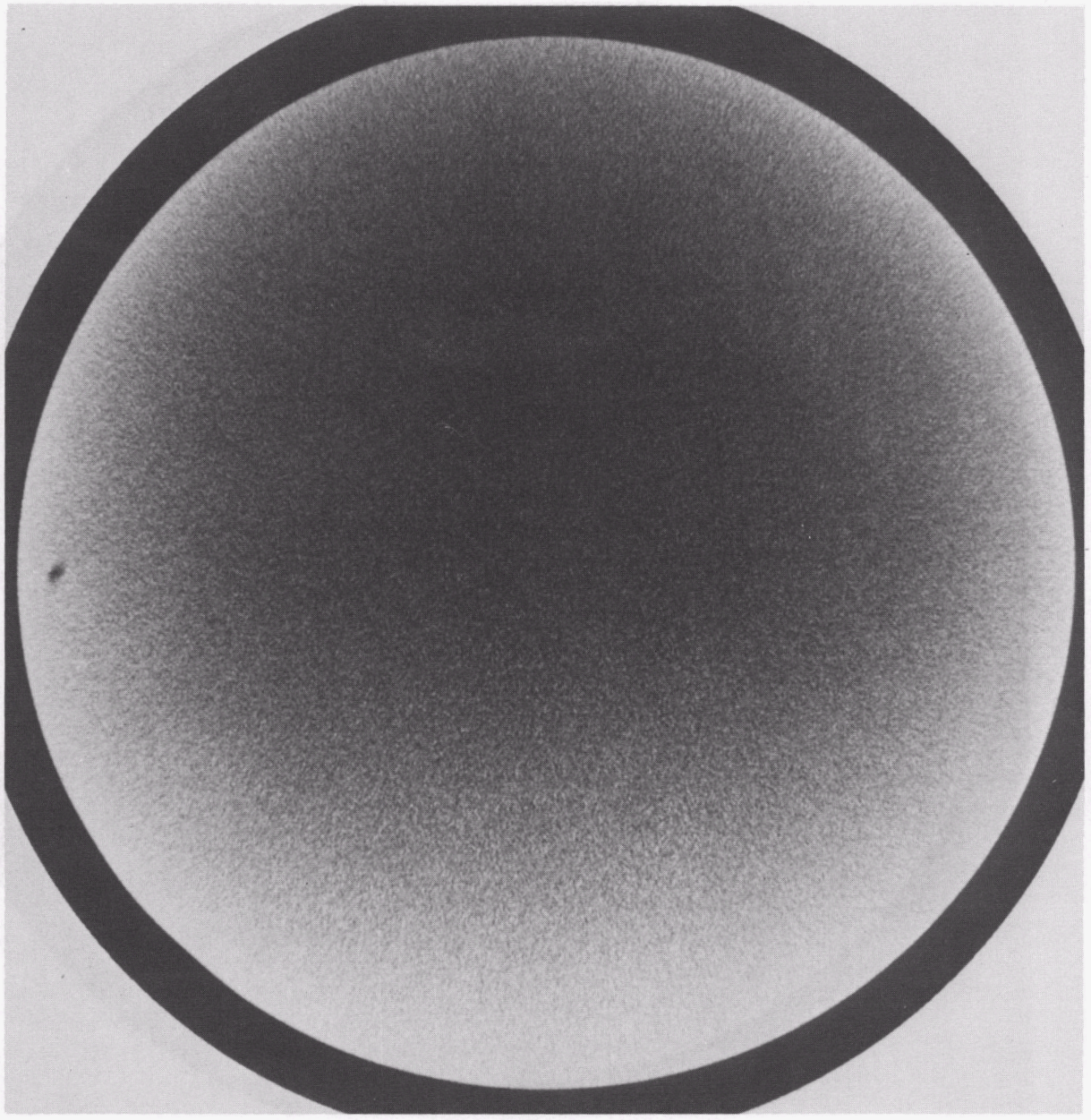

Fig. 10. CT slice through the diameter of sample 37.

YP14570

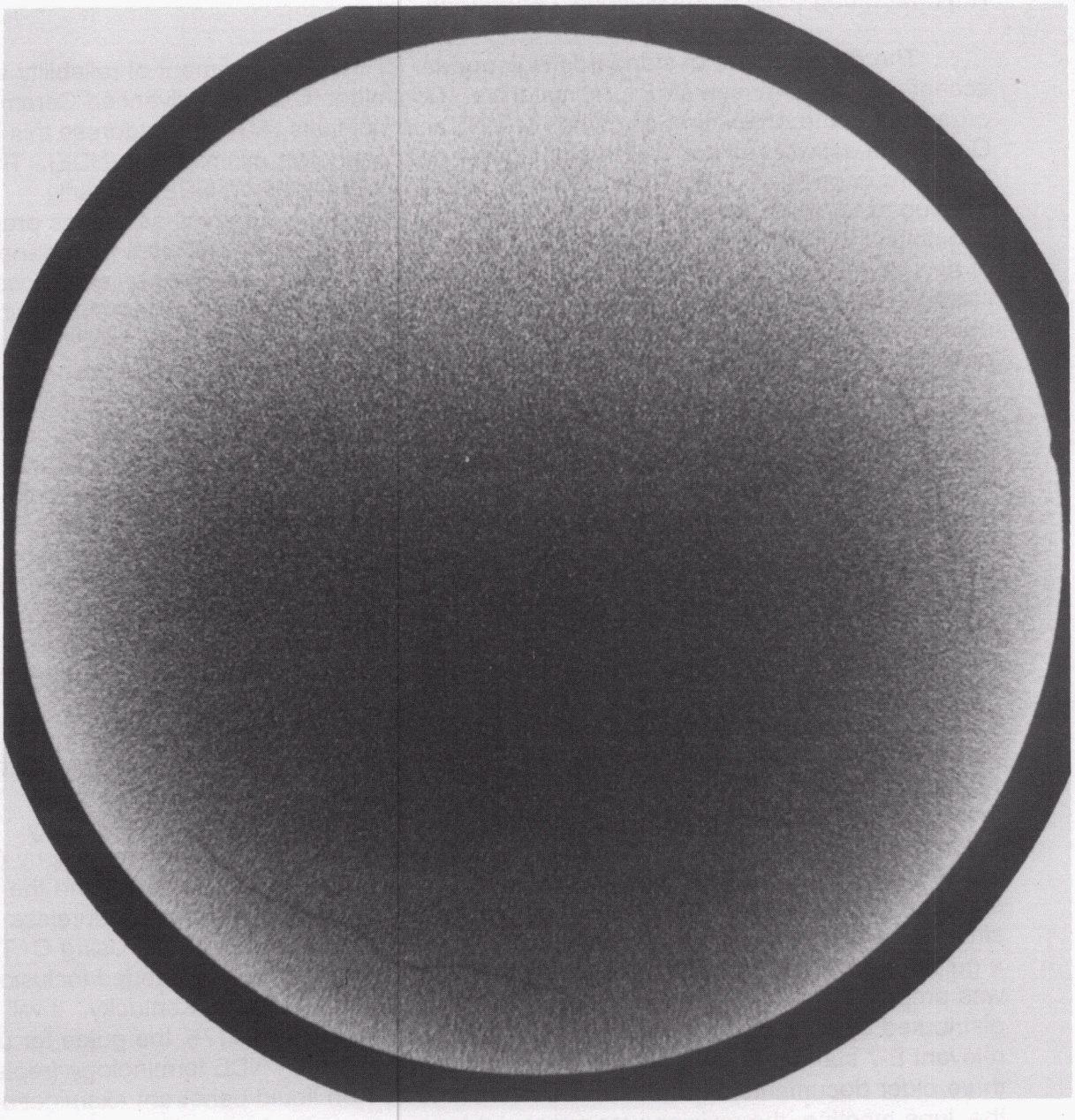

Fig. 11. CT slice through the diameter of sample 36.

NDE Standards for Advanced Ceramics

R. W. McClung (Oak Ridge National Laboratory)

The development of standards is important for the establishment of reliability and acceptance of advanced structural materials. Committee C-28, on Advanced Ceramics, is organized in the American Society for Testing and Materials (ASTM) to address this issue. One of the activities of the C-28 Committee is nondestructive examination (NDE). The Task Group on NDE (TGNDE) is reviewing existing standards on NDE (primarily developed for metals) to determine potential applicability for ceramics as well as preparing original standards. Use of existing or modified standards is more efficient than generation of new documents and will ensure the input of a large body of NDE expertise. Close liaison is established with ASTM Committee E-7 on Nondestructive Testing (NDT), and documents are in various stages of review, recommendations for change modification, and balloting. R. W. McClung is a member of both committees and the official liaison.

Liaison and technical support have been continued between ASTM Committees C-28 and E-7. To date, 31 NDE standards have been reviewed in detail with recommendations made to E-7 for modifications to identified documents. Successful action is complete on 27 documents; the others require action by C-28. A table of ultrasonic velocities in typical ceramic materials prepared by C-28 and submitted to E-7 for incorporation in an existing NDE standard has been accepted by ASTM. A change requested by C-28 related to thickness measurements by ultrasonics has been incorporated into an E-7 standard and successfully passed E-7 ballots and the August 1992 Society ballot. After a preliminary review of an E-7 standard on electronic evaluation of ultrasonic instruments, E-7 opinion was requested on the relevancy of the standard to instruments at frequencies higher than 25 MHz. The higher frequencies are more common for ceramics. The response reflected a need for modest changes to the standard to be relevant for higher frequencies (and ceramics NDE). Comments submitted to E-7 after review of five E-7 standards on liquid-penetrant examination have been incorporated into the standards and approved by E-7 and the August 1992 Society ballots. C-28 requests for specific definitions related to X-ray computer tomography (CT) have resulted in approved, balloted definitions incorporated in CT standards and the E-7 standard on NDT terms. A document on fabrication of seeded voids in pressureless sintered ceramics, designated C1212, has also been approved by ASTM. Using C1212 as a guide, a draft standard for ceramic reference specimens containing seeded inclusions was prepared and discussed at the June 1992 meeting in Louisville, Kentucky. It will be distributed by mail for comments by the TGNDE. A revision of C1175, the guide for use of relevant E-7 standards, was drafted to add a new standard on NDE terminology (replacing three older documents) and to add five new standards on liquid-penetrant examination. At the June meeting, the revision was approved for concurrent subcommittee and committee letter ballot. After agreements were reached at the June meeting, work in progress in C-28 includes the draft standard on reference specimens containing seeded inclusions, amplified outlines for draft standards on reference specimens with laser-drilled holes and precision measurements of ultrasonic velocity, and development of radiographic equivalence factors for ceramics. The latter, after development, will be submitted to E-7 for incorporation in an existing standard.

X-ray Computed Tomographic Imaging – W. A. Ellingson, D. L. Holloway, E. A. Sivers (Argonne National Laboratory) J. Ling, (Ceramic Research Institute, Shanghai, China) J. P. Pollinger (Garrett Ceramic Components of Allied-Signal Aerospace Corporation)

Objective/scope

The objective of this program is to develop X–ray computed tomographic (CT) imaging technology for application to structural ceramic materials. This technique has the potential to map short–range (<5-mm) and long–range (>5-mm) density variations (to perhaps 0.5–1%), detect and size high– and low–density inclusions, and detect and size (within limits) cracks in green–state and densified ceramics. Use of three dimensional (3-D) CT (volume CT) imaging allows interrogation of the full volume of a component and is noncontacting. It is also relatively insensitive to specimen shape and thus can be used to inspect components with complex shapes, such as turbocharger rotors, rotor shrouds, and large individual turbine blades.

Technical progress

The work accomplished during this reporting period covers the application of X-ray CT with the Argonne National Laboratory (ANL) three dimensional (3-D) microfocus system to phase II of the research program conducted to detect whisker distributions (likely to be manifested and detected as density variations) in as-cast pressure-slip-cast $SiC(w)/Si_3N_4$ (Garretts Ceramic Components GN-10 material). This is a continuing joint project between Garrett Ceramic Components of Allied-Signal Aerospace Corporation of Torrance, California.

All of the specimens of $SiC(w)/Si_3N_4$ billets (length/diameter ratio = 1.5 and 2.67) made by pressure slip-casting have now been examined. For all cases in these two sets, the casting pressure was 40 psi and the mold type was plaster of paris. The configuration of the casting is shown in Fig. 1. Note that the dewatering was in two directions: radially and axially (bottom only).

The two sets of specimens and their casting parameters are given in Table 1.

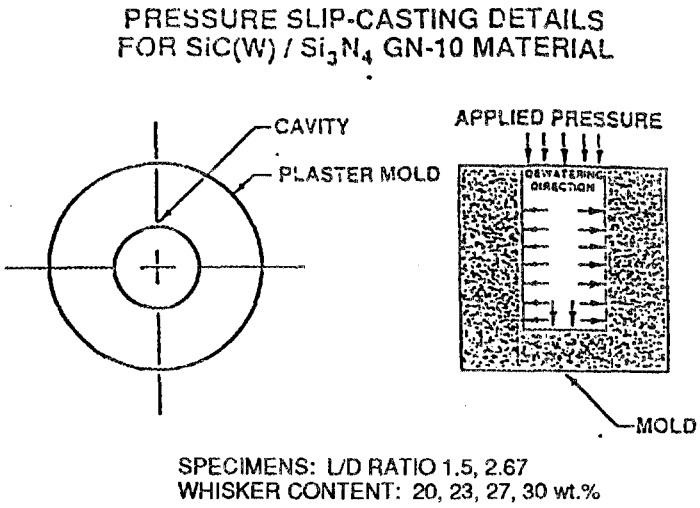

Fig. 1. Schematic diagram of dewatering/mold configuration for pressure-slip-cast SiC(w)/Si_3N_4 GN-10 ceramic materials

Table 1. Casting data[a]

Billet Identification	Whisker Content vol.%	Slip Solids Content vol.%	Slip Viscosity cps	Bulk density at demolding g/cm^3
SET 1 L/D = 1.5				
91A–013	20	69.8	135	2.07
S–910002	23	68	93	2.47
S–910362	27	65	105	2.15
S–910373	30	63	362	2.30
SET 2 L/D = 2.67				
S920030–2	20	69.8	191	1.09
S920033–2	23	68	167	1.04
S920042–1	27	65	96	1.79
S920048–2	30	63	136	1.67

[a]Mold type: Plaster of paris
Casting time: 50 min
Whisker type: American Matrix, HF-Etched
Pressure level: 0.276 MPa (40 psi)

We also compared data that were obtained from two other specimens earlier in this research effort. These data are presented in Table 2.

During this reporting period, we finished the destructive and nondestructive analysis of all the specimens in the Phase II research. We completed the analysis of the L/D = 2.67 specimens for the whisker concentrations of 20, 23, 27, and 30 vol.% whiskers. The data are presented in Figs. 2-5 for 20, 23, 27, and 30 vol.% whiskers, respectively.

In addition, we conducted an initial comparison of the effect of L/D ratio on several radial density gradients by X-ray CT and as measured to destruction. These data are shown in Figs. 6 and 7. Figure 6 shows the effect of L/D ratio for 27 vol.% whiskers. Figure. 7 shows the effect of L/D ratio for 30 vol.% whiskers. Note that the 30 vol.% whisker for L/D = 1.5 is much larger than for L/D = 2.67. But for L/D = 2.67, no significant effect is noted on L/D ratio.

Table 2. Casting parameters used for earliest specimens of $SiC(w)Si_3N_4$

Billet	T-8a	T-12a
Whisker Content	20 vol.%	30 vol.%
Size	25 mm dia 75 mm long	25 mm dia 75 mm long
L/D	3.0	3.0
Whisker	Tateho	Tateho
Slip Visc.	482 cps	274 cps
Casting Pressure	0.103 MPa (15 psi)	0.103 MPa (15 psi)
Solids Content	54.6%	53.3%

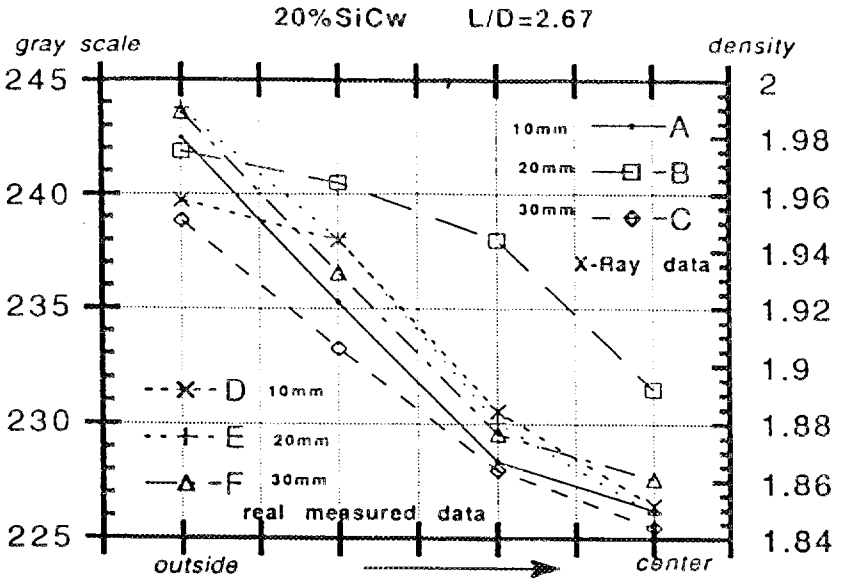

Fig. 2. Radial density gradient for 20 vol.% whiskers as measured by X-ray CT gray-scale changes, and destructive density measurements at three axial location: 10, 20, and 30 mm from bottom.

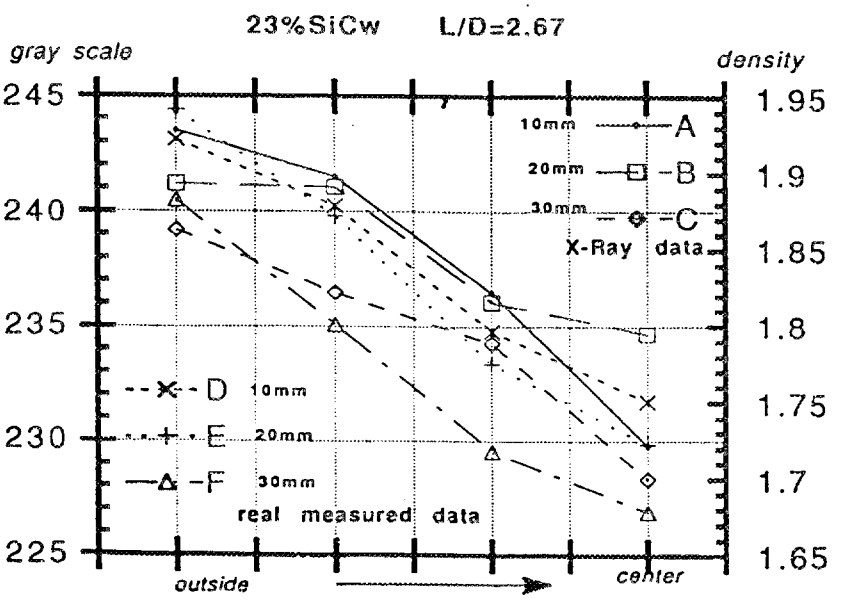

Fig. 3. Radial density gradient, as measured by X-ray CT gray-scale changes and destructive analysis of specimen with 23 vol.% whiskers.

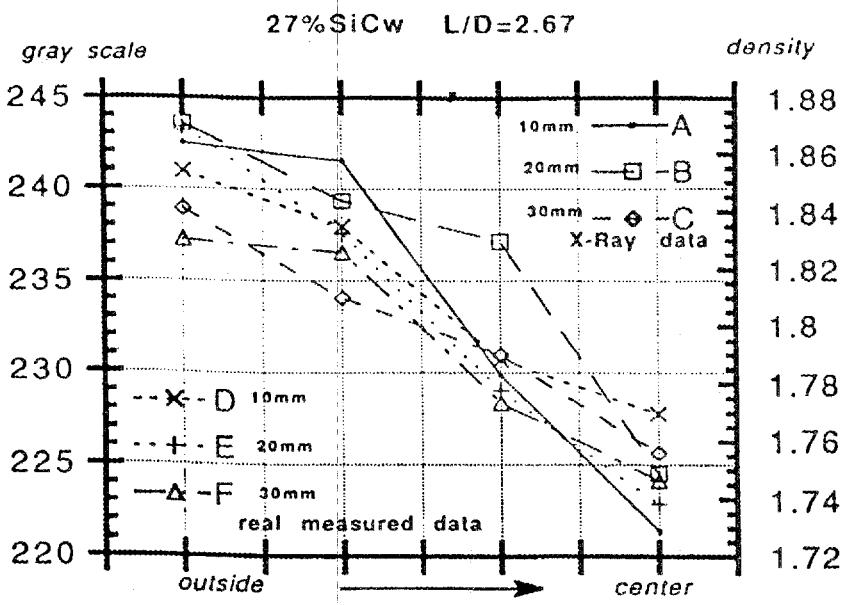

Fig. 4. Radial density gradient for 27 vol.% whiskers as measured by X-ray CT gray-scale changes and destructive density measurements at three axial locations: 10, 20, and 30 mm from bottom.

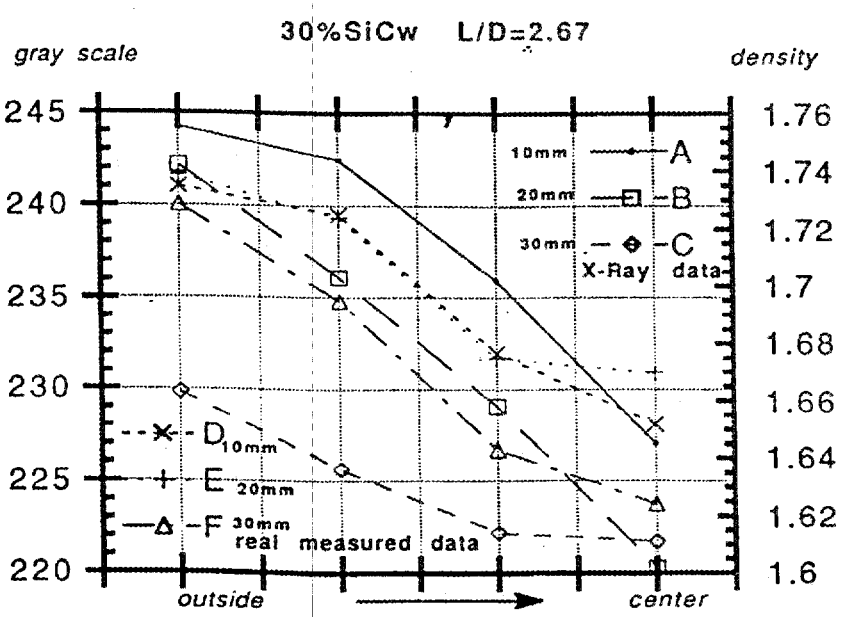

Fig. 5. Radial density gradient, for 30 vol.% whisker specimen as measured by X-ray CT gray scale changes and destructive density measurements at three axial locations: 10, 20, and 30 mm.

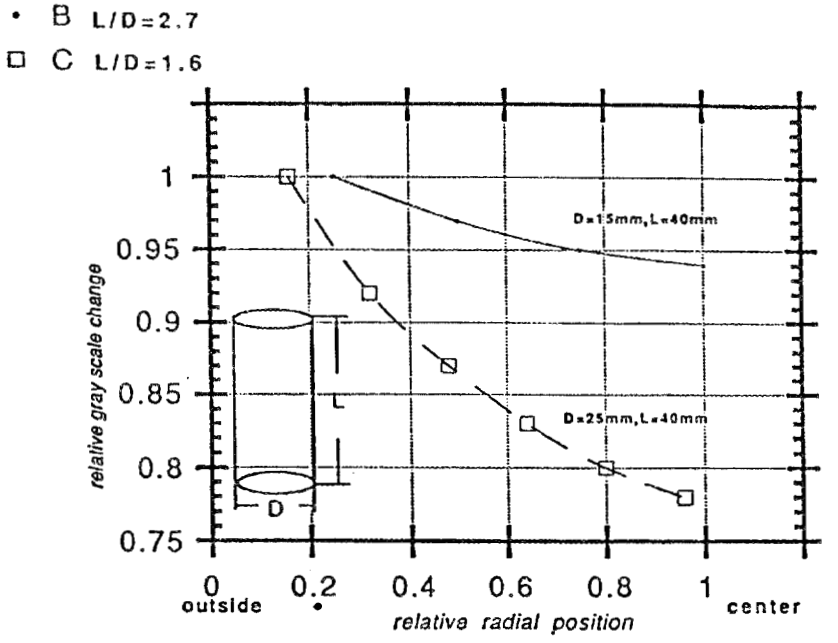

Fig. 6. Radial density gradient, as measured by X-ray CT gray-scale changes, for two L/D ratio billets with 27 vol.% whiskers.

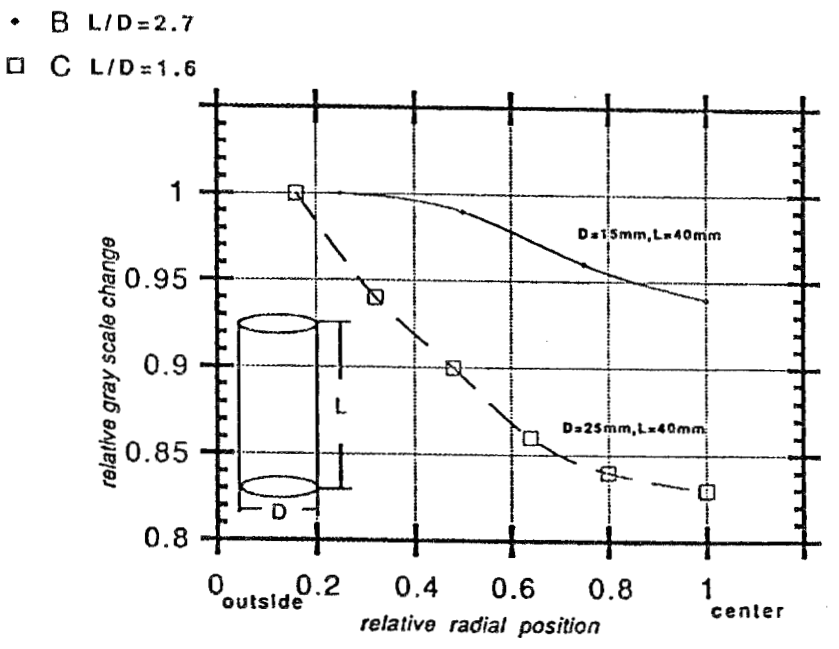

Fig. 7. Radial density gradient, as measured by X-ray CT gray-scale changes, for two L/D ratio billets, with 30 vol.% whiskers.

Because we encountered difficulties when we tried to acquire experimental NDE data on the initial set of specimens made at 25-mm diameter, L/D = 1.5, data comparison has taken longer than anticipated. The reason for this delay was that we originally tried to use one data set for both NMR imaging and X-ray CT imaging. The NMR imaging experiment resulted in the original 20 and 23 vol.% whisker specimens being cut in half, with some loss in the fiducial markings originally used by the X-ray CT data facility.

We have tried to reconstruct the reference positions used on these two samples so we could perform the X-ray CT analysis. However, as you can see by the large scatter in the data, we clearly lost some of the reference markings.

Figure 8 shows schematic diagrams of the two halves of the 20 and 23 vol.% billets.

Figure 9 shows the destructively measured density data and X-ray CT gray-scale data. The comparison is not good for several possible reasons. First, the X-ray CT data sets were not of high quality due to misalignment and poor center- of-rotation measurement, which was not discovered until later. We will attempt to make a correction to improve these data during the next period.

As noted in Specimen Set 2, L/D = 2.67, where we have good reference points, X-ray CT data and destrustively measured data correlate very well.

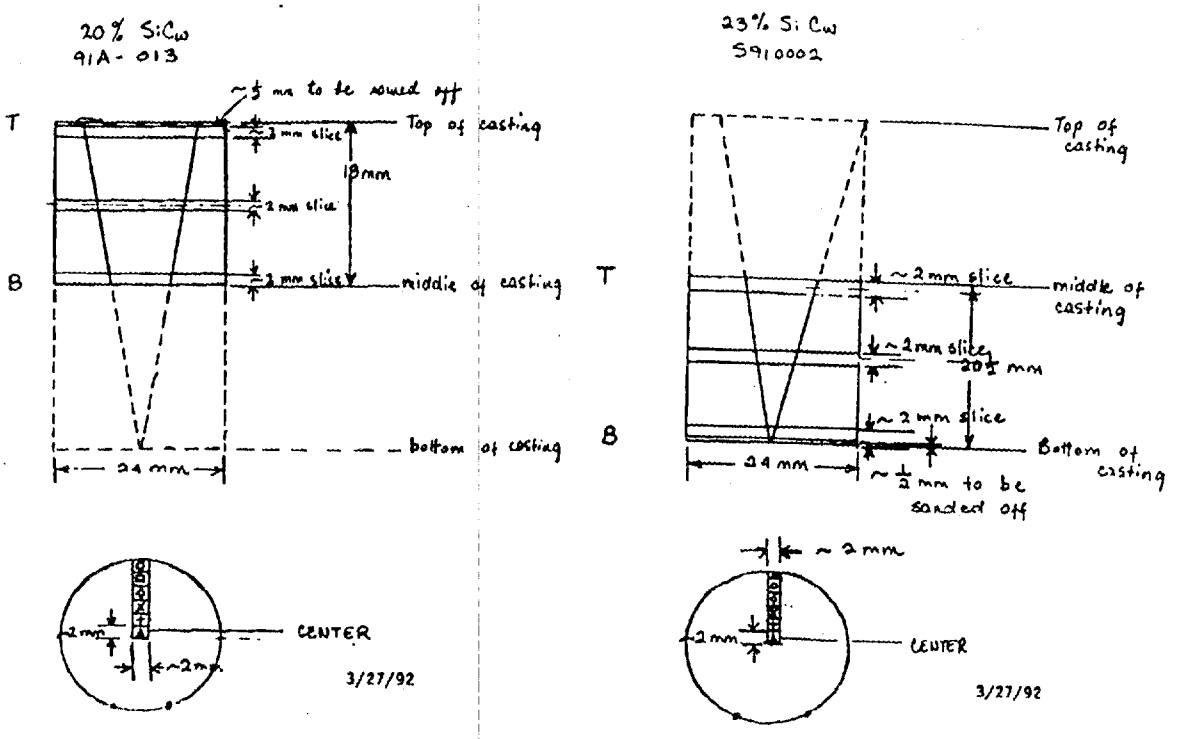

Fig. 8. Schematic diagram showing location of remaining billet halves and where destructive data were taken for L/D = 1.5 specimens.

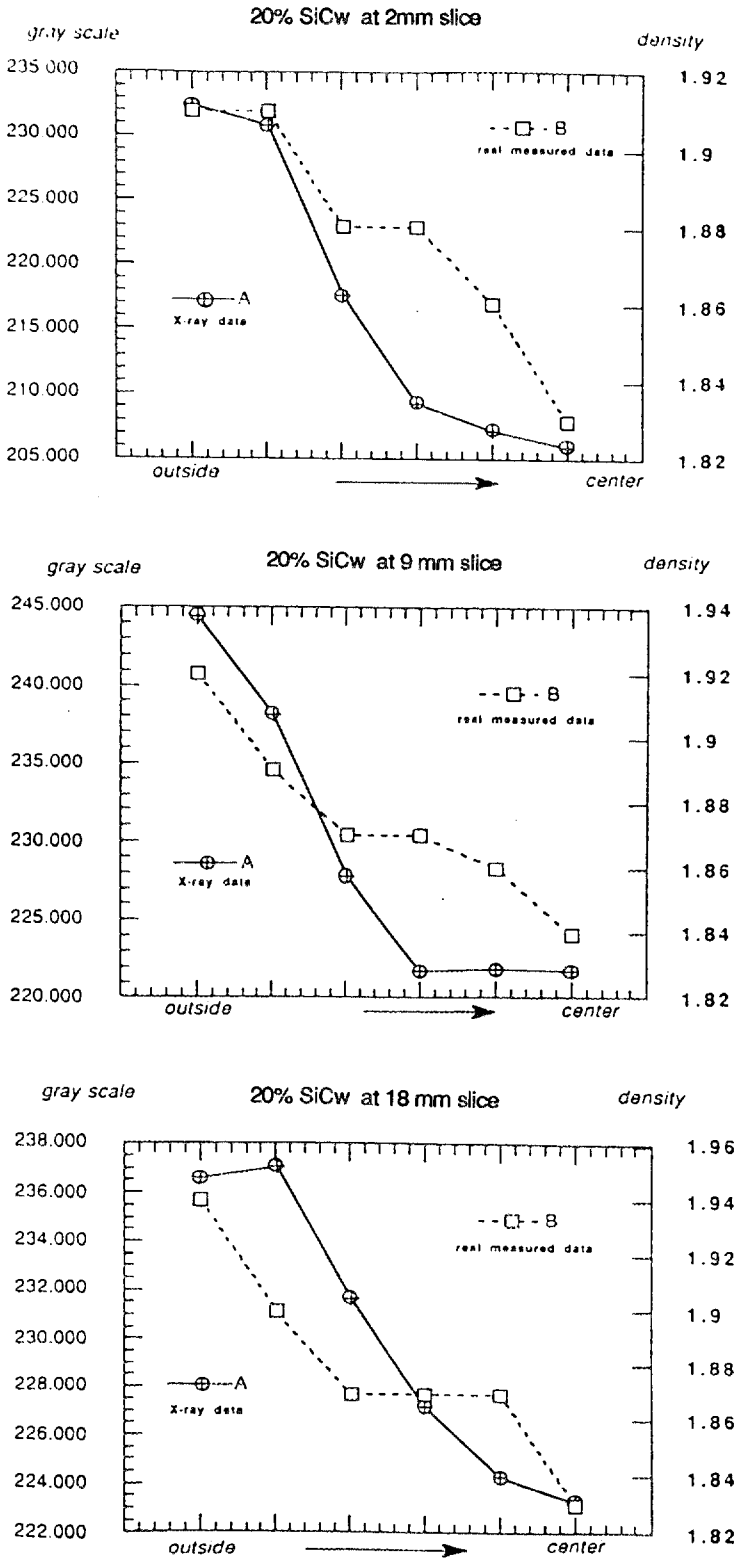

Fig. 9. Radial density distribution for 20 wt.% SiC(w) specimen of L/D = 1.5, as determined by destructive evaluation and as by X-ray CT.

Nuclear Magnetic Resonance Imaging – S. L. Dieckman, A. C. Raptis, W. A. Ellingson (Argonne National Laboratory), and H. Yeh and J. P. Pollinger (Garrett Ceramic Components of Allied-Signal Aerospace Corporation)

Objective/Scope

The objectives of this task are to (1) utilize NMR imaging techniques to study the distribution of whiskers and other possible variations in composite pressure-slip-cast green-state (as-cast) billets, (2) conduct destructive analysis of the same billets (to be performed by Garrett Ceramic Components a Division of Allied Signal Corp.), and (3) correlate the results obtained from the NMR imaging techniques with those obtained from both three dimensional (3-D) X-ray and optical microscopy.

Technical Highlights

In the previous reporting periods, 3-D NMR images were acquired of the proton distribution in benzene-imbibed, as-cast SiC(w)/Si_3N_4 whisker-reinforced composite specimens. Imaging studies were performed on 20 and 23 wt.% whisker-reinforced as-cast composite specimens. The data were acquired by a 3-D NMR imaging technique that is based on two-phase encoding and one readout gradient. This technique has the advantage of sampling the data space equally in three dimensions. Additionally, unlike conventional slice-selection techniques, this 3-D technique allows quick (< 0.5 ms) data acquisition after initial excitation by the RF pulse. This is crucial in these studies because the signals observed from the benzene in this heterogeneous mixture decay away rather quickly (≈1.0 ms) due to microscopic magnetic inhomogeneities caused by large differences in magnetic susceptibility of the benzene and the Si_3N_4.

NMR image data were acquired and reconstructed with 1 mm resolution in each of the three dimensions. Photographs of "thin 2-D slices" extracted from the 3-D images of the 20 and 23 wt % specimens are presented in Figs. 1A-1F. The thin sections correspond to locations where destructive analysis was performed. The gray-scale intensities, and thus concentration of the benzene filler fluid, is greater in the center of the specimen in each instance. In the slices selected from the bottom of the specimen (Fig. 1C and Fig. 1F), acquisition artifacts and RF inhomogeneities caused increased intensity along the sides of the specimen in the phase encoding direction (vertical in the photos). This common artifact, results from large differences in magnetic susceptibility of the ceramic and the filler fluid. The low-frequency noise, which has a blocky appearance in Figs. 1C and 1F is due to undersampling and truncation in the phase encoding domain.

In this period, we completed a comparison of the density data obtained through destructive analysis of the specimens and gray-scale intensities obtained through nondestructive NMR imaging studies. The destructive analysis, performed by Garrett

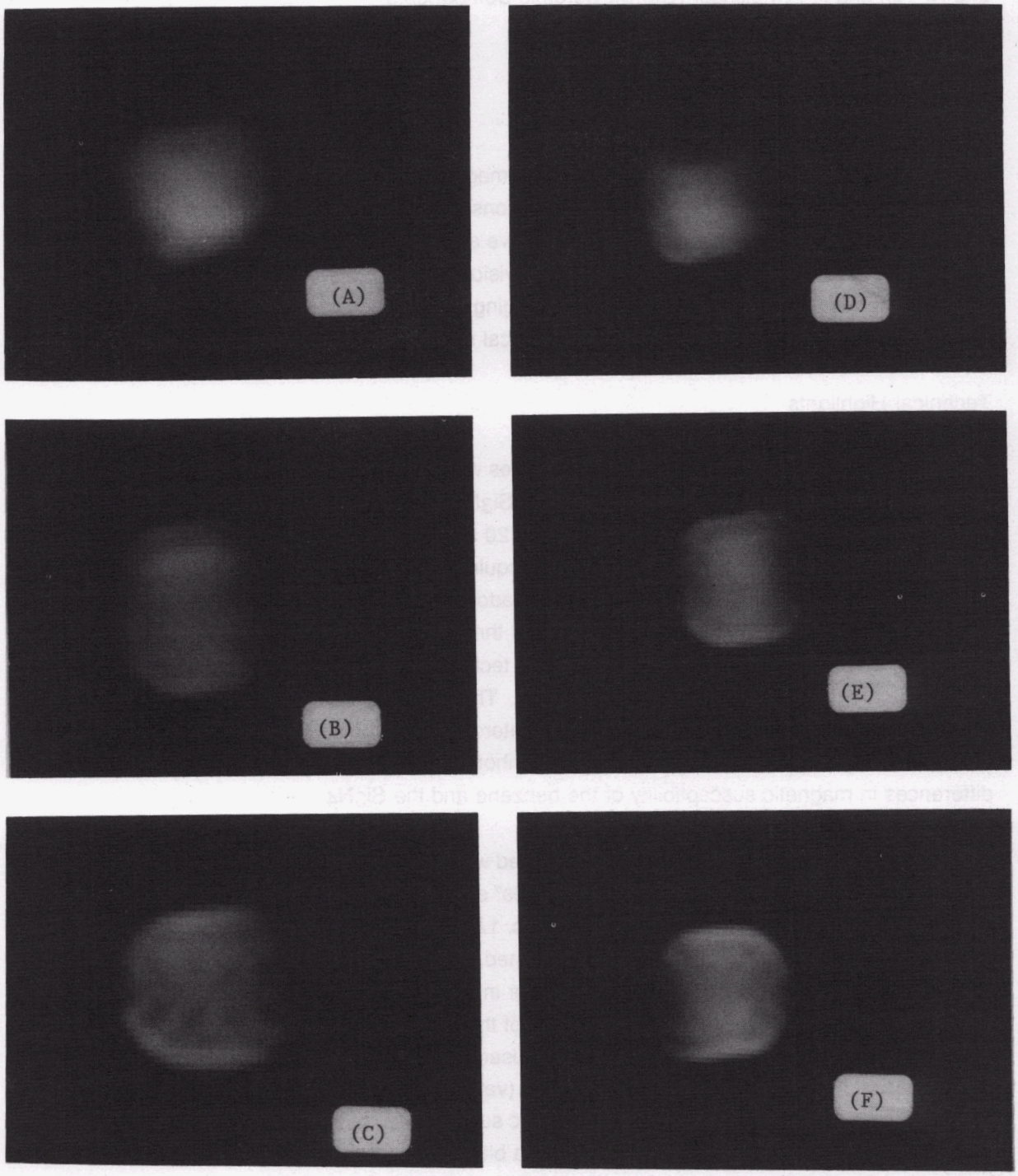

Fig. 1. Photographs of "thick slices" taken from 3-D images of 20 and 30 wt.% whisker composite specimens. The photos correspond to areas (A) 2 mm, (B) 9 mm, and (C) 28 mm from the top of the 20 wt.% specimen, and (D) 18 mm, (E) 28 mm, and (F) 40 mm from the top of the 23 wt.% specimen.

Ceramics Processing Division, Allied-Signal Company, Torrance, CA, was accomplished by sectioning specimens into 2 X 2 X 2 mm cubes at locations near the center and at each end of the specimens. Six specimens were analyzed from each of six separate locations. The resulting densities varied approximately 5% (from 1.84 to 1.94 g/cm^3) across the specimen; however, no indication of relative error in the measurement was given. To provide equivalent spatial resolution in both analysis techniques, the NMR image data were averaged in three dimensions to provide a 2 mm cubic resolution.

Density and NMR gray-scale-intensity data are plotted as a function of radial distance from the center of the specimen for each of the six specimen slices in Figs. 2A-2E. Density measurements varied in a roughly monotonically increasing manner from the center to the outer edge of the specimen. Likewise, the NMR gray scale data decreased with increasing specimen density.

NMR imaging can be performed to determine primarily the distribution of material within the specimen (i.e., nuclei per mm^3). Because this is not a direct measurement of the specimen density, a direct comparison of NMR and density data is generally not possible without performing the imaging experiments with a series of porosity and density calibration standards constructed of the identical composite materials. With the use of such standards, it should be possible to compensate for various physical, instrumental, and experimental limitations and uncertainties, such as chemical shift artifacts, magnetic susceptibility artifacts, magnetic field inhomogeneities, RF inhomogeneities, and nuclear relaxation variations. However this is not possible on Argonne's instrument because of limitations in magnet bore available for the specimen and standards. In addition, given the wide line width (due to magnetic susceptibility), these experiments would not be feasible on commercial imaging systems, which lack the necessary gradient strength and response times. However, while a rigorous (i.e., mathematical) comparison of the gray-scale intensities as a function of density is thus not possible under these conditions, it is clear that the plots in Figs. 2A-2E are qualitatively correct. Thus, this experimental series was indeed successful.

During this period, we also submitted a statement of work for continued effort in magnetic resonance imaging, (i.e., Phase III) "Application of NMR to Gel-Cast Ceramics Processing." This statement details a two-year effort to be performed at Argonne National Laboratory in collaboration with Dr. Ogbemi O. Omatete from the Materials and Ceramics Division at Oak Ridge National Laboratory. The purpose of this work is to evaluate the potential of NMR spectroscopy and imaging to affect development and process control of near-net-shape gel-cast ceramics. In this effort, NMR spectroscopy and imaging will be employed for both the in-situ monitoring of the polymerization process and the nondestructive evaluation of the resultant components. The thrust of this experimental series will be aimed at (1) determining the origin of variability in physical properties (i.e., strength, viscosity, and porosity) among different specimens

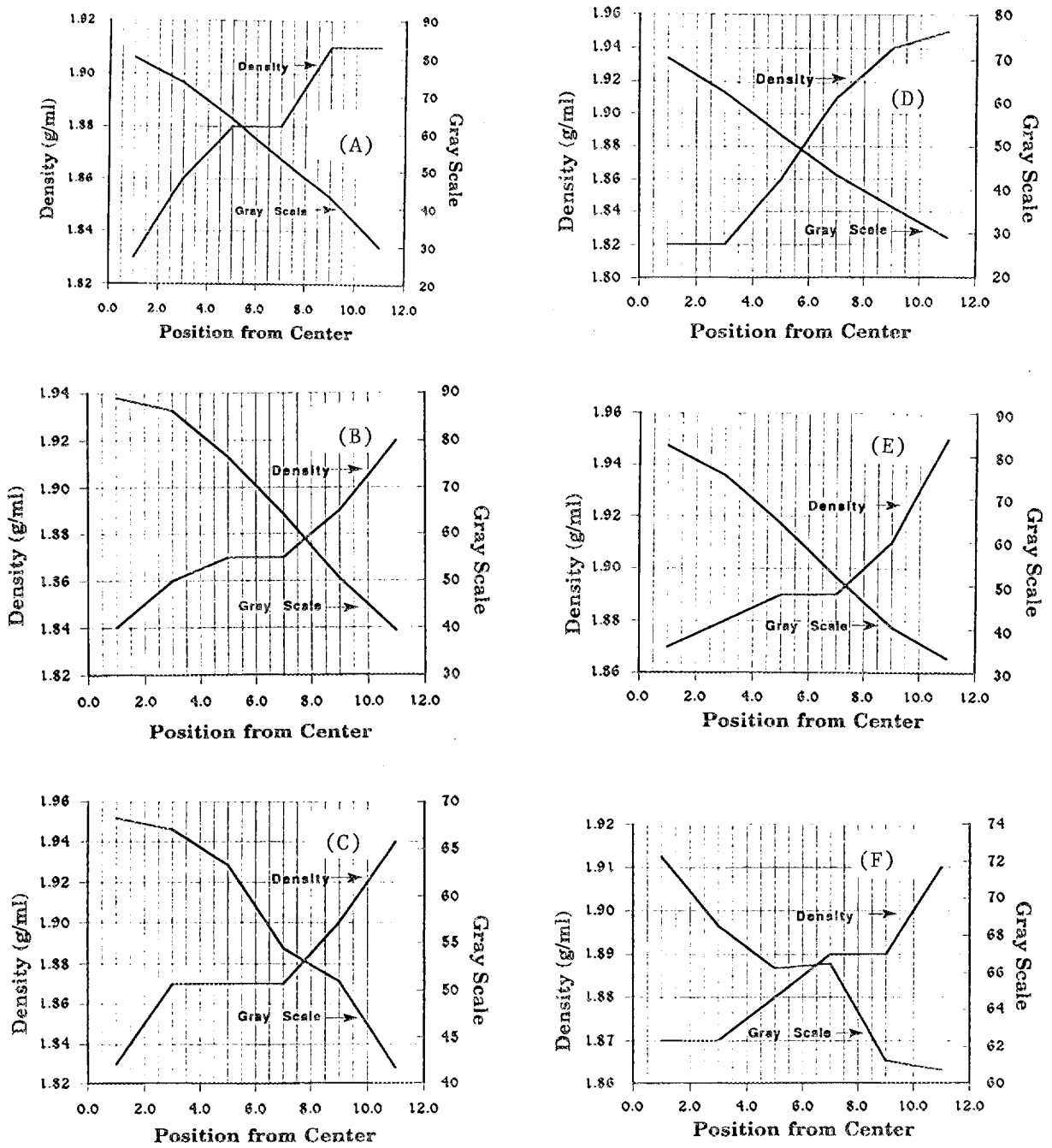

Fig. 2. Plots of density and gray-scale intensity vs. radial distance from the center of the specimen for 20 and 23 wt.%-whisker specimens. The plots correspond to areas (A) 2 mm, (B) 9 mm, and (C) 28 mm from the top of the 20 wt.% specimen, and (D) 18 mm, (E) 28 mm, and (F) 40 mm from the top of the 23 wt.% specimen.

and component compositions, and (2) detecting and tracing flaws throughout the manufacturing process.

The specific objectives encompassed here can be organized into five parts: (1) in-situ spectroscopic monitoring of the gelation process by measuring appropriate NMR parameters (i.e., T_1, T_{1r}, and T_2), (2) multidimensional mapping of polymer and polymerization homogeneity, (3) real-time imaging of the polymerization process; (4) nondestructive evaluation of voids and flaws in the resultant components, and (5) measurement of physical properties (such as degree of polymerization, viscosity, and specimen strength) via correlation with measureable nuclear spin relaxation parameters (T_1, T_{1r}, and T_2).

Status of Milestones

Milestones have been completed for Phase II.

Trips/Communications/Visits

None

Problems Encountered

None.

MILESTONE SCHEDULE (3.5.1.6)

3.5.1.6.08	Complete NMR Imaging of two slip-cast billets	8/15/91
3.5.1.6.09	Submit initial report on correlation between NDE data and destructive testing.	6/15/92
3.5.1.6.10	Complete NMR imaging of remaining billets	6/15/92

4.0 TECHNOLOGY TRANSFER

4.1 TECHNOLOGY TRANSFER

4.1.1 Technology Transfer

Technology Transfer
D. R. Johnson (Oak Ridge National Laboratory)

Technology transfer in the Ceramic Technology Project is accomplished by a number of mechanisms including the following:

Trade Shows - A portable display describing the program has been built and has been used at numerous national and international trade shows and technical meetings.

Newsletter - A Ceramic Technology Newsletter is published regularly and sent to a large distribution.

Reports - Semiannual technical reports, which include contributions by all participants in the program, are published and sent to a large distribution. Informal bimonthly management and technical reports are distributed to the participants in the program. Open-literature reports are required of all research and development participants.

Direct Assistance - Direct assistance is provided to subcontractors in the program via access to unique characterization and testing facilities at the Oak Ridge National Laboratory.

Workshops - Topical workshops are held on subjects of vital concern to the ceramics community.

International Cooperation - This program is actively involved in and supportive of the cooperative work being done by researchers in West Germany, Sweden, the United States, and, most recently, Japan under an agreement with the International Energy Agency. This effort is ultimately aimed at development of international standards and includes physical, morphological, and micro-structural characterization of ceramic powders and dense ceramic bodies, and mechanical characterization of dense ceramics.

IEA ANNEX II Management
V. J. Tennery (Oak Ridge National Laboratory)

Objective/scope

The purpose of this task is to organize, assist, and facilitate international research cooperation on the characterization of advanced structural ceramic materials. A major objective of this research is the evolution of ceramic property measurement standards. This task, which is managed in the United States by ORNL, now includes a formal International Energy Agency (IEA) Annex agreement identified as Annex II between the United States, Germany, Sweden, and Japan. The original annex included four subtasks: (1) information exchange, (2) ceramic powder characterization, (3) ceramic chemical and physical characterization, and (4) ceramic mechanical property measurements. In the United States, a total of 13 industrial and government laboratories have participated and contributed their resources to this research. The research in Subtasks 2, 3, and 4 is now complete. During CY 1990, agreements were reached for Japan to join the Annex and for research in two new subtasks to be initiated. These include, Subtask 5, Tensile and Flexural Properties of Ceramics, and Subtask 6, Advanced Ceramic Powder Characterization.

A proposal for future (Subtask 7) research interest in Mechanical Properties of Structural Ceramics was sent to current U.S. participants. This proposal includes extensive work to correlate the effects of machining parameters upon resultant fracture strength and fracture statistics. The research plan was based upon discussions of the Executive Committee at the Nagoya, Japan, meeting. To date, a total of seven industrial and two federal laboratories have agreed to participate in the proposed work. In addition, several discussions have been held with potential participants on ceramic powder characterization (possible future Subtask 8). The international representatives from Germany, Japan, and Sweden were then sent a research plan for future mechanical property research, based upon the U.S. proposal following the instructions of the Executive Committee at the meeting in Nagoya in October 1992, to determine if they were interested in future research in Mechanical Properties in the Annex. In addition, letters were sent to a representative of the Commission of The European Communities. This proposal will be discussed at the IEA Executive Committee Meeting to be held at the Annual Automotive Contractors' Coordination Meeting (CCM) in Dearborn, Michigan, on November 5, 1992.

Technical progress

Subtask 5, Flexural and Tensile Properties of Ceramics

United States

Analysis of the flexural strength data and tensile strength data is proceeding.

All tensile specimens (5 each) from the international partners [Sweden (ABB material), Germany (ESK material), and Japan (SSN-H material)] of this research were fractured (August 3-6, 1992, by Michael Jenkins).

Germany, Sweden, and Japan

The tensile specimens from Sweden were received on July 10, 1992.

The minutes were received from the IEA Swedish Subtask 5 Meeting held in Göteborg on June 4, 1992. The five tensile specimens (ABB) from Sweden were received on July 10, 1992.

The completed data on the fracture strength test of the 30 GN-10 flexure specimens fractured by Sweden (as part of the exchange) have been received (September 28, 1992).

The specimens were received from Japan, on May 11, 1992, after new gages were applied. The earlier set had serious misalignment problems with the gages. For this new specimen set, the gages have been applied properly.

Subtask 6, Advanced Ceramic Powder Characterization

Major responsibility for this subtask in the United States is at the National Institute of Standards and Technology (NIST), and a detailed report of progress on this subtask is provided in the section of this report submitted by the NIST.

Data analysis, revision of the report on procedure compilation, and future program planning were three major activities during this period.

Preliminary statistical analysis of the powder characterization data has been developed. A draft report containing this information was discussed at the technical leaders meeting in Jülich, Germany, during the period July 6-7, 1992. Comments of the technical leaders were incorporated into this report for distribution to the participants. Primarily, the draft report contains repeatability and reproducibility data for those procedures for which sufficient data are available. Using this analysis, the technical leaders are engaged in detailed data analysis to be included in the final report. Draft inputs on conclusions and recommendations on powder characterization data analysis have been received from technical leaders. Currently, these inputs have been undergoing extensive rewriting and editing. Our plan is to send the draft conclusions and recommendations to participants for their comments by October 30, 1992. In addition, we have received partial inputs from technical leaders on data analysis, which will be incorporated in the final report.

The interim report (for limited release), *Procedures on Ceramic Powders Characterization*, was distributed to participants for consideration of forwarding to standards-setting bodies in the participating countries (April 1992). Mr. Schulz received approval for the limited release of the report from Ms. Borg, Sweden (June 1, 1992). Mr. Schulz received approval for the limited release of the report from Mr. Hiroshi Terasawa, Japan (July 30, 1992). Dr. Seitz, on behalf of Germany, has consented to approve this report, with the requested revisions, for distribution to participants and standards-setting bodies. The final version of the original interim report was received on September 25, 1992, by V. J. Tennery from S. G. Malghan for publication and distribution. This process is now under way.

A set of two questionnaires was sent to the participants of Subtask 6 to seek their input to the future work on powders characterization. Over 75% of the total responses were received. The major highlights of the interest areas for future work are improvement of selected procedures for chemical and physical properties analysis and survey of secondary properties of powders. The technical leaders have been engaged in planning

of future activities related to powders characterization. At the Jülich meeting, various ideas were discussed and a tentative plan was adopted for further evaluation. A questionnaire is being prepared for sending to the participants to seek their input to the program.

References

None

Status of milestones

The date for Milestone 411511 was changed to November 30, 1992, due to compiling the data from the fracturing of the international specimens.

Milestone 411513 has been changed to state: Complete draft final reports for Subtasks 5 and 6. The date has been changed to June 30, 1993, due to the schedule for receiving completed data from the international participants.

Communications/visits/travel

None

Publications and presentations

"IEA Annex II, Subtask 5 - Status of Tensile Strength Analysis GN-10 Silicon Nitride, at 25°C," was presented by V. J. Tennery at the Ceramic Material Testing Coordination Meeting, Allison Gas Turbines, Indianapolis, Indiana, May 5, 1992.

Characterization of Ceramic Powders

S. G. Malghan, L.-S. Lum, J. F. Kelly, E. Begley and S. M. Hsu
(National Institute of Standards and Technology)

Objective/Scope

Ceramics have been successfully employed in engines on a demonstration basis. The successful manufacture and use of ceramics in advanced engines depends on the development of reliable materials that will withstand high, rapidly varying thermal stress loads. Improvement in the characterization of ceramic starting powders is a critical factor in achieving reliable ceramic materials for engine applications. The production and utilization of such powders require characterization methods and property standards for quality assurance.

The objectives of the NIST program are: (1) to assist with the division and distribution of ceramic starting powders for an international round-robin on powder characterization; (2) to provide reliable data on physical (dimensional), chemical and phase characteristics of powders; and (3) to conduct statistical assessment, analysis and modeling of round-robin data. This program is directed toward a critical assessment of powder characterization methodology and toward establishment of a basis for the evaluation of fine powder precursors for ceramic processing. This work will examine and compare by a variety of statistical means the various measurement methodologies employed in the round-robin and the correlations among the various parameters and characteristics evaluated. The results of the round-robin are expected to provide the basis for identifying measurements for which Standard Reference Materials are needed and to provide property and statistical data which will serve the development of internationally accepted standards.

Technical Progress

During this reporting period, the major activities were on preparation of statistical analysis report, preparation of procedures compilation report, preparation of a plan for continuation activities, and development of ASTM procedures. In addition, based on these data, the technical leaders are engaged in developing preliminary conclusions and recommendations, and detailed analysis of data.

Data Analysis: A draft report containing statistical evaluation of IEA Subtask 6 data has been completed. This report contains estimates of repeatability and reproducibility for each set of data that permitted statistical analysis. For example, the following statements for particle size distribution measurement for SNT silicon nitride powder by Sedigraph have been developed:

Mean of laboratory means = 0.93 μm
Standard deviation of laboratory means = 0.09 μm

Repeatability: The difference between two single results found by one operator using the same apparatus within the shortest feasible

time interval will exceed the repeatability value of 0.17 on average not more than once in 20 cases in the normal and correct operation of the method.

Reproducibility: Single results reported by two laboratories will differ by more than the reproducibility value of 0.28 on average not more than once in 20 cases in the normal and correct operation of the method.

This report in draft form has been distributed to technical leaders to enable them to develop preliminary conclusions. Subsequently, the report was distributed to all participants by incorporating suggestions from the technical leaders.

The technical leaders held a meeting in Jülich, Germany to review data and to discuss preliminary conclusions and recommendations. In addition to Prof. H. Hausner, German technical leader, Dr. B. Stojanik attended the meeting, since he will be taking over after Prof. Hausner's retirement in 1992. In conjunction with this meeting, a joint-meeting of the German participants was held. In general, the German participants were enthusiastic about the Subtask 6 progress. However, due to economic downturn and slow progress of advanced ceramic applications, new priorities may be implemented. One such priority is inclusion of alumina in the powder characterization project since alumina ceramics are commercially important. In addition, some participants may withdraw from future activities, while new companies are expected to join.

Procedures Compilation Report: The technical leaders discussed the procedure compilation report and concluded that its early release will assist the efforts of standards setting bodies. Hence, agreed to follow-up on expediting the signing-off of the report by their national representatives. German participants expressed that their comments were not fully reflected in this report. Hence, a revised report was prepared. This report included, all the comments of German participants at appropriate locations. Subsequently, Prof. Hausner at Berlin University, has reviewed the revised report and recommended its acceptance by KFA. In the meantime, the latest version of the report has been sent to Dr. Tennery, ORNL, for its publication.

Inputs were received from technical leaders on the draft conclusions and recommendations. Based on these inputs, we have developed the draft statements. The set of eleven conclusions and recommendations will be reviewed by the technical leaders, and subsequently sent to participants for their input. Some of the highlights are: over half of the procedures studied have yielded excellent data; some of the procedures can be adopted by standards setting bodies or for the production of standard reference materials; and some procedures require additional effort; samples preparation prior to subjecting the sample to instrumental analysis is a key element requiring additional effort.

Future Activities: Discussions with participants in each country have been in progress to develop a follow-up to Subtask 6 program. In addition to discussions in each participating country, recently the technical leaders met with CEN Working Group 2 on powders characterization. At this meeting, detailed discussions were held with the chairman, Philippe Poirier who had just retired from Rhone Poulenc. Representatives from Belgium, France, Germany, Sweden were present at this meeting. Steve Hsu gave an overview of the IEA program, and made the distinction between pre-standardization activity and the actual standardization process. The IEA activity would survey methods, collect data, conduct inter-laboratory comparisons of data, and identify issues to be standardized. These results will then be turned over to the standards setting bodies and they would decide what to standardize. Hopefully, activities such as IEA and VAMAS would shorten the time required for reaching international consensus in the ISO process. Dr. Poirier reviewed the CEN powder activities (CEN TC184 WG2). They are working on the following items:

1. Impurities in alumina
2. Impurities in barium titanate
3. Oxygen in non-oxides (aluminum nitride)
4. Grain size distribution
5. Density
6. Compaction
7. Sintering

The general feeling in CEN was that powder characterization alone was insufficient to fully describe the ceramic powders. In order to arrive at a complete specification of the powders, one needed to develop measurement standards for compaction and sintering. Poirier described this as the ceramic aspect as distinct from the normal powder aspects. They welcomed the IEA activity and would like to readily use the IEA results. They strongly agreed that the IEA activity should feed into the standard setting bodies. They suggested that while CEN could not join the IEA activity, individual members could, and this would further facilitate the ties and make IEA more useful to them. Considerable discussions ensued about the procedural issues.

As a result of a number of discussions with the technical leaders and Subtask 6 participants, a set of two questionnaires were developed: 1. primary properties of powders; 2. secondary properties of powders. The primary properties constitute particle size distribution, phase composition by x-ray diffraction, metallic impurities, and halides. The purpose of this task is to improve intermethod data comparison and develop improved sample preparation procedures. The secondary properties constitute measurement of properties during dispersion, and slurry preparation, and evaluation of spray dried powders and green bodies. Until now 26 participants have responded to the questionnaires, which were designed to seek information from participants in terms of availability of equipment, their willingness to participate in procedure tightening and round robin study. The level of participation appears to be about the same in group 1 and 2.

The U.S. participants have more interest in group 2 and Japan's participants have expressed more interest in group 1. There is some interest, especially from Germany, to include alumina as an optional powder.

ASTM Activities: Five procedures, developed by the ASTM C-28.04 subcommittee, are being prepared to submit for subcommittee and main-committee ballot. These procedures were prepared without using IEA data or procedures. The committee expects that these procedures can serve as starting materials. At a later stage, when the IEA data become available, these draft procedures can be further improved, and the final procedures can be developed.

Status of Milestones

Milestone 411513 has been delayed to June 1993 to incorporate detailed analysis.

Publications/Presentations

Procedure Compilation report for release to the standards setting bodies.

Communications/Visits

S. M. Hsu and S. G. Malghan attended technical leaders meeting and CEN-IEA Subtask 6 technical leaders joint meeting.

Ceramic Mechanical Property Test Method Development

George D. Quinn (National Institute of Standards and Technology)

Objective/Scope

This task is to develop mechanical test method standards in support of the Ceramic Technology for Advanced Heat Engines and Advanced Turbine Technology Applications Programs. The prime DOE contractors and subcontractors will be surveyed to assess their needs and capabilities. Test method development should also consider the general USA structural ceramics community as well as foreign laboratories and companies, but emphasis will be placed on the needs on the DOE community.

Draft recommendations for practices or procedures shall be developed based upon the needs identified above and circulated within the DOE ceramics heat engine community for review and modification. Round robins will be conducted as necessary, but shall be well-focussed, limited in scope and not interfere with ongoing IEA round robins. Procedures developed in this program shall be presented as ATTAP or CTAHE "standard procedures." Alternatively, (and eventually) these will be advanced for final standardization by ASTM or by the U.S. Army as possible MIL STD's.

Technical Highlights and Results

Previous work in this project has contributed to the following completed standards:

1. ASTM C-1198-91 "Dynamic Young's Modulus, Shear Modulus, and Poisson's Ratio for Advanced Ceramics by Sonic Resonance," by S. Gonczy, G. Quinn and J. Helfinstine.
2. ASTM C-1161-90 "Standard Test Method for Flexural Strength of Advanced Ceramics at Ambient Temperature,"
3. ASTM C-1211-92 "Standard Test Method for Flexural Strength of Advanced Ceramic at Elevated Temperature," by G. Quinn in cooperation with Mr. M. Foley, Norton; Mr. T. Richerson, Allied-Signal; and Dr. M. Ferber, ORNL.
4. MIL HDBK 790 "Fractography and Characterization of Fracture Origins in Advanced Structural Ceramics," with J. Swab and M. Slavin, U. S. Army, MTL.

During this six month period, the "Standard Practice for Characterizing Fracture Origins Limiting Defects in Advanced Structural Ceramics" was completed and published by the U. S. Army MTL. This project was a collaborative undertaking with NIST and with M. Slavin and J. Swab of U. S. Army MTL. Over 200 copies were distributed, but the demand has been so great that there has been a second printing of 300 additional copies.

The MIL HDBK is intended to meet a number of needs. It presents general fractographic concepts and can help a beginner quickly learn the procedures to find fracture origins. Figure 1 shows one of the illustrations that is meant to serve this purpose. The MIL HDBK will also serve the needs of the engineering and materials science communities as well. The document gives a framework for characterizing the fracture origins once they are found as shown in Figures 2 and 3. A list of flaw definitions, Figure 4, will help materials scientists, engineers, reliability analysts, and data base analysts. Recommendations for sampling and recording information are given. The guidelines and requirements of this handbook are consistent with the standard practice for reporting strength data and Weibull analysis now under development in ASTM subcommittee C28.02.

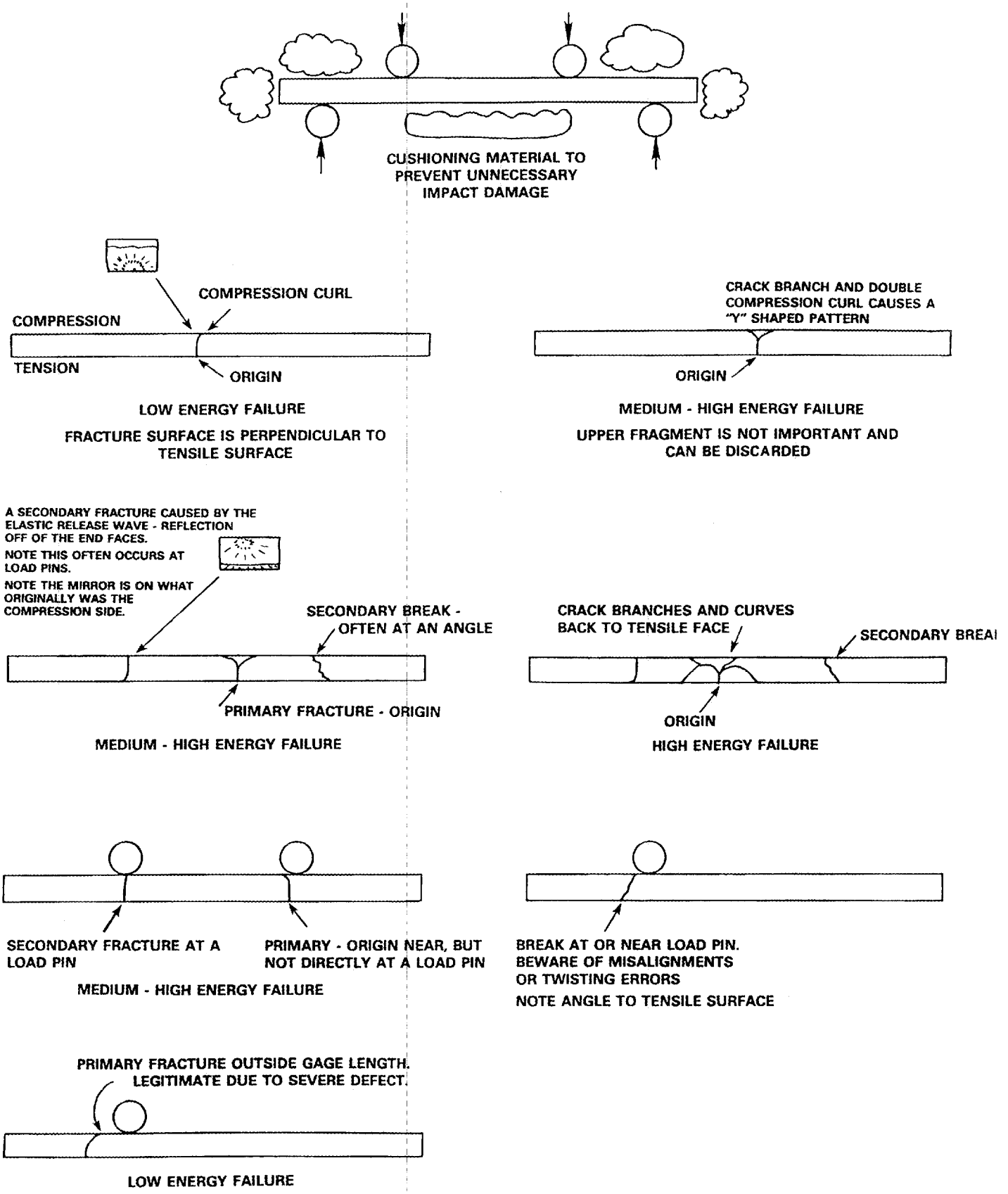

Figure 1. The fractography MIL HDBK includes schematics that will help fractographers find the primary fracture origin.

Required Flaw Characterization Scheme

1. Identity

Including the Spatial Distribution

2. Location

Volume (bulk)
Surface
Near Surface
Edge

3. Size

Optional
Diameter
Qualitative
or
Quantitative

Examples:

Specimen#	Strength (MPa)	Flaw Characterization		
		Identity	Location	Size
17	375	Pore-volume dist.	Volume	~40μm
18	420	Pore-volume dist.	Surface	~50μm
19	380	Mach. dam.-surf.	Surface	~20μm

Figure 2. The characterization scheme for fracture origins.

FLAW CHARACTERIZATION

Specimen	1. Identity	2. Location	3. Size
#17 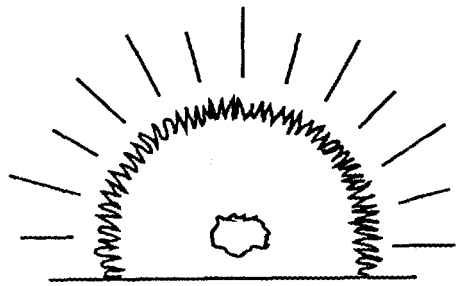	PORE VOLUME DIST.	VOLUME	~ 40 μm Diameter
#18 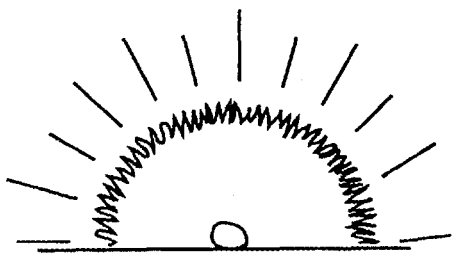	PORE VOLUME DIST.	SURFACE	~ 50 μm Diameter
#19 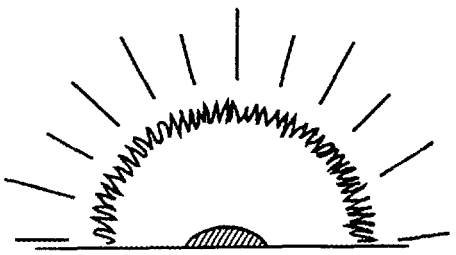	MACHINING DAMAGE SURFACE DIST.	SURFACE	~ 20 μm Deep × ~ 60 μm Long
#20 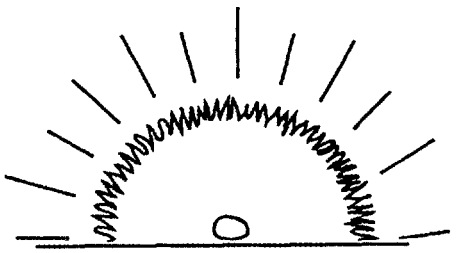	PORE VOLUME DIST.	NEAR SURFACE	~ 35μm Diameter
#21 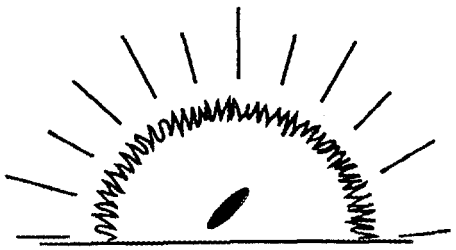	LARGE GRAIN VOLUME DIST.	VOLUME	~ 20 μm × ~ 50 μm

Figure 3. Examples of how the characterization scheme for fracture origins is applied.

Flaw	Code
3.2 **INHERENTLY VOLUME-DISTRIBUTED FLAWS.**	
3.2.1 Pore. A discrete cavity or void in a solid material.	P^V
3.2.2 Porous seam. A 2-dimensional area of porosity or microporosity.	PS^V
3.2.3 Porous region. A 3-dimensional area of porosity or microporosity.	PR^V
3.2.4 Agglomerate. A cluster of particles, or whiskers or a combination thereof, into a larger solid mass.	A^V
3.2.5 Inclusion. A foreign body from other than the normal composition enclosed in the matrix.[7]	I^V
3.2.6 Second-phase inhomogeneity. A microstructural irregularity related to the non-uniform distribution of a second phase, e.g., an atypically large pocket of a second phase or a zone of composition having a crystalline phase structure different than the matrix material.	$2P^V$
3.2.7 Large grain(s). A single (or cluster of) unusually large grain(s).	LG^V
3.2.8 Crack. A line of fracture without complete separation[7]	CK^V

Flaw	Code
3.3 **INHERENTLY SURFACE-DISTRIBUTED FLAWS.**	
3.3.1 Machining damage. Surface microcracks or damage resulting from the machining process, i.e., striations, scratches, impact cracks. (NOTE: surface and subsurface damage are intrinsic to the machining damage).	MD^S
3.3.2 Handling damage. Scratches, chips, cracks, etc., due to the handling of the specimen.	HD^S
3.3.3 Pit. A flaw created by a reaction with the environment e.g., corrosion, thermal cycling, etc.	PT^S
3.3.4 Surface void. A void which is located at the surface and is a consequence of processing, i.e., surface reaction layer, as distinguished from a volume-distributed flaw.	SV^S

Flaw	Code
3.4 **MISCELLANEOUS.**	
3.4.1 Other. A flaw specific to a material.	@
NOTE: the code used for Other types of flaws is up to the discretion of the user and should be carefully defined by the user.	
3.4.2 ?????. An uncertain or undetermined flaw.	?

Figure 4. A list of definitions of flaw types in the fractography MIL HDBK.

The first steps in introducing this document to ASTM Committee C-28 were taken in June at the Louisville meeting. At that time it was decided in C-28.02 that the flaw definitions should be referred to the Terminology subcommittee, C28.91, for a subcommittee ballot.

One of the interesting aspects of characterization of fracture origins is the need to distinguish origins that are due to abnormal microstructural features, such as gross inclusions or a large grain (exaggerated grain growth), from microstructural features that are "ordinary" or "mainstream" microstructural features. The latter are part of the ordinary microstructure of the material, but happen to be at the large end of the size distribution for such feature. The difference between these flaw types is shown in Figure 5. As ceramics become stronger and flaw management techniques more successful, then the ordinary microstructural flaw type will prevail. Of course, these will be difficult to detect on fracture surfaces against the background microstructure. Several of the materials being developed in the CTAHE program seem to have reached this state. In lieu of finding any obvious fracture origins (abnormal features) in flexure bars, engineers have often resorted to calling such origins machining damage. This is not necessarily correct.

Work continued on preparing the standard: "Reporting Uniaxial Strength Data and Estimating Weibull Distribution Parameters for Advanced Ceramics," by S. Duffy and G. Quinn. The extensive help that Curt Johnson of General Electric has contributed in the way of constructive criticism and analytical support (especially the efficiency of MLE versus LSQ) prompted the authors to list C. Johnson as a coauthor of this document.

The draft standard utilizes maximum likelihood analysis to estimate the Weibull parameters and thus is able to assign confidence bounds to the estimates. Unbiasing factors are applied to the estimate of the Weibull modulus, but there is no need to do such for the characteristic strength (since the bias is small). A specific scheme of graphically depicting the data is recommended. For the case of a single flaw population, this draft standard will be completely consistent with, and will yield identical Weibull values and confidence intervals as a formal German DIN standard: DIN 51-110 Part 3. This is an important contribution to consistency in international standardization.

The C-28 standard is also very ambitious in that it also mandates that fractography be applied to establish whether or not multiple flaw populations are present. It has been the experience of nearly all DOE participants that multiple flaw populations are the norm, not the exception. Therefore, the USA standard incorporates censored statistics to permit a proper analysis of multiple flaw populations (a procedure that the DIN standard does not include.) As a consequence, the statistical standard requires the existence of a fractography standard. The following standards are thus interrelated as shown in Figure 6.

There are some trade-offs in the C-28 statistics draft standard, however. Unbiasing factors for the estimates, and the confidence bounds for these estimates are not known for multiple flaw population problems. Unidentified origins must be treated in some fashion as well. Fractures outside "gage lengths" must be properly dealt with. It is well known, and technically accepted that fractures outside the inner span should be included in flexure strength data, *and stresses should not be corrected when using Weibull analysis.*

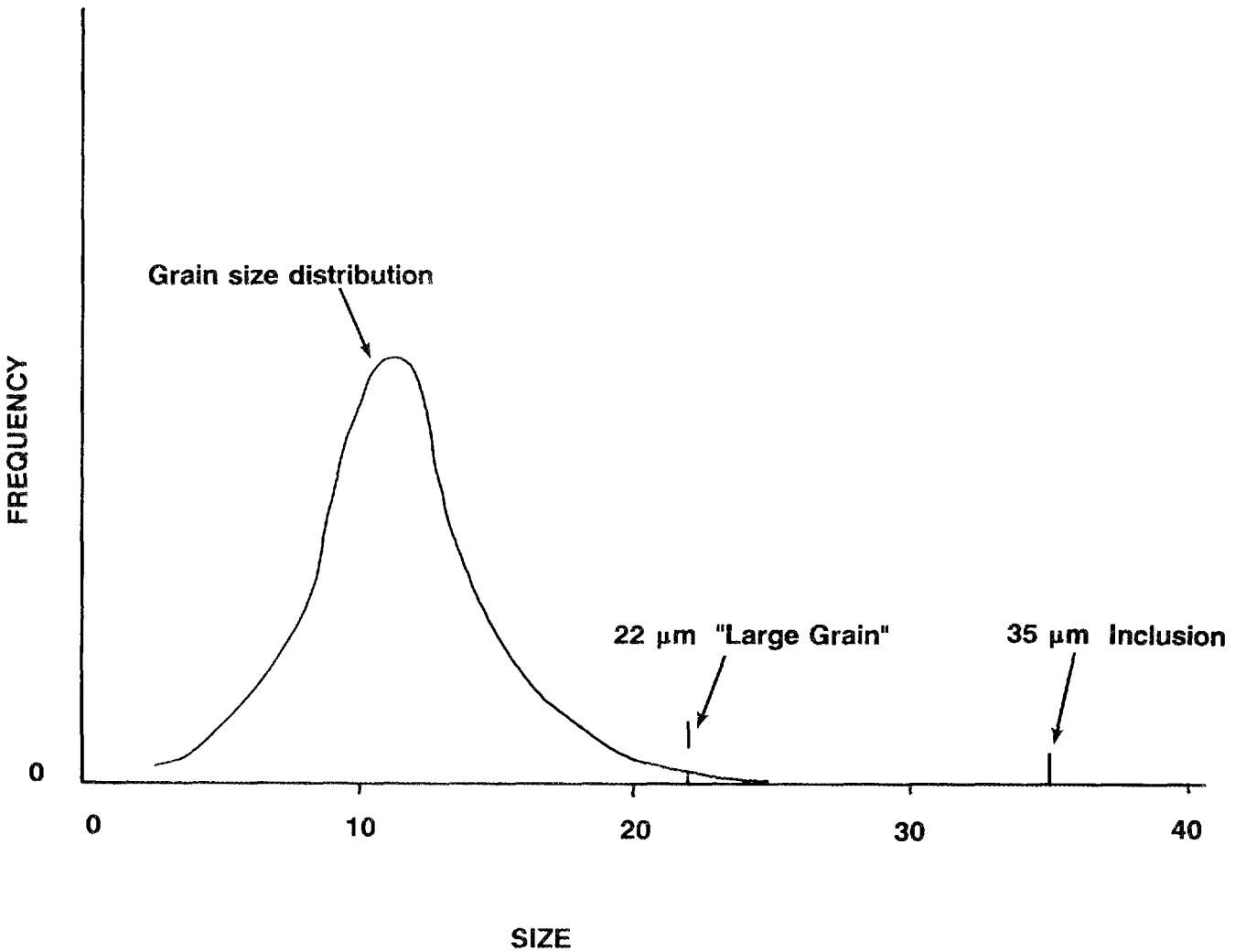

Figure 5. Mainstream or Ordinary versus Abnormal microstructural features as fracture origins. In a given material, the fracture origin in one specimen is a 22 micron, large grain. In another specimen, the origin is a 35 micron inclusion. The 35 micron inclusion is not part of the ordinary microstructure, whereas the 22 micron sized large grain is.

Draft #5 was submitted for a subcommittee C-28.02, Design and Evaluation, ballot in late March. One negative ballot and five affirmatives with comments were obtained. These were reviewed at length by S. Duffy at the C.28 meeting in Louisville in June. As a result, the following revisions were made and incorporated into draft #6 which was submitted in September for a new, concurrent C28 and C28.02 ballot. The equation for scaling strength for specimen size has been corrected to properly use either the K-factor or effective volume (surface) approaches. A revised report template was included which will help clarify when bias and confidence interval factors should be (unimodal flaw populations) and should not be used (multiple flaw population). A summary of the practice is now included. A number of words or expressions were polished up. Finally, and most importantly, the section on how to treat unidentified fracture origins was extensively rewritten and expanded into an appendix by C. Johnson and G. Quinn.

Standardization of fracture toughness testing has commenced. This is a very contentious issue since very strong preferences and opinions have developed over the years. Much of the work in recent years has focussed on fracture toughness of composites or R-curve phenomena. There is at the moment, only a small amount of actual work ongoing on optimizing or refining the measurement of fracture toughness for monolithic ceramics.

During this six month period, the final report on a VAMAS (Versailles Advanced Materials and Standards) round-robin exercise was published. Some of the results were presented in the last semiannual report for this project. The successful results for the IS and SEPB methods have spurred new initiatives to standardize these methods in ASTM. Mr. Jonathan Salem of NASA-Lewis has been appointed overall leader of this activity by Dr. C. Brinkman, the C28.01, Properties and Performance, subcommittee leader.

Work in the present task has concentrated on refinement of the controlled surface flaw method (Fig. 7) This is one of the five candidates for an ASTM fracture toughness standard. Extensive testing has indicated that a slight tilt (1/2 degree) to the indenter orientation can be extremely beneficial in causing the initial precrack to stand out clearly on a fracture surface. Superb results have been obtained on a sintered alumina, hot pressed silicon nitride, sintered silicon nitride, and sintered silicon carbide. Work continues on making this test method more user friendly, and a round-robin is planned for Oct. 1992.

An earlier VAMAS round robin revealed that there is inconsistency in measured hardness on advanced ceramics. A new initiative leading to an ASTM draft standard for microhardness has commenced. Intensive work on preparing a hardness Standard Reference Material has been underway in an internal project at NIST. Preparation of a draft hardness standard will follow.

A round-robin on quantitative microscopy was commenced in May 1992 under the auspices of VAMAS. This exercise was completed in September. The project evaluated the average grain size of unimodal and a bimodal microstructures, as well as the grain size distribution and percent porosity. This project was coordinated in the USA by NIST. The USA participants were Coors, Norton-St. Gobain, Allied-Signal, Carborundum, NASA-Lewis, U.S. Army MTL, and Alfred University.

A chapter on Standardization of Mechanical Properties Tests for Advanced Ceramics was prepared by C. Brinkman and G. Quinn for a book on mechanical properties of

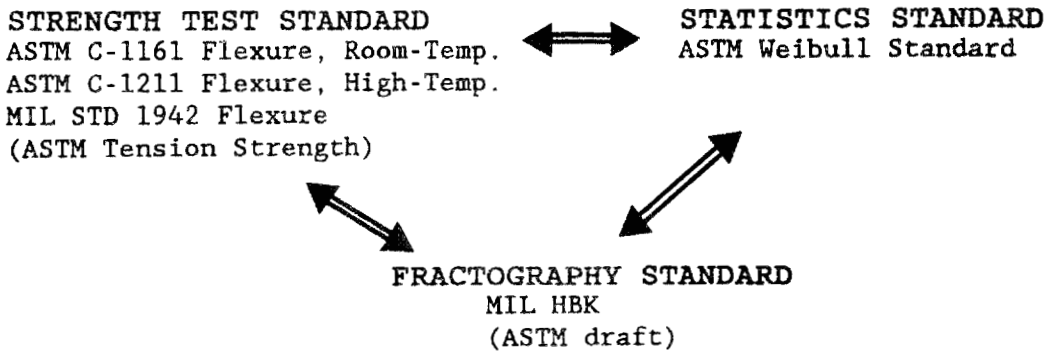

Figure 6. The strength testing standards, the fractography handbook, and the Weibull analysis standard are interrelated.

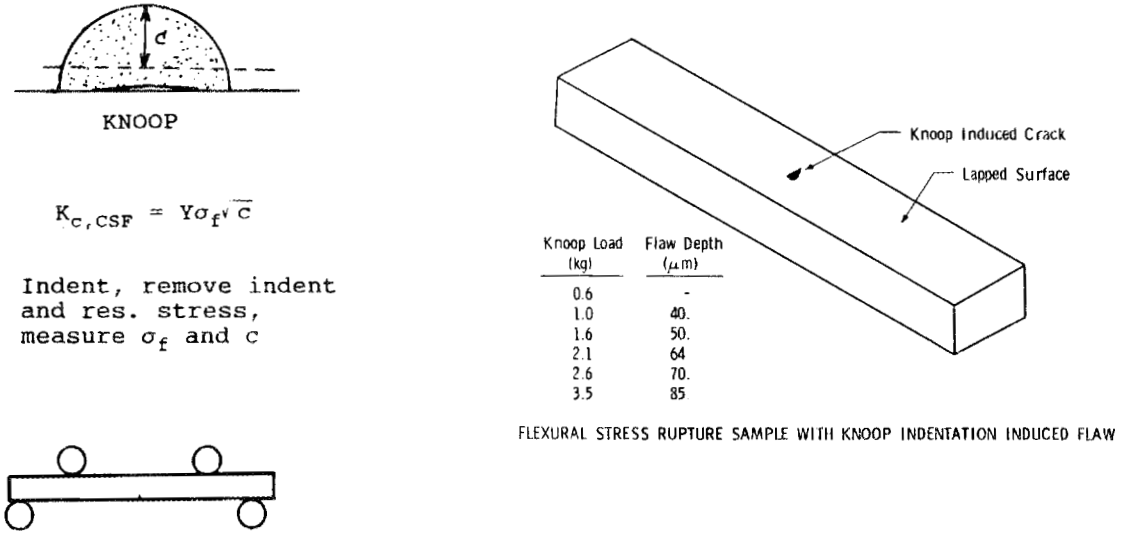

Figure 7. Schematic of the Controlled Surface Flaw (CSF) method.

ceramics being published by Marcel Dekker. A similar paper for an ASME conference in the Spring of 1993 is being written.

An overview article on the status of ASTM committee C28 was written by G. Quinn and published in the November issue of the Ceramic Bulletin.

Status of Milestones

All milestones are on schedule.

Communications/Visits/Travel

1. G. Quinn attended an ASTM E-24 meeting in Pittsburgh in May to help coordinate preparation of the fracture toughness standard.
2. S. Duffy of NASA-Lewis visited NIST to collaborate on the Weibull standard.
3. Mr. Jakob Kubler of the Swiss lab EMPA visited NIST in April to discuss the planned fracture toughness round-robin project.
4. A detailed letter from Dr. James Wimmer of Allied Signal/Garrett was received which had a number of excellent suggestions for future standards work.

Problems encountered

None, except that the controlled surface flaw method with a Knoop indenter will not work on zirconia. A modified indentation method is being studied.

Publications/Presentations

1. ASTM Standard C-1211, "Standard Test Method for Flexural Strength of Advanced Ceramics at Elevated Temperature," ASTM Annual Book of Standards, Vol. 15.01, March 1992.
2. G. Quinn, "Twisting and Friction Errors in Flexure Testing," Ceramic Engineering and Science Proceedings," July/August, (1992) pp. 319-330.
3. MIL HDBK 790, "Fractography and Characterization of Fracture Origins in Advanced Structural Ceramics," 1 July, 1992. (With M. Slavin and J. Swab)
4. G. D. Quinn, "High Temperature Flexure Fixture for Advanced Ceramics," NIST Internal Report 4864, June 1992.
5. G. D. Quinn, "Room Temperature Flexure Fixture for Advanced Ceramics," NIST Internal Report 4877, August 1992.
6. G. D. Quinn, J. Salem, I. Bar-on, K. Cho, M. Foley, and H. Fang, "Fracture Toughness of Advanced Ceramics at Room Temperature," J. Res. NIST, 97, (1992) pp. 579-607.

INTERNAL DISTRIBUTION

Central Research Library (2)
Document Reference Section
Laboratory Records Department (2)
Laboratory Records, ORNL RC
ORNL Patent Section
M&C Records Office (3)
L. F. Allard, Jr.
L. D. Armstrong
D. L. Balltrip
R. L. Beatty
P. F. Becher
T. M. Besmann
P. J. Blau
A. Bleier
E. E. Bloom
K. W. Boling
R. A. Bradley
C. R. Brinkman
V. R. Bullington
R. S. Carlsmith
P. T. Carlson
G. M. Caton
S. J. Chang
R. H. Cooper, Jr.
S. A. David
J. H. DeVan
J. L. Ding
M. K. Ferber
F. M. Foust
W. Fulkerson
R. L. Graves
D. L. Greene
H. W. Hayden, Jr.
E. E. Hoffman
C. R. Hubbard
M. A. Janney
D. R. Johnson (5)
F. W. Jones
D. Joslin
R. R. Judkins
M. A. Karnitz
B. L. Keyes
H. D. Kimrey, Jr.
T. G. Kollie
K. C. Liu
E. L. Long, Jr.
W. D. Manly
R. W. McClung
D. J. McGuire
J. R. Merriman
T. A. Nolan
A. E. Pasto
J. L. Rich
C. R. Richmond
G. L. Riner
J M Robbins
G. V. Rogers, Jr.
M. L. Santella
A. C. Schaffhauser
S. Scott
E. J. Soderstrom
D. P. Stinton
R. W. Swindeman
V. J. Tennery
T. N. Tiegs
J. R. Weir, Jr.
B. H. West
S. G. Winslow
J. M. Wyrick
C. S. Yust

EXTERNAL DISTRIBUTION

Pioneering Research Information Center
E.I. Dupont de Nemours & Co., Inc.
Experimental Station
P.O. Box 80302
Wilmington DE 19880-0302

James H. Adair
University of Florida
Materials Science & Engineering
317 MAE Bldg.
Gainesville FL 32611-2066

Donald F. Adams
University of Wyoming
Mechanical Engineering Department
P.O. Box 3295
Laramie WY 82071

Jalees Ahmad
AdTech Systems Research Inc.
Solid Mechanics
1342 N. Fairfield Road
Dayton OH 45432-2698

Yoshio Akimune
NISSAN Motor Co., Ltd.
Materials Research Laboratory
1 Natsushima-Cho
Yokosuka 237
JAPAN

Mufit Akinc
Iowa State University
322 Spedding Hall
Ames IA 50011

Ilhan A. Aksay
Princeton University
A313 Engineering Quadrangle
Princeton NJ 08544-5263

R. G. Alexander
BASE
26 Malvern Close
Kettering Northants NN16 AJP
UNITED KINGDOM

Richard L. Allor
Ford Motor Company
Materials Systems Reliability Department
P.O. Box 2053, Room S-2031
Dearborn MI 48121-2053

Joseph E. Amaral
Instron Corporation
Corporate Engineering Office
100 Royale Street
Canton MA 02021

Edward M. Anderson
Aluminum Company of America
North American Industrial Chemical Div.
P.O. Box 300
Bauxite AR 72011

Norman C. Anderson
Ceradyne, Inc.
Ceramic-to-Metal Division
3169 Redhill Avenue
Costa Mesa CA 92626

Don Anson
BCL
Thermal Power Systems
505 King Avenue
Columbus OH 43201-2693

Thomas Arbanas
G.B.C. Materials Corporation
580 Monastery Drive
Latrobe PA 15650-2698

Frank Armatis
3M Company
Building 60-1N-01
St. Paul MN 55144-1000

Everett B. Arnold
Detroit Diesel Corporation
Mechanical Systems Technology
13400 Outer Drive West
Detroit MI 48239-4001

Richard M. Arons
PA Consulting Group
279 Princeton Road
Hightstown NJ 08550

Bertil Aronsson
Sandvik AB
S-12680
Stockholm Lerkrogsvagen 19
SWEDEN

Dennis Assanis
University of Illinois
Department of Mechanical Engineering
1206 W. Green Street
Urbana IL 61801

V. S. Avva
North Carolina A&T State University
Department of Mechanical Engineering
Greensboro NC 27411

Patrick Badgley
Adiabatics, Inc.
3385 Commerce Drive
Columbus IN 47201

Sunggi Baik
Pohang Institute of Science & Technology
P.O. Box 125
Pohang 790-600
KOREA

John M. Bailey
Consultant
Caterpillar, Inc.
P.O. Box 1875
Peoria IL 61656-1875

Bob Baker
Ceradyne, Inc.
3169 Redhill Avenue
Costa Mesa CA 92626

Frank Baker
Aluminum Company of America
Alcoa Technical Center
Alcoa Center PA 15069

J. G. Baldoni
GTE Laboratories, Inc.
40 Sylvan Road
Waltham MA 02254

Clifford P. Ballard
AlliedSignal Aerospace Company
Ceramics Program
P.O. Box 1021
Morristown NJ 07962-1021

B. P. Bandyopadhyay
University of North Dakota
Mechanical Engineering Department
Grand Forks ND 58202-8359

P. M. Barnard
Ruston Gas Turbines Limited
P.O. Box 1
Lincoln LN2 5DJ
ENGLAND

Harold N. Barr
Hittman Corporation
9190 Red Branch Road
Columbia MD 21045

Renald D. Bartoe
Vesuvius McDanel
510 Ninth Avenue
Box 560
Beaver Falls PA 15010-0560

David L. Baty
Babcock & Wilcox - LRC
P.O. Box 11165
Lynchburg VA 24506-1165

Donald F. Baxter, Jr.
ASM International
Advanced Materials & Processes
Materials Park OH 44073-0002

M. Brad Beardsley
Caterpillar Inc.
Technical Center Bldg. E
P.O. Box 1875
Peoria IL 61656-1875

John C. Bell
Shell Research Limited
Thornton Research Centre
P.O. Box 1
Chester CH1 3SH
ENGLAND

Albert H. Bell, III
General Motors Technical Center
30200 Mound Road
Engineering Building/W3 Turbine
Warren MI 48090-9010

M. Bentele
Xamag, Inc.
259 Melville Avenue
Fairfield CT 06430

Larry D. Bentsen
BFGoodrich Company
R&D Center
9921 Brecksville Road
Brecksville OH 44141

Joseph C. Bentz
ENCERATEC
2525 Sandcrest Drive
Columbus IN 47203

Louis Beregszazi
Defiance Precision Products
P.O. Drawer 428
Defiance OH 43512

Tom Bernecki
Northwestern University
1801 Maple Avenue
Evanston IL 60201-3135

Charles F. Bersch
Institute for Defense Analyses
1801 N. Beauregard Street
Alexandria VA 22311

Ram Bhatt
NASA Lewis Research Center
21000 Brookpark Road
Cleveland OH 44135

Deane I. Biehler
Caterpillar Inc.
Engineering Research Materials
P.O. Box 1875, Bldg. E
Peoria IL 61656-1875

John W. Bjerklie
Consolidated Natural Gas Service Co. Inc.
Research Department
Pittsburgh PA 15222-3199

William D. Bjorndahl
TRW, Inc.
One Space Park
Building 01, Room 2040
Redondo Beach CA 90278

Keith A. Blakely
Advanced Refractory Technologies, Inc.
699 Hertel Avenue
Buffalo NY 14207

Edward G. Blanchard
Netzsch Inc.
119 Pickering Way
Exton PA 19341

Bruce Boardman
Deere and Company Technical Center
3300 River Drive
Moline IL 61265

Russell Bockstedt
Hoechst Celanese Corporation
150 JFK Parkway
Short Hills NJ 07078

M. Boehmer
DLR German Aerospace Research Estab.
Postfach 90 60 58
D-5000 Koln 90
GERMANY

Lawrence P. Boesch
EER Systems Corp.
1593 Spring Hill Road
Vienna VA 22182-2239

Donald H. Boone
Boone & Associates
2412 Cascade Drive
Walnut Creek CA 94598-4313

Tom Booth
AlliedSignal, Inc.
AiResearch Los Angeles Division
2525 West 190th Street
Torrance CA 90509-2960

Tibor Bornemisza
Sundstrand Power Systems
4400 Ruffin Road
San Diego CA 92186-5757

J.A.M. Boulet
University of Tennessee
Engineering Science and Mechanics
Knoxville TN 37996-2030

H. Kent Bowen
Massachusetts Institute of Technology
77 Massachusetts Avenue, Room E40-434
Cambridge MA 02139

Leslie J. Bowen
Materials Systems
53 Hillcrest Road
Concord MA 01742

Steven C. Boyce
Air Force Office of Scientific Research
AFOSR/NA Bldg. 410
Bolling AFB DC 20332-6448

Gary L. Boyd
Ceramic Engineering Consulting (CEC)
328 Sneath Way
Alpine CA 91901

Steve Bradley
UOP Research Center
50 E. Algonquin Road
Des Plaines IL 60017-6187

Michael C. Brands
Cummins Engine Company, Inc.
P.O. Box 3005, Mail Code 50179
Columbus IN 47201

Raymond J. Bratton
Westinghouse Science & Technology Ctr.
1310 Beulah Road
Pittsburgh PA 15235

John J. Brennan
United Technologies Corporation
Silver Lane, MS:24
East Hartford CT 06108

Jeff D. Bright
Ceramatec, Inc.
2425 South 900 West
Salt Lake City UT 84108

Terrence K. Brog
Coors Ceramics Company
4545 McIntyre Street
Golden CO 80403

Gunnar Broman
317 Fairlane Drive
Spartanburg SC 29302

Al Brown
High-Tech Materials Alert
P.O. Box 882
Dayton NJ 08810

Jesse J. Brown
VPI & SU
Center for Advanced Ceramic Materials
Blacksburg VA 24061-0256

Sherman D. Brown
University of Illinois
Materials Science and Engineering
105 South Goodwin Avenue
Urbana IL 61801

S. L. Bruner
Ceramatec, Inc.
2425 South 900 West
Salt Lake City UT 84119

Adolfo Brusaferro
Keramont Corporation
4231 S. Fremont Avenue
Tucson AZ 85714

Walter Bryzik
U.S. Army Tank Automotive Command
R&D Center, Propulsion Systems Div.
Warren MI 48397-5000

S. T. Buljan
GTE Laboratories, Inc.
40 Sylvan Road
Waltham MA 02254

S. J. Burden
2572 Devonwood
Troy MI 48098

Curt V. Burkland
AMERCOM, Inc.
8928 Fullbright Avenue
Chatsworth CA 91311

Bill Bustamante
AMERCOM, Inc.
8928 Fullbright Avenue
Chatsworth CA 91311

Oral Buyukozturk
Massachusetts Institute of Technology
77 Massachusetts Avenue, Room 1-280
Cambridge MA 02139

David A. Caillet
Ethyl Corporation
451 Florida Street
Baton Rouge La 70801

Frederick J. Calnan
Heany Industries, Inc.
249 Briarwood Lane
Scottsville NY 14546

Roger Cannon
Rutgers University
P.O. Box 909
Piscataway NJ 08855-0909

Scott Cannon
P.O. Box 567254
Atlanta GA 30356

Harry W. Carpenter
1844 Fuerte
Fallbrook CA 92028

David Carruthers
Kyocera Industrial Ceramics Company
P.O. Box 2279
Vancouver WA 98668-2279

Calvin H. Carter, Jr.
Cree Research, Inc.
2810 Meridian Parkway
Durham NC 27713

J. David Casey
35 Atlantis Street
West Roxbury MA 02132

Jere G. Castor
J. C. Enterprise
5078 N. 83rd Street
Scottsdale AZ 85250

James D. Cawley
Case Western Reserve University
Materials Science & Engineering Dept.
Cleveland OH 44106

Thomas C. Chadwick
Den-Mat Corporation
P.O. Box 1729
Santa Maria CA 93456

Ronald H. Chand
Chand Kare Technical Ceramics
2 Coppage Drive
Worcester MA 01603

Robert E. Chaney
EG&G Idaho, Inc.
Idaho National Engineering Laboratory
P.O. Box 1625
Idaho Falls ID 83415-3525

Frank C. Chang
U.S. Army Materials Technology Lab
AMTL-EMM
405 Arsenal Street
Watertown MA 02172

Robert M. Chapman
AlliedSignal Aerospace Company
1001 Pennsylvania Avenue, N.W.
Suite 700 South
Washington DC 20004

William Chapman
Williams International Corporation
2280 W. Maple Road
Walled Lake MI 48390-0200

Charlie Chen
LECO Corporation
P.O. Box 211688
Augusta GA 30917

Frank Childs
EG&G Idaho, Inc.
Idaho National Engineering Laboratory
P.O. Box 1625
Idaho Falls ID 83415-3527

William J. Chmura
Torrington Company
59 Field Street
Torrington CT 06790-4942

Tsu-Wei Chou
University of Delaware
201 Spencer Laboratory
Newark DE 19716

R. J. Christopher
Ricardo Consulting Engineers
Bridge Works
Shoreham-By-Sea West Sussex BN43 5FG
ENGLAND

Joel P. Clark
Massachusetts Institute of Technology
Room 8-409
Cambridge MA 02139

Giorgio Clarotti
Commission of the European Communities
DGXII-C3, MO75, 1-53; 200 Rue de la Loi
B-1049 Brussels
BELGIUM

W. J. Clegg
ICI Advanced Materials
P.O. Box 11
The Heath, Runcorn Cheshire WA7 4QE
ENGLAND

Joseph Cleveland
GTE Products Corporation
Hawes Street
Towanda PA 18848-0504

Gloria M. Collins
ASTM
1916 Race Street
Philadelphia PA 19103

William C. Connors
Sundstrand Aviation Operations
Materials Science & Engineering Dept.
4747 Harrison Avenue
Rockford IL 61125-7002

John A. Coppola
Carborundum Company
Niagara Falls R&D Center
P.O. Box 832
Niagara Falls NY 14302

Normand D. Corbin
Norton Company
Advanced Ceramics
Goddard Road
Northboro MA 01532-1545

Douglas Corey
AlliedSignal, Inc.
2525 West 190th Street, MS:T52
Torrance CA 90504-6099

Keith P. Costello
Chand/Kare Technical Ceramics
2 Coppage Drive
Worcester MA 01603-1252

Ed L. Courtright
Pacific Northwest Laboratory
MS:K3-59
Richland WA 99352

Anna Cox
Mitchell Market Reports
P.O. Box 23
Monmouth Gwent NP5 4YG
UNITED KINGDOM

J. Wesley Cox
BIRL
1801 Maple Avenue
Evanston IL 60201-3135

Art Cozens
Instron Corporation
3414 Snowden Avenue
Long Beach CA 90808

Robert C. Craft
American Ceramic Society, Inc.
735 Ceramic Place
Westerville OH 43081-8720

Mark Crawford
New Technology Week
4604 Monterey Drive
Annandale VA 22003

Richard A. Cree
Markets & Products, Inc.
P.O. Box 14328
Columbus OH 43214-0328

Les Crittenden
Vesuvius McDanel
Box 560
Beaver Falls PA 15010

William J. Croft
U.S. Army Materials Technology Lab
405 Arsenal Street
Watertown MA 02172

M. J. Cronin
Mechanical Technology, Inc.
968 Albany-Shaker Road
Latham NY 12110

Gary M. Crosbie
Ford Motor Company
1430 Culver Avenue
S-2079, SRL Building
Dearborn MI 48121-4036

Floyd W. Crouse, Jr.
U.S. Department of Energy
Morgantown Energy Technology Center
P.O. Box 880
Morgantown WV 26505

John Cuccio
AlliedSignal, Inc.
Auxiliary Power
P.O. Box 5227, MS:1302-2Q
Phoenix AZ 85010

Raymond A. Cutler
Ceramatec, Inc.
2425 South 900 West
Salt Lake City UT 84119

Stephen C. Danforth
Rutgers University
P.O. Box 909
Piscataway NJ 08855-0909

Sankar Das Gupta
Electrofuel Manufacturing Co., Ltd.
9 Hanna Avenue
Toronto Ontario MGK-1W8
CANADA

Charles Davis
Sverdrup Technology, Inc. MSFC
620 Discovery Drive
Huntsville AL 35806

Frank Davis
AlliedSignal Aerospace Company
7550 Lucerne Drive, #203
Middleburg Heights OH 44130

Robert F. Davis
North Carolina State University
Materials Engineering Department
P.O. Box 7907
Raleigh NC 27695

Thomas DeAngelis
Carborundum Company
Niagara Falls R&D Center
P.O. Box 832
Niagara Falls NY 14302

George DeBell
Ford Motor Company
Material Systems Reliability Dept.
P.O. Box 2053, Room S-2023
Dearborn, MI 48121-2053

Michael DeLuca
AMP-AKZO
West Lane
Aquebogue NY 11931

Gerald L. DePoorter
Colorado School of Mines
Metallurgical & Materials Engineering
Golden CO 80401

J. F. DeRidder
Omni Electro Motive, Inc.
12 Seely Hill Road
Newfield NY 14867

Nick C. Dellow
Materials Technology Publications
40 Sotheron Road
Watford Herts WD1 2QA
UNITED KINGDOM

L. R. Dharani
University of Missouri-Rolla
224 M.E.
Rolla MO 65401

Douglas A. Dickerson
Union Carbide Specialty Powders
1555 Main Street
Indianapolis IN 46224

John Dodsworth
Vesuvius Research & Development
Technical Ceramics Group
Box 560
Beaver Falls PA 15010

B. Dogan
Institut fur Werkstofforschung
GKSS-Forschungszentrum Geesthacht
Max-Planck-Strasse
D-2054 Geesthacht
GERMANY

Jean-Marie Drapier
FN Moteurs S.A.
Material and Processing
B-4041 Milmort (Herstal)
BELGIUM

Kenneth C. Dreitlein
United Technologies Research Center
Silver Lane
East Hartford CT 06108

Robin A.L. Drew
McGill University
3450 University Street
Montreal Quebec H3A 2A7
CANADA

Winston H. Duckworth
BCL
Columbus Division
505 King Avenue
Columbus OH 43201-2693

Bill Durako
Sundstrand Aviation Operations
P.O. Box 7002
Rockford IL 61125-7002

Ernest J. Duwell
3M Abrasive Systems Division
3M Center
St. Paul MN 55144-1000

Chuck J. Dziedzic
Coors Ceramics Company
17750 West 32nd Avenue
Golden CO 80401

Robert J. Eagan
Sandia National Laboratories
Engineered Materials and Processes Ctr.
P.O. Box 5800
Albuquerque NM 87185-5800

Jeffrey Eagleson
Lanxide Corporation
1001 Connecticut Avenue, N.W.
Washington DC 20036

Harry E. Eaton
United Technologies Corporation
Silver Lane
East Hartford CT 06108

Harvill C. Eaton
Louisiana State University
240 Thomas Boyd Hall
Baton Rouge LA 70803

Christopher A. Ebel
Carborundum Company
Technology Division
P.O. Box 337
Niagar Falls NY 14302

J. J. Eberhardt
U.S. Department of Energy
Office of Transportation Materials
CE-34, Forrestal Building
Washington DC 20585

Jim Edler
Eaton Corporation
26201 Northwestern Highway
P.O. Box 766
Southfield MI 48037

G. A. Eisman
Dow Chemical Company
Ceramics and Advanced Materials
52 Building
Midland MI 48667

William A. Ellingson
Argonne National Laboratory
Materials Science & Technology Div.
9700 S. Cass Avenue
Argonne IL 60439

William S. Ellis
Machined Ceramics
629 N. Graham Street
Bowling Green KY 42101

Glen B. Engle
Nuclear & Aerospace Materials Corp.
16716 Martincoit Road
Poway CA 92064

Jeff Epstein
Ceramic Technologies, Inc.
12739 Ashford Knoll
Houston TX 77082

Kenneth A. Epstein
Dow Chemical USA
800 Building
Midland MI 48667

Art Erdemir
Argonne National Laboratory
9700 S. Cass Avenue
Argonne IL 60439

E. M. Erwin
Lubrizol Corporation
1819 East 225th Street
Euclid OH 44117

Kenji Esaki
Toyota Technical Center U.S.A., Inc.
2000 Town Center, Suite 500
Southfield MI 48075

John N. Eustis
U.S. Department of Energy
Industrial Energy Efficiency Division
CE-221, Forrestal Building
Washington DC 20585

W. L. Everitt
Kyocera International, Inc.
8611 Balboa Avenue
San Diego CA 92123

Gordon Q. Evison
332 S. Michigan Avenue
Suite 1730
Chicago IL 60604

John W. Fairbanks
U.S. Department of Energy
Office of Propulsion Systems
CE-322, Forrestal Building
Washington DC 20585

Tim Fawcett
Dow Chemical Company
Advanced Ceramics Laboratory
1776 Building
Midland MI 48674

Robert W. Fawley
Sundstrand Power Systems
Division of Sundstrand Corporation
P.O. Box 85757
San Diego CA 92186-5757

John J. Fedorchak
GTE Products Corporation
Hawes Street
Towanda PA 18848-0504

Jeff T. Fenton
Vista Chemical Company
900 Threadneedle
Houston TX 77079

Larry Ferrell
Babcock & Wilcox
Old Forest Road
Lynchburg VA 24505

Raymond R. Fessler
BIRL
1801 Maple Avenue
Evanston IL 60201

Ross F. Firestone
Ross Firestone Company
188 Mary Street
Winnetka IL 60093-1520

Sharon L. Fletcher
Arthur D. Little, Inc.
15 Acorn Park
Cambridge MA 02140-2390

Thomas F. Foltz
Textron Specialty Materials
2 Industrial Avenue
Lowell MA 01851

Renee G. Ford
Materials and Processing Report
P.O. Box 72
Harrison NY 10528

John Formica
Supermaterials
2020 Lakeside Avenue
Cleveland OH 44114

Edwin Frame
Southwest Research Institute
P.O. Drawer 28510
San Antonio TX 78284

Armanet Francois
French Scientific Mission
4101 Reservoir Road, N.W.
Washington DC 20007-2176

R. G. Frank
Technology Assessment Group
10793 Bentley Pass Lane
Loveland OH 45140

David J. Franus
Forecast International
22 Commerce Road
Newtown CT 06470

Marc R. Freedman
NASA Lewis Research Center
21000 Brookpark Road, MS:49-3
Cleveland OH 44135

Douglas Freitag
LTV Missiles Division
P.O. Box 650003, MS:WT-21
Dallas TX 75265

Brian R.T. Frost
Argonne National Laboratory
9700 S. Cass Avenue, Bldg. 900
Argonne IL 60439

Lawrence R. Frost
Instron Corporation
100 Royall Street
Canton MA 02021

George A. Fryburg
Norton/TRW Ceramics
7A-4 Raymond Avenue
Salem NH 03079

Xiren Fu
Shanghai Institute of Ceramics
1295 Ding-xi Road
Shanghai 200050
CHINA

John Gahimer
P.O. Box 1302
Dublin OH 43017

J. P. Gallagher
University of Dayton Research Institute
300 College Park, JPC-250
Dayton OH 45469-0120

Garry Garvey
Golden Technologies Company Inc.
4545 McIntyre Street
Golden CO 80403

Joy A. Garwood
Norton Company
Advanced Ceramics
Goddard Road
Northboro MA 01532-1545

Richard Gates
NIST
Materials Bldg., A-256
Gaithersburg MD 20899

H. Maury Gatewood
Reynolds Metals Company
P.O. Box 27003
Richmond VA 23261

L. J. Gauckler
ETH-Zurich
Sonneggstrasse 5
CH-8092 Zurich 8092
SWITZERLAND

George E. Gazza
U.S. Army Materials Technology Lab
Ceramics Research Division
405 Arsenal Street
Watertown MA 02172-0001

D. Gerster
CEA-DCOM
33 Rue De La Federation
Paris 75015
FRANCE

John Ghinazzi
Coors Technical Ceramics Company
1100 Commerce Park Drive
Oak Ridge TN 37830

Robert Giddings
General Electric Company
P.O. Box 8
Schenectady NY 12301

A. M. Glaeser
University of California
Lawrence Berkeley Laboratory
Hearst Mining Building
Berkeley CA 94720

Joseph W. Glatz
Naval Air Propulsion Center
Systems Engineering Division
P.O. Box 7176, PE24
Trenton NJ 08628

W. M. Goldberger
Superior Graphite Company
R&D
2175 E. Broad Street
Columbus OH 43209

Allan E. Goldman
U.S. Graphite, Inc.
907 W. Outer Drive
Oak Ridge TN 37830

Stephen T. Gonczy
Allied Signal Research
P.O. Box 5016
Des Plaines IL 60017

Jeffrey M. Gonzales
GTE Products Corporation
Hawes Street
Towanda PA 18848-0504

Robert J. Gottschall
U.S. Department of Energy
ER-131, MS:G-236
Washington DC 20545

Earl Graham
Cleveland State University
Department of Chemical Engineering
Euclid Avenue at East 24th Street
Cleveland OH 44115

John W. Graham
Astro Met, Inc.
9974 Springfield Pike
Cincinnati OH 45215

William A. Graham
Lanxide Corporation
P.O. Box 6077
Newark DE 19714-6077

Robert E. Green, Jr.
Johns Hopkins University
Materials Science and Engineering
Baltimore MD 21218

Lance Groseclose
General Motors Corporation
Allison Gas Turbine Division
P.O. Box 420, MS:W-5
Indianapolis IN 46206

Thomas J. Gross
U.S. Department of Energy
Transportation Technologies
CE-30, Forrestal Building
Washington DC 20585

Mark F. Gruninger
Union Carbide Corporation
Specialty Powder Business
1555 Main Street
Indianapolis IN 46224

Ernst Gugel
Cremer Forschungsinstitut GmbH&Co.KG
Oeslauer Strasse 35
D-8633 Roedental 8633
GERMANY

Donald L. Guile
Corning Glass Works
SP-DV-1-9
Corning NY 14831

John P. Gyekenyesi
NASA Lewis Research Center
21000 Brookpark Road, MS:6-1
Cleveland OH 44135

Nabil S. Hakim
Detroit Diesel Corporation
13400 Outer Drive West
Detroit MI 48239

Philip J. Haley
General Motors Corporation
P.O. Box 420, MS:T12A
Indianapolis IN 46236

Judith Hall
Fiber Materials, Inc.
Biddeford Industrial Park
5 Morin Street
Biddeford ME 04005

Y. Hamano
Kyocera Industrial Ceramics Corp.
5713 E. Fourth Plain Blvd.
Vancouver WA 98661

Y. Harada
IIT Research Institute
10 West 35th Street
Chicago IL 60616

R. A. Harmon
25 Schalren Drive
Latham NY 12110

Norman H. Harris
Hughes Aircraft Company
P.O. Box 800520
Saugus CA 91380-0520

Alan M. Hart
Dow Chemical Company
1776 Building
Midland MI 48674

Pat E. Hart
Battelle Pacific Northwest Laboratories
Ceramics and Polymers Development Sec.
P.O. Box 999
Richland WA 99352

Stephen D. Hartline
Norton Company
Advanced Ceramics
Goddard Road
Northboro MA 01532-1545

Michael H. Haselkorn
Caterpillar In.
Technical Center, Building E
P.O. Box 1875
Peoria IL 61656-1875

N. B. Havewala
Corning Inc.
SP-PR-11
Corning NY 14831

John Haygarth
Teledyne WAA Chang Albany
P.O. Box 460
Albany OR 97321

Norman L. Hecht
University of Dayton Research Institute
300 College Park
Dayton OH 45469-0172

Peter W. Heitman
General Motors Corporation
P.O. Box 420, MS:W-5
Indianapolis IN 46206-0420

Robert W. Hendricks
VPI & SU
210 Holden Hall
Blacksburg VA 24061-0237

Wynne Henley
Hertel Cutting Technologies Inc.
1000 Clearview Court
Oak Ridge TN 37830

Thomas L. Henson
GTE Products Corporation
Chemical & Metallurgical Division
Hawes Street
Towanda PA 18848

Thomas P. Herbell
NASA Lewis Research Center
21000 Brookpark Road, MS:49-3
Cleveland OH 44135

Marlene Heroux
Rolls-Royce, Inc.
2849 Paces Ferry Road, Suite 450
Atlanta GA 30339-3769

Robert L. Hershey
Science Management Corporation
1255 New Hampshire Ave., N.W.
Suite 1033
Washington DC 20036

Hendrik Heystek
Bureau of Mines
Tuscaloosa Research Center
P.O. Box L
University AL 35486

Robert V. Hillery
GE Aircraft Engines
One Neumann Way, M.D. H85
Cincinnati OH 45215

Arthur Hindman
Instron Corporation
100 Royall Street
Canton MA 02021

Jon Hines
American Ceramic Society, Inc.
735 Ceramic Place
Westerville OH 43071-8720

Hans Erich Hintermann
CSEM
Rue Breguet 2
Neuchatel 2000
SWITZERLAND

Shinichi Hirano
Mazda R&D of North America, Inc.
1203 Woodridge Avenue
Ann Arbor MI 48105

Tommy Hiraoka
NGK Locke, Inc.
1000 Town Center
Southfield MI 48075

John M. Hobday
U.S. Department of Energy
Morgantown Energy Technology Center
P.O. Box 880
Morgantown WV 26507

Clarence Hoenig
Lawrence Livermore National Laboratory
P.O. Box 808, Mail Code L-369
Livermore CA 94550

Thomas Hollstein
Fraunhofer-Institut fur Werkstoffmechanik
Wohlerstrabe 11
D-7800 Freiburg
GERMANY

Richard Holt
National Research Council of Canada
Structures and Materials Laboratory
Ottawa Ontario K1A OR6
CANADA

Michael Horgan
Materials Engineering Magazine
1100 Superior Avenue
Cleveland OH 44114

Woodie Howe
Coors Technical Ceramics Company
1100 Commerce Park Drive
Oak Ridge TN 37830

Stephen M. Hsu
NIST
Gaithersburg MD 20899

Hann S. Huang
Argonne National Laboratory
9700 S. Cass Avenue
Argonne IL 60439-4815

Gene Huber
Precision Ferrites & Ceramics
5576 Corporate Drive
Cypress CA 90630

Harold A. Huckins
Princeton Advanced Technology, Inc.
56 Finley Road
Princeton NJ 08540

Fred R. Huettic
Advanced Magnetics Inc.
45 Corey Lane
Mendham NJ 07945

Brian K. Humphrey
Lubrizol Petroleum Chemicals Co.
3000 Town Center, Suite 1340
Southfield MI 48075-1201

Robert M. Humrick
Dylon Ceramic Technologies
3100 Edgehill Road
Cleveland Heights OH 44118

Lorretta Inglehart
National Science Foundation
Division of Materials Research
1800 "G" Street, N.W., Room 408
Washington DC 20550

Michael S. Inoue
Kyocera International, Inc.
8611 Balboa Avenue
San Diego CA 92123-1580

Osama Jadaan
University of Wisconsin-Platteville
1 University Plaza
Platteville WI 53818

Said Jahanmir
NIST
Materials Science & Engineering Lab
Gaithersburg MD 20899

Curtis A. Johnson
General Electric Company
P.O. Box 8
Schenectady NY 12301

Sylvia Johnson
SRI International
333 Ravenswood Avenue
Menlo Park CA 94025

Thomas A. Johnson
Lanxide Corporation
P.O. Box 6077
Newark DE 19714-6077

W. S. Johnson
Indiana University
One City Centre, Suite 200
Bloomington IN 47405

Walter F. Jones
Air Force Office of Scientific Research
Bolling Air Force Base
Washington DC 20332-6448

Jill E. Jonkouski
U.S. Department of Energy
9800 S. Cass Avenue
Argonne IL 60439-4899

L. A. Joo
Great Lakes Research Corporation
P.O. Box 1031
Elizabethton TN 37643

A. David Joseph
SPX Corporation
700 Terrace Point
Muskegon MI 49443

Adam Jostsons
Australian Nuclear Science & Technology
New Illawarra Road
Lucas Heightss New South Wales
AUSTRALIA

Matthew K. Juneau
Ethyl Corporation
451 Florida Street
Baton Rouge LA 70801

Hartmut Kainer
Didier-Werke AG
Anlagentechnik Wiesbaden
D-62 Wiesbaden
GERMANY

Tom Kalamasz
Norton/TRW Ceramics
7A-4 Raymond Avenue
Salem NH 03079

Lyle R. Kallenbach
Phillips Petroleum
Mail Drop:123AL
Bartlesville OK 74004

Nick Kamiya
Kyocera Industrial Ceramics Corporation
25 Northwest Point Blvd., Suite 450
Elk Grove Village IL 60007

Roy Kamo
Adiabatics, Inc.
3385 Commerce Park Drive
Columbus IN 47201

Chih-Chun Kao
Industrial Technology Research Institute
195 Chung-Hsing Road, Sec. 4
Chutung Hsinchu 31015 R.O.C.
TAIWAN

Keith R. Karasek
AlliedSignal Aerospace Company
50 E. Algonquin Road
Des Plaines IL 60017-5016

Martha R. Kass
U.S. Department of Energy
Oak Ridge Operations
Building 4500N, MS:6269
Oak Ridge TN 37831-6269

Robert E. Kassel
Ceradyne, Inc.
3169 Redhill Avenue
Costa Mesa CA 92626

Allan Katz
Wright Laboratory
Metals and Ceramics Division
Wright-Patterson AFB OH 45433

R. Nathan Katz
Worcester Polytechnic Institute
100 Institute Road
Worcester MA 01609

Tony Kaushal
Detroit Diesel Corporation
13400 Outer Drive West, Speed Code:L-04
Detroit MI 48239

Ted Kawaguchi
Tokai Carbon America, Inc.
375 Park Avenue, Suite 3802
New York NY 10152

Noritsugu Kawashima
TOSHIBA Corporation
4-1 Ukishima-Cho
Kawasaki-Ku Kawasaki 210
JAPAN

Lisa Kempfer
Penton Publishing
1100 Superior Avenue
Cleveland OH 44114-2543

Frederick L. Kennard, III
General Motors Corporation
AC Rochester, Department 32-24, EB
1300 N. Dort Highway
Flint MI 48556

David O. Kennedy
Lester B. Knight Cast Metals Inc.
549 W. Randolph Street
Chicago IL 60661

George Keros
Photon Physics
3175 Penobscot Building
Detroit MI 48226

Pramod K. Khandelwal
General Motors Corporation
Allison Gas Turbine Division
P.O. Box 420, MS:W05
Indianapolis IN 46206

Jim R. Kidwell
AlliedSignal, Inc.
Auxiliary Power
P.O. Box 5227
Phoenix AZ 85010

Shin Kim
Korea Institute of Machinery & Metals
66 Sangnam-dong, Changwon
Kyungnam 641-010
KOREA

W. C. King
Mack Truck, Z-41
1999 Pennsylvania Avenue
Hagerstown MD 21740

Carol Kirkpatrick
MSE, Inc.
P.O. Box 3767
Butte MT 59702

Tony Kirn
Caterpillar Inc.
Defense Products Department, JB7
Peoria IL 61629

James D. Kiser
NASA Lewis Research Center
21000 Brookpark Road, MS:49-3
Cleveland OH 44135

Max Klein
900 24th Street, N.W., Unit G
Washington DC 20037

Richard N. Kleiner
Coors Ceramics Company
4545 McIntyre Street
Golden CO 80403

Stanley J. Klima
NASA Lewis Research Center
21000 Brookpark Road, MS:6-1
Cleveland OH 44135

Chris E. Knapp
Norton Advanced Ceramics of Canada Ltd.
8001 Daly Street
Niagara Falls Ontario L2G 6S2
CANADA

Albert S. Kobayashi
University of Washington
Mechanical Engineering Department
Mail Stop:FU10
Seattle WA 98195

Shigeki Kobayashi
Toyota Central Research Labs, Inc.
Nagakute Aichi 480-11
JAPAN

Richard A. Kole
Z-Tech Corporation
8 Dow Road
Bow NH 03304

E. Kostiner
University of Connecticut
Chemistry Department, U-60
Storrs CT 06269-3060

Joseph A. Kovach
Eaton Corporation
32500 Chardon Road
Willoughby Hills OH 44094

Kenneth A. Kovaly
Technical Insights Inc.
P.O. Box 1304
Fort Lee NJ 07024-9967

Ralph G. Kraft
Spraying Systems Company
North Avenue at Schmale Road
Wheaton IL 60189-7900

Arthur Kranish
Trends Publishing Inc.
1079 National Press Building
Washington DC 20045

A. S. Krieger
Radiation Science, Inc.
P.O. Box 293
Belmont MA 02178

Pieter Krijgsman
Ceramic Design International Holding B.V.
P.O. Box 68
Hattem 8050-AB
THE NETHERLANDS

Waltraud M. Kriven
University of Illinois
105 S. Goodwin Avenue
Urbana IL 61801

Edward J. Kubel, Jr.
ASM International
Advanced Materials & Processes
Materials Park OH 44073

Dave Kupperman
Argonne National Laboratory
9700 S. Cass Avenue
Argonne IL 60439

Oh-Hun Kwon
North Company
Advanced Ceramics
Goddard Road
Northboro MA 01532-1545

W. J. Lackey
GTRI
Materials Science and Tech. Lab
Atlanta GA 30332

Jai Lala
Tenmat Ltd.
40 Somers Road
Rugby Warwickshire CV22 7DH
ENGLAND

Hari S. Lamba
General Motors Corporation
9301 West 55th Street
LaGrange IL 60525

Richard L. Landingham
Lawrence Livermore National Laboratory
P.O. Box 808, L-369
Livermore CA 94550

Charles J. Landry
Chand Kare Technical Ceramics
712 Flat Hill Road
Lumenburg MA 01462

James Lankford
Southwest Research Institute
6220 Culebra Road
San Antonio TX 78228-0510

Stanley B. Lasday
Business News Publishing Co.
1910 Cochran Road, Suite 630
Pittsburgh PA 15220

Mark S. Laser
Solar Turbines, Inc
2211 Erie Street
San Diego CA 92110

S. K. Lau
Carborundum Company
Technology Division
P.O. Box 832, B-100
Niagara Falls NY 14302

Edward A. Lauder
Advanced Composite Materials Corporation
1525 S. Buncombe Road
Greer SC 29651-9208

J. Lawrence Lauderdale
Babcock & Wilcox
1850 "K" Street, Suite 950
Washington DC 20006

Jean F. LeCostaouec
Textron Specialty Materials
2 Industrial Avenue
Lowell MA 01851

Benson P. Lee
Interscience, Inc.
9718 Lake Shore Boulevard
Cleveland OH 44108

Burtrand I. Lee
Clemson University
Olin Hall
Clemson SC 29634-0907

June-Gunn Lee
KIST
P.O. Box 131, Cheong-Ryang
Seoul 130-650
KOREA

Ran-Rong Lee
Ceramics Process Systems Corporation
155 Fortune Boulevard
Mildford MA 01757

Stan Levine
NASA Lewis Research Center
21000 Brookpark Road, MS:49-3
Cleveland OH 44135

Alan V. Levy
Lawrence Berkeley Laboratory
One Cyclotron Road, MS:62-203
Berkeley CA 94720

Ai-Kang Li
Materials Research Laboratories, ITRI
195-5 Chung-Hsing Road, Sec. 4
Chutung Hsinchu 31015 R.O.C.
TAIWAN

Winston W. Liang
Hong Kong Industrial Technology Centre
78 Tat Chee Avenue
4/F, HKPC Building -- Kowloon
HONG KONG

Robert Licht
Norton Company
Advanced Ceramics
Goddard Road
Northboro MA 01532-1545

E. Lilley
Norton Company
Advanced Ceramics
Goddard Road
Northboro MA 01532-1545

Laura J. Lindberg
AlliedSignal Aerospace Company
Garrett Fluid Systems Division
P.O. Box 22200
Tempe AZ 85284-2200

Leonard C. Lindgren
General Motors Coporation
Allison Gas Turbine Division
P.O. Box 420, Speed Code:T-20A
Indianapolis IN 46206-0420

Hans A. Lindner
Cremer Forschungsinstitut GmbH&Co.KG
Oeslauer Strasse 35
D-8633 Rodental 8866
GERMANY

Ronald E. Loehman
Sandia National Laboratories
Chemistry & Ceramics Department 1840
P.O. Box 5800
Albuquerque NM 87185

Jeffrey C. Logas
Winona State University
115 Pasteur Hall
Winona MN 55987

Bill Long
Babcock & Wilcox
P.O. Box 11165
Lynchburg VA 24506

William D. Long
Wacker Chemicals (USA), Inc.
ESK Engineered Ceramics
50 Locust Avenue
New Canaan CT 06840

L. A. Lott
EG&G Idaho, Inc.
Idaho National Engineering Laboratory
P.O. Box 1625
Idaho Falls ID 83415-2209

Raouf O. Loutfy
MER Corporation
7960 S. Kolb Road
Tucson AZ 85706

Gordon R. Love
Aluminum Company of America
Alcoa Technical Center
Alcoa Center PA 15960

Lydia Luckevich
Ortech International
2395 Speakman Drive
Mississauga Ontario L5K 1B3
CANADA

James W. MacBeth
Carborundum Company
Structural Ceramics Division
P.O. Box 1054
Niagara Falls NY 14302

H. MacLaren
General Electric Company
1000 Western Avenue
Lynn MA 01910

George Maczura
Aluminum Company of America
3450 Park Lane Drive
Pittsburgh PA 15275-1119

David Maginnis
Tinker AFB
OC-ALC/LIIRE
Tinker AFB OK 73145-5989

Frank Maginnis
Aspen Research, Inc.
220 Industrial Boulevard
Moore OK 73160

Tai-il Mah
Universal Energy Systems, Inc.
4401 Dayton-Xenia Road
Dayton OH 45432

Kenneth M. Maillar
Barbour Stockwell Company
83 Linskey Way
Cambridge MA 02142

Lorenzo Majno
Instron Corporation
100 Royall Street
Canton MA 02021

S. G. Malghan
NIST
I-270 & Clopper Road
Gaithersburg MD 20899

Lars Malmrup
United Turbine AB
Box 13027
Malmo S-200 44
SWEDEN

John Mangels
Ceradyne, Inc.
3169 Redhill Avenue
Costa Mesa CA 92626

Murli Manghnani
University of Hawaii
2525 Correa Road
Honolulu HI 96822

Russell V. Mann
Matec Applied Sciences, Inc.
75 South Street
Hopkinton MA 01748

William R. Manning
Champion Aviation Products Division
P.O. Box 686
Liberty SC 29657

Ken Marnoch
Amercom, Inc.
8928 Fullbright Avenue
Chatsworth CA 91311

Robert A. Marra
Aluminum Company of America
Alcoa Technical Center
Alcoa Center PA 15069

Chauncey L. Martin
3M Company
3M Center, Building 60-1N-01
St. Paul MN 55144

Steve C. Martin
Advanced Refractory Technologies, Inc.
699 Hertel Avenue
Buffalo NY 14207

Kelly J. Mather
William International Corporation
2280 W. Maple Road
Walled Lake MI 48088

James P. Mathers
3M Company
3M Center, Bldg. 201-3N-06
St. Paul MN 55144

Ron Mayville
Arthur D. Little, Inc.
15-163 Acorn Park
Cambridge MA 02140

F. N. Mazadarany
General Electric Company
Bldg. K-1, Room MB-159
P.O. Box 8
Schenectady NY 12301

James W. McCauley
Alfred University
Binns-Merrill Hall
Alfred NY 14802

Louis R. McCreight
2763 San Ramon Drive
Rancho Palos Verdes CA 90274

Colin F. McDonald
McDonald Thermal Engineering
1730 Castellana Road
La Jolla CA 92037

B. J. McEntire
Norton Company
TRW Ceramics
Goddard Road
Northboro MA 01532-1545

Chuck McFadden
Coors Ceramics Company
600 9th Street
Golden CO 80401

Thomas D. McGee
Iowa State University
110 Engineering Annex
Ames IA 50011

Carol McGill
Corning Inc.
Sullivan Park, FR-02-08
Corning NY 14831

T. C. McLaren
Cameron Forged Products Company
P.O. Box 1212
Houston TX 77251-1212

James McLaughlin
Sundstrand Power Systems
4400 Ruffin Road
P.O. Box 85757
San Diego CA 92186-5757

Matt McMonigle
U.S. Department of Energy
Improved Energy Productivity Division
CE-231, Forrestal Building
Washington DC 20585

J. C. McVickers
AlliedSignal, Inc.
Auxiliary Power, Bldg. 1303-206
P.O. Box 5227, MS:9317-2
Phoenix AZ 85010

D. B. Meadowcroft
"Jura," The Ridgeway
Oxshott
Leatherhead Surrey KT22 OLG
UNITED KINGDOM

Joseph J. Meindl
Reynolds International, Inc.
6603 W. Broad Street
P.O. Box 27002
Richmond VA 23261-7003

Michael D. Meiser
AlliedSignal, Inc.
Ceramic Components
P.O. Box 2960, MS:T21
Torrance CA 90509-2960

George Messenger
National Research Council of Canada
Building M-7
Ottawa Ontario K1A OR6
CANADA

D. Messier
U.S. Army Materials Technology Lab
SLCMT-EMC
405 Arsenal Street
Watertown MA 02172-0001

Arthur G. Metcalfe
Arthur G. Metcalfe and Associates, Inc.
2108 East 24th Street
National City CA 91950

R. Metselaar
Eindhoven University
P.O. Box 513
Endhoven 5600 MB
THE NETHERLANDS

David J. Michael
Harbison-Walker Refractories Company
P.O. Box 98037
Pittsburgh PA 15227

Ken Michaels
Chrysler Motors Corporation
P.O. Box 1118, CIMS:418-17-09
Detroit MI 48288

Bernd Michel
Institute of Mechanics
P.O. Box 408
D-9010 Chemnitz
GERMANY

David E. Miles
Commission of the European Communities
rue de la Loi, 200
B-1049 Brussels
BELGIUM

Carl E. Miller
AC Rochester
1300 N. Dort Highway, MS:32-31
Flint MI 48556

Charles W. Miller, Jr.
Centorr Furnaces/Vacuum Industries
542 Amherst Street
Nashua NH 03063

R. Minimmi
Enichem America
2000 Cornwall Road
Monmouth Junction NJ 08852

Michele V. Mitchell
AlliedSignal, Inc.
Ceramic Components
P.O. Box 2960, MS:T21
Torrance CA 90509-2960

Howard Mizuhara
WESGO
477 Harbor Boulevard
Belmont CA 94002

Helen Moeller
Babcock & Wilcox
P.O. Box 11165
Lynchburg VA 24506-1165

Francois R. Mollard
Concurrent Technologies Corporation
1450 Scalp Avenue
Johnstown PA 15904-3374

Phil Mooney
Panametrics
221 Crescent Street
Waltham MA 02254

Geoffrey P. Morris
3M Company
3M Traffic Control Materials Division
Bldg. 209-BW-10, 3M Center
St. Paul MN 55144-1000

Jay A. Morrison
Rolls-Royce, Inc.
2849 Paces Ferry Road, Suite 450
Atlanta GA 30339-3769

Joel P. Moskowitz
Ceradyne, Inc.
3169 Redhill Avenue
Costa Mesa CA 92626

Brij Moudgil
University of Florida
Material Science & Engineering
Gainesville FL 32611

Christoph J. Mueller
Sprechsaal Publishing Group
P.O. Box 2962, Mauer 2
D-8630 Coburg
GERMANY

Thomas W. Mullan
Vapor Technologies Inc.
345 Route 17 South
Upper Saddle River NJ 07458

M. K. Murthy
MkM Consultants International
10 Avoca Avenue, Unit 1906
Toronto Onntario M4T 2B7
CANADA

David L. Mustoe
Custom Technical Ceramics
8041 West I-70 Service Road, Unit 6
Arvada CO 80002

Curtis V. Nakaishi
U.S. Department of Energy
Morgantown Energy Technology Center
P.O. Box 880
Morgantown WV 26507-0880

Yoshio Nakamura
Faicera Research Institute
3-11-12 Misono
Sagamihara, Tokyo
JAPAN

K. S. Narasimhan
Hoeganaes Corporation
River Road
Riverton NJ 08077

Samuel Natansohn
GTE Laboratories, Inc.
40 Sylvan Road
Waltham MA 02254

Robert Naum
Applied Resources, Inc.
P.O. Box 241
Pittsford NY 14534

Malcolm Naylor
Cummins Engine Company, Inc.
P.O. Box 3005, Mail Code 50183
Columbus IN 47202-3005

Jeffrey T. Neil
GTE Laboratories, Inc.
40 Sylvan Road
Waltham MA 02254

Fred A. Nichols
Argonne National Laboratory
9700 S. Cass Avenue
Argonne IL 60439

H. Nickel
Forschungszentrum Juelich (KFA)
P.O. Box 1913
Juelich 1-5170 BRD NRW
GERMANY

Dale E. Niesz
Rutgers University
Center for Ceramic Research
P.O. Box 909
Piscataway NJ 08855-0909

David M. Nissley
United Technologies Corporation
Pratt & Whitney Aircraft
400 Main Street, MS:163-10
East Hartford CT 06108

Bruce E. Novich
Ceramics Process Systems Corporation
155 Fortune Boulevard
Milford MA 01757

Daniel Oblas
50 Meadowbrook Drive
Bedford MA 01730

Don Ohanehi
Magnetic Bearings, Inc.
1908 Sussex Road
Blacksburg VA 24060

Robert Orenstein
General Electric Company
55-112, River Road
Schenectady NY 12345

Norb Osborn
Aerodyne Dallas
151 Regal Row, Suite 120
Dallas TX 75247

Richard Palicka
Cercom, Inc.
1960 Watson Way
Vista CA 92083

Muktesh Paliwal
GTE Products Corporation
Hawes Street
Towanda PA 18848

Joseph E. Palko
General Electric Company
55-113, River Road
Schenectady NY 12345

Joseph N. Panzarino
Saint-Gobain/Norton Industrial Ceramics
Northboro Research Center
Goddard Road
Northboro MA 01532-1545

Pellegrino Papa
Corning Inc.
MP-WX-02-1
Corning NY 14831

Terry Paquet
Boride Products Inc.
2879 Aero Park Drive
Traverse City MI 49684

E. Beth Pardue
MPC
8297 Williams Ferry Road
Lenior City TN 37771

Soon C. Park
3M Company
Building 142-4N-02
P.O. Box 2963
St. Paul MN 55144

Harmut Paschke
Schott Glaswerke
Christoph-Dorner-Strasse 29
D-8300 Landshut
GERMANY

James W. Patten
Cummins Engine Company, Inc.
P.O. Box 3005, Mail Code 50183
Columbus IN 47202-3005

Robert A. Penty
Eastman Kodak Company
901 Elmgrove Road
Rochester NY 14653

Robert W. Pepper
Textron Specialty Materials
2 Industrial Avenue
Lowell MA 01851

Peter Perdue
Detroit Diesel Corporation
13400 Outer Drive West, Speed Code L-04
Detroit MI 48239-4001

Bruce Peters
Dow Chemical Company
Building 52
Midland MI 48667

John J. Petrovic
Los Alamos National Laboratory
Group MST-4, MS:G771
Los Alamos NM 87545

Frederick S. Pettit
University of Pittsburgh
Pittsburgh PA 15261

Ben A. Phillips
Phillips Engineering Company
721 Pleasant Street
St. Joseph MI 49085

Richard C. Phoenix
Ohmtek, Inc.
2160 Liberty Drive
Niagara Falls NY 14302

Bruce J. Pletka
Michigan Technological University
Metallurgical & Materials Engineering
Houghton MI 49931

John P. Pollinger
AlliedSignal, Inc.
Ceramic Components
P.O. Box 2960, MS:T21
Torrance CA 90509-2960

P. Popper
High Tech Ceramics International Journal
22 Pembroke Drive - Westlands
Newcastle-under-Lyme Staffs ST5 2JN
ENGLAND

F. Porz
Universitat Karlsruhe
Institut fur Keramik Im Maschinendau
Postfach 6980
D-7500 Karlsruhe
GERMANY

Harry L. Potma
Royal Netherlands Embassy
Science and Technology
4200 Linnean Avenue, N.W.
Washington DC 20008

Bob R. Powell
General Motors Research Laboratories
Metallurgy Department
Box 9055
Warren MI 48090-9055

Stephen C. Pred
ICD Group, Inc.
1100 Valley Brook Avenue
Lyndhurst NJ 07071

Karl M. Prewo
United Technologies Research Center
411 Silver Lane, MS:24
East Hartford CT 06108

Peter E. Price
Industrial Materials Technology, Inc.
P.O. Box 9565
Andover MA 01810

Joseph M. Proud
GTE Laboratories, Inc.
40 Sylvan Road
Waltham MA 02254

Vimal K. Pujari
Norton Company
Advanced Ceramics
Goddard Road
Northboro MA 01532-1545

George Quinn
NIST
Ceramics Division, Bldg. 223
Gaithersburg MD 20899

Ramas V. Raman
Ceracon, Inc.
1101 N. Market Boulevard, Suite 9
Sacramento CA 95834

Charles F. Rapp
Owens Corning Fiberglass
2790 Columbus Road
Granville OH 43023-1200

Dennis W. Readey
Colorado School of Mines
Metallurgy and Materials Engineering
Golden CO 80401

Wilfred J. Rebello
PAR Enterprises, Inc.
12601 Clifton Hunt Lane
Clifton VA 22024

Harold Rechter
Chicago Fire Brick Company
7531 S. Ashland Avenue
Chicago IL 60620

Robert R. Reeber
U.S. Army Research Office
P.O. Box 12211
Research Triangle Park NC 27709

K. L. Reifsnider
VPI & SU
Engineering Science and Mechanics
Blacksburg VA 24061

Paul E. Rempes
McDonnell Douglass Aircraft Company
P.O. Box 516, Mail Code:0642263
St. Louis MO 63166-0516

Gopal S. Revankar
John Deere Company
3300 River Drive
Moline IL 61265

K. Y. Rhee
Rutgers University
P.O. Box 909
Piscataway NJ 08854

James Rhodes
Advanced Composite Materials Corporation
1525 S. Buncombe Road
Greer SC 29651

Roy W. Rice
W. R. Grace and Company
7379 Route 32
Columbia MD 21044

David W. Richerson
2093 E. Delmont Drive
Salt Lake City UT 84117

Tomas Richter
J. H. France Refractories
1944 Clarence Road
Snow Shoe PA 16874

Michel Rigaud
Ecole Polytechnique
Campus Universite De Montreal
P.O. Box 6079, Station A
Montreal, P.Q. Quebec H3C 3A7
CANADA

Barry Ringstrom
Superior Graphite Company
P.O. Box 2373
Smyrna GA 30081

John E. Ritter
University of Massachusetts
Mechanical Engineering Department
Amherst MA 01003

Frank L. Roberge
AlliedSignal, Inc.
Auxiliary Power
P.O. Box 5227
Phoenix AZ 85010

W. Eric Roberts
Advanced Ceramic Technology, Inc.
990 "F" Enterprise Street
Orange CA 92667

Y. G. Roman
TNO TPD Keramick
P.O. Box 595
Einhoven 5600 AN
HOLLAND

Michael Rossetti
Arthur D. Little, Inc.
15 Acorn Park
Cambridge MA 01240

Barry Rossing
Lanxide Corporation
P.O. Box 6077
Newark DE 19714-6077

Steven L. Rotz
Lubrizol Corporation
29400 Lakeland Boulevard
Wickliffe OH 44092

Bruce Rubinger
Global Competitiveness, Inc.
One Devonshire Place, Suite 1011
Boston MA 02109

Robert Ruh
Wright Laboratory
WL/MLLM
Wright-Patterson AFB OH 45433

Robert J. Russell
17 Highgate Road
Framingham MA 01701

L. William Sahley
Supermaterials Company
24400 Highland Road
Richmond Heights OH 44143

Jon A. Salem
NASA Lewis Research Center
21000 Brookpark Road
Cleveland OH 44135

W. A. Sanders
NASA Lewis Research Center
21000 Brookpark Road, MS:49-3
Cleveland OH 44135

J. Sankar
North Carolina A&T State University
Department of Mechanical Engineering
Greensboro NC 27406

Yasushi Sato
NGK Spark Plugs (U.S.A.), Inc.
1200 Business Center Drive, Suite 300
Mt. Prospect IL 60056

Ashok Saxena
GTRI
Materials Engineering
Atlanta GA 30332-0245

David W. Scanlon
Instron Corporation
100 Royall Street
Canton MA 02021

Charles A. Schacht
Schacht Consulting Services
12 Holland Road
Pittsburgh PA 15235

James Schienle
AlliedSignal, Inc.
Auxiliary Power
P.O. Box 5227, MS:1302-2P
Phoenix AZ 85010

John C. Schneider
San Juan Technologies
P.O. Box 49326
Colorado Springs CO 80949-9326

Gary Schnittgrund
Rocketdyne, BA05
6633 Canoga Avenue
Canoga Park CA 91303

Mark Schomp
Lonza, Inc.
17-17 Route 208
Fair Lann NJ 07410

Joop Schoonman
Delft University of Technology
P.O. Box 5045
2600 GA Delft
THE NETHERLANDS

John Schuldies
Industrial Ceramic Technology, Inc.
30 Orchard Way, North
Potomac MD 20854

Robert B. Schulz
U.S. Department of Energy
Office of Transportation Materials
CE-34, Forrestal Building
Washington DC 20585

Murray A. Schwartz
Materials Technology Consulting Inc.
30 Orchard Way, North
Potomac MD 20854

Peter Schwarzkopf
SRI International
333 Ravenswood Avenue
Menlo Park CA 94025

William T. Schwessinger
Multi-Arc Scientific Coatings
1064 Chicago Road
Troy MI 48083-4297

W. D. Scott
University of Washington
Materials Science Department
Mail Stop:FB10
Seattle WA 98195

Nancy Scoville
Thermo Electron Technologies
P.O. Box 9046
Waltham MA 02254-9046

Thomas M. Sebestyen
U.S. Department of Energy
Advanced Propulsion Division
CE-322, Forrestal Building
Washington DC 20585

Brian Seegmiller
Coors Ceramics Company
600 9th Street
Golden CO 80401

T. B. Selover
AICRE/DIPPR
3575 Traver Road
Shaker Heights OH 44122

J. H. Selverian
GTE Laboratories, Inc.
40 Sylvan Road
Waltham MA 02254

Charles E. Semler
Semler Materials Services
4160 Mumford Court
Columbus OH 43220

Thomas Service
Service Engineering Laboratory
324 Wells Street
Greenfield MA 01301

Kish Seth
Ethyl Corporation
P.O. Box 341
Baton Rouge LA 70821

Karleen Seybold
AlliedSignal, Inc.
Auxiliary Power
P.O. Box 5227
Phoenix AZ 85010

William J. Shack
Argonne National Laboratory
9700 S. Cass Avenue, Bldg. 212
Argonne IL 60439

Peter T.B. Shaffer
Technical Ceramics Laboratories, Inc.
4045 Nine/McFarland Drive
Alpharetta GA 30201

Richard K. Shaltens
NASA Lewis Research Center
21000 Brookpark Road, MS:302-2
Cleveland OH 44135

Robert S. Shane
1904 NW 22nd Street
Stuart FL 34994-9270

Ravi Shankar
Chromalloy
Research and Technology Division
Blaisdell Road
Orangeburg NY 10962

Terence Sheehan
Alpex Wheel Company
727 Berkley Street
New Milford NJ 07646

Dinesh K. Shetty
University of Utah
Materials Science and Engineering
Salt Lake City UT 84112

Masahide Shimizu
Ceramic Society of Japan
2-2-503 Takiyama 6-chome
Higashikurume-Shi Tokyo 203
JAPAN

John Shipinski
Toyota Technical Center U.S.A., Inc.
Technical Research Department
2000 Town Center, Suite 500
Southfield MI 48075

Thomas Shreves
American Ceramic Society, Inc.
735 Ceramic Place
P.O. Box 6136
Westerville OH 43081-8720

Jack D. Sibold
Coors Ceramics Company
4545 McIntyre Street
Golden CO 80403

Johann Siebels
Volkswagen AG
Werkstofftechnologie
3180 Wolfsburg 1
GERMANY

George H. Siegel
Point North Associates, Inc.
P.O. Box 907
Madison NJ 07940

Richard Silberglitt
Technology Assessment and Transfer, Inc.
133 Defense Highway, #212
Annapolis MD 21401

Mary Silverberg
Norton Company
Goddard Road
Northboro MA 01532-1545

Gurpreet Singh
Department of the Navy
Code 56X31
Washington DC 20362-5101

Maurice J. Sinnott
University of Michigan
5106 IST Building
Ann Arbor MI 48109-2099

John Skildum
3M Company
3M Center
Building 224-2S-25
St. Paul MN 55144

David P. Smith
Hoskins, Rees & Smith
1910 Cochran Road
Pittsburgh PA 15220

Richard H. Smoak
Smoak & Associates
3554 Hollyslope Road
Altadena CA 91001-3923

Jay R. Smyth
AlliedSignal, Inc.
Auxiliary Power
P.O. Box 5227, MS:93-173/1303-207
Phoenix AZ 85010

Rafal A. Sobotowski
British Petroleum Company
Technical Center, Broadway
3092 Broadway Avenue
Cleveland OH 44115

A. G. Solomah
SAC International Ltd.
1445 Bonhill Road, #13
Mississauga Ontario L5T 1V3
CANADA

S. Somiya
Nishi Tokyo University
3-7-19 Seijo, Setagaya
Tokyo 157
JAPAN

Boyd W. Sorenson
DuPont Lanxide Composites
1300 Marrows Road
Newark DE 19711

Charles A. Sorrell
U.S. Department of Energy
Advanced Industrial Concepts Division
CE-232, Forrestal Building
Washington DC 20585

C. Spencer
EA Technology
Capenhurst Chester CH1 6ES
UNITED KINGDOM

Allen Spizzo
Hercules Inc.
Hercules Plaza
Wilmington DE 19894

Richard M. Spriggs
Alfred University
Center for Advanced Ceramic Technology
Alfred NY 14802

Charles Spuckler
NASA Lewis Research Center
21000 Brookpark Road, MS:5-11
Cleveland OH 44135-3191

M. Srinivasan
Material Solutions
P.O. Box 663
Grand Island NY 14702-0663

Gordon L. Starr
Cummins Engine Company, Inc.
P.O. Box 3005, Mail Code:50182
Columbus IN 47202-3005

Jim Stevenson
Windrock, Inc.
835 Innovation Drive
Knoxville TN 37932

Tom Stillwagon
AlliedSignal, Inc.
Ceramic Components
P.O. Box 2960, MS:T21
Torrance CA 90509-2960

Harold L. Stocker
General Motors Corporation
Allison Gas Turbine Division
P.O. Box 420
Indianapolis IN 46206

H. M. Stoller
TPL Inc.
3754 Hawkins, N.E.
Albuquerque NM 87109

Paul D. Stone
Dow Chemical USA
1776 "Eye" Street, N.W., Suite 575
Washington DC 20006

Roger S. Storm
Carborundum Company
Technology Division
P.O. Box 337
Niagara Falls NY 14302-0337

F. W. Stringer
Aero & Industrial Technology Ltd.
P.O. Box 46, Wood Top
Burnley Lancashire BB11 4BX
UNITED KINGDOM

Thomas N. Strom
NASA Lewis Research Center
21000 Brookpark Road, MS:86-6
Cleveland OH 44135

M. F. Stroosnijder
Institute for Advanced Materials
Joint Research Centre
21020 Ispra (VA)
ITALY

Karsten Styhr
30604 Ganado Drive
Rancho Palos Verdes CA 90274

T. S. Sudarshan
Materials Modification, Inc.
2929-P1 Eskridge Center
Fairfax VA 22031

M. J. Sundaresan
University of Miami
P.O. Box 248294
Coral Gables FL 33124

Patrick L. Sutton
U.S. Department of Energy
Office of Propulsion Systems
CE-322, Forrestal Building
Washington DC 20585

Willard H. Sutton
United Technologies Corporation
Silver Lane, MS:24
East Hartford CT 06108

Ron Sviben
100 Indel Avenue
Rancocas NJ 08073

J. J. Swab
U.S. Army Materials Technology Lab
Ceramics Research Division, SLCMT-EMC
405 Arsenal Street
Watertown MA 02172

Robert E. Swanson
Metalworking Technology, Inc.
1450 Scalp Avenue
Johnstown PA 15904

Scott L. Swartz
BCL
Metals and Ceramics
505 King Avenue
Columbus OH 43201

Steve Szaruga
Air Force Wright Aeronautical Lab
WL/MLBC
Wright-Patterson AFB OH 45433-6533

Yo Tajima
NGK Spark Plug Company
2808 Iwasaki
Komaki-shi Aichi-ken 485
JAPAN

Fred Teeter
5 Tralee Terrace
East Amherst NY 14051

Monika O. Ten Eyck
Carborundum Company
Technology Division
P.O. Box 832
Niagara Falls NY 14302

David F. Thompson
Corning Glass Works
SP-DV-02-1
Corning NY 14831

Merle L. Thorpe
Hobart Tafa Technologies, Inc.
146 Pembroke Road
Concord NH 03301

T. Y. Tien
University of Michigan
Materials Science and Engineering
Dow Building
Ann Arbor MI 48103

D. M. Tracey
Norton Company
Advanced Ceramics
Goddard Road
Northboro MA 01532-1545

Dick Trippett
General Motors Corporation
Allison Gas Turbine Division
P.O. Box 420, MS:W-16
Indianapolis IN 46206-0420

L. J. Trostel, Jr.
Box 199
Princeton MA 01541

W. T. Tucker
General Electric Company
P.O. Box 8, Bldg. K1-4C35
Schenectady NY 12301

Masanori Ueki
Nippon Steel Corporation
1618 Ida
Nakahara-Ku Kawasaki 211
JAPAN

Filippo M. Ugolini
ATA Studio
Via Degli Scipioni, 268A
ROMA, 00192
ITALY

Donald L. Vaccari
General Motors Corporation
Allison Gas Turbines
P.O. Box 420, Speed Code S49
Indianapolis IN 46206-0420

Carl F. Van Conant
Boride Products, Inc.
2879 Aero Park Drive
Traverse City MI 49684

Marcel H. Van De Voorde
Commission of the European Communities
P.O. Box 2
1755 ZG Petten
THE NETHERLANDS

O. Van Der Biest
Katholieke Universiteit Leuven
Departement Metaalkunde en Toegepaste
de Croylaan 2
B-3030 Leuven
BELGIUM

Michael Vannier
Washington University, St. Louis
510 S. Kings Highway
St. Louis MO 63110

Stan Venkatesan
Southern Coke & Coal Corporation
P.O. Box 52383
Knoxville TN 37950

V. Venkateswaran
Carborundum Company
Niagara Falls R&D Center
P.O. Box 832
Niagara Falls NY 14302

Dennis Viechnicki
U.S. Army Materials Technology Lab
405 Arsenal Street
Watertown MA 02172-0001

Ted Vojnovich
U.S. Department of Energy
Office of Energy Research, ER-42
Washington DC 20585

John D. Volt
E.I. Dupont de Nemours & Company, Inc.
P.O. Box 80262
Wilmington DE 19880

John B. Wachtman
Rutgers University
P.O. Box 909
Piscataway NJ 08855

Shigetaka Wada
Toyota Central Research Labs, Inc.
Nagakute Aichi 480-11
JAPAN

Janet Wade
AlliedSignal, Inc.
Auxiliary Power
P.O. Box 5227, MS:1303-2
Phoenix AZ 85010

Richard L. Wagner
Ceramic Technologies, Inc.
537 Turtle Creek South Drive, Suite 24D
Indianapolis IN 46227

J. Bruce Wagner, Jr.
Arizona State University
Center for Solid State Science
Tempe AZ 85287-1704

Daniel J. Wahlen
Kohler, Co.
444 Highland Drive
Kohler WI 53044

Ingrid Wahlgren
Royal Institute of Technology
Studsvik Library
S-611 82 Nykoping
SWEDEN

Ron H. Walecki
AlliedSignal, Inc.
Ceramic Components
P.O. Box 2960, MS:T21
Torrance CA 90509-2960

Michael S. Walsh
Vapor Technologies Inc.
2100 Central Avenue
Boulder CO 80301

Chien-Min Wang
Industrial Technology Research Institute
195 Chung-Hsing Road, Sec. 4
Chutung Hsinchu 31015 R.O.C.
TAIWAN

Robert M. Washburn
ASMT
11203 Colima Road
Whittier CA 90604

Gerald Q. Weaver
Carborundum Specialty Products
42 Linus Allain Avenue
Gardner MA 01440-2478

Karen E. Weber
Detroit Diesel Corporation
13400 Outer Drive West
Detroit MI 48239-4001

J. K. Weddell
DuPont Fibers
Experimental Station, E302
Wilmington DE 19880-0302

R. W. Weeks
Argonne National Laboratory
MCT-212
9700 S. Cass Avenue
Argonne IL 60439

Ludwig Weiler
ASEA Brown Boveri AG
Eppelheimer Str. 82
D-6900 Heidelberg
GERMANY

James Wessel
Dow Corning Corporation
1800 "M" Street, N.W., Suite 325 South
Washington DC 20036

Robert D. West
Therm Advanced Ceramics
P.O. Box 220
Ithaca NY 14851

Thomas J. Whalen
Ford Motor Company
26362 Harriet
Dearborn Heights MI 48127

Ian A. White
Hoeganaes Corporation
River Road
Riverton NJ 08077

Alan Whitehead
General Electric Company
1 River Road, 55-111
Schenectady NY 12345

Sheldon M. Wiederhorn
NIST
Building 223, Room A329
Gaithersburg MD 20899

John F. Wight
Alfred University
McMahon Building
Alfred NY 14802

D. S. Wilkinson
McMaster University
1280 Main Street, West
Hamilton Ontario L8S 4L7
CANADA

James C. Williams
General Electric Company
Engineering Materials Technology Labs
One Neumann Way, Mail Drop:H85
Cincinnati OH 45215-6301

Steve J. Williams
RCG Hagler Bailly, Inc.
1530 Wilson Boulevard, Suite 900
Arlington VA 22209-2406

Thomas A. Williams
National Renewable Energy Laboratory
1617 Cole Boulevard
Golden CO 80401

Craig A. Willkens
Norton Company
Advanced Ceramics
Goddard Road
Northboro MA 01532-1545

Roger R. Wills
TRW, Inc.
Valve Division
1455 East 185th Street
Cleveland OH 44110

David Gordon Wilson
Massachusetts Institute of Technology
77 Massachusetts Avenue, Room 3-455
Cambridge MA 02139

Matthew F. Winkler
Seaworthy Systems, Inc.
P.O. Box 965
Essex CT 06426

Gerhard Winter
Hermann C. Starck Berlin GmbH
P.O. Box 25 40
D-3380 Goslar 3380
GERMANY

W. L. Winterbottom
Ford Motor Company
20000 Rotunda Drive
SRL, Room E-3182
Dearborn MI 48121

William T. Wintucky
NASA Lewis Research Center
Terrestrial Propulsion Office
21000 Brookpark Road, MS:86-6
Cleveland OH 44135

David G. Wirth
Coors Ceramics Company
600 9th Street
Golden CO 80401

Thomas J. Wissing
Eaton Corporation
Engineering and Research Center
P.O. Box 766
Southfield MI 48037

James C. Withers
MER Corporation
7960 S. Kolb Road
Building F
Tucson AZ 85706

Dale E. Wittmer
Southern Illinois University
Mechanical Engineering Department
Carbondale IL 62901

Warren W. Wolf
Owens Corning Fiberglass
2790 Columbus Road, Route 16
Granville OH 43023

Egon E. Wolff
Caterpillar Inc.
Technical Center
P.O. Box 1875
Peoria IL 61656-1875

George W. Wolter
Howmet Turbine Components Corporation
Technical Center
699 Benston Road
Whitehall MI 49461

James C. Wood
NASA Lewis Research Center
21000 Brookpark Road, MS:86-6
Cleveland OH 44135

Marrill Wood
LECO Corporation
P.O. Box 211688
Augusta GA 30917-1688

Wayne L. Worrell
University of Pennsylvania
3231 Walnut Street
Philadelphia PA 19104

John F. Wosinski
Corning Inc.
ME-2 E-5 H8
Corning NY 14830

Ian G. Wright
BCL
505 King Avenue
Columbus OH 43201

Ruth Wroe
ERDC
Capenhurst Chester CH1 6ES
ENGLAND

Bernard J. Wrona
Advanced Composite Materials Corporation
1525 S. Buncombe Road
Greer SC 29651

Carl C. M. Wu
Naval Research Laboratory
Ceramic Branch, Code 6373
Washington DC 20375

John C. Wurst
University of Dayton Research Institute
300 College Park
Dayton OH 45469-0101

Neil Wyant
ARCH Development Corp.
9700 S. Cass Avenue, Bldg. 202
Argonne IL 60439

Roy Yamamoto
Texaco Inc.
P.O. Box 509
Beacon NY 12508-0509

John Yamanis
AlliedSignal Aerospace Company
P.O. Box 1021
Morristown NJ 07962-1021

Harry C. Yeh
AlliedSignal, Inc.
Ceramic Components
P.O. Box 2960, MS:T21
Torrance CA 90509-2960

Hiroshi Yokoyama
Hitachi Research Lab
4026 Kuji-Cho
Hitachi-shi Ibaraki 319-12
JAPAN

Thomas M. Yonushonis
Cummins Engine Company, Inc.
P.O. Box 3005, Mail Code 50183
Columbus IN 47202-3005

Thomas J. Yost
Corning Inc.
Technical Products Division, 21-1-2
Corning NY 14831

Jong Yung
Sundstrand Aviation Operations
4747 Harrison Avenue
Rockford IL 61125

A. L. Zadoks
Caterpillar Inc.
Technical Center, Building L
P.O. Box 1875
Peoria IL 61656-1875

Avi Zangvil
University of Illinois
104 S. Goodwin Avenue
Urbana IL 61801

Charles H. Zenuk
Transtech
1340 N. Via Ronda Oeste
Tucson AZ 85715-4830

Carl Zweben
General Electric Company
P.O. Box 8555, VFSC/V4019
Philadelphia PA 19101

Klaus M. Zwilsky
National Research Council
2101 Constitution Avenue
Washington DC 20418

Department of Energy
Oak Ridge Operations Office
Assistant Manager for Energy
Research and Development
P.O. Box 2001
Oak Ridge, TN 37831-8600

Department of Energy (10)
Office of Scientific and Technical
Information
Office of Information Services
P.O. Box 62
Oak Ridge, TN 37831

For distribution by microfiche
as shown in DOE/OSTI-4500,
Distribution Category UC-332
(Ceramics/Advanced Materials).

★U.S. GOVERNMENT PRINTING OFFICE 1993 -759 -176/80005